



<https://theses.gla.ac.uk/>

Theses Digitisation:

<https://www.gla.ac.uk/myglasgow/research/enlighten/theses/digitisation/>

This is a digitised version of the original print thesis.

Copyright and moral rights for this work are retained by the author

A copy can be downloaded for personal non-commercial research or study,
without prior permission or charge

This work cannot be reproduced or quoted extensively from without first
obtaining permission in writing from the author

The content must not be changed in any way or sold commercially in any
format or medium without the formal permission of the author

When referring to this work, full bibliographic details including the author,
title, awarding institution and date of the thesis must be given

Enlighten: Theses

<https://theses.gla.ac.uk/>
research-enlighten@glasgow.ac.uk

**A Study of the Aerodynamic and Mechanical
Interference Effects Between Two Neighbouring Square Towers**

Submitted by

WA-UN ALEXIS LEONG

for degree of Ph.D. of the

University of Glasgow

December, 1987

ProQuest Number: 10970803

All rights reserved

INFORMATION TO ALL USERS

The quality of this reproduction is dependent upon the quality of the copy submitted.

In the unlikely event that the author did not send a complete manuscript and there are missing pages, these will be noted. Also, if material had to be removed, a note will indicate the deletion.



ProQuest 10970803

Published by ProQuest LLC (2018). Copyright of the Dissertation is held by the Author.

All rights reserved.

This work is protected against unauthorized copying under Title 17, United States Code
Microform Edition © ProQuest LLC.

ProQuest LLC.
789 East Eisenhower Parkway
P.O. Box 1346
Ann Arbor, MI 48106 – 1346

To my mother
and
in memory of my father

SUMMARY

Although wind-induced vibration of tall structures has attracted much attention for some time, little is known about the behaviour of such a structure under the influence of fluid flows from structures in close proximity. The little experimental evidence already available suggests that, for certain configurations, the dynamic response of a tall structures can be drastically altered due to the presence of neighbouring structures.

The work presented in this thesis is to study and, to a certain extent, to provide a better understanding of, the effects of aerodynamic interaction between two neighbouring slender tower structures at various positions relative to each other in a series of wind tunnel model tests. Furthermore, it is of particular interest to investigate whether the mechanical interaction, which may take place between the towers through the foundation or perhaps through some other structural linkage, has any effect on the resulting response.

For simplicity reasons, only one type of model with fixed geometry and mechanical properties has been used in this study. The square-section tower model has a height to breadth ratio of 10 to 1 and is constructed with an aluminium, hollow square-section core to which are attached plywood panels to form the correct external geometry. During measurement, the model is mounted on a strain gauge dynamometer and the whole assembly resembles a continuous, elastic cantilever with low natural frequency.

In the study, wind tunnel tests were first carried out on a single tower model in both uniform smooth and turbulent flows, and measurements were then performed with a second dynamically and geometrically identical tower model at various positions relative to the other. From the measurement results, the effects of interference excitation on model forces and responses were compared and quantified.

The wind tunnel tests comprised a broad range of measurements, including:

- Torsional moment and forces acting on the tower models in both longitudinal and transverse directions.
- Translational displacements at the top of the models.
- Velocity fluctuations in the near wake.

For each configuration, the mean and fluctuating response of the models were measured over a velocity range at discrete intervals (or other variables).

Measurements were then repeated at several values of the mean wind speed. In each case, responses from all measuring instruments were sampled and stored in digital form. These data were then analysed off-line to yield results such as probability density functions, correlation functions, power spectrum density functions etc.

The results from the wind tunnel tests indicate that in all the cases being investigated, the response process of each tower is affected by the presence of the other in the flow field. The effects due to the flow interference are characterised by the continuous and discontinuous changes in vortex shedding.

In the close-spaced configurations, with the presence of mechanical interaction, the two towers could behave as a single tower and the response is markedly different from that observed in other configurations.

When the tower models are arranged one behind the other relative to the wind and the in-line distance between them is less than six times the tower's breadth, the downstream tower is effectively shielded by the upstream tower. However, significant fluctuating forces and responses are developed even in these cases. The most vigorous response occurs when the two towers are offset normal to the flow direction and the downstream tower is located at or near the boundary of the wake created by the upstream tower.

When the turbulence intensity of the free-stream is increased uniformly across the wind direction, the flow patterns around the towers are drastically changed. As a result, the response amplitudes, in both single and twin tower configurations, are stronger than those observed in uniform smooth flow.

ACKNOWLEDGEMENTS

It is a pleasure to express my appreciation to my advisor, Mr. T.H. Cain, for his guidance and assistance throughout this work.

Thanks are also given to the workshop staff who manufactured and prepared the models and instrumentation, and in particular, to Mr. A. Smedley for his friendly assistance during the wind tunnel measurements.

I also wish to express my gratitude to Mr. R. Gordon for his valuable advice in experimentation and Mrs. E. Murray-Smith for her assistance in computation.

Finally, I am also greatly indebted to Mr. B. McTaggart for lending me the badly needed B&K Charge Amplifier, and to the staff in the Department who gave me so much help.

CONTENTS

SUMMARY	i
ACKNOWLEDGEMENTS	iii
CONTENTS	iv
NOMENCLATURE	ix
CHAPTER 1: INTRODUCTION	
1.1 Background of the problems studied	1
1.2 Aims and approach of the research project	2
1.3 Thesis layout	3
CHAPTER 2: LITERATURE REVIEW	
2.1 Introduction	5
2.2 Torsional response and flutter	8
2.3 Along-wind response	10
2.4 Cross-wind response	13
2.4.1 Excitation due to incident turbulence (and buffeting)	13
2.4.2 Excitation due to wake (and vortex shedding)	14
2.5 Excitation due to cross-wind displacement	17
2.5.1 Lock-in	17
2.5.2 Galloping	18
CHAPTER 3: DESCRIPTION OF THE EXPERIMENTAL APPARATUS	
3.1 Introduction	21
3.2 The 'Handley-Page' wind tunnel	22

3.3	Production of large scale turbulence in wind tunnel	23
3.3.1	Turbulence generation grid	23
3.3.2	Properties of the wind model	24
3.4	Dynamic modelling of tall structures	27
3.4.1	Description of the aeroelastic models	29
3.4.2	Mechanical linkages	31
3.5	Measurement of unsteady wind forces	31
3.5.1	Description of the force balance column	33
3.6	Supporting structures	35
3.7	Instrumentation	35
3.7.1	Dynamic pressure measurement	35
3.7.2	Strain gauge signal conditioning	36
3.7.3	Displacement measurement	37
3.7.4	Hot-wire anemometry	38
CHAPTER 4: DATA ACQUISITION AND PROCESSING		
4.1	Introduction	42
4.2	General considerations	42
4.3	Data acquisition and control system	45
4.3.1	Analogue-to-digital converter	45
4.3.2	Real-time clock	46
4.3.3	Sample and hold unit	46
4.4	Description of software	47
4.4.1	Run control routines	49
4.4.2	Fast continuous A/D conversion routine	51

4.4.3	Data processing	53
4.4.4	Data analysis	54
4.4.5	Data presentation	57
CHAPTER 5: PRESENTATION AND DISCUSSION OF RESULTS OBTAINED FROM A SINGLE TOWER BLOCK MODEL		
5.1	Introduction	59
5.2	Mechanical response characteristic of the single model system	59
5.2.1	Experimental arrangements	60
5.2.2	The measuring procedure	61
5.2.3	Presentation of Results	62
5.2.4	Determination of natural frequency and damping	64
5.2.5	Determination of natural frequency and damping by other methods	66
5.2.6	Verification of interaction between orthogonal force components	69
5.3	Measurements of model wind loads and corresponding dynamic responses	69
5.3.1	General approach	70
5.3.2	Model forces as functions of mean wind speed and flow characteristics	71
5.3.3	Model responses as functions of mean wind speed and flow characteristics	76
5.3.4	Response characteristics of the second measuring system	78
5.3.5	Model wind loads and responses as a function of angle of incidence of the mean wind	79
5.3.6	Aerodynamic damping	81
5.3.7	Effects of free stream turbulence on the model wind loads and response	83
5.4	Measurements of the flow field in the near wake of the square tower	86

5.4.1	The wake characteristics	86
5.4.2	Variation of the Strouhal number	88
5.4.3	Cross-correlation between velocity fluctuations in the near wake and model response	89
CHAPTER 6: PRESENTATION AND DISCUSSION OF RESULTS OBTAINED FROM TWIN TOWER BLOCK MODELS		
6.1	Introduction	92
6.2	Mechanical response characteristics of the twin model system	93
6.3	Tandem arrangements	95
6.3.1	Model forces in the along-wind direction	95
6.3.2	Model forces in the cross-wind direction	99
6.3.3	Torsional response	102
6.3.4	Dynamic response in the along-wind and cross-wind directions	103
6.3.5	Oscillation loops	105
6.3.6	Orbital motion analysis	106
6.3.7	Interference mechanism (of towers in tandem arrangements)	107
6.3.8	Effects of turbulence	108
6.3.9	Effects of structurally linkage between the towers	109
6.4	Side by side arrangements	110
6.4.1	Model forces and torsional moment coefficients	111
6.4.2	Dynamic response characteristics	113
6.5	Staggered arrangements	114
6.5.1	Model forces and torsional moment coefficients	114
6.5.2	Dynamic response characteristics	117
6.5.3	Interference mechanism (of towers in staggered arrangements)	118

CHAPTER 7: CONCLUSIONS AND RECOMMENDATIONS FOR FURTHER RESEARCH

7.1 Introduction	120
7.2 Conclusions from the results observed in single tower configuration cases	121
7.3 Conclusions from the results observed in twin tower configuration cases	123
7.4 Some uncertainties associated with the apparatus used in the measurements	125
7.5 Recommendations for further research	126
REFERENCES	128
APPENDICES	
A PRINCIPLE OF THE STRAIN GAUGE BALANCE SYSTEM	143
B STATISTICAL PROPERTIES OF RANDOM DATA	145
B.1 Mean and mean square values	145
B.2 Probability density functions	146
B.3 Autocorrelation functions	146
B.4 Power spectral density functions	147
B.5 Cross-correlation functions	148
B.6 Cross-spectral density functions (and coherence functions)	148
C EFFECTS OF VARIATION IN AERODYNAMIC FORCES ON A BODY DUE TO ITS MOTIONS	151

NOMENCLATURE

SYMBOLS	DESCRIPTION
A	Area
B	Breadth of the tower model
b	Bar width
C_F	Force coefficient
C_L	Lift coefficient
C_M	Torsional moment coefficient
$C(f)$	Co-spectral density function
d	(i) Distance between the vortices (ii) Distance from the turbulence generation grid
D_x, D_y	Aerodynamic damping force
E	(i) Stiffness modulus (ii) Voltage
E_x, E_y	Coupling forces between motion directions
$E(\)$	Voltage output from a hot-wire element
F_x, F_y	Force components in the longitudinal and transverse directions respectively
$F(\)$	Function of
f	Frequency
f_s	Sampling frequency
f_v	Vortex shedding frequency
H	Height of the tower model
h	Time interval between each discrete value
I_x	Longitudinal turbulence intensity
K	Geometry constant
k	Surface drag coefficient
L_x	Longitudinal integral scale of turbulence
l	Width between the centres of vortices behind a stationary cylinder

M	Torsional moment
m	Mesh size
N	Total number of digitally recorded data values
N_B	Number of data blocks per channel
N_S	Number of data points per segment
P	Probability density function
$Q(f)$	Quad-spectral density function
$R(\tau)$	Time correlation function
S	Transfer function
$S(f)$	Power spectral density function
St	Strouhal number
T	Total sampling time
X, x	Rectangular Cartesian coordinate, along-wind or longitudinal direction
X_B	Longitudinal spacing ratio between models
Y, y	Rectangular Cartesian coordinate, cross-wind or transverse direction
Y_B	Transverse spacing ratio between models
\bar{U}	Mean flow velocity
\bar{U}_{eff}	Effective cooling velocity
u, v, w	Flow velocity in the x, y and z direction
U_r	Reduced velocity
$W(\)$	Weighing function
Z, z	Rectangular Cartesian coordinate, height

GREEK SYMBOLS

α	Angle of incidence
γ	Power law exponent
$\gamma(f)$	Coherence function
Δ	Increment
Δf	Bandwidth

δ	Logarithmic decrement of structural damping
ϵ	Error
ζ	Damping ratio
θ	Inclined angle of the hot-wire
$\Theta(f)$	Phase angle of cross-spectral density function
μ	Damping coefficient
$\mu(z)$	Deflection mode shape of a structure
π	3.1416
ρ	Density
$\rho(t)$	Autocorrelation coefficient
σ	Standard derivation
τ	Time delay

SUPERSCRIPTS

$\bar{\quad}$	Time mean value
\prime	Fluctuating component
\wedge	(i) Value at which peak response occurred (ii) Average of Peak values
\cdot	Time derivative

SUBSCRIPTS

a	Aerodynamic, e.g. ζ_a is aerodynamic damping
i	ith mode
o	Reference value, e.g. f_o is natural frequency
s	Structural, e.g. ρ_s is structural density
v	Vortex, e.g. f_v is vortex frequency
w	Wind
x,y	Rectangular Cartesian coordinates
∞	Infinity

CHAPTER ONE

INTRODUCTION

1.1 Background of the Problems Studied

Ever since the dramatic failure of the famous Tacoma Narrows Bridge, the phenomenon of wind-induced vibration of tall buildings and structures has been the subject of much research work. Nevertheless, although total failure of tall structures is rare, there have been several reported cases of permanent damage to tall buildings and structures, such as the Great Plains Life Building during the Lubbock Tornado in 1970, the fallen pylon of the Lodemann Bridge after a severe storm in 1972 [1], and many reported cases of interior walls cracked, cladding failure, structural fatigue due to repeating stress and discomfort to the occupants due to movement of a building induced by wind.

In the presence of neighbouring structures situated upstream, the existing evidence indicated that the downstream structures would experience an even stronger adverse effect; for example, the collapse of the three cooling towers in an array of eight at Ferrybridge [2]. These adverse aerodynamic interference effects have been detected in wind tunnel measurements for groups of towers [3], [4] and [5], and a pair of bridge pylons [6] and [7]. Nowadays with tall buildings (or structures) being built upstream (or downstream) of existing structures, particularly on reclaimed land, and in the advent of taller, more slender and flexible structures with less built-in stiffness and damping, it is likely that tall structures could be excited by the turbulence created by the surrounding structures. Therefore it is important for designers or engineers to be able to understand the interference effects between adjacent structures.

On the other hand, in spite of the great significance of this subject in actual practice, there are very few reported results of investigations into the interference effects between adjacent structures. The object of the present project is to explore this relatively unknown area.

The wind-induced responses of tall buildings and structures can be divided into torsional and translational motions in along-wind and cross-wind directions. The last two have been subjected to extensive research throughout the years.

There have been very few reported results on torsional motion, either in wind tunnel or in full scale measurements. This could be expected since most modern buildings and structures have high levels of torsional stiffness, so that normally such response

is insignificant and can be ignored.

Early investigations of along-wind (parallel to the mean flow direction) response of tall buildings and structures were conducted by Davenport and Vickery. They concluded that such response is due primarily to the buffeting by the incident turbulence, and, later, they introduced the concept of gust loading factor through which structural response in the along-wind direction can be calculated. Nowadays, computer programmes are available to predict the along-wind response of tall building up to a high degree of accuracy.

The cross-wind (perpendicular to the mean flow direction) response is mainly due to the action of vortices shed in the wake of the structure. The mechanism of this kind of excitation is more complex and has been extensively examined as a problem in the field of fluid mechanics and as a dynamic system. But despite of all these efforts, there is still no rigorous theory which could describe such response throughout the usual wind speed range.

When a single structure is under investigation, it is often sufficient to consider the cross-wind response only. This is because, in most cases, the wind-induced instabilities occur in the cross-wind direction and the associated response amplitude can be more than an order of magnitude greater than that relating to the along-wind direction [8].

But for the case of a structure located in the vicinity of other structures, torsional and along-wind motions induced by wake buffeting could be significant and should not be ignored [9], [10] and [11]. Furthermore, since there are suspicions that the upstream structure could be affected by the presence of the downstream structure, therefore, in the twin prismatic column system used in the present investigation, both models are instrumented so that responses in all three modes can be measured.

1.2 Aims and Approach of the Research Project

The broad aims of the research project reported in this thesis were as follows:

- (1) To acquire an understanding of the mechanism and characteristics of flow-induced oscillation of a square-section tower structure in both uniform and turbulent flows.
- (2) To measure the effects on the magnitude of responses due to the presence of a prismatic tower structure situated upstream or downstream of a similar tower and the contributions from specified variables (or parameters).

- (3) To investigate the interference effects between neighbouring towers for different configurations, and to quantify the significance of both aerodynamic and mechanical couplings.
- (4) To formulate mathematical equations which, together with the relevant data, may be able to estimate the relative magnitude of response due to wind and other effects.

Because of the complexity of the problem being considered, the number of variables was limited to the following: wind speed, flow types, orientation or incidence of the model to the mean wind, spacing ratios and arrangements between models. Only square-section towers with fixed geometry and mechanical properties were used in the wind tunnel measurements.

During the tests, the data collected comprised two components of force and a torque as measured by a strain-gauged balance column and two displacement components as measured by accelerometers placed at the top of the model towers. Consequently, the tower model-force balance column combination used in these tests resembled an elastic cantilever with three degree of freedom. For each configuration, mean and RMS values of each response were measured at discrete wind velocities. Then, for each configuration, several sets of continuous time-series response signals at chosen mean flow velocities were collected and stored on disc via a micro-computer, and these data were used for later evaluation. A detailed description of these procedures will be presented in a later section.

1.3 Thesis Layout

Chapter 2 describes the types of flow mechanism which cause the oscillation of tall buildings, with references to the literature in each individual field.

The experimental apparatus, including both mechanical and electronic components, are described in detail in Chapter 3.

Chapter 4 discusses the data acquisition system, the procedure for data processing and data analysis. Some of the software used in the study are also briefly discussed.

In Chapter 5, the response of a single tower model in either uniform smooth or uniform turbulent flow are presented. The mechanical characteristics of the measuring system and the wake characteristics behind the tower model are also discussed.

Chapter 6 contains results measured from two tower models placed at various positions relative to each other. The possible excitation mechanisms due to aerodynamic and/or mechanical interference between them are also discussed.

Chapter 7 comprises of a summary of all major conclusions and recommendations for further research.

The last section of the thesis contains a list of references and appendices containing relevant supporting materials.

CHAPTER TWO

LITERATURE REVIEW

2.1 Introduction

Before examining the mechanisms of various aerodynamic instabilities, it is instructive to examine, at least qualitatively, how flow about either a single structure or two identical prismatic structures leads to large positive or negative pressure distributions.

(a) Flow about an Isolated Prismatic Cylinder

Fig. 2.1(a) represents a prismatic structure as viewed from above with uniform flow approaching normal to its front face (i.e. $\alpha = 0$). A qualitative indication of flow lines, including separation regions, is shown. As the flow approaches the structure, it is deflected around the sharp corners and accelerated so that the high velocity fluid separates from the structure, leaving a region of low velocity fluid within the separated region [5].

The mean pressure distribution about the structure is also indicated qualitatively in Fig. 2.1(a). The largest loads occur as negative pressures (acting outward) at the upstream end of the sides, whereas positive pressure (acting inward) covers only the upwind face. Based on the results from other investigations, the maximum instantaneous positive pressure rarely exceeds 110-120% of the stagnation pressure of the approach flow, while the negative pressure can exceed three times the stagnation pressure [5]. Pressure on the rear face of the structure (base pressure) tends to be small and uniform over large areas.

If the section is rotated to a small angle with respect to the mean flow direction, a flow separation region can form on the upstream end of the windward side with reattachment occurring somewhere along the surface, as shown in Fig. 2.1(b). The qualitative mean pressure distribution, as indicated in Fig. 2.1(b), shows that the negative pressures decrease in magnitude along this side in the downstream direction and may become positive after reattachment [12]. Depending on the approaching flow angle, upwind corner geometry and surface roughness, the separation region may not be steady but may fluctuate in time--in particular when it is coupled with the body's oscillatory motions. In extreme conditions the separation region could collapse and re-establish itself alternatively. Under such oscillating conditions, the fluctuating pressure is large in magnitude and the peak pressure loading can be as high as three times the dynamic pressure.

Rockwell [13], who measured the fluctuating pressure on a square section cylinder at various incident angles, showed that the maximum pressure fluctuation due to vortex shedding occurs at $\alpha = 5$ degree and the minimum pressure fluctuation amplitude near the trailing edge of the section appears at $\alpha = 14-15$ degree--when the deflected shear layer has just reattached to the side face. Corresponding to this minimum amplitude is a maximum value of the vortex shedding frequency. Further increase of the incident angle (at $\alpha = 34$ degree according to Ref. [13]), may cause the separation region to disappear completely and produce positive pressures over the entire side surface.

Another source of large negative pressure on a finite length structure are the corner vortices near its free end, as shown in Fig. 2.2. As flow approaches the structure from an angle, the flow over the top of the structure tends to roll into vortices with origin at the leading edge top corner [14]. The negative pressures associated with these vortices are usually high. Besides these, depending on the structure's geometry and the turbulence intensity in the free stream, the vortex sheet shedding from the top corners could play a strong role in determining the wake characteristics [15].

On the other hand, when the turbulence intensity in the approaching flow is increased, results from other wind engineering investigations of structures, such as those of Vickery [16], indicate that the steady and fluctuating forces acting on the structures are markedly influenced. Lee [17] suggested that such changes are due to the intermittent reattachment of the shear layers to the downstream end of the side faces. The subsequent deflection of the shear layers causes the vortex formation to move downstream, thus raising the base pressure and leading to a reduction of the mean drag. Bearman and Obasaju [18], by analysing the traces of fluctuating pressure on stationary and oscillating square-section cylinder, reached the same conclusions.

(b) Flow about Twin Prismatic Cylinders at Various Arrangements

When a nearby structure is included in the consideration, qualitative analysis of the loading effects becomes more complex, and the amplitudes of the induced oscillations are strongly dependent on the relative positions of the structures concerned. The three types of model arrangement used in this study, namely the staggered, tandem and side by side, are schematically shown in Fig. 2.3.

In the staggered arrangement, shown in Fig. 2.3(a), the accelerated flow, after being deflected from the upstream section, impinges on the downstream section. The flow approaching the downstream cylinder will have a higher turbulence level and

result in increased positive pressures on this cylinder. Whereas the higher velocities past the point of separation at the outer corner (point C in Fig. 2.3(a)) may result in higher negative pressure. If vortex shedding is the dominant mechanism of instability, the formation of vortex streets behind the two cylinders is strongly dependent on their positions in the longitudinal and transverse directions. Under certain flow conditions, a critically located downstream cylinder could alter the wake of the upstream cylinder significantly [11].

When one cylinder is placed directly behind the other in tandem arrangement, such as that shown in Fig. 2.3(b), the downstream one can either be contained entirely within the low-velocity wake region of the upstream cylinder or be at a position just outside this region so that a distinct vortex street is formed behind each cylinder. In the former cases, the downstream cylinder will benefit from the shielding provided by the upstream one and experience a decrease in the magnitude of the negative pressure on all sides.

Zdravkovich [19], in an extensive investigation of the flow interference effects between two circular cylinders in various arrangements, identified three regions in which the vortex shedding is considerably modified by and strongly dependent on the arrangements of the two bodies, namely the proximity interference, wake interference and no interference regions, see Fig. 2.4.

He further subdivided the spacing between the two above mentioned tandem arrangements into different flow regimes according to the flow changes in the gap between them. These results are summarised in Fig. 2.5. It must be pointed out that flow about a circular-section cylinder is different from that past a square-section cylinder, but the response characteristics are very similar under the same flow conditions. It is therefore applicable to use the same terms to describe the flow situations though different section cylinders are used.

Likewise, when two cylinders are positioned side by side to the approaching flow direction, as shown in Fig. 2.3(c), Zdravkovich [19] divided the gap between the cylinders into three flow regimes, varying from a single vortex street, in which the two cylinders behave as a single bluff body, to a coupled vortex street in which the vortices are simultaneously formed and coupled in an out-of-phase mode, as illustrated in Fig. 2.5.

According to Rosati [21], the dynamic wind forces acting on structures in atmospheric conditions could come from two main sources [21].

- (1) The time varying loads which can be associated with the following influences.

- buffeting by gusts.
 - buffeting by turbulence and vortices shed by the structure itself, and
 - buffeting by the wake from another structures.
- (2) The forces induced by the elastic motions of the structure, and the resultant forces may be due to vibration in either.
- an uncoupled mode, such as lock-in and galloping type instabilities, or
 - a coupled mode, such as flutter type instability.

In order to simplify the discussion, the following sections are divided in terms of structural responses such as torsional, along-wind and cross-wind motions rather than excitations. The following presentation does not intend to provide a complete historical review of these subjects, but rather to summarise published works directly related to the theme of this thesis.

2.2 Torsional Response

For structural reasons, and also due to human sensitivity to angular motions, torsional response of tall building is an important factor in design. But surprisingly, little information on torsional effects is available to the designer.

In general, aerodynamic moments occur if the line of application of the total wind load does not pass through the elastic centre of the structure. For geometrically symmetric bluff bodies, mean torsional moments can occur due to non-uniformities in the flow field and for wind directions not aligned with the axes of building symmetry, whereas fluctuating torque is caused by unbalances in the instantaneous pressure distributions. The magnitude of both mean and unsteady torque can be accentuated by the presence of geometric and stiffness asymmetries [22].

There is a similar aeroelastic phenomenon known as torsional flutter, in which two degrees of freedom of a structure--rotation and lateral oscillations--couple together in an unstable oscillation [23].

There are a few papers dealing with the analytical study of torsional response of tall structures, such as [24] and [25]. Unfortunately, their formulations were based on quasi-static approach and thereby ignored the important contribution from the wake excitation.

On the experimental side, Nakamura et al. studied the aerodynamic mechanism of torsional flutter of bluff structures, first by using spring-mounted rectangular bar models of various side ratios [26] and, later, repeated with forced oscillating bar models [27]. The results from these measurements reached the same conclusion, showing that the vortex shedding played a significant role in the determination of the onset of torsional oscillation.

Durgin and Tong [28], by using a scale model with adjustable mechanical properties and strain gauges, measured the two bending and torsional motion of a rectangular building in uniform flow. Their results indicated that the instability due to vortex shedding was very sensitive to small misalignment of the mass centre and the elastic axis, and to the ratios of the twist and bending frequencies.

Generally, however, investigations of torsional response of buildings and structures in simulated wind have been mostly limited to specific projects which may have irregular cross-sections and shapes, such as the one presented by Kato and Akiyama [29].

Kareem, who studied the multilevel cross-wind loading on a square section building, estimated the torsional moment acting on the model by integrating the fluctuating pressure forces over its surfaces [107]. Based on his measurements, Kareem [30] outlined the development of torsional loads on a rectangular building.

A similar technique was employed by Isyumov and Poole [22] who subsequently found that changes in the lift force and its centre of action are the major source of torsional moments. Another important finding of their study is that the vortex induced pressure fluctuations on the back side of the cylinder is the major contributor to the dynamic torque.

The effects of changes in the wake on torsional excitation, caused by the presence of other buildings and structures in the vicinity, is also the topic studied by Reinhold et al. [9]. They used sensitive transducers and measured the pressure distribution on the surfaces of square prisms in uniform and turbulent flows. The mean and fluctuating force and torsional moment coefficients were evaluated from numerical integration of the pressure readings. But since the resultant values were based on pressure readings at only three points on each face, the limited number of cases reported could not provide any general conclusion.

More recently, in an extensive study, Blessmann et al. [31] used a heavily instrumented model to study the interaction between two square prisms placed at various positions relative to each other and for various flow conditions. Their results indicated that at a small spacing distance, the amplitude of the torque acting on the

downstream building could be more than three times the values measured for the isolated model.

2.3 Along-Wind Response

Although alternating along-wind forces (i.e. drag) could be induced by vortex shedding, in particular for those circular section structures such as chimneys or piles [32], the in-flow response of isolated tall prismatic buildings and structures is due primarily to the buffeting by the longitudinal component of turbulence in the natural wind which gives rise to changes in speed and direction of the incident wind. Historically, the along-wind response of tall buildings used in structural calculations was based on meteorological and aerodynamic conditions alone, and mechanical properties such as mass distribution, flexibility and damping were ignored. Nevertheless, as the modern structures and tall buildings become more flexible, lighter in weight and lower in damping, the average frequency of the atmospheric gust may become close to the structure's natural frequency and may result in large resonant motions induced by the wind. Hence numerical procedures, based not only on the aerodynamic conditions but also on the mechanical properties of the structure concerned, have been developed since 60's.

Liepmann [33] had pioneered the use of the statistical method to estimate the response of structures to excitation induced by atmospheric turbulence. Davenport applied Liepmann's concepts to solve the tall building along-wind response problem [34], and developed models of the wind flow near the ground for this application.

Later, Davenport proposed a quasi-static spectral model which led to the development of a gust factor approach for estimating tall building along-wind response [35]. But this approach includes a height-independent expression for the spectrum of the longitudinal velocity fluctuation and results in overestimating the response of very tall structures.

Vellozzi and Cohen [36] developed a modified procedure, in which they applied a reduction factor to take account of the fact that the fluctuating pressure on the windward face is not perfectly correlated to that acting on the leeward face. But, owing to the way in which this factor is applied and to the simplifying assumptions concerning the quasi-static part of the response, estimated results from this procedure are in fact less satisfactory than the others.

Vickery [37] subsequently developed a procedure similar to the one in [35], but which is more flexible in the choice of certain meteorological parameters. Consequently,

procedures for estimating along-wind response based essentially on [35] and [36] have been included in the Canadian Structural Design Manual [38] and in the Appendix to the American National Standard A58.1 [39]. More details are given in [40].

Subsequently, computer programmes for estimating along-wind response of tall building have been developed independently by Simiu et al., in [40] and [41]. These programmes employed improved models of the atmospheric turbulence and of the along-wind pressure correlation, which therefore allows more economical designs.

In addition to a computer programme, Ref. [42] also includes graphs which take the dependence of the turbulent fluctuations on height into account and provide a facility for rapid manual calculations. A simplified procedure is also given in [43] to estimate the response of structures with a linear fundamental mode shape. A procedure for estimating the response of point structures is developed by Solari [44].

All the procedures mentioned above are based on the assumption that, around the structure in question, the terrain is approximately horizontal and that its roughness is reasonably low over a large surrounding area. However, if the topography of the surrounding terrain is unusual, or if the building is strongly affected by the flow in the wake of neighbouring buildings, the present analytical procedures become inapplicable and one has to rely on wind tunnel testing.

The effect of an upstream building in a flow field will increase the turbulence intensity, this corresponds to broadening the band-width of the input force spectrum [45]. One of the early wind tunnel investigations to involve twin square cylinders was the technical paper presented by McLaren et al. [46], in which they compared the effect of free stream turbulence on the along-wind force coefficients of twin square-section cylinders at various in-line (tandem) positions. Their results indicated that the interference effects between the cylinders would be reduced when the spacing between them was approximately three times or more the side length of the section, and this position seemed to be independent of the turbulence intensity and section's size. Also, the drag force was reduced as the free stream turbulence intensity increased.

Using a square section cylinder with a circumferential ring of 64 pressure tappings at mid-span and placed first upstream and then downstream with respect to a dummy cylinder alternatively at different spacings, Lee and Flower [47] studied the interference effects on the along-wind and cross-wind forces acting on the instrumented section. From their measurements, they found that the upstream section could be affected by the presence of a downstream section at a distance up

to ten times its width away and, also, that within a spacing ratio of less than 3.7, the downstream prism could experience a thrust against the flow rather than a drag. The combined mean drag from the upstream and downstream sections has values which resemble those given in [46].

In comparison, the mean drag force acting on a pair of circular cylinders at tandem positions, such as the results from Biermann and Herrnstein [48], showed a sudden jump in mean drag value when the cylinders were 3 to 4 diameters apart. They concluded that such a 'kick' on the interference drag was due to two different flow patterns which were related to the spacing between the cylinders. On the other hand, the pressure distribution measurement by Hori [49] also indicated that for close positions, the downstream cylinder could experience a negative drag-thrust force as shown in [47].

More recently, Blessmann and Riera [31] conducted an extensive study of interference effects between square prisms in uniform and turbulent shear flows. Their results indicated the same trends in the variation of along-wind force with spacing ratio, even though they studied a shorter range. In general, they concluded that, due to the presence of a neighbouring building, the wind induced along-wind force on the downstream building could be increased by up to 40%.

Saunders and Melbourne, followed the tests performed by Melbourne and Sharp [50], highlighting the influence of adjacent buildings on dynamic loads by using buffeting factors which are a measure of the wind loads produced by the presence of another structure compared to the loads without the presence of another structure. Their results indicated that there is a substantial increases in both peak loads and dynamic response in the along-wind direction.

Further research into the interference excitation between neighbouring tall buildings was conducted by Bailey et al. [11], in which the increased along-wind and cross-wind response of a tall square building under interference excitation and proximity effects was studied in a series of wind tunnel model tests. An important finding of these measurements is that the dynamic behaviour of the upstream building--particularly in the along-wind direction--could be markedly affected by a critically located downstream building through mutual interference.

In the side by side arrangement, the only published results with a pair of square prisms are those given by Lee and Flower [47]. They showed that as the gap between the prisms was increased from zero, the mean along-wind force fell from a high initial value to a value less than that of an isolated prism. Such reduction is mainly due to the base bleed effect. They also observed that by increasing the

separation (more than one width length), a flow bearing appreciable momentum will inject into the wake region. The flow itself will entrain fluid from the wake and lead to vortex shedding from the prisms' inner side faces. Hence the prisms will be acting as isolated bodies. The mean along-wind force will rise to its datum value and thereafter remain substantially constant.

2.4 Cross-Wind Response

The cross-wind motions of modern tall buildings and structures due to wind result from a nonlinear fluid-structure interaction of incident turbulence, wake dynamics and building cross-wind motion. Although these excitations can be identified separately, they often superimpose in causing instability. Because of the complexity and the number of variables involved, there is, as yet, no analytical method available to calculate accurately the cross-wind response of tall building due to wind.

To simplify the discussion, the following presentation is divided into sections which associate with each type of excitation mechanism.

2.4.1 Excitation due to Incident Turbulence (and Buffeting)

The turbulent properties of the natural wind, which give rise to changes in speed and direction of the incident wind, induce lift and drag forces and pitching moments on buildings and structures. Melbourne [51] pointed out that the significance of the incident turbulence in causing cross-wind response depends on the ability of this turbulence to generate a cross-wind force on the structure by a combination of longitudinal wind velocity and angle of incidence of the mean wind. In general, this means a section with high lift curve slope or pitching moment curve slope such as bridge deck or flat deck roof, as shown in Fig. 2.6.

The mechanism of structural response to excitation from incident turbulence is either via the process of resonant excitation of one or more of the natural structural modes or by a single response to a well correlated discrete gust.

On the other hand, if the unsteady loading on a structure is caused by turbulence shed in the wake of an upstream body, the unsteady loading is usually referred to as wake buffeting. An example of oscillations attributed to wake buffeting can be found in [52].

The quasi-steady spectral approach, similar to those procedures to determine the along-wind response of a structure, is applied to the computation of cross-wind response of structures due to incident turbulence. A summary of such approaches to

the cross-wind motion of bridge decks is given by Davenport [53]. Also Refs. [23] and [54] provide the outlines of procedures to estimate the cross-wind and buffeting response of line-like structures by atmospheric turbulence.

2.4.2 Excitation due to Wake (and Vortex Shedding)

For buildings and structures under wind action, the most common source of cross-wind excitation is associated with vortex shedding. The vortices, which are formed by the unsteady free shear layers, are shed from the sides of the body and give rise to an alternating force on the body. Fig. 2.7 shows a sequence of simultaneous surface pressures and resultant forces acting on a circular section during vortex shedding. This type of excitation is commonly known as vortex excitation.

For any particular structure and under certain conditions, the shed vortices have a primary frequency, f_v , and is defined by the Strouhal relation,

$$St = \frac{f_v B}{\bar{U}_o}$$

in which B is the cross-wind dimension of the section and \bar{U}_o is the mean flow velocity. Fig. 2.8 summarises the variation of Strouhal number of a square-section cylinder with Reynolds number obtained in both air and water [55]. Broadly speaking, the Strouhal numbers show a slight and continuous change around a constant value in the range of Reynolds number between 100 to 2×10^7 . At higher Reynolds number ($> 10^7$), the value of the Strouhal number is 0.13, which is in close agreement with the widely accepted data in the literature [56].

If the vortex shedding frequency approaches and coincides with the natural frequency of the structure, resonant response may occur and this is commonly referred to as the critical speed effect. But because turbulence intensity level and mean wind velocity are varying with height, the excitation of vertical structures due to vortex shedding is effectively broad band. Therefore, it is more appropriate to use the term wake excitation to include all forms of excitation associated with the wake.

Because of its practical importance, excitation of a circular cylinder due to vortex shedding has been subjected to extensive studies throughout the years. An analytical method, starting from basic flow principles and representing the full range of response, has not yet been developed. But empirical models which describe the response behaviour of an elastic body under the action of vortex shedding by a judicious choice of parameters are available.

The first such model was first suggested by Bishop and Hassan [57] in which, by measuring the aerodynamic forces acting on a rigid spring-mounted circular cylinder

in a streaming fluid, they described the time-varying lift coefficient, C_L , in the expression:

$$\ddot{y} + 2\zeta_i(2\pi f_i)\dot{y} + (2\pi f_i)^2y = \frac{1}{2m}\rho u^2 D L C_L$$

where m is the mass, D and L are the diameter and length of the cylinder, ζ_i and f_i are the damping and frequency at the i th mode. The lift coefficient also satisfies a non-linear relation of the form,

$$\ddot{C}_L + (\text{damping term}) + (2\pi f_i)^2 C_L = (\text{forcing term})$$

This empirical model was later modified by Hartlen and Currie [58] and subsequently by Griffin et al. in a successive series of papers [59], [60] and [61]. In Ref. [61], the fluid oscillator model consists of a modified van der Pol equation with four empirical coefficients to be evaluated from observations of the cylinder motion. But this model has been criticised by Dowell [62] for not being consistent from a fluid dynamics point of view. In a recent attempt, Griffin and Koopman [63] and Sarpkaya [64], as well as Dowell [62] solved this problem in such a way that the fluid dynamic parameter is separated from those associated with the structure itself.

On the other hand, there are numerous reports dealing with the fluid dynamic aspects of the vibration problem, such as Toebes [65], Ramberg and Griffin [66] and [67] in which they studied the spanwise velocity correlations and vortex information in the wake of vibrating cylinders. Sallet [68] attempted to develop a theory for the prediction of drag and lift forces on a vibrating cylinder, but questions remain with respect to the validity of this theory [69]. And the works by Howell and Novak [70] represent basic studies of the behaviour of vibrating cylinders in turbulent flows. A comprehensive review of researches on vortex-induced oscillations of a circular cylinder in uniform and shear flows are included in Ref. [71].

In the aspect of wind tunnel investigations of wake excitation of buildings and structures, most studies were conducted in uniform flow conditions, such as those by Fung [72], Scruton [73], Wootton [74] and others. Recently, more effort has been put on the investigation of cross-wind vibration of tall structures in simulated natural wind. A few of the published results include Vickery [75], Vickery and Clark [76] and Rosati [77].

Although there are significant differences in the experimental approaches used, almost all these studies include the measurement of cross-wind forces associated with vortex shedding, and a number of important and fundamental conclusions can be drawn from these results.

First, the free stream turbulence has a profound effect on the cross-wind forces associated with wake excitation. Such effect is due to the shear layer which is modified by the free stream turbulence. This in turn controls the development of the wake and hence the main aerodynamic forces and wake excitation. A detailed description of the effect can be found in Gartshore [78].

Secondly, the structure with long after-body ($\text{width/breath} > 1$) produces a wider bandwidth of the cross-wind force spectrum.

Thirdly, vortex shedding from structures with low height to breath ratio is less organised, which results in a broadening of the cross-wind force spectrum. The effect may be caused by the shedding vortices changing from the arch-type to the Karman type, and is reflected by a change in the variation of Strouhal number with aspect ratio, as shown in [79].

More recently, Saunders [80], using rectangular building models subjected to strong simulated wind perpendicular to one face, revealed that the cross-wind aerodynamic input into the model building is insensitive to the level of its cross-wind motion and the cross-wind response is primarily due to wake excitation. Based on his findings, Saunders and Melbourne [45] demonstrated the use of nondimensioned cross-wind force spectra in predicting the cross-wind response and loading on the building.

The works by Kareem [29], [81] and [107] represent a different direction of studying the wake induced cross-wind oscillations of a tall building model. He used eight pressure transducers to measure fluctuating pressures at various levels throughout the model building height. The multivariate probabilistic and spectral characteristic of the fluctuating pressure field on and around the model are then derived from wind tunnel measurements. By monitoring the cross-correlation between the fluctuating pressure field around the model at various heights, an expression for the integral wind loading function on the building in the time and frequency domains can be developed through statistical integration. The results from the prediction procedure developed in these studies showed good agreement with the experimental results, and could be used to estimate the cross-wind accelerations levels of tall building at the primary design stage.

In the cases when another structure is in the vicinity, all the published results, such as Whitbread and Wootton [3], Blessmann and Riera [31], Lee and Flower [47] and Saunders and Sharp [52], indicated a substantial increase in the cross-wind response, but very few mentioned the change in the structure's response characteristics in the along-wind direction. Only Bailey et al. [11], by using the results of their force spectral measurements and a number of wake spectra,

attempted to explain the flow excitation mechanism between neighbouring bodies.

However, considered conservatively, the results from the measurements of flow interference between two circular-section cylinders may be useful in providing some insight into the effect of flow interference between neighbouring structures. The review by Zdravkovich [82], is by far the most comprehensive dealing with the flow interference between two circular cylinders in different arrangements.

2.5 Excitations due to Cross-Wind Displacement

There are three commonly recognised cross-wind excitations under this heading, namely, flutter, lock-in and galloping. These are usually referred to as wind-induced instabilities which occur when a body in fluid flow deflects under some force and the initial deflection gives rise to succeeding deflections of an oscillatory and/or divergent character. Such aeroelastic instabilities involve aerodynamic forces that act upon the body as a consequence of its motion [23].

The flutter excitation has been discussed under the torsional response section and will not be repeated here.

2.5.1 Lock-In

Under the action of vortices shed from the edges, a bluff body will be driven periodically producing alternating forces on the body, see Fig. 2.7. The alternating forces are strongest in the cross-wind direction but will cause only a small response unless the Strouhal frequency of the alternating pressures approaches the natural frequency of the body.

Lock-in is the phenomenon in which the body mechanical frequency controls the vortex-shedding frequency over a fairly wide range of wind velocities. Lock-in is thought to be associated with the interaction between the cross-wind displacement of the structure and the wake and is related to the critical speed of the vortex shedding. The effect of lock-in upon vortex shedding is shown in Fig. 2.9. A comprehensive review of this phenomenon can be found in papers published by Mair and Maull [83] and Parkinson [84].

The synchronisation of cross-wind force on a structure was first investigated experimentally by Bishop and Hassan [57] on an externally driven circular cylinder in uniform flow. Subsequently there were investigations of this phenomenon by Ferguson and Parkinson [85], Toebes and Ramamurthy [86] and others. These investigations were mostly carried out on two-dimensional bodies driven externally

and the information gathered included measurements of cross-wind forces, and correlation of the pressure fluctuation on the vibrating structures with the velocity fluctuations in the near wake. Their results indicated that, during lock-in, the frequency of oscillation of the structure and the vortex shedding frequency locked together when the amplitude of oscillation reached a certain critical value and the resultant cross-wind force increased significantly, and they concluded that the lock-in is dependent on the amplitude of cross-wind oscillation.

A few experiments dealt with the extent to which lock-in can induce large amplitude cross-wind response of tall buildings and structures. The results from Wootton [74] who conducted a series of tests on a base-pivoted circular model stack, and Novak [87], who measured the cross-wind response of a rectangular prism over a wide range of reduced velocities, showed that lock-in can cause large amplitude cross-wind response over a wide range of reduced velocities close to the critical when the structural damping is low, and is likely to occur on buildings which are operating near the peak of the wake energy spectrum.

2.5.2 Galloping

Galloping is the term used to describe the large amplitude single degree of freedom motion of a structure associated with the sectional aerodynamic force characteristics. Arising from the aerodynamic instability of the bluff cross-sectional shape which has fixed separation points, such as square and rectangular sections, small amplitude oscillations generate forces which become of large amplitude and act in the direction of and in phase with the cross-wind motion.

Fig. 2.10 shows a square section at rest and in transverse motion in the presence of a wind normal to a face and the plane of motion. The cross-wind motion of the section will create an asymmetric surface pressure distribution which results in a force, F_y , in the direction of the motion so that the transverse displacement is further increased. In this condition energy is transmitted to the body from the wind. The induced oscillation, which develops at the natural frequency of the body, will be increased until the energy dissipated per cycle is balanced by the structural damping.

Unlike the wake excitation, the present analytical formulation can predict the galloping response of all structures having a common type of cross section, arbitrary mass and damping. The fundamental assumption of galloping analysis is that the fluid force is quasi-steady which means that for every instant during the oscillation, the aerodynamic force acting on the body is the same as for a static test on the same rigid body at the same angle of incidence of the mean flow. Fig. 2.11 shows the variation of the transverse force coefficient, C_{F_y} , with incidence, α , for a square

prism in smooth flow [88].

Theoretically, galloping can arise when the slope of the graph of transverse force coefficient against incidence, $dC_{F_y}/d\alpha \big|_{\alpha=0}$, is positive and such a body is usually referred to as a soft oscillator. This instability criterion was first applied to galloping by den Hartog [89]. However, this criterion can be a sufficient but not a necessary condition for galloping to occur. If an initial cross-wind displacement is sufficient to generate an effective angle of incidence at which the force is positive, then galloping still occurs even though the section may have zero or negative slope of force coefficient, and such a body can be described as hard oscillator [89].

Parkinson and Brooks [90] were the first to determine the limiting amplitude of galloping in terms of aerodynamic coefficients. Later, Parkinson and Smith [88], basing their work on a quasi-steady assumption, developed a generalised response curve which can be used to determine galloping cross-wind response of structures in smooth flow. Using a similar approach, Novak [91] and [92] proposed the concept of a universal curve which can be used to predict the galloping behaviour of all structures having similar mechanical properties.

The effect of turbulence on galloping was explored by Nakamura and Mizota [25], Novak and Tanska [93] and others. It has generally been concluded that the quasi-steady assumption is valid only at reduced velocities significantly higher than critical and the frequency of the near wake associated with vortex shedding is well above the natural frequency of the structure.

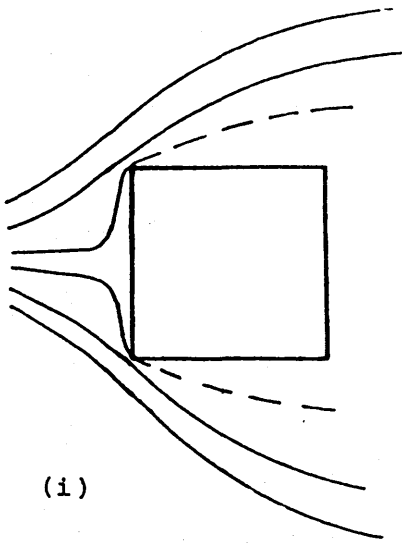
Furthermore, the study of galloping of tall structures in a simulated natural wind condition by Novak and Davenport [94] revealed that galloping response was significantly reduced as turbulent intensity was increased, but vigorous galloping behaviour still existed. Subsequent measurements by Laneville and Parkinson [95], Novak [92] and Novak and Tanaka [93] showed that increased turbulence can transform a body which is a soft oscillator in smooth flow into a hard oscillator in turbulent flow, and a hard oscillator in smooth flow into a soft oscillator in turbulent flow.

More recently, Kwok [8] studied cross-wind oscillations, in particular, the displacement dependent lock-in and galloping behaviour of circular and square building models in uniform and simulated natural wind conditions. It was found that, when the tall building model was operating at close to the critical reduced velocity and particularly for low values of structural damping, displacement dependent lock-in excitation could cause large amplitude cross-wind response. He also proposed a prediction procedure comprising a combination of a random and a sinusoidal lock-in

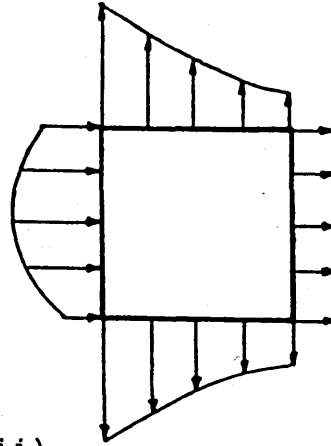
excitation models. The predicted cross-wind response of the towers is close to the measured value.

It was also found that, under certain conditions, the downstream body of two in close proximity may be subjected to galloping oscillations induced by the turbulent wake of the upstream body. A familiar example is the large amplitude oscillation of some ice-coated power line cables in strong wind. This phenomenon is usually referred to as wake galloping [96].

A similar motion-induced excitation has been observed on slender structures in a row with small spacing ratio. This aeroelastic instability is caused by the relative motion of the structures which periodically changes the flow condition. This so-called 'interference galloping', which was first observed by Ruscheweyh [97] and [98], is characterised by an onset flow velocity which depends on the mass-damping parameter, the spacing and an interference galloping criterion which includes the den Hartog galloping criterion and a hysteresis lag angle. In contrast to the classical galloping excitation, the aerodynamic force is not primarily velocity dependent but, instead, it is position dependent.

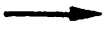


(i)

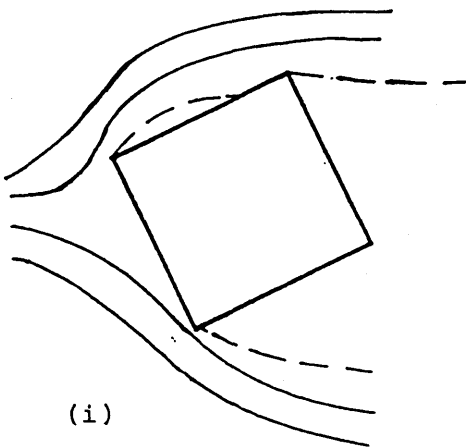


(ii)

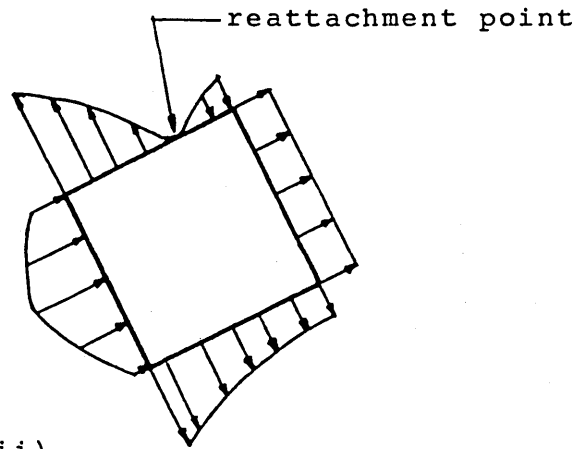
(a) Angle of incidence, $\alpha = 0$ degree



Wind Direction



(i)



(ii)

(b) Angle of incidence, $\alpha > 0$ degree

Figure 2.1 Flow and mean pressure distribution about a square-section cylinder with angle of incidence of the mean wind varying from (a) $\alpha = 0$ to (b) $\alpha > 0$.

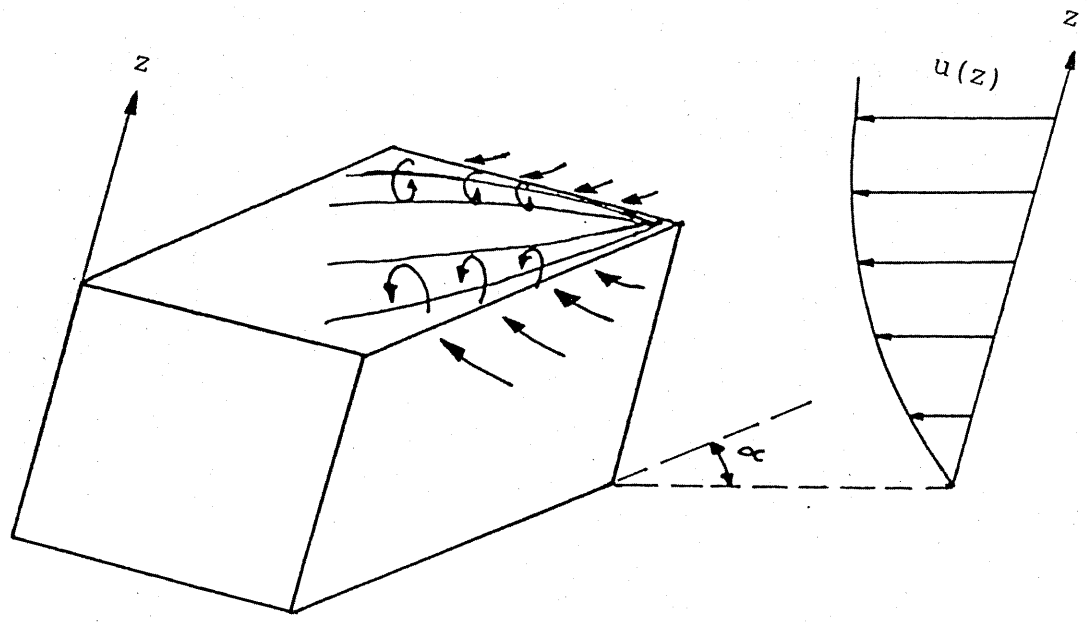


Figure 2.2 Corner vortices generated on the flat-top building roof.

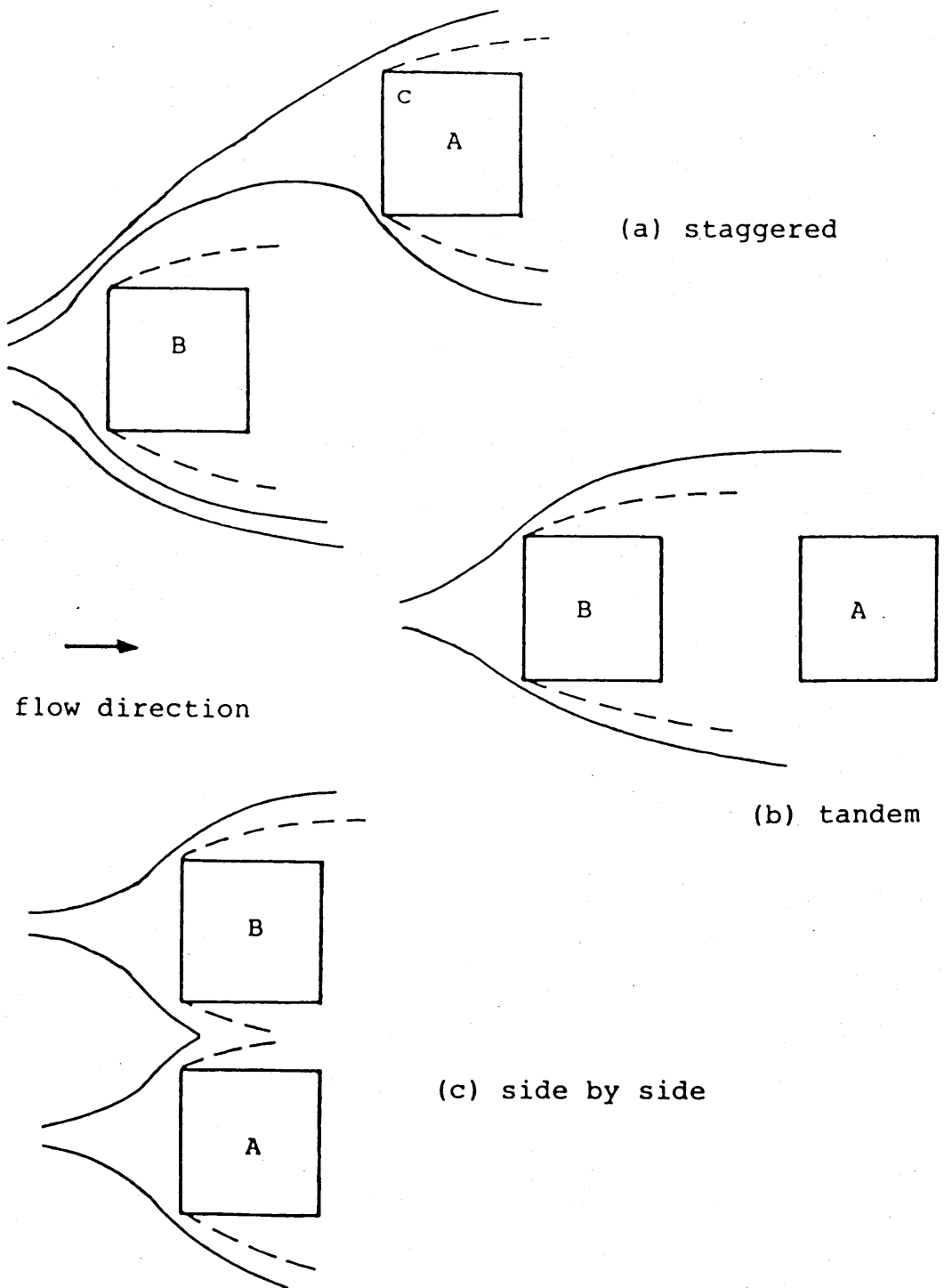


Figure 2.3 Flow about two square-section cylinders at (a) staggered, (b) tandem and (c) side by side arrangements.

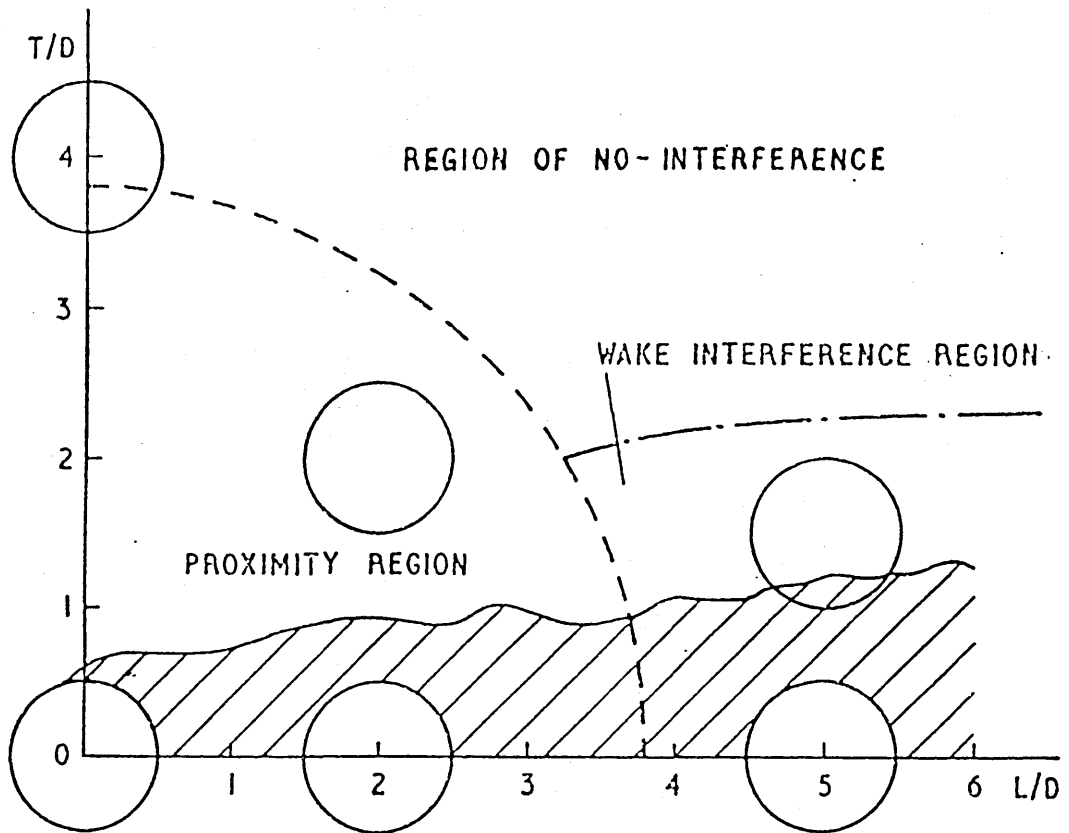


Figure 2.4 Classification of flow regimes in side by side and tandem arrangements for stationary cylinders, from Ref. 19.

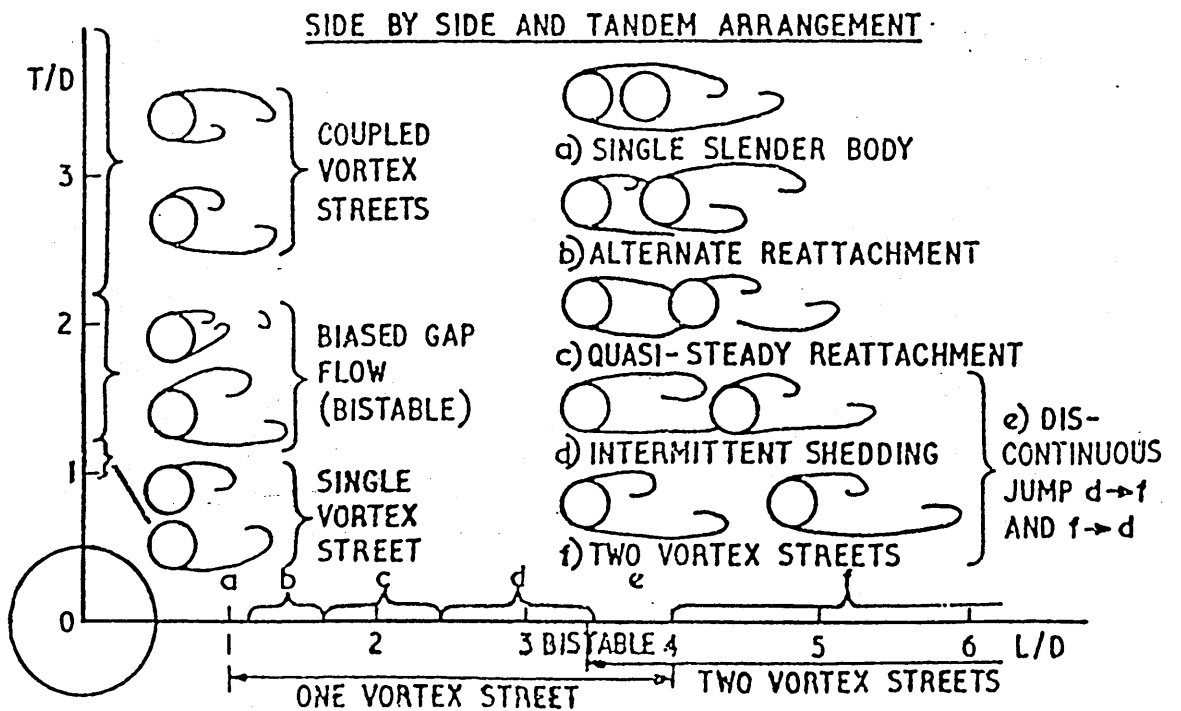


Figure 2.5 Classification of interference regions between two circular cylinders, from Ref. 19.

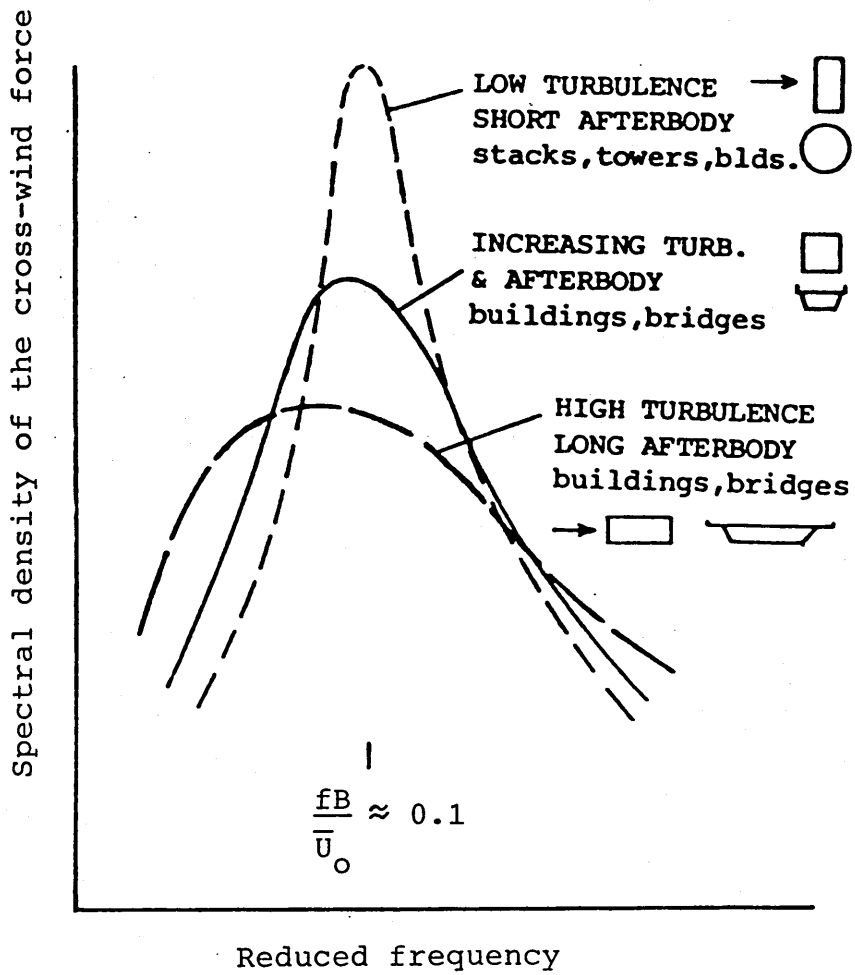


Figure 2.6 A qualitative comparison of the frequency distribution of the cross-wind forces induced by wake excitation for various structures and free stream turbulence, from Ref. 51.

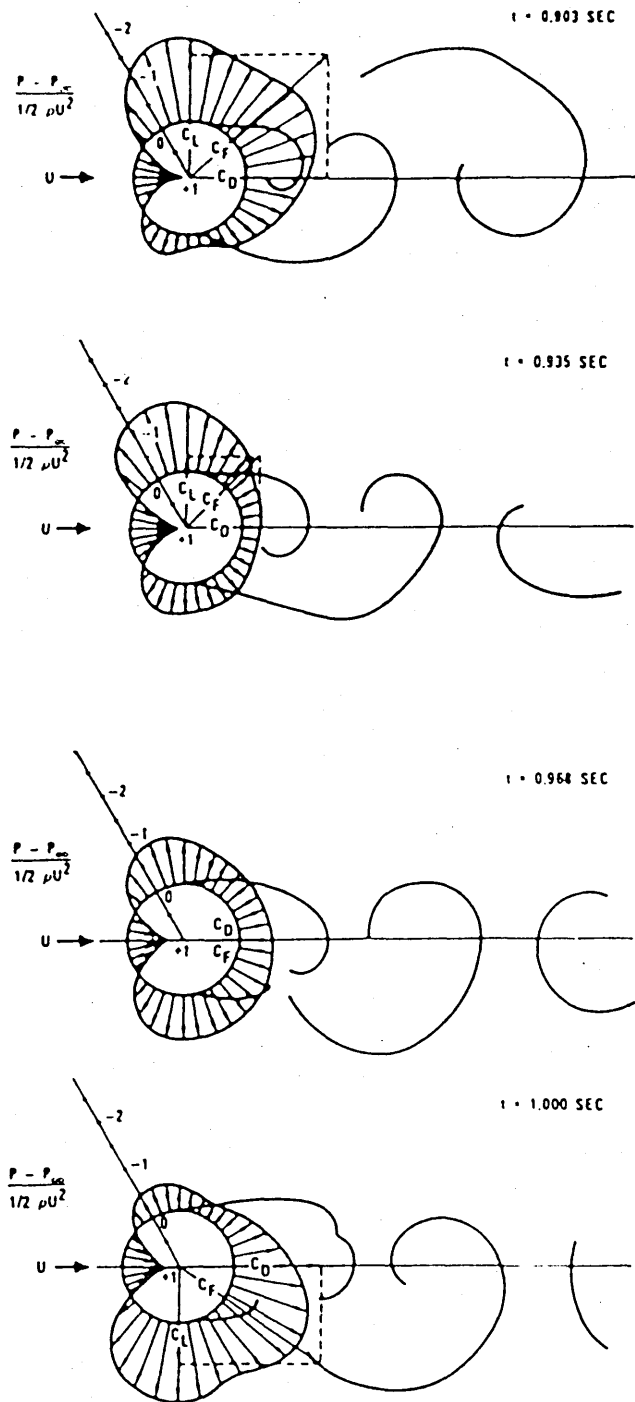


Figure 2.7 A sequence of simultaneous surface pressure fields and wake forms at $Re = 112,000$ for approximately one third of one cycle of vortex shedding (after Drescher, 1956).

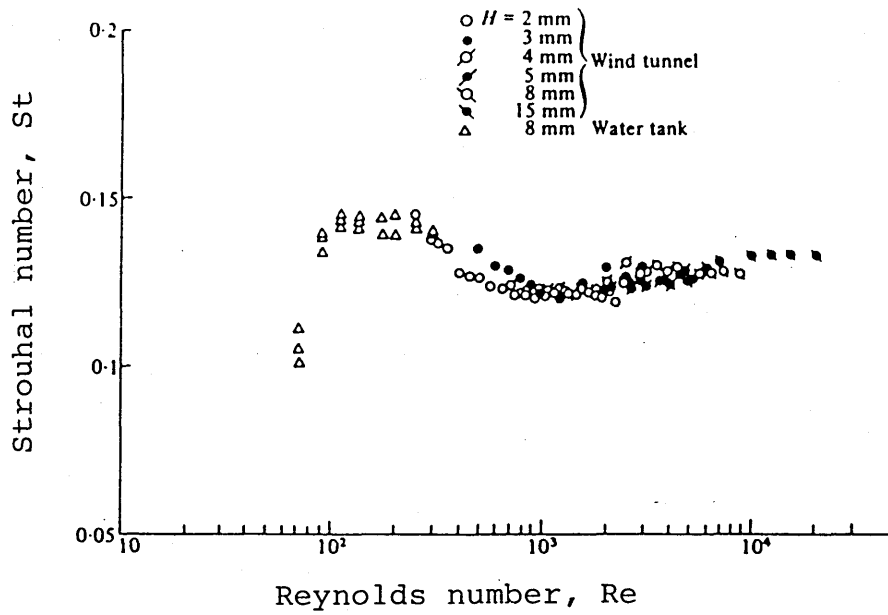


Figure 2.8 Variation of Strouhal number with Reynolds number for a square cylinder, from Ref. 55.

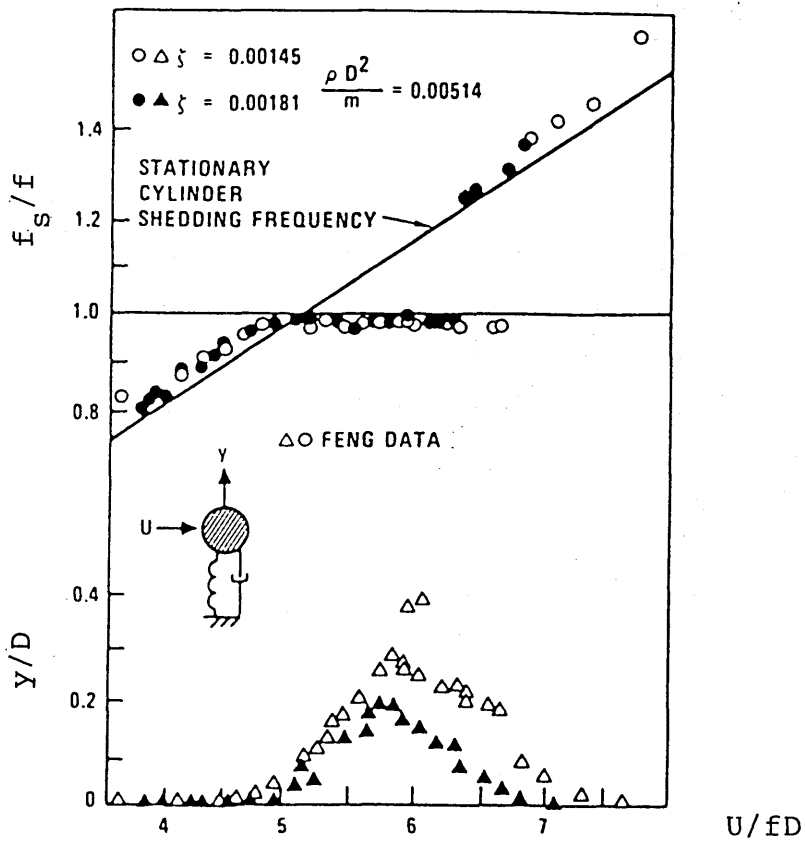


Figure 2.9 Resonance of a rigid circular cylinder with vortex shedding (after Feng, 1968).

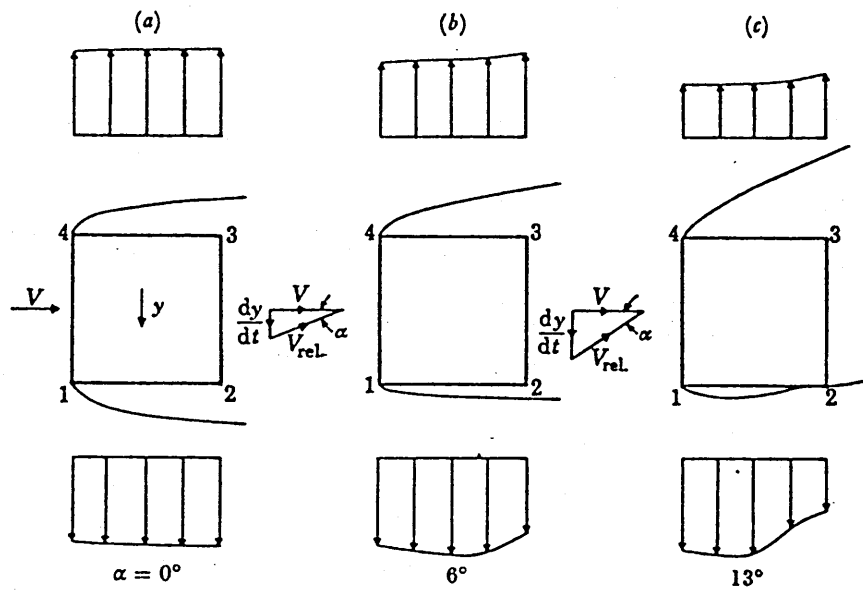


Figure 2.10 Effects of square-section afterbody on separated shear layers during galloping, from Ref. 88.

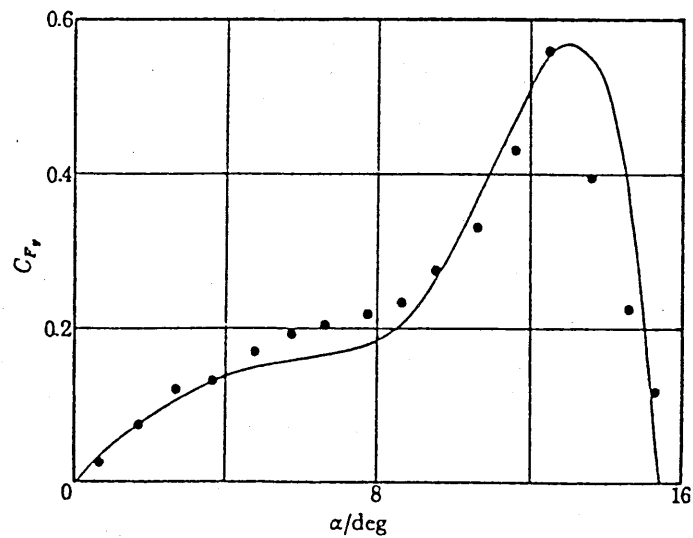


Figure 2.11 Variation of transverse force coefficient with angle of attack for square-section cylinder, from Ref. 88.

CHAPTER THREE

DESCRIPTION OF THE EXPERIMENTAL APPARATUS

3.1 Introduction

Owing to the complexity of the problem, flow-induced oscillations of tall buildings and structures can rarely be predicted on a purely analytical basis. Physical modelling of wind-structure in a wind tunnel, therefore, is still the most accurate and practical means of relating aerodynamic loading on a structure to properties of local wind conditions.

For the results obtained from wind tunnel investigations of wind effects on buildings and structures to be meaningful and applicable in predicting the full scale behaviour requires the measurements to satisfy a number of similarity requirements. The significant differences in the techniques used and assumptions made in this respect are due primarily to the differing facilities and equipment employed.

The following list of the variables and their physical meanings is considered to contain the minimum number of variables required for the present wind tunnel modelling.

U_w is velocity associated with wind structure.

\bar{U}_o is local mean longitudinal velocity.

σ_w is standard deviation of velocity fluctuations.

L_w is length scale associated with the wind structure.

f_w is frequency associated with wind structure.

$S_w(f)$ is power spectral density of longitudinal velocity.

ρ is air density.

μ is air viscosity.

P is pressure.

L_s is length scale associated with the structure.

f_s is frequency associated with the structure.

ρ_s is density of the structure.

E is stiffness modulus of the structure

ξ_s is damping ratio for the structure, and

$D_x . D_y$ is separation between the structures.

Dynamic similarity can be achieved if nondimensional groups derived from these variables are maintained. Extensive treatments of similarity requirements for dynamic wind tunnel modelling can be found in literature, such as Scruton [99], Simiu and Scanlan [22]. The principals employed are [100]:

- (1) The similarity of the mean and turbulent characteristics of the flow;
- (2) geometric similarity of the structure to a scale consistent with the length scaling of the natural wind;
- (3) similarity of aerodynamic forces;
- (4) similarity of inertia forces and stiffness characteristics; and
- (5) similarity of damping forces.

In general, these similarity requirements can be conveniently divided into two groups: one deals with the modelling of the natural wind and the other with the dynamic modelling of the structures. These, together with the force measuring devices and their accessories as used in this study, are discussed in the following sections.

Finally, brief descriptions of the various instruments used are presented at the end of this Chapter together with details of their calibration.

3.2 The 'Handley-Page' Wind Tunnel

The general layout of the Glasgow University low-speed 'Handley-Page' wind tunnel is shown in Fig. 3.1. It is of the atmospheric-pressure closed-return circuit type with a 1.61x2.13 m octagonal, 2.44 m long working section.

This wind tunnel is driven by a fixed pitch fan via a DC motor and is capable of producing wind speed up to 60 m/s for short periods of time and up to 40 m/s for continuous running. The wind speed can be changed continuously by adjusting the amount of current through the motor.

The whole wind tunnel has been refurbished. A re-calibration was carried out and documented by Gordon et al. [101]. Fig. 3.2 and 3.3 show the results from these

tests.

The fan motor, which is mounted on top of a concrete block, obtained its power supply from an AC/DC convertor-generator installed at a separate location. It was observed that, with the convertor-generator switched on, the accelerometers mounted either at the tip of the model or on the support structure with its axis parallel to the wind flow direction (along the X-axis, see Fig. 3.4) could pick up a distinctive noise signal of frequency equivalent to the convertor-generator rotating speed (1480 r.p.m.). There is no way to isolate this interference since it is transmitted through the concrete foundation. Fortunately, the amplitude of this noise signal was relatively small in comparison with the response signal. Therefore, in general, it produced insignificant distortion of the measured responses.

3.3 Production of Large Scale Turbulence in Wind Tunnel

The evidence from recent measurements of wind-induced oscillations of tall buildings and structures proves that the results obtained under smooth uniform flow conditions could lead to overestimation of the response of the actual structures. In fact, a series of wind tunnel tests to determine the response of a square-section tower to both smooth uniform flow and turbulent shear flow, conducted by Whitbread [102], Whitbread and Scruton [103], gave results indicating that:

- The characteristic sharp peak response in smooth flow is replaced in turbulent shear flow by a steady increase in amplitude with wind speed.
- A higher structure damping is required with turbulent flow to achieve the same reduction in amplitude as in smooth flow.
- Reattachment of separated boundary layers can occur in a turbulent flow and have the effect of reducing the width of the wake.

In those cases where two identical tall structures are located close to each other, it is apparent that the oscillatory behaviour of the downstream object is very much dependent on the wake structures created by the upstream object. Therefore, taking measurements in both uniform and turbulent flows will not only produce data for comparing the variations of structural response in different flow conditions, but may also provide vital information about the effects of aerodynamic interference between two neighbouring objects under such flow conditions.

3.3.1 Turbulence Generation Grid

There are basically two methods of producing turbulence in a smooth uniform stream, namely the natural growth and augmented methods. The first method requires a wind tunnel with very long fetch of roughness elements over which a turbulent shear flow boundary layer is developed whereas the augmented method, which requires a relative short fetch length, can produce large scale turbulence by installing tripping devices such as a grid or spires of different shapes or by air injection upstream of the fetch length.

Because of the relative short working length of the Handley-Page wind tunnel, it was found that the only practical way to create a turbulent flow with a sufficiently large intensity and scale was by installing a uniform square mesh grid immediately upstream of the test section. The general arrangement of the grid, the model-balance assembly and its support structures in the wind tunnel working section are shown by the isometric view diagram in Fig. 3.4.

The bar grid was made from rectangular-section wooden beams bolted together by screws and wing-nuts at every point where two bars cross. The dimensions of the bar and mesh size, which is the centre spacing of the bars, were based on the tentative relationship between turbulence intensity and grid dimensions derived by Whitbread [102] and Vickery [104], i.e.

$$\frac{\sigma}{U_o} = 3.27 \left[\frac{d}{b} \right]^{-0.995}$$

and the tentative expression for the longitudinal scale of turbulence, i.e.

$$\frac{L_x}{b} = 0.00813 \left[\frac{d}{b} \right]^{1.39}$$

in which d is the longitudinal distance from the grid and b is the bar width normal to the flow direction. According to Whitbread [102], an isotropic turbulence superimposed on a uniform mean flow was formed at a distance about ten times the mesh size (m) from the grid.

In the present arrangement, the distance between the grid and the centre of the turntable (about midway along the working section) is approximately 1.32 m. This gives the values of b and m to be 0.032 m and 0.14 m respectively. And from these empirical equations, a uniform turbulent flow with turbulence intensity of 9.6% and length scale of 0.46 m should be established at this location.

3.3.2 Properties of the Wind Model

Two wind models have been used in this investigation, termed uniform smooth flow and uniform turbulent flow. The smooth flow was produced by the tunnel in its normal operating form whilst the turbulent flow was generated by inserting a uniform grid ahead of the model. The flow characteristics of these flow models were surveyed by means of a straight hot-wire probe connected to a DISA Constant Temperature Anemometer and Lineariser. Measurements were mostly taken at a height of 0.97 m from the tunnel floor, and at locations where the models would be placed in the later measurements.

The profiles of the longitudinal turbulence intensity and mean velocity ratio measured at locations 6.5 and 9.8 times the mesh size downstream of the grid are presented in Fig. 3.5(a) and (b), respectively. The relative sizes of the grid is also illustrated in this diagram for comparison. Here, the turbulence intensity is defined as the ratio of the standard deviation of the fluctuation, σ_u , to the mean flow velocity, \bar{U}_o , that is

$$\text{Turbulence Intensity} = \frac{\sigma_u}{\bar{U}_o}$$

and \bar{U}_{eff} is the time-average of the mean flow velocity measured by a single hot-wire probe both normal to the flow and along its longitudinal direction, that is

$$\bar{U}_{eff} = \sqrt{(\bar{U} + u')^2 + w'^2 + v'^2}$$

Because a relatively simple turbulence generation technique was employed in this study, the resulting flow formed behind the grid did not have the usual velocity profile as produced by other techniques. However, the absence of a proper mean wind speed profile is not considered to have a significant influence on the dynamic response of very tall structures.

Briefly, the results showed in Fig. 3.5(a) and (b) establish the following facts. Excluding the regions of the developing wall boundary layers, the longitudinal turbulence intensity and mean velocity ratio are almost constant with the height, although the average turbulence intensity within the region is generally 2% lower than the value calculated from the tentative equation. However, the profile of intensity measured at a distance well less than the ten times mesh size limit shows a large non-uniformity along its height. These irregularities may be due to the dispersal of the low velocity wake shed by the individual grid members. The scatter of the values of the mean velocity profile, measured at the same location, provide further evidence of this nonuniformity.

Fig. 3.5(a) also includes the longitudinal turbulence intensity of an full scale wind model, proposed by Davenport [34].

$$\frac{\sigma_u}{\bar{U}_z} = 2.58 \sqrt{k} \left[\frac{z}{z_{10}} \right]^{-\gamma}$$

in which γ is the power law exponent, k is the surface drag coefficient and \bar{U}_z is the mean wind speed at a height z .

For the present profile, the values of γ and k are 0.4 and 0.02 respectively. These values correspond to a terrain with large and irregular objects typical of the centres of large cities, see Ref. [34].

As expected, the profiles of the turbulence intensity vary with the distance from the grid, as shown in Fig. 3.5(a), and in Fig. 3.6(a) in which the centre-line distribution of the turbulence intensities were measured at four separate locations. In these plots, $d/m = 5.77$ and 11.22 represent the shortest and longest distance between the grid and the model stations used in the later measurements. In average, the resulting turbulent flow field shows an average drop of 0.8% of the measured intensity per mesh length. The profile of the uniform smooth flow is also shown in this diagram for comparison. Fig. 3.6(b) also shows the variation of mean velocity ratio, $\bar{U}_{eff} / \bar{U}_o$, with the free stream velocity as a function of measurement location.

These results, except the smooth flow case, also indicate a gradual decrease of turbulence intensity with increase of wind speed. This, together with the relatively large drop in the intensity values measured at locations close to the grid, may again confirm the effects of the low-speed wakes shed by the individual grid members.

Fig. 3.7(a) and (b) show the variations of turbulence intensity and mean velocity ratio with free stream wind speed, measured at $d/m = 7.6$ and at three locations across the flow. The small variation of these values confirms the near uniformity across the flow at that location.

The power spectral density functions of the longitudinal velocity component taken at four positions along the centre line of the working section are given in Fig. 3.8. The longitudinal integral length scale, L_x , which is often used as a measure of the scale of turbulence, was estimated to be 0.63 m by extrapolation of the spectrum measured at the upper part of the profile to zero frequency.

In Fig. 3.9, the longitudinal turbulence spectrum obtained in these measurements has been replotted in the form of $f S_{u'}(f) / \bar{U}_o^2$ versus $f L_x / \bar{U}_o$, with $L_x = \bar{U}_o / 2\pi \hat{f}$ and \hat{f} is the frequency corresponding to the peak value of the normalised spectrum. The spectra of the uniform turbulent flow measured in NPL

wind tunnel [103] and the theoretical expression proposed by Davenport [105] are also shown on the same graph for comparison. And the present turbulent wind model seems to have insufficient spread of energy to both the lower and high numbers.

3.4 Dynamic Modelling of Structures

In general, the types of models used in wind tunnels to study the oscillatory behaviour of tall structures under wind action can be conveniently divided into two groups, namely the conventional 'stick' models or the multi-degree of freedom aeroelastic models.

For modern tall buildings and structures, the fundamental mode of deflection consists of a cantilever and a sway action. Hence, if the response associated with higher modes is neglected, this fundamental deflection can be conveniently approximated by a straight line.

This so called 'stick' approach usually comprises a rigid model, spring mounted near its base, and a set of gimbals located at a point selected to provide a best fit between the model and prototype mode shapes. The other main components are force transducers to measure the wind-induced overturning moment, a ballast weight to adjust for the correct inertia scaling and an electro-magnet to apply eddy-current damping to the model. The models used by Kwok [8] in his studies of wind-induced response of tall slender building was a typical example of this approach.

However, despite its simplicity in design and construction, this type of modelling has several disadvantages, the principal ones being:

- Only one or two fundamental sway modes are included.
- The torsion and the coupling between the translational and torsional degrees of freedom due to both inertial and elastic effects can not be studied.

Furthermore, real buildings are multi-degree of freedom systems with modes higher than the fundamental. The contributions of the higher modes to the response depend largely on the frequency of the exciting force and is significant for tall slender structures under certain wind conditions.

The design and construction of the multi-degree of freedom model is generally more complicated and usually comprises several elastically interconnected 'lumped' masses, each having two translational and one rotational (about a vertical axis)

degrees of freedom. The masses are primarily concentrated at the rigid or flexible floor diaphragms which are connected by flexible columns. And the entire mechanical system is then enclosed by a non-structural cell which forms the exterior geometry.

In most cases, a multi-degree of freedom model is mounted on a balance capable of measuring the mean and dynamic bending moments and torque near the base of the model and is fitted with accelerometer and/or displacement transducers to provide measurements of the sway and rotational motions near the top of the model. The multi-degree of freedom model designed and constructed by Davenport et al. [106] is a typical example of this approach.

However, the need for more instrumentation and greater complexity in design and fabrication make this type of modelling less attractive, unless the objects being studied are complex and the modes of vibration are highly three-dimensional due to inertial and elastic coupling between various degrees of freedom.

In the present study, a pair of force balance columns, which are capable of measuring the two translational forces and one torsional moment, were made available during the model designing stage. Therefore, the primary task was to design and construct a pair of aeroelastic models which could integrate with these columns and form a model-balance system.

Because the main objectives of this investigation are to compare the aerodynamic and/or mechanical coupling effects between neighbouring structures, rather than to measure the actual magnitude of wind loads exerted on them in various conditions, a number of simulation criteria mentioned in the previous section could be relaxed:

- (a) the aeroelastic models used in this study were not intended to simulate any particular building or structure and so values such as dimensions or weight were chosen by engineering judgement,
- (b) because of the balance column, the conventional rigid model-gimbals assembly could not have been used here. On the other hand, the multi-degree of freedom model was rejected on the basis of costs and complexity. The resulting design of the model-balance system is a compromise between these two approaches,
- (c) because of the design approach, the mechanical properties of the complete model-balance system, such as stiffness and damping, were very much dependent on the material used and the method of fabrication, and

- (d) since vortex shedding was considered to be the main source of excitation, it is desirable to keep the critical wind velocity at the lower end of the speed range. In doing so, additional weights were added onto the model to lower its natural frequency. A byproduct of such arrangement is that the higher modes of oscillation could be simulated by the present set-up.

3.4.1 Description of the Aeroelastic Models

The basic design of the aeroelastic models used in this investigation was very much the same as those used by Cain [7] in his studies of the oscillatory behaviour of bridge pylons under wind action. But here, instead of using a steel hollow rectangular section, a duraluminium hollow square-section was employed. The section measured 38x38 mm and 3.2 mm in thickness. The use of a flexible cantilevered beam to form the model's core, not only guaranteed that the two translational motions were parallel to the principle axes, but also provided a twisting mode shape which varies with height.

The core was built-in at both ends. Two intermediate transverse panels (or diaphragms), which like the top plate were made from medium hard wood, were fixed on to the core at equidistant positions along its length. These, together with the four timber stringers cemented at the four corners of each diaphragm, formed a stiff frame to which thin plywood panels could be attached. The plywood panels were fixed by numbers of tiny wood screws and made up the external geometry. The base plate, on the other hand, was made from a specially acquired compressed plywood which is extremely hard but can be machined as normal timber.

In view of the combined effects of the aerodynamic loading and the model's own weight, the cantilevered core and all its attachment plates were fastened together through a combination of bolts, nuts and right angle brackets.

The aerodynamic forces and moments acting on the model were transmitted to the force balance by means of a flanged hollow cylinder. In turn, this cylinder, in appearance very similar to an expansion joint and which has access holes on its surface for the accelerometer output cables, was rigidly anchored to the bottom side of the model's base plate. The mechanical fixture consists of two split sleeve cramps which were clamped tightly onto the cylinder's body by a number of bolts and nuts. The attachment plates on which the sleeves sat were then bolted on to an opposite piece at the free end of the balance column. As a result, the relatively stiff model and dynamometry constituted a cantilever beam system with end load. Details of the construction and fixtures between each component are shown in Fig. 3.10.

The reason for using this rather inconvenient method to link the force balance and the model was because the former was situated under the wind tunnel working section and the latter had to be mounted onto the column balance through a small hole in the tunnel's floor. Once placed in position, the model's bottom face was about 6 mm above the floor surface.

Two miniature accelerometers of the piezo-electric type were mounted on each model at positions near the end of the core section and in directions coinciding with the bending directions. The light-weight output cables were taped onto the core surface and led out of the model through the access holes. One side of the plywood panelling could be easily removed which provided the options of changing the accelerometers or making adjustment after assembly.

To reduce the natural frequency, six lead ballast masses which weighs 1.02 kg altogether were inserted into the core section and fixed at regular interval along its length. It must be pointed out here that the models after completion are completely symmetrical about their vertical axes, and there is no attempt to change this symmetry by applying additional mass.

Two identical aeroelastic models were built for this investigation. Each model was 0.1016 m in width and 1.022 m in length, an aspect ratio of 10. Based on these figures, the frontal area of these model is less than 4% of the working section. Therefore, the blockage effects on the measured values are assumed to be negligible. With the split sleeve cramps and other accessories attached, each model weighs 9.2 kg. The total mass moment of inertia about the two principal axes lying in the bottom face of the model was estimated to be 3.4 kg m^2 . Fig. 3.11 shows the model deflected shape under a static load applied at its tip. The averaged stiffness was estimated to be 12 kN/m.

Unless specified, both tower models were orientated with one face normal to the wind, with the distance between them varied longitudinally (X) and laterally (Y) on a coordinate grid, such as the one shown in Fig. 3.12.

Prior to the design of these aeroelastic models, two prismatic square-section cylinders made from Perspex panels were built and used for preliminary tests. These Perspex models have the same external dimensions except that one spanned the height of the tunnel's working section (2-D model). The deflection shape of the short Perspex model (3-D model) under a static load is also shown in Fig. 3.11 for comparison.

However, because of the time restriction, these Perspex models were only used in the determination of the dynamic properties of the model-balance assembly and

were not used in any wind tunnel measurements. The results from these tests are discussed in the next chapter.

3.4.2 The Mechanical Linkages

To explore the effects on the response of the two models when they are 'explicit' linked together, a mechanical coupling device was built. Basically, the linkage device consists of two split brackets which were clamped on to the models at a selected position. Each bracket had a rubber lining inside to protect the model surface and they were linked to each other by two parallel steel bars. Because of their inherent rigidity, it is unlikely that these bar linkages would be bent under the test conditions, i.e. the relative distance between the tower models at the connected point is constant.

In the present study, this coupling device was only applied when the models were arranged in either tandem or parallel configuration with a spacing ratio of four, see pictures in Fig. 3.13(a) and (b).

3.5 Measurement of Unsteady Wind Forces

The aerodynamic loading on a structure is the combined effects of atmospheric turbulence, wake excitation and forces associated with structural motion. The quasi-static wind loading can be determined by the following experimental methods [107]:

- Pressure measurements.
- Direct measurement of force spectra.
- Indirect determination of force spectra from response measurement.

Direct measurement of wind pressure usually involves a model with a number of pressure tappings on its exterior surface. Mean forces and moments on the model are determined by simply integrating mean pressure values at numerous locations over the entire model. But to obtain overall fluctuating wind loads, a large number of pressure transducers are required for simultaneous monitoring of pressure fluctuations in order to account for the inhomogeneity of the pressure distribution on the model surfaces.

Reinhold [9] avoided the problem of accumulating a large amount of data from each pressure tapping location by performing an analogous summation of the transducer output signals to obtain a signal which represented the resultant fluctuating load.

Kareem [29] and [107] adopted a different approach which required a limited number of transducers to measure pressures at various levels throughout the height of the model building. By monitoring the relationship between pressure at various levels, he subsequently developed an expression for the integral wind loading function through statistical integration.

On the other hand the direct force measurement approach is based on the assumption that the model loads are independent of the dynamic characteristics of the model being only a function of the wind structure and aerodynamic shape of the building.

In order to obtain a reliable measurement of fluctuating forces and moments on a stationary model mounted on a force balance, the resonant frequency of the entire system must be higher than any expected forcing frequency and at the same time the transducer should have a high sensitivity. Whitbread [108] developed such a system using carbon fibre reinforced plastic model and semi-conductor strain gauges. More recently, Tschanz [109] designed a five component high sensitivity, high frequency force balance for measuring quasi-static forces on rigid foam model of buildings.

An alternative approach is to use low frequency models and to determine wind load spectra by measuring the response spectra and appropriate mechanical admittance functions. The main difficulty is that the dynamic properties of the model, such as the damping, have to be known exactly.

The model-balance system used by Saunders and Melbourne [45] in their investigation of tall building response to cross-wind excitation is a typical example. This inverse approach was also adopted by Evans and Lee [110] and [111] in designing their one component balance for measuring the base bending moment on rigid models. The unique feature of their design is that the frequency and damping of the model-balance system could be varied independently. The typical dynamic response of a model-balance combination is shown in Fig. 3.14.

For the present study, the decision to use the elastic force balance columns at the model design stage had dictated the choice of experimental method to measure the wind loading. In fact, with vortex shedding considered to be the main cause of instability, the inverse approach is believed to be the most precise way of characterising the required mode generalised spectral density function. One significant advantage of the resonance testing method is that the model-balance system acts as a well characterised mechanical amplifier in which the useful signal is amplified by the mechanical resonance factor but in which the system noise remains

unaffected, thereby increasing the signal to noise ratio by up to 2 orders of magnitude [110].

3.5.1 Description of the Strain Gauges Force Balance Column

As mentioned earlier, a strain gauged, column type dynamometry system was used here to measure the mean and fluctuating forces and moments acting on the model. The basic principles of a strain gauged dynamometer and torquemeter are explained briefly in Appendix B.

The design and construction of the force balance columns were all carried out at the Department of Aeronautics. The column had a general appearance of a circular cross-section shaft. The analysis of the two lateral forces and one torsional moment was carried out at three different sections. The balance column, without the base plate and other accessories, is shown in Fig. 3.15.

The column had two cut-outs which served to analyse the two lateral forces and which were separated by a distance L . These cuts left a square-section column at the centre and four thin sections at four equidistant positions. These thin strips gave a form of elastic linkage and served to limit the column's deflection whilst increasing the strain gauge signal. Strain gauges were bonded to the faces of the four thin strips with their foil grid parallel to the column axis. The gauges were connected together to form two full Wheatstone bridge circuits and their output unbalance potentials were proportional to the resultant forces in the two lateral directions.

To determine the applied twisting moment, four other strain gauges were bonded to the four sides of the hollow square near to the column's top end. The gauges were placed mutually at right angles to each other and at 45-degrees to the shaft axis. The hollow square had a much smaller cross-sectional area than the shaft and therefore had a larger strain, giving higher sensitivity. Fig. 3.15 shows the sectional views of the cut-outs, the hollow square and the placing of the gauges on its four faces.

The strain gauges used in the present balance transducer system are the TINSLEY linear foil gauges type (8/350/E/C) which has the dimensions of 6.2x3.7 mm and a nominal resistance of 350 ohms. To avoid any possible damage to the assembly from any external disturbance, the gauges, their terminals and the cables connected with the terminal socket were all covered with silicon rubber after completion. Furthermore, the two cut-out regions and the hollow square were shielded by two movable protective covers, see Fig. 3.16.

In assembly, the machined shaft itself was mounted on top of a 0.18 m diameter steel disc via a concentric fixing stud. This fixture was further reinforced with a circular shaft support collar which in turn linked both the shaft and the flange together through four socket head set-screws. During assembly, alignment between each component was checked carefully to ensure that the strain gauges were lying in the planes of the principal axes.

The disc attached to the shaft had a small recess in its under surface which matched a spigot on the upper surface of a similarly sized back disc. This latter was in turn fastened to the foundation. There were 36 equi-spaced holes drilled around the disc circumferences. Therefore, by relocating the fixing screws, the whole model-balance assembly could be rotated to any direction at 10-degree intervals. The balance column was linked with the aeroelastic model by a fixture which is illustrated in Fig. 3.11.

With the top pieces and base discs attached at both ends, the resulting balance column weighs 14.65 kg and is 0.758 m in length. The complete column assembly used for all wind tunnel tests is shown in Fig. 3.16.

Because of its configuration, it is apparent that the mechanical properties of the balance column are identical in all translational directions. However, in order to distinguish the measured bending forces from each other, it is assumed here, unless specified otherwise, that the direction which is parallel to the longer axis of the attachment plate is lateral (i.e. y-direction), see Fig. 3.16 and 3.17.

Static calibration of the balance in both bending directions was obtained by a simple dead-weight pulley system with the balance assembly mounted in a vertical location. Fig. 3.17 shows the amplified strain gauge bridge outputs with loads applied at the tip of the column and at the tip of the aeroelastic model where mounted on top of the balance column. These results illustrate that outputs from the dynamometry are effectively independent of the point of application of the force.

The bridge outputs from the two other bridges are also shown in Fig. 3.17. It is apparent that the mechanical interaction between each gauge set, at least under static loading condition, is negligible small. The static stiffness of the column alone measured in the longitudinal and lateral directions were estimated to be 82 kN/m and 109 kN/m, respectively.

The torque meter was also calibrated with a dead-weight linkage system, but with the balance assembly mounted in a horizontal position. The test arrangement and the amplified strain gauges outputs are shown in Fig. 3.18. The relatively large output from the bridge sensing the force in one lateral direction was due solely to

the weight of the applied loads. The results from the other gauges confirmed the mechanical interaction between each set was small.

3.6 Support Structures

Ideally, the mounting on which the model-balance assemblies stood should be heavy and rigid, so that no motion could be induced through the foundation on one due to the motion of the other. But in practice, the confined space under the working section and the obstruction of other structures had restricted the weight of the support structure. And the final design was constructed in such a way that it could be dismantled or moved if necessary.

The choice adopted here is a space frame structure, as shown in the isometric view in Fig. 3.4. Basically, it comprised two bolt-jointed frames fabricated from 76.2 mm angle pieces. They were linked to each other by several cross members and a 10 mm thick steel plate on top. This top plate also served the purpose of a platform on which the model-balance assembly was mounted. The whole frame structure was bolted to the concrete floor by four foundation bolts along each side.

Two platform plates were prepared, one is 0.23x1.04 m, and the other is 0.36x0.61 m. The longer one was used mainly for cases when the models were arranged in tandem or staggered configurations, whereas the other was for single model or parallel configuration tests.

3.7 Instrumentation

The previous sections have dealt with the reasons behind the choice and design of the wind and structure models. In this section, the various instruments, and their applications in the present work, are briefly discussed.

3.7.1 Dynamic Pressure Measurement

The dynamic pressure in the wind tunnel test section was normally determined by a pitot-static probe which was mounted horizontally on the tunnel side wall and at a position near the working section entrance. The probe was connected to a Furness MDC FC002 micromanometer which had a total pressure range of 10000:1 to an accuracy of 1% in any range, or an absolute accuracy of $\pm 0.49 \text{ N/m}^2$ under steady condition. A digital read-out of the dynamic pressure (in terms of mm H_2O) was also available on the instrument.

In the present data acquisition system, the differential voltage output signal from the micromanometer was amplified by a low-drift operational amplifier before being transmitted to the sample and hold unit (which is described in the next chapter). The output from this amplifier circuit was calibrated against the dynamic pressure as read on the digital display. For simplicity, a linear fit was performed on the data, as shown in Fig. 3.19. The net accuracy of the dynamic pressure measurement was estimated to be $\pm 0.95 \text{ N/m}^2$.

During measurement, the output from the micromanometer was continuously sampled via the A/D convertor. The digitised values were stored on disc as were the inputs from other instruments. In the subsequent processing (whether it is on-line or off-line), the time-averaged flow velocity was determined from the recorded data. The resulting mean flow velocity was then stored in the run information buffer at the beginning of each data file and used for reference purposes, such as the calculation of Reynolds number.

After the installation of the turbulence generation grid, it was found that the pitot-static tube was partially blocked. The solution was to install a second pitot-static tube at the centre of the ceiling turntable. The pressure values measured at these positions showed a difference of less than 1% over the speed range and were therefore considered to be compatible. Fig. 3.19 shows the calibration values measured by the pitot-static tube at the new location, without the turbulence generation grid installed. Due to the blockage effects of the grid, the maximum continuous running wind speed was dropped by one third to about 25 m/s.

3.7.2 Strain Gauge Signal Conditioning

The main purpose of signal conditioning is to boost the transducer output signals to a level that is suitable for processing in the recording equipment. In addition to this, transducers of the strain gauge type also require a separate power source to provide excitation.

For the present work, the measurement of the forces and twisting moments via the force balance columns were performed by the Data Acquisition Ltd. DA 1402 signal conditioning system. This system consists of a stabilised power supply, a monitor unit and six strain gauge conditioning units. In addition to the basic features provided for bridge completion, calibration, energisation etc., each conditioning unit was also equipped with a switchable low-pass filter, over-voltage indication and an add-on amplifier which gives a maximum amplification gain to 10000.

In this set-up, each strain gauge bridge was driven by a constant voltage of 7 volts via the voltage control board in each unit. Amplification of the bridge output signals was performed by the D.C. Differential Instrumentation Amplifier. This amplifier had been designed to provide a 10 V or 50 mA output and a frequency response from D.C. to within $\pm 2\%$ at 20K Hz coupled with high gain and low noise. With an add-on amplifier, each conditioning unit could provide a gain output ranging from 5 to 10000, variable in 6 steps and an offset adjustment of approximately ± 10 V. In order to utilise the full range of the A/D convertor, the offsets of each strain gauge bridge were specifically adjusted prior to every measurement.

To reduce the unwanted noise, the optional low-pass filter was applied to all conditioning units. The plug-in filter board accepted two capacitors, the values of which determined the roll off point for the filter. For the present investigation, the cut-off frequency was set at approximately 100 Hz.

For measuring forces in the translational directions, the gain of each associated conditioning unit was set at 2000. A typical calibration curve showing the outputs of the strain gauge bridges on the model-balance system with force applied alternatively in the two translational directions is shown in Fig. 3.20. For measuring torque, because of the expected low output signal amplitude, the gain was set at 10000. The calibrated output level and estimated net accuracy of the six conditioning units are summarised in Table 3.1.

The bridge balances and offsets were checked frequently, normally before and after every measurement. Except in some cases, their repeatability were good and usually within 5%.

3.7.3 Displacement Measurement

The tip displacements of the tower models were monitored by two accelerometers in each model. They were mounted inside the model with their main axes pointing to the two lateral directions and at positions as near to the top of the model as was practically possible.

The accelerometers used in this investigation were all Bruel & Kjoer piezoelectric type. Three different types of accelerometer were used. There were two miniature size Type 4375 accelerometers which were normally mounted on the downstream model, and two heavier, but more sensitive Type 4339 and Type 4367 general purpose accelerometers. In spite of their sizes, the accelerometers' weight was still very small as compared to the total weight of the model-balance assembly, and should not have altered the dynamic characteristics of the system significantly.

In order to have good dynamic response, the accelerometers were fixed at the models either by steel studs or cement. Furthermore, to ensure that no stray signal was induced in the accelerometer cables by mechanical motion, all internal wiring was taped and properly supported.

For the present measurement, the accelerometers were operated as displacement transducer. The output voltage which they generated was directly proportional to the relative displacement of the pick-up. The amplification and conditioning of these output signals were performed by four individual Bruel & Kjoer Type 2635 charge amplifiers. The 2635 is a four stage amplifier consisting of an input amplifier, low-pass filter amplifier, integrator amplifier and output amplifier. More details can be found in the manufacturer's literature [112].

Calibration of the accelerometer-amplifier system involved two stages. In the first the accelerometer sensitivity, $\mu\text{c}/\text{m}/\text{sec}^2$, was determined by comparing its output with that of an accelerometer of known sensitivity, using a manufacturer provided calibrator. In the second the voltage registered by the A/D convertor was obtained using the reference output incorporated in the charge amplifier. The charge amplifier, according to calculation, had a output sensitivity of 1 mm/V. Finally, the high-pass and low-pass filters incorporated in these amplifiers were set at 1 and 100 Hz, respectively, throughout the tests.

3.7.4 Hot-Wire Anemometry

Hot-wire anemometry is the principal instrument in the measurement of the instantaneous flow velocity. The principle of this technique is based on the convective heat transfer from an electrically heated element to the surrounding fluid. The amount of heat transfer depends on the temperature difference and the geometry of the sensor, as well as on the flow velocity and other physical properties of the fluid. More details on its principles and operation can be found in the literature, such as Bradshaw [113] and Sandborn [114].

For the present work, two types of hot-wire probes were used:

(a) Single-sensor probe.

This is a DISA type 55P11 miniature wire probe. It consists of a single straight wire sensor element placed perpendicular to the probe axis, see Fig. 3.21(a).

(b) Dual-sensor probe.

This is a DISA type 55P61 miniature cross-array probe. It consists of two cross-slanted wire sensing elements, set at 45 and 135 degree angles to the probe axis, see

Fig. 3.22(b).

For simplicity, the hot-wire and its probe body were simply attached to a mounting block which, by means of adjusting the fixing screws, could be moved up and down along a 1.1 m long, vertical laboratory stand. As a precaution, this stand had a heavy base which was stabilised with weights, so that the whole unit was heavy enough to withstand the flow pressure by itself. All adjustments on the hot-wire position had to be done manually.

For measurements in turbulent flow fields with turbulence intensity level less than 20%, it is assumed that the whole flow field can adequately be described in terms of four velocity components, namely \bar{U} , u' , v' and w' , and the simplifying assumptions would give rise to little error in the final result. In general, if linearisation of the anemometer's signal was used, the signal-velocity relationship for the single and cross-slanted wire probe could be summarised as follows [115]:

- For a single hot-wire probe normal to the flow.

$$\bar{U} + \frac{\overline{v'^2}}{2\bar{U}} \approx \bar{U} = \frac{1}{KS} \left[\bar{E} \left(\frac{\pi}{2} \right) - E_o \right]$$

$$u' + \frac{v'^2}{2\bar{U}} = \frac{1}{KS} \left[E' \left(\frac{\pi}{2} \right) \right]$$

- For a cross-slanted hot-wire probe.

$$\bar{U} = \frac{1}{KS} \left[\bar{E} \left(\frac{\pi}{4} \right) - E_o \right] = \frac{1}{KS} \left[\bar{E} \left(3\frac{\pi}{4} \right) - E_o \right].$$

$$u' = \frac{1}{2KS} \left[E' \left(3\frac{\pi}{4} \right) + E' \left(\frac{\pi}{4} \right) \right], \text{ and}$$

$$v' = \frac{1}{2KS} \left[E' \left(3\frac{\pi}{4} \right) - E' \left(\frac{\pi}{4} \right) \right].$$

in which K is a geometry constant, S is a general transfer function and $E(\theta)$ is the anemometer's voltage output from the wire element inclined an angle θ to the flow direction.

The above expressions was based on the assumption that the hot-wire probe was placed in the XY-reference plane. Since the cross-flow velocity component, w' , is usually small, it has been neglected in the above expressions.

The hot-wire energisation and output signal conditioning were usually carried out by the Constant Temperature Anemometer system. The C.T.A. used in the present work was a DISA Type 56C00 multi-channel system, consisting of three C.T.A.

units, three linearisation units, three signal conditioning units and one mean value unit.

Each C.T.A. unit consists of a 56C01 compensating circuit and a 56C16 C.T.A. bridge. The whole unit was designed for use with standard DISA wire probe.

The signal conditioning unit was DISA Type 56N20. It was mainly used for boosting and filtering the measured signals before these were transmitted to the other instruments. The high-pass and low-pass filters incorporated in this unit were set at 1 and 100 Hz, respectively, throughout the tests.

The mean value unit, DISA Type 56N22, was used to measure the D.C. component of the output signals from the C.T.A. units. Because of its great accuracy of measurement, it was also used for the calibration and balancing of the bridges.

The calibration included simultaneous measurements of the mean flow velocity, \bar{U} , and voltage output, E , from the anemometer. Using these two parameters, the constant of the voltage-velocity relationship could be determined. A typical calibration curve is shown in Fig. 3.23.

As shown in Fig. 3.23, the relationship between the anemometer's voltage output and the velocity of flow is not linear. Such non-linearity is generally permissible for measurements having a low degree of turbulence intensity (less than 10%). However where high degrees of turbulence intensity exist, or where two hot-wires are used for simultaneous measurement, then it is necessary to linearise the anemometer's voltage output. The purpose is to avoid any non-linear distortion of the signals and to ensure a reasonable operation.

For linearisation purpose, the general relationship between voltage and velocity is assumed to be given by,

$$E = F(\bar{U})$$

where $F(\bar{U})$ is a general function of the mean flow velocity.

If $\bar{U} = F^{-1}(E)$, then $F^{-1}(E)$ can be considered as a function to describe the relationship between the input voltage and the linearised output voltage.

In the present C.T.A. system, a DISA Type 56N21 lineariser was used to linearise the output signals from the bridge unit before they were transmitted to other units.

In brief, the lineariser implemented the following mathematical expression:

$$y = 10^A + Bx + Ey + Cx + D$$

where A,B,C,D and E are constants and y is the linearised output. Details of the lineariser's principles and functions can be found in the manufacturer's literature [116].

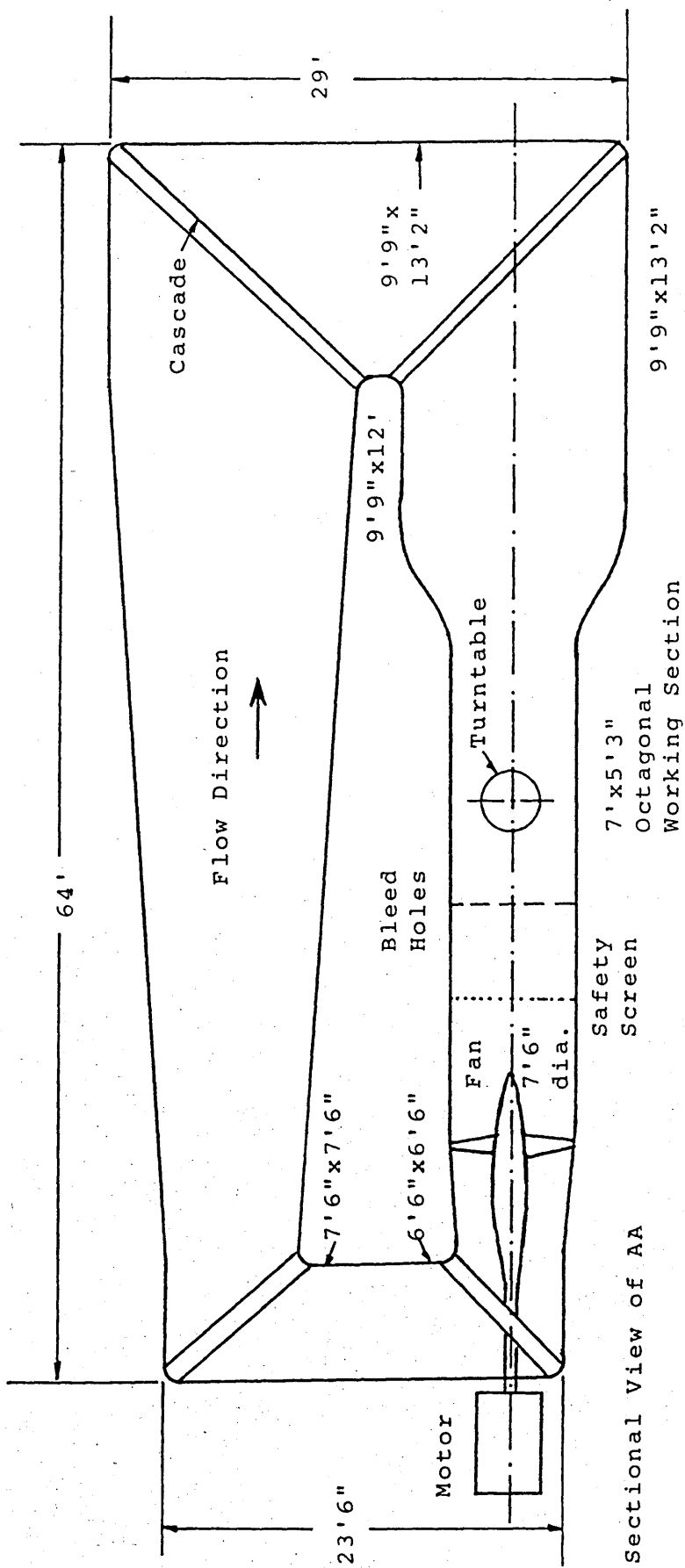
Using the values collected from a previous calibration, these constants were determined by means of an iteration programme and applied to the lineariser through a number of control adjustments. The linearised voltage values showed in Fig. 3.23 is replotted in Fig. 3.23.

In order to utilise the full range of the A/D convertor, the anemometer was usually calibrated to a wind speed much higher than required, i.e. 10 V output for 50 m/s. During measurements, the anemometer was operated at the lower half of its calibrated speed range. The net accuracy of the anemometer in this set-up was estimated to be ± 6.25 mm/s.

	function	mode	twisting moment	x-bending	y-bending
model A + force column balance A (downstream position)	gain setting		10000	2000	2000
	sensitivity		3.053 N-m/V	20.298 N/V	19.002 N/V
	net accuracy/10 ⁻³		7.63 N-m	50.745 N	47.505 N
	stiffness		-----	5.374 kN/m	6.245 kN/m
	natural frequency*		-----		
model B + force column balance B (upstream position)	gain setting		10000	2000	2000
	sensitivity		3.062 N-m/V	19.273 N/V	18.975 N/V
	net accuracy/10 ⁻³		7.655 N-m	48.183 N	47.437 N
	stiffness		-----	5.715 kN/m	5.756 kN/m
	natural frequency*				

* estimated

Table 3.1 Summary of calibration results of the complete model-balance system.



N.B. not in scale

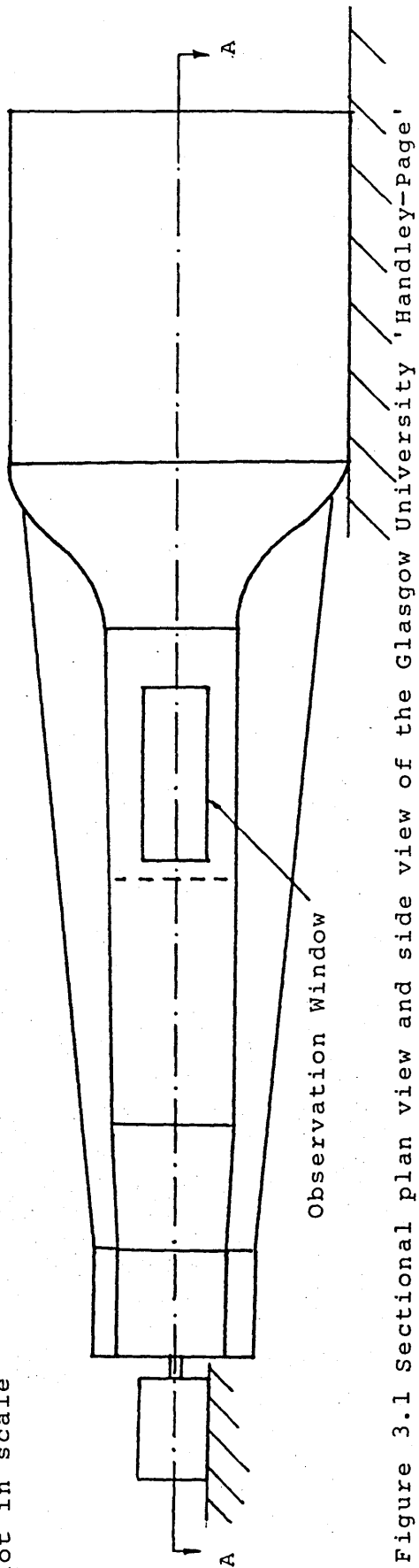
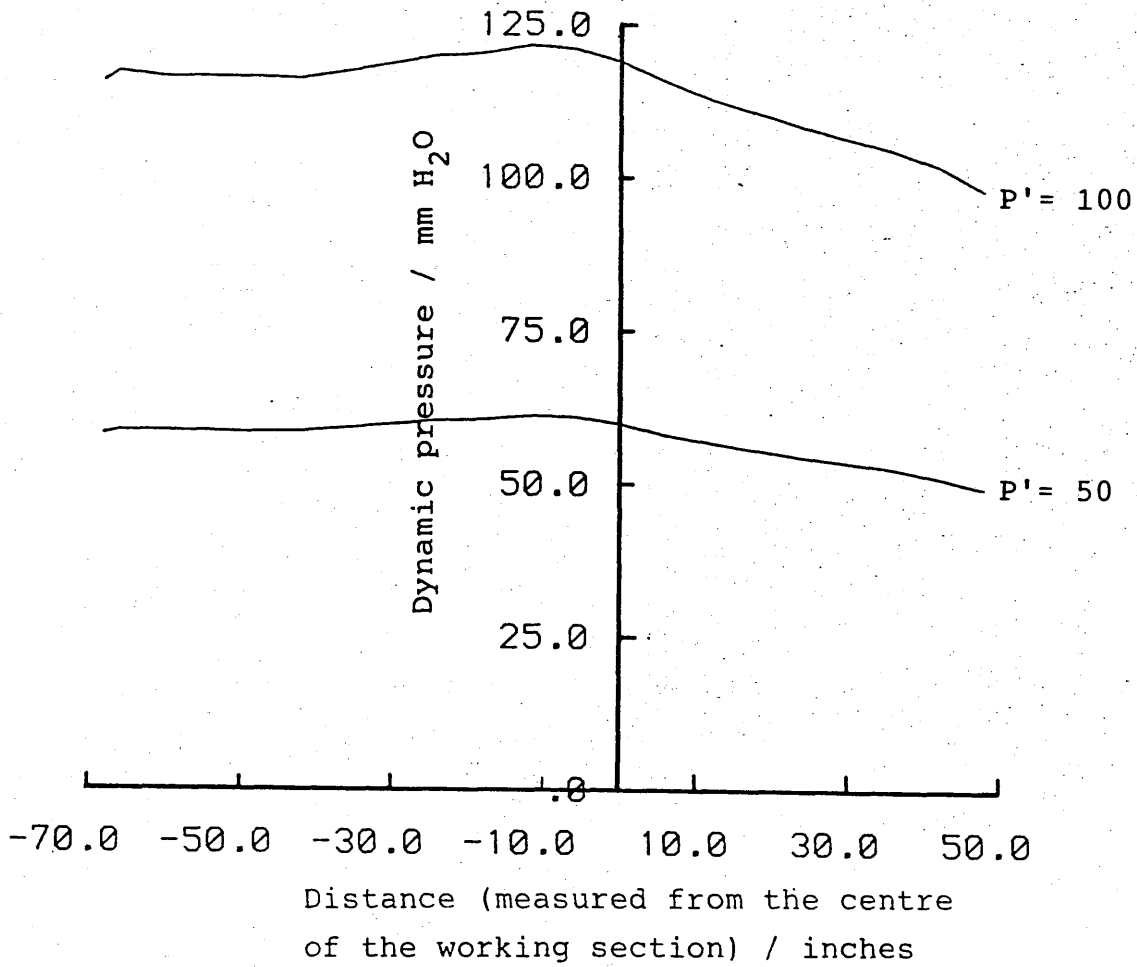
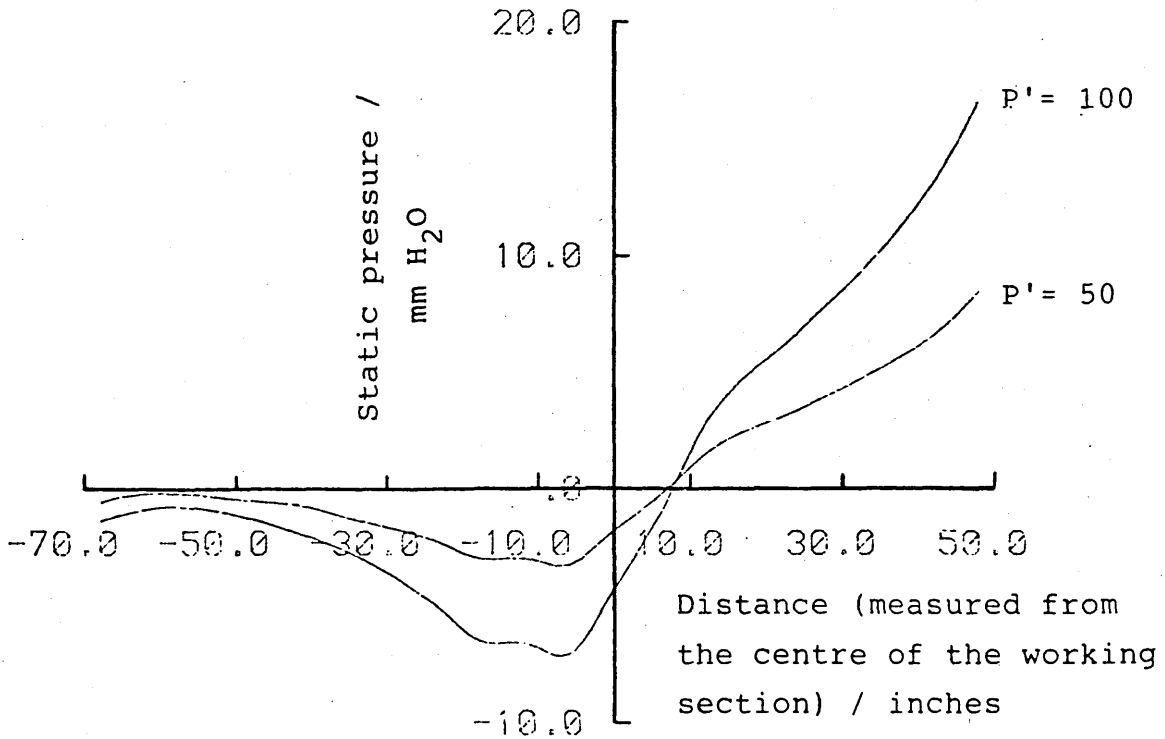


Figure 3.1 Sectional plan view and side view of the Glasgow University 'Handley-Page' 7ft x 5ft3in wind tunnel.

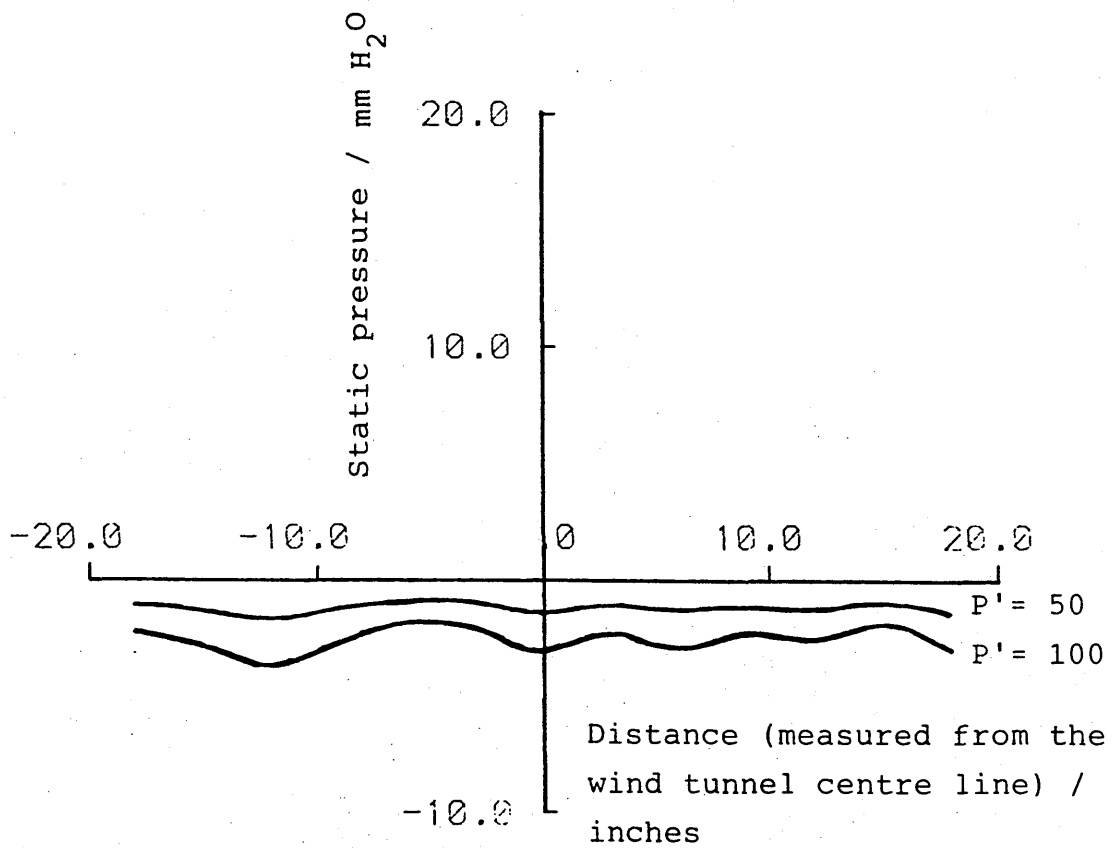


(a) Dynamic pressure vs. distance



(b) Static pressure vs. distance

Figure 3.2 Variation of the (a) dynamic and (b) static pressure measured along the centre line of the working section of the 'Handley-Page' wind tunnel, from Gordon et al. Ref. 101.



Static pressure vs. distance

Figure 3.3 Variation of the static pressure measured across the centre of the working section of the 'Handley-Page' wind tunnel, from Gordon et al. Ref. 101.

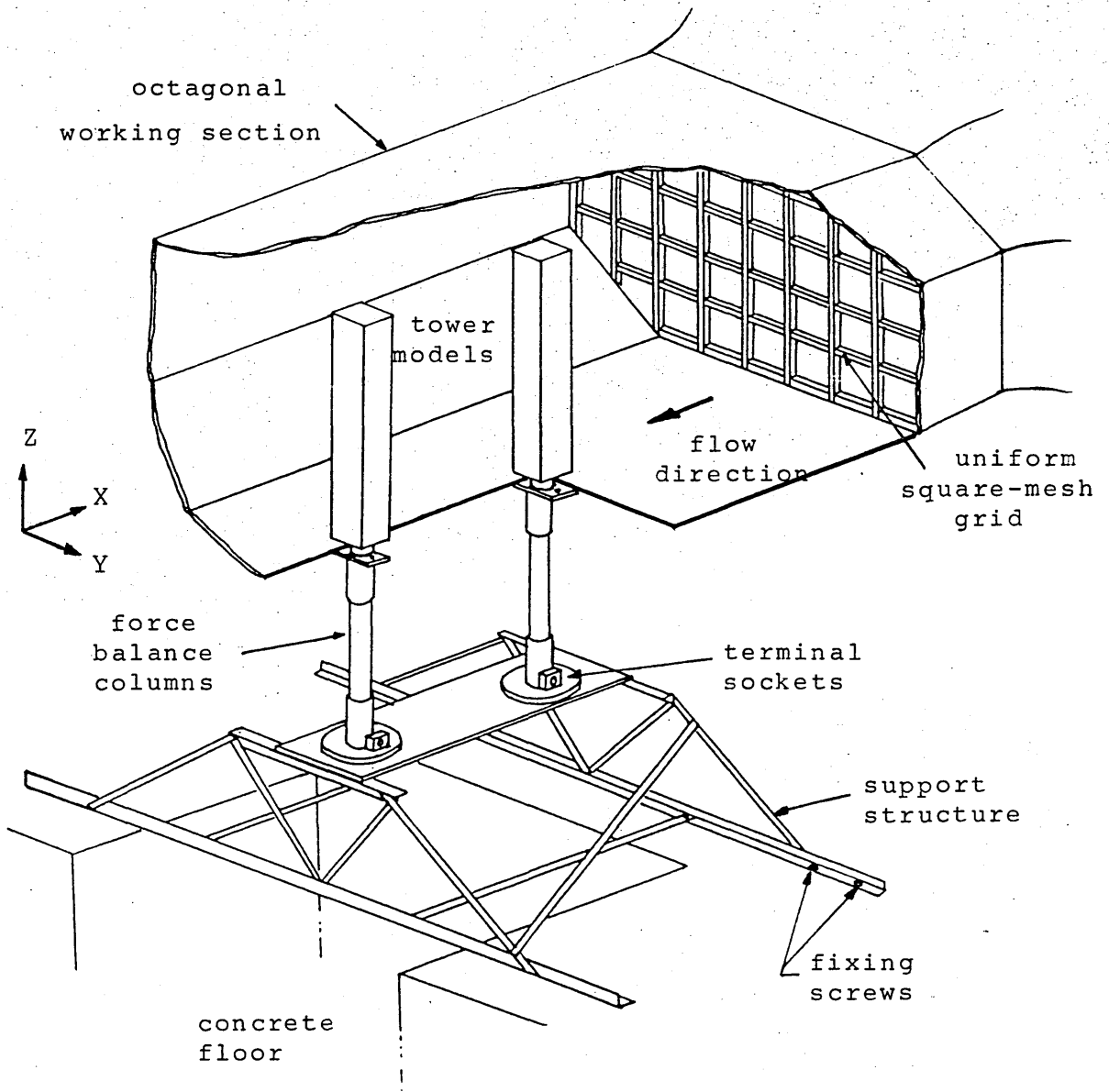


Figure 3.4 An isometric view of the complete experimental set up in the wind tunnel working section.

SYMBOLS

d/m

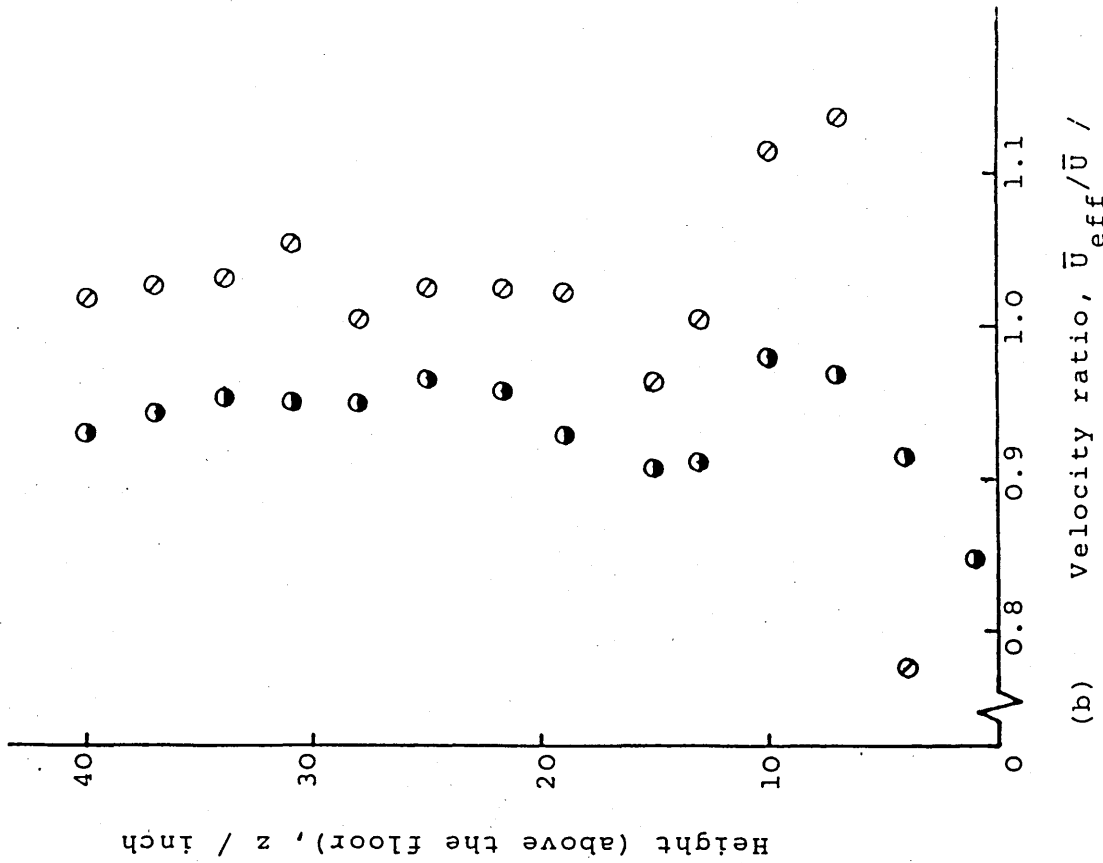
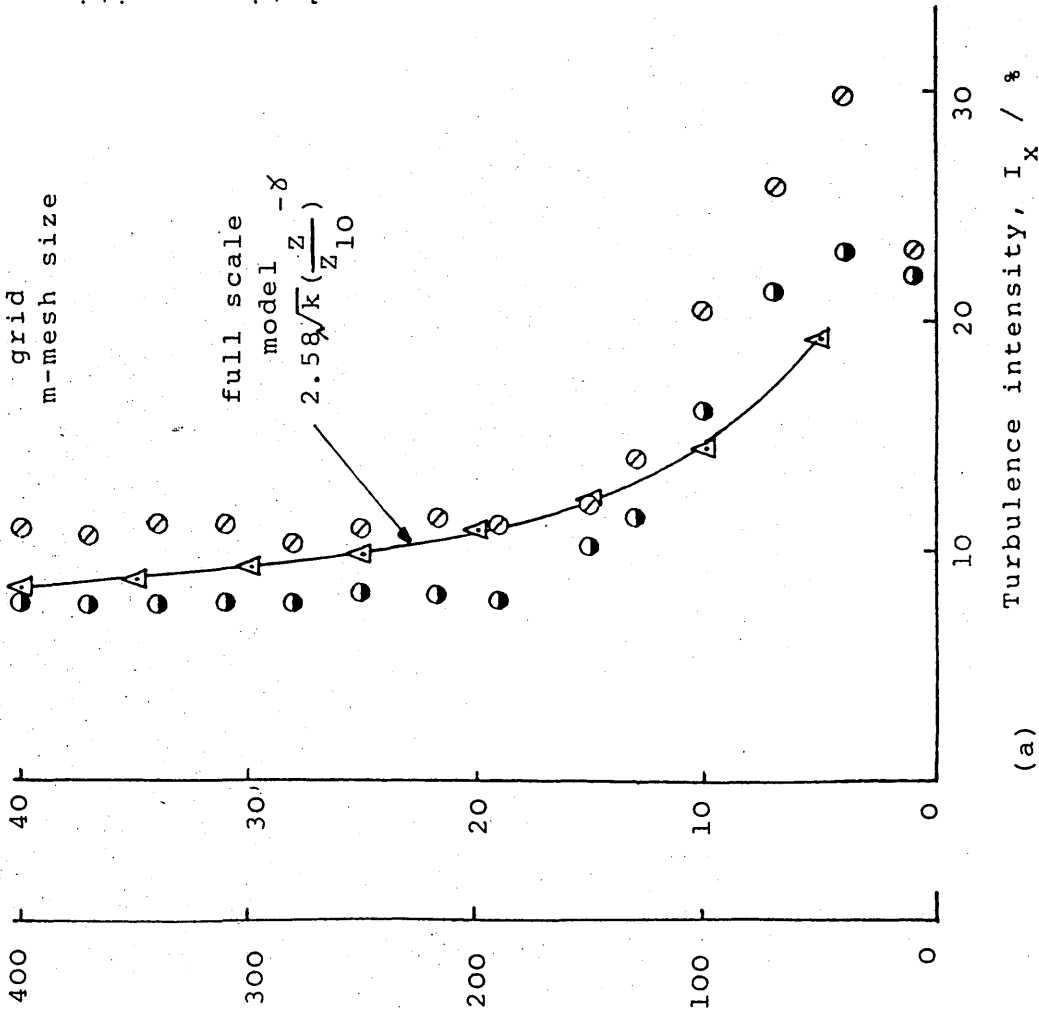
⊙ 6.50

● 9.77

⊙ d-distance from grid
● m-mesh size

full scale /m

model /in



(a) Variation of turbulence intensity and velocity ratio with height at two locations.

(b) Variation of turbulence intensity and velocity ratio with height at two locations.

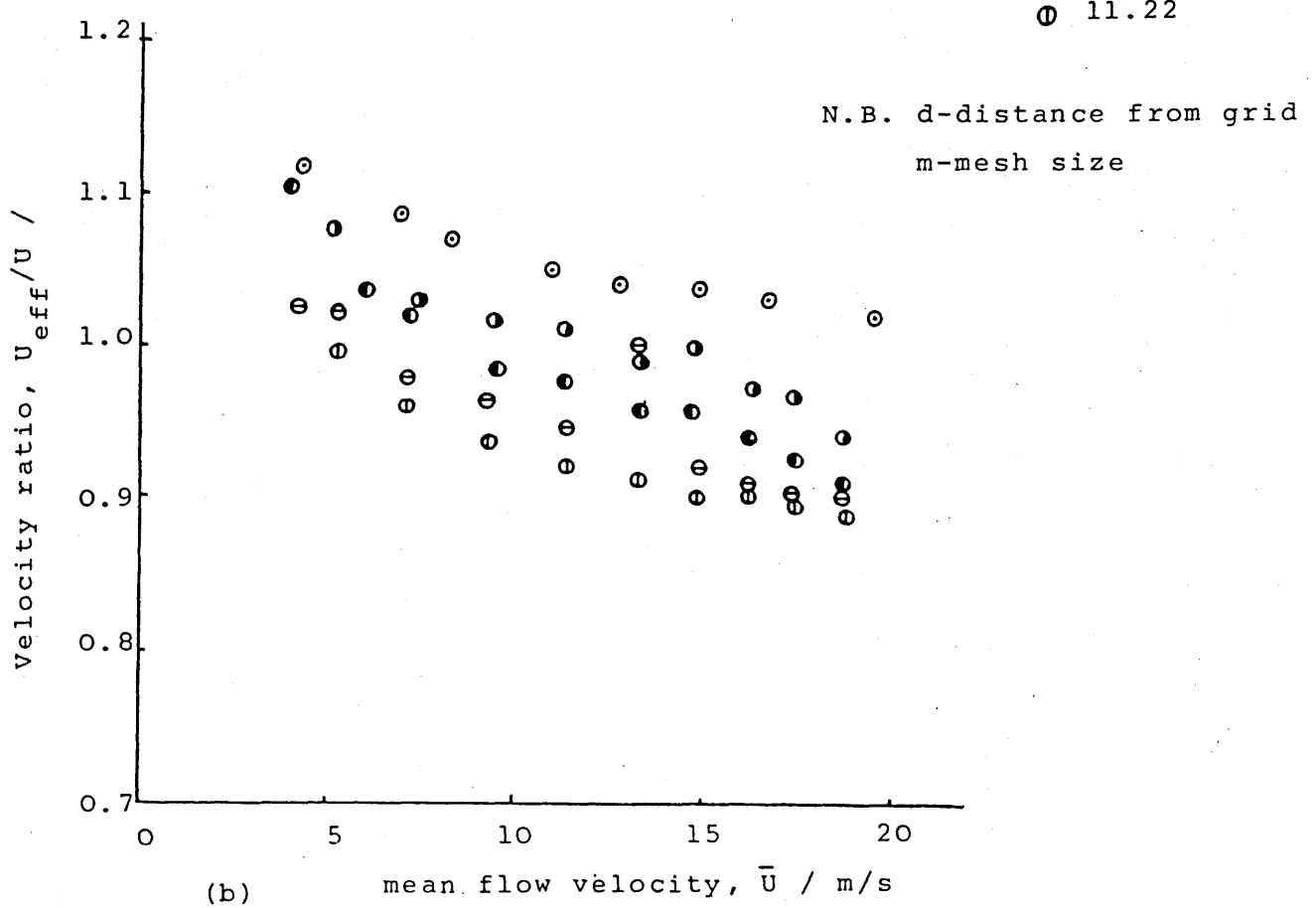
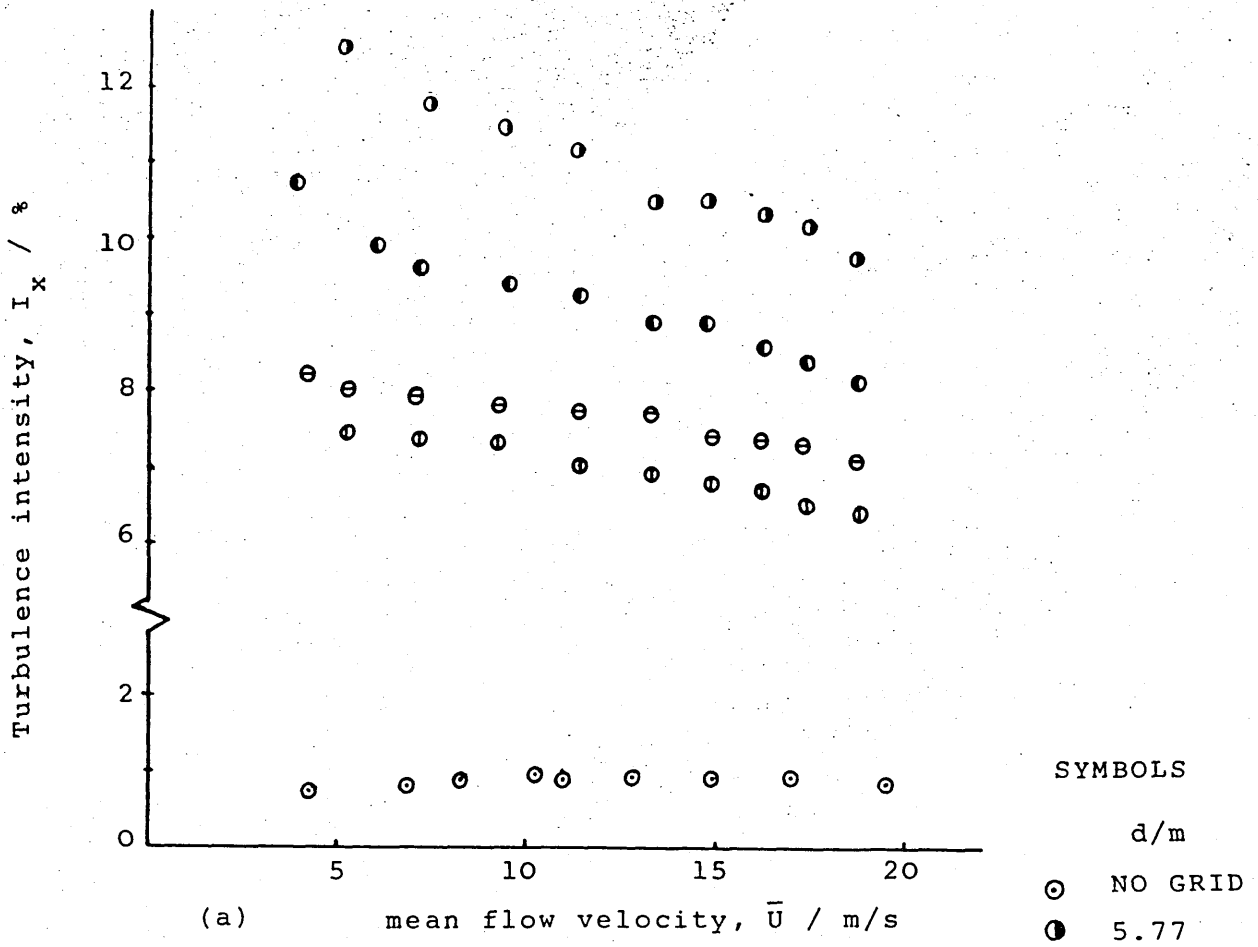


Figure 3.6 Centre-line distribution of turbulence intensity and mean velocity ratio measured at various locations.

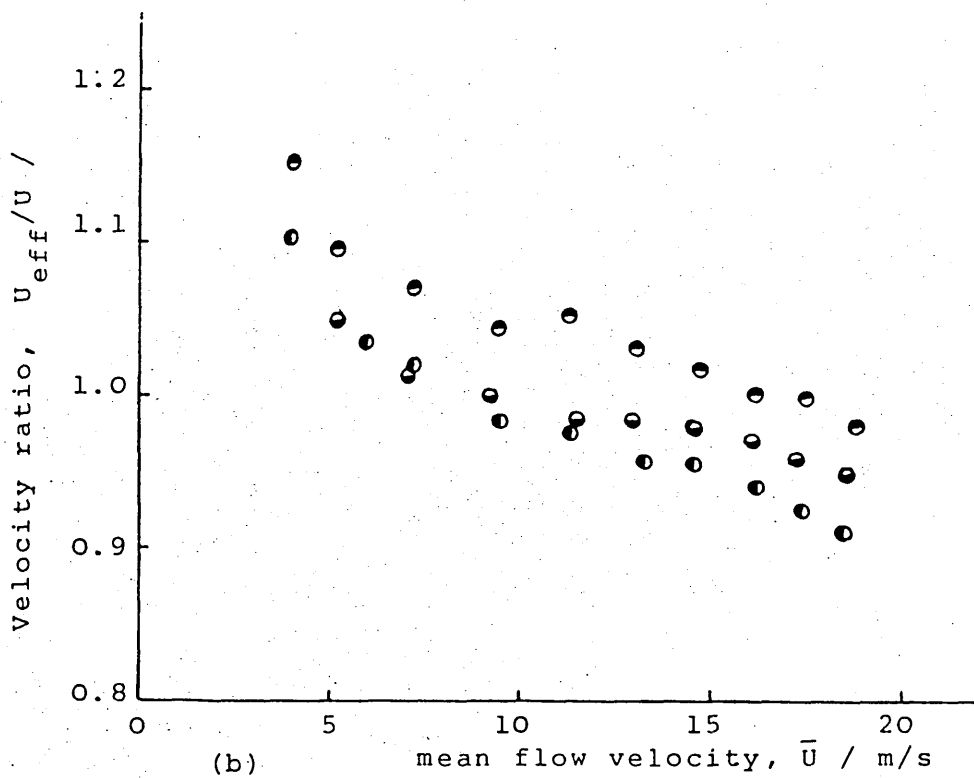
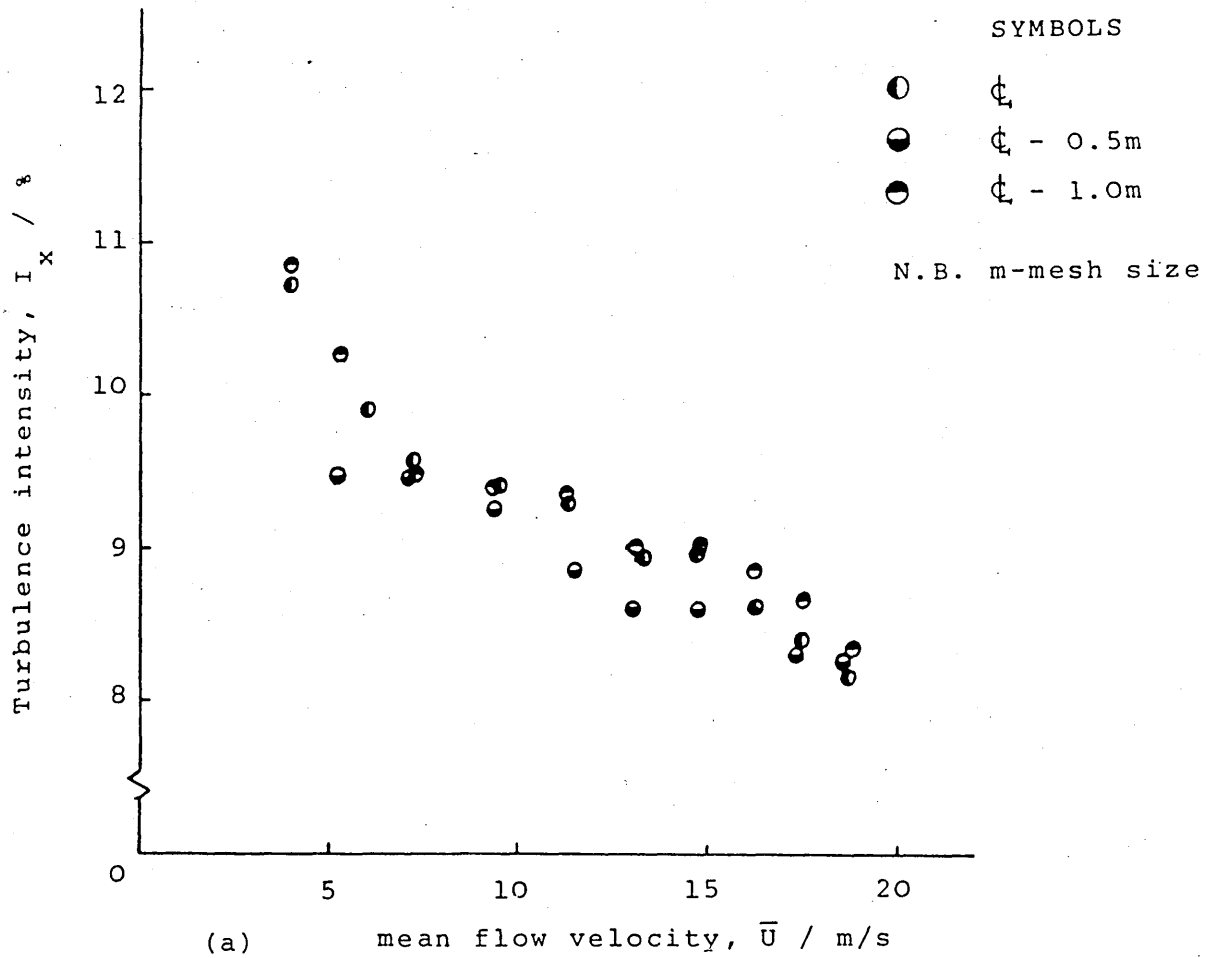


Figure 3.7 Variation of turbulence intensity and mean velocity ratio across the wind flow direction.

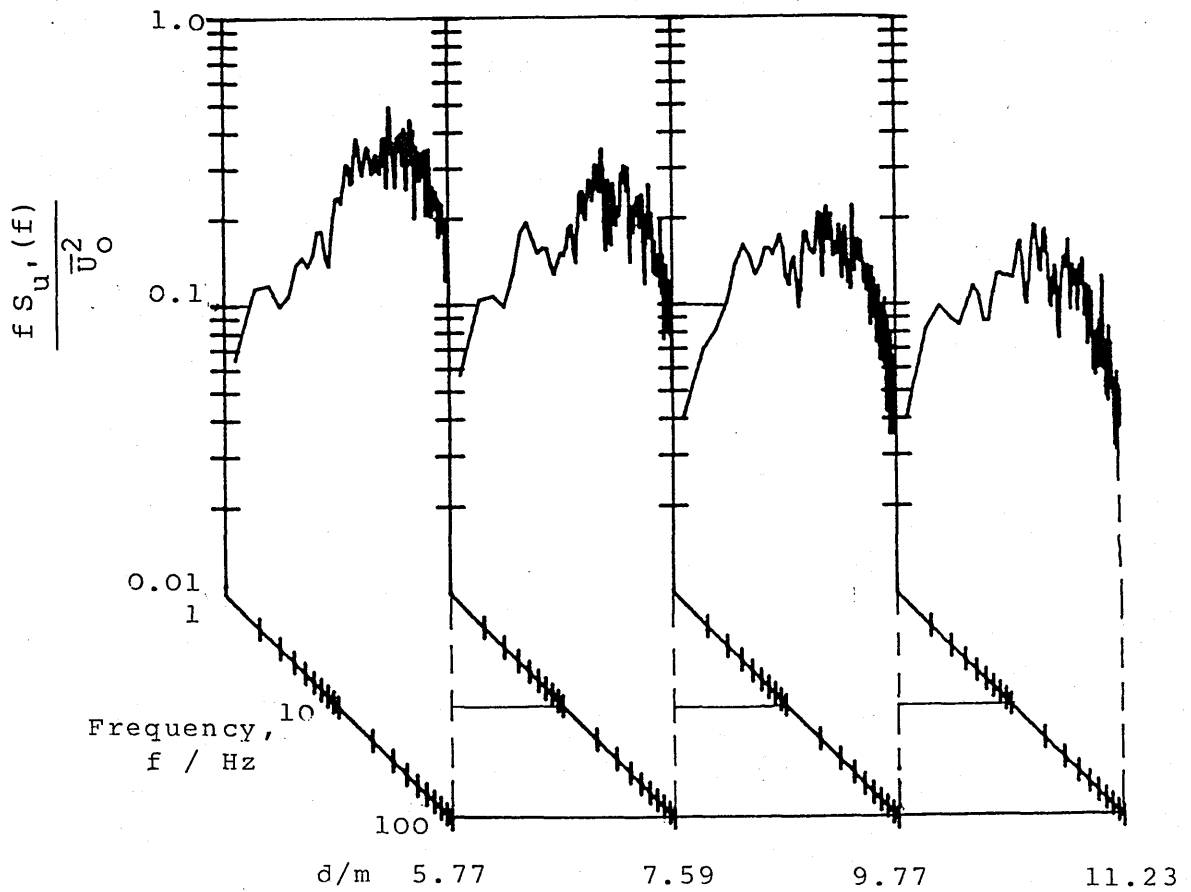
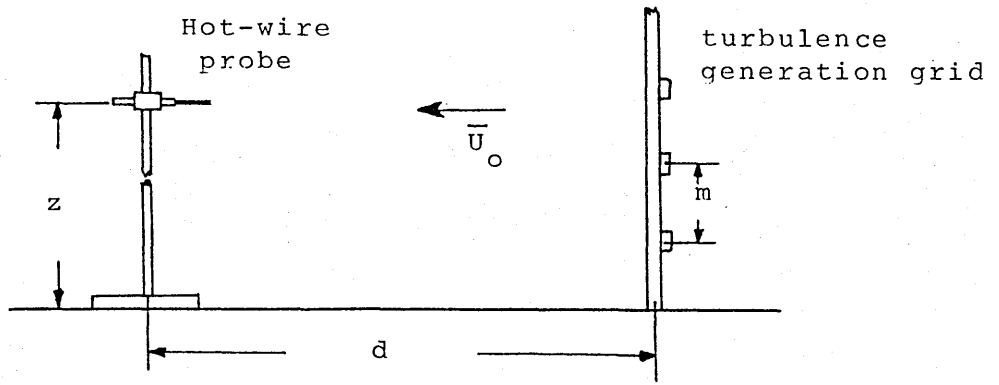


Figure 3.8 Variation of the spectrum of turbulence as a function of longitudinal distance between the turbulence generation grid and the position of the hot-wire probe.

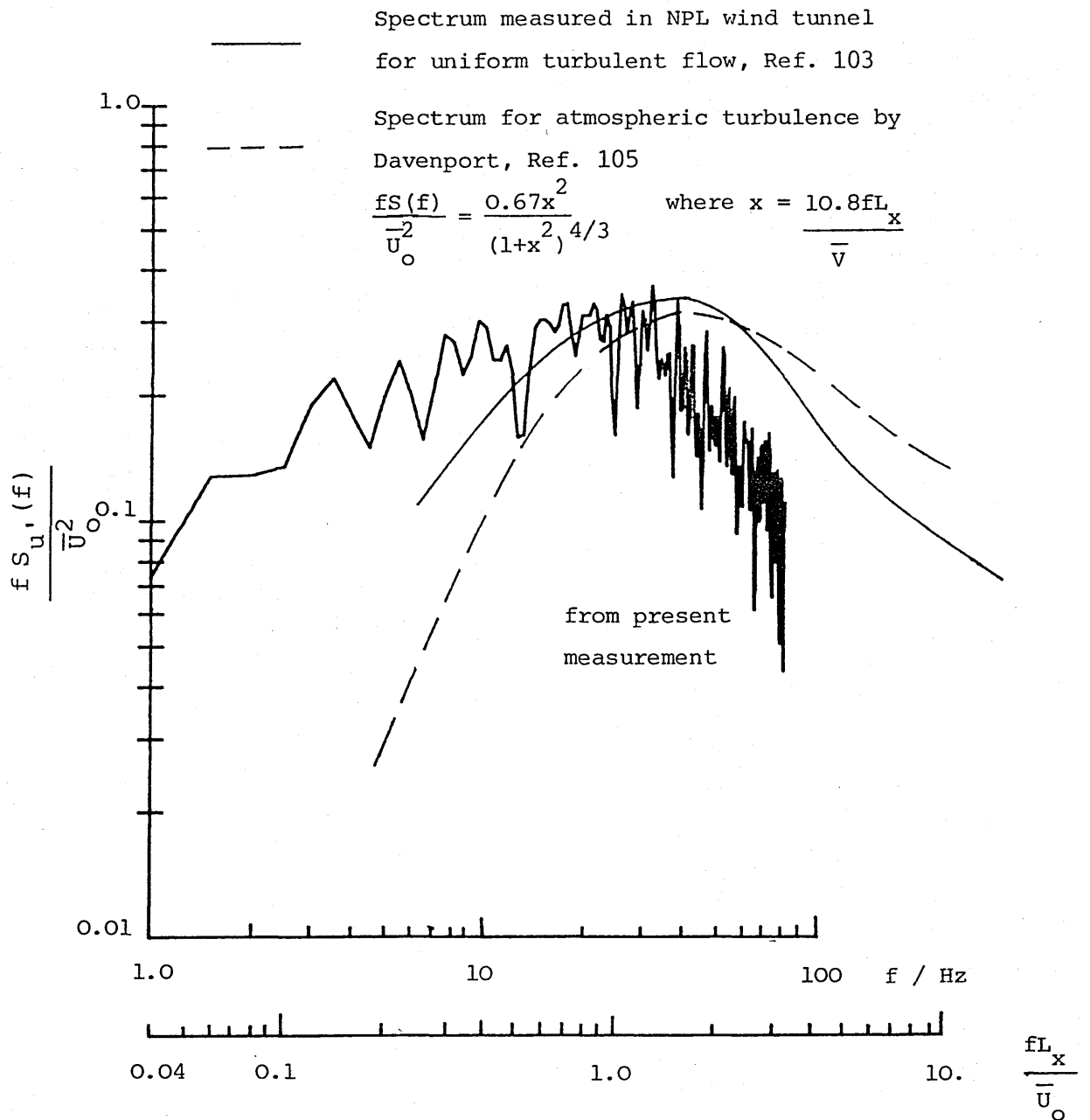


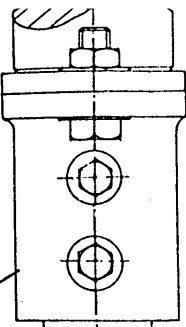
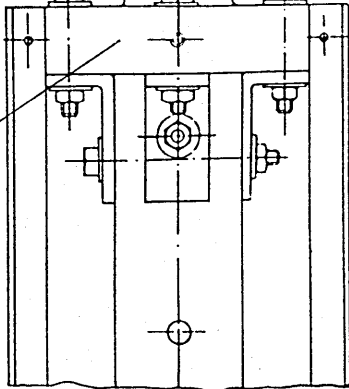
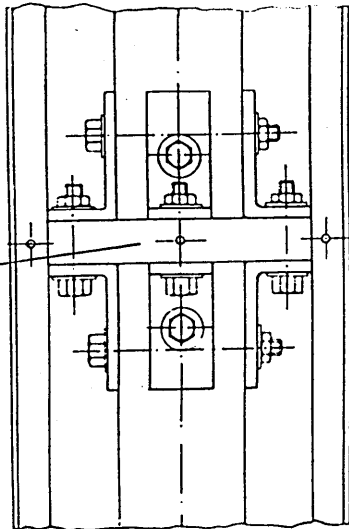
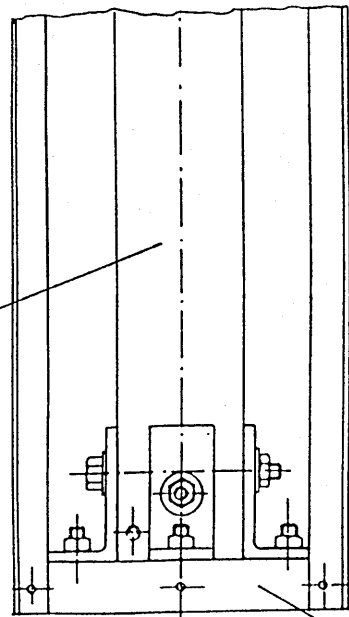
Figure 3.9 A comparison between the spectra of turbulence measured in the Glasgow University wind tunnel, NPL wind tunnel and the theoretical expression proposed by Davenport.

hollow
core section

diaphragm

base plate

split
sleeve cramps

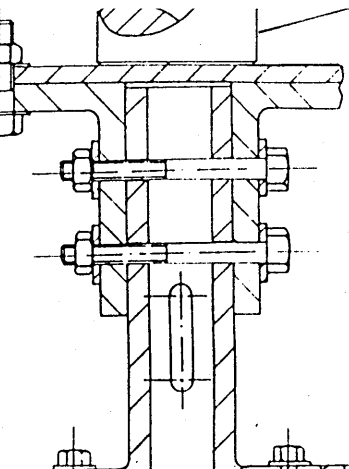
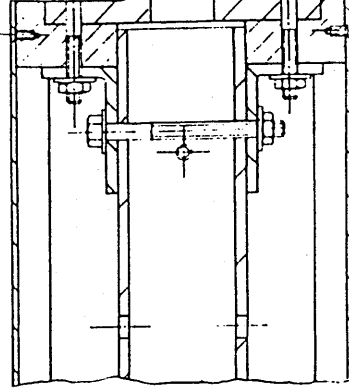
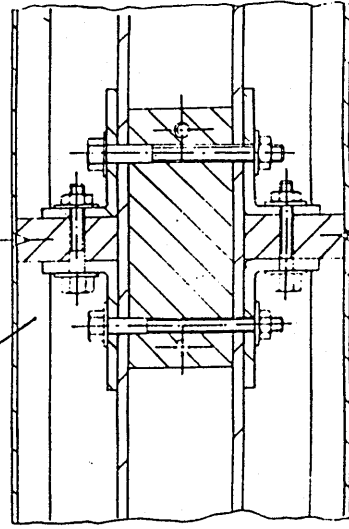
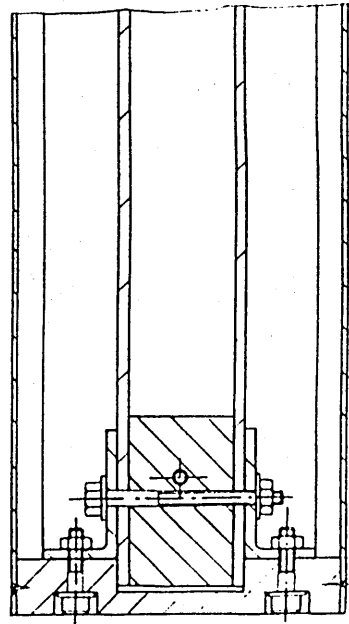


complete model assembly with one panel removed

top plate

flanged
hollow cylinder

stingers



sectional view of AA

plywood panel

force
balance
column

Figure 3.10 An exposed and a sectional view of the complete assembly aeroelastic model.

symbols



x aeroelastic model
= 1.1 (approx.)



+ Perspex model
= .2 (approx.)

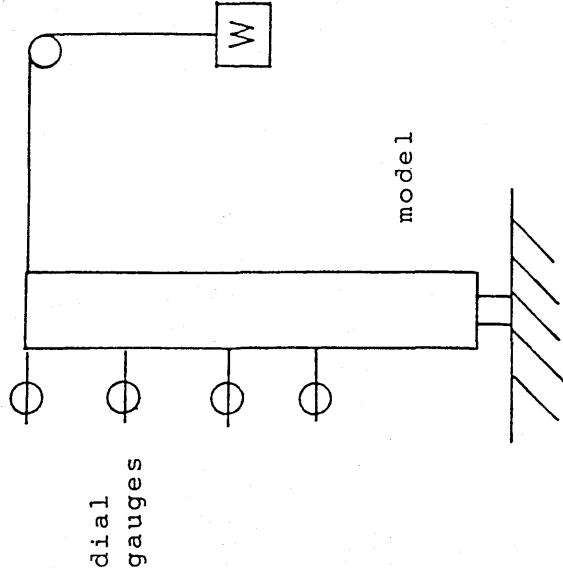
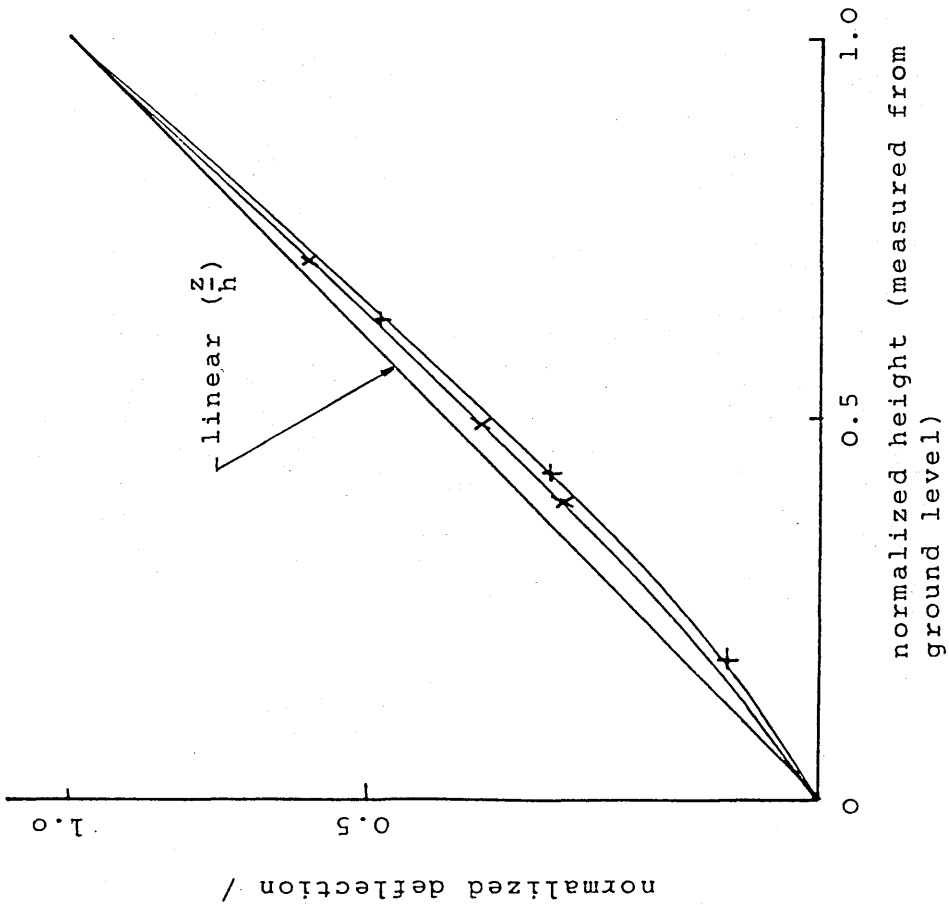


Figure 3.11 Static deflected shapes of the aeroelastic and three-dimensional Perspex model.

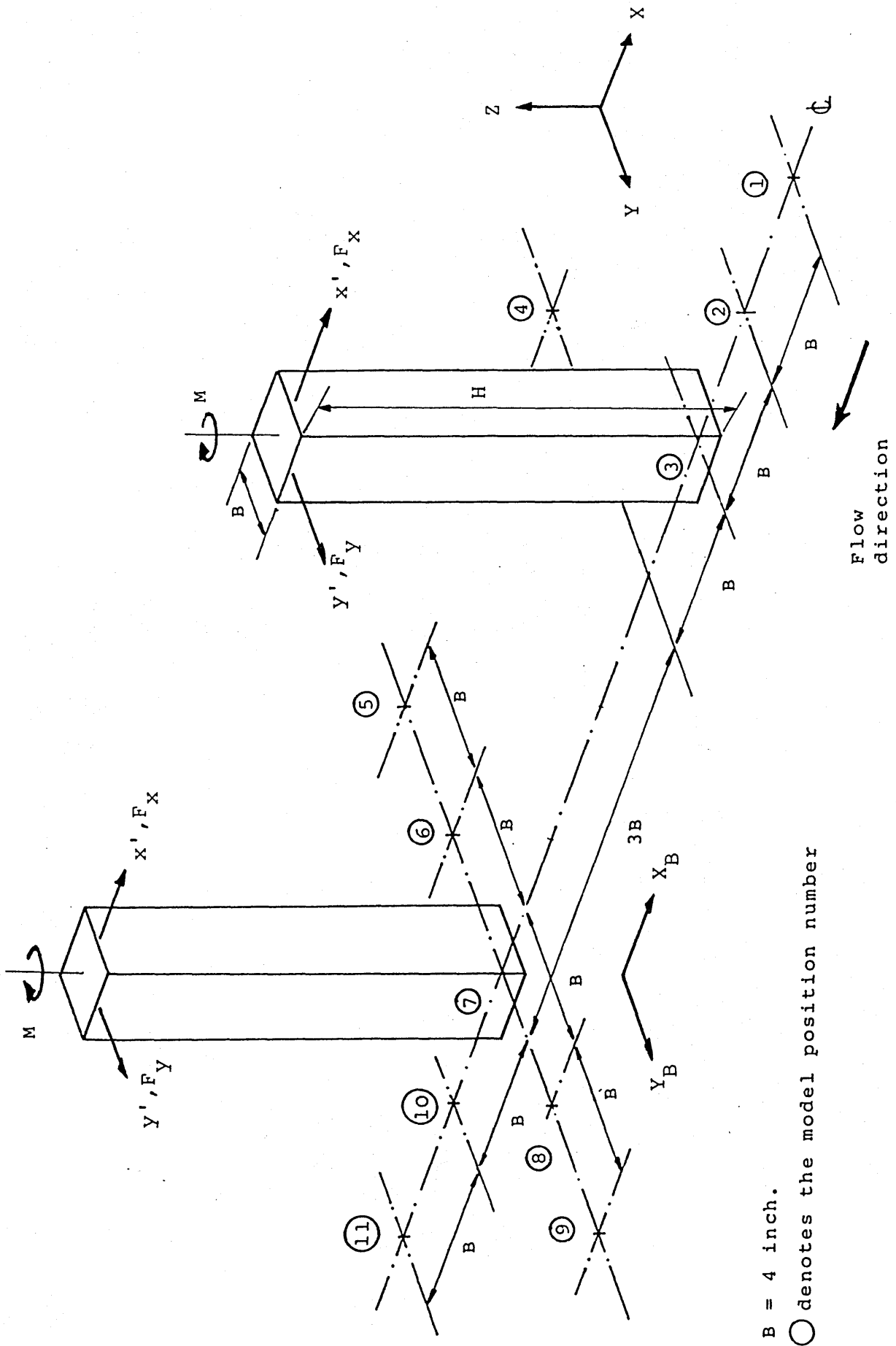


Figure 3.12 Model geometry, spacings and notations with sign conventions used in the wind tunnel measurements.

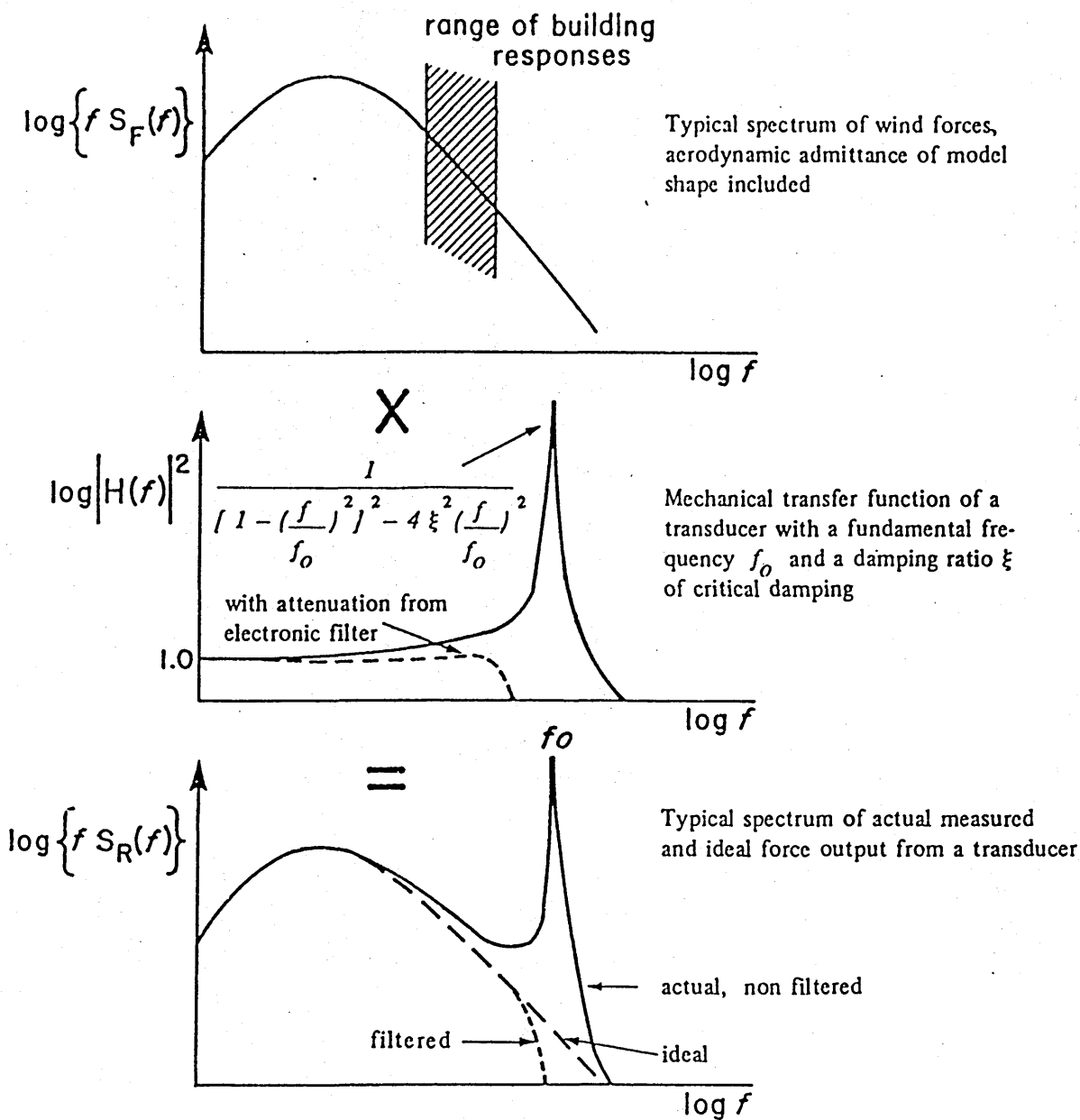


Figure 3.14 Dynamic response of a model-balance combination, from Ref. 109.

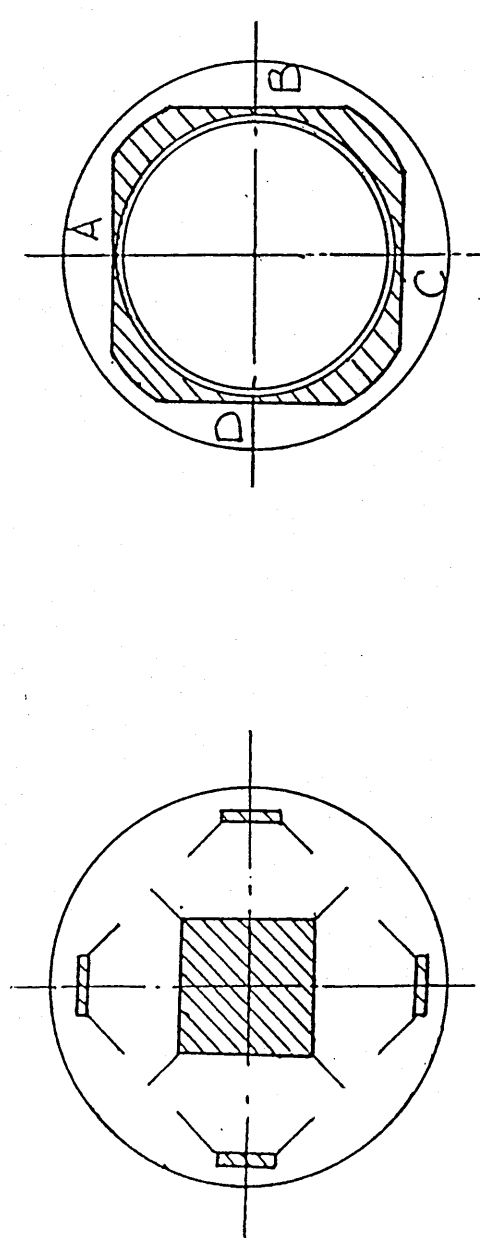
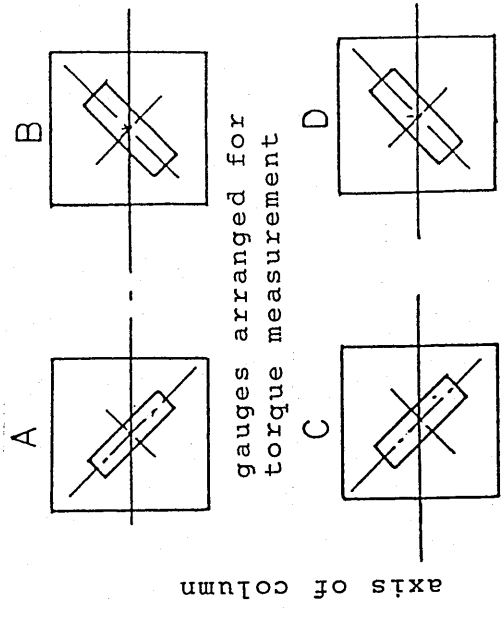
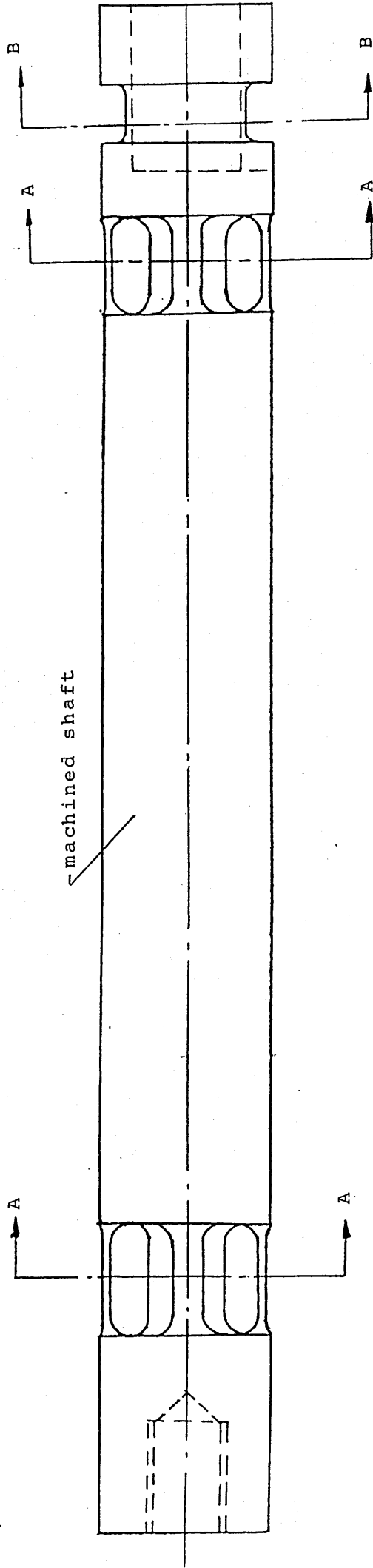


Figure 3.15 An exposed view of the machined shaft part of the force balance column.

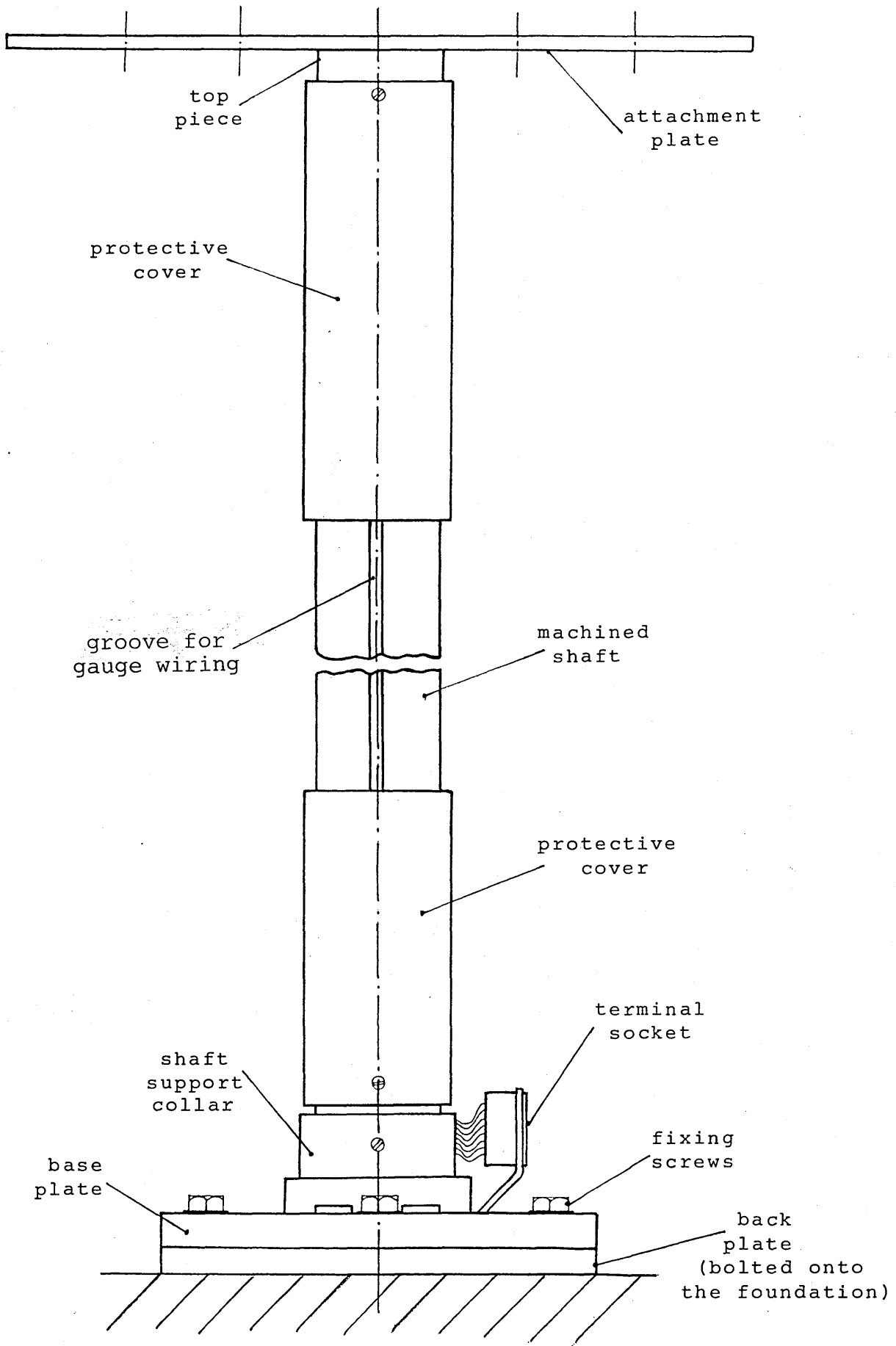


Figure 3.16 A schematic diagram of the complete force balance column.

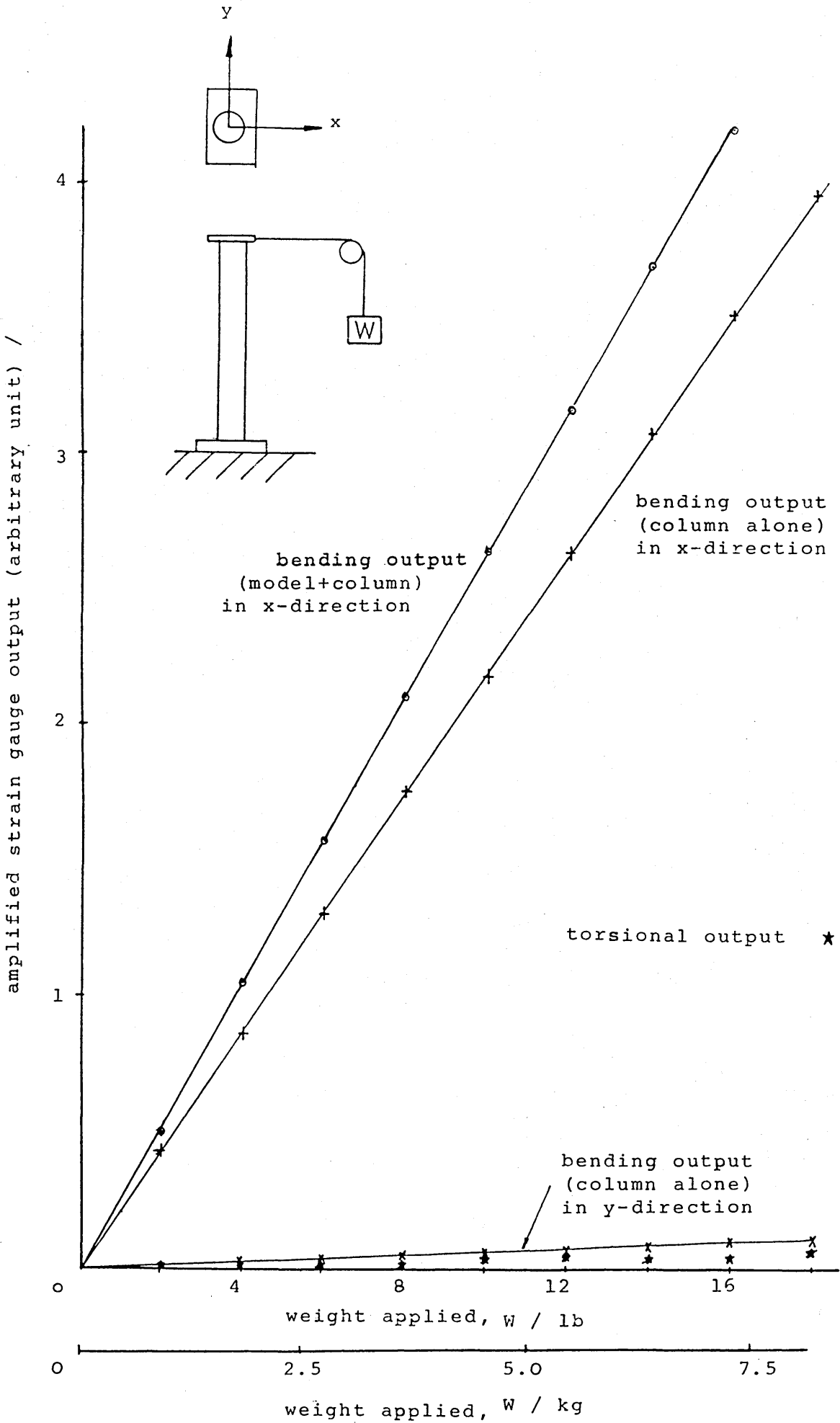


Figure 3.17 A typical calibration of the output from the strain gauge sets with a static force applied.

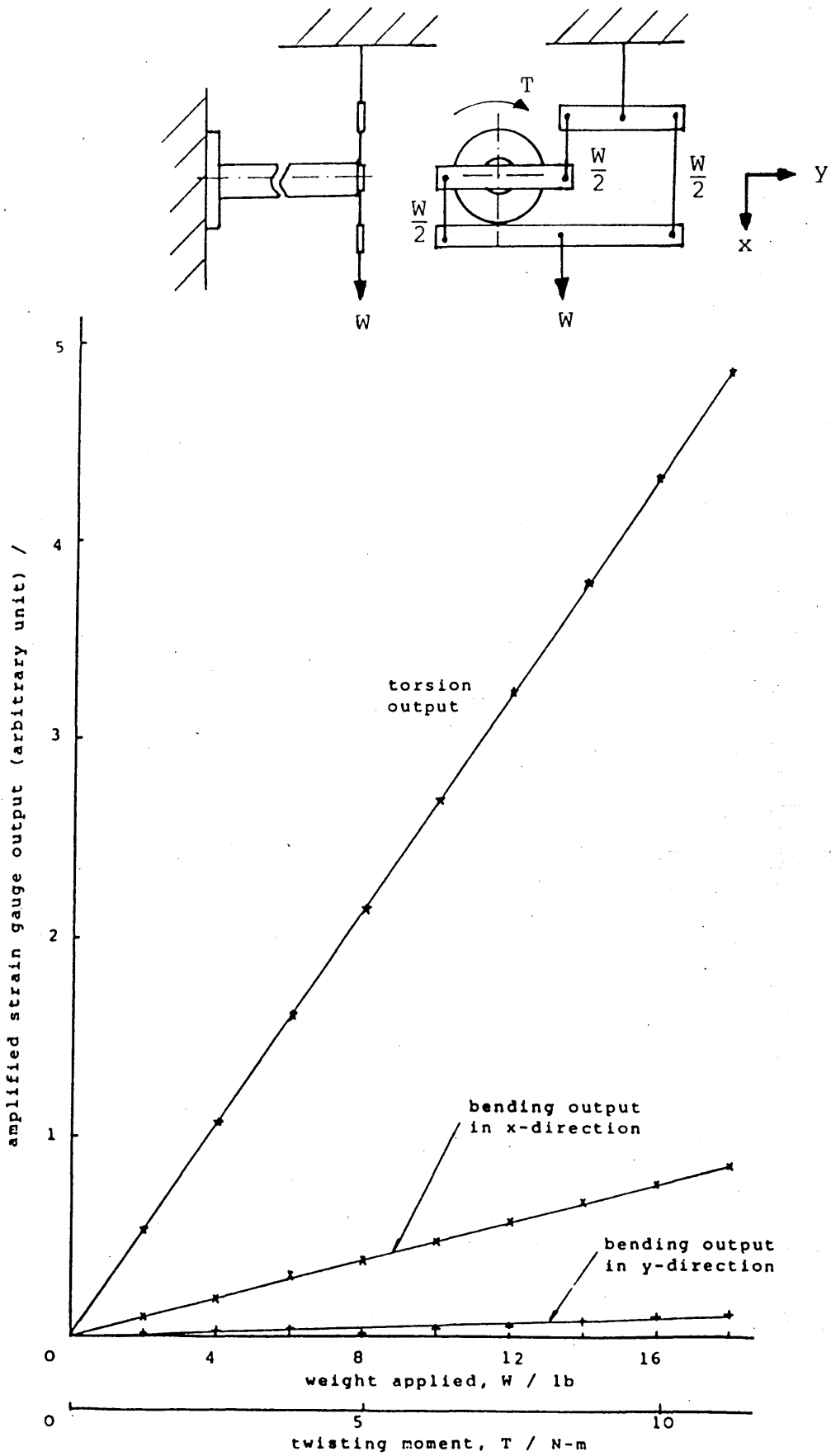


Figure 3.18 A typical calibration of output from the strain gauge sets with a static twisting moment applied.

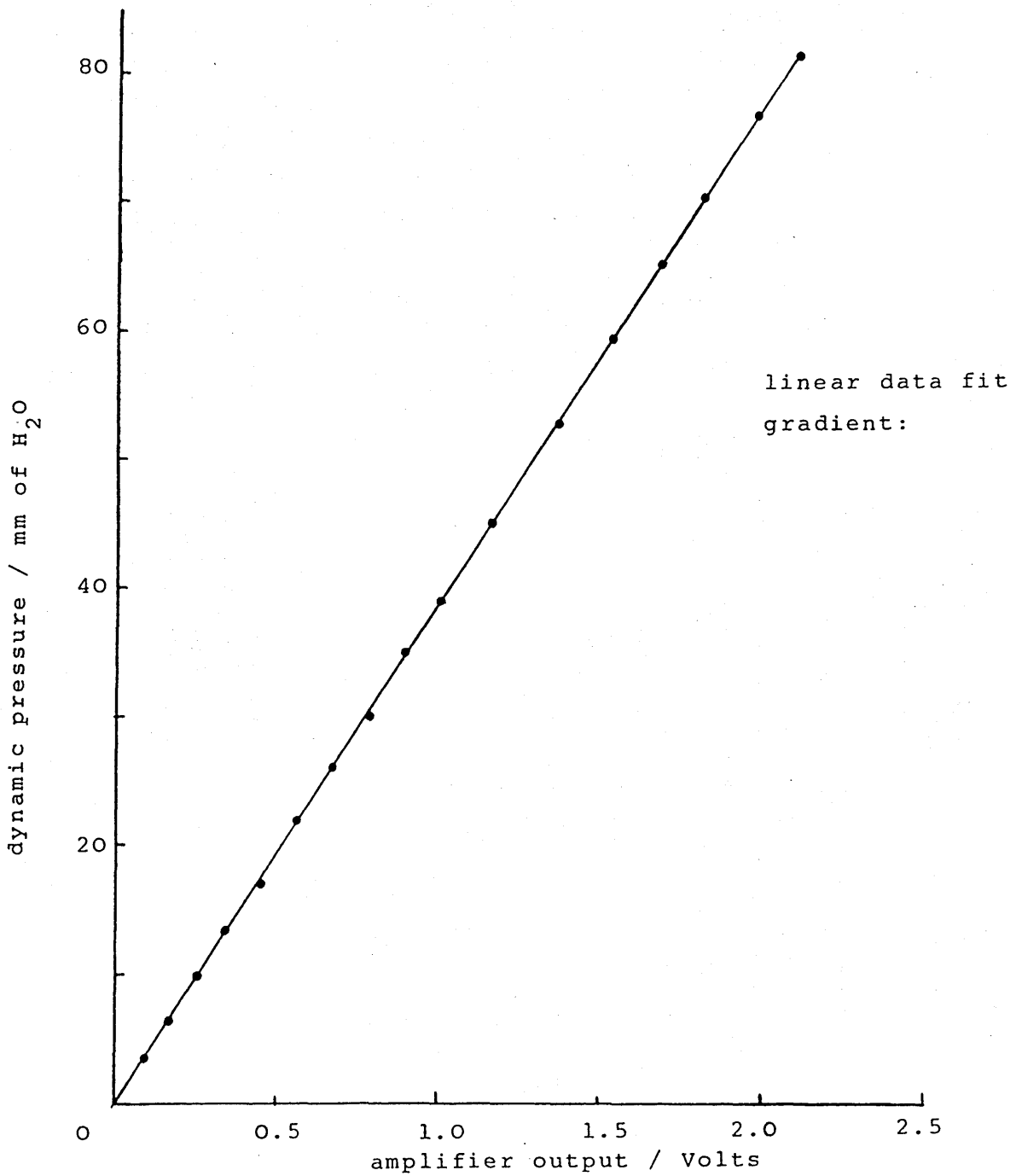
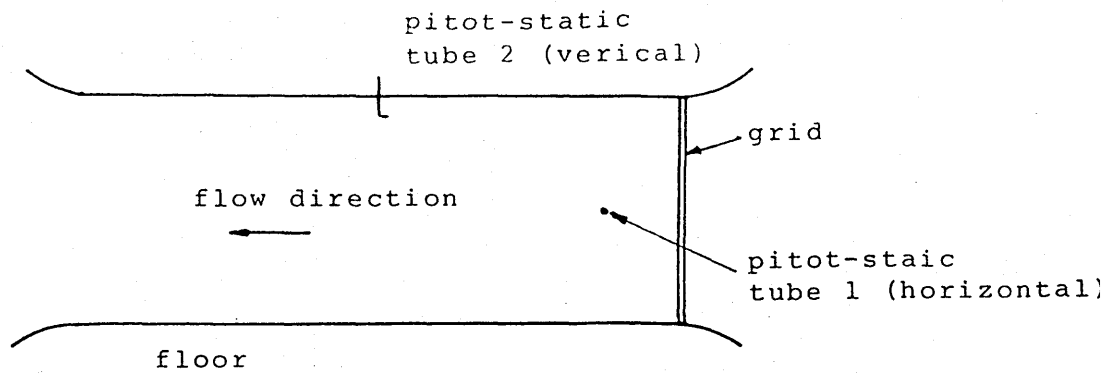


Figure 3.19 A typical calibration curve of dynamic pressure in the wind tunnel working section.

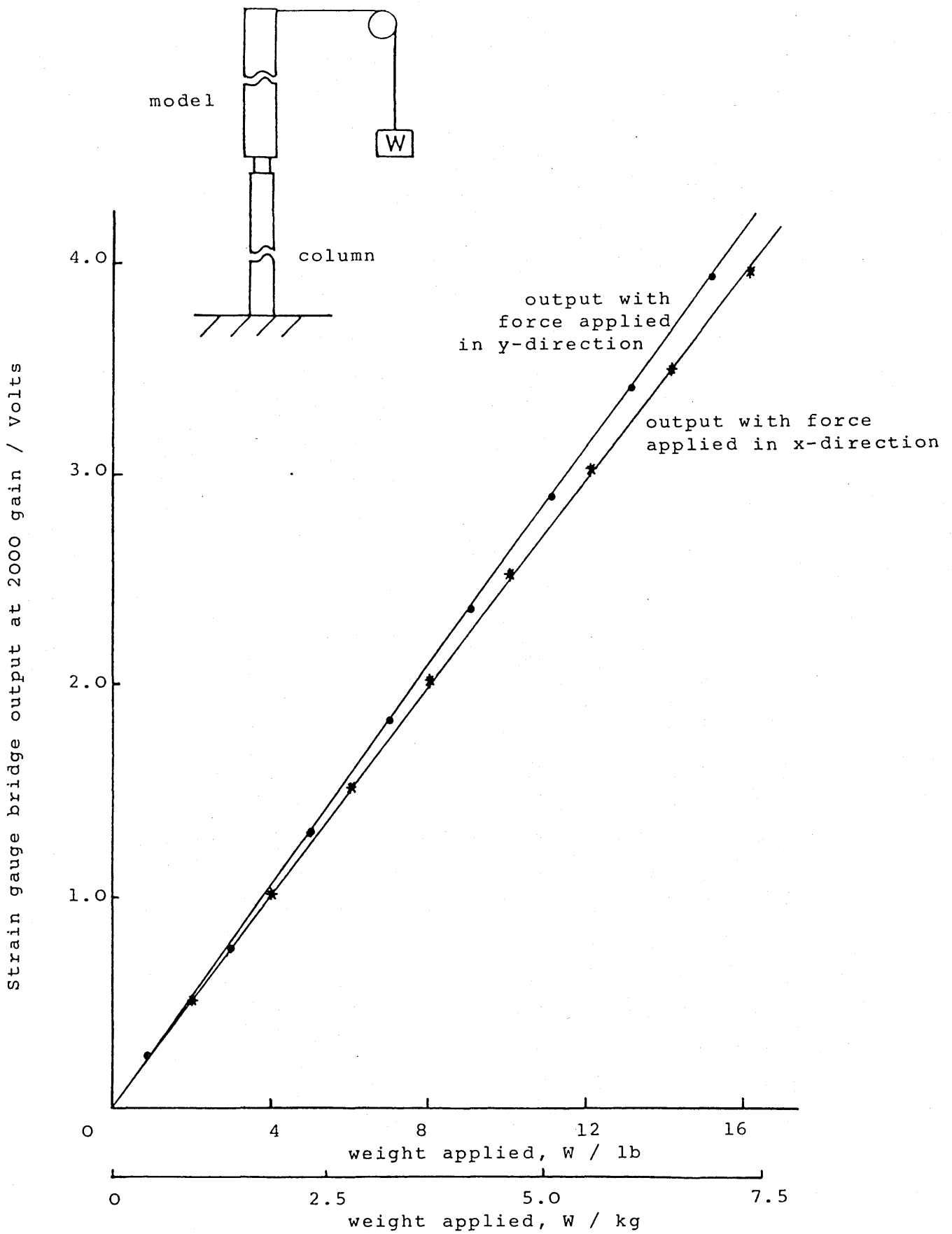


Figure 3.20 A typical calibration of output from the model-balance assembly with a static force applied to the tip of the model.

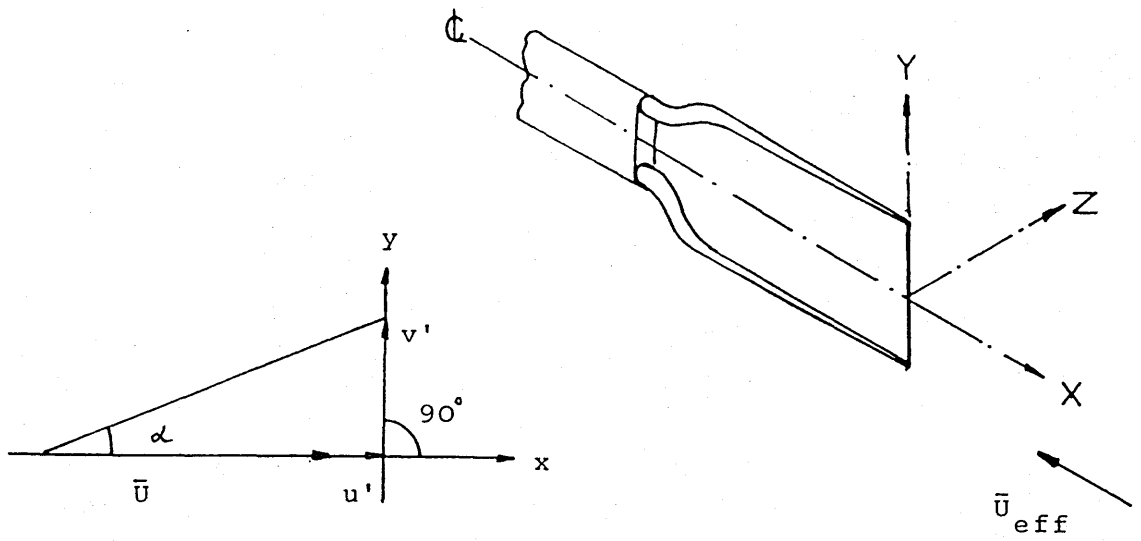


Figure 3.21 A schematic diagram of a single hot-wire probe and its associated flow field.

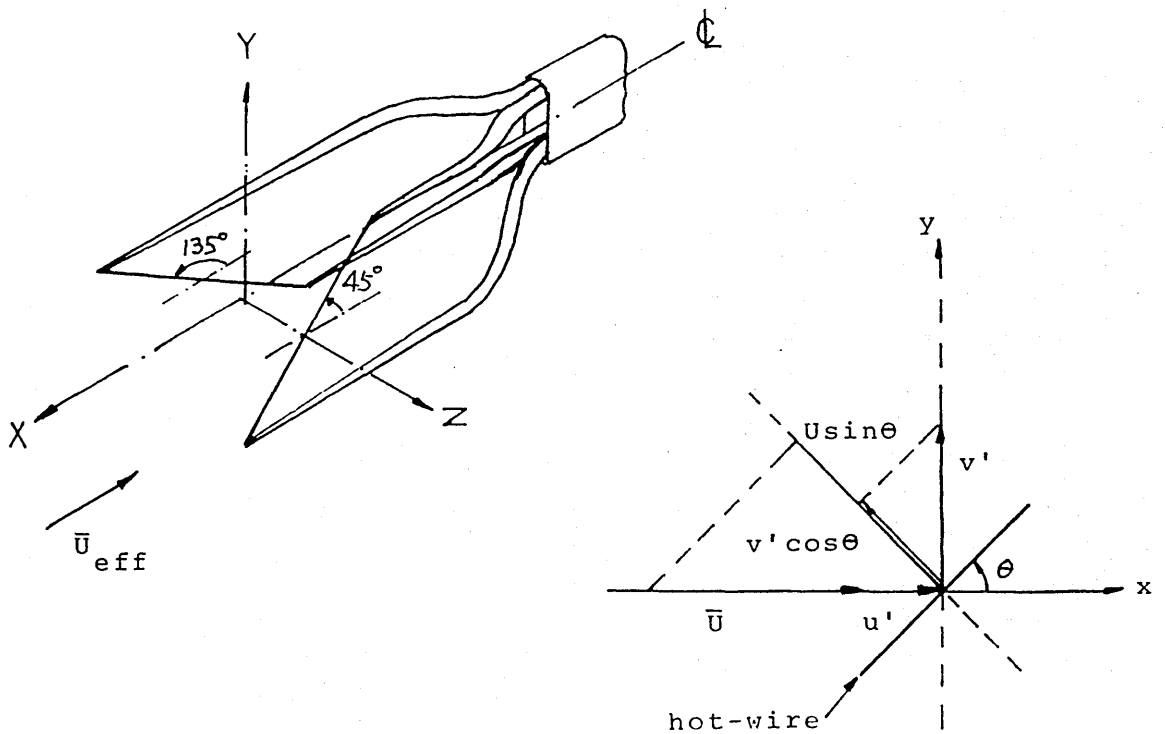


Figure 3.22 A schematic diagram of a cross-slanted hot-wire probe and its associated flow field.

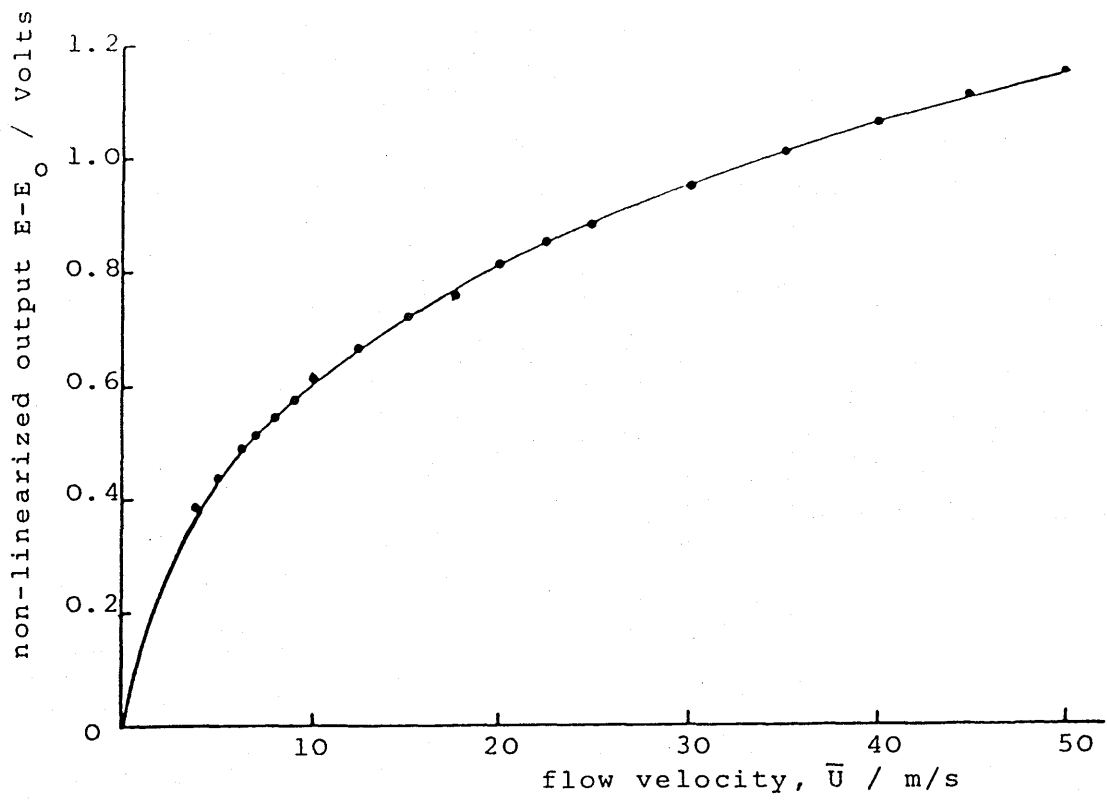


Figure 3.23 A typical non-linear calibration of a hot-wire output.

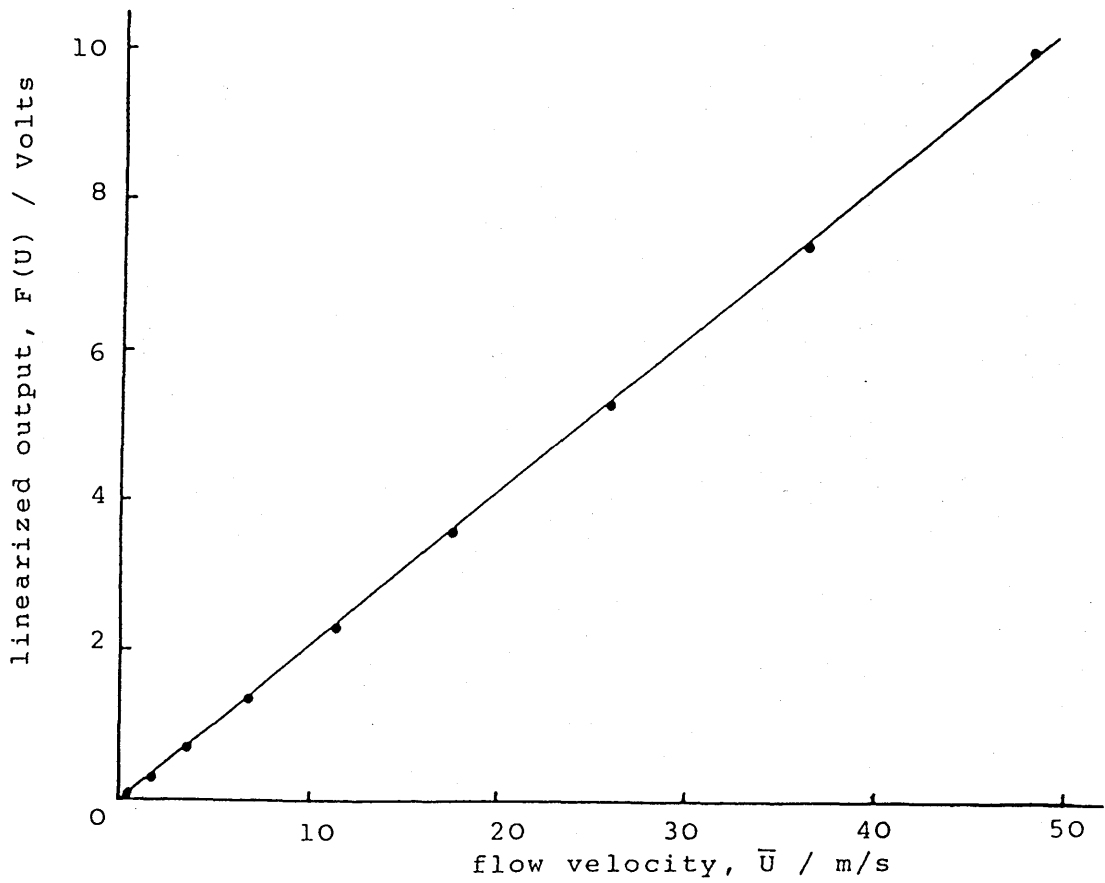


Figure 3.24 A typical linearized curve of a hot-wire output.

CHAPTER FOUR

DATA ACQUISITION AND PROCESSING

4.1 Introduction

In this chapter, an outline of basic signal measurement is first presented and then followed by a detailed account of the data acquisition and control system used in the present investigation. The heart of this system is a Digital Equipment Corporation Modular Instrument Computer (MINC-11) whose major functions are to digitise the conditioned analogue signals from the instruments and to store the data on floppy discs for further processing.

Normally, the complete system consists of a number of laboratory modules: an analogue-to-digital converter (MNCAD); a multiplexer (MNCAM); a real-time clock (MNCKW); a digital-to-analogue converter (MNCAA) and IEEE instrument bus interface (IBV11-A) for communication between each module, together with two specially designed peripheral devices: a multi-channel signal conditioner and a sample and hold module. For the present investigation, because only a few input channels were required, this system was proportionally scaled-down.

During measurements, the analogue signals from each assigned instrument were continuously sampled and recorded on disc via the microcomputer. The recorded data were either processed in real-time to unveil its basic statistical properties or kept on file for later evaluation. The various statistical functions used for describing the basic properties of random data, as required in the present investigation, are discussed in Appendix B.

In the second half of this chapter, the structures and functions of some selected computer programmes used for data logging, data processing, data analysis and data presentation are discussed in detail.

4.2 General Considerations

Any observed data representing a physical phenomenon can be classified as being either deterministic or nondeterministic. Deterministic data are those that can be described by any explicit mathematical relationship (such as a sinusoidal wave), whereas the nondeterministic data are random in nature (such as background noise) and must be described in terms of probability statements and statistical averages. A typical random process time-signal is schematically illustrated in Fig. 4.1 and

Fig. 4.2 shows the various forms of random process. Detailed description of the meaning and physical significance of these random process can be found in Ref. [117]

In the present study, the data recorded from the measurements include output voltage signals from a manometer (velocity), strain gauge bridges (forces and torsional moments), accelerometers (displacements) and hot-wire anemometer (wake energy). Even though the wave forms of these measured values varied considerably for different measuring conditions, it is reasonably to believe that those data recorded are stationary. This means that the mean values and autocorrelation functions of all measured data are independent of the time of measurement and the properties of the data can be determined from time average of individual sample records [117].

For a random signal of a repetitive nature, such as the one shown in Fig. 4.1, the measured value, $x(t)$, can be separated into a static or time-invariant component and a dynamic or fluctuating component, such as

$$x(t) = \bar{x} + x'(t)$$

where $x(t)$ is a voltage signal which can represent velocity, displacement or force.

In order to preserve this voltage signal in storage, such as on a floppy disc, the input signal must be converted into an electrical impulse with a numerical value corresponding to the strength of the source signal. The process of obtaining a series of discrete numerical values from a continuous function is called digital sampling.

As for example, Fig. 4.1 illustrates the discrete values, x_i , being derived from a continuous time history record, $x(t)$, at regular time interval, t_i , i.e.

$$t_i = t_0 + ih \quad \text{for } i = 1, 2, \dots, N.$$

where N is the sample size of the data recorded and t_0 is the initial point which is arbitrary.

The regular time interval between each discrete value, as shown in Fig. 4.1, is a distance h apart and is determined by the data sampling frequency, i.e.

$$\text{sampling interval, } h = \frac{1}{f_s}$$

where f_s is the rate (or frequency) with which an analogue signal is converted to digital values.

In digital processing, if the sampling frequency is $1/h$ samples per second, then the frequency components in the record can be unambiguously identified at up to $f_s = 1/2h$ samples per second only. This is generally called the Nyquist frequency.

For any frequency f , where $0 < f < f_s$, power spectral density at a frequency above f_s , defined by $(2f_s + f)$, $(4f_s + f)$ etc. will be aliased with f . The effects of aliasing is to falsely distort the resultant power spectral density functions.

The most practical method to avoid aliasing is either by filtering the data prior to digitisation to reduce the amplitudes of the high frequency components or by faster sampling (such as choosing f_s equal to the highest frequency of interest).

For the present measurements, the sampling frequency, f_s , was set at 320 Hz, i.e. the Nyquist frequency was 160 Hz, despite the fact that the fundamental oscillatory frequency of the tower models is less than 10 Hz. However, this value was a compromise after considering the disc storage capacity and the likelihood of high frequency components existing in the recorded data. Likewise, the low-pass filters incorporated with each measuring instrument were all set at 150 Hz or less, according to the instrument type. A summary of some basic statistics concerned with data sampling is shown in Table 4.1.

During measurements, the analogue signals from the assigned instruments were digitised by the A/D converter and written onto the floppy disc in the user volume (DY1:) via the control programme. In order to standardise the data processing sequence, the sampled values were recorded and processed in blocks. Each block contains 256 word (1 word = 2 bytes). Thus, a one-sided, single density formatted disc could hold 964 blocks of data, or, in other words, 493K bytes. But it was found that because of the double data buffering, in which data transfer to disc took place during dormant periods between data sampling, the space required on the disc must be twice the amount of data to be recorded. This meant that, with necessary space reserved for the run control programme, the size of each data file could not be greater than 450 blocks. In fact, in order to optimise the processing speed, each data file was limited to 396 blocks. For a twelve channels simultaneous input, this was equivalent to 26.4 seconds of sampling time for each channel.

This amount of data collected from each channel was considered to satisfactorily represent the non-stationary characteristics of the random data at an acceptable level and, at the same time, to provide sufficient resolution for the power spectral density analysis. [118].

4.3 Data Acquisition and Control System

The data acquisition and control system used in the present study was originally designed to investigate the aspects of dynamic stall of helicopter rotor blades. The centre of this system was the DEC MINC-11 microcomputer which was used for data acquisition, data manipulation, monitoring and controlling the associated peripheral devices. The integrated hardware/software system included a 30-channel band-limited signal conditioner which amplified signals from pressure transducers, a 31-channel sample and hold module to eliminate time-skew errors between channels, and other standard laboratory interface modules. The latter comprised a multi-channel analogue-to-digital converter, a 16-channel multiplexer which combined with the A/D converter provided 32-channel single-ended inputs, a real-time clock, a 4-channel digital-to-analogue converter to control external events and IEEE instrument bus interface for communications to or from the MINC to any instrument connected with the bus. A schematic diagram of the complete set-up, including data logging and presentation, can be found in Ref. [119].

The present MINC-11 microcomputer had been fully upgraded with a LSI-11/23 16-bit microprocessor with 64K bytes of RAM, a FPF-11 floating point hardware, a memory management unit (MMU) for 18-bit memory addressing which increased its indirectly accessible storage capacity to 256K bytes. The self-contained RX02 dual floppy disc system had a 1.0M byte capacity and half of this was available for user software and data.

The microcomputer was usually linked with a VT105 terminal for direct input/output communication and a VT100 terminal for graphical output. The latter was also equipped with a VT640 retro-graphics unit and screen hard-copy was obtained via a Riva Printgraphics module and an Anadex dot matrix printer. Later, a second MINC system which did not have a proper graphic terminal was available at the Department for analysing data. A multi-colour Gould graphic plotter was connected with the second MINC for making high quality prints. The complete system which had been scaled down for the present measurements, is shown schematically in Fig. 4.3.

In this investigation, a maximum of twelve channels was used at any one time, so that only the following laboratory modules and peripheral devices were utilised to interface with external equipment.

4.3.1 Analogue-to-Digital Converter

The MNCAD was a successive approximation type converter which translated the instantaneous value of a voltage applied to one of its inputs into a 12-bit binary value accessible to the system computer. This unit had an auto-zeroing circuit that made the A/D conversion with unusually high stability and accuracy.

The maximum input voltage was ± 5.12 Volts with converted resolution of ± 1.25 mV (or one part in 4096). The conversion time was approximately $30 \mu\text{s}$, but channel selection and transfer of the sampled value to memory increased this to $35 \mu\text{s}$ per channel.

This unit also contained a 16-channel multiplexer which could be configured for either 16 single-ended channels or 4 single-ended plus 6 differential channels.

4.3.2 Real-Time Clock

The MNCKN real-time clock was used as time-base generator. The programmable counter could be driven by a variety of events occurring either inside or outside the MINC system.

In the present system, at each time the clock overflows, a negative going TTL clock pulse was sent to the pulse shaper at the sample and hold unit through a connector. As explained by Galbraith et al. [120], the pulse was first inverted and differentiated to give a large positive pulse which in turn triggered all nineteen monostables into action. The subsequent conversion was then started on the 31 sample and hold circuits simultaneously. The real-time clock could be linked with the A/D converter via user software.

4.3.3 Sample and Hold Unit

It was found that if the input skew rates were high, and the A/D conversion was relatively slow in a multi-channel A/D conversion system, the time-skew errors between channels could be significant. It had been found that a single A/D conversion (from signal conversion to storage in memory) required approximately $44 \mu\text{s}$. For a 32-channel input, this was equivalent to $32 \times 44 = 1.41$ ms between the first and last converted channels. Even in the present measurements with only twelve input channels and without using the multiplexer, the time skew error was still around 0.42 ms.

To overcome this error, a multi-channel analogue sample and hold device was designed and built by Galbraith et al. [120] to interface between signal conditioners and multiplexer, and, hence, to provide simultaneous sampling on all channels.

For the present work, the sample and hold was linked between the various instruments and the A/D converter via two multi-pin sockets. The sweep sampling was controlled by the TTL clock pulse from the real-time clock which was suitably buffered to activate the circuitry. A detailed account of the design and construction of this unit can be found in Ref. [120].

4.4 Description of Software

In any computer based experimental study, the development and choice of the appropriate computer routines for a particular task are vitally important. In the following sections, the structure and functions of some selected computer programmes used for data acquisition, reduction, analysis and presentation are discussed in detail.

Because of the amount of data to be processed, it is ideal that a high speed computer with a large storage capacity should be available. In this respect, the present MINC-11 microcomputer system described in the previous sections is relatively slow and has very limited data storage capacity (compare with a hard disc system which can hold 20M bytes).

With this inherent limitation in mind, different methods were examined to try and alleviate these restrictions. For example, instead of using the conventional FORTRAN formatted direct access file for data handling, an unformatted binary direct access file contained in the system library routines (SYSLIB) was used extensively in most routines, giving a read/write speed increase of about one order of magnitude and a two fold reduction in disc storage space required.

Since only formatted values could be transmitted between computers (such as from MINC-11 to ICL2976) and the transfer process, even for a small data file, could involve a considerable time penalty, in the present study, all the recorded data were analysed and presented by the MINC-11 microcomputer alone.

The operating system used on the MINC-11 microcomputer system was the DEC RT-11 version 4.0. All the software used in the present work were written in either FORTRAN IV or MACRO-11 assembly language. In general, the FORTRAN programmes were used for the control, data analysis and presentation sequences and a number of MACRO assembly programmes were called as subroutines for data acquisition and general laboratory module programming.

Although the MINC-11 microcomputer has a wide range of software for data acquisition (REAL-11/MNC) and data analysis (such as SLPLIB), from previous

investigations the software for laboratory module programming was found to be somewhat inflexible and, thereby, limited the data handling speed considerably. A decision was taken to write some specific routines in MACRO assembly code to optimise the sampling sequence for the data acquisition requirements and thereby increase the maximum sampling rate.

The enhanced software package contained subroutines in four areas: (a) analogue to digital conversion routines, (b) digital to analogue conversion routines, (c) software clock routines and (d) general checking and utility programmes. A detailed description and listing of these subroutines can be found in Ref. [121].

Because of the different requirements of the present application, the fast A/D conversion routine listed in Ref. [121] had to be modified. A brief account of the modification is presented in the following sections.

The upgraded MINC-11 microcomputer has a maximum memory capacity of 256K bytes, but the actual memory space which can be directly addressable for real time data and programme is only 64K. However, memory above the 64K bytes boundary can still be addressed via the MMU or the virtual data arrays by using the Single Job (SJ) or Foreground/Background (F/B) monitor. In practice, after loading the necessary control programme, approximately 12K bytes (or 64K A/D samples) were left for actual data storage. To alleviate this restriction, double data buffering, in which data was transferred to disc during the time intervals between sampling, was used in conjunction with the data logging sequences.

The use of double data buffering had some drawbacks. One was that the maximum A/D sampling speed was reduced by half. Fortunately the reduced sampling rate was still higher than the present measurements required. The other shortcoming was the space created on the floppy disc must be twice the amount of the free blocks required for the data file. This imposed a limitation on the data file size of 450 blocks.

From the beginning, it was assumed that oscillation of the tower structure model under wind was random but stationary. In order to locate the resonant response region and to examine the oscillatory behaviour before and after this region, a large number of measurement points was required.

In practice, for every model configuration or flow condition, the response signals were measured and analysed by two separate procedures:

- Static measurement-in which the response signals, either in terms of force or displacement, were sampled and averaged by an on-line analysis. Only the

resultant mean or mean-square values were kept for presentation. Results from this measurement gave a complete picture of the model's response within the wind speed range and served the purpose of choosing the measurement points for the dynamic measurements.

- Dynamic measurement-in which the time history signals from the assigned instruments were sampled and stored on discs via the microcomputer for off-line processing. Because of the data size, only a limited number of such files for each test could be stored for analysis. The recorded values were processed by various routines, as depicted in the block diagram of Fig. 4.4, before the various statistical properties of the response signals could be obtained.

In general, the programme used for the present study could be divided into the following three basic categories:

- (a) data acquisition and run control routines.
- (b) data reduction and analysis routines, and
- (c) presentation routines.

A detailed description of the functions of some routines within each category are presented in the following sections.

4.4.1 Run Control Routines

Two types of FORTRAN programme were employed to control the sequence of events for:

- (1) Static measurement (such as MEAN08)
- (2) Dynamic measurement (such as ADEIGH)

The primary aims of these tests were to record the models' response as measured by the assigned instruments over a sufficient long duration and, from the subsequent results, to assess the behaviour of the models in different flow conditions. Therefore, during measurements, the microcomputer had to be able to sample and to store large amounts of digitised signals in file continuously. In both types of tests, the same high speed A/D conversion routine was used and the major differences were the subsequent steps in handling the recorded data.

According to the number of models used, the number of input channels required might be changed. For this reason, all the monitoring instruments were connected to the sample and hold module with BNC plugs. This arrangement made the input

changes from one type to another much easier and introduced less disturbance. In general, the first input channel (no. 0) was always connected to the manometer via the linear amplifier.

The structures of these run control programmes are discussed briefly below.

(a) Static Measurement

At the beginning, the user was prompted to input, through keyboard, the run parameters, including: output file name, number of channels required, input types, instrument calibration values and wind tunnel temperature. These parameters, together with the calculated results from the recorded data, were stored in a formatted direct access file for future presentation.

In order to make the tests less time consuming, the measurement of forces (including twisting moment) and displacements for every testing combination were done by two separated runs.

Immediately before switching on the wind tunnel, the offsets of each channel were sampled at f_s over a four seconds period, and the averaged values were then stored in the buffer and printed out for reference. When the actual data gathering was ready to proceed, entry was then made into the relevant subroutine, such as ADCS08, which is discussed in the next section.

In all static tests, whatever the number of channels used, the sampling time was set at 29.6 seconds. The resulting raw A/D samples, whose size depended on the number of channels used, were stored on disc via the unformatted binary direct access file.

Once the data logging had been completed, the raw A/D data were read back into the programme buffer in blocks. The initial steps involved conversion to units according to the input types and this was done by applying the offset, calibration and correction factors to the raw data.

The time-averaged value of each input was then calculated. This process was repeated until all the data blocks had been covered. The calculated values were then averaged, giving the actual mean value of each input over the whole sampling period.

To determine the mean-square values, the same read-conversion process was repeated again, but this time each recorded value was subtracted by its corresponding mean value before it was squared. At the end, the resulting values became the mean-square values.

The resultant mean and mean-square values of each input channel were first printed on paper via the dot-matrix printer and then sent to an output file on disc for presentation.

Once this was completed, the user was prompted to alter the variable parameter, such as wind velocity or the model's incident angle, and the whole procedure was repeated until the desired number of measurement points had been reached.

Finally, after switching off the wind tunnel, each input channel was sampled and averaged as at the initial stage. This was to make sure that the offsets of each monitoring instrument had not shifted significantly during measurement.

A flow chart illustrating the sequence of steps in a static test is shown in Fig. 4.5.

(b) Dynamic Measurement

The setting up sequence of this routine was similar to the static test except that more run parameters, such as models' positions, hot-wire probe location etc., had to be inputted through the keyboard. This run information, together with the offset values measured before switching on the wind tunnel, were recorded as real numbers in the first block of the output file. The data blocks after the initial run information block contained the raw A/D conversions as sequential samples from channel 0 to the number of channel required, see Fig. 4.6.

During the subsequent data reduction and analysis processes, the values stored in the run information block were used to generate the required channel values in appropriate units from the raw A/D conversions. The information block was also updated at each step so that vital information could be passed from one processing routine to another.

When the actual data logging was ready to proceed, entry was made into the relevant subroutine, such as ADCS08. At each clock overflow, the inputs from each channel were sampled and the raw A/D conversions were read into the programme's buffer until half of the buffer was full. Then the control dropped to the next FORTRAN statement which began a section of code to transfer the data to the disc (DY1:) via the unformatted direct access file. The other half of the buffer continued to fill with data during this transfer. This process terminated when the required number of data blocks was reached.

A simple flow chart with indication at each stage is shown in Fig. 4.7.

4.4.2 Fast Continuous A/D Conversion Routine

The high speed A/D conversion subroutine from Ref. [120], as its name implied, demanded the sampling of the 32 multiplexed channels and the transferring of the digitised data to floppy disc in the minimum time period. The resultant subroutine had a maximum aggregate rate (number of channels x sampling rate per channel) of 20480 Hz.

Although the measurements in the present study required the A/D conversion routine to have a moderate sampling speed, the most important requirement was that the digitised data should be transferred to floppy disc without interrupting the sampling sequence.

The basic structure of the present conversion routine resembled those, such as ADSC16, described in Ref. [121], but had some extra features which originated from Hacker [122]. In here, the modified conversion routine was operating in conjunction with two associated routines, namely WAITFD which provided a simple buffer management scheme and STOPIT which terminated the conversion routine.

In operation, the FORTRAN control programme first called in the fast continuous A/D conversion routine (such as ADCS08). It required four parameters, namely the buffer name, buffer's length, clock frequency selector value and clock overflow value. The last two variables were determined via the REAL-11/MNC subroutine XRATE. The next call was the wait-for-data routine, WAITFD, which executed a tight loop for the data movement. Once half the data buffer was filled, this subroutine activated the process to transfer the raw A/D values to floppy disc (DY1:) via the unformatted binary direct access file. During data transfer, the other half of the buffer continued to fill with new data. After the transfer had been completed, the control programme returned to the WAITFD subroutine until all required data was collected. The A/D conversion process was terminated by calling the termination routine STOPIT.

The data sampling sweep of the assigned input channels was controlled through the programmable real time clock module, which was set to overflow at the predetermined sampling rate. In the control sequence, the clock started after entry to the A/D conversion subroutine, and the first sweep was initiated on the first clock overflow. Thereafter, sweeps through the input channels were continued on each clock overflow until the data collecting process was terminated.

The basic structure of the A/D conversion subroutines used in the present study were all identical, only the number of input channels to be swept was adjusted according to the requirements.

A flow chart diagram which illustrates the various features in this subroutine is shown in Fig. 4.8

4.4.3 Data Processing

As mentioned in the previous sections, the raw A/D values stored in each data file has to be reduced to their fluctuating components, $x'(t)$, before being processed by other programmes. The FORTRAN routine, PROCES, served this purpose. During the process, the basic statistic parameters of the recorded data from each input channel, together with some other test parameters, were computed.

At programme entry, the run number was requested as input. Once the required data file was located, the run information buffer was read.

The whole reduction process required the stored sampled values to be read into the memory buffer twice. In the first run, the sampled values were read and processed in blocks. The number of data blocks to be processed each time depended on the number of input channels used in measurements.

Each data block contained 256 words (or 256 A/D values) which were first converted to floating point values in units corresponding to the input types. This was done by applying the offsets, calibration and correction factors to the data. The resulting values were then sorted and summed up one after another. The same process was repeated for all channels until all recorded data in file had been processed. The calculated values at the end were averaged again to produce the actual mean values of each input channel over the whole sampling period.

The next step was to remove the mean value, \bar{x} , from the original digitised signals and to find the mean square values. The procedure to transfer data and to convert into real values was exactly the same as before. The only difference was that the original raw A/D values were replaced by the fluctuating values which were read from disc via the unformatted direct access file.

For those data files which contained values from the two element hot-wire measurements, the two coupled voltage output signals, $E'(\pi/4)$ and $E'(3\pi/4)$, were also reassembled at this stage. The resulting values were read back as two individual fluctuating velocity components.

To save space, the output fluctuating values were recorded on disc as integer numbers (2 bytes). As in the case of the input data file, each output data block contained 256 words.

Finally, the run information buffer was updated with values such as the time-averaged mean and RMS values of each input channel, and test parameters such as mean flow velocity, Reynolds number etc. These parameters were dependent on the run-time temperature observed at the beginning of each test. The updated run information block was then recorded as the first block in the processed data file and was then directly available for use by the following analysis and plotting routines.

4.4.4 Data Analysis

The present work on investigating the interference effects between neighbouring towers has concentrated mainly on parametric comparison of statistical properties of the responses in both time and frequency domains. The following routines computed these functions, whose mathematical significance has already been mentioned in Appendix B, from the recorded data.

To standardise the analysis sequences, the same initialisation procedure was adopted for all analysis routines. At the entry of these programmes, the user was prompted to input data file number (i.e. FPR***.DAT). Once found, the run information buffer, which was recorded as the first block in the data file, was read.

After that, dependent on the routine used, the user was prompted to choose the input channel whose data were going to be analysed.

During the read-in stage, the recorded values were transferred to the computer buffer in blocks which varied with the number of input channels used. The values from the selected channel were then picked, converted to real values and kept in a temporary buffer before moving into the analysing stage.

In all the analysis routines used in this work, these data read-in and preparation procedures were repeated until all the data blocks stored in file had been processed.

(a) Averaged Peak Displacement.

The peak-to-peak displacement (or vibration amplitude) of a slender body under wind actions is valuable in that it is a useful quantity in assessing the maximum stress on the structure.

The FORTRAN programme, NDPEAK, was operated in conjunction with the peak-processing subroutine (PEAK) from the software package (SLPLIB). This peak-processing algorithm is a procedure to detect increasing and decreasing trends in a set of data. Output from this subroutine is then directly related to the alternating peaks and crests of input signal waveform.

Since this subroutine was sensitive to small signal fluctuations, only the sampled values from the accelerometers were processed by this programme. The resulting peaks and crests corresponded to the peak displacements in the longitudinal and lateral directions.

When all the stored data from a selected channel had been processed, the peak and crest values were then averaged. The mean, RMS, and the largest and smallest values were then printed on paper via the dot-matrix printer.

(b) Probability Density Function

The main application of this measurement, as described in Appendix B, is to establish the probability characteristics of some physical data.

The FORTRAN programme, PDD, which employed the interval histogramming subroutine (HISTI) from the software package (SLPLIB), examined the recorded data from the selected channel and called one count if the examined data had a value within one of the prescribed intervals. The net result was equivalent to the histogram of the recorded data.

After processing all the stored data from the requested channel, the resulting probability density function was normalised and plotted on the graphical terminal for inspection. The user had the option to store these values in a user specified file for future presentation.

(c) Power Spectral Analysis

Estimation of the power spectral density of discrete samples from either a deterministic or a stochastic process, as discussed in Appendix B, is a useful procedure to unveil the general frequency composition of the physical data.

In the present study, two FORTRAN programmes, namely POWERS and COPOWS, were employed for computing the power spectral density functions (and other relevant functions) of single and joint data records, respectively. These two programmes were adopted from Ref. [123] having been modified extensively for the present applications.

The programme, POWER, was an implementation of the 'Blackman-Tukey' method and followed a procedure originally described by Rader [124]. This 'standard' method was used here to provide an estimation of the autocorrelation function of a recorded signal, and an estimation of the power spectrum by computing the discrete Fourier transform of a windowed version of the correlation function.

The second programme, COPOWS, was based on the overlapped fast Fourier Transform (FFT) technique described by Carter et al. [125]. This so-called 'direct' method was used here to estimate the various second order statistics between two recorded signals, including results such as auto- and cross-power spectral density functions, phase angle, coherence function and generalised cross-correlation.

It has been shown that during the computation, some smooth weighting function had to be applied to each data segment in order to reduce errors caused by side lobe leakage. In programme COPOWS, a so-called Henning window was applied to every data segment before processing. For a one side spectrum, the Hanning weighting function is defined as [125],

$$W(t) = \frac{1}{2} \left[1 - \cos \left(\frac{2\pi t}{N_s} \right) \right]$$

in which N_s is the number of data points in each segment. However, this weighting function had the apparent drawback of wasting the valuable data and had to be overcome by applying backward overlapping (50% in this case) during the process.

More detailed description of these two methods may be found in the standard texts such as Bendat and Piersol [117] and Newland [118].

The general layouts of the auto- and cross-power spectral analysis programmes are shown by block diagrams in Fig. 4.8 and 4.9, respectively.

From Ref. [117], the normalised standard error for a one sided spectrum is,

$$\epsilon = \frac{1}{N_B}$$

in which N_B is the number of data blocks per channel. In the present measurement, the error was estimated to be equal to 0.123 for all tests.

Because of the restricted memory space and to obtain greater flexibility in handling the computed values, the results produced by these two programmes were stored in disc via the unformatted direct access file. In each output file, the first data block contained the updated run information and additional information such as types and sizes of the resultant data contained in each file. The subsequent data blocks contained the computed values, usually correlation values first and followed by spectral density functions. Moreover, the processed values were recorded as real numbers (4 bytes) word length which was double the size of the input raw data.

4.5 Data Presentation

As mentioned in the previous sections, there were two MINC systems available for analysing and presenting the recorded data. But, because of their different hardware configurations, each machine used its own customised plotting package. A family of FORTRAN IV programmes, which utilised these packages, was implemented for use on these MINC microcomputers.

In general, using the VT100 graphical terminal, the plotting routines provided a 'quick look' presentation of the data. Only the desired outputs were reproduced on paper via the dot-matrix printer. Because of its relatively poor quality, only a fraction of the results presented in this study was produced by this system. Consequently, because of the absence of a proper graphic terminal in the other MINC system (the one based at Department), all the graphical output was done without on-line examination. This meant that many of the graphs produced were found to be useless.

To make the presentation short, only those plotting routines which took data from a separate file are discussed. With this in mind, the following routines have been written:

- (a) Mean values (or coefficients) versus flow velocity.
- (b) auto- and cross-correlation functions versus time displacement.
- (c) power spectral density and other related functions versus frequency.

In order to allow a direct comparison between results for different settings, these routines had the option to put several sets of data on the same graph. To save space, the coordinate of each data set was displaced by a certain amount in either x- or y-direction. And to preserve clarity, the x-axis and the coordinate of all data points were rotated by 30 or 45 degrees clockwise. The result is a semi-three-dimensional presentation of the two-dimensional data, their visual differences are demonstrated in Fig. 4.11.

- (a) Mean values versus flow velocity

To standardise the presentation, the time-averaged values of the strain gauge bridges' outputs had been expressed as mean force coefficients and mean moment coefficients about the prism centre. For the fluctuating components, the coefficients were obtained by using the root mean square (RMS) values of the fluctuating forces and moments. The force and moment coefficients per unit length are defined as follows:

$$C_{F_y} = \frac{F_y}{\frac{1}{2} \rho \bar{U}_o^2 B}$$

$$C_{F_x} = \frac{F_x}{\frac{1}{2} \rho \bar{U}_o^2 B}$$

$$C_M = \frac{M}{\frac{1}{2} \rho \bar{U}_o^2 B^2}$$

where F_y and F_x are force components perpendicular to the sides (at zero angle of attack, F_y equals lift and F_x equals drag). The quantity $\frac{1}{2} \rho \bar{U}_o^2$ represents the free stream dynamic pressure. Whereas the mean and fluctuating displacement values were usually presented normalised by the width of the square section, B. Because of considerable data scattering, the results presented in this study were all smoothed by applying a running-average weighting function [126]. The five-term weighted-average formula is defined as,

$$y_i = \frac{1}{9} \left(y_{i-2} + 2 y_{i-1} + 3 y_i + 2 y_{i+1} + y_{i+2} \right)$$

in which Y_i denotes the smoothed value at the i th point.

(b) Auto- and cross-correlation function versus time displacement

As mentioned in Appendix B, the correlation functions were usually normalised and had values between ± 1 . In order to have a better presentation of the wave form variations, the coordinate of each data set was displaced along the y-axis. During the analysis, the results were computed in the time domain range between 0-750 msec. for a single data record and ± 750 msec. for analysing joint data records.

(c) Power spectral density (and related functions) versus frequency

These frequency based functions were all computed in a range between 0-160 Hz. with a frequency resolution of 0.625 Hz/data point. For the power spectral density functions, the values were usually presented either in decibel (db) or in their normalised form, such as:

$$\text{Force} : \frac{f S_F (f)}{\left[\frac{1}{2} \rho \bar{U}_o^2 B \right]^2}$$

$$\text{Moment} : \frac{f S_M (f)}{\left[\frac{1}{2} \rho \bar{U}_o^2 B^2 \right]^2}$$

$$\text{Displacement} : \frac{f S_x (f)}{\sigma_x^2}$$

$$\text{Velocity} : \frac{f S_u (f)}{\bar{U}_o^2}$$

Number of channels assigned	12 (maximum)
Sampling rate/channel	320 Hz
Nyquist frequency	160 Hz
Number of data blocks/channel	33
Degree of freedom, 2N	66
Total number of data points	101376
Sampling time, T	26.4 secs.
Band width.	0.038

Table 4.1 Statistics of the input measured values.

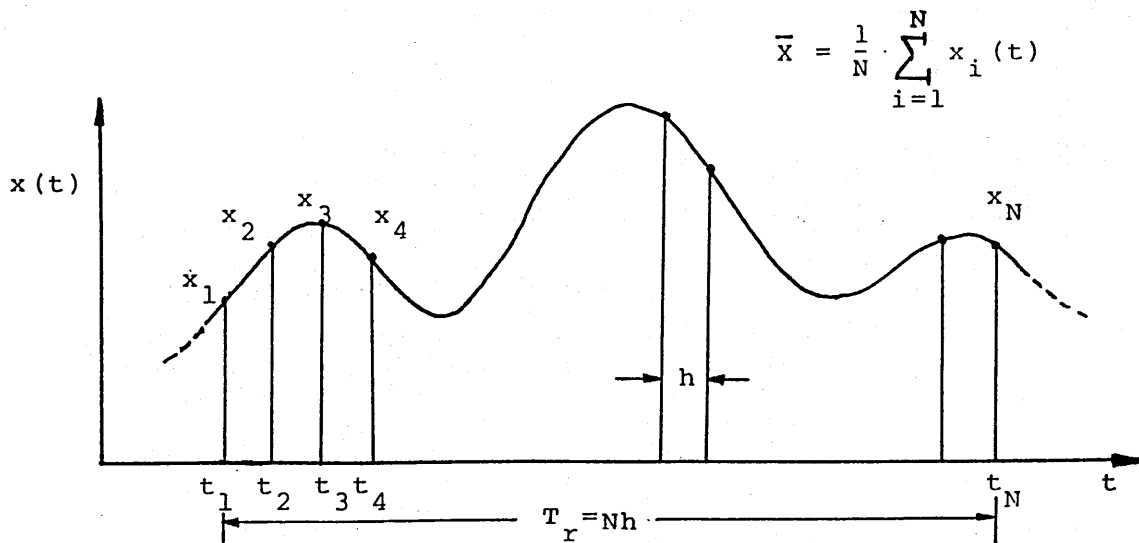


Figure 4.1 Sampling of a continuous record.

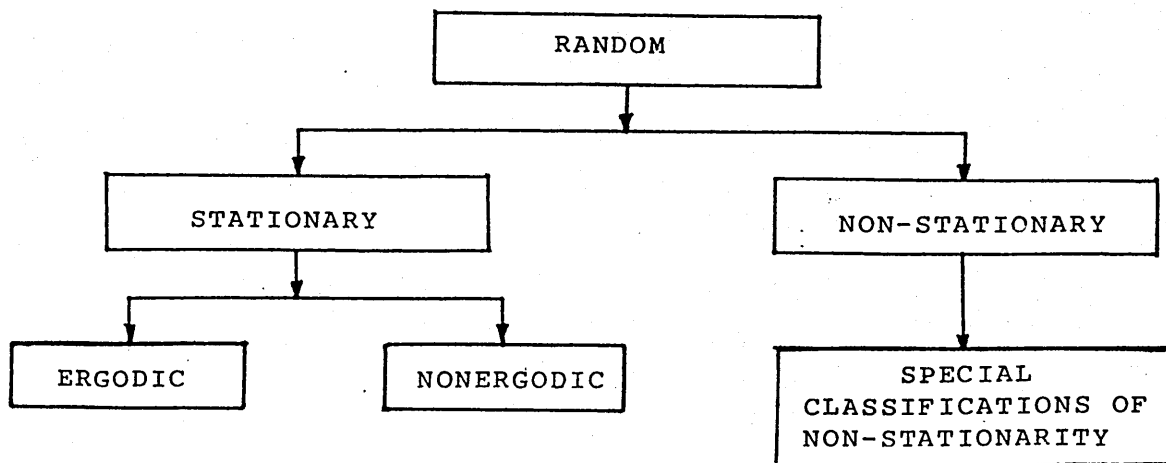


Figure 4.2 Classifications of random data.

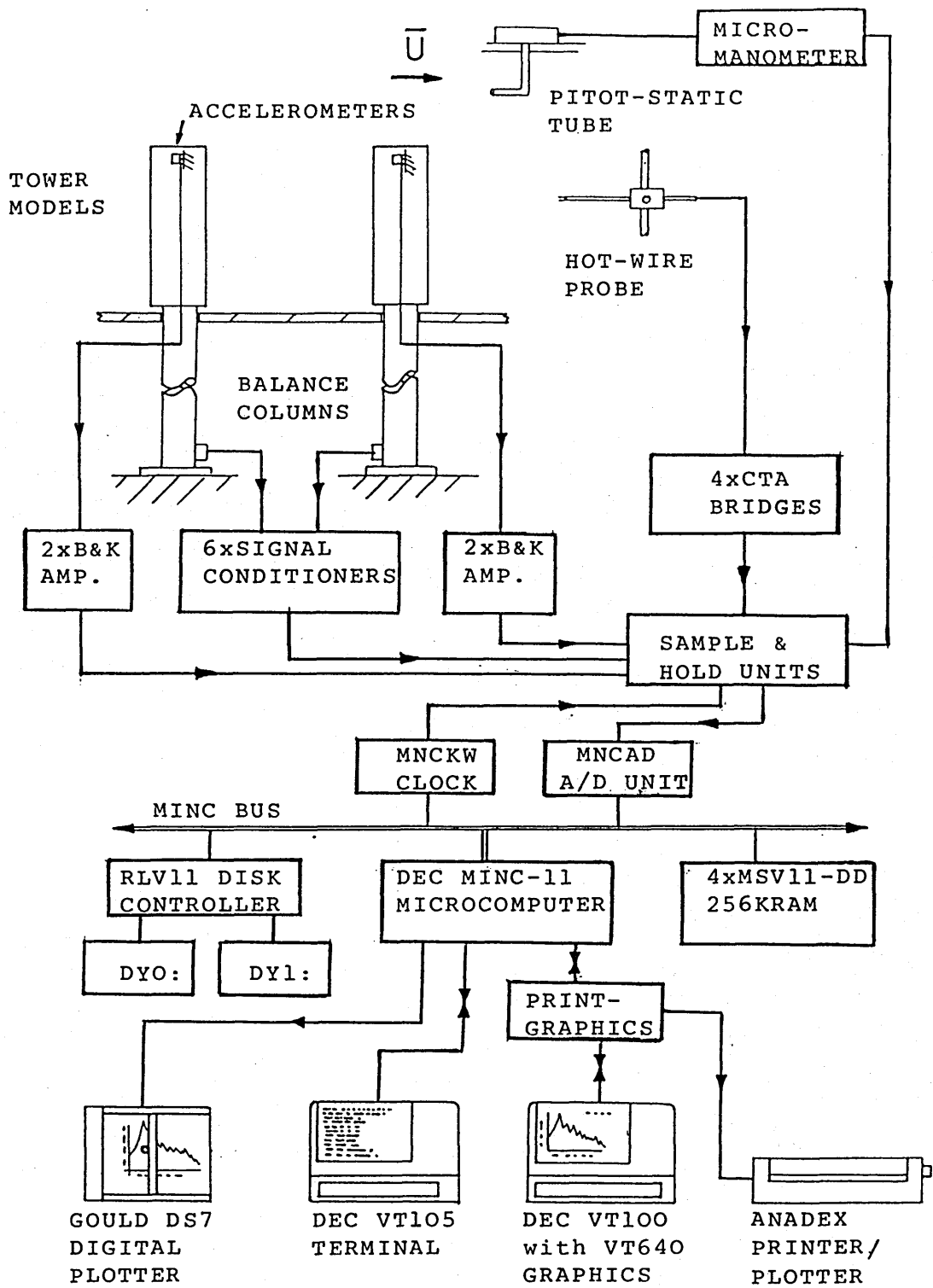


Figure 4.3 General arrangement of data acquisition and control system.

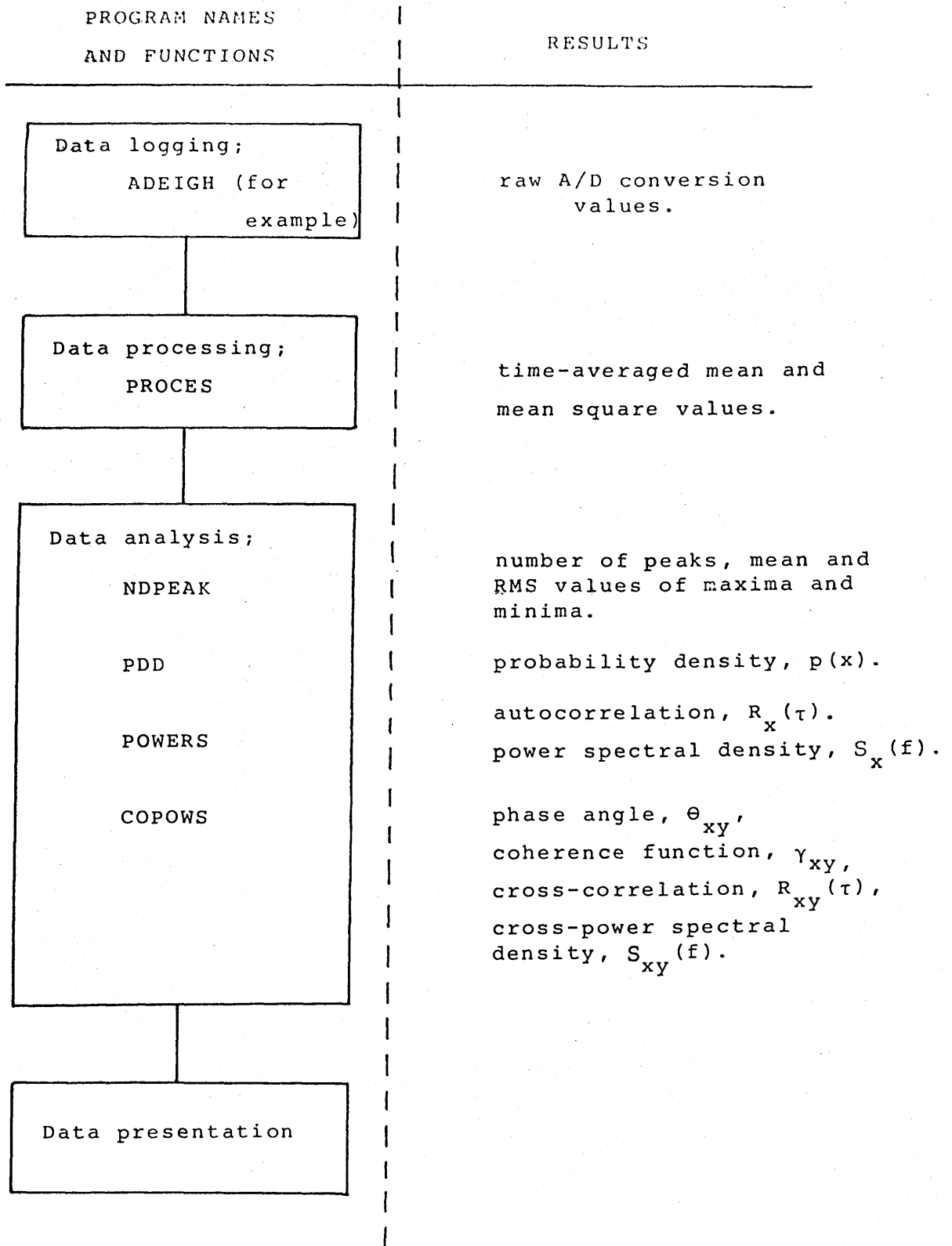


Figure 4.4 Block diagram showing the program used and its products at each processing stage.

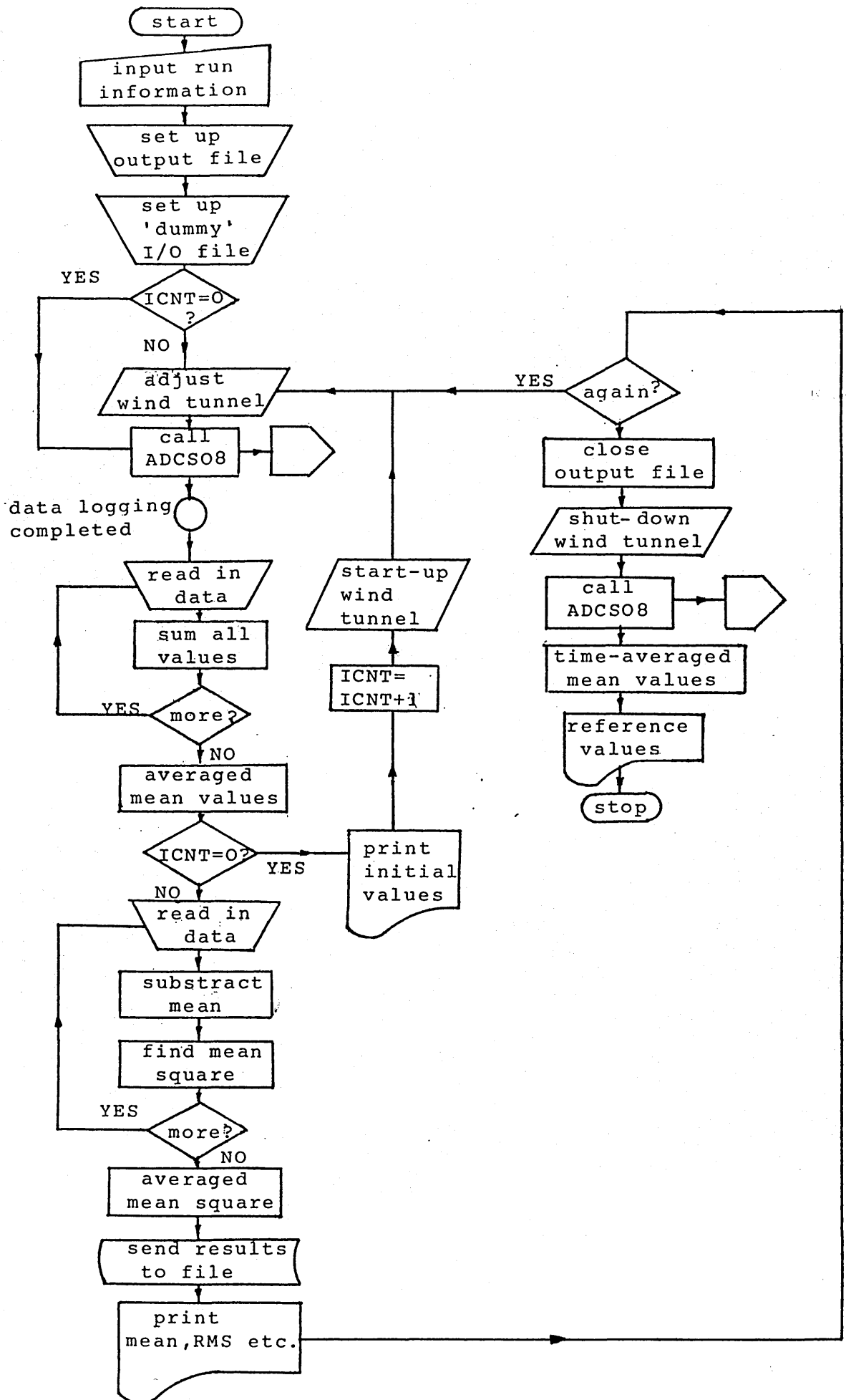


Figure 4.5 Flow-chart for the mean values measurement using eight input channels.

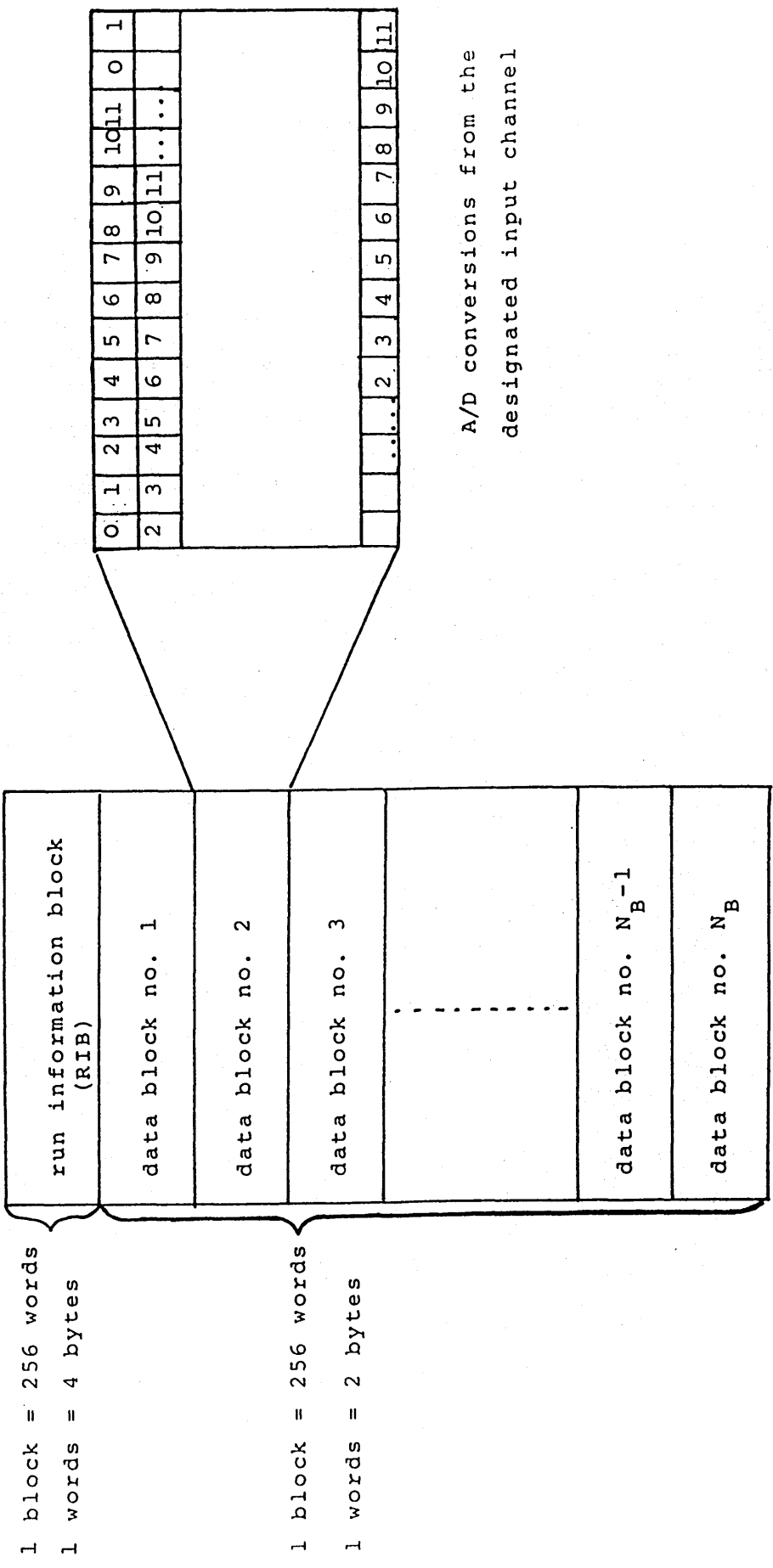


Figure 4.6 Sequence of data blocks and A/D conversions in a raw/processed data file.

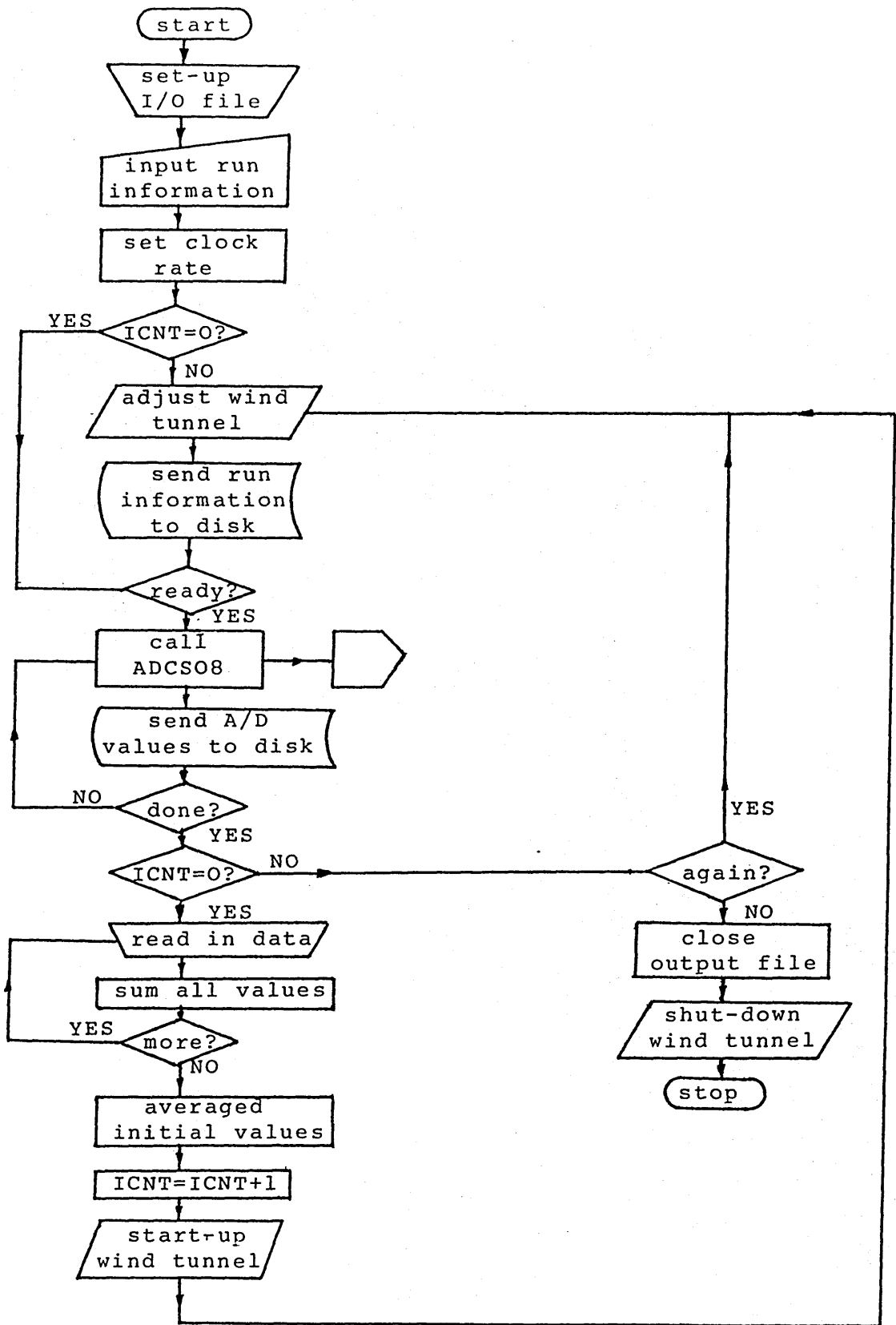


Figure 4.7 Flow-chart for the dynamic values measurement using eight input channels.

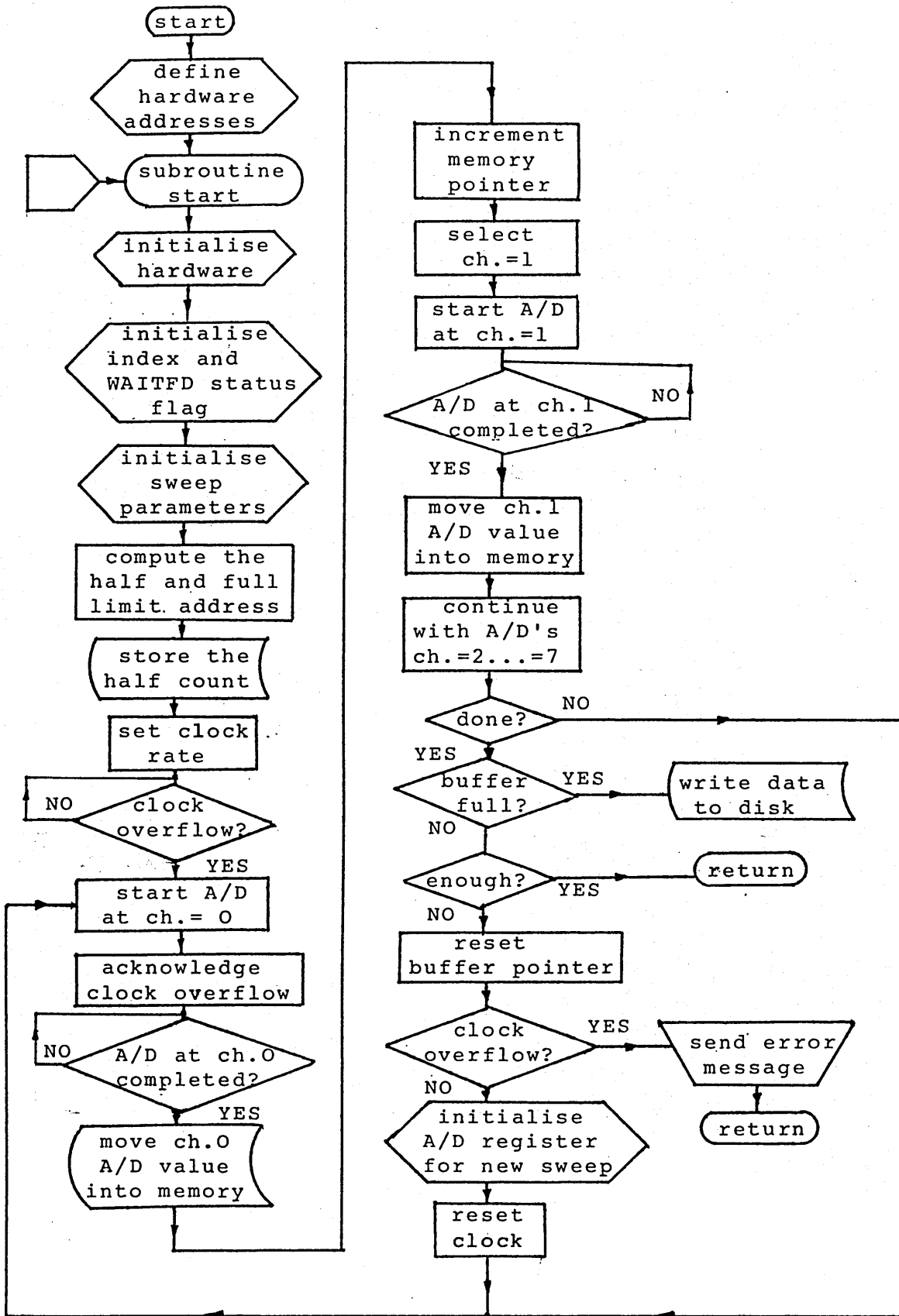


Figure 4.8 Flow-chart for the fast continuous A/D conversion subroutine.

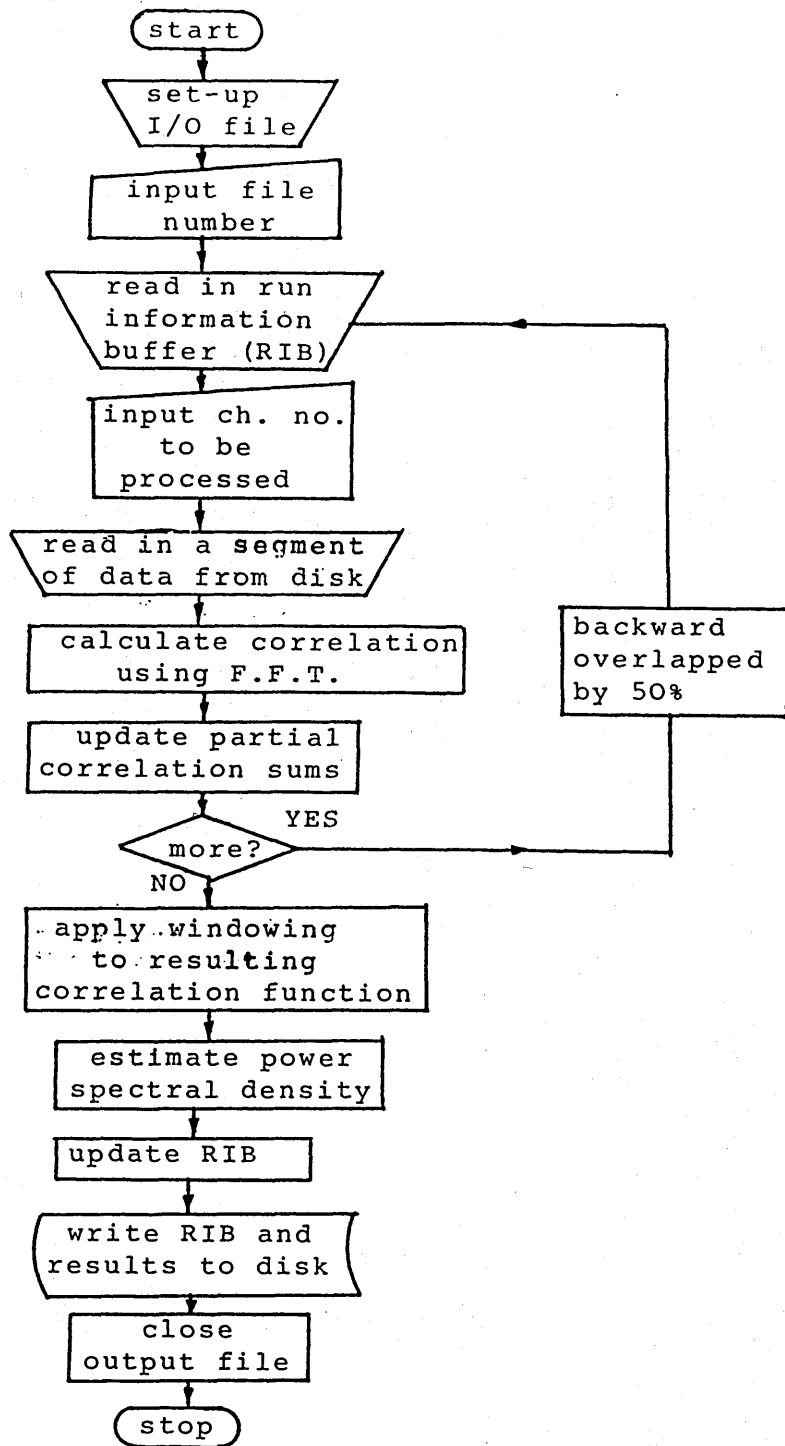


Figure 4.9 Flow-chart diagram for program 'POWERS'.

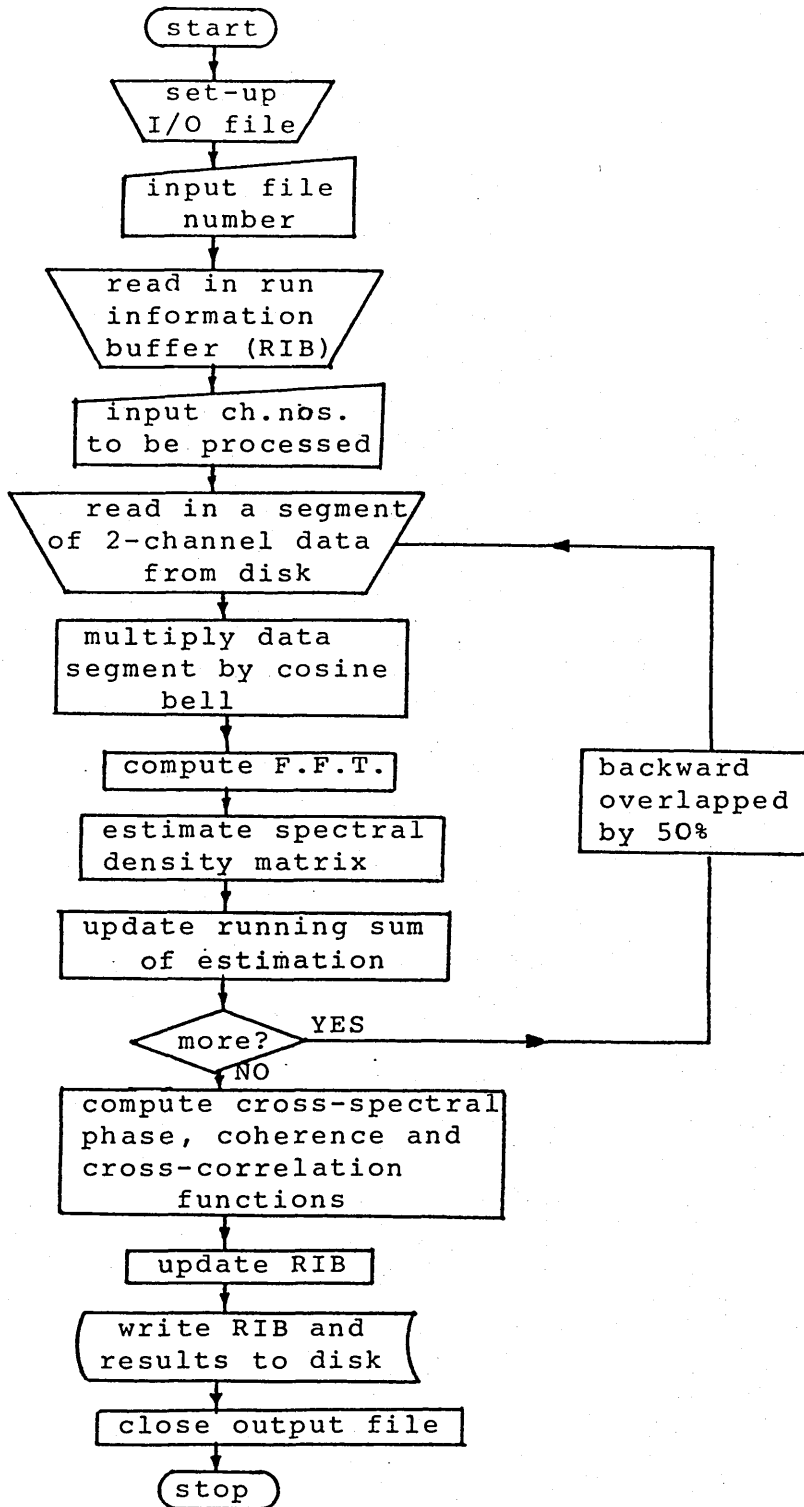
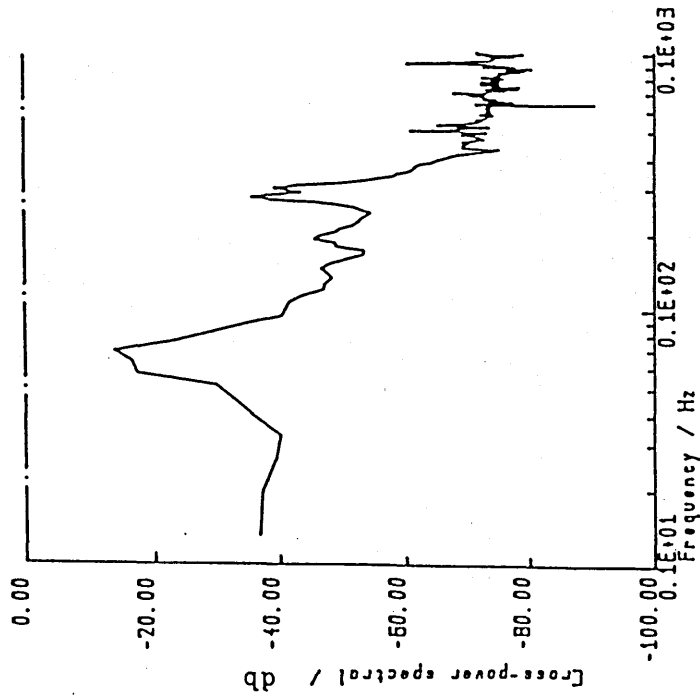
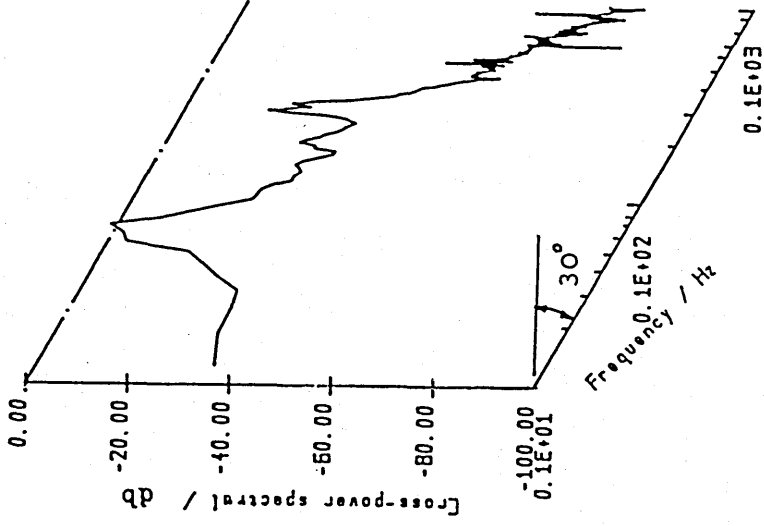


Figure 4.10 Flow-chart diagram for program 'COPOWS'



Normal two-dimensional presentation



Semi-three-dimensional presentation

Figure 4.11 A visual comparison of the normal presentation and the one with its X-axis (and the data point coordinate) to be rotated by 30-degree clockwise.

CHAPTER FIVE

PRESENTATION AND DISCUSSION OF RESULTS OBTAINED FROM A SINGLE TOWER BLOCK MODEL

5.1 Introduction

The experimental results presented in this chapter are divided into three separate sections as follows.

- (a) results of the structural dynamic analysis conducted on either the partial or complete model-balance assembly.
- (b) results of the aerodynamic response of a square tower model under different but carefully controlled operating conditions, and
- (c) wake characteristic in the near wake region and its correlation with the structure motions.

The main objective of the first test was to determine the system's response to vibrational force at different frequencies and, from the results obtained, to assess the dynamic properties of the whole system. The objective of the second test was primarily to evaluate the system's response to aerodynamic excitation in simulated natural wind conditions and to establish the subsequent response characteristics.

Some of the results presented here were collected as further support for the conclusion drawn in an early chapter while some of the work provided background information relevant to the theme of the thesis.

5.2 Mechanical Response Characteristic of the Single Model System

Because of the low-frequency response characteristics of the combined elastic model-strain gauge dynamometer used in this investigation, the model wind-loads and corresponding dynamic response are the combined end-results of both wind characteristics and structural action.

One very useful experimental technique for the study of the dynamic behaviour of machines and structures concerns the measurement of what is loosely termed 'mechanical impedance'. Broadly speaking, this term defines the relationship between forces and motion at various points, both with respect to amplitude and phase. Table 5.1 lists the general definitions of terms used for complex dynamic ratios of force and motion [127] and [128].

The general main applications of impedance testing are:

- To determine the natural frequencies and mode shapes.
- To determine the specific material properties such as damping capacity or dynamic stiffness.
- To establish a basis for an analytical model.

A wide variety of techniques have been suggested to determine the mechanical impedance of a given system. But for reasons of simplicity, the resonance test, which is also known as the 'peak-amplitude' method, was employed in this study. This method is, basically, to excite the system harmonically and measure its response at chosen locations over a range of frequency.

In the following sections, after a brief discussion of the experimental set-up, results from the dynamic testing, either in terms of mobility or compliance of the system, are presented. Using the same apparatus setting, the dynamic coupling of the orthogonal force components which were measured via the strain gauges, were also examined.

5.2.1 Experimental Arrangements

The elastic model and force balance column used in these tests were completely assembled as described in Chapter Three. In order to study the contribution from each component, each part, with the exception of the model, was excited either individually or in combination with others. A representation of the complete system, including the measuring instruments, is shown in Fig. 5.1.

In this study, the word 'complete' is referred to a fully assembled model-balance combination mounted at the centre of the platform. The mounting rig was bolted to the concrete floor in a way exactly similar to the one used in later wind tunnel investigations. In doing so, the effect on the entire assembly due to the presence of the rig could be investigated.

(a) The Forcing System

Electrical excitation was chosen for this work in preference to mechanical because of the advantage of having continuously variable amplitude, frequency stability and fineness of control. The exciting force was supplied to the loading device via a Goodmans (model V50) electrodynamic vibrator, driven through a custom built low-frequency power amplifier (rated 100W) by a SE LAB Type 2001 frequency oscillator/response analyser. The oscillator had a steady frequency output ranging

from 0.01 to 999 Hz.

The voltage applied to the shaker, and hence the amplitude of the force applied to the system, was controlled by adjusting the oscillator output which ranged from 0.01 to 10 Volts. And, as for the frequency, the output voltage was read from a built-in digital indicator. There was no other adjustment between the oscillator and amplifier.

(b) The Response Measurements

The force produced by an electromagnetic vibrator is usually found by measuring the current passing through it. But this method was not suitable for this type of work and instead a B&K type 8200 force transducer was incorporated to give a direct reading of force transmitted to the loading system.

The Type 8200 is a small, permanently preloaded transducer suitable in measuring force in the range from 1 KN tensile to 5 KN compressive. In the present arrangement, the transducer was attached to the testing structure using its threaded spigot and linked with the exciter's head via an 9.5 mm diameter cylindrical push rod. In this way the force transmitted by the exciter to the whole assembly was measured. Before taking the actual measurements, the calibrated values of the transducer quoted by the manufacturer were checked.

Because of the relatively low frequency loading employed, a B&K Type 2628 LF charge amplifier was employed here to amplify the signal from the transducer. The operating principles of this type of conditioning device were similar to those (Type 2635) described in Chapter Three, except that it was specially designed for handling very low frequency or quasi-static signals.

To measure the point movement or displacement at a particular location on the structure, a B&K Type 4321 accelerometer and Type 2635 charge amplifier were used. Details of these instruments and their operation can also be found in Chapter Three. During measurement, the signal from the accelerometer was fed to either a voltmeter or other recording device via the conditioning unit. Therefore, a measured voltage corresponding to the structure motion or displacement could be obtained.

5.2.2 The Measuring Procedure

As mentioned before, the basic procedure of a resonance test is to excite the system harmonically and measure its response at particular points over a range of frequencies. The amplitude of response depended not only on the dynamic characteristics of the system, but also on the amplitude (as well as the location and

frequency) of the force applied to it.

The voltage applied to the vibrator was set at 4 Volts for most of the tests. This value was chosen after several trials and found to produce the best response over the given frequency range.

As illustrated in Fig. 5.1, the exciting force was transmitted to the structure via the push rod and force transducer. It should be noted that for these preliminary dynamic tests in which the mounting rig was not involved, the structure under test was usually bolted to a rigid foundation. The force application point was chosen at a location such as the top end of the balance column whether the elastic model was attached to it or not. On the other hand, when the model-balance assembly was mounted on top of the test rig, the excited force was then usually applied to a point at the middle of the upper cross-supporting frame.

During measurement, the miniature accelerometers were placed at certain positions within the structural system to pick up the resulting acceleration signals. The relative positions of these accelerometers, which detected the transfer response of the test rig, force balance column and the two independent lateral deflections at the top of the model, are denoted by numbers and shown in Fig. 5.1. The term transfer values referred to the cases in which force and motion were measured at different points.

Because an adequately stiff mounting for the exciter was not immediately available and also because of a tight time schedule, all response tests on the mounting frame were performed with the exciting force applied to the system in the longitudinal direction.

The signal frequency for the present tests was varied manually from 3 Hz to 100 Hz at regular interval. Subsequently, more data points were taken for frequencies close to the observed resonance values.

5.2.3 Presentation of Results.

As mentioned in the previous sections, the structural response was picked up by transducers at various locations within the system. The resulting signals, both force and acceleration, were led to the ultra-violet (U.V.) recording oscillograph via the conditioning amplifiers. To avoid confusion of recording too many traces at one time, the signals were selected through a switching box. The response amplitude (peak-to-peak) of each trace was measured from the oscillograph paper and converted to its actual value with appropriate units.

For measuring the phase angle, the accelerometer signal was fed to the frequency analyser which, by taking in a pure sinusoidal signal from the oscillator and using it as a reference, measured the phase between the excitation and the structural response. The phase angle, in terms of degree and its corresponding quadrant, was read from the analyser's built-in phase meter.

It should be noted that the terms 'longitudinal' and 'transverse' were used here to describe responses measured with respect to the model axes, because the terms 'along-wind' and 'cross-wind' were not applicable once the body was rotated. However, at zero angle of incidence, the two conventions corresponded and also coincided with the X- and Y-axes of the wind-tunnel reference coordinates.

(a) Amplitude and Phase Angle Plots

For a linear system, it can be shown that the ratio of amplitude of response to amplitude of exciting force is independent of the amplitude involved. The 'peak-amplitude' is then taken to be the 'maximum displacement per unit amplitude of force' [129]. This ratio may (loosely) be called compliance (for displacement/force) or mechanical admittance (for motion/force). In this study, the accelerating responses were measured at locations as shown in Fig. 5.1. The compliance curves, as the one shown in Fig. 5.2, are the resulting ratio of the tip deflection to force plotted against the forcing frequency.

It should be emphasised again that the results presented here only define the system's transverse response to longitudinal excitation. Inevitably, such 'induced' response was much smaller than it would have been if the force had been applied in the same direction. Therefore, the results presented here are not a direct measure of the system's transverse response but rather a reasonable representation of its dynamic behaviour under such conditions. Whereas the resulting amplitude may contribute little to the determination of the actual dynamic properties.

For comparison, the compliance curves of the finite length Perspex model-balance assembly are shown in Fig. 5.4. Apart from the model, the measuring conditions and technique were identical in both cases.

It could be seen that these compliance curves showed a number of 'peaks', each in the vicinity of a natural frequency. Comparing the longitudinal responses of Figs. 5.2 and 5.4, it was obvious that the elastic model combination had a lower damping and therefore higher response than the Perspex model combination. Their differences will be examined further in later sections.

Nevertheless, the peak-amplitude method has a serious defect in that no account is taken of the change in the phase lag of the response behind the exciting force. Since this change is most marked when the system is passing through resonance, information can be derived from the analysis of a simple phase angle plot. In fact, the phase angle plots could yield as much information regarding the natural frequency and damping as those of peak-amplitude [129].

Two graphs showing the variation in phase angle (degree by which the displacement is lagging behind the force) over the frequency range corresponding to the peak amplitude curves are shown in Figs. 5.3 and 5.5. These again relate to the accelerometer positions shown on the system in Fig. 5.1 and correspond to the peak-amplitude curves in Figs. 5.2 and 5.4, respectively.

It can be seen that in these curves, resonance is accompanied by a phase change from nearly zero degree to nearly 180 degree or from nearly 180 degree to nearly 360 degree. This is due to the fact that the measurement points were either in phase or antiphase with the displacement at the point of excitation at the resonant frequency.

5.2.4 Determination of Natural Frequency and Damping

The first piece of information to be extracted from an amplitude plot, such as those shown in Figs. 5.2 and 5.4, was the natural frequency. This being usually identified as the value of the frequency at which a peak was recorded.

This is not an exact result and is influenced by two factors. These were, first, the effect of damping which coupled the modes, and secondly the contribution from other (extraneous) modes at that frequency. However, for a system with relatively light damping and widely spaced frequencies, such effects were small. Table 5.2 lists the natural frequencies obtained from the compliance curves showed in Figs. 5.2 and 5.4.

These figures illustrated that the complete model-balance system had different natural frequencies about each of its principal axes. Such imperfection was expected because of the directional construction differences at the model-balance connection joint. Furthermore, the design and construction of the test rig, which is illustrated in Fig. 3.4, is actually stiffer along its transverse axis (i.e. perpendicular to the free stream direction). This might have a contribution towards these differences.

In Fig. 5.2, the natural frequencies of the first three longitudinal modes are identified, namely at 5.85, 21.6 and 32.2 Hz. In the transverse direction, two peaks are positively identified, namely those at 6.4 and 28.5 Hz.

The transverse response curve also showed a peak between the two identified above. This peak, referred as p' in Fig. 5.2, had a frequency value which coincided exactly with one measured in the longitudinal direction. Nevertheless, such a peak was not found in the case when the elastic model was replaced with the Perspex model, as shown in Fig. 5.4. Further evidence was obtained from the strain gauge measurements. The gauges output, measured with and without the elastic model attached, are shown in Fig. 5.6(a) and (b), respectively. It is evident that the small peak occurred only when the elastic model is attached to the force balance column. Therefore, it is concluded that the peak, p' , was most likely caused by the coupling effects between the two motion directions of the assembly at that particular frequency.

On the other hand, the compliance curves in Fig. 5.4 indicated that the Perspex model-balance assembly had a fundamental frequency slightly higher than those for the elastic model assembly, namely 7.3 and 7.8 Hz compared to 5.85 and 6.4 Hz. This could be solely due to the weight difference between the two models used.

The second piece of information which could be derived from the amplitude plots was the damping coefficients. The structural damping is a measure of the energy of vibration dissipated per cycle; it arises from the movement of the foundations in the ground, fretting of the joints and hysteresis effects within the structural materials.

Pendered et al. showed that [129], if each peak is assumed to represent motion in only one mode, then the damping coefficient may be calculated from the sharpness of the peak.

Under this assumption, the dimensionless damping coefficient, μ_s , is given by,

$$\mu_s = 2\zeta = \frac{\Delta f}{\hat{f}_i}$$

in which ζ is the damping ratio, Δf is the bandwidth and \hat{f}_i is the peak frequency at i th mode. In literature, such as [130], this is also known as the half power point method and the reciprocal of the damping coefficient is called the Q factor. The presence of motion in off-resonant modes introduced some error into the use of this method.

Figs. 5.7-5.10 show the transfer mechanical admittance (mobility) curves from various tests, including the mounting rig alone; the force balance dynamometer; the model-balance assembly and the complete assembly. In each case, the accelerometer was placed in the system as the accompanying diagram illustrated. The change in the number of peaks (number of modes), their locations (natural frequencies) and their amplitudes (damping) have clearly demonstrated the influence

of each additional part on the resulting mechanical characteristic of the system. The information derived from these plots is given in Table 5.2.

5.2.5 Determination of Natural Frequency and Damping by Other Methods

As seen in the previous sections, the damping coefficients estimated by the half power point method required very accurate measurement of the vibration amplitude for excitation frequencies in the resonant regions. But, if the structure under testing had low damping (high Q factor), then it would be a difficult task to assess the peak amplitude and hence there might be significant errors in the half power point location, and a large percentage error in the bandwidth because it was so small.

To reduce such errors, Pendered et al. [129] suggested an alternative approach utilising the phase angle plots. At first, by assuming that for a single mode, the stiffness and inertia forces balance out and the excitation force overcomes the damping force only, then the frequency at which the resonant condition occurred would be the natural frequency. Thus in Figs. 5.3 and 5.5, the natural frequency is given by the interaction of the phase angle curve with the line (i.e. $arg(\theta) = 90$ or 270 degree).

And just as the sharpness of the peaks of the amplitude curves gave a measure of freedom from damping, the coefficients of damping may also be calculated from the slope of the phase angle curve at this point. And the damping coefficient is given by [129].

$$\mu_i = \frac{2}{f_i \times (\text{slope at } f_i)}$$

Compared with the peak-amplitude method, in this approach it was only necessary to plot the phase angle curve over a small range of frequency to obtain both pieces of information. Furthermore, because the phase angle was independent of the amplitude of either the exciting force or response motion, only the phase angle reading had to be taken for each frequency considered. The major analytical advantage of this method, however, lay in the fact that the determination of the natural frequency did not depend upon the accurate location of a 'peak'.

Nevertheless, just as there is the difficulty of accurately locating a peak in an amplitude curve, the estimated value obtained from the phase angle approach was hampered by the difficulty of measuring the slope with sufficient precision. Moreover, the values obtained from both of these two methods were affected somewhat by the coupling of the modes and presence of motion in off-resonant modes.

Pendered and Bishop [129] proposed an improved version of the amplitude approach to estimate damping. In this the effect of off-resonant vibration was considered but, as demonstrated by the same authors, unless the location of a peak in a curve was precisely located, the improvement was small.

The natural frequencies and damping values, estimated from the peak-amplitude plots, listed in Table 5.2, were examined and compared with those from their corresponding phase angle plots. The resulting values showed little discrepancy and were therefore not listed here.

Another convenient way of assessing the damping in a structure was by means of the free-decay method. In this approach, the structure was simply set into free oscillation by a step perturbation (or by pushing the model structure to one side, releasing it and allowing it to vibrate freely) with the flow at rest. The damping was represented by the natural logarithm of the amplitude ratio of successive cycles of oscillation.

Using this technique, it was usually impossible to excite any mode other than the fundamental mode, which also dominated the response, since all the higher modes were damped out quite quickly. The damping ratio, ζ , was determined by analysing the decay traces.

In the present wind tunnel studies, the free-decay method was a more convenient way to estimate the damping of the model structure because it did not require an external exciter. In fact, in the subsequent measurements, the damping values were obtained in this way for every testing configuration just prior to any actual measurement taking place. A typical trace of such exponential decay oscillation is shown in Fig. 5.11.

To reduce the work loads, a FORTRAN programme was written and used in conjunction with the DEC microcomputer. The main function of this routine was to take in signals from the accelerometers via their conditioning units and to plot the actual displacement traces on the associated graphical terminal. By locating the peaks on the curve and measuring their amplitudes, the logarithmic decrement, δ , could be found, i.e.

$$\delta = \ln \left(\frac{\text{amplitude of motion}}{\text{amplitude of motion one cycle later}} \right)$$

Note that $\delta = 2\pi\zeta/\sqrt{1-\zeta^2}$, and for low damping $\delta \approx 2\pi\zeta$.

But if the peaks of the vibration-decay trace were ill-defined, then it was very difficult to obtain a good estimation of the damping using this conventional

technique. Because of this, a method which estimated the damping from the enclosed area ratio and which was first proposed by Russel [131], was used here to complement the free-decay values.

In this method, as illustrated in Fig. 5.11, a smooth curve of AB' of the form, $x = x_o \exp(-\zeta 2\pi ft)$ was drawn to envelope the peaks. The area enclosed by AB'CD was then measured with a planimeter. If area AB'CD = a' and ABCD = a , then

$$\frac{a'}{a} = \frac{(1 - \exp(-\zeta 2\pi f_o T))}{(2\pi f_o \zeta)}$$

From a table of a'/a versus $2\pi f_o T$, see [131], the value of $2\pi f_o T$ for a particular area ratio could be read off. Since the period, T , and fundamental frequency, f_o , were known, then the damping ratio, ζ , could be calculated.

Table 5.2 also lists the average values of natural frequency and damping determined by the free-decay oscillation method.

It can be seen that the fundamental frequency of the complete assembly measured from the amplitude plots were 5.85 Hz in the longitudinal direction and 6.4 Hz in the transverse direction. These might be compared with the values obtained from the free-decay method, namely 6.25 Hz and 6.76 Hz respectively. No definite explanation can be offered for the discrepancy of about 6% between these two sets of values. However, the difference in the natural frequencies about each of the system's principal axes measured from the amplitude plots (0.55 Hz) was close to that obtained from other method (0.5 Hz).

To explore the directional effect on the measured damping values, the model-balance assembly was rotated from zero degree to 90 degree at 15 degree interval. At each setting, the values of natural frequency and damping were measured by means of the free-decay method. Fig. 5.13(a) and (b) show the variation of the damping ratios, estimated from both upper and lower traces, with the angle of inclination between the two lateral directions of the model and the wind tunnel reference axes. The data showed in these diagrams were taken from two sets of readings using the same equipment and technique, but measured at different times.

These results clearly indicated that the measured damping ratios could not be correlated to the model incident angle. In view of such inconsistency, it is concluded that the inherent damping inside the model-balance assembly was not of the viscous type alone, but might be a combination of viscous and coulomb (dry friction) type damping. To confirm this, the amplitude of the peaks from Fig. 5.11 was replotted in natural logarithm against time, see Fig. 5.12. The nonlinearity near the end of the

line confined the existence of the coulomb type damping in this trace.

5.2.6 Verification of Interaction between Orthogonal Force Components

In Chapter Three, the calibration of the strain gauges output from the force balance column indicated that the interactions between orthogonal gauges under static conditions were very small. To check the coupling effects under the dynamic conditions, the tests described in the previous section were repeated with readings from the strain gauge circuits being taken. Outputs from the longitudinal and transverse strain gauge sets are shown in Fig. 5.14(a) and (b), respectively. In both cases, the tests were performed either with or without the elastic model attached and with excitation force applied in the longitudinal direction.

The spectra of the complete assembly in these diagrams showing the first three longitudinal modes and the first two transverse modes corresponded to those found in the compliance curves.

It is evident from these curves that the transverse strain gauge set produces a significant output when the forced excitation is applied to the assembly longitudinally. In fact, in the fundamental mode, the peak output amplitude from both longitudinal and transverse bridge systems is about the same. This could mean that the whole system is oscillated in both planes. But it also means that the excitation energy could be transferred from one principal axis to another. Nevertheless, the magnitude of such interaction effects is difficult to evaluate and therefore, in this study, no correction is applied to the measured responses. On the other hand, the widely spaced peaks at the higher modes suggest that there is little interaction between the force components at higher modes.

5.3 Measurements of Model Wind Loads and Corresponding Dynamic Responses

A tall, elastic structure exposed to the natural wind may be set into vibration by the action of the wind. Oscillations may be induced by some form of aerodynamic instability or by the regular shedding of vortices.

In general, the longitudinal (or in-line with the wind direction) vibration of an isolated structure is primarily excited by the random fluctuation of the wind velocity associated with turbulence, and the transverse (cross-wind) oscillation is mainly caused by the periodic shedding of large vortices into the wake of the structure. Changes in the transverse force component and its centre of action are the major source of torsional oscillation about its elastic axis.

The amplitude of oscillation of a structure responding to a particular aerodynamic force is dependent on the structural mass and damping. The aerodynamic force itself depends on many factors, including the shape of the structure, Reynolds number, reduced wind velocity and the amplitude of the structural motion.

The present measurements, by using a closed-return wind tunnel and aeroelastic model incorporating torsional and translational degrees of freedom, were aimed to investigate the followings:

- Wind-induced loadings and responses of a tall square tower model as functions of mean wind speed and flow characteristics of the approaching airstream.
- Effects of flow incident angle on the model wind loads and its response.

5.3.1 General Approach

By using an elastic model-balance system, a series of measurements were performed in order to determine the mean and fluctuating wind loads, including torque and translational bending forces induced by the action of the wind. It should be mentioned here that, because neither the model nor the long dynamometer on which it was mounted were rigid, the mode shape of the complete assembly could not be described by a straight-line deflection shape. Therefore the linear relationship between excitation and response, through which the displacement spectrum at the top of the model can be determined from the force spectrum or vice versa [8], is not applicable here.

Because of this reason, the translational responses at the top of the model were measured by accelerometers mounted near its end. The resulting acceleration signals were integrated to yield the equivalent displacement signals by the conditioning units.

On monitoring the mainly resonant responses from the model, the random signals obtained from the strain-gauge transducers and accelerometers were found to be narrow-band and had dominant frequencies near the system's fundamental mode. The wake spectrum was determined from velocity fluctuations measured in the near-wake region using a linearised hot-wire anemometer. Signals obtained from such measurements usually showed characteristics similar to wide-band noise. Analysis of these wide-band random signals was confined to the region of interest, from DC to 150 Hz.

To assess the effects of free stream turbulence on the model response, measurements were carried out for the following cases: (1) uniform smooth flow,

i.e. clear wind tunnel with turbulence intensity less than 1% and (2) uniform turbulent flow, i.e. with turbulence generating grid installed inside the wind tunnel. The construction of the square mesh grid and the resulting wind structure have been described in Chapter Three.

In the smooth flow situations, the mean wind speed upstream of the model normally varied between 5 m/s and 30 m/s. This gives a full range of reduced velocity, $\bar{U}_r = \bar{U}_o / f_o B$, varying from 7.8 to 46.9. For simplicity reasons, the fundamental frequency, f_o , is taken as 6.3 Hz about each of the model principal axes. This figure is close to those obtained from the displacement spectrum analysis which gave a dominant frequency of 6.25 Hz in both lateral directions.

By installing a square mesh grid at the entrance of the working section, a second wind speed range between 4 m/s and 20 m/s was obtained and a corresponding range of reduced velocity from 6.3 to 31.3.

Unless specified, all values measured in the time domain were normalised according to their natures and expressed as functions of mean wind speed, \bar{U}_o , and reduced velocity, \bar{U}_r , whereas the normalised spectra (or other functions in the frequency domain) were presented in terms of frequency, f .

In the following discussions, the terms 'longitudinal' and 'transverse' are preferred to describe responses with respect to body axes because the terms 'along-wind' and 'cross-wind' are strictly in the directions parallel and normal to the mean wind and are not applicable once the body is rotated. At zero angle of incidence, longitudinal and transverse are equivalent to along-wind and cross-wind respectively.

5.3.2 Model Forces as Functions of Mean Wind Speed and Flow Characteristics

The aerodynamic forces and torque characteristics of the 10x1x1 square tower are established by measuring the wind-induced loadings via the force balance dynamometer on which the model was mounted. The time-averaged mean and fluctuating (RMS) coefficients of torsional moment and bending forces in the two translational directions, measured in both smooth and turbulent flows, are presented as functions of reduced velocity in Figs. 5.15(a)-(f) and 5.16(a)-(f), respectively.

Other results determined by analysing the time-series data for a number of wind tunnel tests, such as probability density functions and auto-power spectra, are presented in Figs. 18-21. Detailed description of the software routines used in the data analysis and presentation can be found in Chapter Four.

(a) Torsional Moment Coefficient

Conventionally, wind loads used for structural design are taken to be either uniformly or symmetrically distributed. But actual overall wind loads are seldom uniformly distributed even for buildings with symmetric geometries. Mean torsional moments for such buildings can occur due to non-uniformities in the flow field and for wind directions not aligned with the axes of building geometry, whereas the fluctuating torques are caused by unbalance in the instantaneous pressure distributions [22].

Nevertheless, in the present measuring system, the eccentricities between the centre of pressure distribution and the section's elastic centre are very small. This, together with the high torsional rigidity inherent from its design, means that the amplitude of the fluctuating signals from the torsional strain-gauges is small, as illustrated by the RMS coefficient curve in Figs. 5.15(d) and 5.16(d).

However, it is apparent that, for the range of reduced velocity of the tests, the variation of mean torsional moment acting on the tower in smooth flow correlates with the variation of the transverse force component.

A similar response pattern was observed by Isyumov et al. [22]. By applying pneumatic averaging of the local pressure distribution around square and rectangular section building models, they found that changes in the transverse force component and its centre of action are the major sources of torsional moments. An important finding is that pressure fluctuations on the back face induced by vortex shedding can provide an important contribution to the dynamic torque. The latter may also be associated with flow re-attachment intermittencies for shapes with relatively short afterbodies. But the absence of pressure tappings on this model meant that the effect due to pressure fluctuations could not be verified in this investigation. However, as illustrated by the normalised torsional moment spectra in Figs. 5.20(a) and 5.21(a), torsional vibration due to the mechanism of vortex shedding is prominent.

It should be mentioned here that because of the low strain-gauge outputs and high amplification factor (5 times higher than those in measuring forces) set at the conditioning units, the signal-to-noise ratio is relatively low. It is clear that in some cases, the amplitude level of the background noise was higher than that from the gauges. The noise came from two sources: the AC/DC generator motor which has a rotational speed of 25 Hz and the 50 Hz from the main supply picked-up during digitisation.

Probably because of these reasons, the probability density distributions of the torsional signals, shown in Figs. 5.18(a) and 5.19(b) at various reduced velocities, may reveal nothing about the dynamic torque but merely the effects due to the background interferences.

Presented in Figs. 5.20(a) and 5.21(a) are the normalised torsional moment spectra of the square tower in smooth and turbulent flow conditions. Despite the disruption from the noise, there is a peak response at the frequency which coincides with the natural frequency of the measuring system. This, together with a marked increase at the critical reduced velocity (also reflected in the mean value curve) suggests that the wake excitation, and in particular the vortex excitation, is the dominant excitation mechanism.

Furthermore, the resulting torque spectra from turbulent flow is about an order of magnitude bigger than those measured in smooth uniform flow. This indicates that velocity fluctuations in the approaching flow could increase the torque resulting from asymmetrical pressure fluctuations, as is generally believed.

(b) Longitudinal and Transverse Force Coefficients

In the past, wind tunnel modelling of tall slender structures was usually designed to permit vibration in the cross-wind direction only, the assumption being that the structural response was predominant in that direction. But the recent experimental works by Perera [132] and Sykes [133], in which they showed that coupling between the lateral and longitudinal modes of vibration could lead to an effective increase in structural damping, had made such assumption open to doubt.

It is therefore not surprising that results obtained from the present measuring system, which incorporated torsional and translational degrees of freedom, could be radically different from those obtained with models having a single mode of vibration. However, the results presented here are always compared with those from other works and, whenever possible, an explanation of their similarities and discrepancies is given.

To begin with, variations of the fluctuating force coefficients of the square tower as functions of the reduced velocity, measured in both smooth and turbulent flows, are presented in Figs. 5.15(e)&(f) and 5.16(e)&(f). A marked increase in the force amplitude, in both along-wind and cross-wind directions, is evident at a critical reduced velocity of about 10.8 in smooth flow and 11.4 in turbulent flow. The cause of peak response at and near the critical reduced velocity is attributable to vortex excitation when the frequency of the shedding vortices approaches the natural frequency of the structure.

It must be pointed out that, due to the model's inertia and its substantial displacement at and near to the critical reduced velocity, the output from the strain gauge dynamometer could not, in this circumstance, be a measure of the actual amplitude of the aerodynamic force acting upon it.

On the other hand, the simultaneous occurrence of the peak response in the along-wind direction at the critical reduced velocity is consistent with the behaviour pattern observed by Lee [134]. As shown in Appendix C, if the natural frequencies about each of the principal axes are nearly equal and if the incident wind is not exactly aligned with either of these axes, then at the critical wind velocity when the total damping of the cross-wind vibration is very small, coupling can occur between the along-wind and cross-wind motions. The amount of energy transferred is dependent on the angle between one of the axes and the direction of the initial excitation.

Figs. 5.15(e) and 5.16(e) show the considerable along-wind component which is produced by this type of energy transfer at the expense of the cross-wind motion. In the absence of this effect, as shown in [134], the cross-wind amplitude would be larger and only a small amount of along-wind motion due to buffeting would be present. These results are generally in line with those obtained by Perera [132] and Sykes [133].

Changes in wind exposure for the square tower from uniform smooth flow to uniform turbulent flow results in a considerable increase in wind loading. Simply speaking, at the critical reduced velocity, there is a 1.8 times increase in the along-wind direction and 3.3 times in the cross-wind direction. More about the effects of free stream turbulence on the aerodynamic response characteristics is given in later sections.

As shown in Fig. 5.15(b), the average value of the along-wind force coefficient in smooth flow is approximately 1.5. This is about 10% lower than the value given by ESDU [135] in which the along-wind force coefficient was measured from surface-mounted square block of the same aspect ratio.

The discrepancy is getting even bigger in the turbulent flow cases. As shown in Fig. 5.16(b), the along-wind force coefficient, averaged over the entire speed range, is 0.81 and is about 33% less than the value estimated from ESDU [135] for the same turbulence intensity. Differences in test conditions, in particular the wind model used in the turbulent flow measurements, and the omission of the oscillation due to vortex shedding and other instability mechanisms may all contribute to the higher along-wind force given by ESDU.

For most modern tall buildings and structures under normal wind action, excitation associated with the wake is considered to be the dominant mechanism, and the response process is usually well represented by a normal, i.e. Gaussian distribution. This is clearly illustrated by the amplitude traces of the strain-gauges signals, shown in Fig. 5.17, and their subsequent probability distribution plots, shown in Figs. 5.18 and 5.19, in both smooth and turbulent flows at various reduced velocities.

The Gaussian distribution, which is calculated from the mean and variance of the recorded digital data and is drawn in solid line, is presented on these plots for comparison. It is evident that the wind-induced loading on the square tower, either in smooth or turbulent flow and in both the along-wind and cross-wind directions, follows the theoretical distribution quite well.

But, at and near the critical reduced velocity and when the shedding frequency approaches the natural frequency of the structure, the model will respond to the fluctuating forces and oscillate with appreciable amplitude in the cross-wind direction. Under such conditions, there is a significant interdependence of variables in the cross-wind excitation and response. Excitation due to the oscillating wake is magnified by the presence of other wind-induced instability mechanisms, such as displacement dependent lock-in. According to Kwok [8], lock-in is a phenomenon whereby the cross-wind displacement of a structure causes an increase in the wake energy which in turn increases the cross-wind response of the structure. The resulting motion of the tower not only affects the frequency of vortex shedding but also increases its axial correlation, thus increasing the total excitation acting on the body.

Consequently, the response near the peak usually departs from the normal distribution; the resonant response usually resembles that of a sine wave, such as those described in Appendix B. The same is true about the input force. This phenomenon is illustrated by the strain-gauge traces in Fig. 5.17, and its probability distribution in the cross-wind direction at $\bar{U}_r = 10.89$, as shown in Fig. 5.18. The sinusoidal nature of the model response near the peak also provides the information so that the displacement amplitude at the tip of the model may be calculated from known parameters [137].

In the turbulent flow situation, a similar response pattern is observed at the critical reduced velocity of about 11.7. It is evident that the sinusoidal type distribution occurred in both along-wind and cross-wind directions (but is less well-defined than in smooth flow). This suggests that energy transfer (coupling) between the two translational directions is stronger in turbulent flow than in smooth flow.

It is also interesting to note that in uniform smooth flow, a mode higher than the fundamental mode of vibration exists at reduced velocity of about 45.

The normalised along-wind and cross-wind force spectra, in both smooth and turbulent flows and at various reduced velocities, are presented in Figs. 5.20 and 5.21. As happened in the torsional moment measurements, the signals from the longitudinal strain-gauges were relatively weak and were 'masked' by noise from background interferences. However, the energy contribution from the noise reduced as the signal-to-noise ratio level improved. For the whole range of reduced velocity there is a pronounced peak at and near to the natural frequency and may represent the resonant response in the along-wind direction. However, in turbulent flow, the peak values are one order higher in magnitude than those obtained in smooth flow. This may simply be the effect of buffeting excitation due to the incident turbulence in the along-wind direction.

In the cross-wind direction, the normalised force spectra under both wind exposures have similar basic shapes. A typical spectral peak at and near the natural frequency of the measuring system suggests that the model is subjected to a strong wake excitation. Change of the turbulence intensity level in the incident flow shows little impact on the resonant peaks at the critical reduced velocity but results in a considerable broadening of the normalised cross-wind force spectrum, as shown in Figs. 5.20 and 5.21. The latter is likely to be caused by a reduction in correlation of the vortex shedding process associated with increase in turbulent intensity. Peaks corresponding to a higher mode of oscillation are observed in the cross-wind force spectrum in both smooth and turbulent flows at reduced velocities higher than 20. The second peak amplitude gradually increased as the reduced velocity increased. Its frequency is estimated to be at somewhere between 29-30 Hz.

5.3.3 Model Responses as Functions of Mean Wind Speed and Flow Characteristics

Standard deviation of the fluctuating displacement response at the top of the square tower was measured for reduced velocity ranges from 8 to 40 in uniform smooth flow and 5 to 30 in uniform turbulent flow. Variations of the normalised tip deflections in the longitudinal and transverse directions, measured with the mean wind either normal (0 degree), or at 45 or 90 degrees to one face of the square tower, are presented in Fig. 5.22(a)-(c) respectively as a function of the reduced velocity.

Fig. 5.22(a) represents a typical response diagram for the vortex-excitation of a square tower model in smooth flow. At wind speed below the critical value, the

response is of very small amplitude and is random in character. But as the wind speed increased to a value for which the frequency of the shedding of complementary pairs of vortices is close to the natural frequency of the structure, a sharp increase in oscillation amplitude appears. The amplitude peak occurs at a reduced velocity of about 10.8 and the amplitude of oscillation is fairly constant. On further increasing the wind speed, the response then falls to a low level with the amplitude again becoming random. As expected, the oscillations at the peak amplitude occur almost entirely in the transverse direction whereas the longitudinal component of amplitude increases almost proportionally to the reduced velocity. A similar response pattern in transverse response of a square tower was reported by Melbourne [51] and Kwok [8].

With the turbulence intensity in the free stream increased, the transverse response is increased by 20% at the critical velocity of about 11.5, see Fig. 5.23(a). It is interesting to note that in both uniform smooth and turbulent flows, high RMS values of oscillations are maintained at flow speed above that at which the peak occurred and tend to increase with wind speed.

With one edge of the square tower pointing towards the oncoming flow ($\alpha = 45$ degrees), two strong vortices are shed from the front corner [17]. The separated flow over the top of the tower is then interacting with the shear layers coming from other directions. The characteristic peak response disappears and the model response simply increases as the wind speed is increased. On the other hand, the effect of turbulence in the free stream is to 'wash out' the tip effect and allow coherent vortex formation. The result is an overall increase in the response magnitude as shown in Fig. 5.23(b).

Comparing the curves of Fig. 5.22(c) (in which the model-balance assembly was rotated by 90 degrees from its normal orientation) with those of Fig. 5.22(a), the results indicate that the energy transferred between the two motion directions is more effective in one direction than in the other and as the amount of energy transferred increases, so does the effective damping in the transverse direction.

In order to visualise the tip movement of the square tower in both smooth and turbulent flows, X-Y plots of the amplitude traces are drawn at various reduced velocities and presented in Figs. 5.24 and 5.25. It should be mentioned here that the traces presented in these diagrams represent about 3 seconds of the recorded digital data (one-tenth of the total). For reference purposes, the normalised along-wind and cross-wind responses which are calculated from data over the whole sampling period are also presented in Figs. 5.24 and 5.25 as a function of the reduced velocity. Each X-Y plot is denoted with a letter which also indicates the relative position of

each data set in terms of reduced velocity.

It is clearly shown in these plots that in the smooth flow, the response is dominant in the transverse direction at reduced velocity below 30. With the along-wind component becoming bigger in response to the incident turbulence, the oscillations become elliptical along the transverse direction. The almost constant-amplitude sinusoidal response at and near the critical reduced velocity is further evidence to support that vortex shedding is the basic exciting mechanism of the model oscillations in both types of flow.

At higher reduced velocities, the resonant-like elliptical response occurs less regularly and is interrupted by short bursts of normally distributed response. In fact, at high reduced velocity, the dynamic response characteristic of the tower is very similar in both smooth and turbulent flows.

5.3.4 Response Characteristics of the Second Measuring System

In most of the published reports of the wind-tunnel investigations of the interference excitation between neighbouring tall buildings, measurements were usually taken on an instrumented model and referred to as the 'principal' building. The other model, which is referred to as the 'interfering' building, was used to provide interference by locating it at any position upstream and downstream of the identical principal building.

It was decided at the beginning of this study that results measured simultaneously from a pair of fully instrumented models would give a more accurate representation of the prototype and a better understanding of the excitation mechanism involved under all flow conditions. Therefore, an aeroelastic square tower model and a strain-gauged force balance column with specifications exactly identical to those described in Chapter Three, were built. The aerodynamic response characteristics of this system are discussed in this section.

For convenience, from now on, the interfering tower model is always located upstream and is referred to as system B, the downstream tower model being referred to as system A, see Fig. 3.12.

However, despite all the efforts to keep the two assembled systems identical, results from the initial tests indicated that the damping of system B was significantly higher than that of system A and, consequently, the displacement response of system B was reduced.

It was not clear at that time what caused this high damping. In an attempt to eliminate the problem, the strain gauge dynamometer was stripped to pieces and rebuilt. However, after many frustrated attempts, it was finally decided that dry friction, which may be caused by a slightly bigger clearance between the contact surfaces of each component, was the major cause. The problem was partially solved by tightening up some key components of the column. And it is fair to say that the resulting mechanical characteristics of system B are close, but do not exactly match those of system A.

The mean and fluctuating torsional moment and force coefficients, measured by system B in smooth uniform flow, are presented in Fig. 5.26(a)-(f) as a function of reduced velocity. The basic shapes of these curves are similar to those obtained from system A, as shown in Fig. 5.15(a)-(f). The apparent increase of wind loads in the cross-wind direction, at the expense of a decrease in the along-wind direction, reflects the effects due to the energy transference between the two motion directions.

For comparison, the normalised tip deflections of the square tower measured by the two systems in smooth uniform flow are shown in Fig. 5.27(a) and (b). It is evident that for the range of reduced velocity, the transverse response characteristics of the two measuring systems are close to each other.

Measurements were also performed on system A which, unlike the results presented above, was mounted on the test rig with long platform. The resultant transverse response is plotted in Fig. 5.28(a) in dotted line. The offset of the peak at the critical reduced velocity suggests a shift of the natural frequency of the complete system due to a combination of effects resulting from the long platform's weight and geometry.

5.3.5 Model Forces and Responses as a Function of Angle of Incidence of the Mean Wind

The response characteristics of the 10x1x1 square tower in both smooth and turbulent flows at various reduced velocities were measured over a 90 degree range of angle of incidence of the mean wind at 5 degree interval. The results presented include the mean and fluctuating torsional moment and transverse force coefficients, and the normalised transverse displacement at the top of the model.

(a) Normalised Transverse Response

Standard deviation transverse response of the square tower in the smooth flow wind model was measured at $\bar{U}_r = 10.9, 23.6$ and 39.2 , and in the turbulent flow wind

model at $\bar{U}_r = 11.8$ and 23.6, as shown in Fig. 5.28(a) and (b) respectively. The reduced velocities were chosen to be representative of operating conditions in which either vortex excitation or wake excitation is the dominant excitation mechanism.

As the angle of incidence of the mean wind is increased, there is an increased tendency for the separated shear layer to re-attach to the windward face of the square tower. The effects of re-attachment are a reduction in excitation forces and hence a decrease in the transverse response. It is evident in Fig. 5.28(a) that the decrease in response is considerable and is quite rapid over the first 20 degrees.

For flow normal to one face, that is at zero angle of incidence, the response amplitude is generally higher in turbulent flow than in smooth flow. It is also interesting to note that in smooth flow, as shown in Fig. 5.28(a), the transverse response has its highest amplitude when the angle of incidence of the mean wind is about 10 degree from normal to one face. A similar phenomenon was observed by Rosati [21] and Kwok [8] in their studies of the response characteristic of a slender square tower, but at different incident angles.

(b) Torsional Moment and Transverse Force Coefficients

As mentioned in the previous sections, wind-induced torque acting on a prismatic building can occur due to non-uniformities in the mean flow and for wind directions not aligned with the axes of building symmetry. With one face normal to the mean wind, the centres of mean pressure are approximately at the middle of each face. A small change of the incident angle of the approaching flow, either due to transverse body motion or velocity fluctuations in the mean flow, could rapidly shift the centre of pressure forward along the windward face towards the leading corner. The variation of the magnitude and line of action of the transverse force resulting from fluctuations in approaching flow is illustrated by the rapid rate of change in the mean torsional moment over the first 30 degrees, as shown in Fig. 5.29(a). Whereas the effect of the change in angle of incidence in uniform flow is less dramatic.

As seen from Fig. 5.30, the maximum value of the fluctuating torque occurs at zero angle of incidence and the magnitude is gradually reduced to a minimum at and around 45 degree. In turbulent flow, the torsional moment coefficient is about an order of magnitude higher than those in uniform smooth flow. This again suggests that the torque fluctuations tend to be related to velocity fluctuations in the approaching airstream.

Transverse force coefficients of the square tower, measured in both uniform smooth and turbulent flows at three reduced velocities, are plotted in Fig. 5.29(b) as a function of angle of incidence of the mean wind. The negative force coefficient at

small angles of incidence and negative slope at zero angle of incidence are typical for square-section bodies. Hence for a quasi-steady approximation, the square tower satisfies Den Hartog's criterion for galloping instability, that is

$$\left. \frac{dC_{F_y}}{d\alpha} \right|_{\alpha=0} < 0.$$

and is expected to be susceptible to galloping in both smooth and turbulent flows. More about the effects of transverse force and free stream turbulence on model stability is given in the following sections.

Also shown in Fig. 5.29(b) is the transverse force coefficient of a surface-mounted square-section cylinder of the same aspect ratio, given by ESDU [135]. It can be seen that the agreement between the negative force coefficients measured at small angles of incidence is generally good, but the gap increases quite rapidly after the first 20 degree. Differences in test conditions and the type of model used may both contribute to the fact that a higher transverse force response was given by ESDU.

5.3.6 Aerodynamic Damping

It has been established in Appendix C that the aerodynamic force acting on a square-section body is proportional to the slope of the transverse force coefficient versus angle of incidence of the mean wind. The aerodynamic force can be quantified in the form of an equivalent aerodynamic damping, as discussed in Appendix C. A generally accepted criterion of structural stability is that large amplitude oscillation, such as galloping, will occur if the resulting damping, that is structural damping plus aerodynamic damping, equals or is less than zero. As defined in Chapter Two, galloping is the term used to describe large amplitude single degree of freedom motions associated with a sectional aerodynamic force characteristic which produces a force in the direction of and in phase with the cross-wind motion. And it has been shown in Refs. [91]-[95] that galloping of slender structures is very dependent on turbulence and is confined to relative low values of structural damping and high reduced velocities in natural wind conditions.

It is generally believed that a square-section body is prone to galloping in both smooth and turbulent flows. Therefore it was important to determine whether the square tower model used in this test could develop galloping at high reduced velocity. This can be done by applying a quasi-steady linear approximation to the aerodynamic force associated with the transverse force characteristics obtained from the present measurement.

As a first approximation in which non-linearity is neglected, the equivalent aerodynamic damping for the complete structure in the cross-wind direction (eqn. C.1 in Appendix C) can be expressed as,

$$\zeta_a = \frac{-1}{8\pi} \frac{\rho}{\rho_s} \frac{\bar{U}_o}{fB} \int_0^1 \frac{\bar{U}_z}{\bar{U}_o} \frac{dC_{F_y}}{d\alpha} \mu^2(z) dz$$

in which the velocity profile can be replaced by a standard power law expression,

i.e. $\bar{U}_z/\bar{U}_o = (z/H)^\gamma$. For a slender building it is often possible to assume a linear deflection mode shape and a constant value for $dC_{F_y}/d\alpha$ over the whole height of the building. The above expression can be reduced to,

$$\zeta_a = \frac{-3}{8\pi(3+\gamma)} \frac{\rho}{\rho_s} \frac{\bar{U}_o}{fB} \frac{dC_{F_y}}{d\alpha} \quad \text{---(5.1)}$$

Kwok [8] measured the transverse forces acting on a 18x1x1 square tower at different angles of incidence of the mean wind in three types of flow, namely, uniform smooth flow, turbulent boundary layer flow and rod-generated turbulent flow. The transverse force coefficients from his tests are reproduced in Fig. 5.31. The transverse force coefficients from measurements made in the present experiment and similar force coefficient measurements made by Laneville and Parkinson [95] on a two-dimensional square prism in grid-generated turbulent flow are also presented in Fig. 5.31. For similar conditions, the comparisons are generally quite reasonable.

From his measurements, Kwok established that for flow normal to one face, there was considerable galloping response in both the turbulent flows but there was no galloping in uniform smooth flow until the angle of incidence of the mean wind was about 9 degree from normal. He postulated that, at zero angle of incidence, the aerodynamic force resulting from the negative slope of the transverse force coefficient was sufficient to cause galloping in the turbulent boundary layer flow but was not enough in the uniform smooth flow. It was not until the angle of incidence of the mean wind was about 9 degree that the negative slope of the transverse force coefficient was sufficient to cause galloping in the smooth flow.

In comparison, for the values obtained from the present measurements, as shown in Fig. 5.31, it is apparent that at zero angle of incidence, the aerodynamic force resulting from the negative slope of the transverse force coefficient was sufficient to cause galloping type response in the turbulent flow but was not enough in the uniform smooth flow.

In turbulent flow, the negative slope is highest at zero angle of incidence. By applying eqn. 5.1, the negative aerodynamic damping is estimated to be -0.7% of its

critical value at the highest operating reduced velocity. This value is lower than the structural damping at 3.4% critical, as shown in Table 5.2. Hence the resulting damping is high enough to prevent galloping from happening. Because of the smaller negative slope value at zero angle of incidence, it is even less likely that galloping could develop in the uniform smooth flow. Therefore, it can be concluded that excitation due to galloping does not occur in this investigation.

5.3.7 Effects of Free Stream Turbulence on the Model Wind Loads and Responses

Observations made in the present series of experiments do not agree entirely with earlier works on the effects of free stream turbulence on model responses, such as those by Vickery [12] and Kwok [8]. It is generally known that parameters such as the height to breadth ratio of the model tested and the Reynolds number may affect the resulting response amplitude [138], but probably the most important factor that can have considerable influence on the model response is the mechanical response characteristic of the model or the measuring system itself. This is illustrated here by the fact that under the given conditions, the present model does not display galloping behaviour. Whereas the square tower model used in Kwok's measurements was prone to excitation due to galloping.

The aim of the following discussion is not to investigate the cause of these discrepancies in detail but rather to establish a physical mechanism to explain the effects of free stream turbulence on the aerodynamic response characteristics of a square tower.

It is well known that the addition of turbulence to the flow can raise or lower the drag (along-wind force) and base pressure coefficient of bluff bodies, depending on the turbulent intensity and the geometry of the body [13].

Gartshore [78] suggested that the effect of increasing free stream turbulence is to increase the mixing in the shear layers and hence increase the rate of entrainment of the surrounding fluid. Both the increased entrainment and the growth of inherent instabilities would cause the mean shear layers to thicken. In addition to this, it is also possible that increased entrainment will produce a lower pressure behind the body which will cause the radius of curvature of the shear layers to decrease so that the layers will be bent further inward towards the body sides. The result of either or both of these processes is that there will be an intermittent re-attachment of the mean shear layer to the side face. The subsequent deflections of the shear layers cause the vortex formation region to move downstream, thus raising the base pressure. The more complete pressure recovery on the side faces and a rise in the base pressure lead to a reduction in the drag force, as shown by Lee [13]. In this

study, the reduction of drag due to incident turbulence is clearly demonstrated by the results shown in Figs. 5.15(b) and 5.16(b).

Furthermore, the modification of the separated shear layers also controls the development of the wake and hence the mean aerodynamic force and the wake excitation. It is therefore possible to explain the effects of free stream turbulence on the transverse force coefficient characteristics, such as those shown in Fig. 5.31, and the subsequent large amplitude response, in terms of the increase in entrainment described above.

At a small angle of incidence, as illustrated by the sketch in Fig. 2.1(b), there is a partial re-attachment of the shear layer on the windward face of the square-section. The enclosed separation bubble on the windward side causes higher local suction than those on the opposite side face, and hence a positive transverse force (or negative lift) is developed. The maximum transverse force is believed to occur when re-attachment at the trailing edge of the body becomes permanent. Rockwell [16], using a two-dimensional square-section prism, has found that the incident angle at which the steady re-attachment at the trailing edge occurred is in the range of 14-15 degrees from the direction of the mean wind. At higher angle of incidence, the re-attachment point of the shear layer moves forward and may result in a smaller separation area with decreasing positive transverse force magnitude.

On the other hand, increasing the amount of turbulence in the flow increases the rate of entrainment into the wake and decreases the radius of curvature of the shear layers, so the value of the angle at which the enclosed separation bubble is established on the body side face is likely to be smaller in turbulent flow. The effect of incident turbulence intensity on the separation-reattachment phenomenon has been investigated by Akins et al. [139]. By using the same argument, more substantial re-attachment and hence a higher transverse force should be expected in turbulent flow than in uniform smooth flow at small angle of incidence [8].

Kwok's results, which are presented in Fig. 5.31, provide evidence that earlier permanent re-attachment will take place in the turbulent boundary layer flow. But the corresponding maximum transverse force coefficient is significantly smaller than that measured in the smooth flow. Kwok suggested that this might be largely due to the presence of both a velocity profile and a turbulence intensity profile in the turbulent boundary layer flow. In the absence of these variations, such as grid-generated turbulent flow in which both the velocity and turbulence are more uniform, the effect of earlier re-attachment due to increase in free stream turbulence is more significant. This is supported by the results obtained from the present experiment which shows a significant increase of model response in uniform

turbulent flow than in uniform smooth flow.

On the other hand, the cross-wind oscillation of the tower is equivalent to a rotation of the section by a cyclically varying small angle to the mean wind, and so the vibration does make the re-attachment intermittent. The flow around an oscillating square-section cylinder (which was driven in the cross-wind direction mechanically) was visualised using smoke. And photographs in Fig. 5.33 show the close-up view of the wake for an amplitude ratio of 0.25 and a reduced velocity in the middle of the lock-in range. Comparing the flow pattern observed behind a fixed square-section cylinder, the vortices in the oscillating case are more clearly defined.

As illustrated in these pictures, the separated shear layers roll up from the upstream corners to form vortices and appear to be re-attached to the body side faces. The size of the separation bubbles enclosed by the shear layers tends to be contracted and expanded with the section's periodic motion. When the cylinder's displacement reaches its apex, the fully grown vortex is discharged into the wake at the oscillating frequency. However, in the present measurement, it is difficult to distinguish the effects due to body motion (rotation) from those of free stream turbulence. The relative importance of the two factors certainly requires further investigation.

For a square tower, it is believed that the wake excitation is the dominant mechanism and this has been shown to be most intense at the critical reduced velocity. However, with the presence of a negative aerodynamic damping, the total damping of the system could be significantly reduced and, consequently, the response due to wake excitation would be increased to a sufficient large magnitude to enable the motion of the tower to maintain an effective angle of incidence at which the slope of the transverse force coefficient is considerably more negative. In comparison, the negative slope of the transverse force coefficient in the turbulent flow is at a maximum at zero angle of incidence and decreases as the angle is increased. For similar conditions in the uniform smooth flow, the maximum aerodynamic force resulting from the negative slope of the transverse force coefficient is found at an angle of incidence about 13 degree from the normal of a face. By assuming that the cross-wind motion of the tower is sinusoidal, the maximum effective angle of incidence due to its motion is estimated to be about 6.5 degrees in turbulent flow and 5 degrees in smooth flow.

As shown in Fig. 5.31, the variation of negative slope of the transverse force coefficient in the first 10 degree in both smooth and turbulent flows is very small indeed. Thus it can be seen that at and near zero angle of incidence, the negative aerodynamic force (damping) resulting from the negative slope of the transverse force coefficient is significantly higher in the turbulent flow than for similar

conditions in the uniform smooth flow (i.e. the resulting total damping of the system is less in turbulent flow), and consequently a marked increase in model response is observed in the turbulent flow.

It is therefore concluded that wake excitation, when assisted by the reduction of total damping associated with the transverse force characteristics, can be very effective in causing large amplitude response. It is thought that a similar mechanism is applicable to the response characteristics of the square tower in both uniform smooth and turbulent flow, but the effect is more noticeable in the latter cases.

5.4 Measurements of the Flow Field in the Near Wake of the Square Tower

It is concluded from the previous sections that for tall, elastic buildings and structures, the major source of wind-induced excitation is usually associated with vortex shedding. This is referred to as wake excitation. It is therefore of considerable interest to investigate the wake characteristic downstream of an oscillating tower and to correlate the tower's response with the velocity fluctuations in the near wake, in particular when the vortex shedding frequency is at or close to the frequency of the body oscillation. The relationship between the free stream velocity and the frequency at which vortices are shed from a bluff body is usually defined by the Strouhal number, $St = f_v B / \bar{U}_o$, in which f_v is the frequency of shedding.

5.4.1 The Wake Characteristic

Measurements of the velocity fluctuations in the near wake of the 10x1x1 square tower was made with a linearised DISA hot-wire anemometer, which is the most common type of instrumentation used in an investigation of this nature. A single vertical hot-wire probe was used in this measurement which would respond to the longitudinal turbulence as well as the cross-flow associated with vortex shedding. Details of the hot-wire anemometer and its calibration are given in Chapter Three.

It was felt that it would be of considerable interest to explore the wake characteristic, in terms of turbulence level and energy contents in the spectrum, in the area surrounding the tower model so that regions of strong or weak wake interference could be identified. Hot-wire measurements were made at 19 different positions. One of these was located upstream of the model and the measurements represented the undisturbed mean wind flow. The rest were at various grid positions behind the model. Fig. 5.33 depicts this arrangement.

Also shown in Fig. 5.33 are the averaged turbulence intensity and Strouhal number of the flow at these positions, averaged over a range of mean wind speed. In view of these values, the flow field around the square tower may be conveniently divided into two regions according to the turbulence intensity at the positions of measurement, as illustrated in Fig. 5.33.

As expected, the hot-wire signal measured at the position upstream of the model or downstream but at $y/B \geq 2$ is almost unaffected by the presence of the model. In region I, which included the positions of measurement from E to J, the probe is located near the wake boundary so that it is able to detect any periodicity in the velocity fluctuations. The fluctuation intensity in this proximity region is usually less than 10% and a well-defined spectral peak at the shedding frequency is always present in the spectra measured at these positions. The distinct spectral peak in the spectra suggests the presence of the vortex-shedding cross-wake oscillation.

In region II, which is usually referred to as the wake-interference region, the turbulence level is usually high. It is interesting to note that on the wake centre-plane, the intensity rises in the near-wake and increases downstream for a short distance. A maximum is reached at approximately $3B$ behind the rear face of the model.

A similar flow phenomenon was observed by Davies et al. [18] who used a pulse-wire anemometer to measure the velocity fluctuations behind a $6 \times 1 \times 1$ square tower in three types of flow. Their results, illustrated by means of streamlines and three-dimensional plots, revealed that a closed circulation, free stagnation zone was formed immediately behind the tower. The distance to the position of maximum fluctuation was $4B$ and this position coincided with the closure of the wake circulation. It seems to be that the 'bubble' is dependent on the flow entrainment from both the side shear layers and the separated shear layer over the top of the block. In the presence of a turbulent shear flow, the circulation zone is noticeable shortened and the distance to maximum fluctuations is reduced to $1.5B$. However, the maximum turbulence level in the re-circulation region is not dependent on the turbulence in the approaching flow.

The results obtained from these measurements, together with those from Davies et al. [18], suggests that wake buffeting on the downstream tower block will be significant at certain downstream positions. Also it is likely that if the downstream tower is located inside the re-circulation zone of the upstream tower then it may be subjected to a strong forward 'pushing' force due to flow reversals within this region.

Within the wake-interference region, it is also evident that the velocity fluctuations could contain more than one prominent frequency component. For this reason, the Strouhal number estimated from the shedding frequency at these positions is intermittent and sometimes has a value much bigger than it should be, as shown in Fig. 5.33. Furthermore, within the wake-interference region but outside the recirculation zone, the wake tends to be relaxed and starts to decay as it moves further downstream.

Based on this observation, the hot-wire probe was therefore placed at a location just outside the wake region but close enough to detect any periodicity due to the velocity fluctuations. The position of the hot-wire relative to the tower is shown in Fig. 5.34. The vertical position of about 75% of the height of the model was less likely to be affected by flow entrainment from the top of the tower. The relative low turbulence intensity at this position also ensures satisfactory functioning of the hot-wire instruments.

Wake spectra of the square tower in both uniform smooth and turbulent flows are shown in Fig. 5.35(a) and (b) respectively at various reduced velocities. Also shown with these spectra are the Strouhal number and turbulence level of the wake at the position of measurement.

It is clearly illustrated in these spectra that a spectral peak features prominently at and around a reduced frequency of 0.087 in smooth flow and 0.091 in turbulent flow. The presence of this spectral peak is further evidence to support the view that the cross-wind force acting on the tower is induced by the wake. As expected, the peak occurs at the critical reduced velocity when the vortex shedding frequency and the natural frequency of the tower are close together. It must be pointed out, however, that these wake spectra do not provide a direct measure of the force acting on the tower but, rather, they give a reasonable representation of the energy available in the wake.

5.4.2 Variation of the Strouhal Number

It is generally believed that the Strouhal number of a square prism has a constant value over a wide range of Reynolds numbers. The most widely accepted value is about 0.13 for a two-dimensional cylinder [55] and 0.10 for a three-dimensional prism [18]. Nevertheless, these values are much higher than those found in this measurement, as shown in Fig. 5.35.

When a bluff structure is self-excited by periodic vortex shedding forces or wake capture, there is a complex non-linear interaction between the wake and the body.

The vibration itself causes an increase in the magnitude of the forces and the additional aerodynamic force is probably associated with the intermittent re-attachment of the shear layers on the body surfaces (as illustrated by the pictures in Fig. 5.33), thereby causes increased circulation. Dependent upon both the displacement amplitude and the frequency of oscillation, the resulting vortices in the wake are larger and stronger than would be the case if the cylinder were stationary. Komatsu et al. [140] termed the vortex shed from the leading edge of an oscillating body and synchronised with its motion as a 'motion-induced vortex'.

Steinman [141] hypothesised that if vortices are shed at or near each end of the amplitude range, the normal width of the vortex street is increased by the ratio,

$$\frac{(p + 2y)}{p} = 1 + \frac{2y}{1.3B}$$

in which p is the width between the centers of the two rows of vortices behind a stationary cylinder and y is the half amplitude of oscillation. Consequently, the increase in distance between the shedding vortices due to the body's motion decreases the shedding frequency. Hence, the maximum amplitude of oscillation can not be attained even though the Strouhal frequency for a stationary cylinder exactly equals the natural frequency of an elastic body. The ratio between the Strouhal number \hat{St} at which peak vibration occurs and the Strouhal number, St , for a stationary cylinder is [142],

$$\frac{\hat{St}}{St} = \frac{1}{1 + 5.4 \frac{y}{B}}$$

For a typical displacement of 30% of the section's width, the Strouhal number of a square prism is estimated to be 0.09, and this figure is close to those values obtained in this investigation.

This argument is further supported by the evidence that, at a high angle of incidence, the oscillation amplitude of the square tower is significantly reduced and the resulting Strouhal number of the wake is very close to those measured behind a stationary prism.

5.4.3 Cross-Correlation between Velocity Fluctuations in the Near Wake and Model Response

It is evident from the wake spectra presented in the previous sections that there is a close relationship between the model response and the velocity fluctuations in the near wake of the square tower, especially at and close to the critical reduced velocity when large amplitude cross-wind oscillations occur. This section presents the level

of the cross-correlation between the model response in the two lateral directions and the velocity fluctuations in the wake. During measurement, the signals from the accelerometers and the hot-wire anemometer were measured simultaneously and recorded digitally on disc for off-line analysis. Details about cross-correlation analysis procedure and computer programmes can be found in Chapter Four.

Briefly, the most convenient method to express the cross-correlation is by regarding the normalised cross-spectral density function, more simply referred to as cross-spectra, as a function of frequency. However, if the wake spectrum $S_u(f)$ is considered to be the excitation function and the cross-wind (or along-wind) displacement spectrum $S_y(f)$ is the response function, then the squared coherence function between input $u(t)$ and the output $y(t)$ is defined as,

$$\gamma_{yu}^2(f) = \frac{|S_{yu}(f)|^2}{S_u(f) S_y(f)}$$

In this section, both the cross-spectrum and square-root of the coherence function of the cross-correlation analysis are examined in detail. For convenience, the latter is simply referred to as the coherence function.

It must be pointed out, however, that the interdependence between excitation and response process is likely to be non-linear and hence the input-output relationship can not be rigidly defined. Therefore the main emphasis of this analysis is to identify the area which exhibits strong coherence between wake and the model responses and to relate this to the pertinent excitation mechanism.

Fig. 5.36(a) and (b) show the coherence function between the velocity fluctuations in the near wake and either the along-wind or cross-wind dynamic response of the square tower in uniform smooth flow. For the range of reduced velocity, it can be seen that the near wake and the cross-wind response display a relatively strong coherence at close to the shedding frequency, f_v , as shown in Fig. 5.36(b). It is interesting to note that the strongest coherence between the wake velocity fluctuations and the cross-wind displacement is not at the critical reduced velocity. This may be the result of the fact that at the critical reduced velocity, there is a large amount of energy to be transferred between the two lateral motions. Consequently, the along-wind response is markedly increased at the expense of the response in the cross-wind direction. This is supported by the evidence that at the critical reduced velocity, there is a significant increase of the coherence between the wake and the along-wind response at the natural frequency of the tower. In turbulent flow, similar response characteristics at the critical reduced velocity are observed, as shown in Fig. 5.37(a).

At high reduced velocities, the increases in cross-wind response caused a significant increase in wake energy at the natural frequency of the tower. It is therefore not unexpected to find that there is a relatively strong coherence at the natural frequency in these operating conditions.

The cross-power spectra between the velocity fluctuations in the near wake and the dynamic response in either the along-wind or cross-wind direction, measured in both the smooth and turbulent flows, are shown in Figs. 5.38 and 5.39 respectively. It is evident that there is a noticeable narrowing and an increase in magnitude of the spectral peak when the vortex shedding frequency and the natural frequency of the tower are close together. That is at operating reduced velocities at or close to the critical value of 10.8 in smooth uniform flow, and 11.7 in uniform turbulent flow. The narrowing of the spectral peaks suggests that the correlation of the vortices along the axial direction are improved by the effects due to the displacement dependent lock-in.

It is evident that the wake energy decreases as the operating reduced velocity of the tower exceeds the critical value. However, it has been shown in the previous sections that the wake excitation in the presence of negative aerodynamic damping is significant for a square tower at high operating reduced velocities and in particular for low values of structural damping. The resultant large amplitude response causes a significant redistribution of the wake spectra. And it can be seen in Figs. 5.38 and 5.39 that there is marked increase in wake energy at the natural frequency of the tower as well as a significant decrease in wake energy at the vortex shedding frequency. Although the increase in wake energy available for wake excitation at the natural frequency of the tower is small, such an increase will be sufficient to cause an increase in cross-wind response. And it is interesting to note that at operating velocities much higher than the critical, the motion of the tower can still have a significant influence on the vortex shedding process and energy distribution in the wake.

<p>Dynamic Mass (apparent Weight)</p> $\frac{F}{a} \quad / \quad \frac{Ns^2}{m}$	<p>Acceleration through Force</p> $\frac{a}{F} \quad / \quad \frac{m}{Ns^2}$
<p>Mechanical Impedence</p> $\frac{F}{v} \quad / \quad \frac{Ns}{m}$	<p>Mobility (Mechanical Admittance)</p> $\frac{v}{F} \quad / \quad \frac{m}{Ns}$
<p>Stiffness</p> $\frac{F}{d} \quad / \quad \frac{N}{m}$	<p>Compliance</p> $\frac{d}{F} \quad / \quad \frac{m}{N}$

Table 5.1 Terminology for complex dynamic ratios of force and motion, from Ref. 127.

	arrangements	mode 1	mode 2	mode 3	
using peak-amplitude method	test rig alone	$f_1=22.5$ Hz $\zeta_1=0.03$			
	force balance column alone	$f_1=14.12$ Hz $\zeta_1=0.084$			
	model-balance assembly	$f_1=4.5$ Hz $\zeta_1=0.027$	$f_2=21.0$ Hz $\zeta_2=0.059$		
	longitudinal complete elastic model- balance assembly	$f_1=5.85$ Hz $\zeta_1=0.029$	$f_2=21.6$ Hz $\zeta_2=0.014$	$f_3=33.2$ Hz $\zeta_3=0.028$	
		transverse	$f_1=6.4$ Hz $\zeta_1=0.031$	$f_2=28.5$ Hz $\zeta_2=0.019$	
	longitudinal complete perspex model-balance assembly	$f_1=7.3$ Hz $\zeta_1=0.034$	$f_2=22.6$ Hz $\zeta_2=0.042$	$f_3=33.3$ Hz $\zeta_3=0.04$	
		transverse	$f_1=8.0$ Hz $\zeta_1=0.044$	$f_2=28.5$ $\zeta_2=0.027$	
	using free-decay method	longitudinal complete elastic model-balance assembly	$f_1=6.25$ Hz $\zeta_1=0.016$		
			transverse	$f_1=6.76$ Hz $\zeta_1=0.014$	

Table 5.2 Data derived from the peak-amplitude and free-decay oscillation plots.

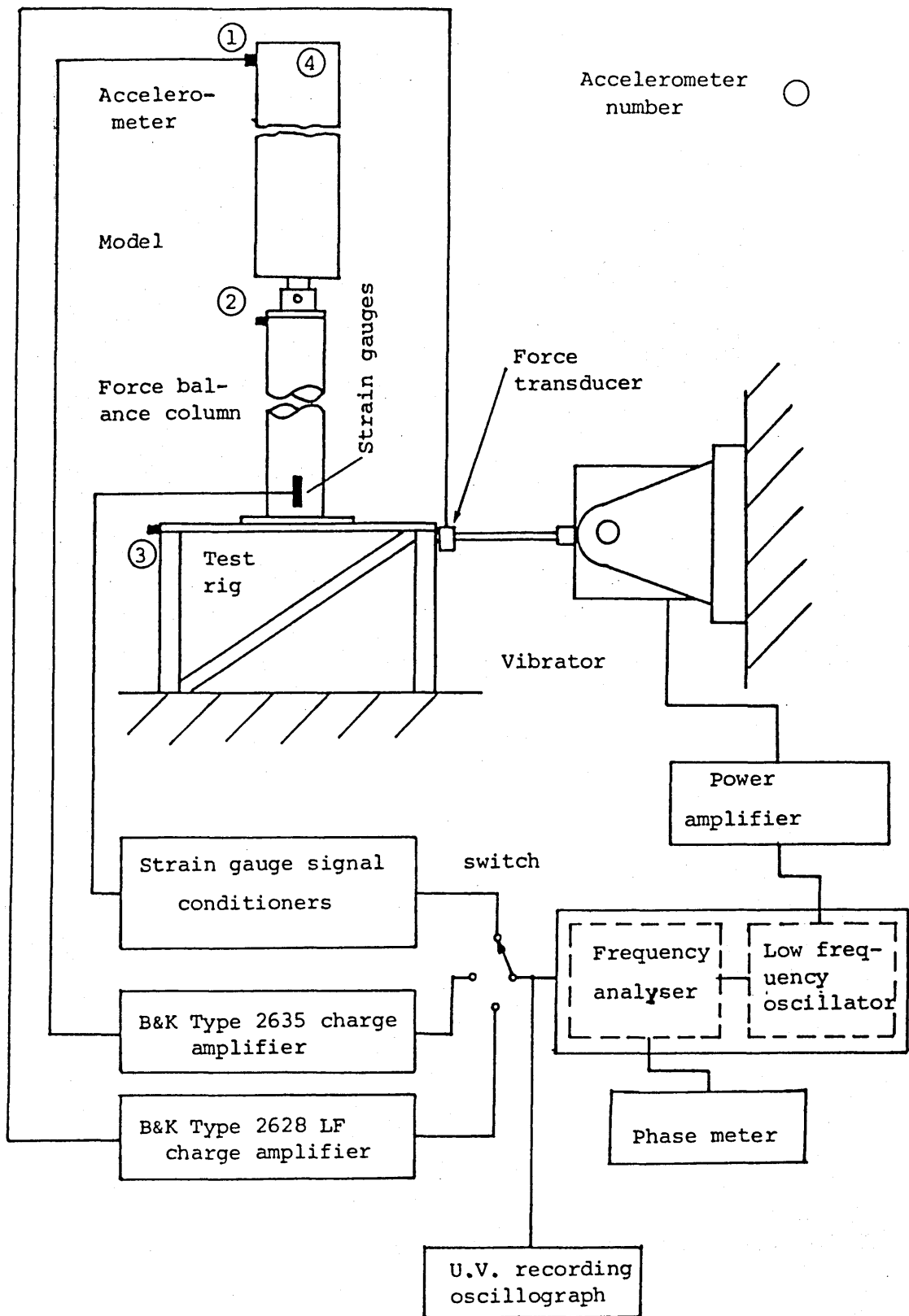


Figure 5.1 Block diagram of dynamic model measurement arrangement.

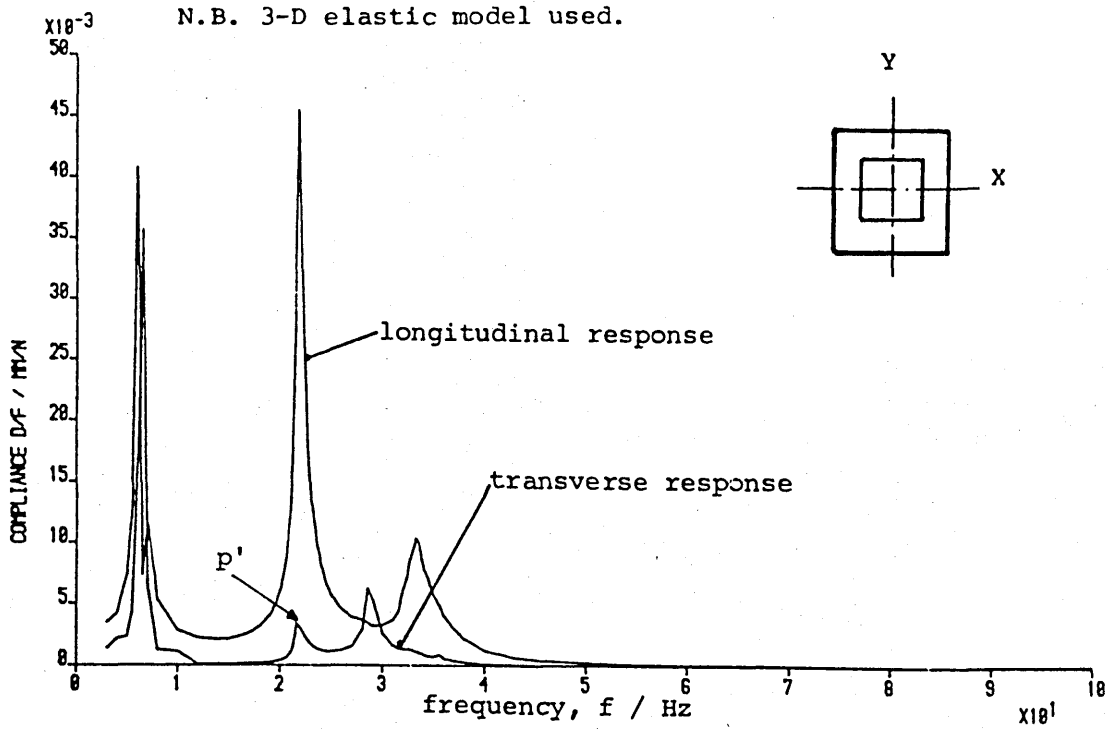


Figure 5.2 Transfer impedance measured at the free end of the complete model-balance assembly with excitation force applied to the test rig along its longitudinal (x-) direction.

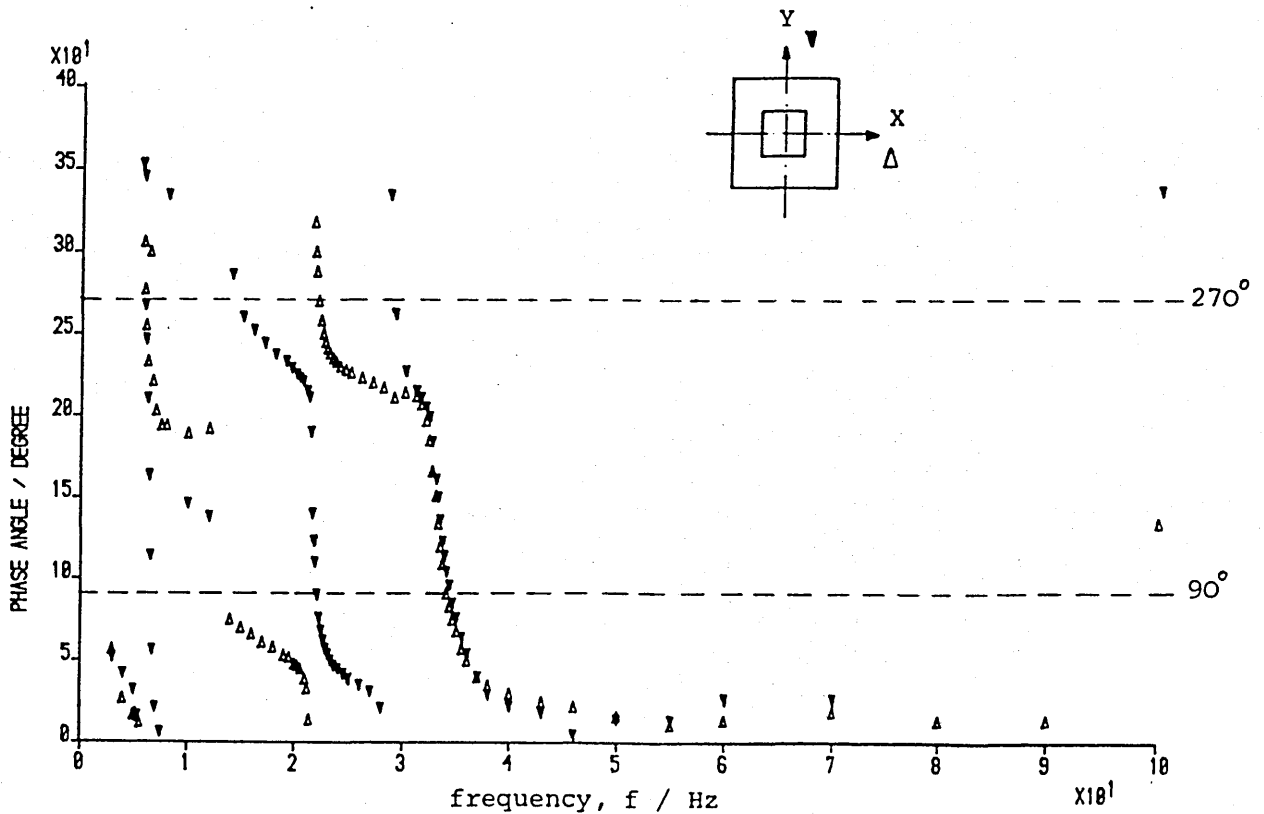


Figure 5.3 Phase angle plot (degree of displacement lagging behind force), measured at the free end of the model along its longitudinal and transverse directions and with excitation applied in longitudinal direction.

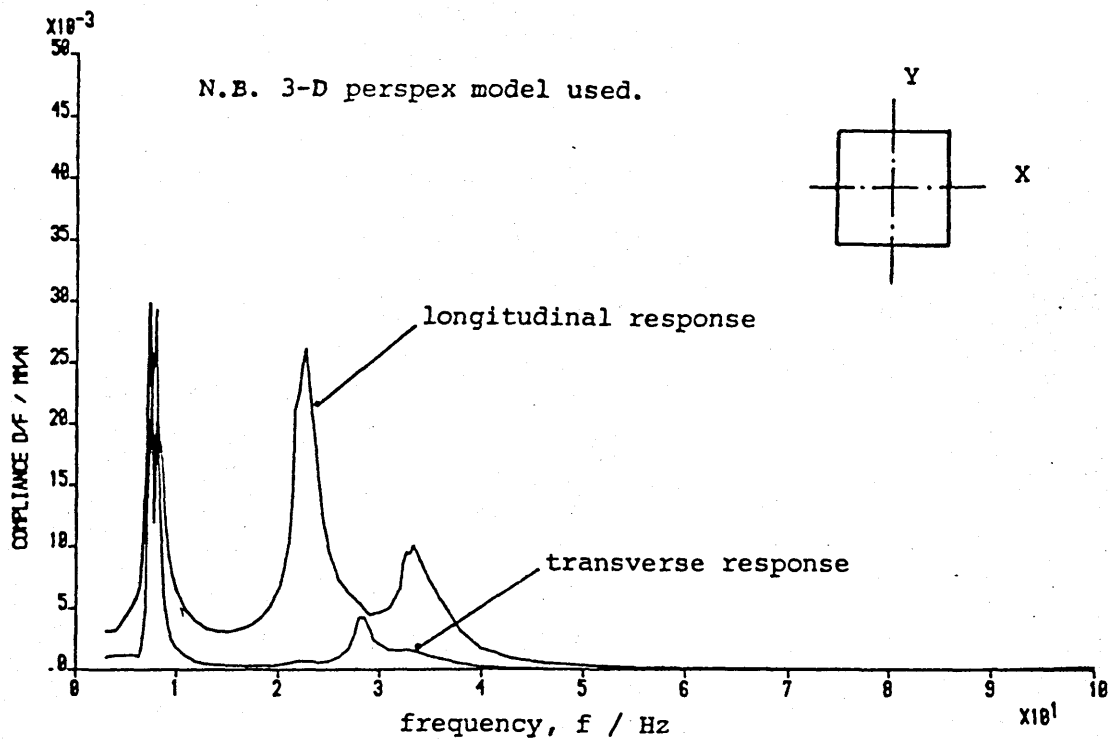


Figure 5.4 Transfer impedance measured at the free end of the complete model-balance assembly with excitation force applied to the test rig along its longitudinal (x-) direction.

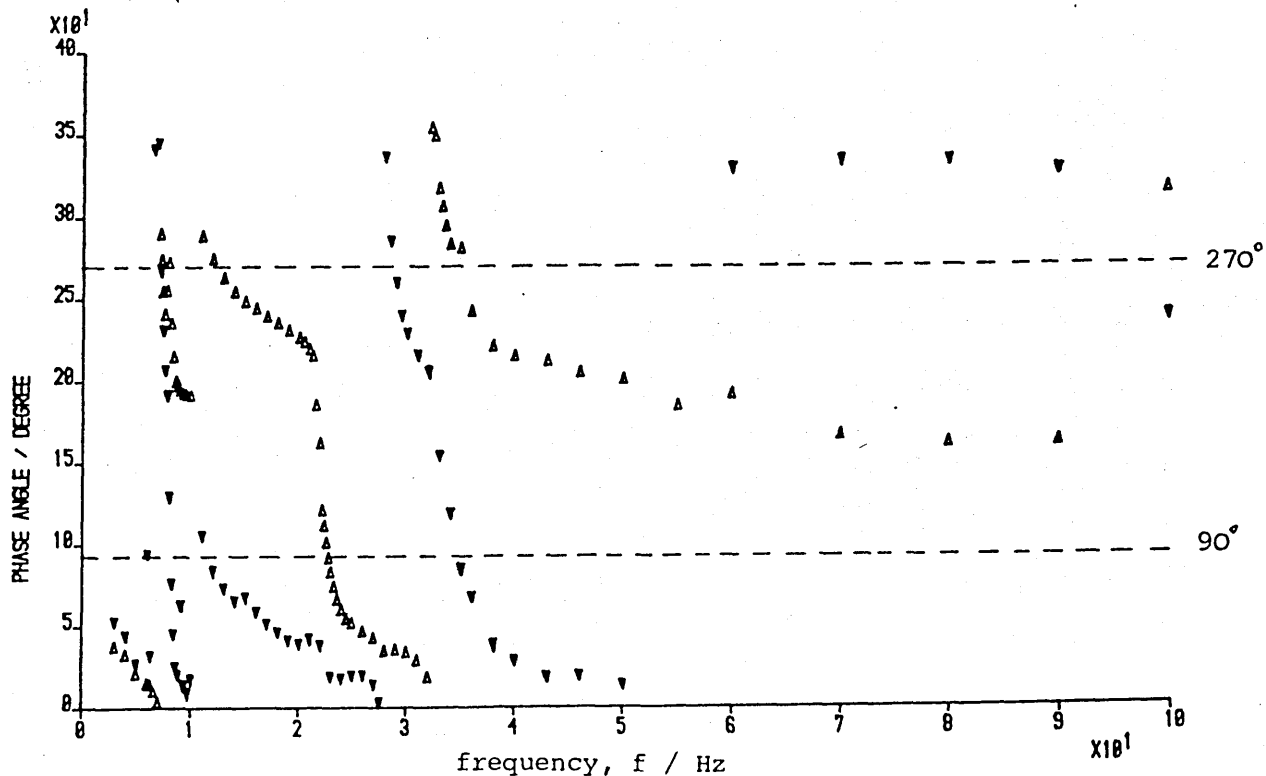
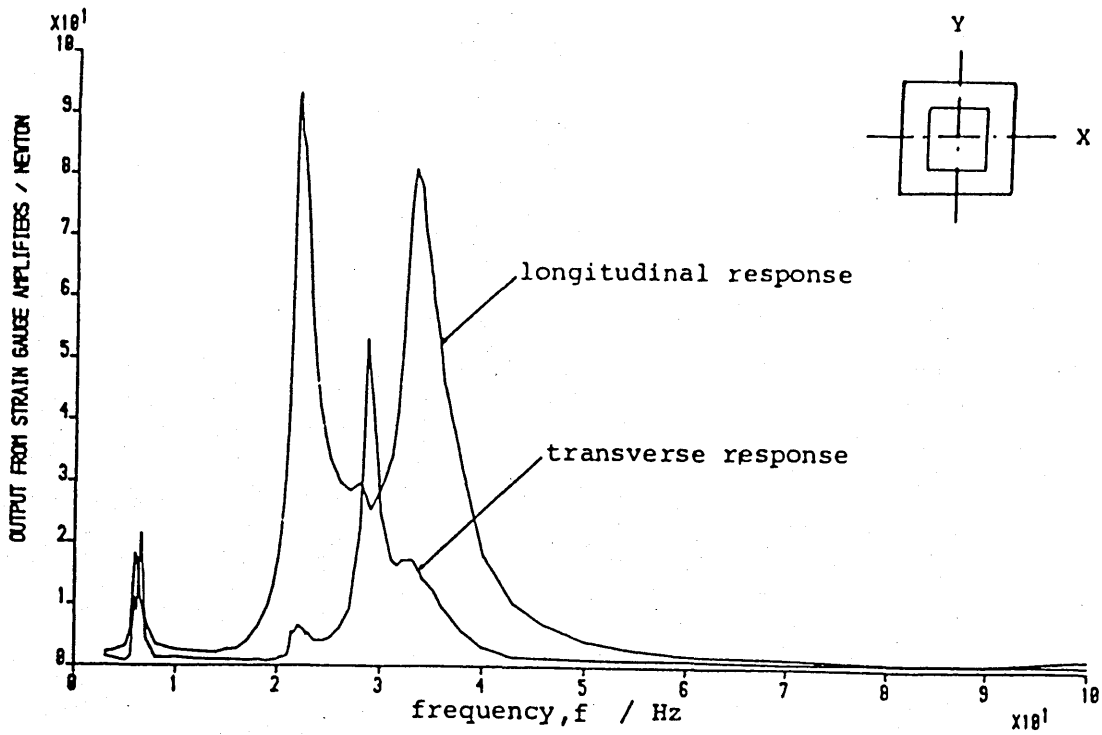
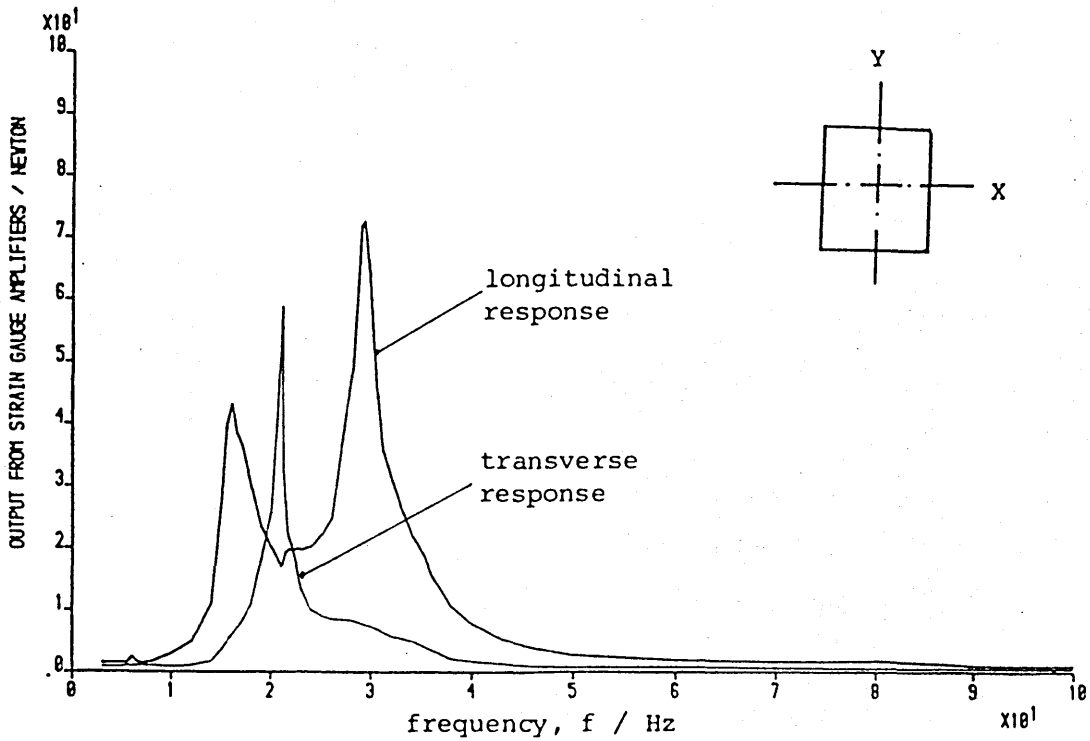


Figure 5.5 Phase angle plot (degree of displacement lagging behind force), measured at the free end of the model along its longitudinal and transverse directions and with excitation applied in longitudinal direction.



(a) With an elastic model attached to the force balance column.



(b) Without model attached to the force balance column.

Figure 5.6 Output from the longitudinal and transverse strain gauge set (a) with and (b) without model attached to the force balance column.

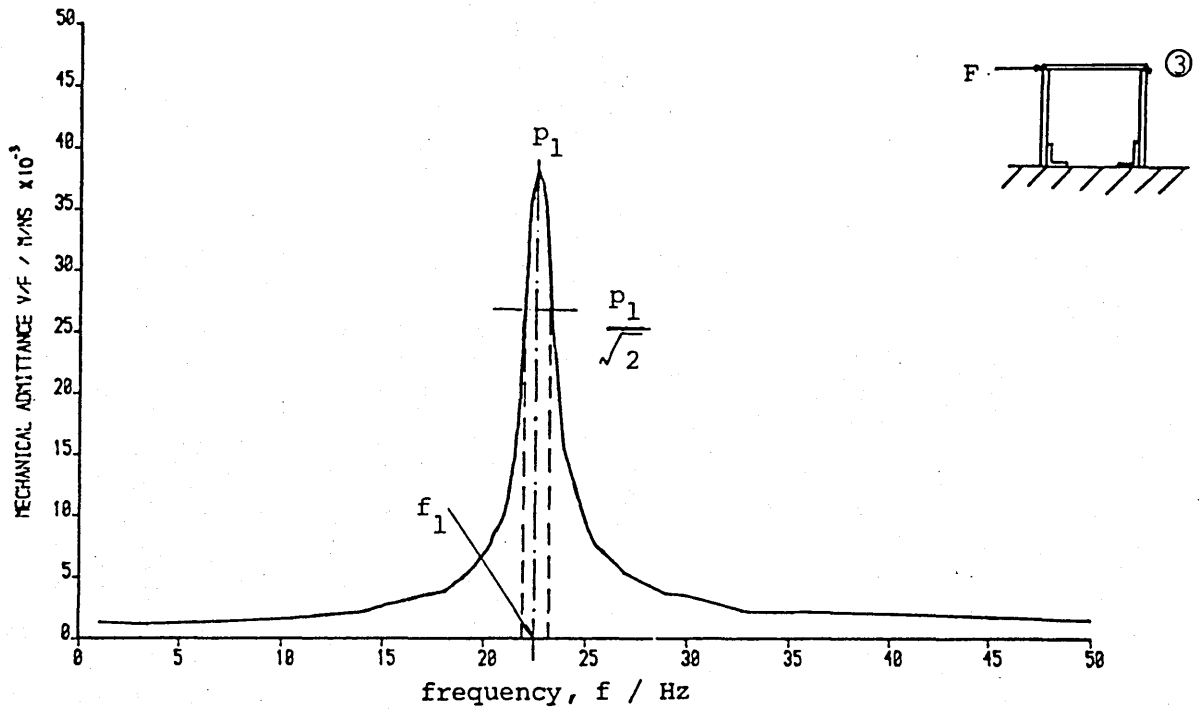


Figure 5.7 Transfer impedance measured at the test rig (station 3) with excitation applied along its longitudinal direction.

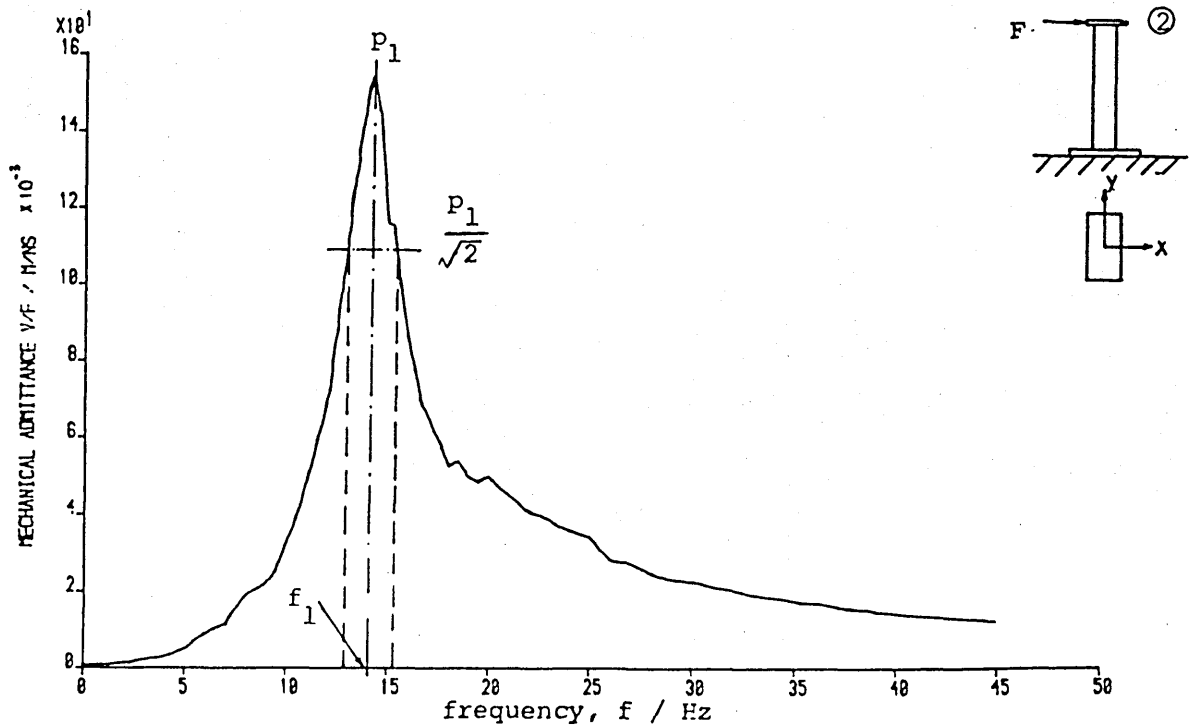


Figure 5.8 Transfer impedance measured at the top of the force balance column (station 2) with excitation applied along its longitudinal direction.

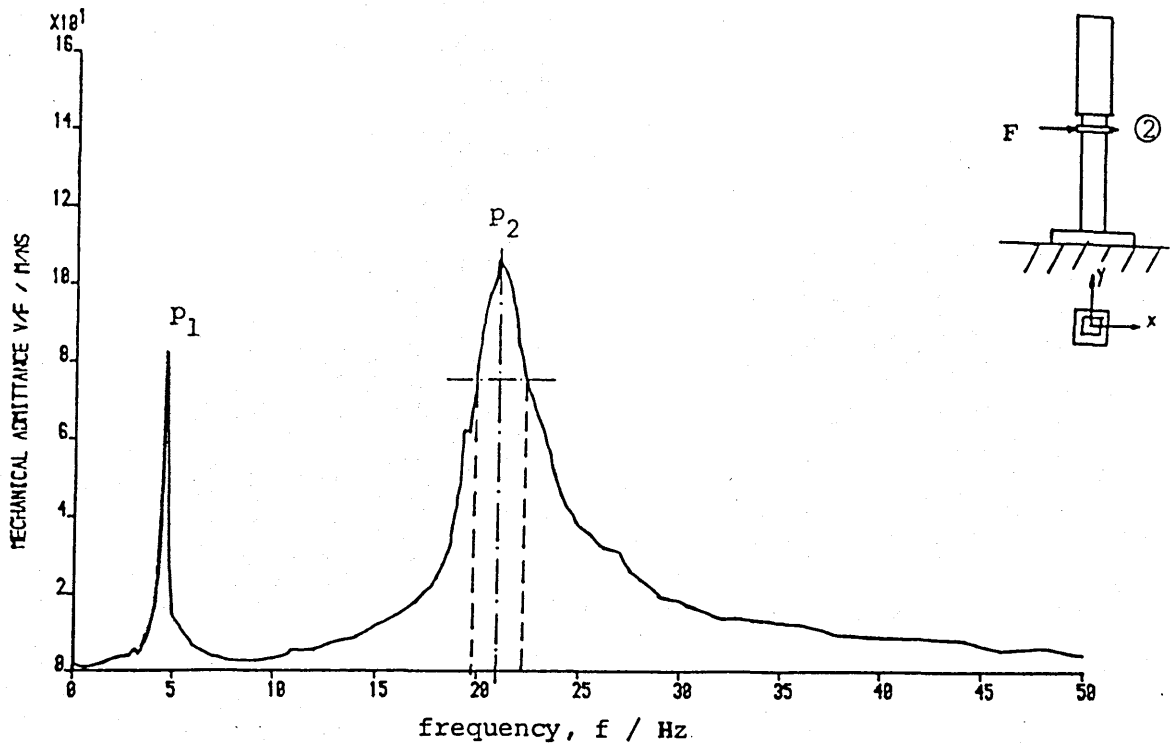


Figure 5.9 Transfer impedance measured at the elastic model-balance assembly (at station 2) with excitation applied along its longitudinal direction.

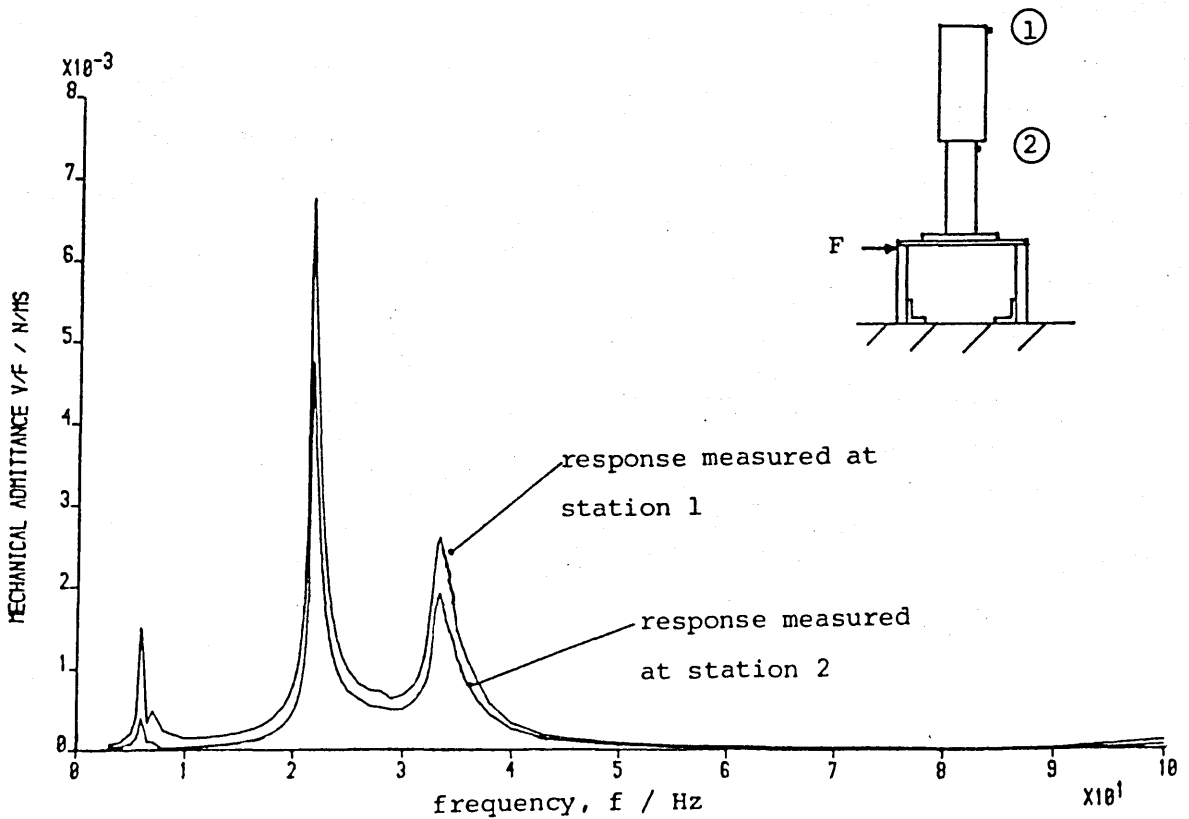


Figure 5.10 Transfer impedance of the complete model-balance assembly measured by accelerometers at station 1 and 2, excitation applied along its longitudinal direction.

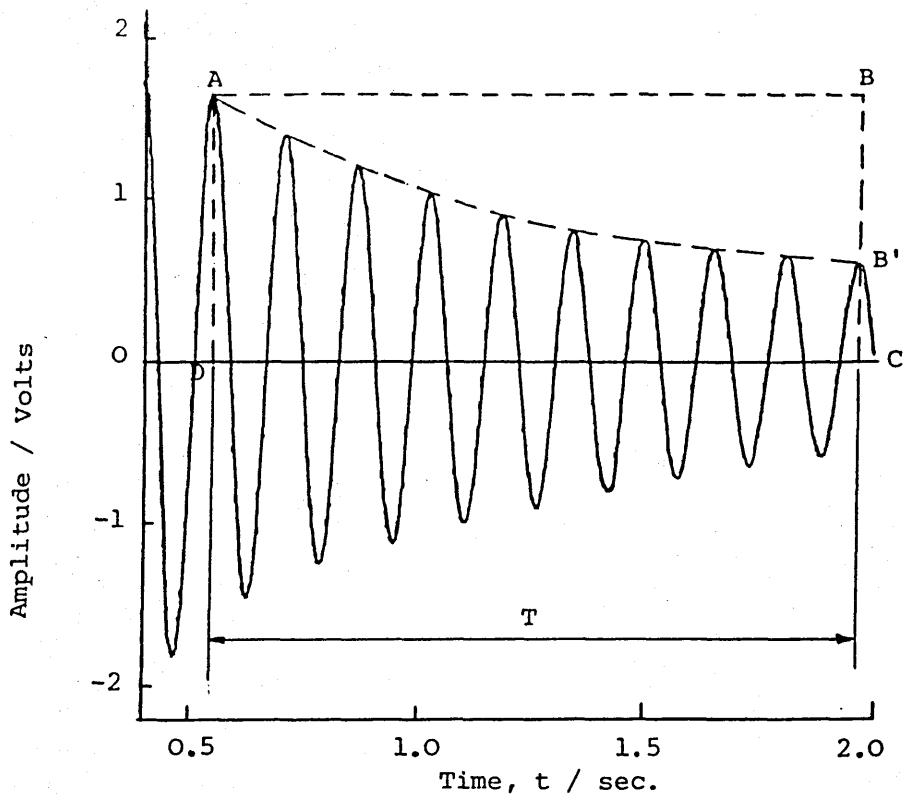


Figure 5.11 A typical trace of a free-decay oscillation measured by accelerometers at the free end of the complete model-balance assembly.

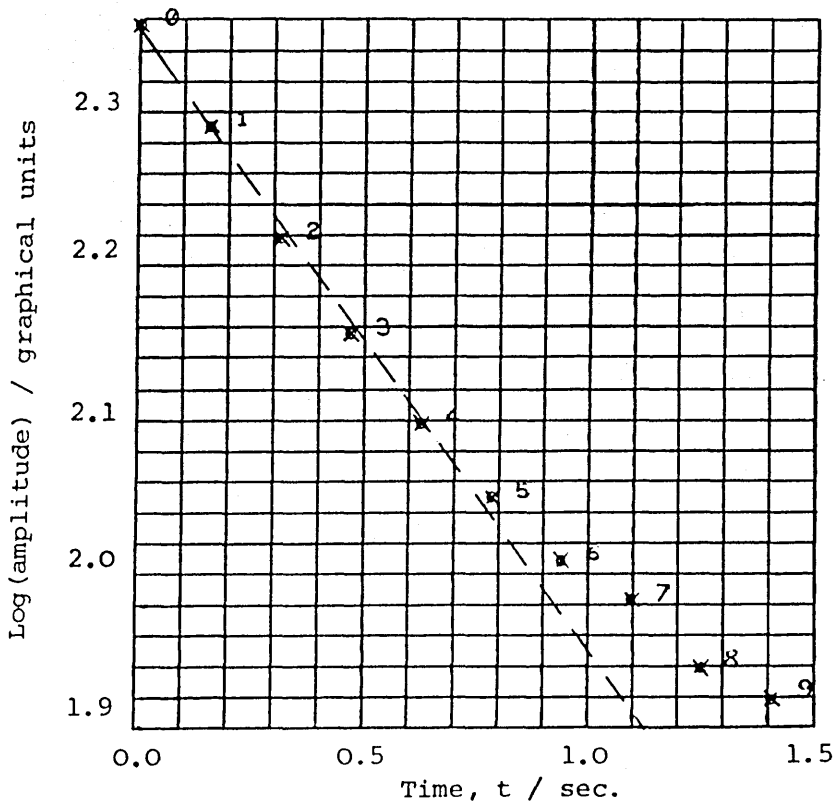
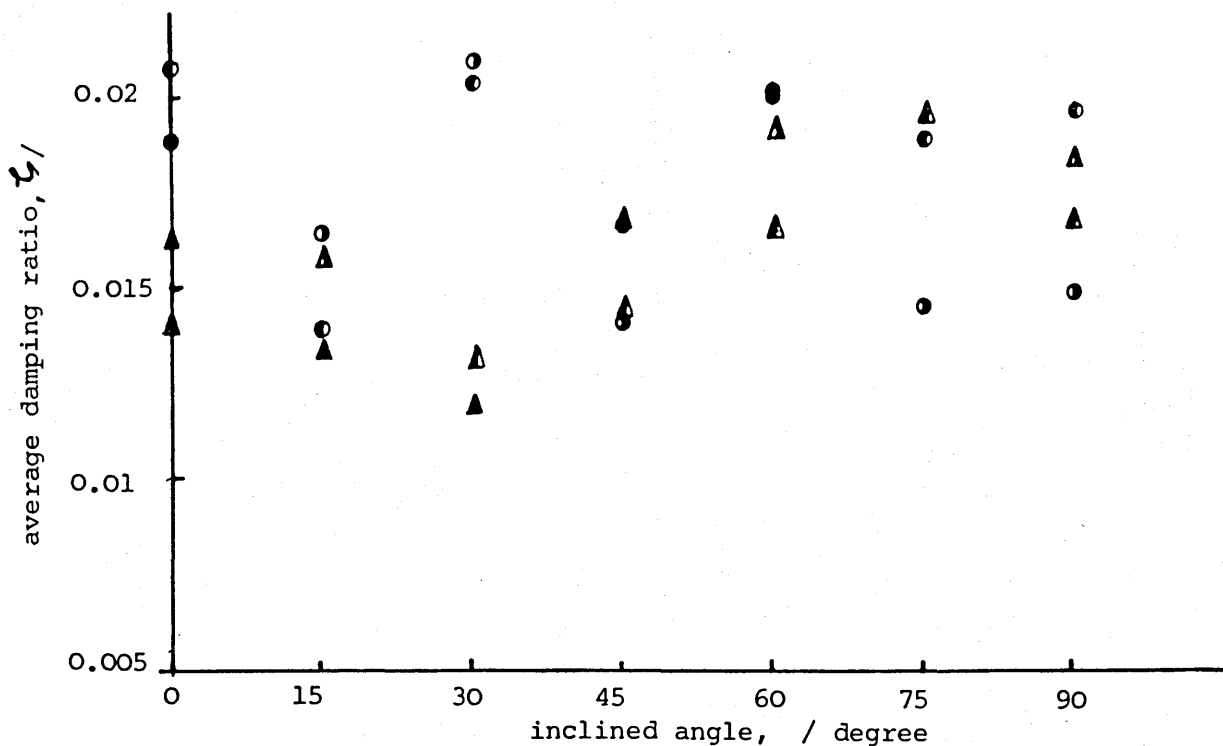
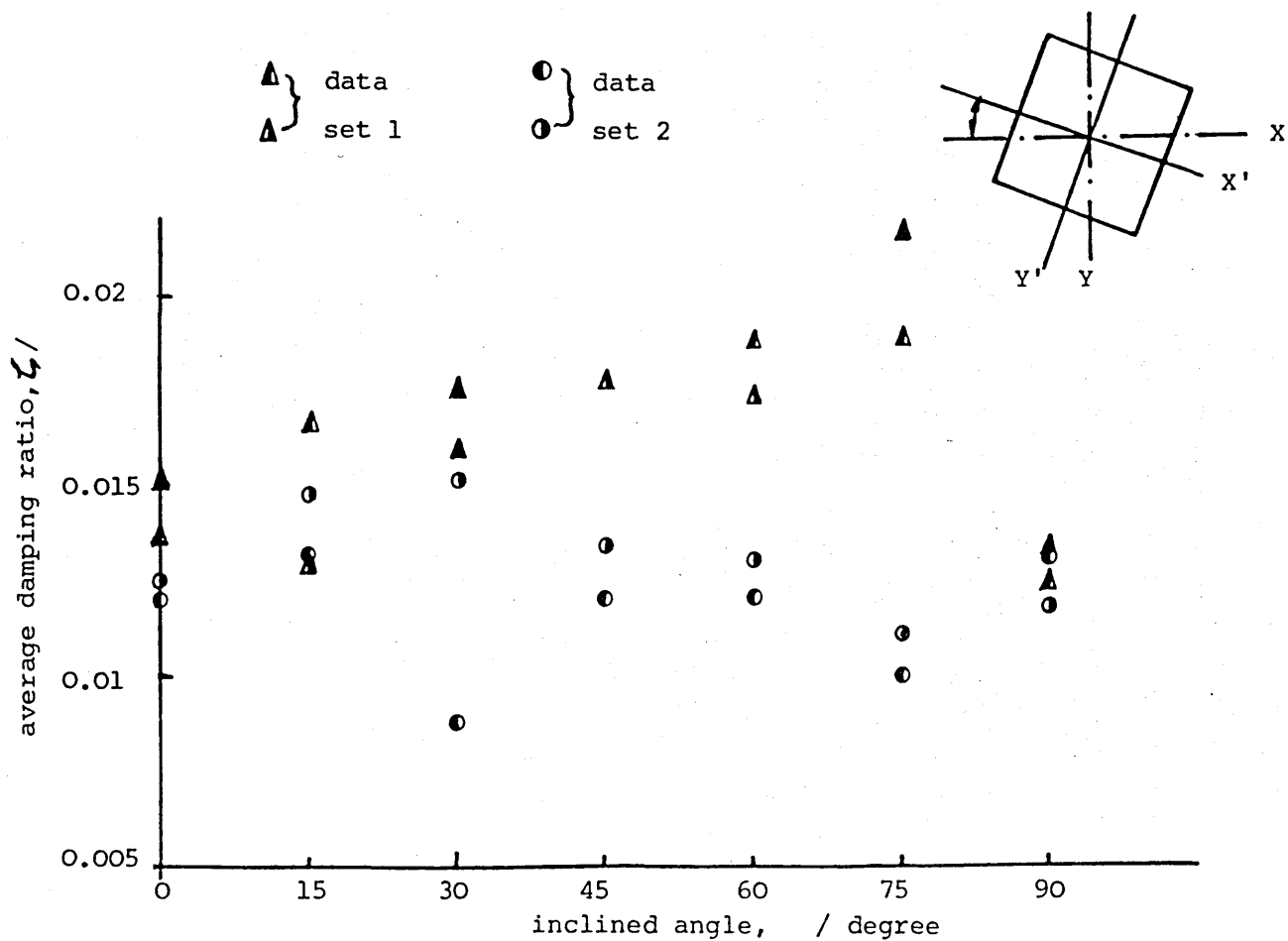


Figure 5.12 Plot of the natural logarithm of the peak amplitudes measured from the above trace against time.

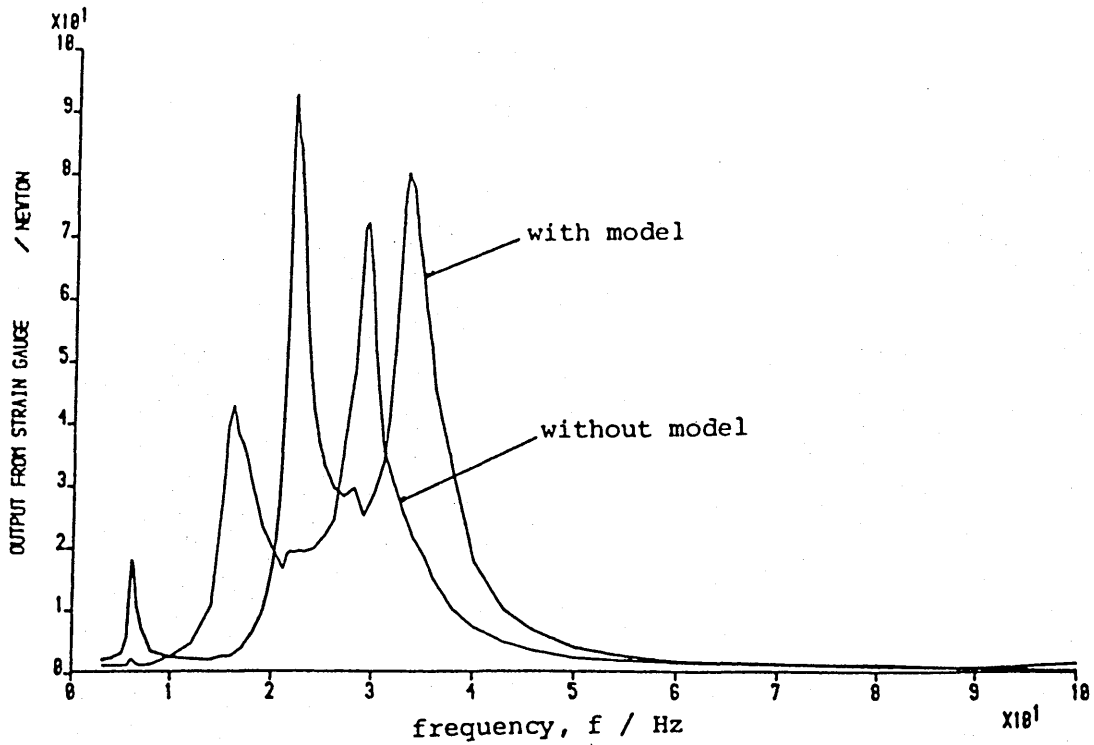


(a) Average values measured in longitudinal (X-) direction.

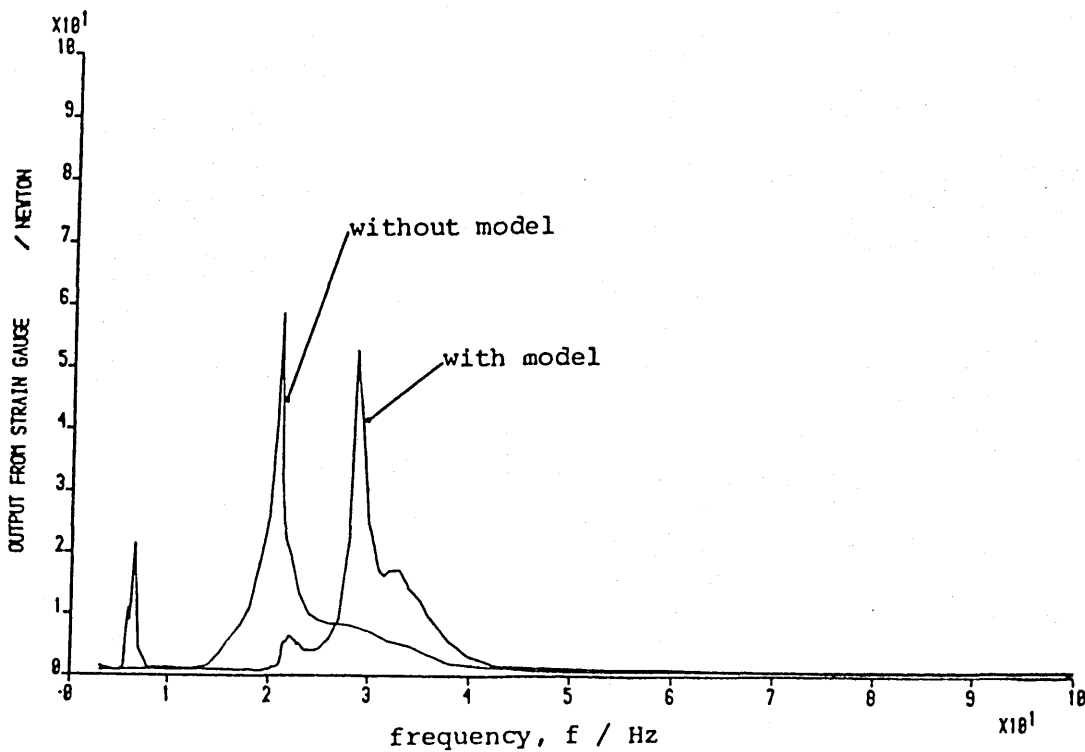


(b) Average values measured in transverse (Y-) direction.

Figure 5.13 Variation of damping ratio with the model's inclined angle (measured with respect to the wind tunnel reference axis).



(a) Output from the longitudinal strain gauge set.



(b) Output from the transverse strain gauge set.

Figure 5.14 Comparison of output from (a) the longitudinal and (b) the transverse strain gauge set either with or without the elastic model attached, excitation applied in longitudinal direction.

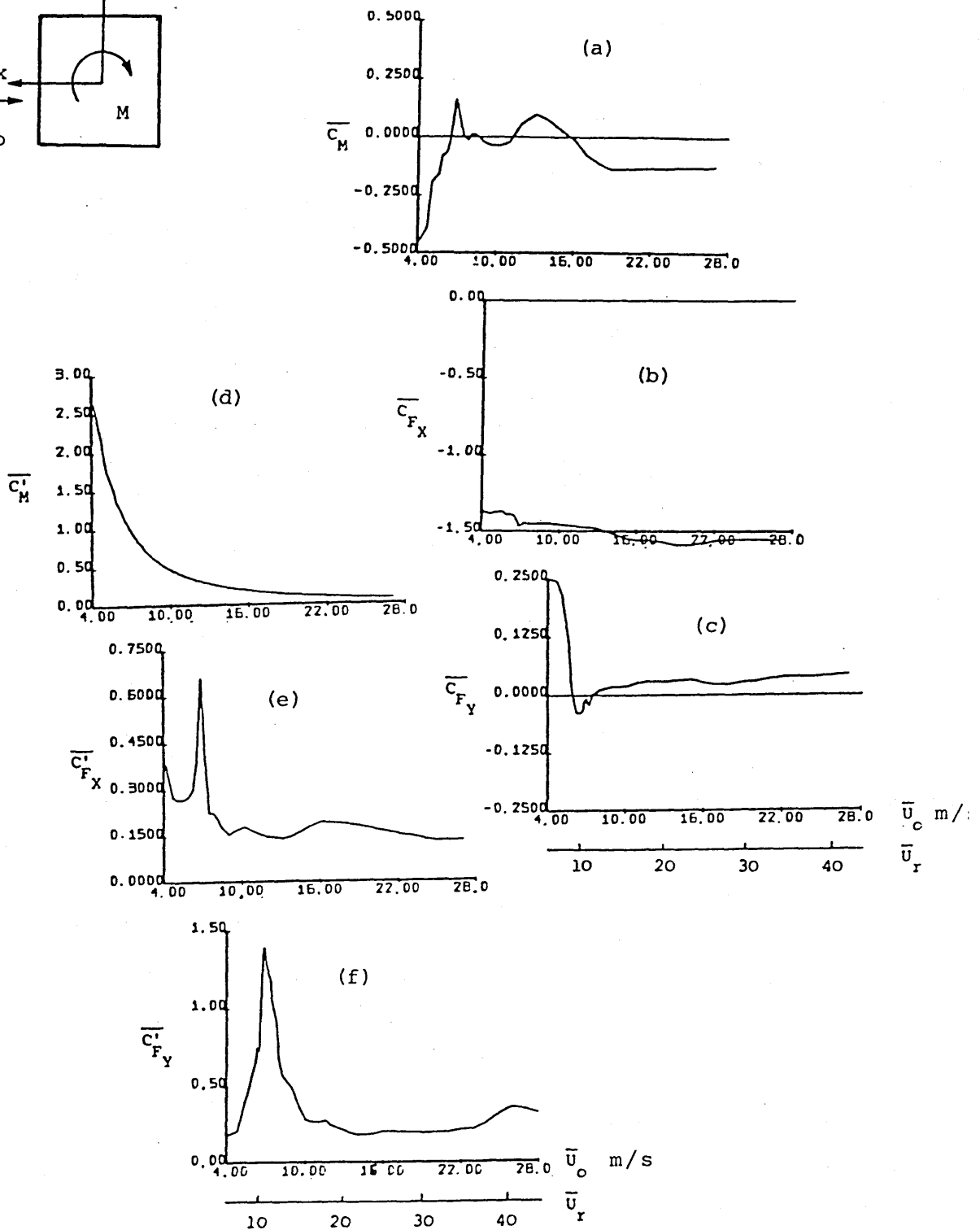
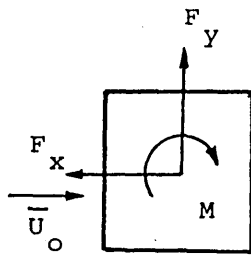


Figure 5.15 Mean and RMS coefficients of torsional moment, longitudinal and transverse force for the 10x1x1 square tower model in uniform smooth flow.

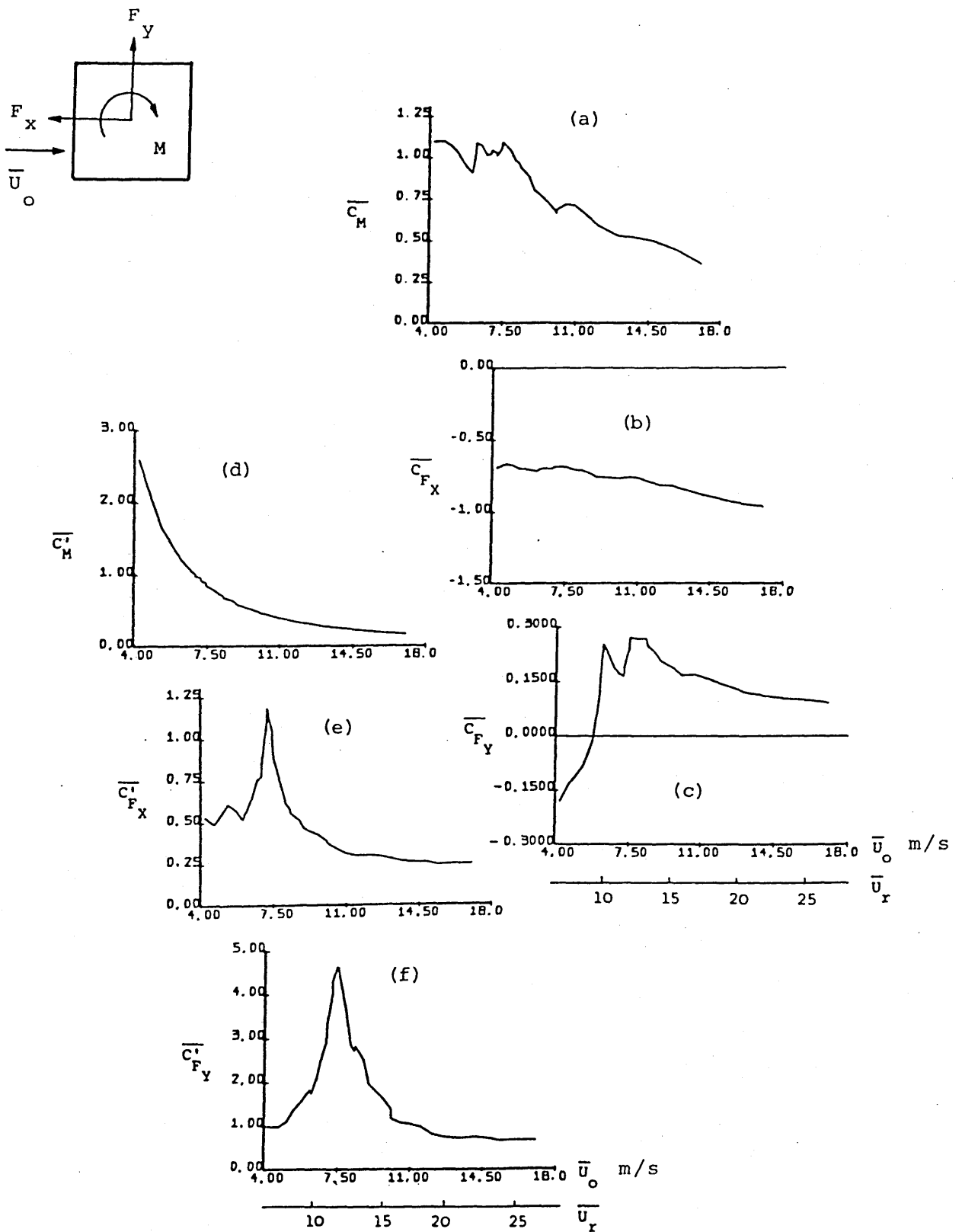


Figure 5.16 Mean and RMS coefficients of torsional moment, longitudinal and transverse forces for the 10x1x1 square tower model in uniform turbulent flow.

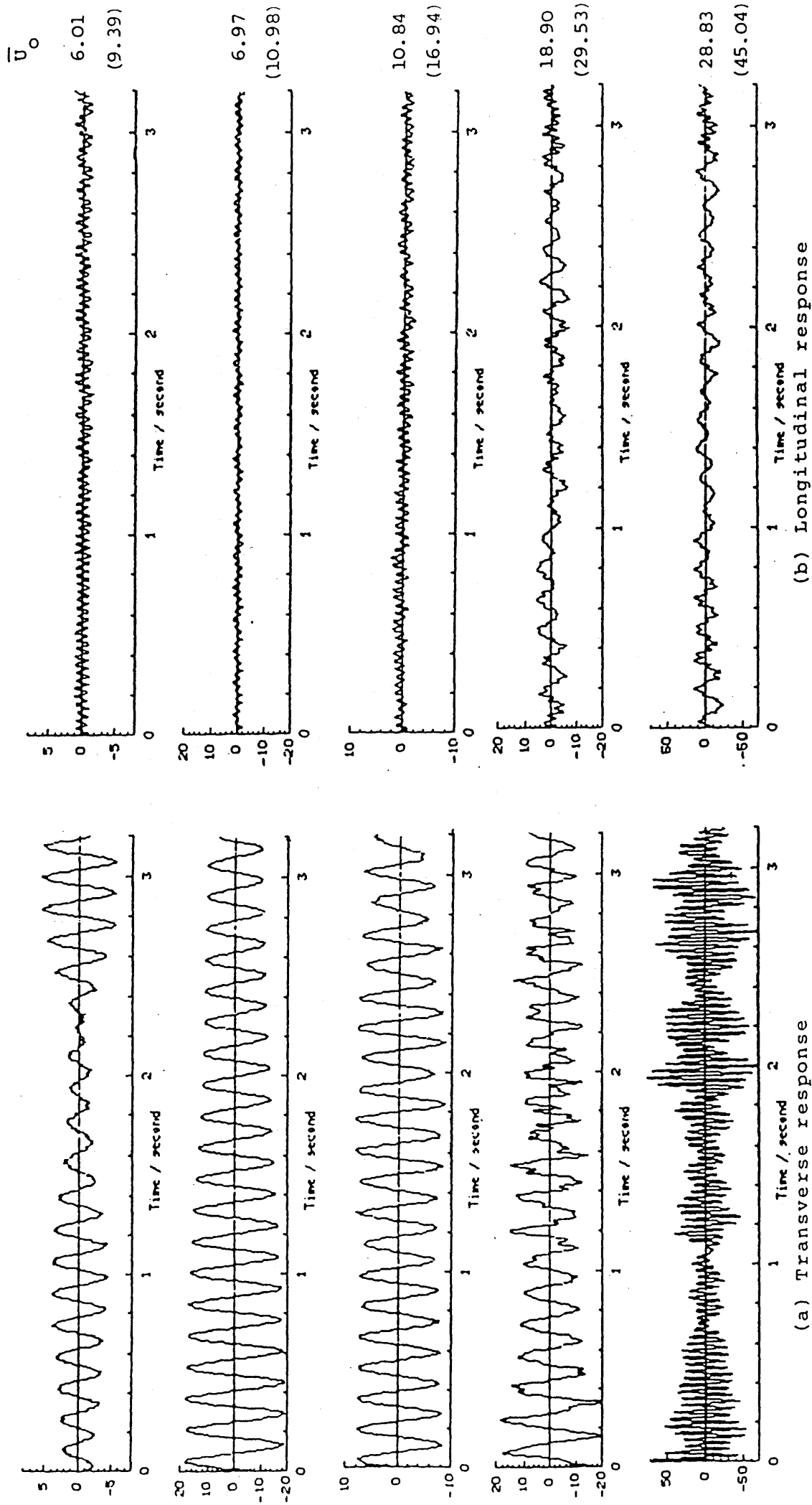


Figure 5.17 Traces of response from the longitudinal and transverse strain gauge sets measured in uniform smooth flow for various reduced velocities.

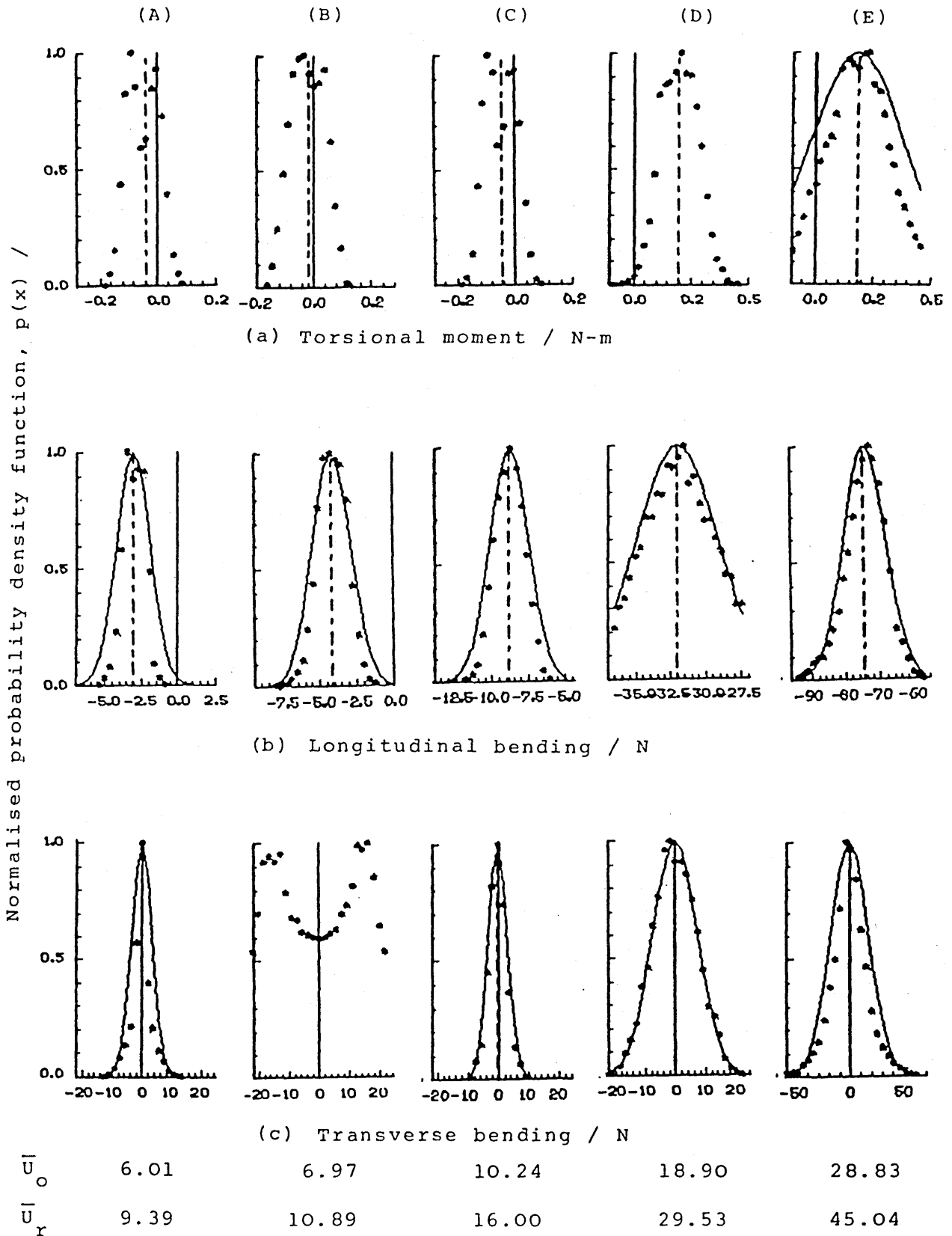


Figure 5.18 Probability density function of output from (a) torsional, (b) longitudinal and (c) transverse bending strain gauge signals measured in uniform smooth flow for various reduced velocities.

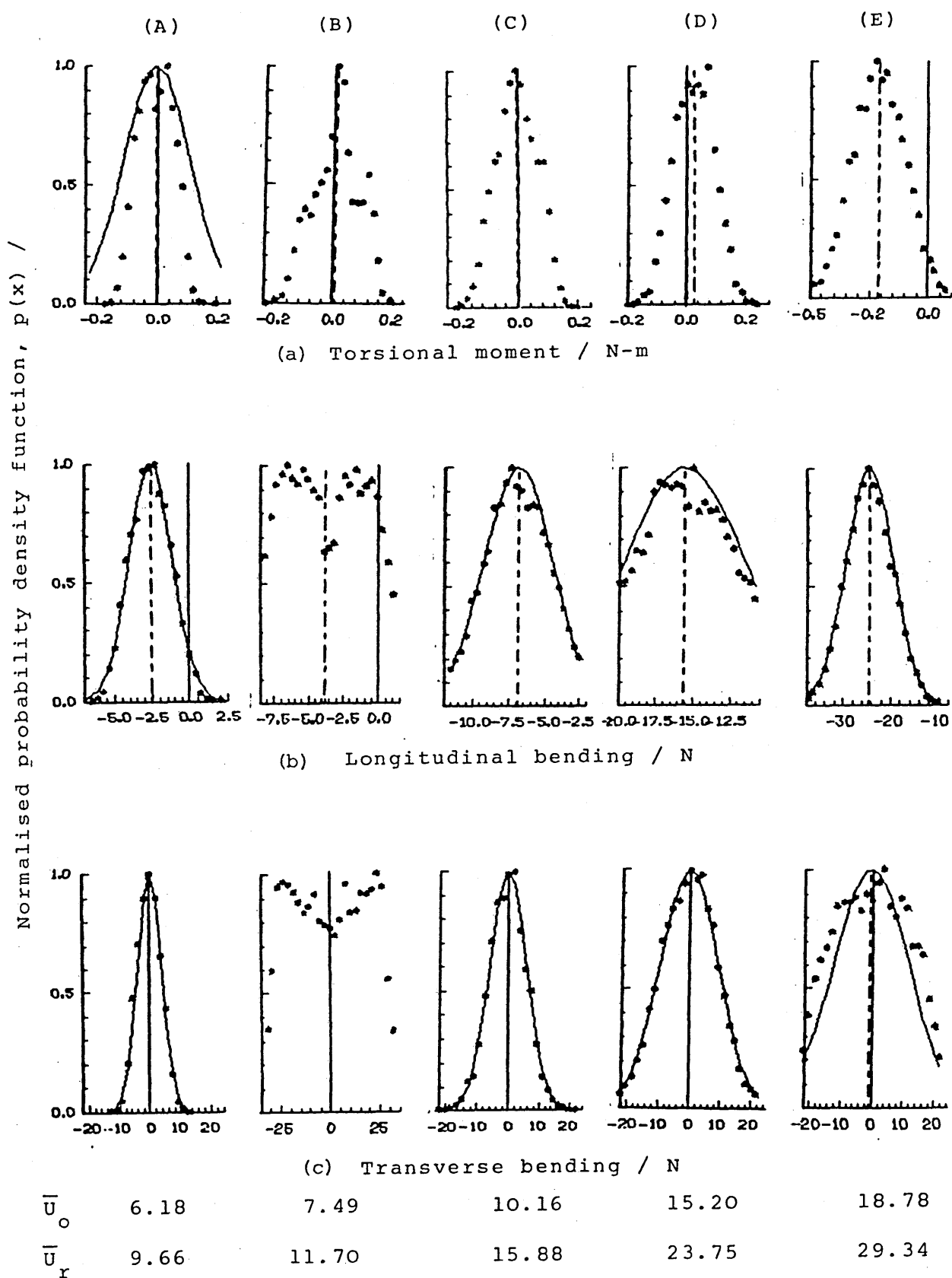
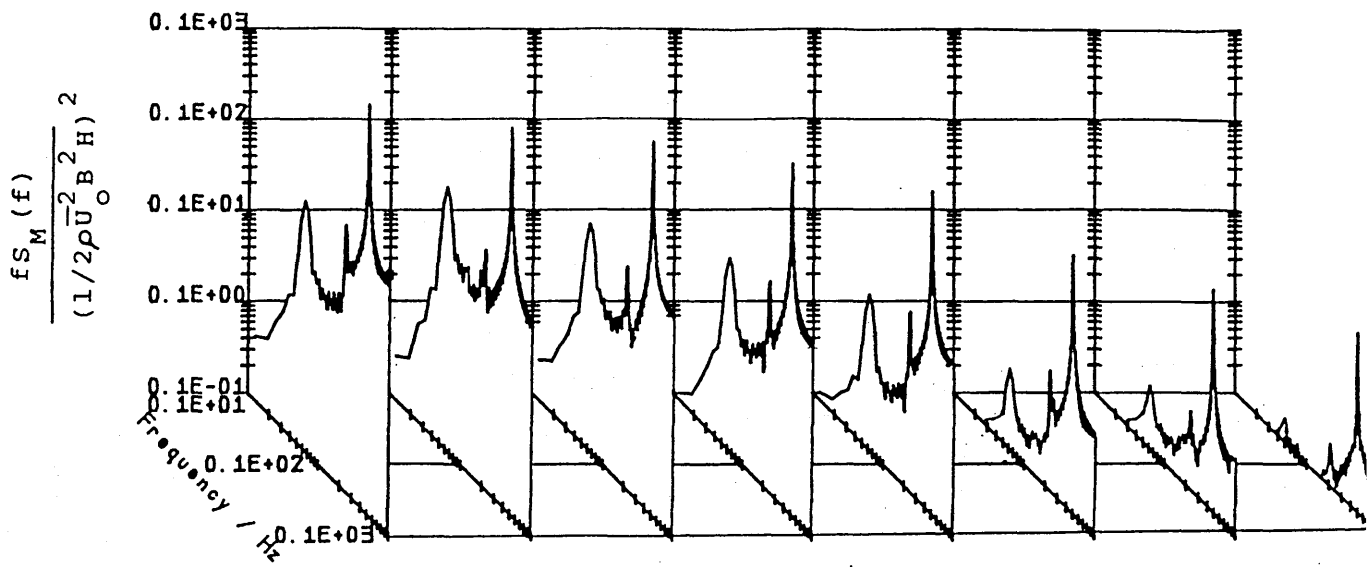
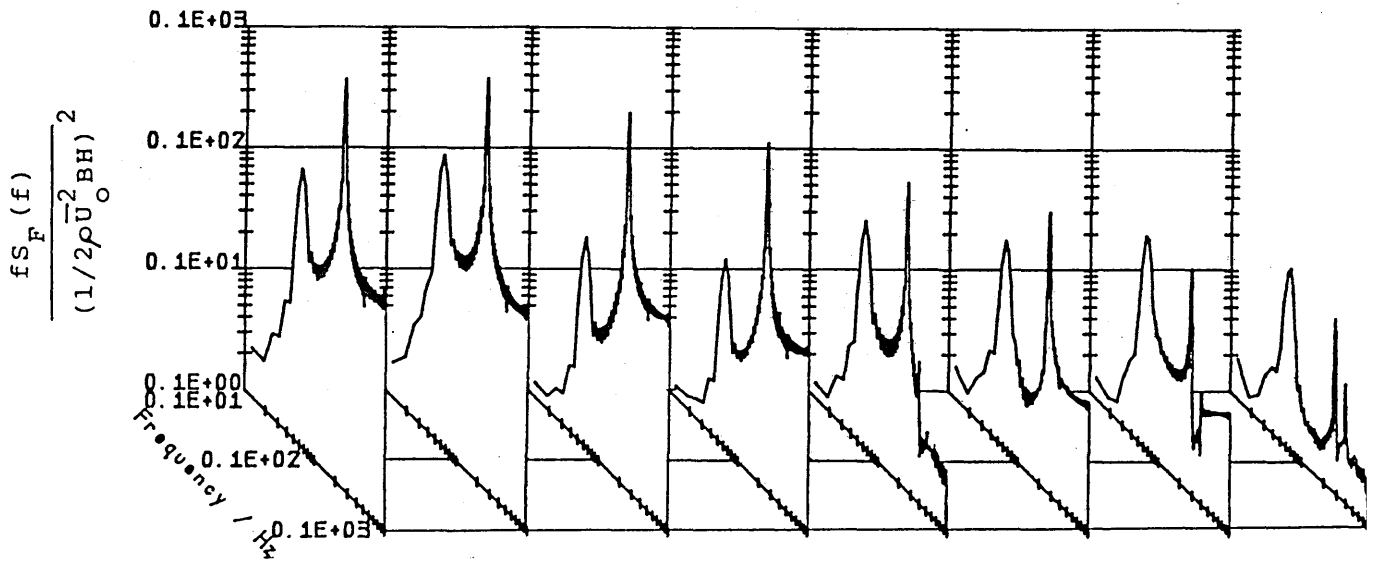


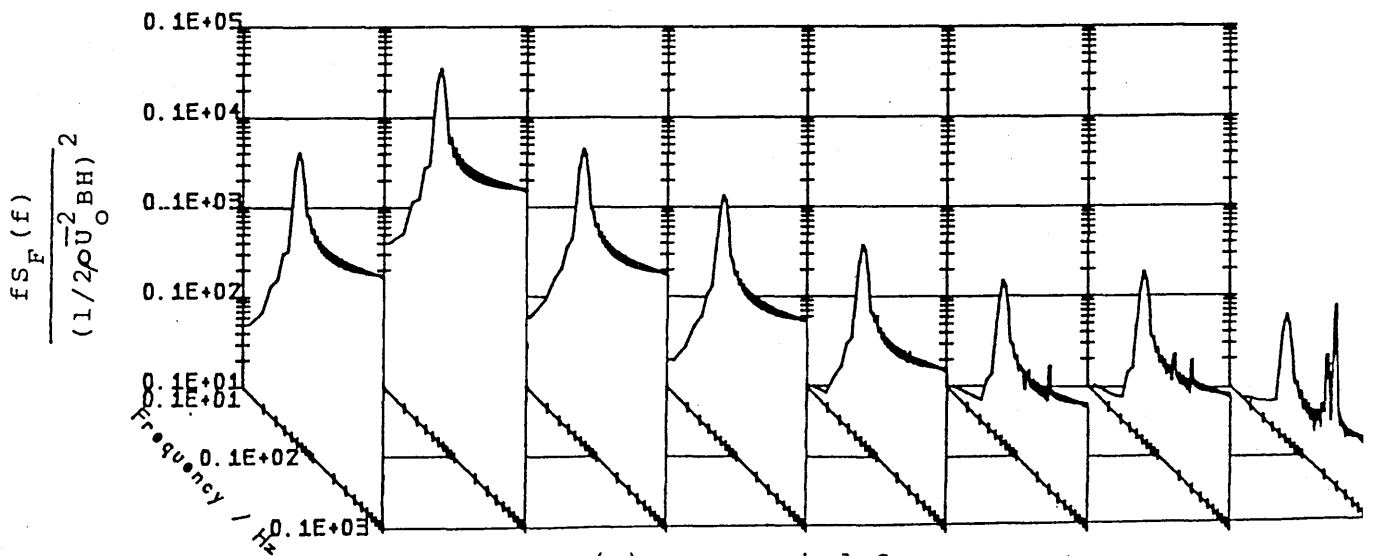
Figure 5.19 Probability density function of output from (a) torsional, (b) longitudinal and (c) transverse bending strain gauge signals measured in uniform turbulent flow for various reduced velocities.



(a) torsional moment spectra



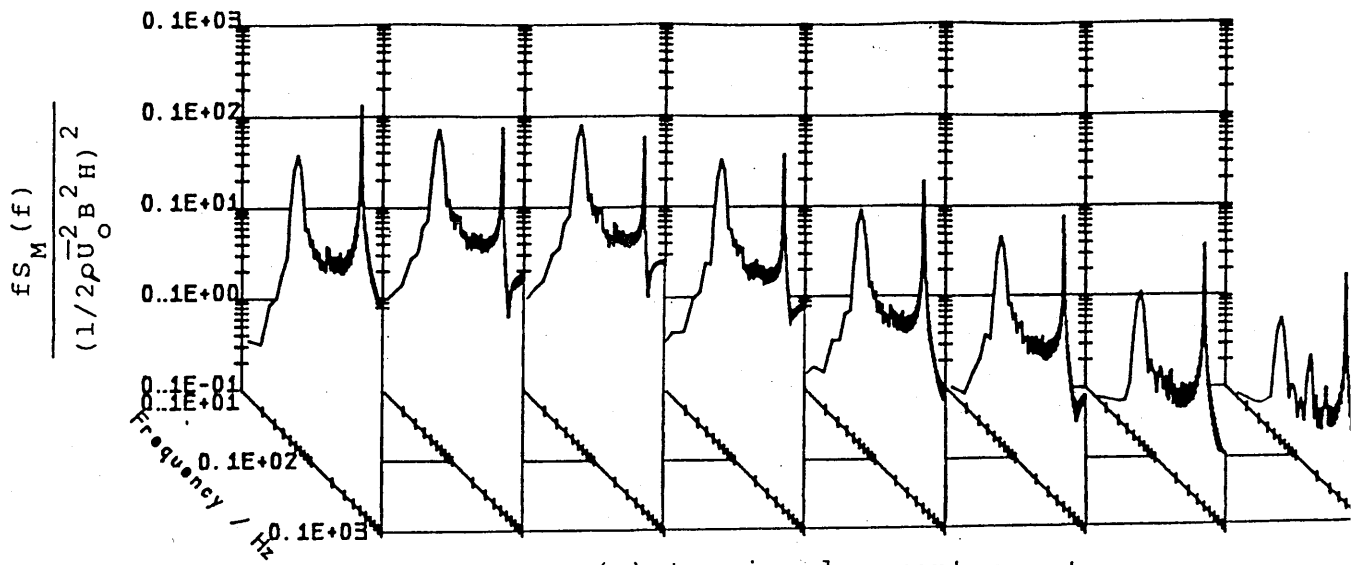
(b) along-wind force spectra



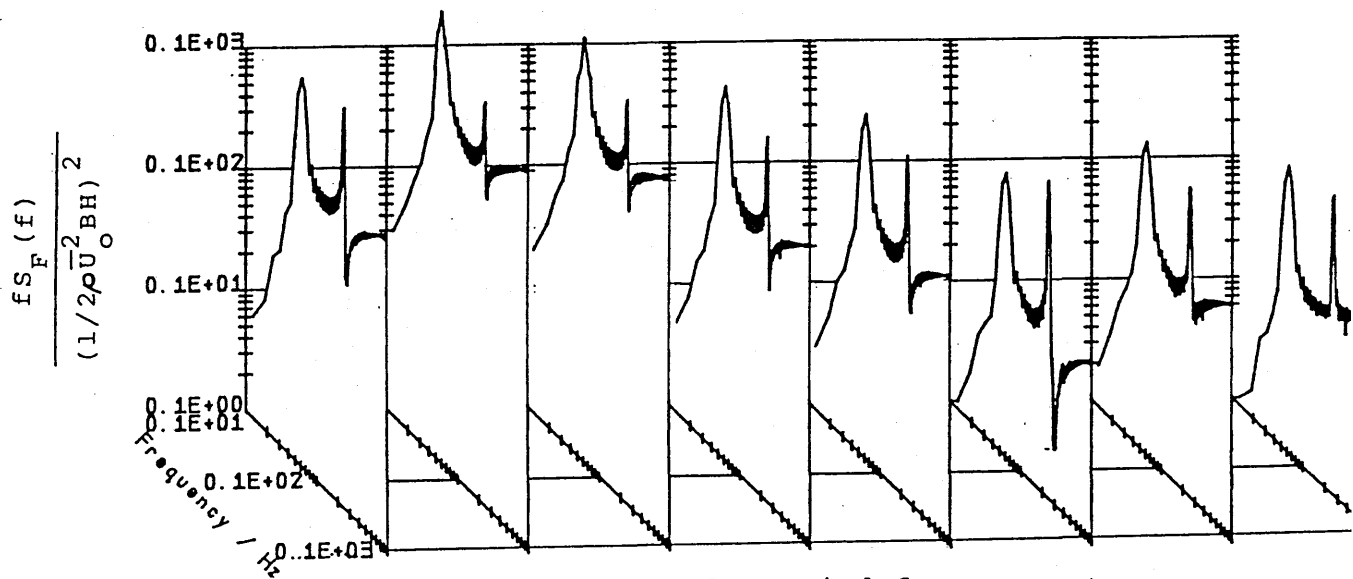
(c) cross-wind force spectra

\bar{U}_0	6.01	6.97	7.62	8.60	10.24	15.11	18.97	25.0
\bar{U}_r	9.39	10.89	11.90	13.44	16.00	23.61	29.64	39.2

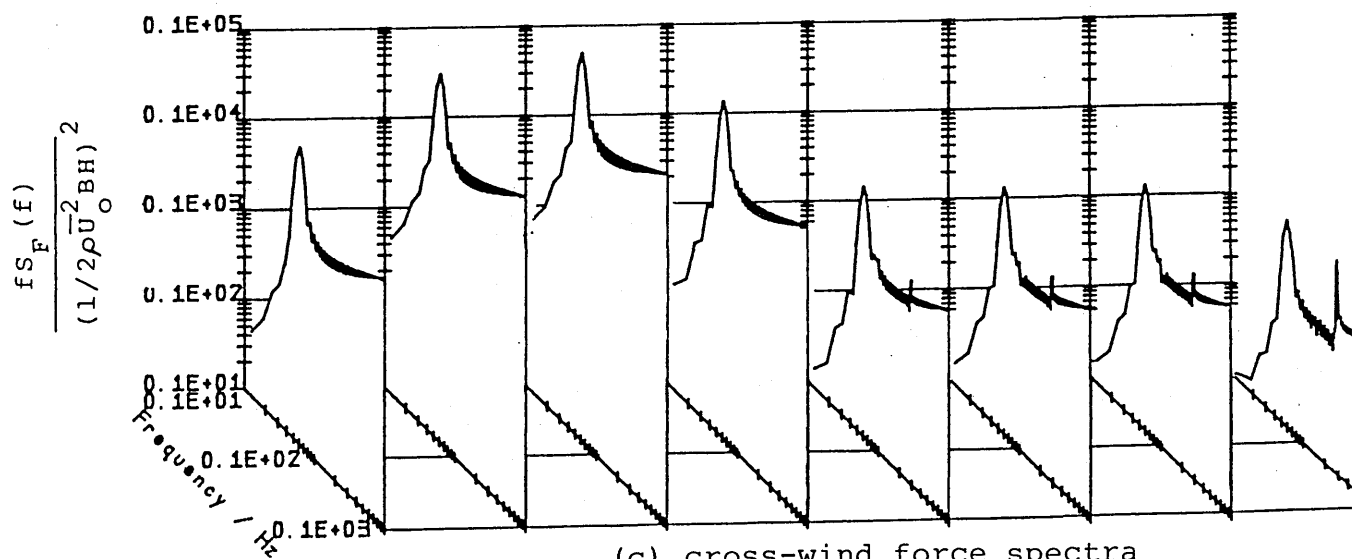
Figure 5.20 Normalised torsional moment, longitudinal and transverse force spectra for the 10x1x1 square tower model measured in uniform smooth flow for various reduced velocities.



(a) torsional moment spectra



(b) along-wind force spectra



(c) cross-wind force spectra

\bar{U}_0	6.18	7.07	7.59	8.52	10.16	12.72	15.20	18.7
\bar{U}_Y	9.65	11.04	11.86	13.31	15.87	19.87	23.74	29.3

Figure 5.21 Normalised torsional moment, longitudinal and transverse force spectra for the 10x1x1 square tower model measured in uniform turbulent flow for various reduced velocities.

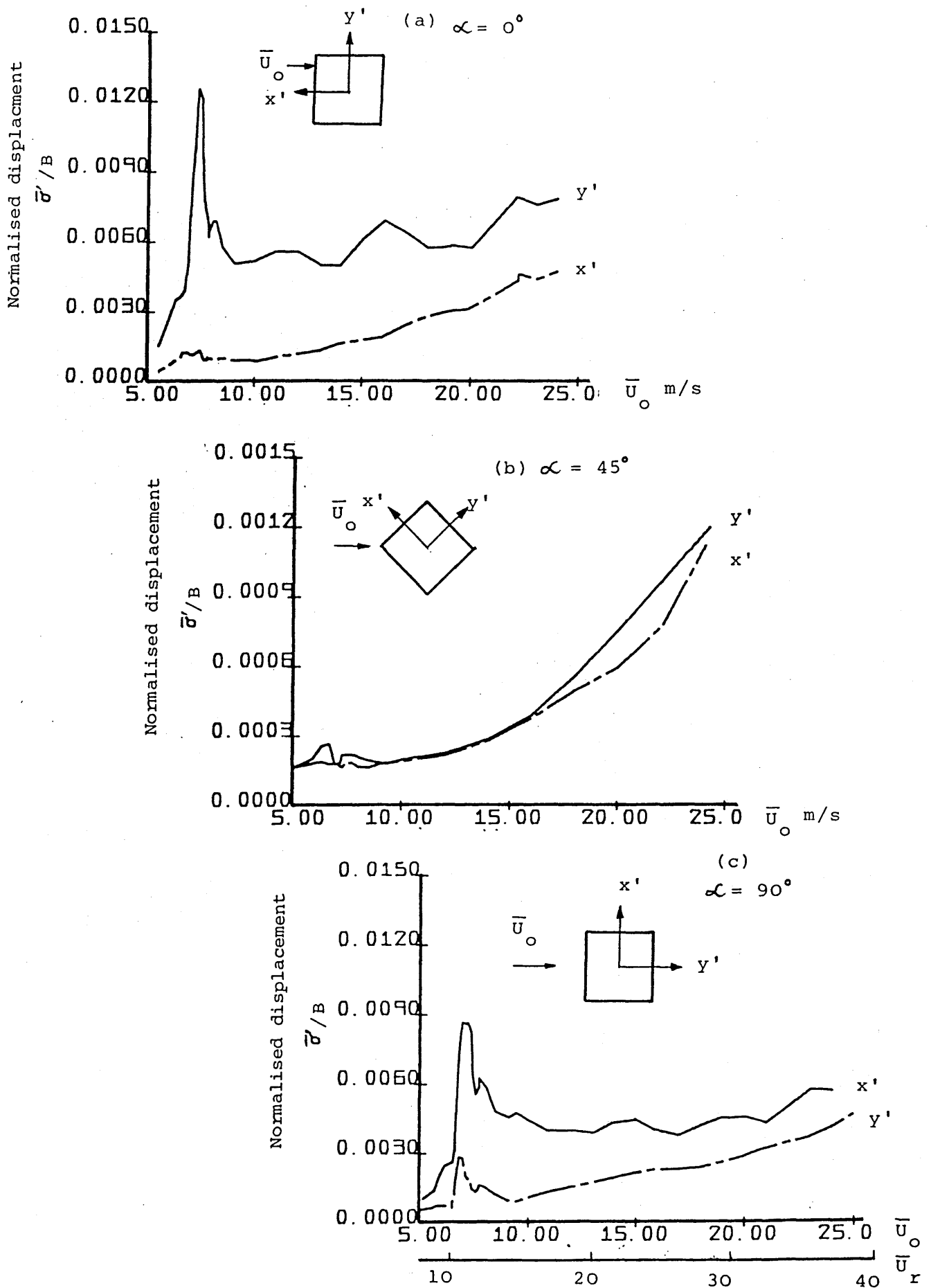


Fig. 5.22 Normalised longitudinal and transverse displacement at the top of the square tower model in uniform smooth flow, measured at (a) $\alpha = 0^\circ$, (b) $\alpha = 45^\circ$ and (c) $\alpha = 90^\circ$ and as a function of the mean wind.

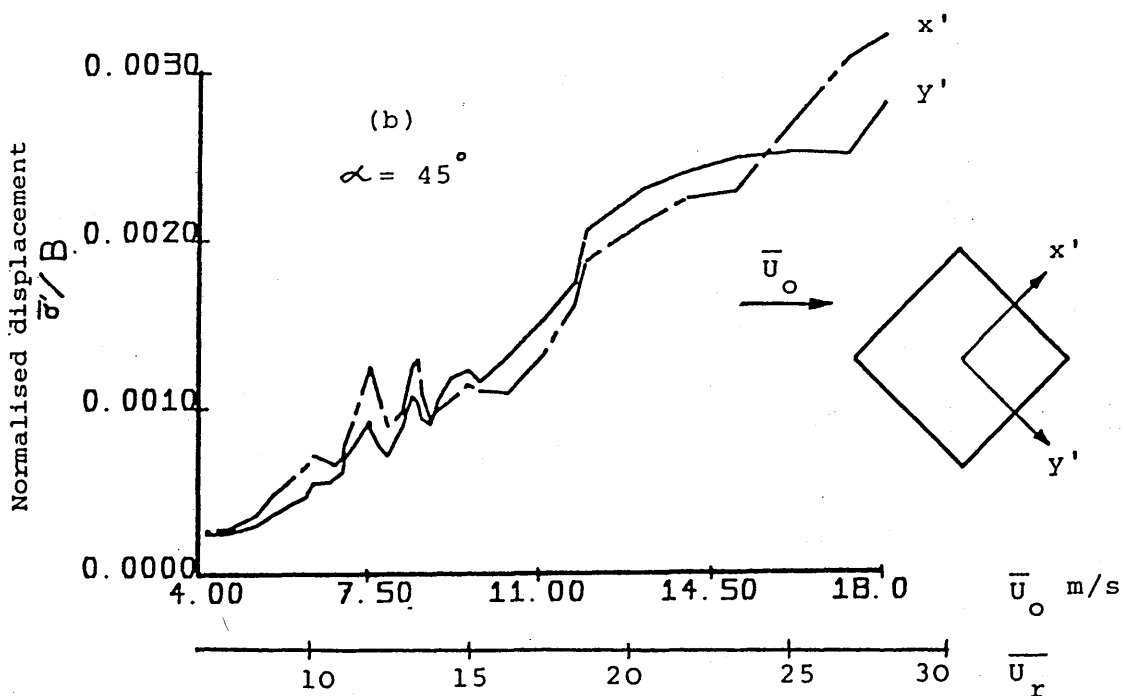
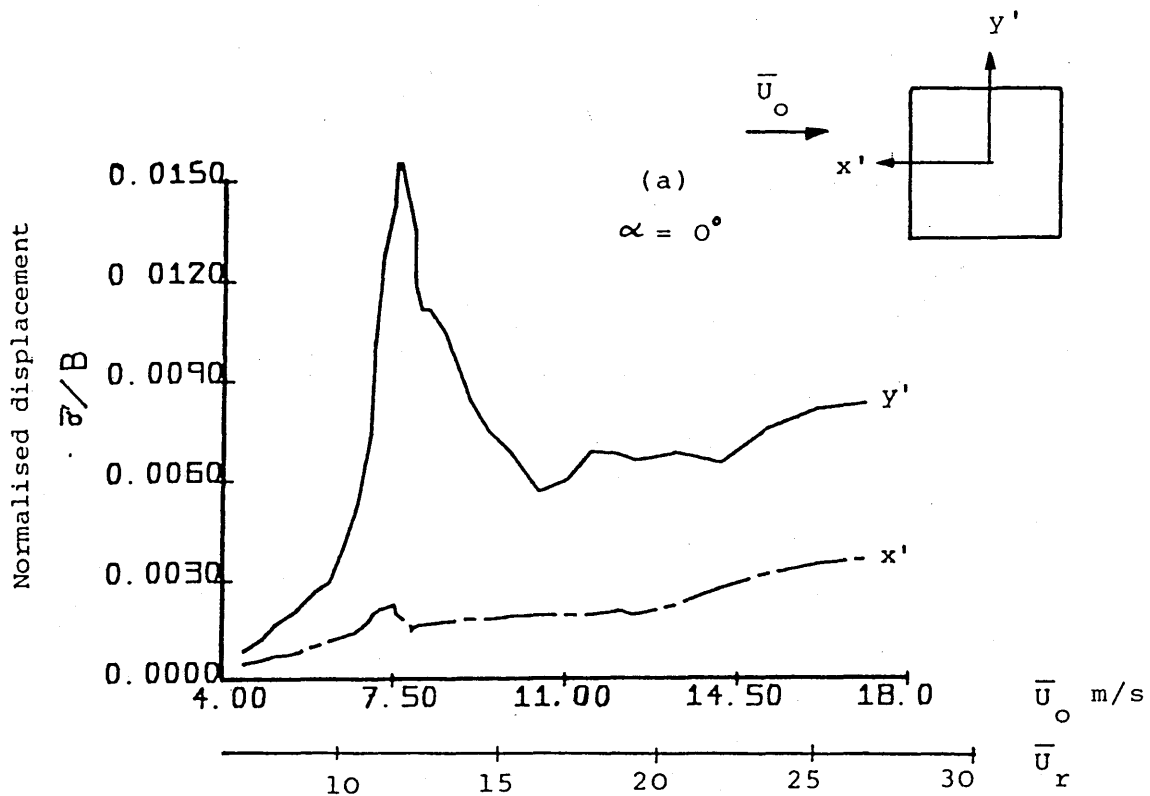


Figure 5.23 Normalised longitudinal and transverse displacement at the top of the square tower model in uniform turbulent flow, measured at (a) $\alpha = 0^\circ$ and (b) $\alpha = 45^\circ$ and as function of the mean wind.

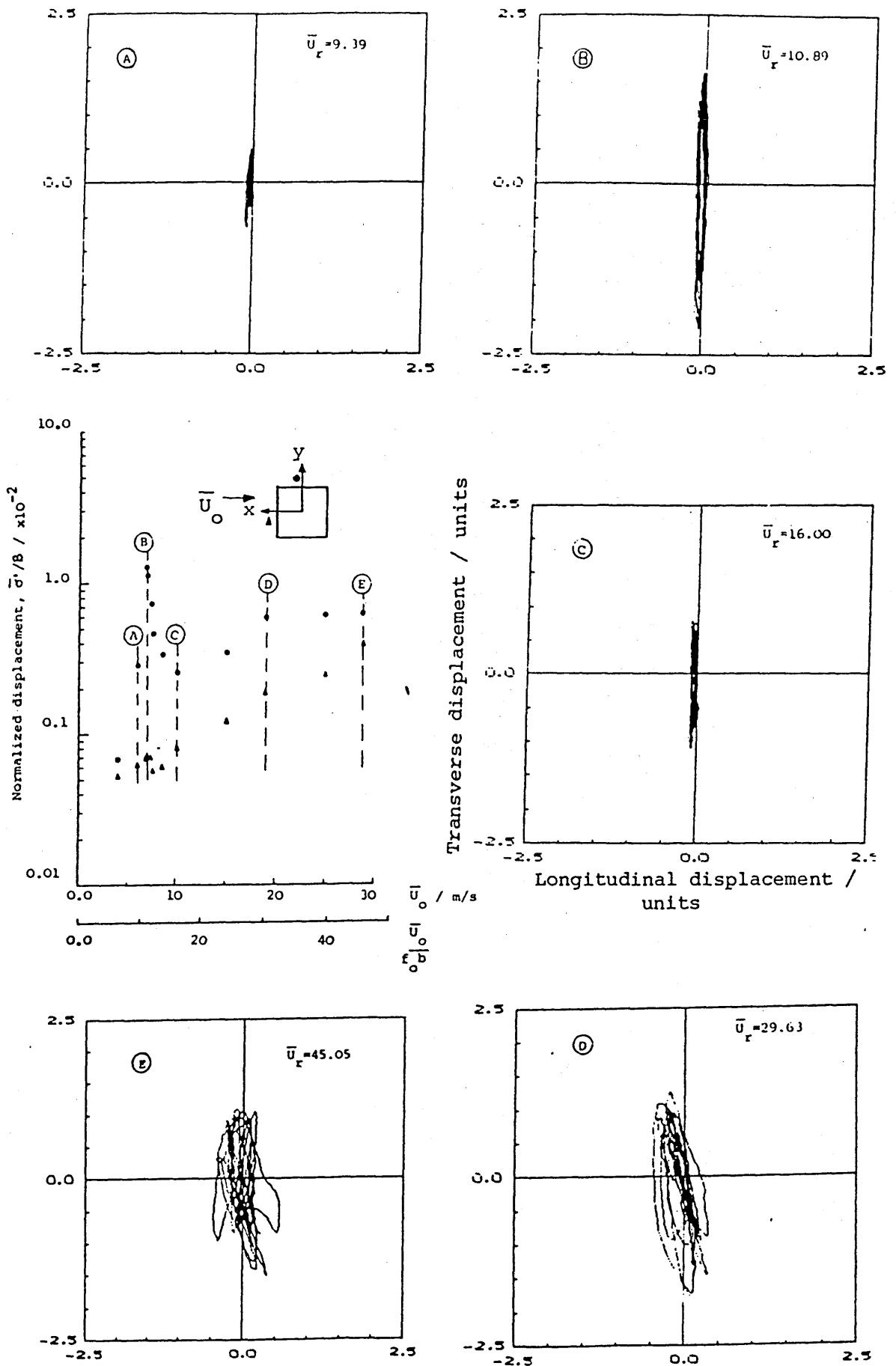


Figure 5.24 X-Y plots of displacement at the top of the 10x1x1 square tower model measured in uniform smooth flow for various reduced velocities.

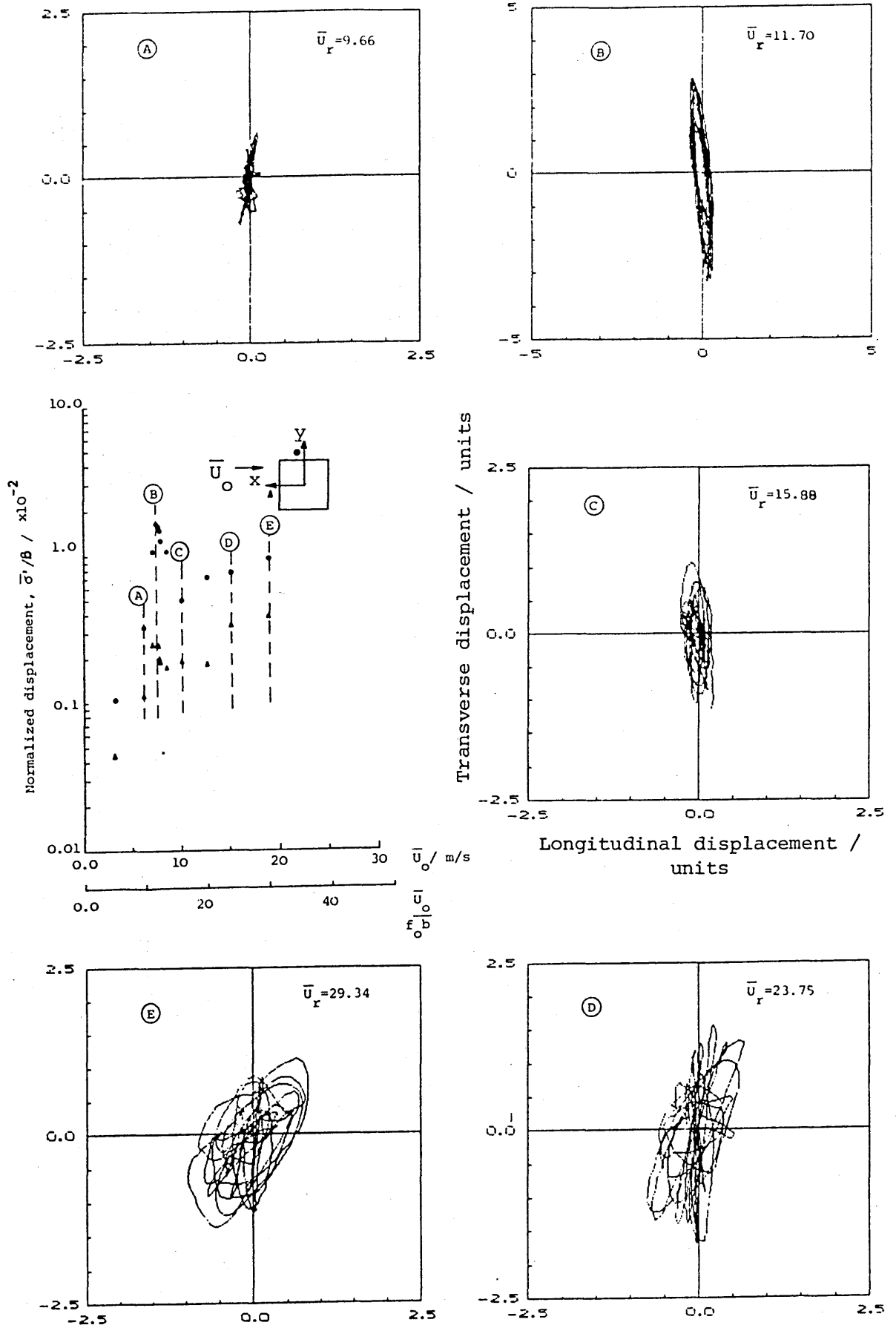


Figure 5.25 X-Y plots of displacement at the top of the 10x10x1 square tower model measured in uniform turbulent flow for various reduced velocities.

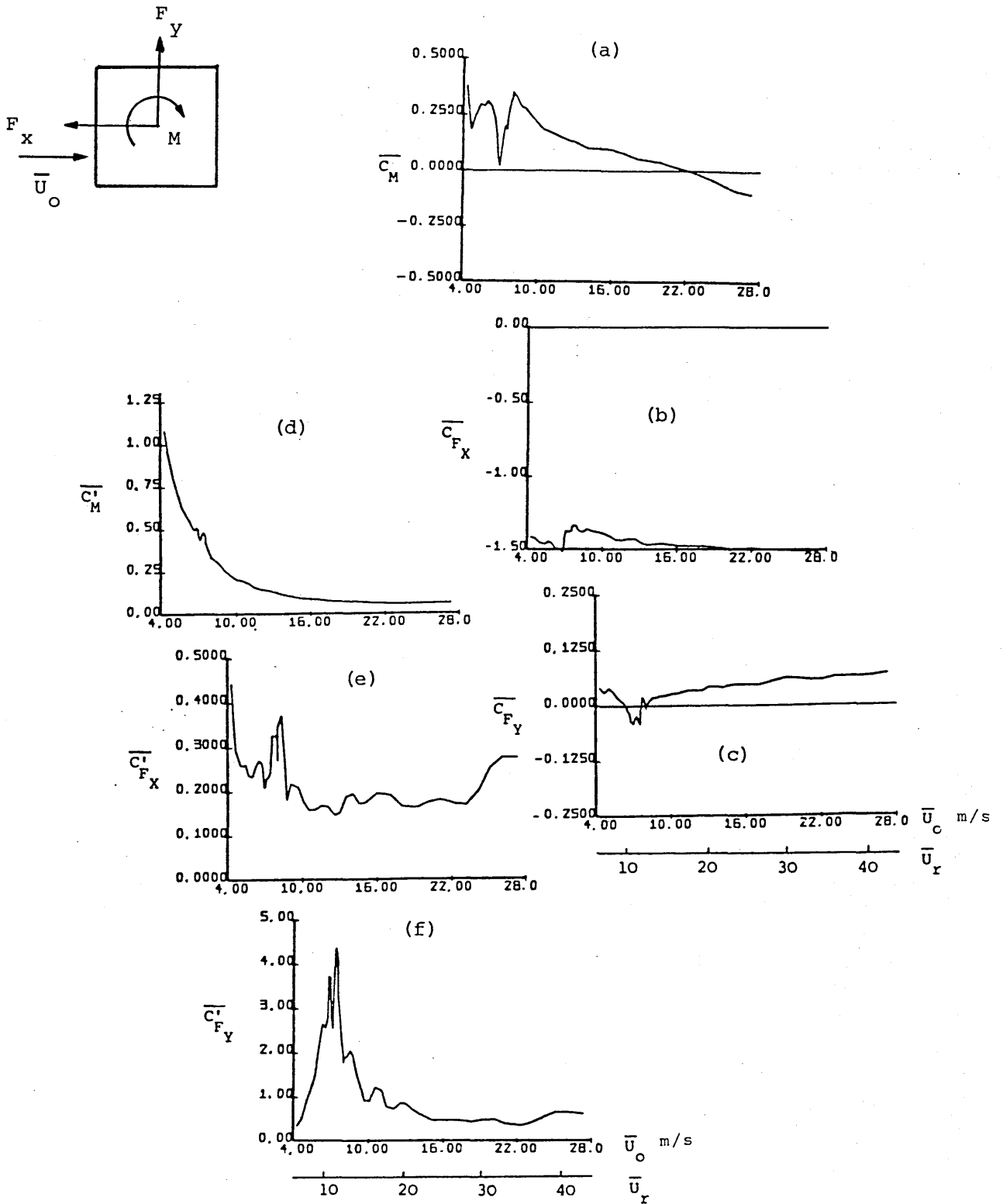


Figure 5.26 Mean and RMS coefficients of torsional moment, longitudinal and transverse force of the 10x1x1 square tower model in uniform smooth flow. (N.B. the second model-balance system was used in this test)

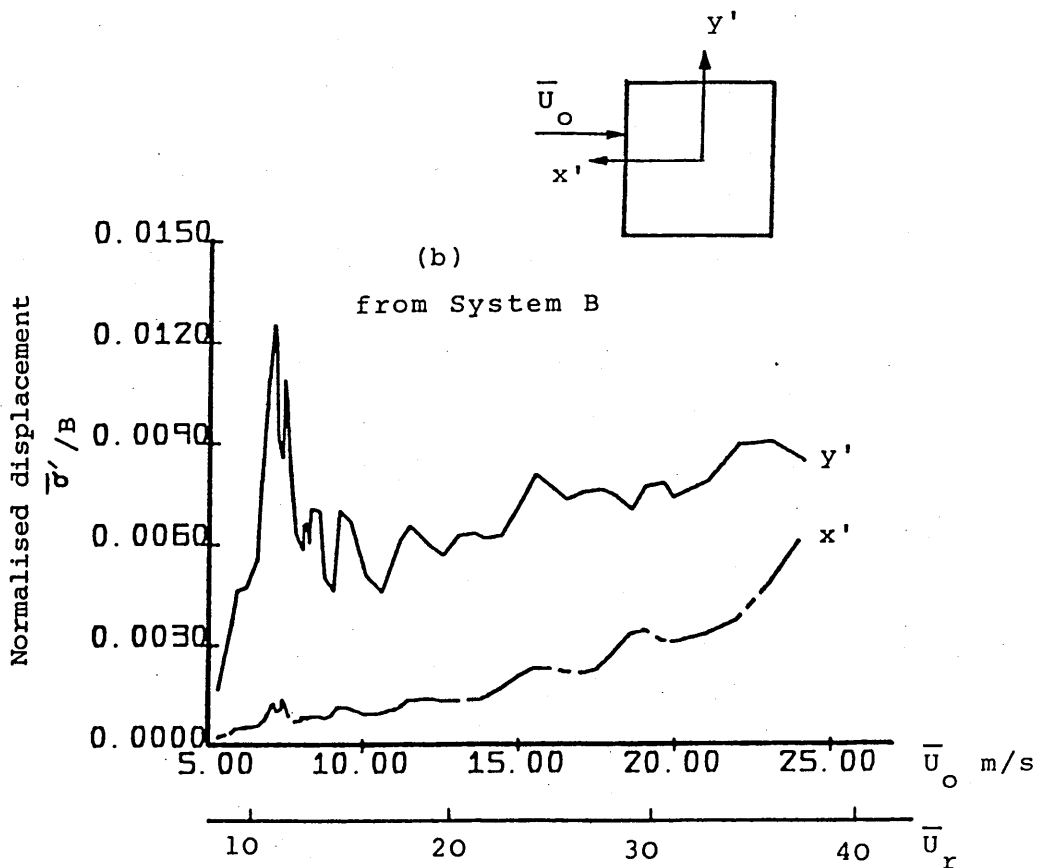
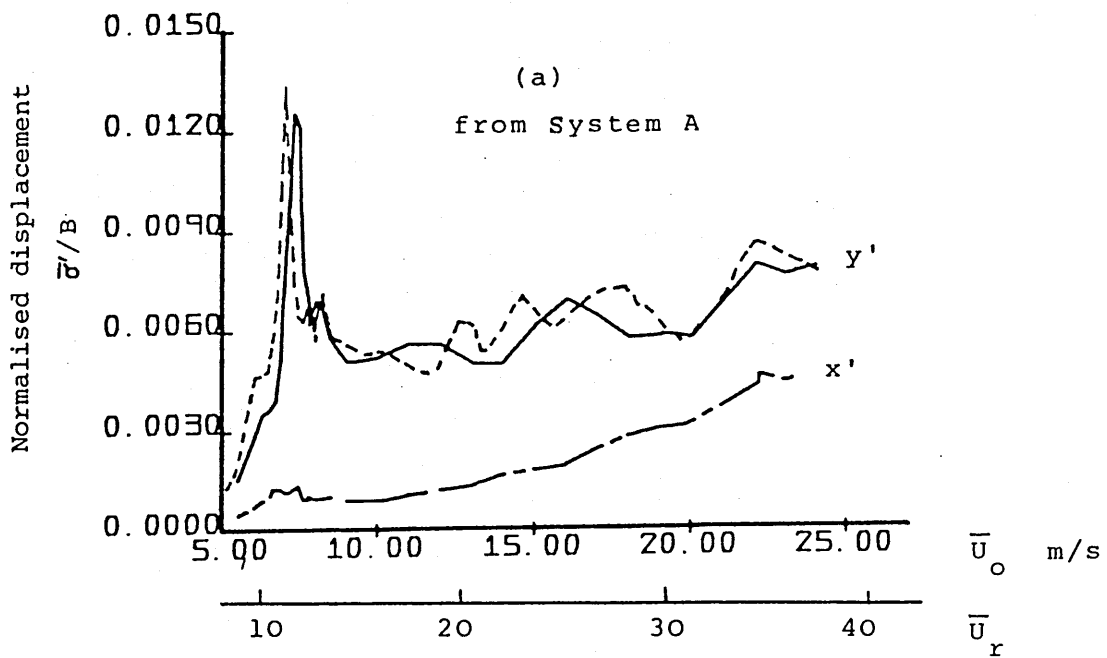


Figure 5.27 Comparison of the normalised displacement at the top of the two model-balance systems used in this study in uniform smooth flow.

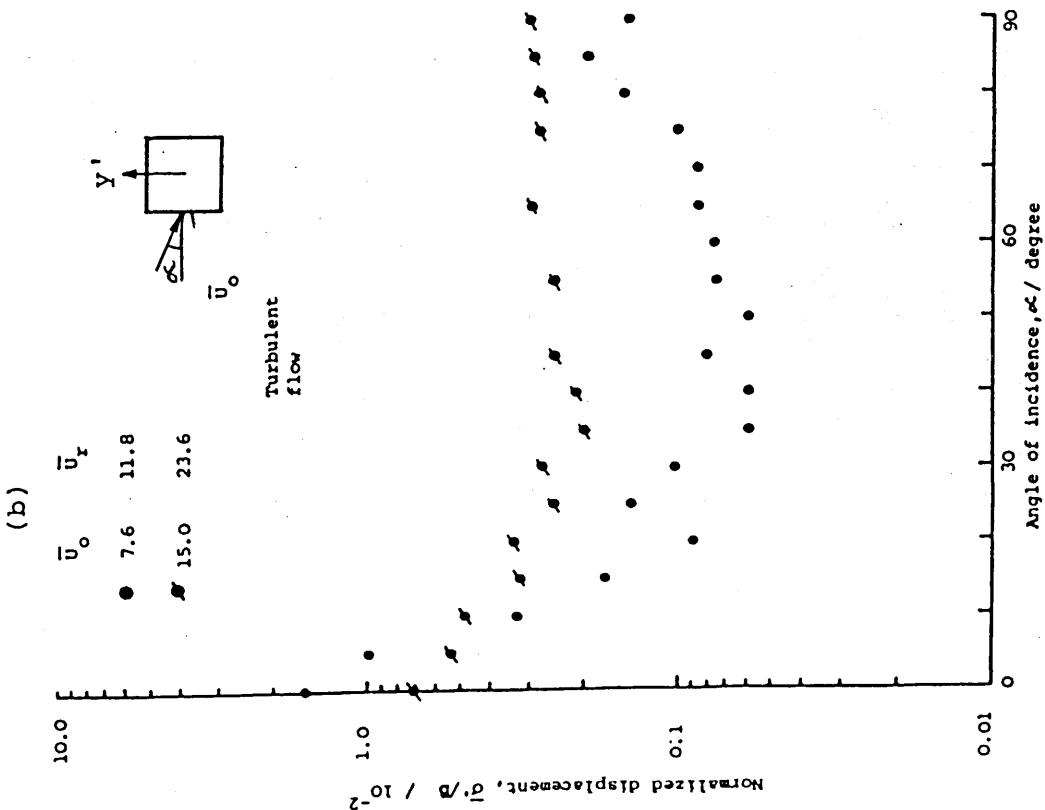
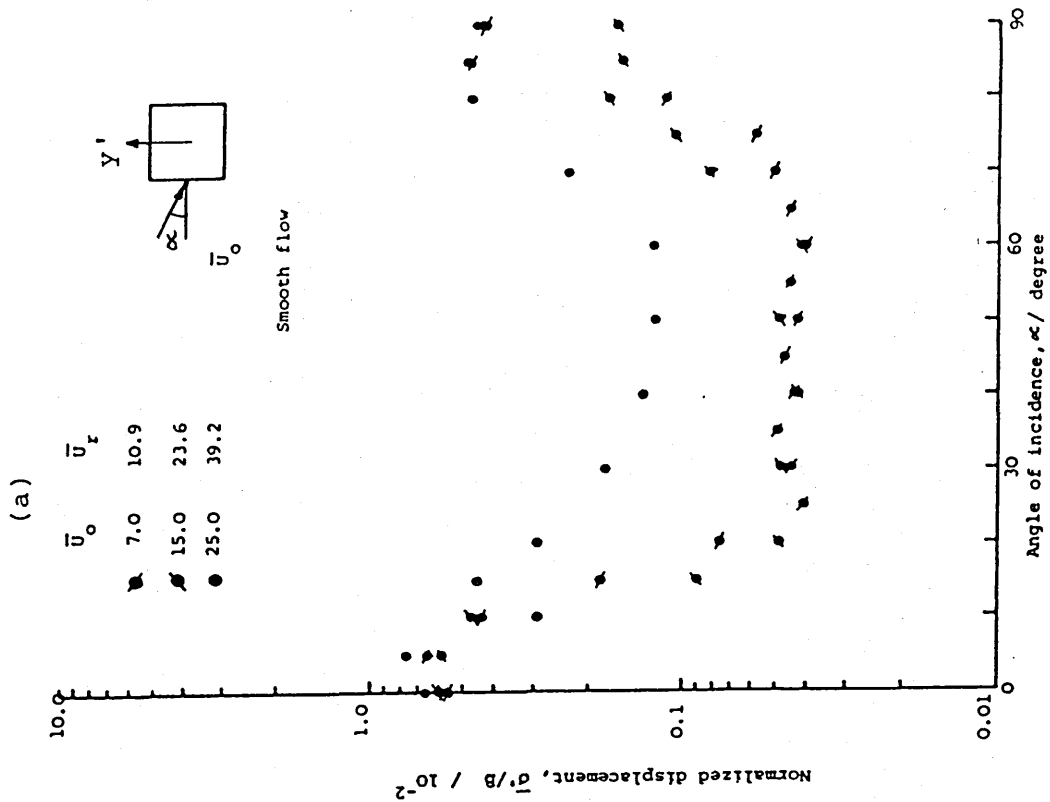


Figure 5.28. Variation of the normalised transverse response at the top of the 10x1x1 square tower with angle of incidence of the mean wind in (a) uniform smooth and (b) uniform turbulent flow for various reduced velocities.

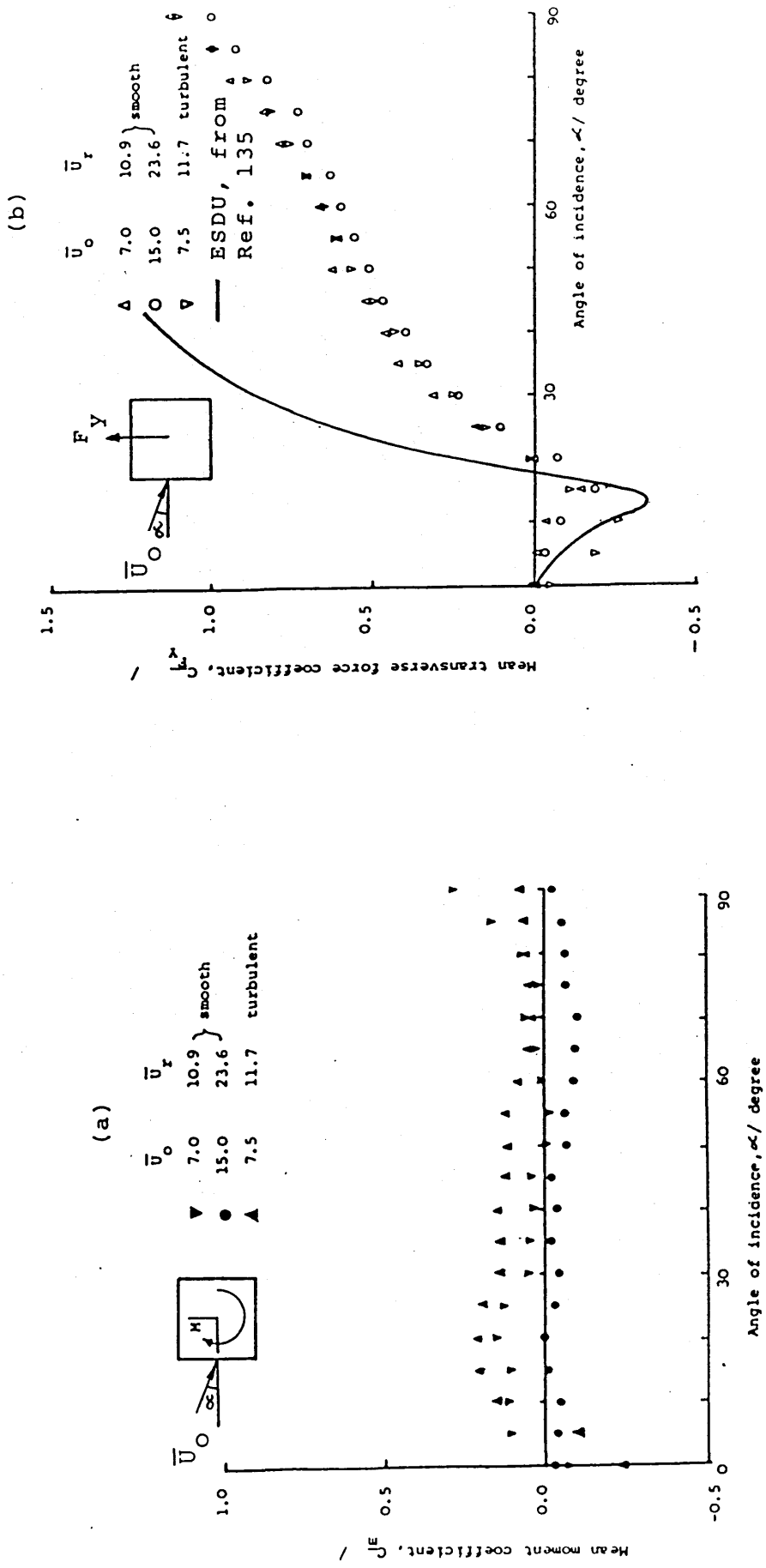


Figure 5.29 Variation of the mean torsional moment and transverse force coefficients of the 10x1x1 square tower with angle of incidence of the mean wind in both uniform smooth and turbulent flows for various reduced velocities.

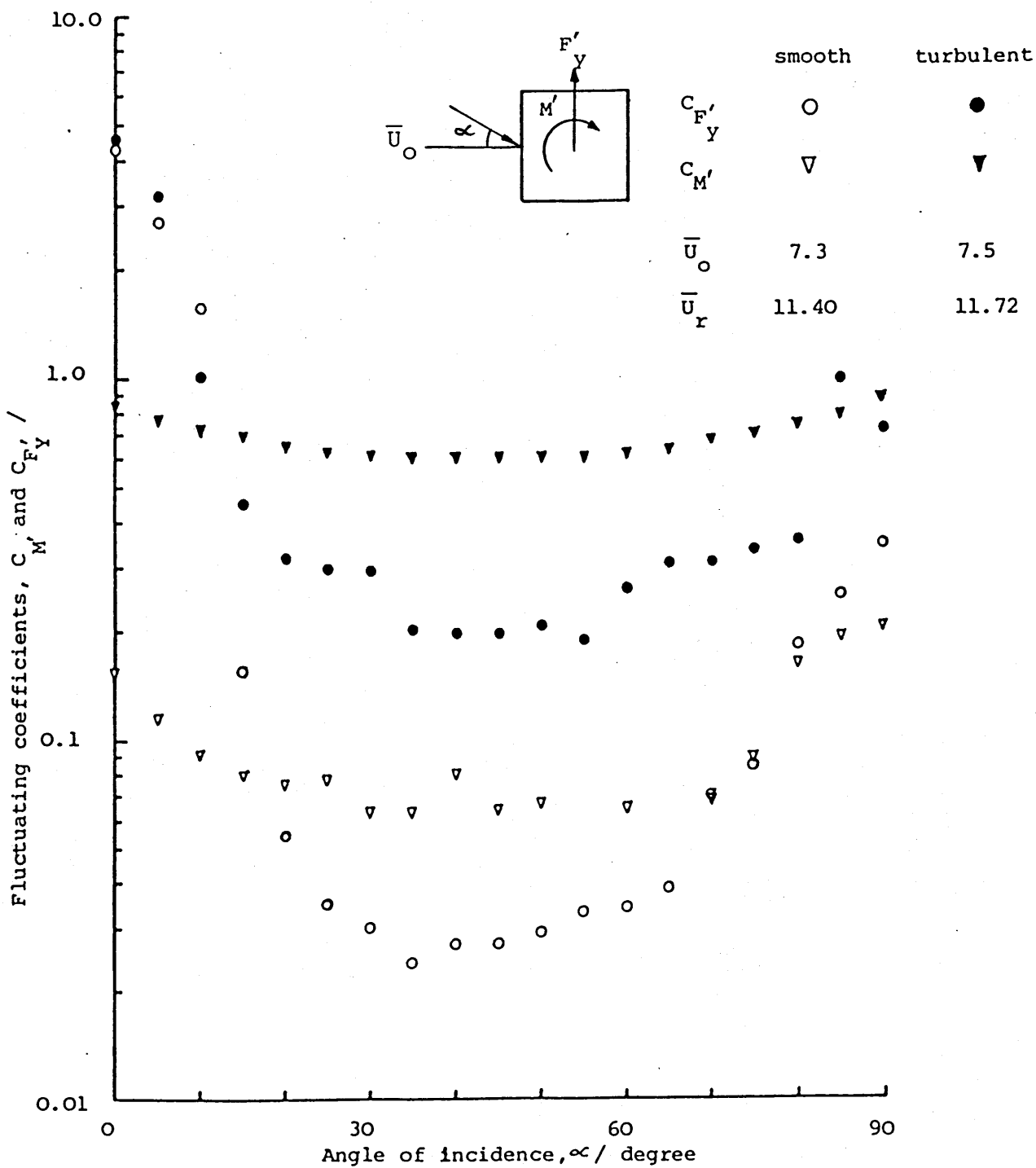
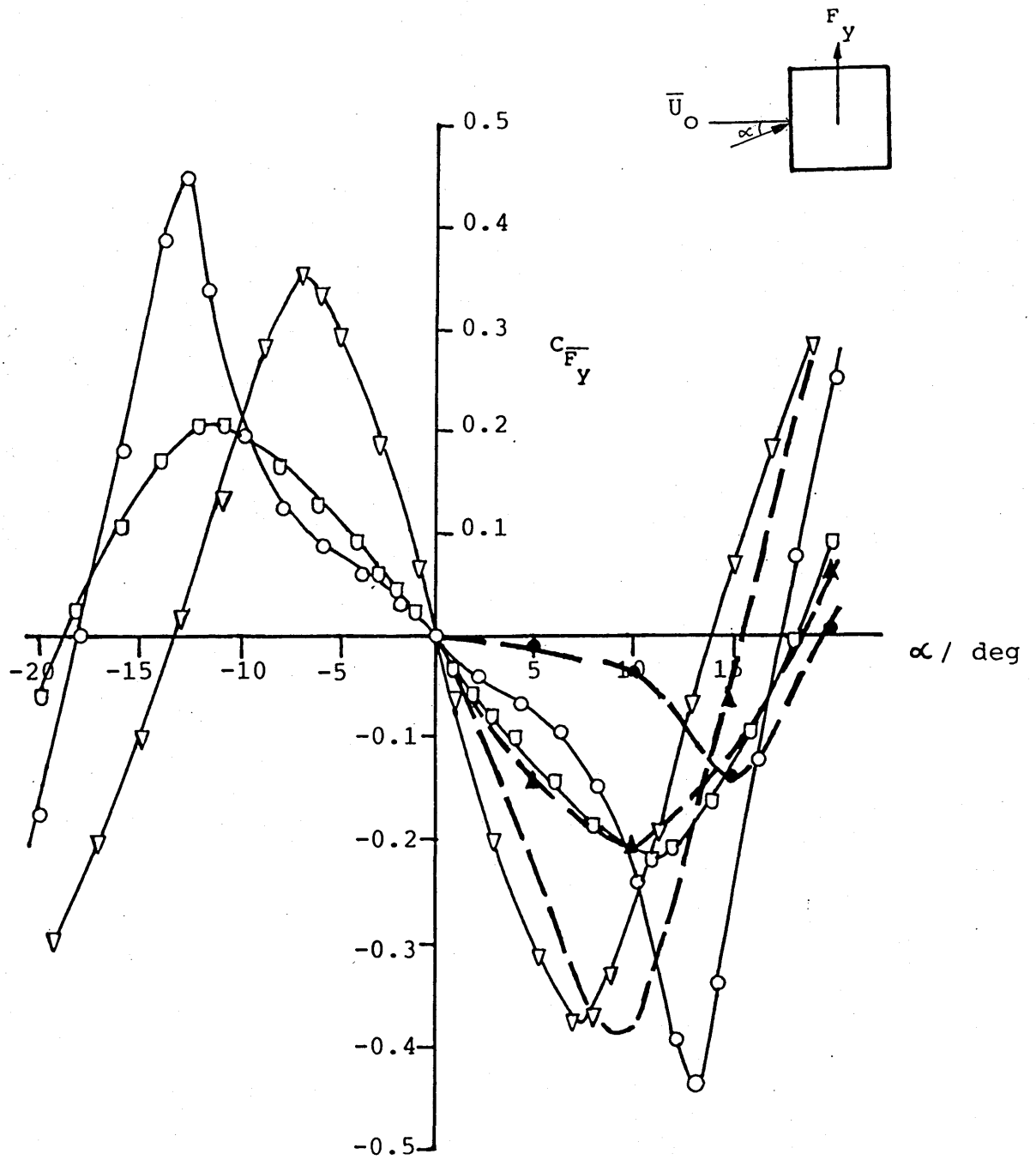


Figure 5.30 Variation of fluctuation torsional moment and transverse force coefficients of the square tower model with angle of incidence of the mean wind in both uniform smooth and turbulent flows at two reduced velocities.



	symbol	turbulence intensity	
From Kwok	○	uniform smooth flow	0.01
Ref. 8	◻	turbulent boundary layer flow	0.07
	△	rod-generated turbulent flow	0.09
From Laneville and Parkinson Ref. 95	---	two-dimensional square section grid-generated turbulent flow	0.09
From present measurements	—●—	smooth uniform flow	0.01
	—▲—	grid-generated turbulent flow	0.09

Figure 5.31 Comparison of the mean transverse force coefficients of a square-section tower in different types of flow.

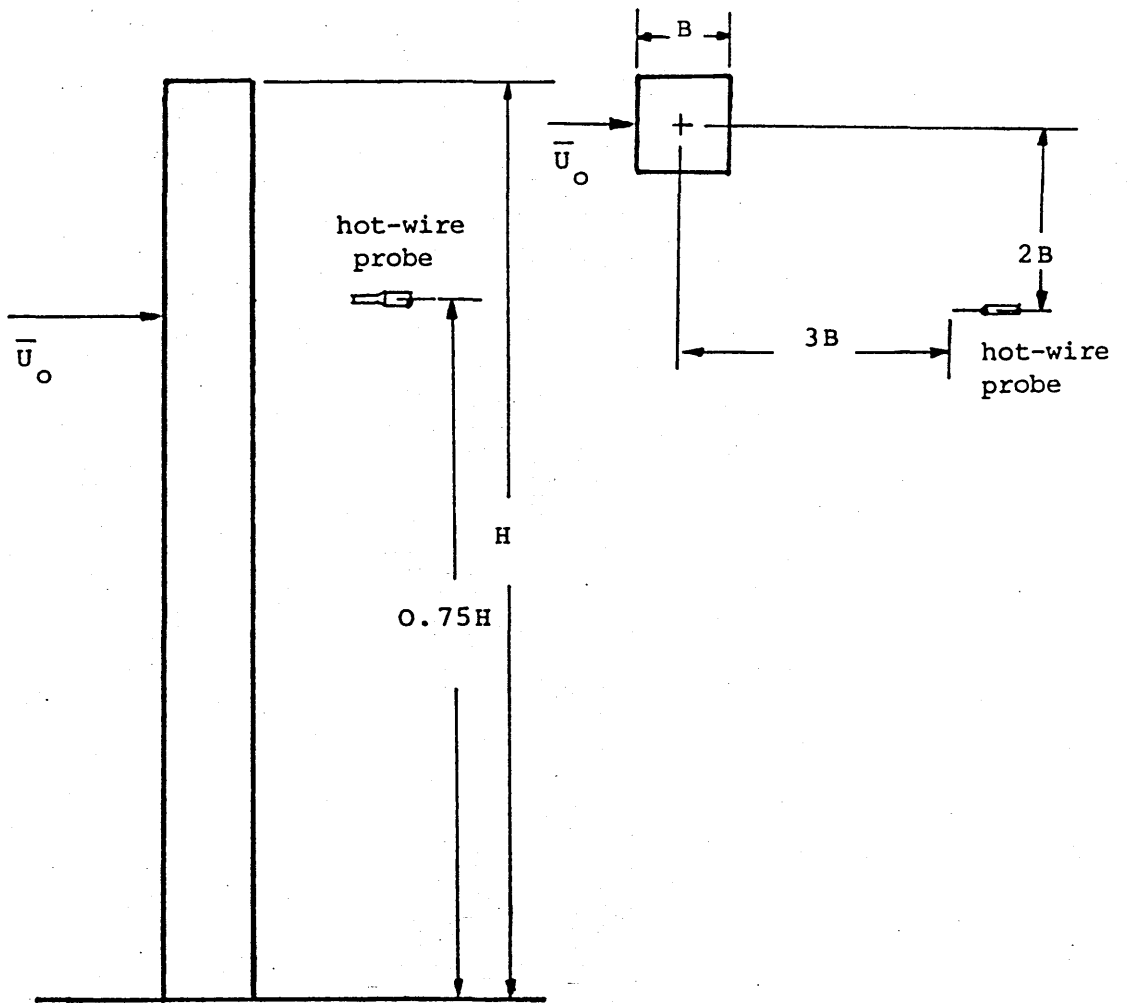


Figure 5.34 Relative position of the hot-wire probe for measuring velocity fluctuations in the near wake behind the 10x1x1 square tower model.

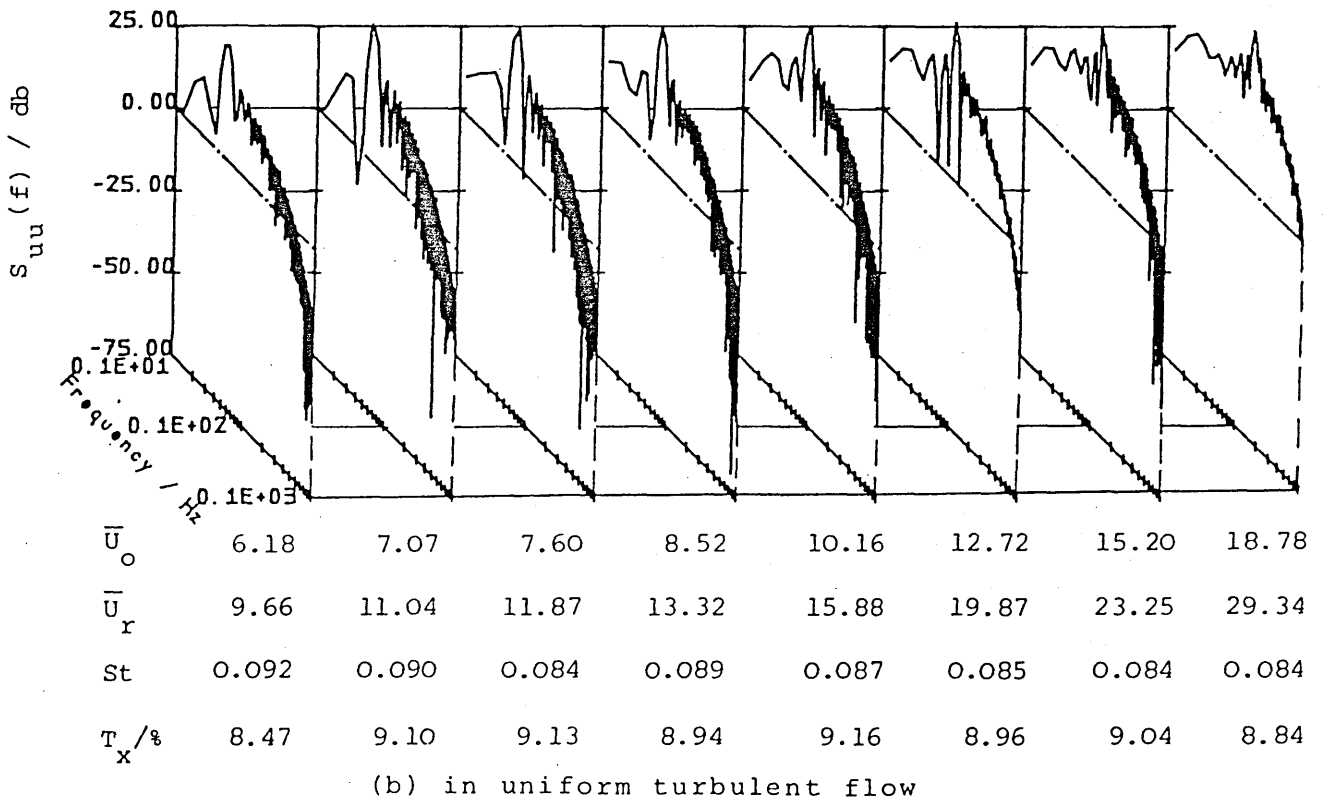
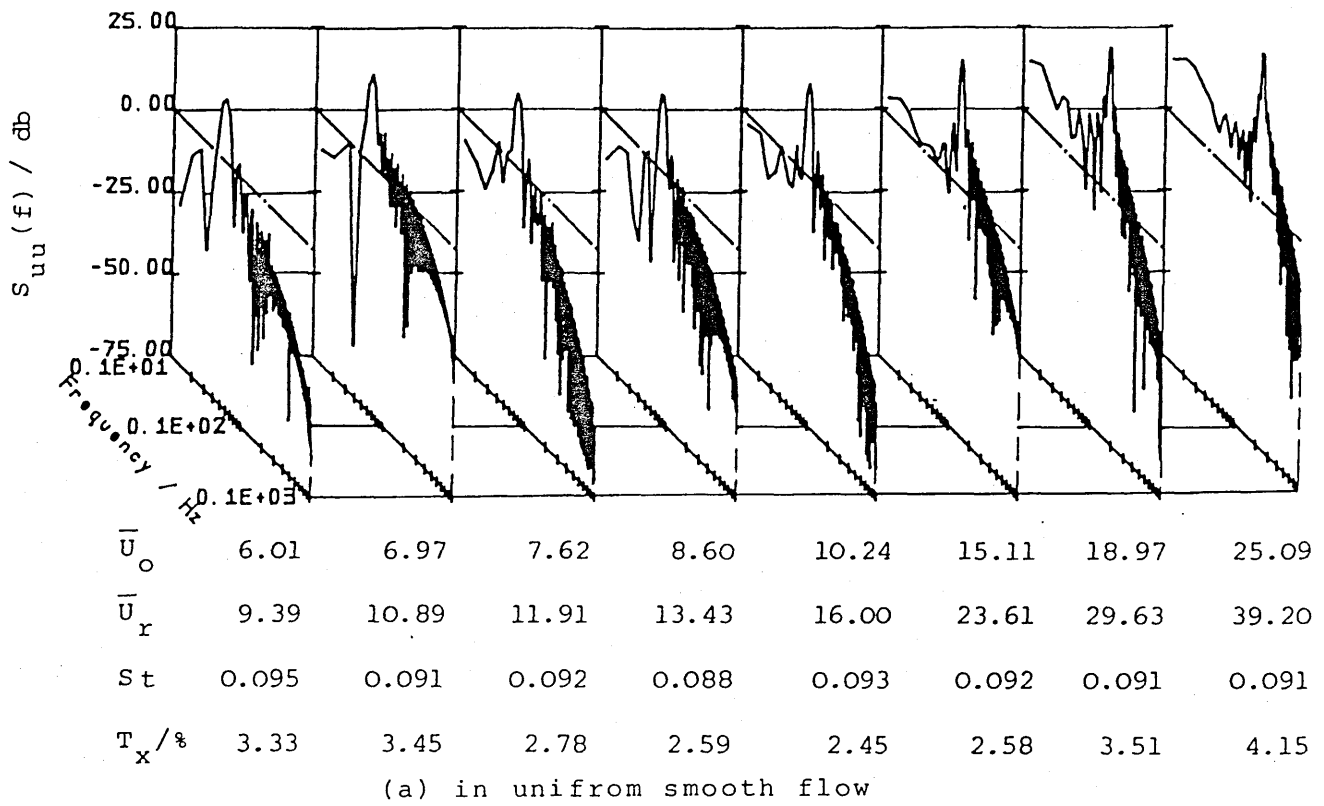
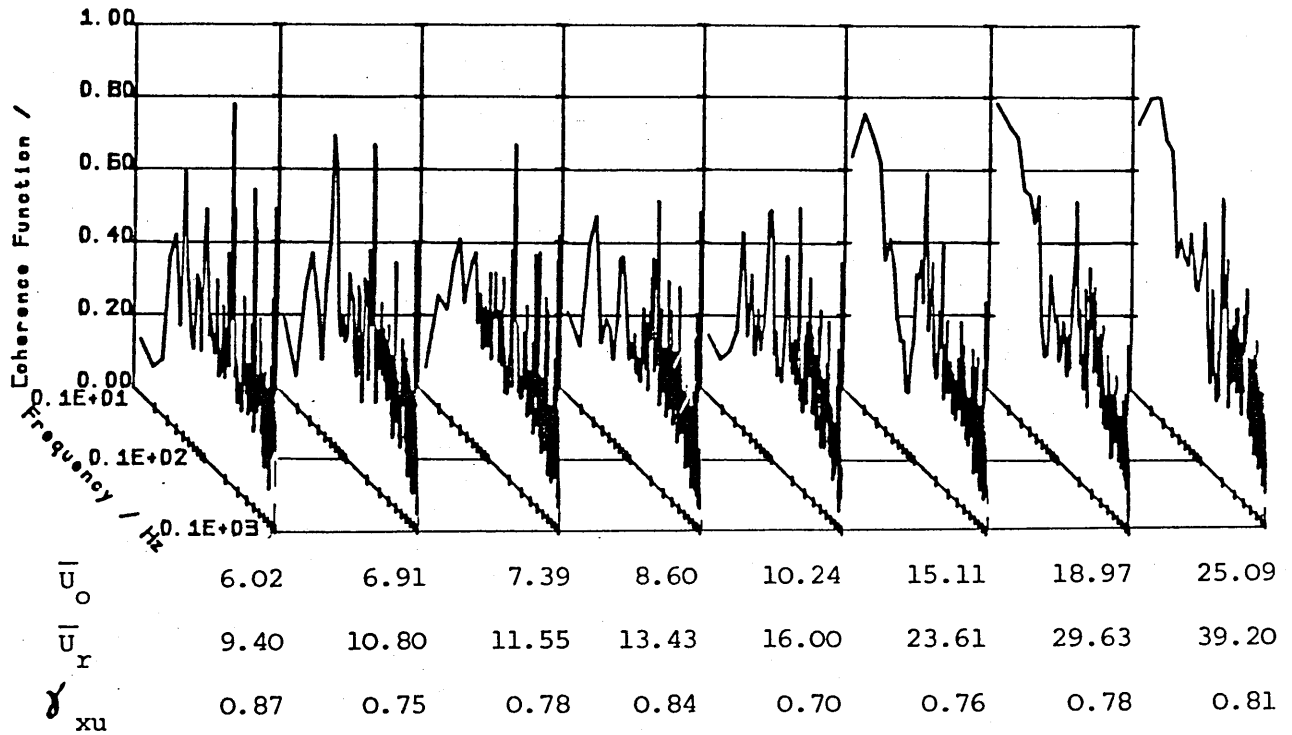
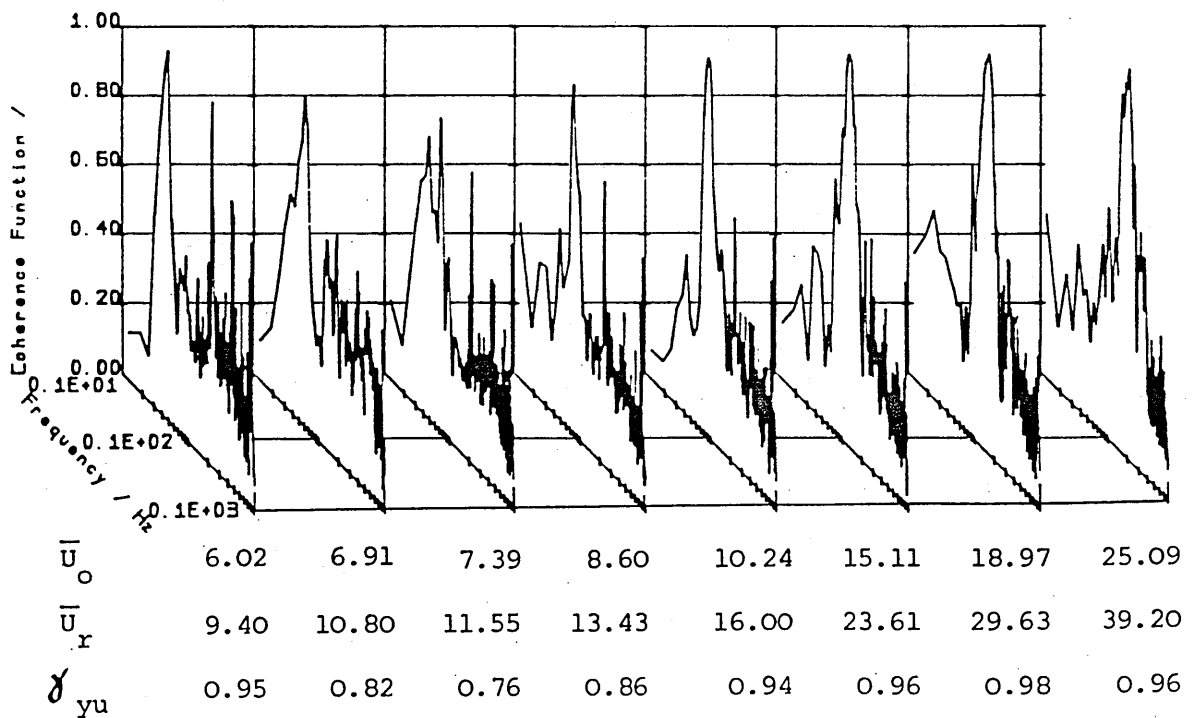


Figure 5.35 Wake spectra of the 10x1x1 square tower in the (a) uniform smooth and (b) uniform turbulent flow for various reduced velocities.

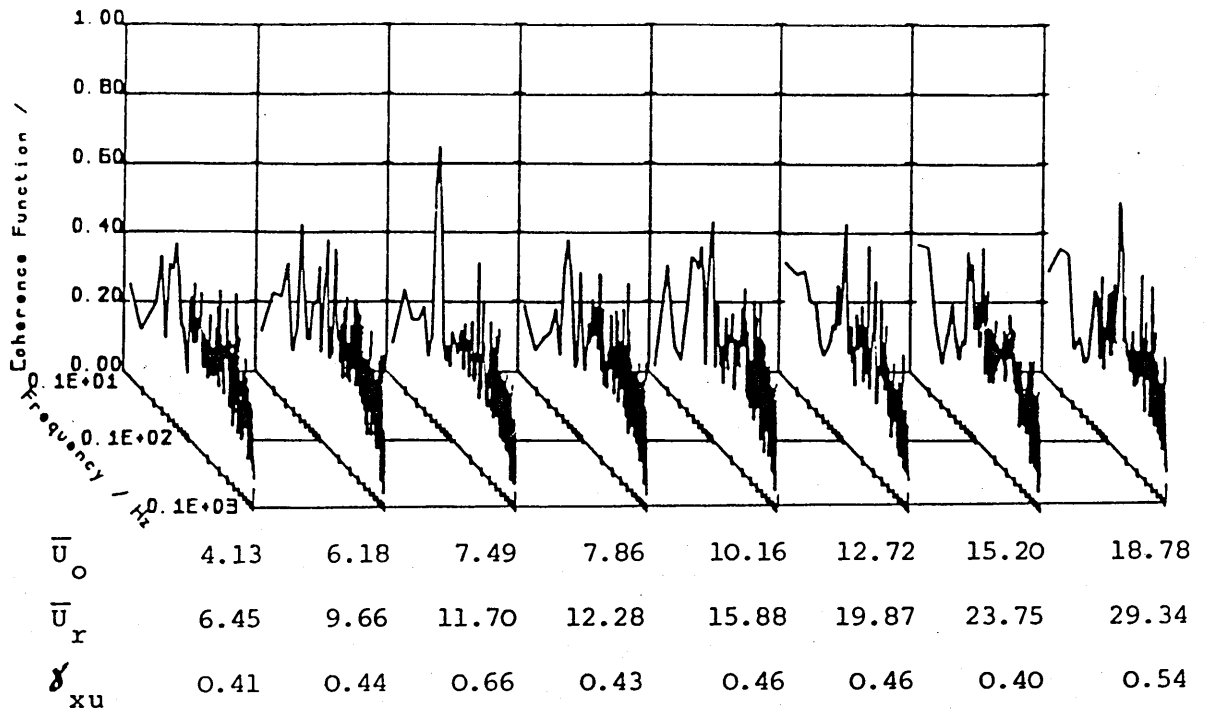


(a) velocity fluctuations and along-wind response

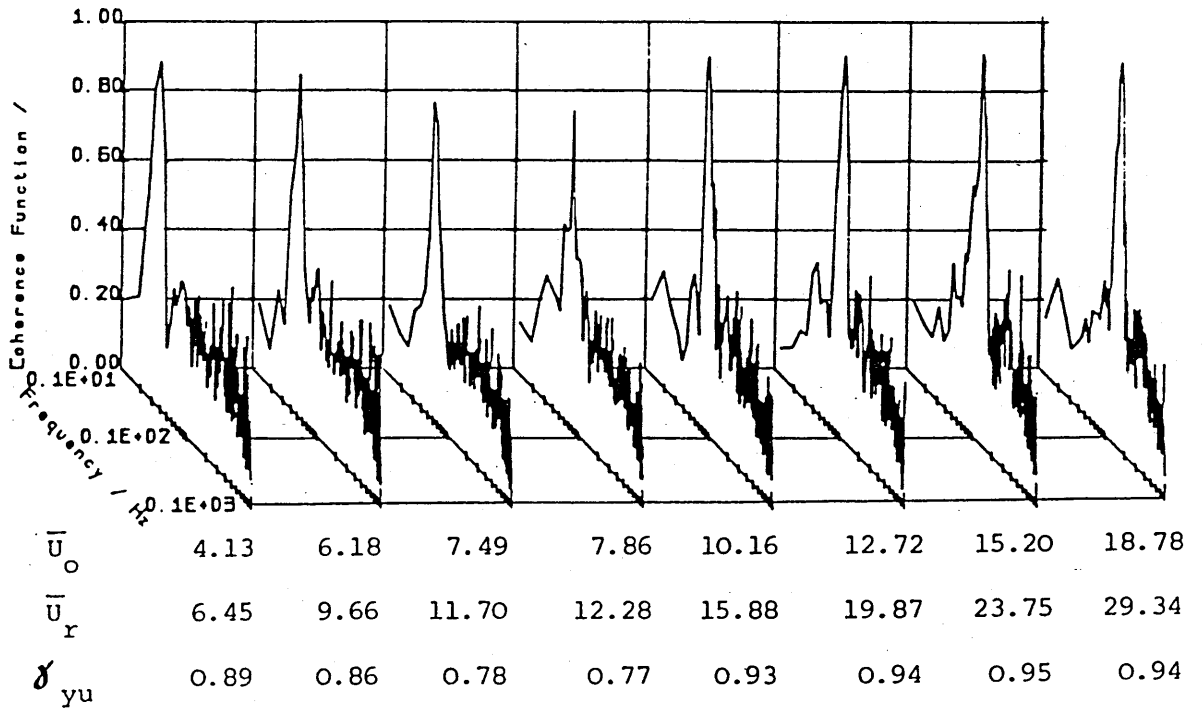


(b) velocity fluctuations and cross-wind response

Figure 5.36 Coherence function between velocity fluctuations in the near wake and (a) along-wind and (b) cross-wind response of the 10x1x1 square tower in uniform smooth flow.

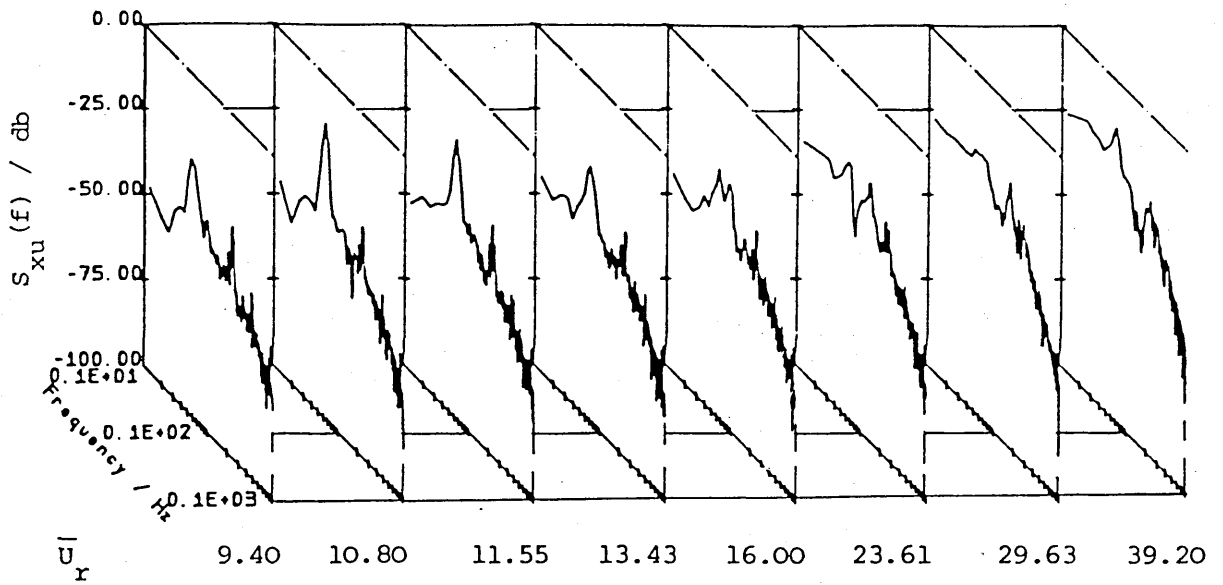


(a) velocity fluctuations and along-wind response

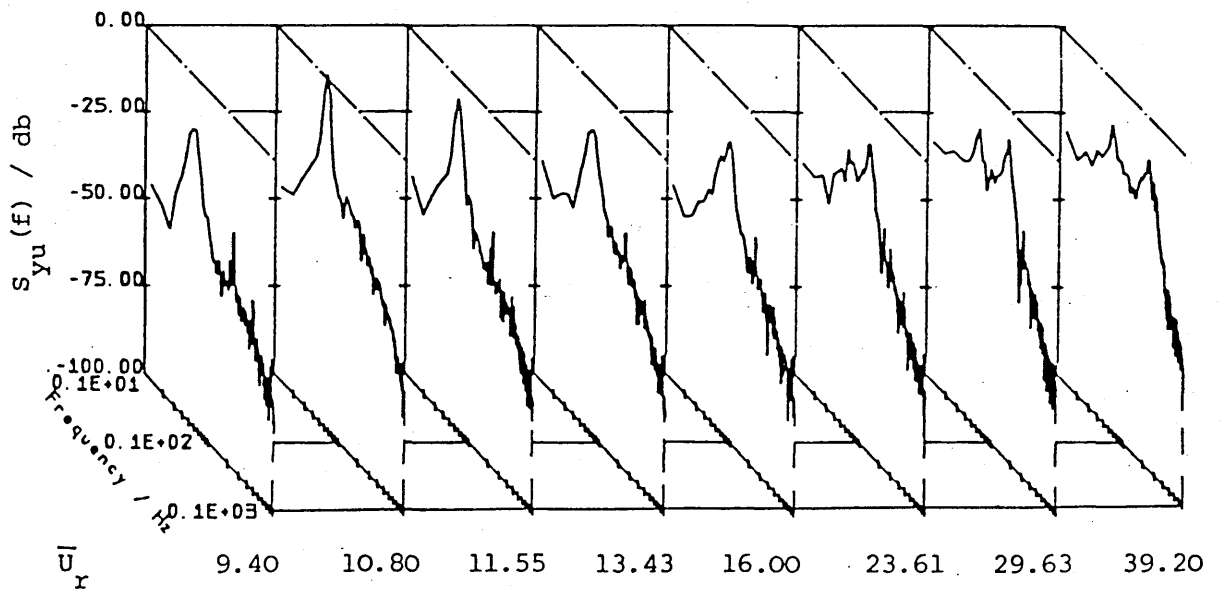


(b) velocity fluctuations and cross-wind response

Figure 5.37 Coherence function between velocity fluctuations in the near wake and (a) along-wind and (b) cross-wind response of the 10x1x1 square tower in uniform turbulent flow.

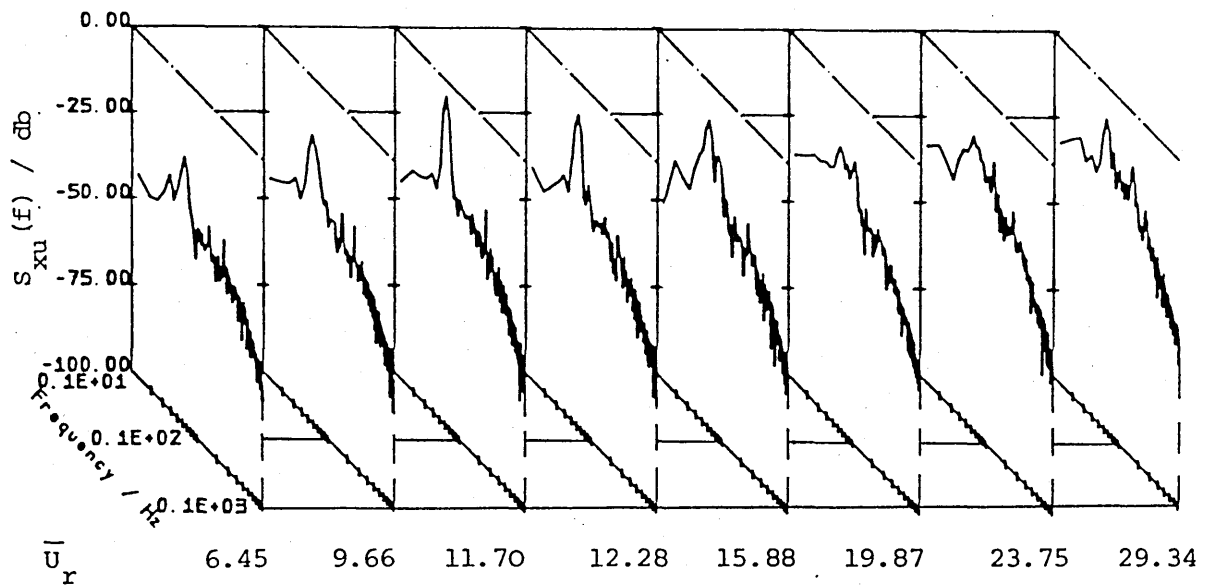


(a) velocity fluctuations and along-wind response

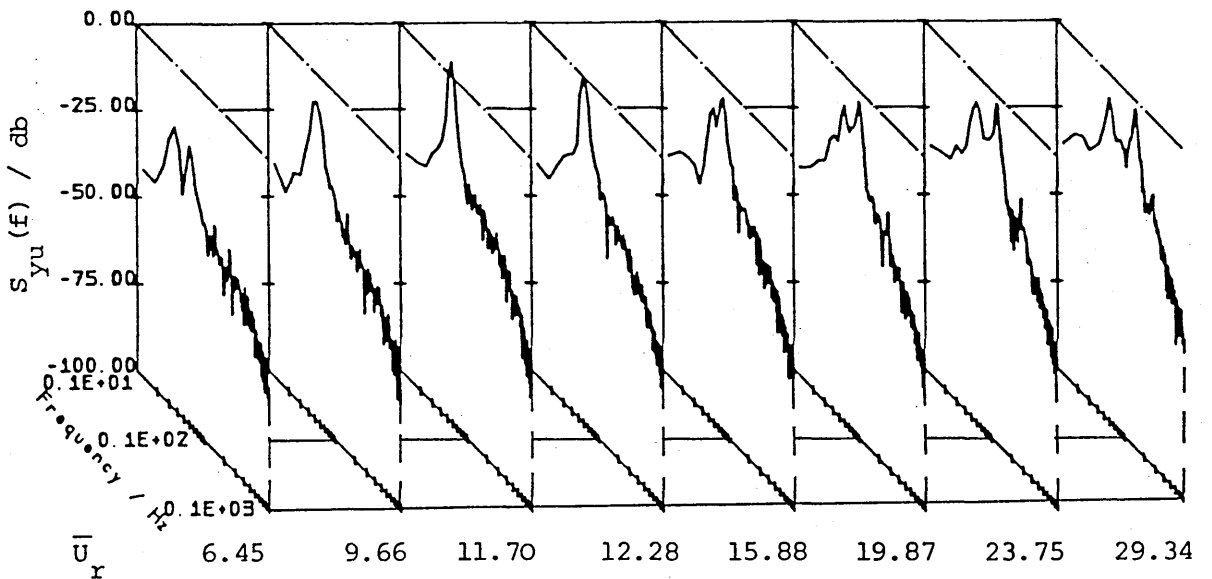


(b) velocity fluctuations and cross-wind response

Figure 5.38 Cross-power spectra of velocity fluctuations in the near wake and (a) the along-wind and (b) the cross-wind response of the 10x1x1 square tower in uniform smooth flow.



(a) velocity fluctuations and along-wind response



(b) velocity fluctuations and cross-wind response

Figure 5.39 Cross-power spectra of velocity fluctuations in the near wake and (a) the along-wind and (b) the cross-wind response of the 10x1x1 square tower in uniform turbulent flow.

CHAPTER SIX

PRESENTATION AND DISCUSSION OF RESULTS OBTAINED FROM TWIN TOWER BLOCK MODELS

6.1 Introduction

The construction of tall flexible buildings with low damping has generated special problems for designers due to the increased susceptibility of these buildings to dynamic effects induced by wind. These problems are becoming even more complex due to the concentration of tall buildings in city centres, where the increased dynamic response of one building under interference excitation from neighbouring tall buildings and structures is significant.

The interaction of neighbouring tall buildings, commonly referred to as interference or proximity effects, is the result of coupling of the fluid flow through the group. In general, the interference between neighbouring structures depends on their positions relative to the approaching wind; the resultant effects may be either partial, when only one building is affected, or combined, when all are mutually interfered.

This Chapter deals with the wind loading and dynamic response of two neighbouring square tower blocks in a series of wind tunnel tests. Unlike most other studies on the subject of interference between buildings when measurements were usually taken on the so-called 'principal' model, the two elastic tower models employed in these tests were fully instrumented so that for each the torque, along-wind and cross-wind forces and displacements in the two translational directions could be measured. With such a facility, the problem of mutual interference from the upstream building or interference from the downstream building coupled by the fluid could be thoroughly investigated. It is also the aim of this study to determine the contribution from the interaction effects, arising from the inherent mechanical coupling between the models through the mounting structure and the case when they were structurally coupled by rigid cross members. The observed behaviour is described by the resultant model forces and model response in both the time and frequency domains. Using a number of wake spectra, a possible excitation mechanism which describes the interactions between the towers will be suggested.

Unless specified otherwise, both tower models were orientated with one face normal to the wind, with the distance between them varied longitudinal (X) and laterally (Y) on a coordinate grid, as illustrated in Fig. 3.12. Seventeen different model configurations were tested during the course of this investigation. They can be conveniently divided into four groups:

- (a) Tandem configurations--one tower block is placed behind the other along a common centre-line in the direction of flow at seven longitudinal spacings, i.e. $X_B = 2, 3, 4, 5, 6, 7$ and 8 .
- (b) Side by side configurations--the two tower models are arranged side by side to the approaching flow at two transverse spacings, i.e. $Y_B = 2$ and 4 .
- (c) Staggered configurations--this arrangement is restricted to one transverse spacing at three longitudinal positions, i.e. $Y_B = 1, X_B = 2, 4$ and 6 .
- (d) Miscellaneous--this includes tests in which the models were structurally coupled at either upper or lower ends by rigid substructures, and cases in which the angle of incidence was 45 degree off the mean wind. Furthermore, measurements were also made when the sway motions of the upstream model were restricted (wedged).

In addition, most of the model configurations were also studied in both the uniform smooth and turbulent flows. A summary of the model arrangements and the data files which had been collected for the off-line analysis is given in Table 6.1.

In the following sections, after a brief discussion of the mechanical response characteristics of the combined system, the test results are presented in groups according to the model arrangements. It should be noted that, because of the amount of data obtained, only a fraction which are considered to be most significant will be presented here.

6.2 Mechanical Response Characteristics of the Twin Models System

In the original planning, it was aimed to keep the interactions due to mechanical coupling between the two model-balance assemblies as small as possible, so that the two systems were free to oscillate independently and interference between them could only be caused by the fluid. But because of the inertia of the combined system and the elastic behaviour of the space frame structure on which it is mounted, the existence of a weak mechanical interaction between the two towers is inevitable. This section describes how such coupling could affect the responses measured by these systems.

Because of the shortage of proper equipment and inadequate space to mount the vibrator, the dynamic structural test methods described in the last Chapter could not be applied here. Instead, the interactions between the models were investigated by the free-decay vibration method with the flow at rest. The displacement signals

which were measured by the accelerometers at the tops of the models were recorded and stored in digital form in real time by the microcomputer. The displacement amplitude traces shown in Fig. 6.1(a) and (b) are the typical responses at the top of the two models with initial perturbation (produced by hand) applied to the downstream model (model A).

In view of the time-history traces shown in Fig. 6.1, it is evident that the phenomenon known as beating is encountered. In brief, beating means that when one part of a coupled system is set in oscillation, its vibration dies away very slowly while the vibration of the other part of the system slowly builds up, the vibration is then slowly transferred back to the first system and the process is repeated. A more familiar example of this phenomenon is the periodic transfer of energy between two identical pendulums when they are coupled by a spring or by a rod that in turn is suspended from a rigid support by two lengths of string [143]. The periodic transfers of vibrations suggests that the two systems (whether they are pendulums or elastic models) are weakly coupled.

In general, beating occurs at a frequency small compared with the natural frequencies of either system. In this twin models set-up, the beating frequency in the longitudinal and transverse direction is estimated to be at 0.45 and 0.65 Hz, respectively. In most of the cases studied, it appeared that the beating frequencies were unaffected by the model spacings but were likely to be influenced by the rigidity of the foundation on which the model systems were mounted.

It is felt that it would be of considerable interest to cross-correlate the response of the model on which the initial excitation was applied with the resultant response on the other model. Figs. 6.2 and 6.3 are the resulting co-spectra and coherence functions at various spacings. In these measurements, perturbation (produced by hand) was applied to model A either in its along-wind or cross-wind direction, as stated in these diagrams. It must be pointed out, however, that the input is in fact the response of the system on which the force is applied. Therefore, this analysis is not a direct measure of the transfer function but rather a representation of the energy available in the system.

As shown in Fig. 6.2, the cross-power spectrum analysis reveals that there is a peak response at the natural frequency of the combined system. This frequency is 6.35 (± 0.49) Hz and is close to the fundamental frequency of an isolated modelling system. As expected, the correlation is generally stronger in the cross-wind direction between the two systems than in the along-wind direction. Unfortunately, the effect due to beating is at a frequency too low to be shown on these plots.

The coherence function of the responses measured from the two systems in both along-wind and cross-wind direction are shown in Fig. 6.3(a) and (b) for various spacings. In these plots, the coherence is noticeably different from unity in the vicinity of the resonance. This is partially due to the non-periodicity of the signals and the impedance mismatch between the input and output response. Whereas the gradually decrease of coherence at high frequency is primarily a result of the poor signal energy available.

In the cases when the two models were structurally coupled, the pattern of energy transfer between them is completely different. It is because the combined system behaves as a single structure. Consequently, the phenomenon of beating also disappeared in these cases.

6.3 Tandem Arrangements

There are an infinite number of possible arrangements of two bodies with one placed behind the other at any longitudinal spacing. However, in the present measurements, because of the restrictions imposed by the apparatus and other reasons, only seven tandem arrangements have been investigated. The longitudinal distance between the centres of the towers varies from two times to eight times the breadth (B) of the tower at regular intervals. The relative positions of the towers in these arrangements are illustrated by the schematic diagram shown in Fig. 3.12.

On the other hand, despite the fact that only a limited number of configurations was investigated, the positions of the towers have covered the close-proximity region when they are sufficiently close to each other and the wake interference region when the rear tower is in the wake of the front one. The results from the measurements made, including bending forces, torsional moment, displacement response at the tip of the tower and the wake which they created, are presented in the following sections.

6.3.1 Model Forces in the Along-Wind Direction

(a) Along-Wind Force Coefficient

The appearance of drag (or along-wind force) reduction due to the presence of an upstream body has been well known for a long time, but the effect for bodies in tandem positions was not investigated until recently, in particular, by Zdravkovich [19] for circular cylinders and Reinhold et al. [9] for square cylinders. In this study, this so called shielding effect is clearly illustrated by the collection of

curves presented in Fig. 6.4(a) and (b) in which the time-mean along-wind force coefficients versus mean wind velocity at seven tandem arrangements are shown.

It should be noted that these graphs (force coefficient versus mean wind velocity)--and the subsequent plots of mean or fluctuating response against mean wind flow--are all arranged in such a way that results from different configurations can be accommodated within one single diagram. Therefore the effects due to spacings or other variables can be directly compared.

To provide an even better visualisation of how the force coefficients varied with the longitudinal distance between the towers, the mean force coefficients are averaged over the given velocity range and plotted against the spacing ratios, as shown in Fig. 6.6. The drag force coefficient of a single tower in both types of flow are also shown in Fig. 6.6 for comparison.

At small spacing ratio ($X_B < 3$), the amplitude of drag force acting on the upstream tower is about the same as those on the single isolated tower in smooth flow, but the averaged drag coefficient drops gradually as the distance between the towers is increased and reaches a minimum at a position about 5 to 6 times the tower's breadth. Beyond that, the drag coefficient returns to the single tower value and tends to be unchanged as the separation is increased further.

On the other hand, the drag force coefficient of the downstream tower is well below that measured from a single tower. At the closest positions where the rear tower is likely to be located within the shear layers emanated from the front tower, the former even experiences a positive drag--thrust force, as shown in Fig. 6.6. This, in effect, is the result of the negative pressure in front of the rear tower exceeding that on the base side behind. Consequently, this also implies that the flow in the gap between the towers is almost stagnant. But as the spacing between them increases, the amplitude of drag on the downstream tower gradually builds up in response to the more vigorous flow activity within the gap region. For a certain distance of separation, the flow pattern around the two towers seems to change suddenly and the force amplitude on the downstream tower is drastically increased. The sudden change of force amplitude at this position also seems to coincide with the fluctuation which occurs on the upstream tower.

At this critical position (a spacing of between $5B$ to $7B$), the action of the wake vortices from the front tower on the rear tower is prominent. But the resulting forces on the latter is intermittent, as shown in Figs. 6.4(b) and 6.5(b). In fact, because of the uncertainty in choosing a proper drag coefficient value for the downstream tower at $X_B = 6$, the data point in Fig. 6.6 is deliberately omitted and

replaced by dotted line. A similar flow phenomenon has been observed by Zdravkovich [19], Hori [49] for circular cylinders in smooth flow. However, the critical spacing they found is shorter at 3.5 times the diameter behind the front cylinder.

Beyond the critical spacing, the drag coefficient of the rear tower approaches the values found on an isolated tower in turbulent flow. This result is expected because at this distance, tower A is likely to be at a position completely outside the region enclosed by the shear layers from the front tower and instead, is engulfed by the turbulent wakes trailing behind them.

Because of these reasons, the amplitude of the fluctuating along-wind force coefficient of the rear tower is likely to be high at and around the critical position. And this is clearly demonstrated by the results presented in Fig. 6.5(a) and (b). Another unusual feature of this measurement is also found at the 6B configuration, as a number of peaks of amplitude over a narrow range of reduced velocity on the downstream tower is observed. This is in marked difference from the traces with a single, well-defined peak of instability, such as the one shown on the downstream tower at $X_B = 5$. This is further evidence to confirm that 6B is the critical spacing and that at this distance strong aerodynamic interference occurred between the two towers.

Furthermore, the evidence presented so far suggests that there are two distinct types of flow pattern, i.e. one in which there is almost no flow in the gap between the towers and the other in which a fully developed flow approaches the downstream tower, and the change of flow patterns takes place only when the two towers are at a certain distance apart. In the subsequent sections, this feature will be discussed in more details.

(b) Along-Wind Force Spectrum

As compared to the single tower cases, the along-wind force spectra of both the upstream and downstream towers are changed substantially by the presence of the other tower. Presented in Fig. 6.7(a) and (b) are the normalised along-wind force spectra of the two towers at four different configurations and for various reduced velocities.

Because of the resonant characteristics of the model-balance assembly, there is always a peak on the force spectrum at the natural frequency of the system. This peak of amplitude represents the energy associated with the wake or the strength of the applied excitation, the magnitude of which depends on the relative positions of the two towers and the flow conditions.

Comparing the variation of peak amplitude at the shedding frequency of the towers in tandem arrangements with those measured for a single tower, the similarity can be seen, there being a pronounced peak at the critical reduced velocity. The exception is the force spectrum of the downstream tower at $X_B < 6$. For such an arrangement, the amplitude of the peak at the shedding frequency seems to be unchanged over a wide range of reduced velocity. The pronounced peak which indicates the resonant oscillation of the system is missing. This, together with the low force fluctuation recorded, suggests that the flow in the gap between the towers is stagnant, as mentioned before.

However, the peak induced in the along-wind force spectra for the two tower cases is about an order of magnitude bigger than those obtained from an isolated tower--relative to their respective peaks at and around the resonant reduced velocity. Because of the stronger force signals, the peaks representing the amplitudes of the background noise have been significantly reduced to the extent of being completely eliminated in some cases.

On the upstream tower, the results shown in Fig. 6.7(a) indicate that the amplitudes of the peak at the critical reduced velocity (\hat{U}_r , which is the same as in the cross-wind direction) decreased as the spacing ratio increased, but this trend is reversed at $X_B = 6$ and beyond.

At $X_B = 6$, the amplitudes of the force spectra measured for the towers--in particular the downstream one--are significantly increased, apparently in response to the large along-wind force fluctuations, as shown in Fig. 6.5(b). If the distance between the towers is extended further (such as 8B), both the force and force spectrum indicate that the two towers behave as a single tower with resonance occurring at $\bar{U}_r = 11.67$. Nevertheless, the peak amplitude of the front tower in this arrangement is much larger than it would be on the single tower. Since aerodynamic interference between the towers in this arrangement is likely to be small, it is thought that this may be attributed to the transfer of motion energy from one tower to another via the supporting structures. But how this mechanical interference works and its magnitude are not known at this stage.

In contrast, the peak amplitude of the downstream tower in this arrangement has a value approaching that measured from a single tower in uniform turbulent flow. This again can be attributed to the fact that the rear tower is submerged within the wake created by the upstream tower. In fact, the flow approaching the downstream tower has a dominant frequency caused by the vortex shedding and the subsequent displacement response of the upstream tower. But due to the fact that both towers are mechanical identical, it is difficult to identify or quantify the contribution of the

wake interference from the present measurements. On the other hand, the apparent strong response of the downstream tower at $X_B = 8$ is in contradiction with the results presented by Bailey and Kwok [11], in which they measured the aerodynamic interference between two square buildings. In fact, at the same spacing ratio, they observed no peak induced in the along-wind force spectrum of the downstream tower. However, the results presented in Fig. 6.7(a) and (b) at least confirm the existence of the two flow patterns which previously have not been observed in other people's measurements [9] and [11].

6.3.2 Model Forces in the Cross-Wind Direction

(a) Cross-Wind Force Coefficient

It has been shown in the previous Chapter that wake excitation, in particular the one associated with vortex shedding, is the major excitation mechanism of square tower blocks in both smooth and turbulent flows. In the twin tower cases, with one directly behind the other, vortex excitation has again been shown to be playing a major role in the transverse oscillations of prismatic towers [11]. But due to the combined effect of other factors, the oscillation magnitudes of the towers are substantially increased and the critical velocities at which instabilities occurred vary with the spacing.

The results presented in Fig. 6.8 show the variation in the time-mean force coefficient of the two towers in the cross-wind direction with the mean wind velocity at seven tandem configurations. As expected, generally the force coefficients show very little variation over the full range of reduced velocity tested and seem to be unaffected by the presence of the other tower—whether it is at the upwind or downwind positions. The only exception is at the 6B arrangement when both towers experience transverse mean forces which are acting on them in opposite directions. The force coefficient for the downstream tower is velocity dependent which seems to suggest that at and near the critical spacing, where the two vortex street flows begin to develop, the vortex-induced oscillation of the downstream tower is disrupted by the shedding coming from the upstream tower. The vortex shedding behind the front tower seems to persist for some time and then it is intermittently suppressed and replaced by the reattachment flow regime. The subsequent oscillation of the downstream tower becomes more vigorous but less regular.

The effects of the intermittent shedding on the downstream tower is more obvious in the plots of the RMS coefficients of the fluctuating cross-wind force against mean wind velocity, as the one shown in Fig. 6.9. Comparing these results with those

measured from a single tower in smooth flow, shown in Fig. 5.15, it can be seen that the peak amplitudes in the twin tower cases are significantly increased--ranged from 3.5 to 10 times bigger. The critical reduced velocities vary from 8.54 at $X_B = 5$ to 15.34 at $X_B = 3$. And in most cases, the maximum fluctuations of both towers occur at the same velocity.

At the spacing of $6B$, the cross-wind force fluctuation amplitudes are not the highest but they are the most energetic with a clump of peaks spreading over a narrow range of reduced velocity. These results are further evidence to support the view that the intermittent reattachment takes place on the downstream tower. Beyond the critical spacing range, discrete peaks of amplitude appear at the critical reduced velocity on both towers indicating that they are forming their own vortex streets. Since both models used in these tests are identical, the wake from the upstream one could induce a more correlated vortex shedding along the downstream structure which in turn produces an enhanced vortex-induced motion. Consequently, at $X_B = 8$, the fluctuating force amplitude of the downstream tower is about 100% stronger than the upstream one, as shown in Fig. 6.9.

On the other hand, when the two towers are spaced $2B$ apart, the resultant fluctuating cross-wind force coefficients show two distinct instability regions. The first is at $\bar{U}_r = 11.05$ and corresponds to the flow velocity at which the vortex shedding frequency coincides with the natural frequency of the system. The second instability region occurs at $\bar{U}_r = 17.43$ and is probably the result of mechanical coupling between the two towers. In fact, such coupled mode between towers is evident in other arrangements, but the effects seem to be more pronounced at close spacing (i.e. $X_B < 4$). More about this feature will be discussed in the subsequent sections.

(b) The Wake Behind the Downstream Tower

In order to investigate the effects on vortex shedding of the presence of a tower at upstream positions, the fluctuation of the flow velocity in the wake behind the downstream tower is measured by the use of a single hot-wire anemometer at position shown in Fig. 6.10. The mounting and operation of the hot-wire anemometer are discussed in Chapter 3. The power spectral density analysis is applied to find the Strouhal frequencies: namely, frequencies having a dominant power existing in the fluctuation of the wake. Results of the analysis are presented in Fig. 6.10 in which the Strouhal number is plotted against the spacing ratio for various reduced velocities. The Strouhal numbers measured in the wake of a single tower in both types of flows are also shown for comparison.

It is evident that the vortex shedding is detected in the whole range of spacing behind the downstream tower. At $X_B = 2$, the Strouhal numbers are well below those measured in the wake behind a single tower in uniform smooth flow but, as the spacing between the towers is increased, they gradually increase and approach the single tower values.

In the 5B arrangement, the Strouhal numbers are spread over a wide range of values (from 0.07 to 0.1). This is a clear indication of the existence of the bistable nature of the flow at and around the critical spacing where intermittent shedding from the upstream tower disrupts the vortex shedding on the rear one. The velocity dependent nature of this phenomenon is also evident. At greater spacings, regular velocity fluctuations are observed behind the downstream tower and the resulting Strouhal numbers have values close to those measured in the single tower cases.

However, one important feature shown by these results is the low Strouhal number value found at the 2B configuration. This value (the average is about 0.06) is equal to the Strouhal number of a two-dimensional rectangular section with a breath to width ratio approximately equal to 2.5, Otsuki et al. [56]. The close resemblance of the response characteristics, such as those shown in the force measurements in Fig. 6.9, also suggests that at $X_B = 2$, the two towers (which combined together have a breath/width ratio equals to 3) behave as a single tower. And according to Zdravkovich [19], two cylinders at close spacing could behave as a single slender body with a different Strouhal number. But the questions of how the two towers couple together and the way they oscillate can not be answered at this stage.

(c) Cross-Wind Force Spectrum

Presented in Figs. 6.11(a) and (b) are the normalised cross-wind force spectra of the upstream and downstream towers at $X_B = 2, 4, 6$ and 8 for the range of reduced velocity covered. For $\bar{U}_r < 20$, the power spectra show discrete peaks at the natural frequency of the model-balance system at 6.5 Hz. The magnitudes of these peaks depend on number of factors, such as vortex strength, turbulence intensity of the incident flow and the induced motion (or inertia) of the models themselves.

If the variations of the resonant peak amplitudes with reduced velocity in each arrangement are examined, it is evident that over the large spacing ratio range, both towers behaves as an isolated tower with a prominent peak at the critical reduced velocity. However, the normalised peak value of the downstream tower at $X_B = 8$ is about 60% bigger than the upstream one at the same reduced velocity. This confirms the effect of vortex enhancement on the rear tower caused by the vortex shedding from the front tower.

At the smaller spacings, the normalised peak values of both towers seem to be unchanged with the flow over a narrow range of reduced velocity. This, together with the close resemblance of the fluctuating cross-wind force coefficients, suggests that the towers are interlocked through some mechanism. The nature of this interference mechanism is not clear at this stage but its effect seems to be decreased as the spacing between the towers is increased.

On the other hand, although the power spectra in both translational directions are of similar basic shape, the intensities of the oscillations are dissimilar. In fact, the normalised peak value of the spectrum obtained in the cross-wind direction is one to two orders of magnitude bigger than the corresponding one measured in the along-wind direction, as shown in Fig. 6.7(a) and (b) and Fig. 6.11(a) and (b). However, due to incident turbulence, the along-wind spectra of the downstream tower do have a much broader-band of response and, in most cases, the energy appears to have diffused into a frequency range above the resonant.

As the reduced velocity increases beyond 20, a number of peaks appear in the spectra at frequencies between 29 and 30 Hz. At very high reduced velocities, the amplitudes of these peaks are so big that they surpass those at the shedding frequency. After examining the recorded force signals and dynamic characteristics of the combined measuring system, it is concluded that these peaks are the results of oscillations of the system at higher mode. Since it is not certain about the strain gauge dynamometer's behaviour at oscillatory mode higher than fundamental, the phenomena is therefore not to be discussed any further in this presentation.

6.3.3 Torsional Response

The results of the investigation into the torsional response of the towers in tandem arrangements are presented in Figs. 6.12 to 6.14. In Fig. 6.12, the coefficients of the time-mean torsional moment are plotted against the mean wind velocity. It is obvious that the magnitudes of the mean torsional moments acting on the towers are markedly different. Nevertheless, there is no obvious explanation for the irregular variations shown for the coefficient on the front tower. Over the same range of reduced velocity, the variation of torsional moment on the rear tower is relatively smooth.

On the other hand, at the 6B configuration, the coherence between the towers seems to be improved and there are appreciable increases in the torsional response of both towers. Comparing these curves with the force variations measured in the along-wind and cross-wind directions in the same configuration, gives a clear indication that the torsional response of a tower is closely related to its oscillation in

the translational directions.

Blessmann et al. [31] investigated the interaction effects between neighbouring tall buildings and found that there were substantial increases in the maximum torsional moment due to the presence of another structure in the vicinity. But the results they presented in [31] only covered the spacing ratio range up to 3B. Furthermore, they determined the forces and moment acting on the models by integrating the pressure readings and therefore they avoided the troubles of noise and low output signals which persist in the present method of measurement.

To complete the scope of measurements, the RMS coefficients of the fluctuating torsional moment of the towers are also shown in Fig. 6.13. But, due to the low signal outputs, the accuracy is suspect and not much information should be drawn from these results.

Presented in Fig. 6.14(a) and (b) are the normalised torsional moment spectra of the towers in four tandem arrangements. As mentioned before, the low strain-gauge output reduces the signal-to-noise ratio, so that it is not unexpected when the spectra obtained exhibit corruption by noise. This is particularly illustrated by the power spectra of the upstream tower at $X_B = 4$ and 6 in which the discrete peak at 50 Hz is the noise caused by the mains. In the same arrangements, the normalised peak values for the downstream tower at the shedding frequency are marginally bigger indicating that the torsional moment on the tower is also responding to the increased turbulence in the incident flow.

In the two other arrangements shown in Fig. 6.14, the energy associated with torsion is considerably bigger. In most cases, the peak amplitude at the resonant reduced velocity is one order bigger in magnitude than those found in the single tower cases. This suggests that vortex shedding, probably with enhancement from the upstream tower, is the main contribution to the torsional response.

6.3.4 Dynamic Response in the Along-Wind and Cross-Wind Directions

The results of the investigation into the oscillatory behaviour of the towers in the along-wind and cross-wind directions are presented in Figs. 6.15 and 6.16, respectively. In each of these diagrams, variation in the normalised RMS values of the fluctuating displacement response measured at the top of the front and rear towers in various tandem arrangements are shown. The mounting and operation of the accelerometers are the same as described in Chapter Five.

On the upstream tower, there is a clear indication of vortex excitation in the along-wind direction with peaks of amplitude occurring at reduced velocities which are

almost identical to those observed in the force measurements. Whereas, on the downstream tower, the along-wind component of amplitude increases almost proportionally to the reduced velocity. The peak of amplitude, which signals the occurrence of vortex shedding on the downstream tower, appears again at the critical reduced velocity as the spacing between the two towers increases beyond 5B.

In the cross-wind direction, the response characteristics of both towers over the full range of reduced velocity show a surprising resemblance to each other, and the peak amplitudes at the resonant reduced velocity of both towers in each arrangement are different by a very small amount, as shown in Fig. 6.16.

In the 2B arrangement, it is interesting that the normalised value of the peak at $\bar{U}_r = 17.43$ is almost five times bigger than the peak at $\bar{U}_r = 11.05$. On the other hand, in the 3B arrangement, two distinct peaks are observed at $\bar{U}_r = 13.47$ and 15.29. These have not been observed in the force measurements. In view of the close similarity of the response characteristics of the towers, this could be further evidence to support that at close positions, the towers are coupled together via the supporting structure and subsequently behave as a single slender body. In fact, as shown by Ikenouchi [6] and Novak [87], the existence of two instability regions is one of the characteristics of the aerodynamic instability of rectangular cylinders. However, the magnitude of such mechanical interference seems to be decreased as the distance between the towers increased, although the effects of such coupling is evident in all arrangements.

Beyond the critical spacing (at $X_B = 7$ or 8), oscillations due to vortex shedding formed behind the two towers are evident. The stronger and broader-band of response on the downstream tower at these positions is the result of the incident turbulence or 'resonant buffeting' when the vortex shedding behind the upstream tower strongly affects and synchronises with the vortex shedding behind the downstream one.

To illustrate the amplification in response due to the presence of other buildings in the vicinity, a term called the buffeting factor is usually used. The buffeting factor suggested by Saunders and Melbourne [45] has been defined as,

$$BF = \frac{\text{overturning moment (with neighbouring structure present)}}{\text{overturning moment (isolated structure)}}$$

The along-wind and cross-wind response of the towers (in terms of buffeting factor) under mutual interference at various tandem arrangements are presented in Figs. 6.17 and 6.18, respectively. In this presentation, the overturning moment is

replaced by the average values of the tower's maximum displacement in each cycle over a period of time. In fact, the maximum deflexions at the tip of the tower in each oscillatory cycle are represented by the peaks or troughs on the displacement amplitude traces, such as those shown in Fig. 6.1. The procedure to identify and quantify the peaks or troughs from the off-line data file is discussed in Chapter Four.

In Fig. 6.17, the along-wind response is characterised by BFs greater than 1.0 over the full range of reduced velocity tested. As expected, the in-line oscillations of the downstream tower are markedly amplified due to the increased turbulence in the incident flows. Nevertheless, for $\bar{U}_r < 20$ (in particular within the instability region), the variation of BFs with mean wind velocity is less orderly, with values scattering from just less than one to well over ten times that measured on the isolated tower under the same flow conditions.

The causes of such irregular fluctuations may be due to the fact that the narrow-band response of the single tower is replaced by a broader band response in the twin tower cases. Furthermore, the peak response of the models in the twin tower configuration is not always occurring at the same critical reduced velocity as in the single tower cases.

A similar pattern with data points scattered above and below the unity line are observed in the cross-wind response, as shown in Fig. 6.18. However, at $\bar{U}_r > 20$, the response curves are characterised almost entirely by BFs less than 1.0.

6.3.5 Oscillation Loops

In order to visualise the relationship between the oscillatory amplitudes and the tower locations, the mean values of the maximum tip displacement of the towers in the along-wind and cross-wind directions (the data used in Figs. 6.17 and 6.18) are employed again in Fig. 6.19. In this diagram, the axes of each ellipse represent the mean maximum displacement of either the front or the rear tower in that direction at the critical reduced velocity which is also given alongside in brackets. The results presented in Fig. 6.19 covers the tests with towers in either tandem or staggered arrangements and in both uniform smooth and turbulent flows. The response of the single tower in both types of flow is also shown for comparison. These elliptical loops are drawn on the same scale so that the change in amplitudes can be readily assessed. It must be emphasised that these loops are for illustration only; in some cases, they are neither regular nor have axes parallel to each other.

As expected, the variation in the size of these loops is closely related to the response curves shown in Figs. 6.15 and 6.16. The exceptionally large responses of the towers in the 2B configuration are evident. However, the general trend is that for $X_B < 6$, the oscillatory amplitude of the front tower is always larger than the rear one, whereas beyond the critical spacing, the trend is reversed. It seems to be that, apart from the critical spacing where the flow around the towers is drastically changed, there is an optimal spacing at $X_B = 4$ where the oscillations of the towers are smallest. Finally, the increased response in the along-wind direction due to interference from the other tower--as compared to isolated tower cases--is clearly shown in this diagram.

6.3.6 Orbital Motion Analysis

As described in the previous chapter, the true movement of the tower can be reconstructed from signals obtained from accelerometers set at right angles to each other. Such polar diagram can provide characteristic information about the oscillatory behaviour of the towers under different flow conditions. Three sets of such X-Y plots which show the orbital motion of both towers at $\bar{U}_r = 10.8, 12.1$ and 15.3 are shown in Fig. 6.20. This range of values is chosen so that the dynamic responses of the towers at and away from the critical reduced velocity are shown.

The resultant traces are equivalent to the Lissajous' patterns derived from two sine waves and the phase relationship between them can be determined from the loop's size [130]. (For example, if the amplitudes of the two inputs are the same and there is no phase difference between them, then the resultant oscillation loop is represented by a straight line and is inclined to 45 degree to both axes). Fig. 6.20 shows that the phase difference between the displacement components in the along-wind (X) and cross-wind (Y) directions on the upstream tower is negligible, but it is considerable bigger on the downstream tower. In fact, the latter has a phase angle varying from approximately 30 degrees at $\bar{U}_r = 10.8$ to 90 degrees at $\bar{U}_r = 12.1$. The beating effects, whose presence indicates energy transfer between the translational directions and between the two measuring systems, are evident. Outside the instability region, the orbital motion of the towers becomes less orderly, as shown in Fig. 6.20(c).

A similar response characteristic is observed on the towers in other arrangements. In short, at and near the critical reduced velocity, there is no phase difference between the displacement components for the front tower in the along-wind and cross-wind directions. But outside the synchronised range or on the downstream tower, the phase difference is considerable.

This technique can be applied further to examine the oscillatory behaviour of the whole assembly as a single object (two tower measuring systems linked by the frame structure). This is done by replacing the along-wind displacement component with the cross-wind component for the other tower. The resultant trace represents the phase relationship between the motion of the towers in that direction. Presented in Figs. 6.21 and 6.22 are the cross-wind displacement plots of the towers in 4B and 6B configurations at two reduced velocities. The time-based displacement amplitude traces are also shown alongside.

In the 4B arrangement, the flat loop shown in Fig. 6.21 indicates that there is only a small phase difference between the cross-wind motions of the two towers. In contrast, in the 6B arrangement, the phase difference between the cross-wind motions of the two towers is not regular but, rather, varies vigorously with time, indicating that one of them (such as the downstream tower) is excited by a force which is not in unison with the other. However, at and near the resonant reduced velocity, the variation of the phase angle seems to be confined within the first 90 degrees. But outside the instability region, the unison between the motions vanishes and the phase angles have values varying from 0 to 180 degree.

In general, the results obtained from this analysis confirm again that at small spacing, the towers behave as a coupled system, and such coupling effects are decreased as the distance between the towers is increased.

6.3.7 Interference Mechanism (of Towers in Tandem Arrangements)

From the results presented so far, there is convincing evidence that the response of towers in tandem arrangements is much bigger than that of an isolated tower under the same flow conditions. This is mainly due to the mutual interference between the towers, resulting from either the continuous and discontinuous changes in vortex shedding or mechanical coupling through the supporting structures. The latter is revealed by the beating which indicates the transfer of energy between the translational axes and measuring systems. Unfortunately, the magnitude of such coupling effects is not known. Therefore, the present discussion will be confined to the interference effects due to aerodynamic forces only.

Since the resulting oscillations induced by the vortex shedding are considerably modified by and strongly depend on the relative positions of the two towers, several flow interference regimes can be linked to the observed vortex shedding response from the seven tandem arrangements being investigated.

(a) When the two towers are close together, the downstream tower is completely enclosed by the shear layers emanating from the upstream tower. Under such conditions, it is possible that the two towers behave as a single slender body with a different Strouhal number. And their responses, particularly in the cross-wind direction, seem to be reinforced by the mechanical coupling effects.

(b) When the towers are further apart, quasi-steady reattachment of the separated shear layers from the front tower can take place on the rear one. The two towers are effectively interlocked aerodynamically. Under such conditions, vortex shedding is suppressed behind the front tower and its formation behind the rear tower is severely disrupted by the reattachment.

The flow pattern around the towers in (a) and (b) is characterised by its single vortex street.

(c) When the spacing between the towers is increased further, there is a critical position where the distance between the towers just exceeds that between adjacent vortices. The flow pattern around the towers is radically altered and intermittent reattachment of shear layers on to the rear tower occurs.

The critical spacing is characterised by the sudden change of response on the downstream tower in the along-wind direction.

(d) If the distance between the towers is increased beyond the critical, the effects due to shear layer reattachment will vanish. Instead, individual vortex streets are formed behind the towers. However, the commencement of vortex shedding behind the front tower has strong effects on the vortex shedding process behind the rear one. The typical response shows that the rear tower oscillates with a larger amplitude than the front one. And the flow pattern around the towers is characterised by the formation of two vortex streets.

6.3.8 Effects of Turbulence

Tests were also conducted in uniform turbulent flow to examine the effects of high background turbulence on interference excitation. Presented in Fig. 6.23 are the results for the dynamic response at the top of the towers in four tandem arrangements (one of these is the case when the towers are coupled by a rigid link at the upper ends). As usual, the oscillations at the peak amplitudes occur almost entirely in the cross-wind direction. In most cases, the along-wind component of amplitude increases almost proportionally to the reduced velocity.

It is interesting that in the 2B arrangement, there is none of the signs that would normally be expected of vortex excitation. In fact, no peak of amplitude occurs at any particular velocity. Instead, in the subsequent 4B and 6B arrangements, there is a clear indication of the peak of instability at the critical reduced velocity which is at 12.0 and 11.46, respectively. The peak amplitudes are also appreciably larger than those measured in smooth flow. If the magnitudes of response in both types of flow are compared, the increase in the twin tower cases is much bigger than that for the isolated tower cases under the same flow conditions. The effects of turbulence on interference excitation is also illustrated by the oscillation loops shown in Fig. 6.19. The marked increase in the along-wind component on the downstream tower in the 6B arrangement is clearly evident.

On the other hand, the measurement of the time-mean along-wind force on the towers in these three tandem arrangements did not reveal the critical position where the drag value for the downstream tower is suddenly altered. Instead, the variation of the mean drag values for both towers is linearly proportional to their spacings. The Strouhal number measured behind the rear tower, as shown in Fig. 6.10, has values close to those measured behind an isolated tower under the same flow conditions.

In contrast, the along-wind force coefficients for the upstream tower are higher than those measured on a single tower. This could be the result of the fact that the front tower is always close to the turbulence generation grid. And as the measurements in Chapter Three have shown, the turbulence intensity inside the wind tunnel is directly proportional to the distance between the grid and the position where the measurement is taken.

In short, from the experimental results found in this investigation, it is concluded that the turbulence in the flow has an enhancement effect on the excitation caused by a neighbouring tower. But a critical spacing between towers, in which the flow around them is drastically altered, has not been found.

6.3.9 Effects of Structurally Linkage Between the Towers

Tests were also conducted with the tower models coupled together by a rigid substructure clamped to their upper or lower parts to examine the effects of model configuration on the aerodynamic instability. Descriptions and illustrations of the linkage used in these tests can be found in Chapter Three. From the wind tunnel experiments on the coupled tower models, such as those shown in Fig. 6.24, it is evident that the vortex induced oscillation is still the dominant aerodynamic instability but, with the additional substructure, the along-wind response has been

damped out. However, compared to the free oscillations, the effect of structurally coupling the towers on the cross-wind oscillations is small.

When the two towers are explicitly coupled together, they in effect become parts of a linked structure. It is therefore not unexpected to find that the amplitudes of response on both towers are very similar. In fact, results from an orbital motion analysis--such as the one shown in Fig. 6.25--illustrate that their cross-wind motions are in perfect unison. Beating, which is usually associated with energy transfer between freely oscillating towers, is completely eliminated. This is also in agreement with the results obtained from the mechanical response characteristics measurements, such as those described in section 6.1.

In addition, in an attempt to examine the effects of the front tower's motion on the rear tower, measurements were performed with the sway motion of the former restricted by a pair of wedges. But, as the results presented in Fig. 6.26 show, the amplitudes of response of the downstream tower, as well as its response characteristic, are not appreciable affected by the motion of the upstream tower.

6.4 Side By Side Arrangements

In the parallel arrangements, where the two tower models are arranged to face the wind side by side, the formation of vortex streets can only be affected by the proximity interference. And Zdravkovich in [19] suggested that, within the interference region, flow behind the cylinders could be divided into three flow regimes, such as the one depicted in Fig. 2.5.

- (a) single vortex street,
- (b) biased gap flow, and
- (c) coupled vortex streets.

But as shown in Refs. [19] and [46], the single vortex street occurs only when the spacing between the towers is very small ($Y_B < 1.2$ for circular cylinders), therefore it is unlikely to find such interference in the present setting. Due to various reasons, only two side by side arrangements, namely $Y_B = 2$ and 4, have been investigated. But like the measurements performed on the towers in tandem arrangements, all the experiments were conducted in both uniform smooth and turbulent flows, and with their upper parts structurally coupled. Results from these measurements are presented in the following sections.

6.4.1 Model Force and Torsional Moment Coefficients

Fig. 6.27(a) and (b) show plots of the time-mean along-wind force (or drag) coefficients on the towers at various side by side configurations tested in both types of flow. In the close-spaced arrangement, the average drag coefficients (over the whole range of reduced velocity) of model A and B are -1.36 and -1.6, respectively. Compared with the average drag value on an isolated tower, the difference is less than 7%. Discrepancies of similar amplitude are also found in other arrangements (with or without the rigid substructures attached). It is therefore likely that such discrepancies are caused by the measurement techniques rather than caused by any proximity interference. In fact, as the results of the experiments conducted on two circular cylinders by Biermann and Herrnstein [48] and on square prisms by Lee and Fowler [47] have shown, effects of proximity between two parallel towers on their drag values could be significant only when they are very close to each other (i.e. $Y_B < 1.5$).

In the turbulent flow, the average mean drag coefficients on both towers in all three arrangements are of much the same value which is about 60% higher than the result of a similar test on an isolated tower. Again, this high value can not be explained by the presence of gap flow, since a similar magnitude of discrepancy is observed in the wide-spaced arrangements. Neither can this be explained by the variation of turbulence intensity, since the longitudinal distance between the turbulence generating grid and the twin towers is the same as that used in the single tower measurements.

The variations in the coefficient of the time-mean cross-wind force on the towers with mean wind velocity in both types of flow are shown in Fig. 6.28(a) and (b). In the structurally coupled cases the mean cross-wind force experienced by the towers in both types of flow is substantially constant. From the fluctuating force measurements (results are not shown here), a prominent peak of instability which signals the commencement of vortex induced oscillations is found at a reduced velocity of about 8.88 in smooth flow and 10.29 in turbulent flow. As expected, the magnitude of these peaks are the same on both towers.

It is interesting to note that in smooth flow, the mean cross-wind forces on the towers spaced $2B$ apart are acting in the same direction whereas, in turbulent flow, the towers experience cross-wind forces acting in opposite directions. This phenomenon can be explained by the fact that in smooth flow, the tendency of the flow to form a separation bubble on the inner face of the tower is impeded by the proximity of the other tower. Hence a large, stronger, separation bubble is formed on the tower's outer side face rather than on its inner side face. Consequently, wide

and narrow wakes are formed behind the towers and divided by a biased flow through the gap.

In contrast, in turbulent flow, the incident flow entrains fluid from the wakes and leads to vortex shedding from the inner side faces of the towers. The accelerated flow through the gap brings the pressure in this region down, thus causing a force of attraction between the towers. The recurrence of vortex induced oscillations of the towers in turbulent flow is confirmed by the peak of instability observed in the subsequent fluctuating force measurements in the cross-wind direction.

Ishigai, et al [144] using the Schlieren optical method, photographed the flow pattern around two circular cylinders in various side by side arrangements and showed that at a certain distance apart, the biased flow in the gap is bistable and the wide and narrow wake can intermittently interchange between the two towers. The bistable nature of the wake is also found in the present arrangement and is confirmed by the measurement of the vortex shedding frequency behind one of the towers.

In smooth flow and for the close-spaced arrangement, the frequency of the wake--when reduced to a Strouhal number--varies widely. The average Strouhal number, which is given in Fig. 6.29, is well above the values measured behind a single tower. Conversely, in turbulent flow, because of the establishment of periodic flow behind the towers, the value of the resultant Strouhal number is about the same as for the single tower.

When the transverse spacing between the towers is increased to $4B$, the effects of the interference due to gap flow on the mean cross-wind force are proportionally reduced but are still evident, as shown by the results in Fig. 6.28. From the wake measurement, as shown in Fig. 6.29, the vortex streets are then well established.

Presented in Fig. 6.30(a) and (b) are the values of the time-mean torsional moment on the towers measured in both types of flow. Because of the low interference between the towers (except in the coupled cases), it is expected to find a torsional response similar to that measured on an isolated tower in the same flow conditions. But in view of the results presented in Fig. 6.30, it is obvious that the torsional responses of the two towers are drastically different. Such peculiar behaviour could only be explained by the fact that the signals from the torsional strain gauges are very small. In particular, as mentioned before, the measuring system B (on which model B is attached) seems to have electronic characteristics worse than the other system. This means that it is more vulnerable to the interference caused by the background noises. Therefore, the vigorous torsional response registered by model B, as shown in Fig. 6.30, could be the result of the noise.

6.4.2 Dynamic Response Characteristics

The results of the investigation into the oscillatory behaviour of the towers in both uniform smooth and turbulent flows are presented in Figs. 6.31 and 6.32. For the condition of the two towers spaced $2B$ apart in smooth flow, there is none of the signs that would normally be expected of vortex excitation of the single tower. No peak of amplitude occurs at any particular reduced velocity in both along-wind and cross-wind directions, as shown in Fig. 6.31. In turbulent flow, due to the entrainment of fluid from the wakes, vortices are formed behind the towers. And there is a clear indication on the response curves, as shown in Fig. 6.32, that a peak of instability occurs at the critical reduced velocity, although the peak amplitudes are much smaller than would be found on a single tower. In short, the results presented here seem to suggest that for small transverse spacing, the vortex-induced oscillations tend to be suppressed by the proximity interference.

When the transverse spacing between the towers is increased to $4B$, distinct vortex streets are formed behind the towers. The oscillation amplitudes--in particular at and near the resonant reduced velocity--are much stronger. As shown in Figs. 6.31 and 6.32, the oscillations at these peak amplitudes occur almost entirely in the cross-wind direction whereas the along-wind component of amplitude increases almost proportionally to the reduced velocity. But, unlike the results found on a single tower in these types of flow, the magnitudes of the peaks in turbulent flow are smaller than in smooth flow.

Zdravkovich [19], on studying the interference between two circular cylinders showed that, if the cylinders spacing is just greater than that corresponding to the biased gap flow regime, distinct vortex streets are formed behind the towers. And they can be coupled in an out-of-phase mode with the vortices simultaneously formed and shed from the gap side and then simultaneously on the outer side. To explain this flow behaviour, it may be easier to employ the orbital motion analysis and look at the phase relationship between the motions of the towers in the same direction.

The two traces presented in Fig. 6.33 are composed from the cross-wind displacement signals of the two towers separated $4B$ apart, with and without their upper ends structurally connected. As mentioned in the previous analysis, when the two towers are linked by the rigid substructures, they in effect become parts of a linked structure and their motions are in perfect unison (phase difference is zero). By contrast, the phase difference between the freely oscillating towers in this arrangement is almost 180 degrees out-of-phase. From this result, it is therefore concluded that the coupled vortex streets can develop on square towers in side by

side arrangements.

6.5 Staggered Arrangements

In general, the term 'staggered' applies to all possible combinations of longitudinal and transverse spacings between two parallel cylinders (or towers) positioned at right angle to the approaching flow direction, while neither one is directly behind the other at any longitudinal spacing nor do they face the flow side by side at any transverse spacing. In effect, this means that there are an infinite number of possible arrangements between the two bodies. It is therefore not surprising that, although the staggered arrangement is most likely to be found in engineering applications, it has attracted the least research interest.

In the present study, due to various reasons, only three staggered configurations between the two towers have been investigated, namely at $X_B = 2, 4$ and 6 and $Y_B = 1$ (which are referred to as (2.1)B, (4.1)B and (6.1)B arrangements in the following discussion). As in the previous measurements, all experiments are conducted in both uniform smooth and turbulent flows. Results from these measurements are presented in the following sections.

6.5.1 Model Force and Torsional Moment Coefficients

The variation in the coefficients of the time-mean and RMS values of the fluctuating along-wind force on the towers with mean wind velocity in uniform smooth flow are presented in Fig. 6.34(a) and (b), respectively. Results of similar measurements from tests conducted in turbulent flow are shown in Fig. 6.35. From these results, it is evident that the mean values, with the possible exception of those from the towers in the (6.1)B arrangement, are fairly constant over the entire range of reduced velocity. It may therefore be more convenient to explain the variation of mean drag force with spacings in term of their averaged values.

In smooth flow, the average mean drag coefficients of the upstream tower at the three staggered positions are $-1.30, -1.13$ and -1.17 respectively. These values are about the same as those found on the upstream tower in the tandem arrangements at these spacings, see Fig. 6.6. But in the (2.1)B arrangement, the mean drag coefficient of the downstream tower is -1.15 which is much higher than the value measured on the downstream tower in tandem arrangement at this spacing. Nevertheless, this result is not unexpected because, in this configuration, the flow impinging on the downstream tower has been accelerated by the presence of the upstream tower. Furthermore, the former is located outside the low-velocity wake

region which, as illustrated by the results obtained from towers in tandem arrangements, has beneficial shielding effects. In fact, the magnitude of the drag force experienced by the tower at this position is about mid-way between the values measured for a single tower in smooth and turbulent flows.

On the other hand, when the longitudinal spacing between the towers is increased to $4B$, the mean drag coefficient on the rear tower is reduced to -0.39 . This value is about the same as those found for a single tower in turbulent flow. This indicates that the downstream tower is submerged in the wake created by the front tower. The magnitude of the drag force on the rear tower is further reduced when the tower is deeper in the wake, such as in the $(6.1)B$ arrangement. In both the $(4.1)B$ and $(6.1)B$ configurations, the flow approaching the downstream tower has a high turbulence level. The effects of incident turbulence on the towers are further illustrated by the variation of the RMS values of the fluctuating along-wind force, such as those shown in Fig. 6.34(b). As compared to results for towers in tandem arrangements at the same spacings, the amplitudes of the peak of instability, which occurs at a reduced velocity of 10.04 in the $(4.1)B$ arrangement and 11.33 in the $(6.1)B$ arrangement are markedly increased, see Fig. 6.19.

In turbulent flow, the magnitude of the mean drag force acting on the upstream tower is almost the same as measured for the upstream tower in tandem arrangement at the same longitudinal spacings. Whereas the rear tower, such as the one in the $(2.1)B$ configuration, behaves as a single tower in turbulent flow. But when the longitudinal spacing between the towers is increased, both the mean and fluctuating values of the along-wind force are increased.

The time-average and fluctuating cross-wind force coefficients for the towers in smooth flow at three staggered positions are presented in Fig. 6.36. The main feature seen in these results is that the mean cross-wind force (lift) acting on the front and rear towers are in opposite directions (with a negative lift directly towards the axis of the upstream tower wake). These results are similar to those shown on the towers in side by side arrangements and, possibly, may be explained by the forces evolving in the same way. More about this feature, including the interference mechanism, will be discussed in the later sections.

On the other hand, in the $(2.1)B$ configuration, the formation of vortices behind the upstream tower is disrupted by the presence of the downstream tower. The subdued vortex excitation is clearly illustrated by the amplitudes of the fluctuating cross-wind force on the towers, as those shown in Fig. 6.36(b). The close proximity of the two towers also means that there may exist an internal gap flow between them, and, due to their motions, the flow through the gap could be disrupted in a

way similar to that found in close-spaced side by side arrangements. The bistable nature of the gap flow is illustrated by the high Strouhal frequency which is measured by a single hot-wire probe positioned downstream of the rear tower. The averaged value of the Strouhal number, together with those measured in other types of flow, is presented in Fig. 6.29(a).

In turbulent flow, due to the partial reattachment of the shear layers on the rear body, the wake formed behind the front tower is narrower. The proximity effects between the towers is therefore reduced. Conversely, the magnitude of the mean cross-wind force on the downstream tower is stronger and is acting in the same direction as that on the front tower.

When the longitudinal spacing is increased to $4B$ and $6B$, the rear tower is then located in the wake-interference region. Distinct vortex streets are formed behind the towers and the oscillatory amplitudes are significantly increased, as seen in Figs. 6.36(b) and 6.37(b). The most vigorous oscillation is likely to take place when the downstream tower is near the wake boundary. Unfortunately, with only three staggered configurations being investigated, it is difficult to locate the wake boundary which may extend from the near wake region to far downstream. However, the oscillatory behaviour of the rear tower in the $(6.1)B$ arrangement resembles that shown in Figs. 6.8 and 6.9 for the tandem arrangements at spacings near the critical.

Isyumov et al. [22], in examining the anatomy of the wind-induced torsional moments on tall buildings, suggests that the changes in the cross-wind force (lift) and its line of action resulting from fluctuations in the approaching flow are the main sources which cause mean torsional moments on buildings of square and rectangular cross-section. The results presented in Fig. 6.37, in which the variation in the coefficients of the time-mean torsional moment on the towers with mean wind velocity in both types of flow is shown, seem to confirm that observation.

In smooth flow, the magnitude of the mean torsional moment on the towers gradually increases as the longitudinal spacings between them is increased. The changes in magnitude in each arrangement tend to be well correlated with the fluctuating magnitude of the forces acting on the towers in the cross-wind direction. In fact, the torsional response of the towers in the $(6.1)B$ arrangement resembles those shown in Fig. 6.12 for the tandem arrangements at spacings close to the critical.

In turbulent flow, due to the change in the flow pattern around the towers, the effects of wake interference is also changed. The strongest torsional load is found

on the towers in the (4.1)B configuration. It must be pointed out that the vertical scales of Fig. 6.37(a) and (b) are different. The maximum torsional loads on the towers in the (4.1)B arrangement in turbulent flow are about the same as those obtained on the towers in (6.1)B arrangement in smooth flow. As mentioned before, due to combined adverse factors such as high torsional rigidity and high background noise levels, changes in the dynamic torque on the towers, which are very small always, can not be measured accurately and, therefore are not shown here.

6.5.2 Dynamic Response Characteristics

In smooth flow, the variations of the normalised displacement at the top of the towers in both along-wind and cross-wind directions at two staggered configurations are presented in Fig. 6.39. Unlike the results observed for the towers in tandem arrangement at the same longitudinal spacing, the cross-wind oscillation amplitudes of both towers in the (2.1)B arrangement is substantially reduced, although the critical reduced velocity at which the amplitude peaks occurred is still about the same. In contrast, the peak amplitude of the displacement response of the towers in the (4.1)B arrangements is much bigger and prominent, in both translational directions, than those observed in tandem arrangement at the same longitudinal spacing.

When the intensity of the free stream turbulence is increased, the response characteristics of the towers in the (4.1)B and (6.1)B arrangements, such as those shown in Fig. 6.40, resemble those shown in Fig. 6.23 for the tandem arrangements at the same longitudinal spacings. It is evident that in the (2.1)B configuration, vortex induced oscillations of the towers are completely suppressed, as no peak of amplitude occurred at any reduced velocity. The relative peak amplitudes of the towers in all three arrangements and in both types of flow are summarised by the plots of the oscillation loops in Fig. 6.19.

Another noticeable feature of these measurements is the significant increase of the streamwise component on the upstream tower in both (2.1)B and (4.1)B arrangements, although the RMS values of the normalised response are still much smaller than those in the cross-wind direction. In order to examine this feature in more detail, three sets of the X-Y plots, representing the tip movement of the upstream and downstream towers spaced $4B$ apart at different reduced velocities, are presented in Fig. 6.41. The remarkable change in the response of the front tower, as compared to that of the rear one, is clearly evident. Also, it is evident from these plots that the instantaneous magnitude of the along-wind component is much bigger than the cross-wind component, and the maximum oscillation occurs

when the mean flow velocity approaches the critical reduced velocity.

Another prominent feature of these plots is that the axis of the oscillation loop is almost parallel to the diagonal line between the two towers. The inclined angle between the diagonal line and the mean flow direction is also known as the angle of stagger. When the longitudinal spacing between the towers is reduced, for example in the (2.1)B configuration, the tilting of the oscillation loops on the upstream tower is increased and remains parallel to the new stagger angle. In both cases, the oscillation on the downstream tower is predominantly in the cross-wind direction with only a small increase in the streamwise direction.

A similar oscillatory behaviour of two square buildings in close proximity was observed by Bailey et al. [11] in his investigation of the interference excitation between twin tall buildings. He noted that when the two buildings were spaced $1.5B$ longitudinally and $1.22B$ transversely apart, the oscillation on the upstream tower became elliptical along the diagonal line between the two buildings with the along-wind component slightly larger. In his presentation he did not indicate the oscillatory behaviour of the downstream building for such a configuration. He concluded that this type of oscillation is the result of the flow through the gap between the two buildings. The rhythmically varying width of this gap apparently added to the excitation process.

In the uniform turbulent flow, there is a change in the flow around the towers due to the increase of turbulent mixing in the shear layers. The resultant resonant oscillations of both towers are predominantly in the cross-wind direction, as shown in Fig. 6.42 in which the oscillation loops of the towers at three reduced velocities are given. In fact, the amplitude of the cross-wind oscillation of the upstream tower in the (4.1)B configuration is the biggest for all configurations investigated.

However, as shown in Fig. 6.19, when the longitudinal spacing of the towers is increased to $6B$, there is also a significant increase of the streamwise component on the downstream tower in both types of flow. This is largely due to the the fluctuating high velocity flow formed near the edge of the wake created by the upstream tower.

6.5.3 Interference Mechanism (of Towers in Staggered Arrangements)

From the results presented in the previous sections, there is a clear indication that the interference effects of the wake flow velocity on the downstream tower is as important as the magnitude of the incident turbulence intensity. In addition, although the response amplitude of the towers is increased by interference in most

of the twin tower configurations, the strength of vortex shedding could be severely reduced rather than increased in some situations. This feature is particularly common when the two towers are close to each other, either in the side by side or staggered configurations, but not when one is directly behind the other.

A plausible explanation is that this is the result of the fluid entrainment into the wake boundary of the upstream tower. As the sketch of the two staggered towers in Fig. 2.3 illustrates, the flow rate around the downstream tower is unaffected on its outer side but is increased on its inner side due to the entrainment between the inner side and the fully formed wake of the upstream tower. When the towers are sufficiently close to each other, the position of the downstream tower could create a channel wide enough for the wind to converge and stream between them, altering the wake characteristics of the upstream tower. Consequently, both along-wind and cross-wind response are affected by this proximity effect, with large elongated movement, as those shown in Fig. 6.41, along the diagonal line between the towers. Furthermore, the slight asymmetry of flow around the towers induced by the entrainment of fluid into the upstream wake boundary causes the cross-wind force components (lift) on them.

When the longitudinal spacing between the towers is increased, effects due to the close proximity vanish. Instead, distinct vortex streets are likely to be formed behind each tower and wake interference effects the response of both towers.

In turbulent flow, due to the increase in the turbulent mixing in the shear layers and the subsequent reduction in their radius of curvature, the flow patterns around the towers are drastically altered. It seems that wake interference dominates in all the configurations being investigated. In addition, from the results observed on the towers in both side by side and staggered arrangements, it is clear that an increase in the turbulence of the undisturbed flow has an enhancement effect on the coherent structure of the wake of the upstream tower, increasing its effectiveness in causing both resonant oscillation and interference excitation. In contrast the increase in turbulence caused by the introduction of the upstream tower has no strong impact on the downstream tower's response.

Model configuration	Spacing ratios		File name	Remark
	X _B	Y _B		
TANDEM	2	0	FIN267- FIN274	
	3	0	FIN361- FIN368	
	4	0	FIN201- FIN208	
	4	0	FIN210- FIN215	linkage at upper ends
	4	0	FIN216- FIN221	linkage at lower ends
	5	0	FIN223- FIN230	
	6	0	FIN237- FIN244	
	6	0	FIN231- FIN236	upstream model wedged
	7	0	FIN245- FIN252	
	8	0	FIN259- FIN266	
	8	0	FIN253- FIN258	$\alpha = 45$ degree
STAGGERED	2	1	FIN275- FIN282	
	4	1	FIN283- FIN290	
	6	1	FIN291- FIN298	
SIDE BY SIDE	0	2	FIN355- FIN360	
	0	4	FIN345- FIN350	
	0	4	FIN351- FIN354	linkage at upper ends

Table 6.1 Summary of the model combinations investigated in this study and the resultant data file names from dynamic measurements.

Model configuration	Spacing ratios		File name	Remark
	X _B	Y _B		
TANDEM	2	0	FIN325- FIN330	
	4	0	FIN313- FIN318	
	6	0	FIN319- FIN324	
STAGGERED	2	1	FIN331- FIN334	
	4	1	FIN307- FIN312	
	6	1	FIN301- FIN306	
SIDE BY SIDE	0	2	FIN335- FIN338	
	0	4	FIN339- FIN344	

N.B. Unless specified, angle of attack, $\alpha = 0$ degree

Table 6.1 Summary of the model combinations investigated in this study and the resultant data file names from dynamic measurements.
(cont'd)

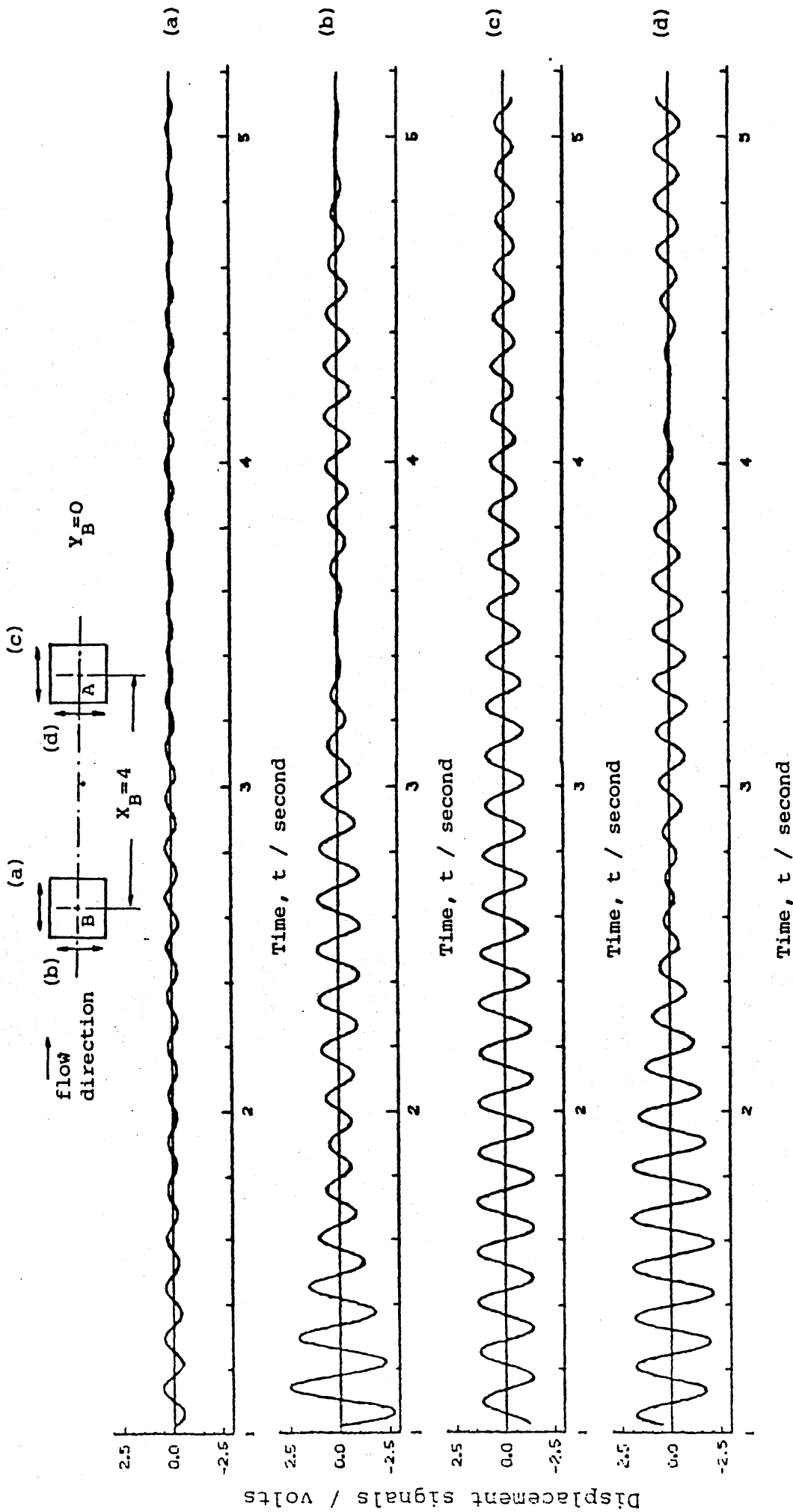


Fig. 6.1(a) Typical amplitude traces of the free-decay vibrations measured at the top of the models with initial perturbation applied to the tip of model A along its transverse direction.

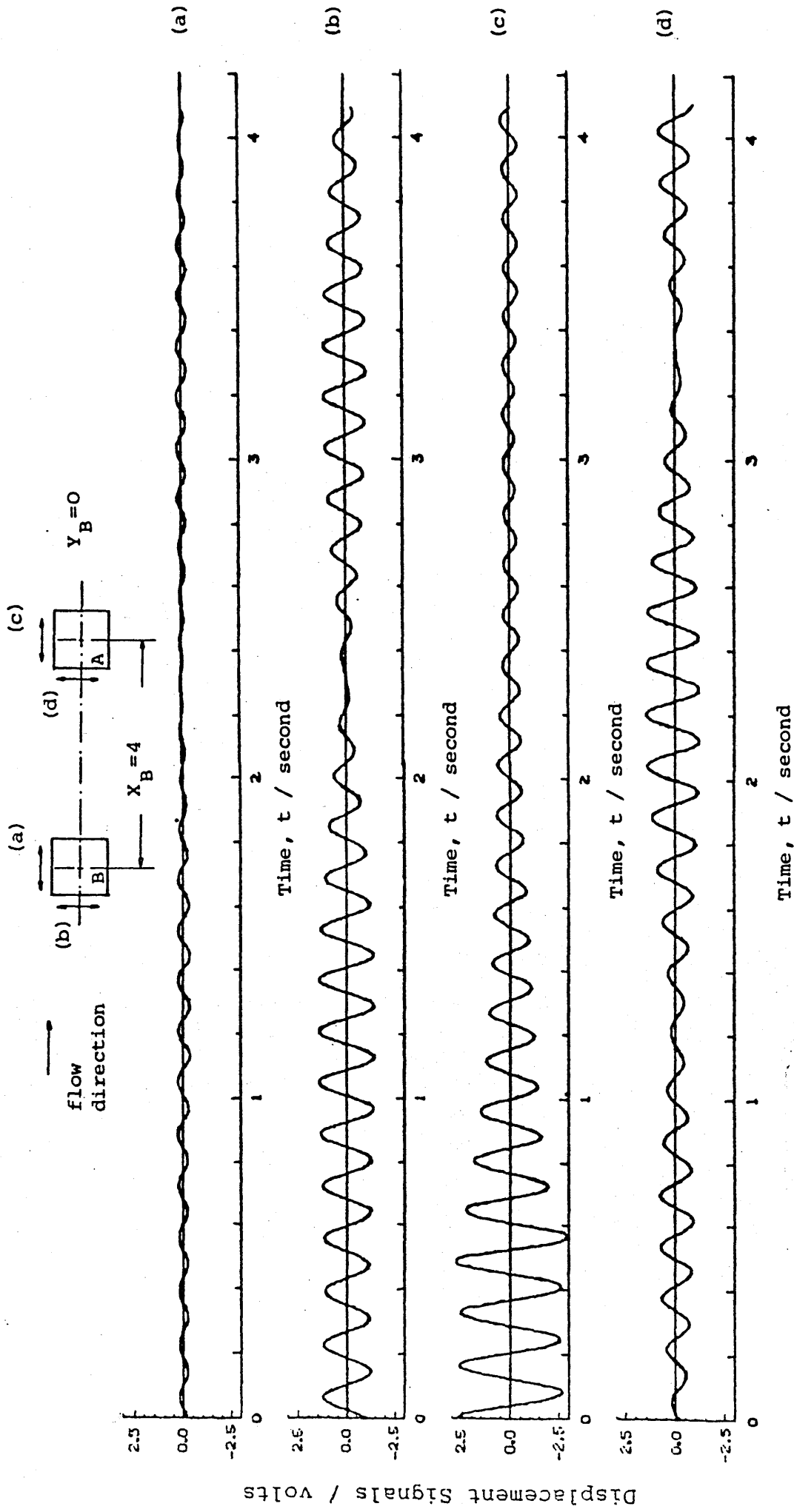
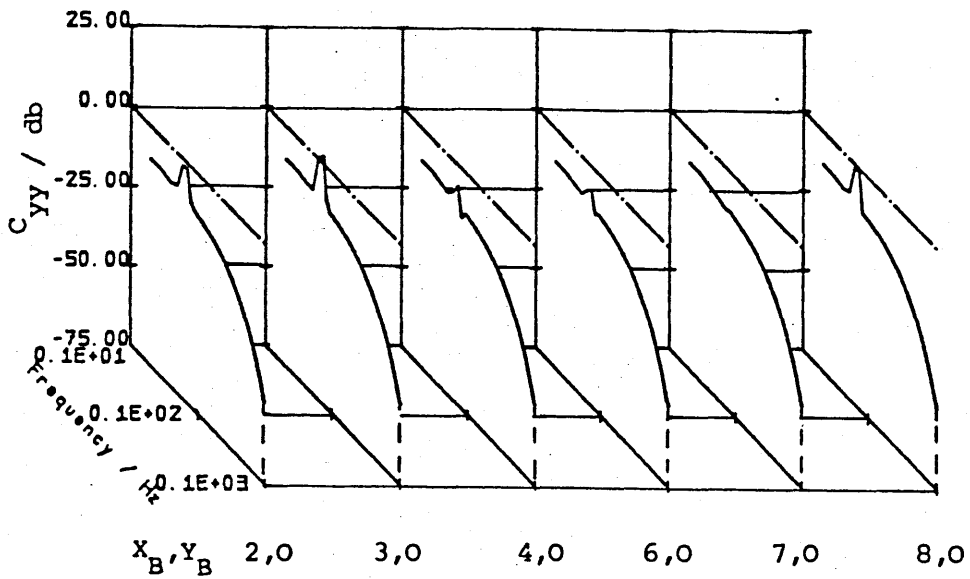
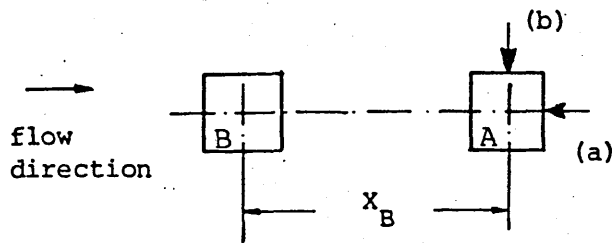
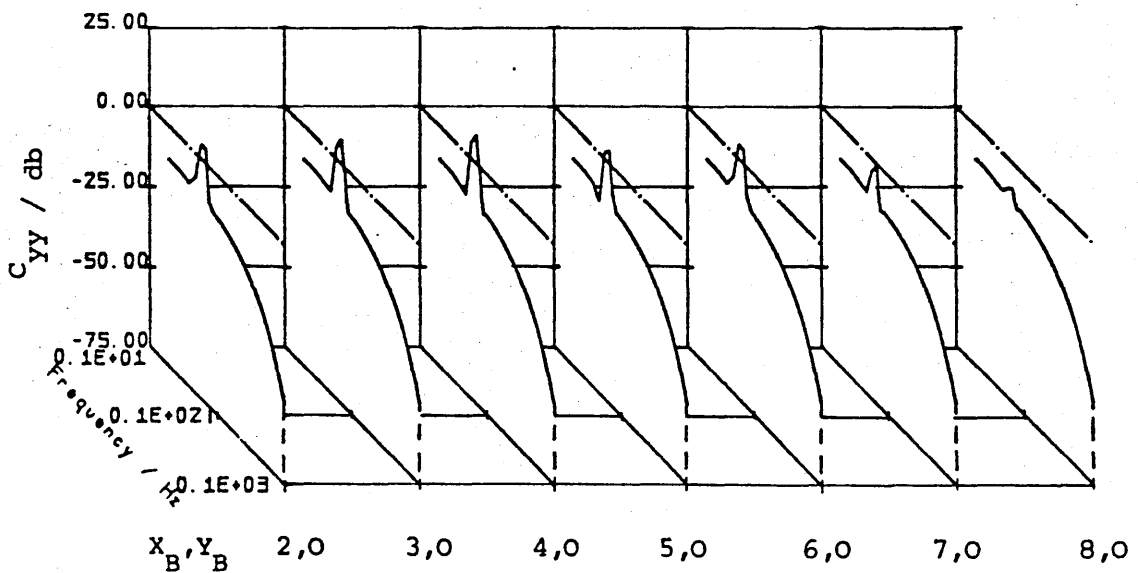


Fig. 6.1(b) Typical amplitude traces of the free-decay vibrations measured at the top of the models with initial perturbation applied to the tip of model A along its longitudinal direction.



(a) excitation applied and response measured in the longitudinal direction.



(b) excitation applied and response measured in the transverse direction.

Figure 6.2 Cross-power spectrum functions of (a) longitudinal and (b) transverse responses between model A and B with initial perturbation applied to A along its (a) longitudinal and (b) transverse direction at various spacings.

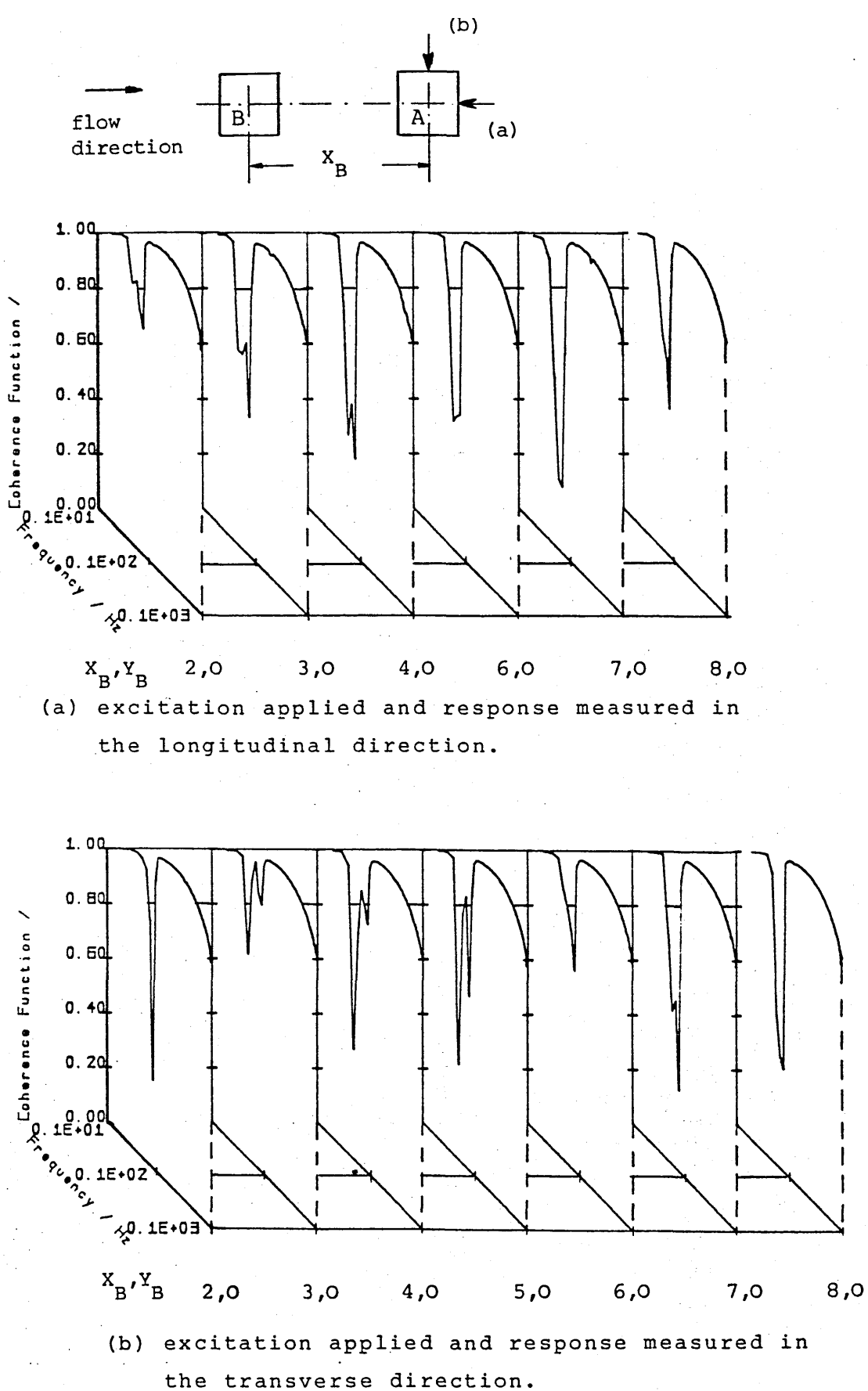
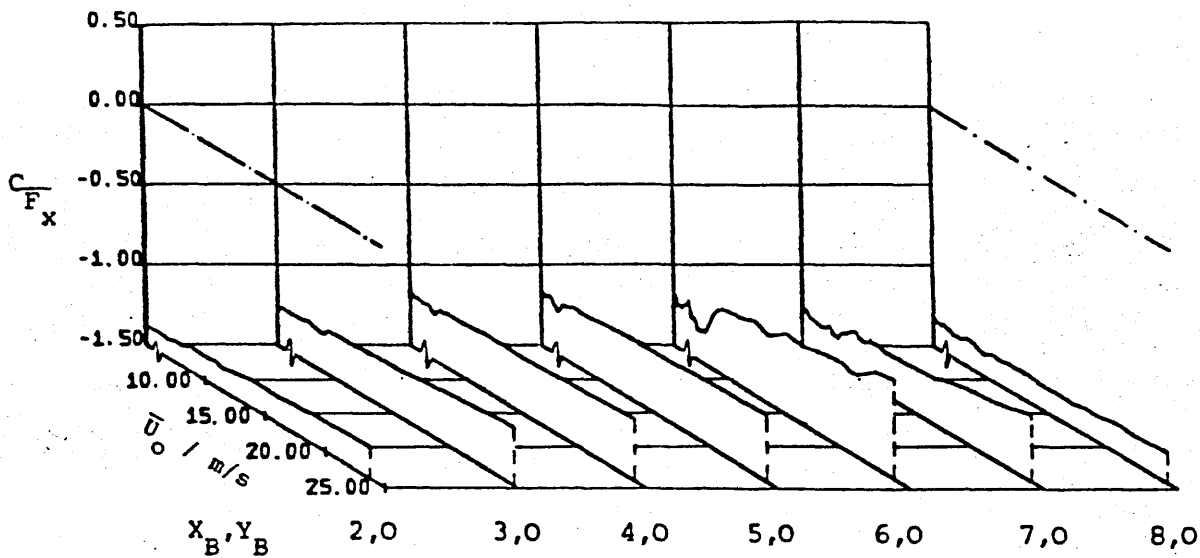
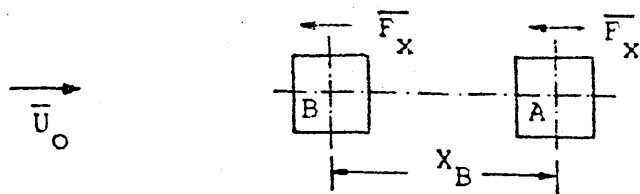
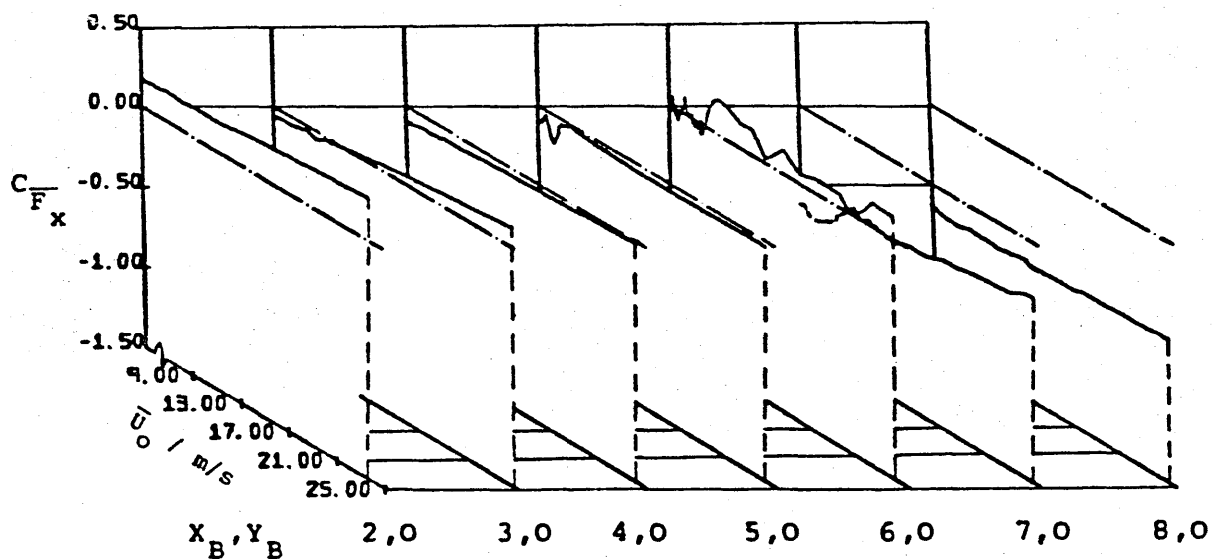


Figure 6.3 Coherence functions of (a) longitudinal and (b) transverse responses between model A and B with initial perturbation applied to A along its (a) longitudinal and (b) transverse direction at various spacings.

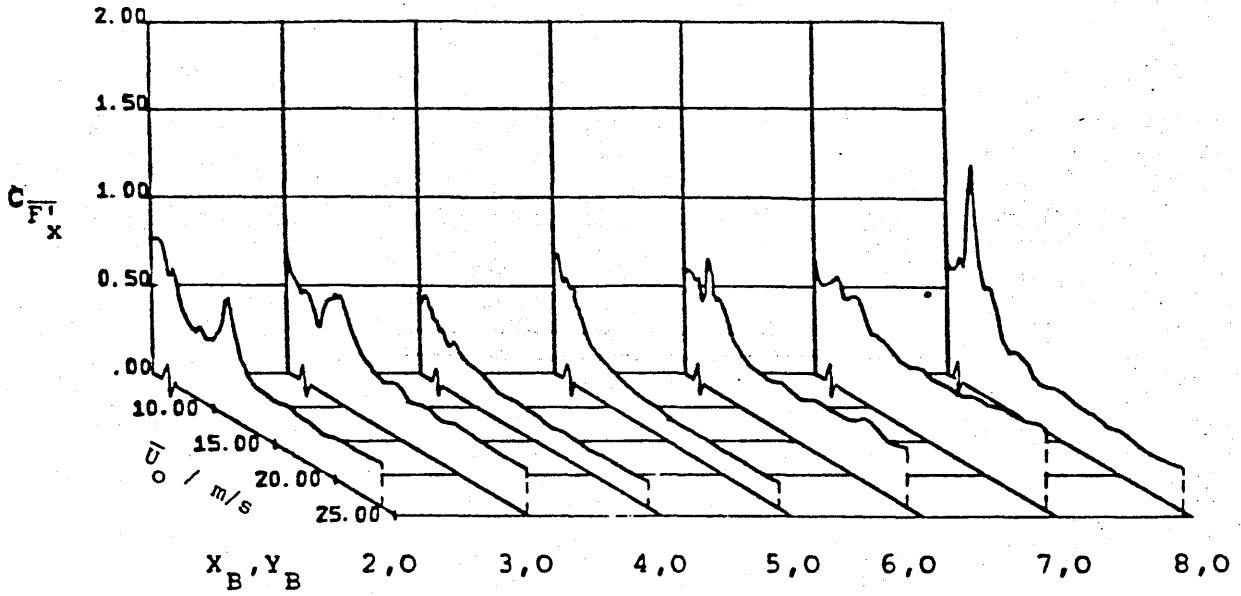
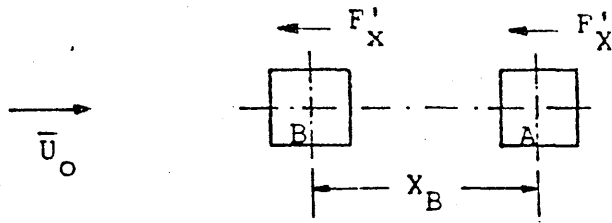


(a) Time-mean along-wind force coefficients of tower B

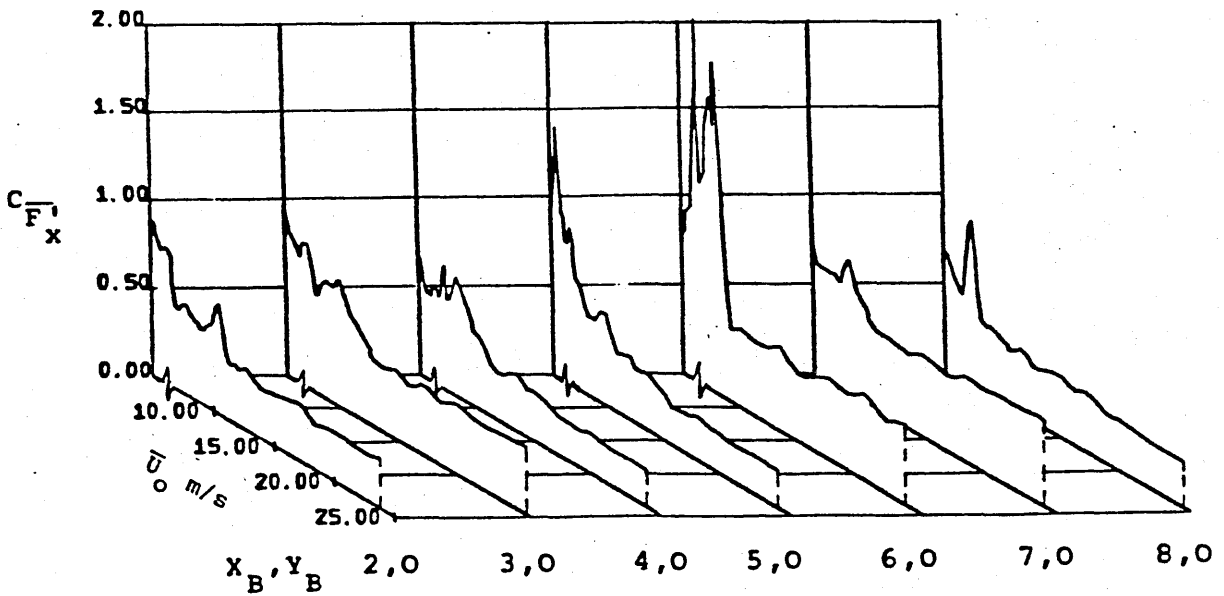


(b) Time mean along-wind force coefficients of tower A

Figure 6.4 Variation in the coefficients of the mean along-wind force on (a) the upstream and (b) the downstream tower with mean wind velocity in uniform smooth flow for various tandem arrangements.



(a) RMS fluctuating along-wind force coefficients of tower B



(b) RMS fluctuating along-wind force coefficients of tower A

Figure 6.5 Variation in the coefficients of the RMS values of the fluctuating along-wind force on (a) the upstream and (b) the downstream tower with mean wind velocity in uniform smooth flow for various tandem arrangements.

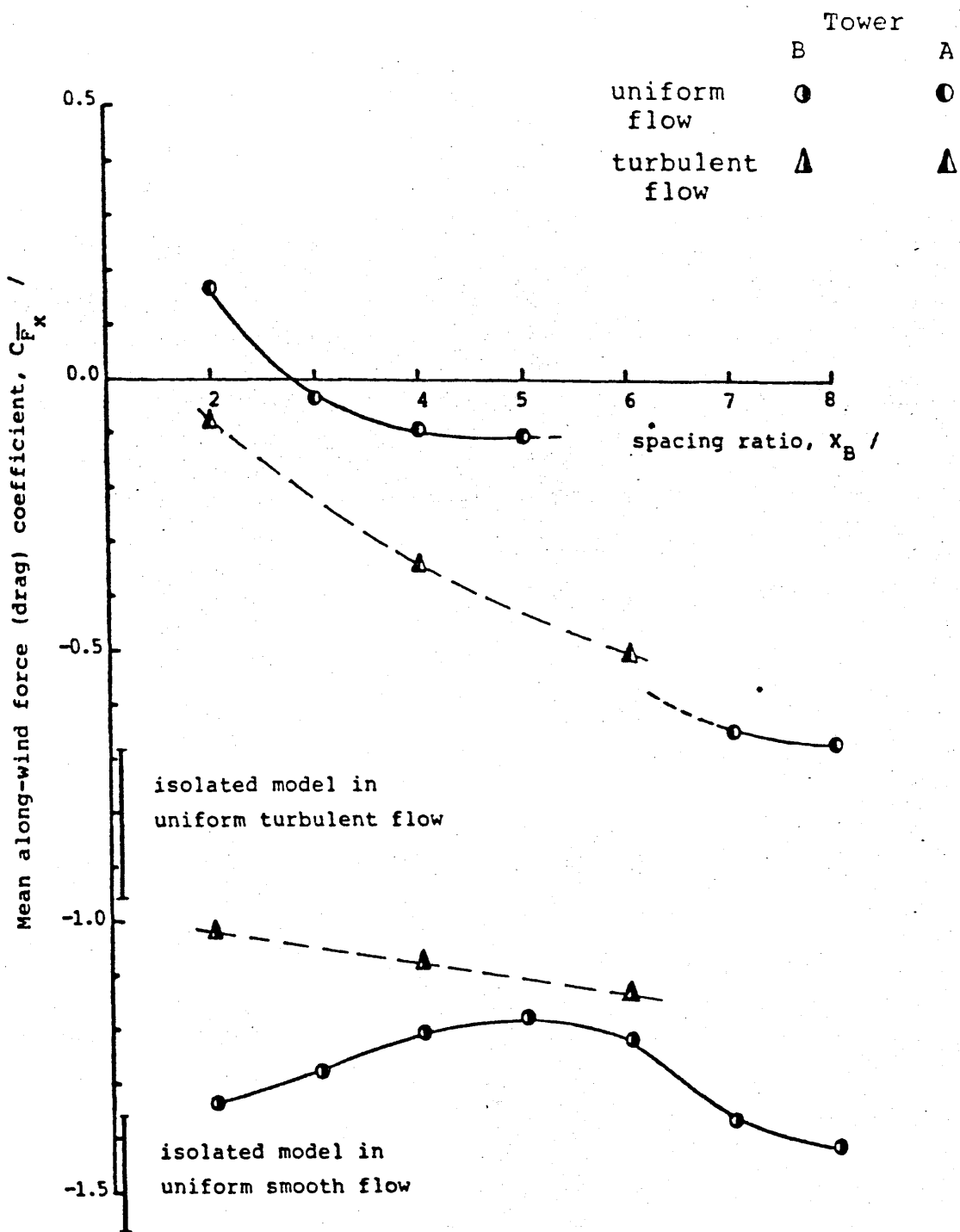
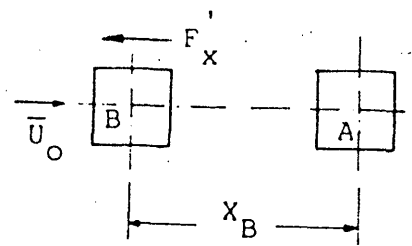
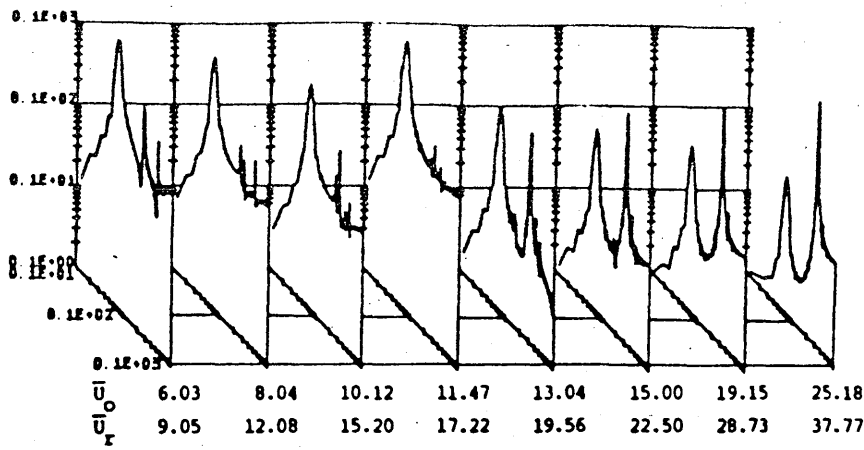
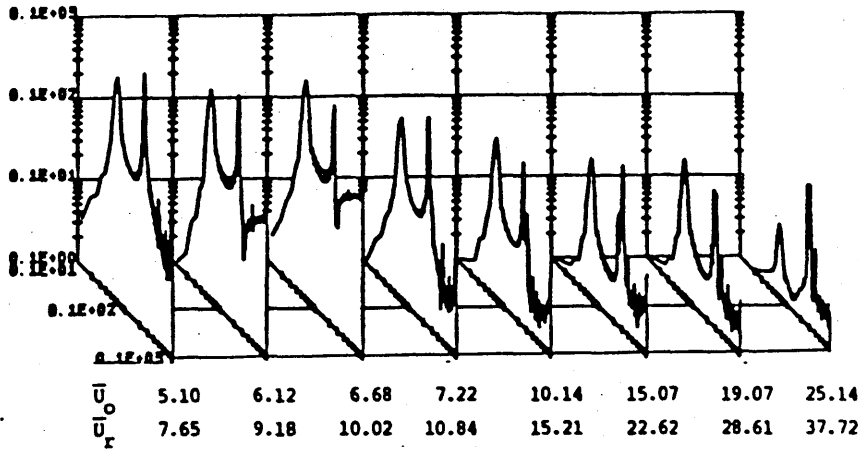


Figure 6.6 Variation of the mean along-wind force (drag) coefficients of the two towers in tandem arrangement with spacing ratio in both uniform smooth and turbulent flows.



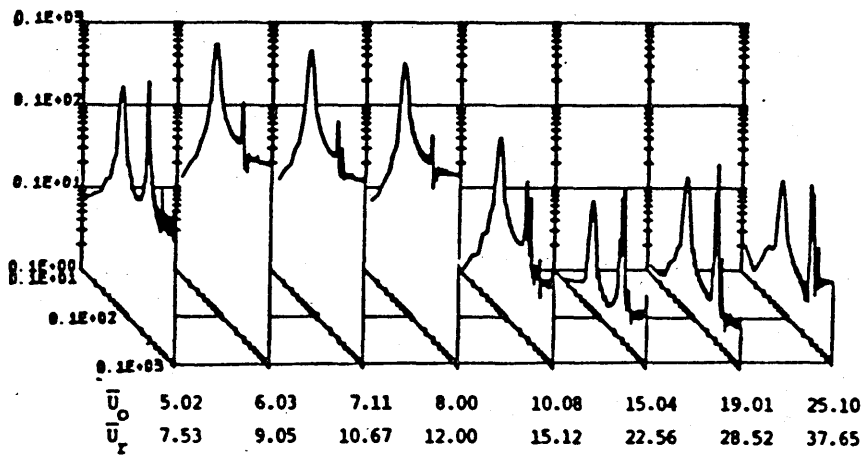
(a) $X_B = 2$

$$\hat{U}_r = 11.05/17.43$$



(b) $X_B = 4$

$$\hat{U}_r = 9.11$$



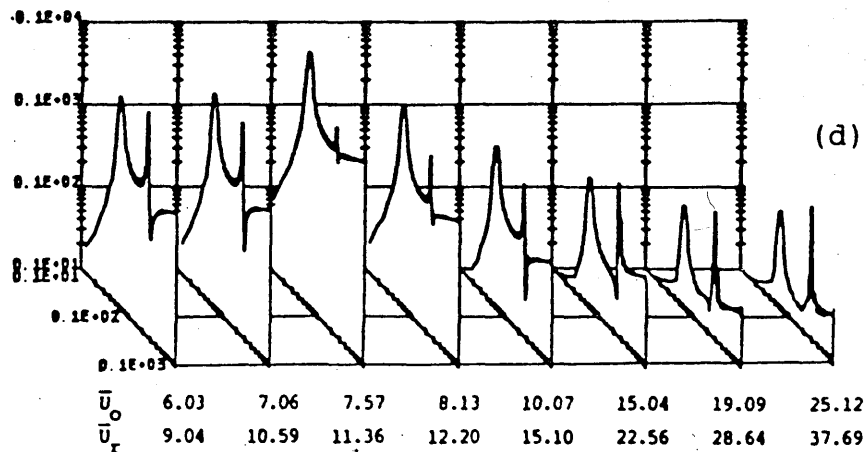
(c) $X_B = 6$

$$\hat{U}_r = 11.84$$

$$\frac{f S_F(f)}{\left(\frac{1}{2} \rho \bar{U}_0^2 B H\right)^2}$$

\bar{U}_0, \bar{U}_r

f



(d) $X_B = 8$

$$\hat{U}_r = 11.67$$

Fig. 6.7(a) A collection of normalised along-wind force spectra for the upstream tower at four tandem configurations in uniform smooth flow for various reduced velocities.

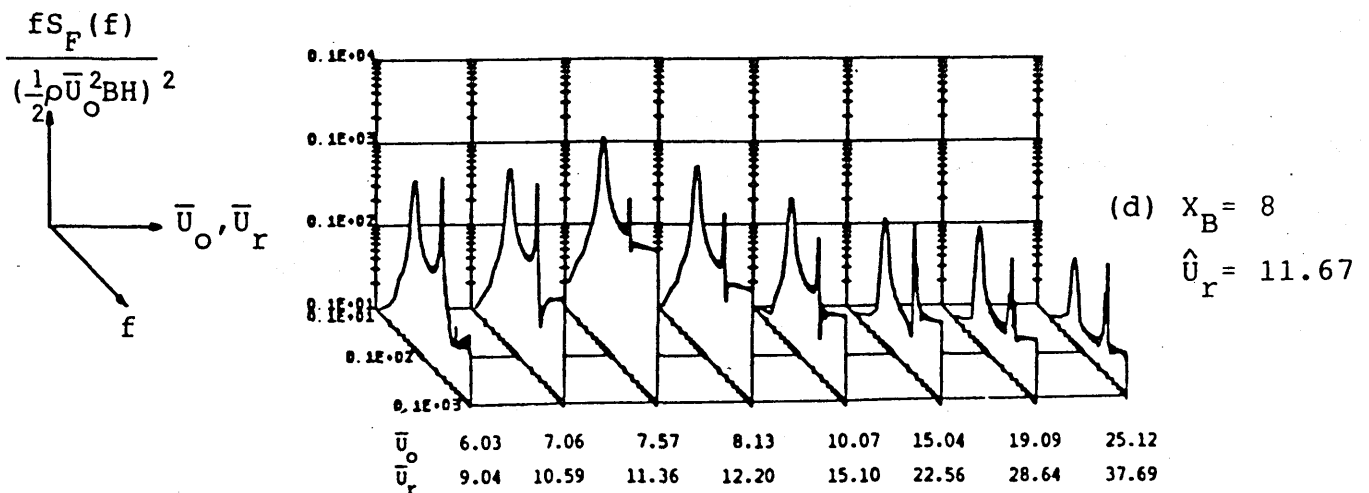
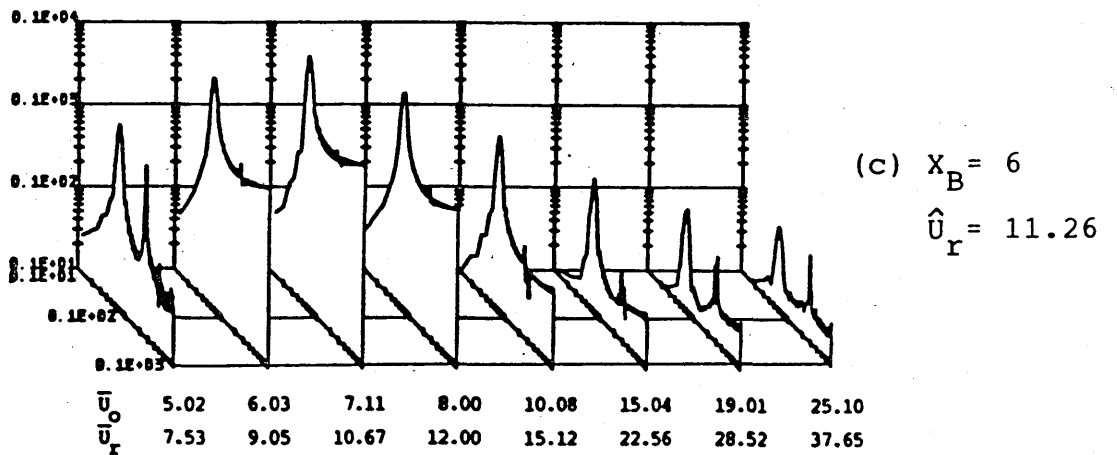
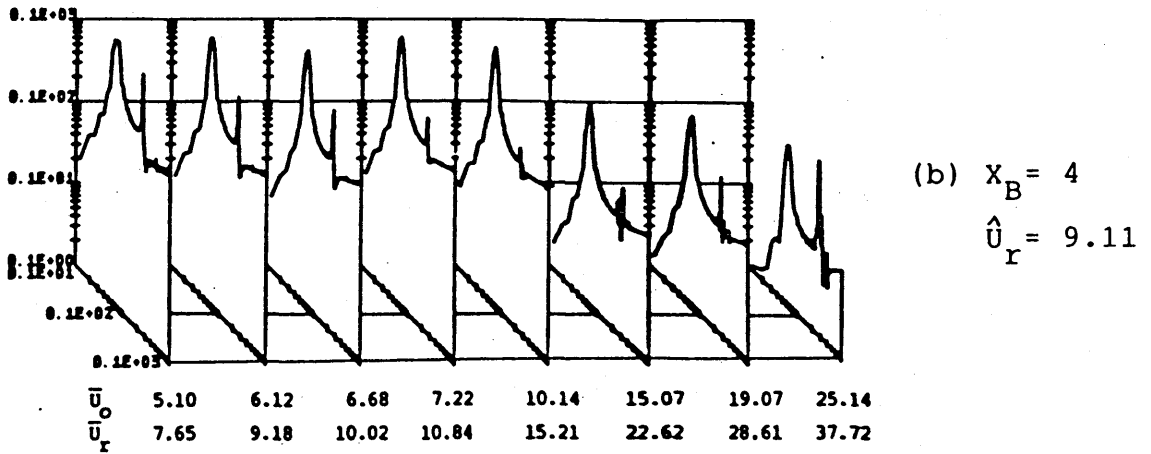
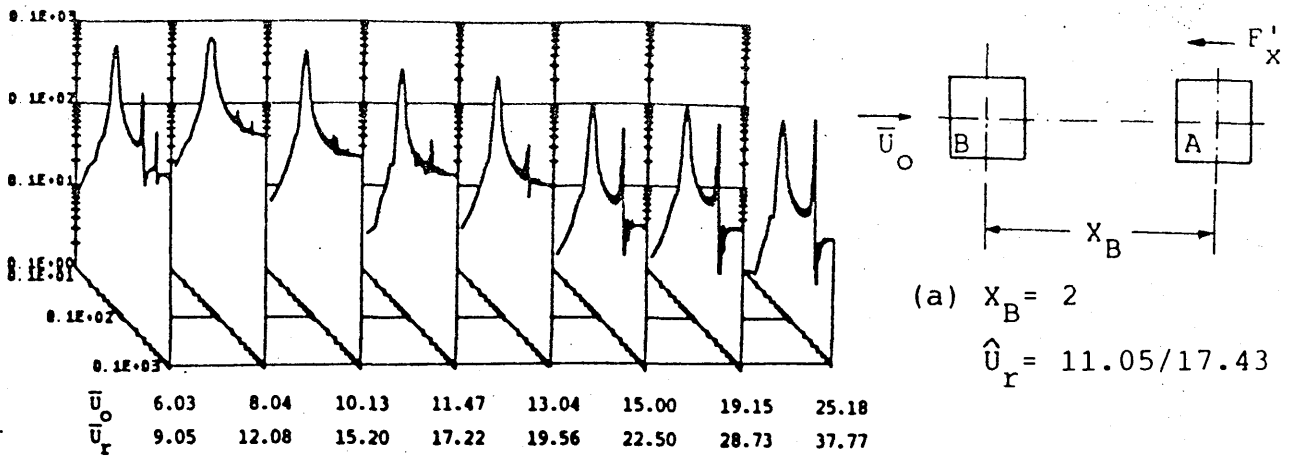
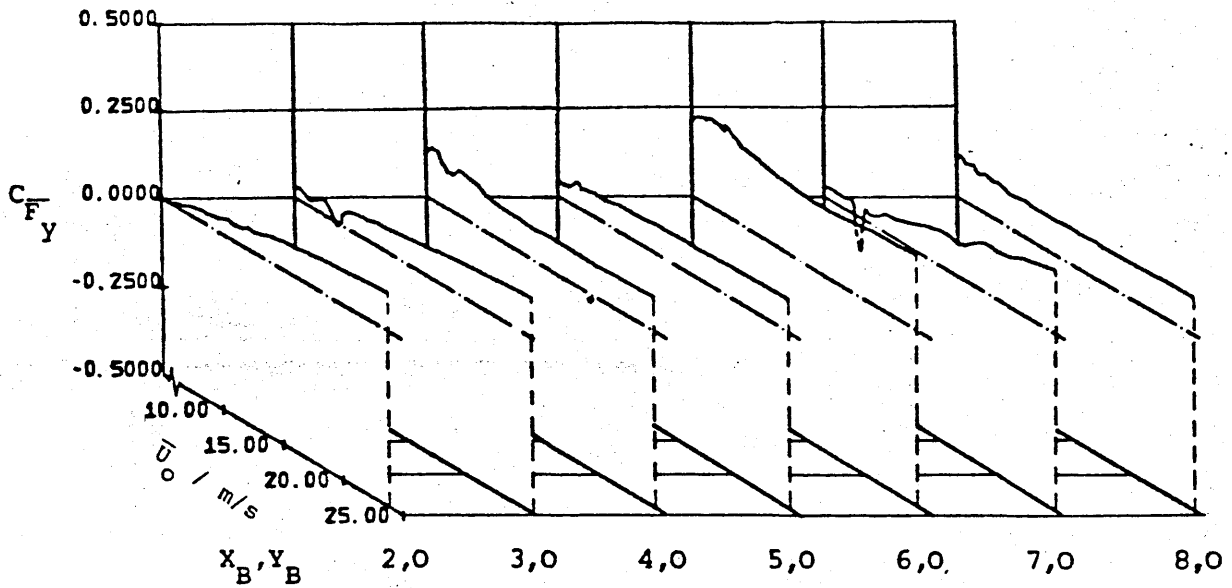
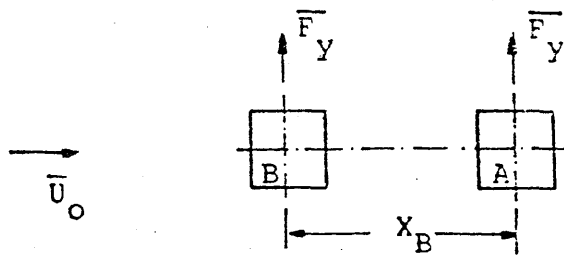
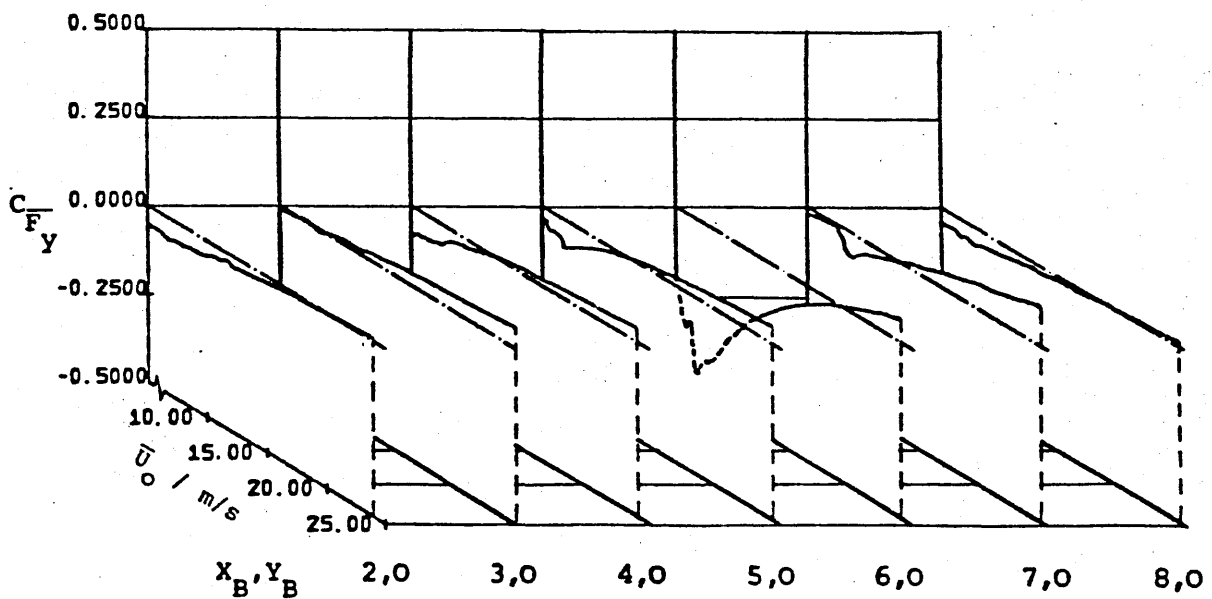


Fig. 6.7(b) A collection of normalised along-wind force spectra for the downstream tower at four tandem configurations in uniform smooth flow for various reduced velocities.

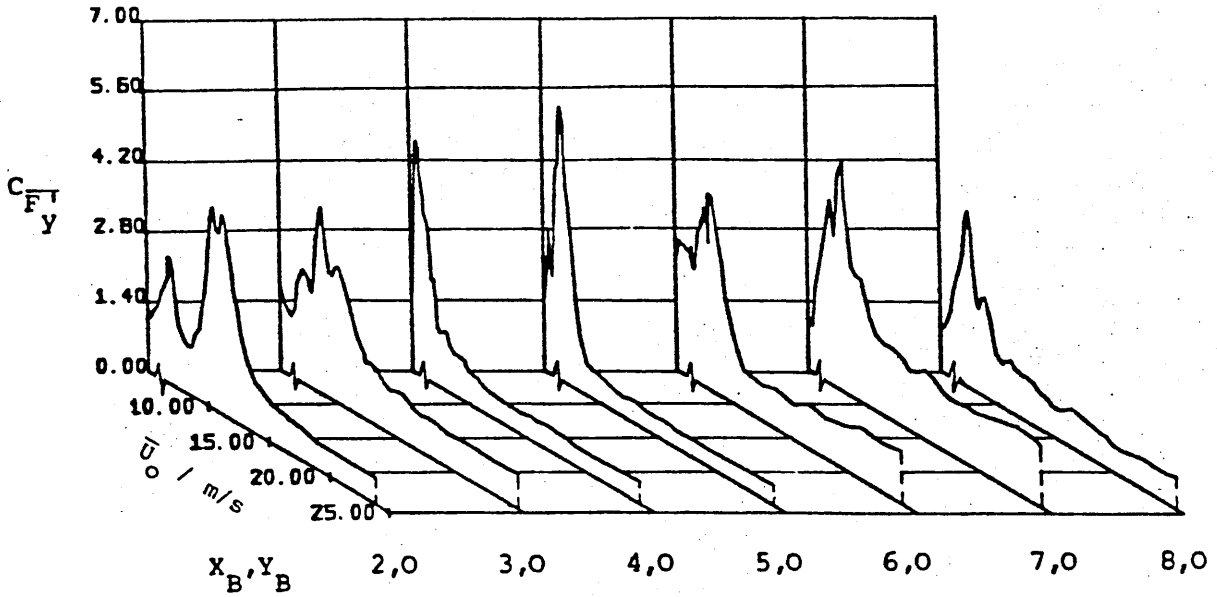
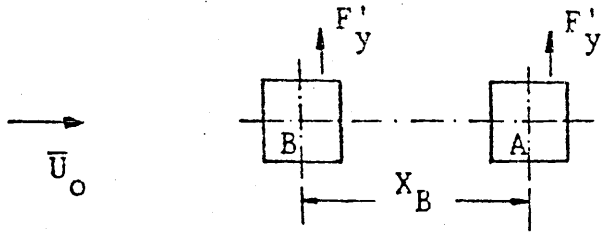


(a) Time-mean cross-wind force coefficients of tower B

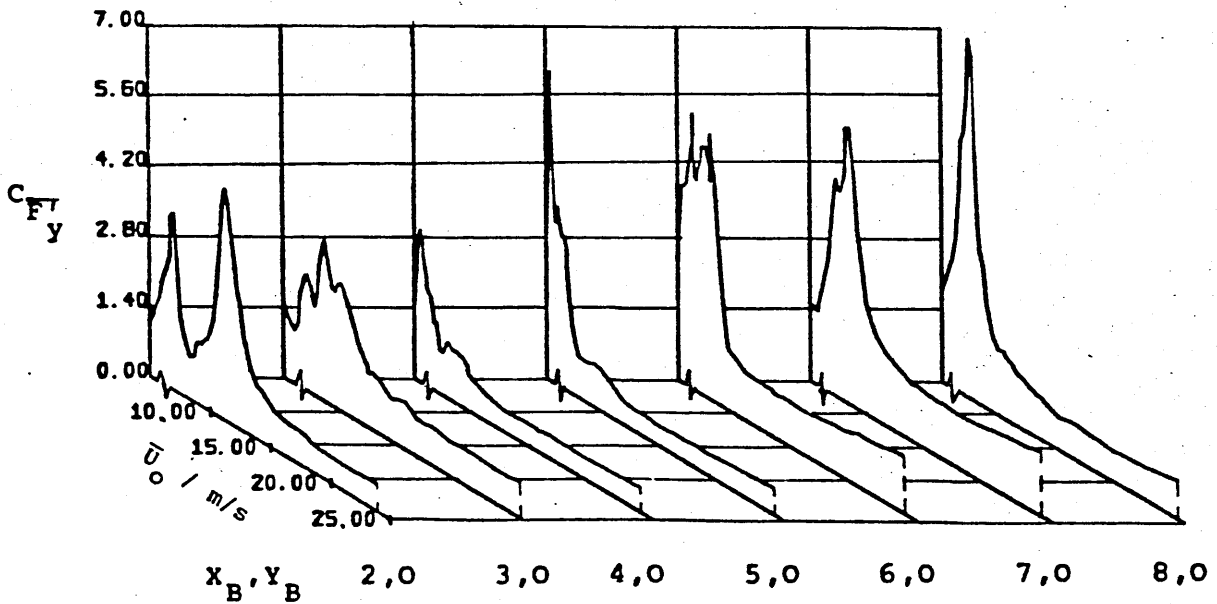


(b) Time-mean cross-wind force coefficients of tower A

Figure 6.8 Variation in the coefficients of the mean cross-wind force on (a) the upstream and (b) the downstream tower with mean wind velocity in uniform smooth flow for various tandem arrangements.



(a) RMS fluctuating cross-wind force coefficients of tower B



(b) RMS fluctuating cross-wind force coefficients of tower A

Figure 6.9 Variation in the coefficients of the RMS values of the fluctuating cross-wind force on (a) the upstream and (b) the downstream tower with mean wind velocity in uniform smooth flow for various tandem arrangements.

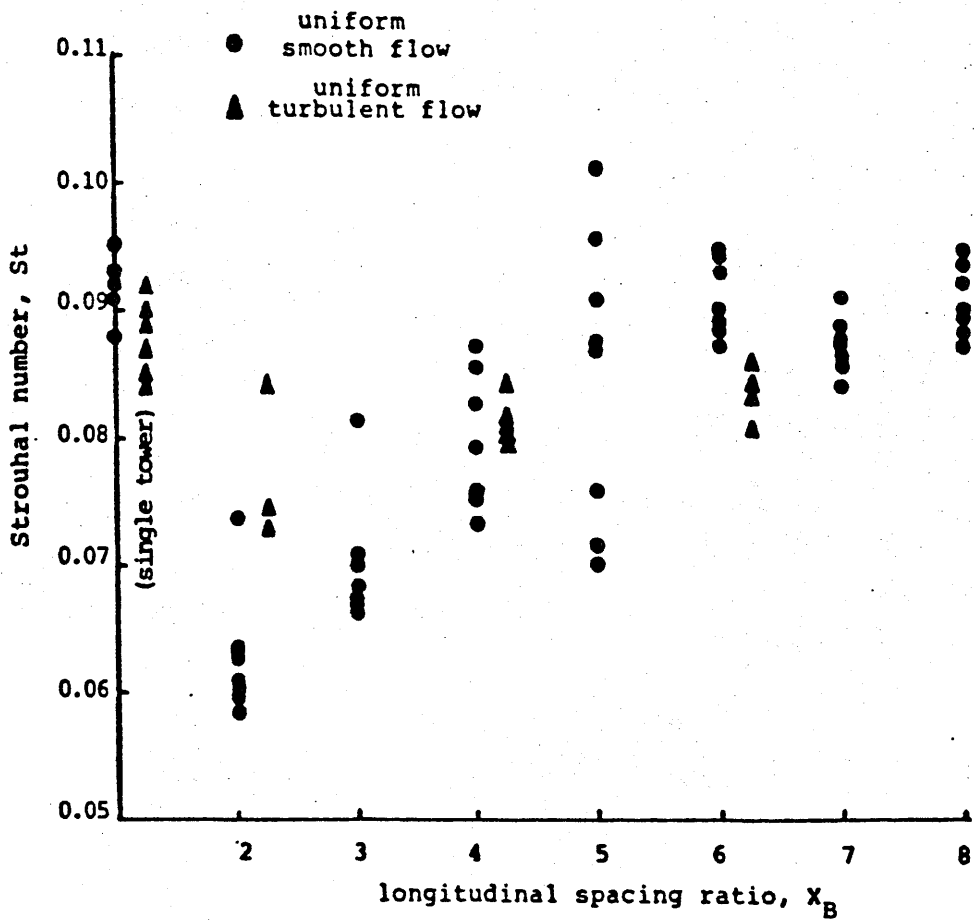
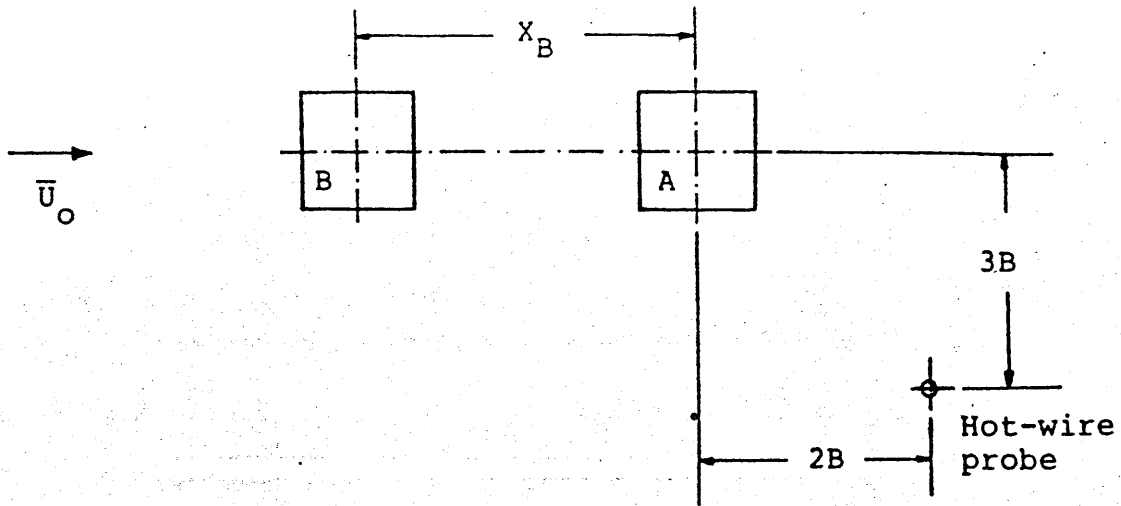


Figure 6.10 Strouhal number behind the downstream tower in tandem arrangements in both uniform smooth and turbulent flows.

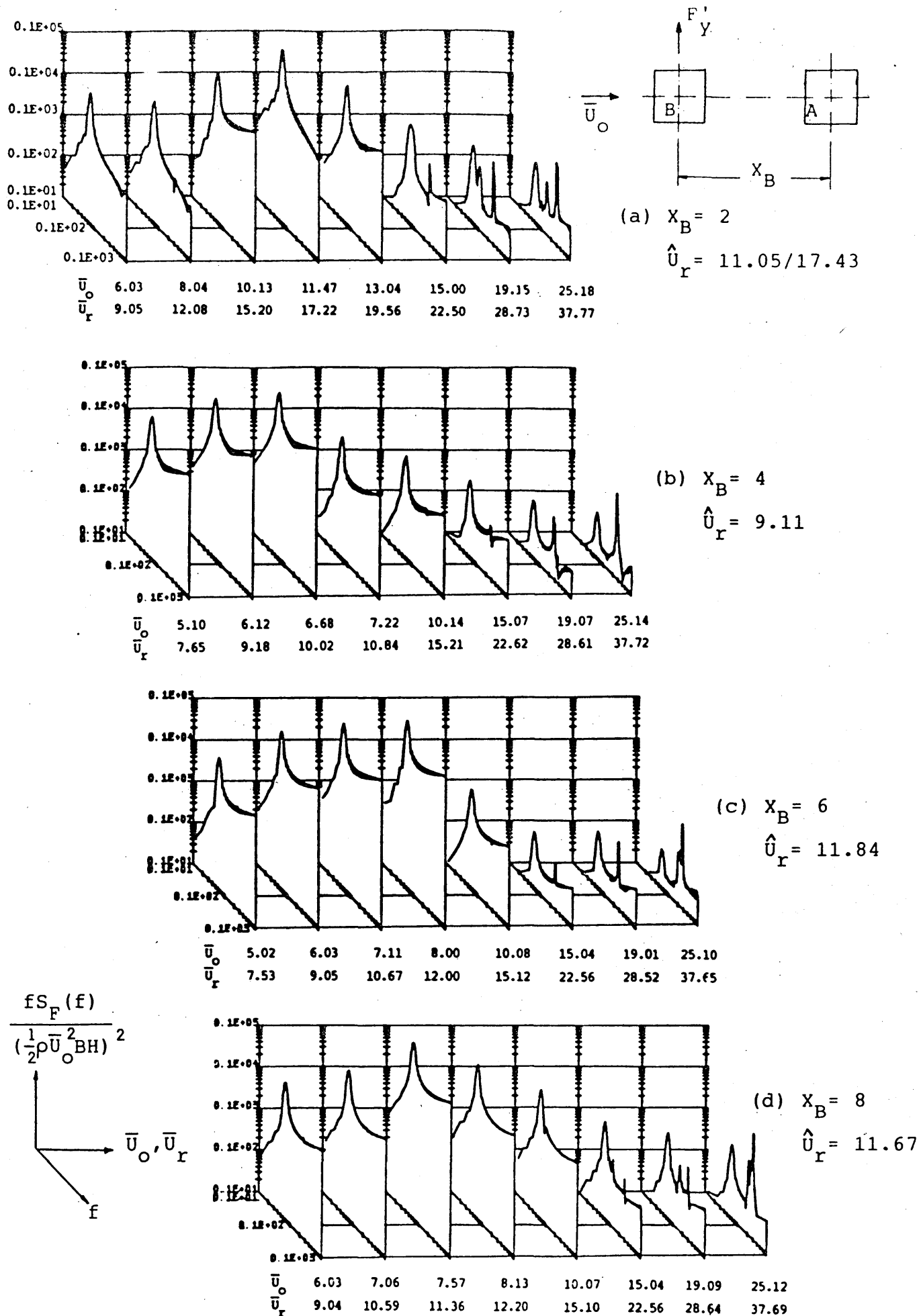
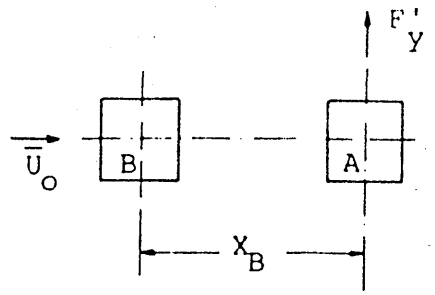
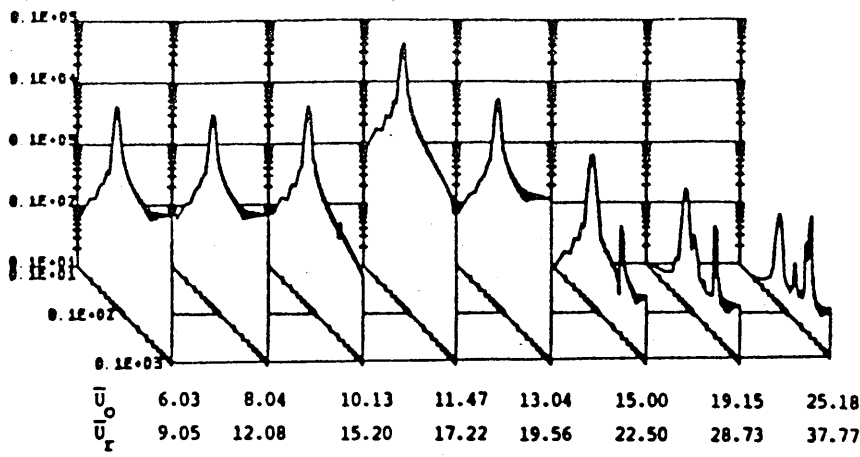
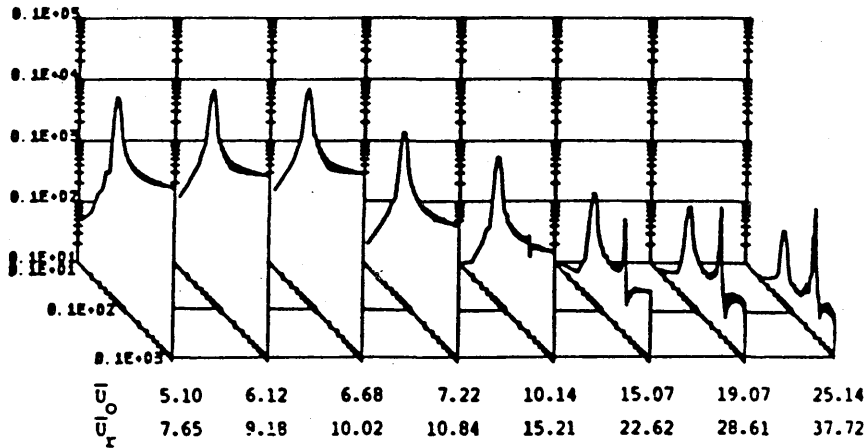


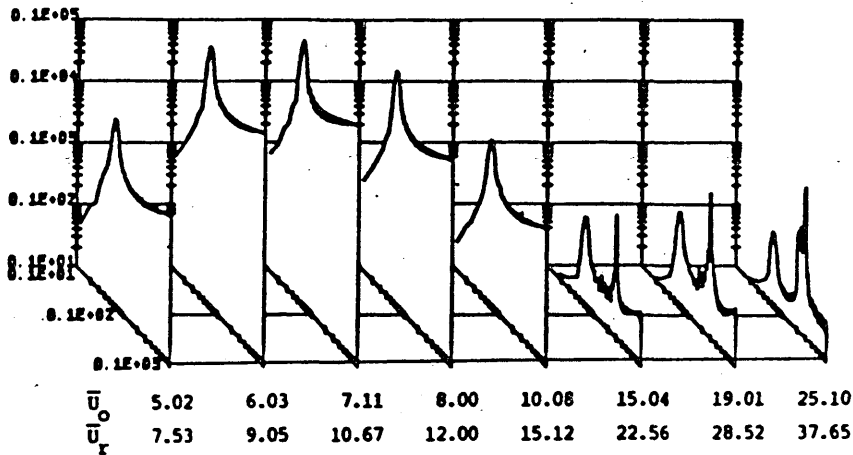
Fig. 6.11(a) A collection of normalised cross-wind force spectra for the upstream tower at four tandem configurations in uniform smooth flow for various reduced velocities.



(a) $X_B = 2$
 $\hat{U}_r = 11.05/17.43$

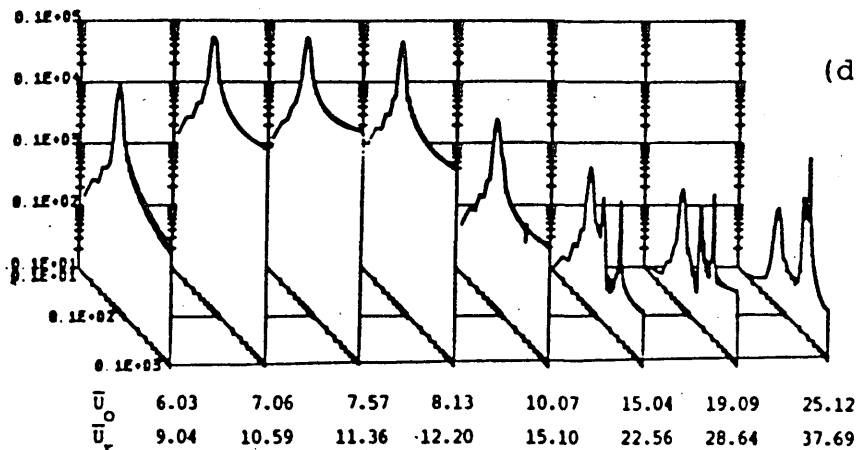
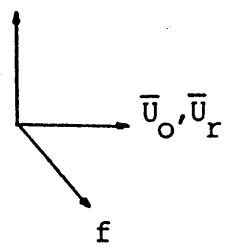


(b) $X_B = 4$
 $\hat{U}_r = 9.11$



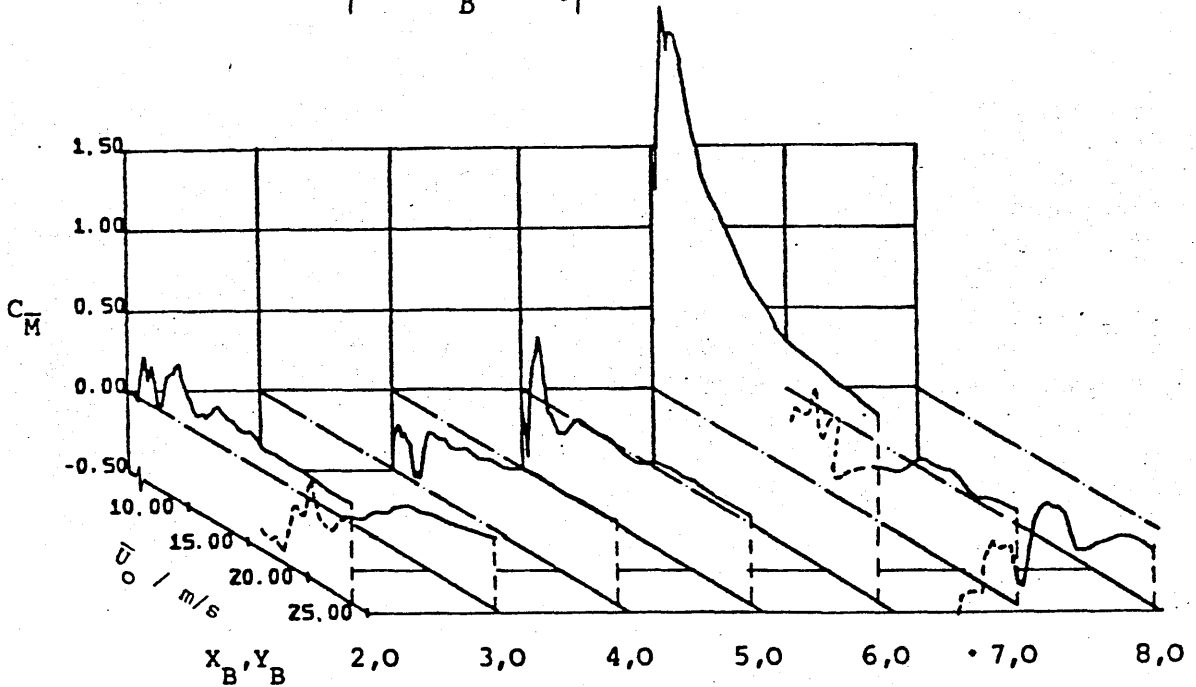
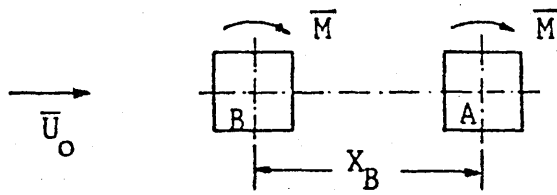
(c) $X_B = 6$
 $\hat{U}_r = 11.55$

$$\frac{f S_F(f)}{(\frac{1}{2} \rho \bar{U}_0^2 B H)^2}$$

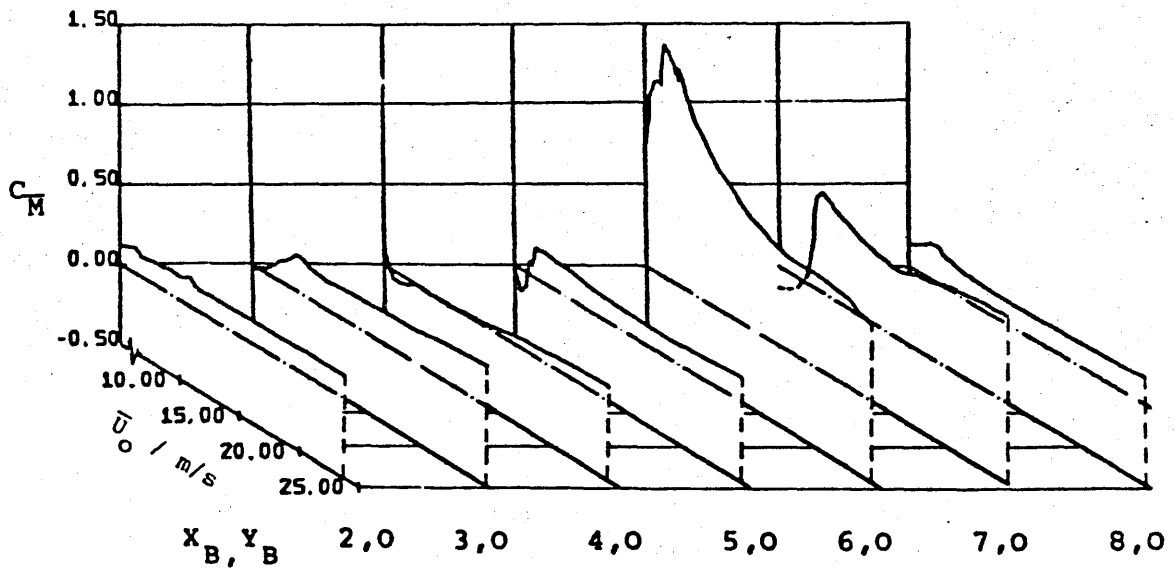


(d) $X_B = 8$
 $\hat{U}_r = 11.67$

Fig. 6.11(b) A collection of normalised cross-wind force spectra for the downstream tower at four tandem configurations in uniform smooth flow for various reduced velocities.

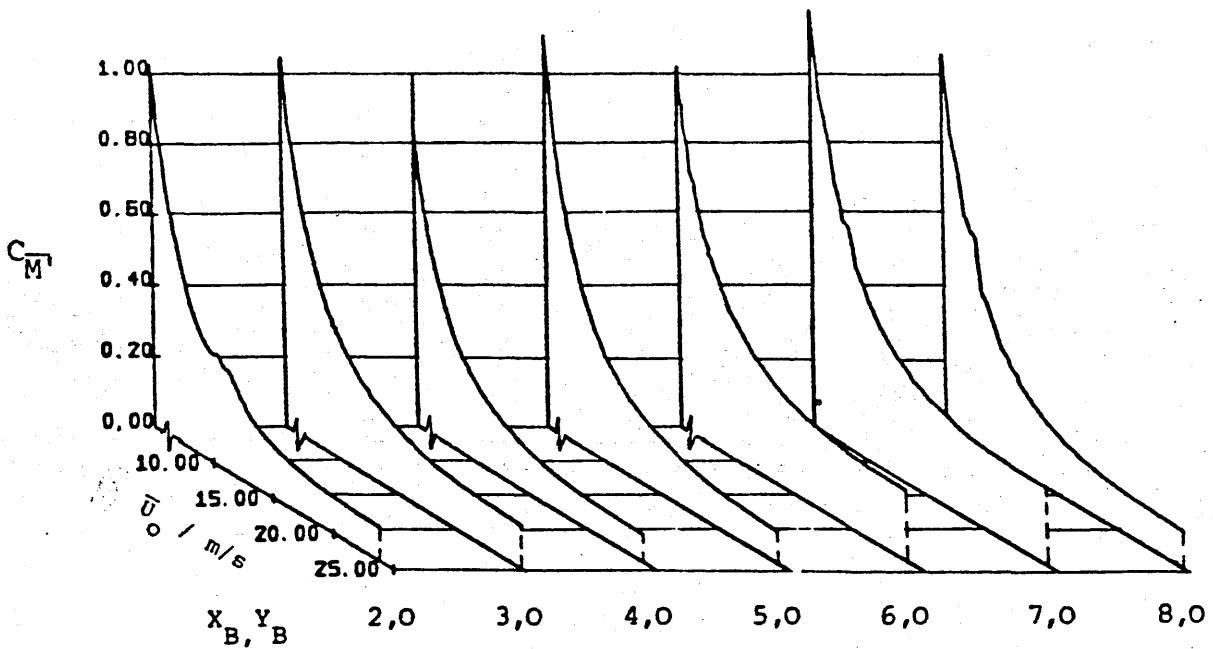
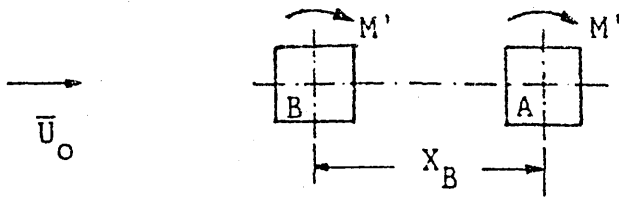


(a) Time-mean torsional moment coefficients of tower B

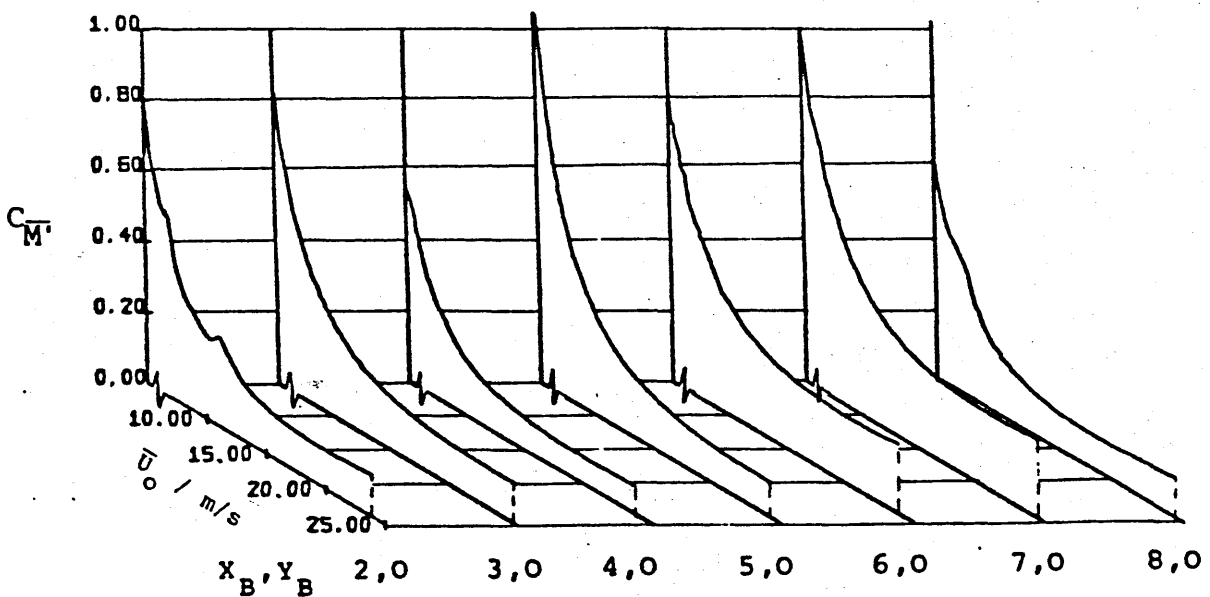


(b) Time-mean torsional moment coefficients of tower A

Figure 6.12 Variation in the coefficients of the mean torsional moment on (a) the upstream and (b) downstream tower with mean wind velocity in uniform smooth flow for various tandem arrangements.

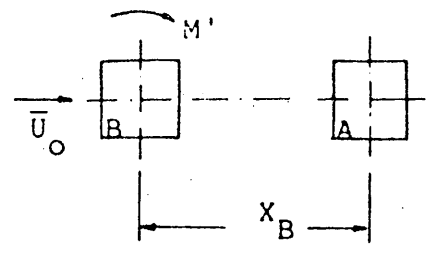
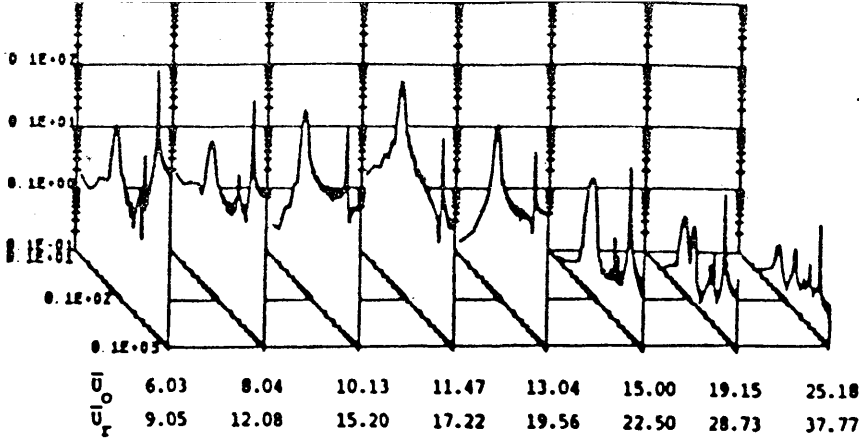


(b) RMS fluctuating torsional moment coefficients of tower A

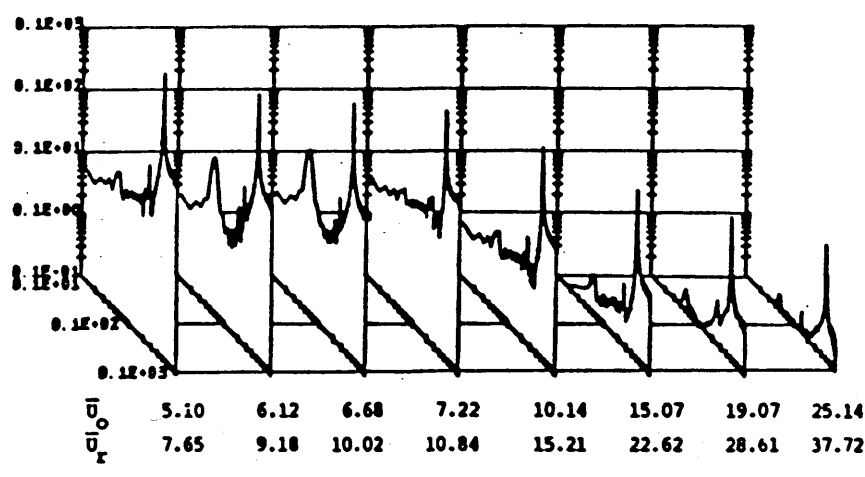


(a) RMS fluctuating torsional moment coefficients of tower B

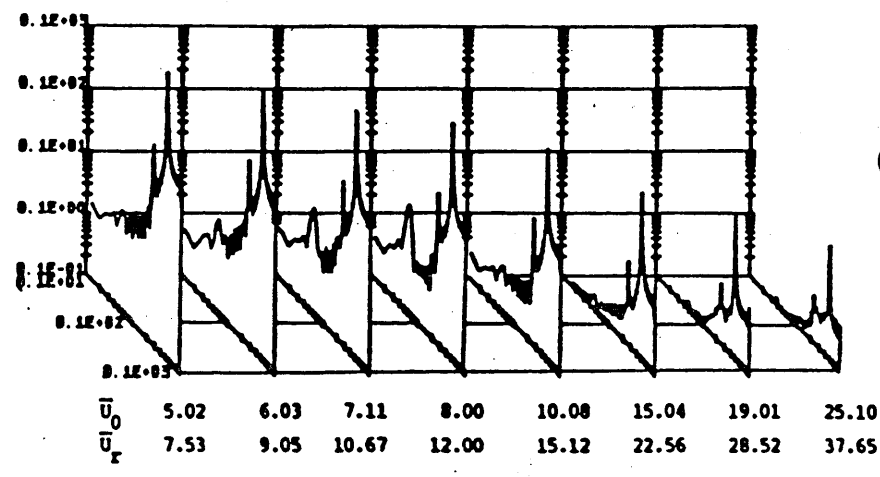
Figure 6.13 Variation in the coefficients of the RMS values of the fluctuating torsional moment on (a) the upstream and (b) the downstream tower with mean wind velocity in uniform smooth flow for various tandem arrangements.



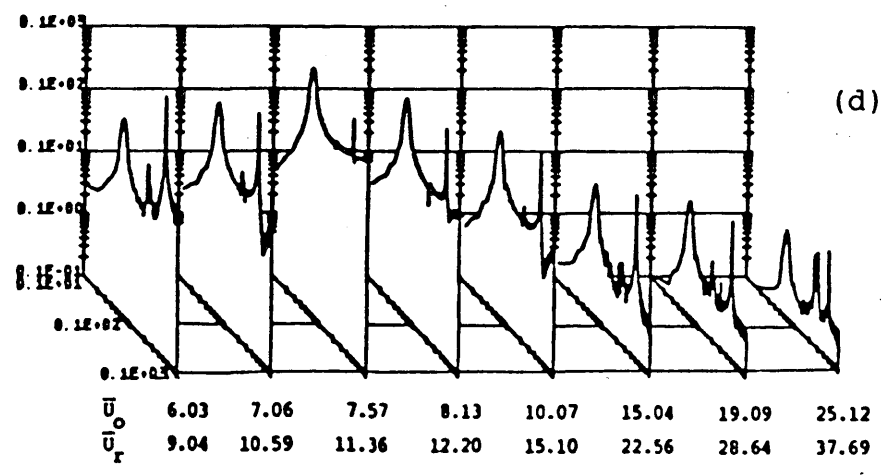
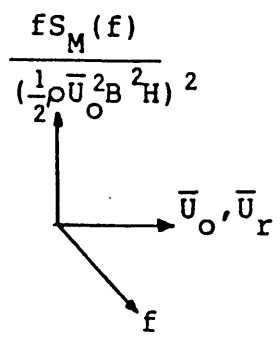
(a) $X_B = 2$
 $\hat{U}_r = 11.05/17.43$



(b) $X_B = 4$
 $\hat{U}_r = 9.11$

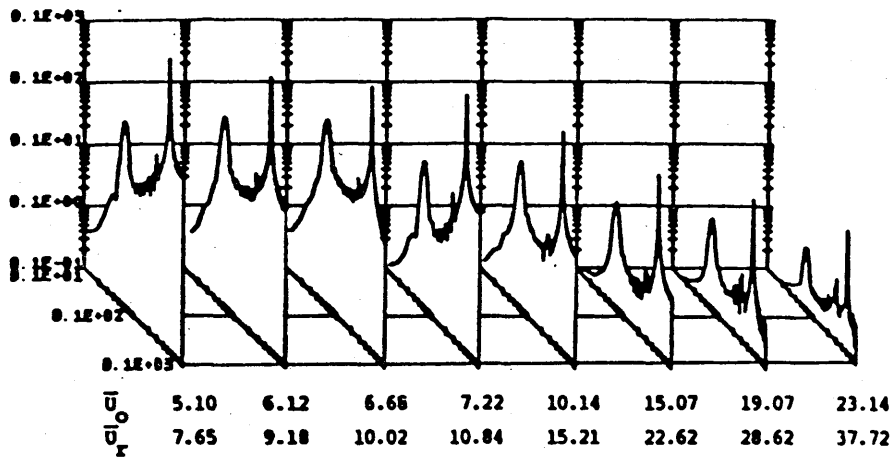
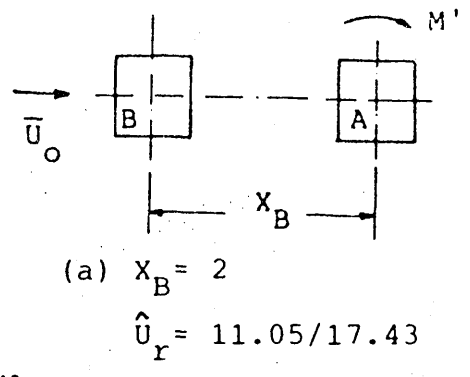
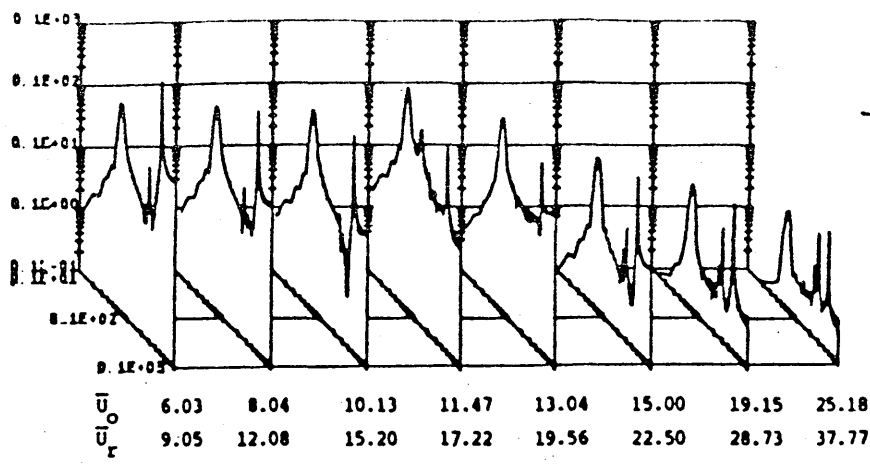


(c) $X_B = 6$
 $\hat{U}_r = 11.84$

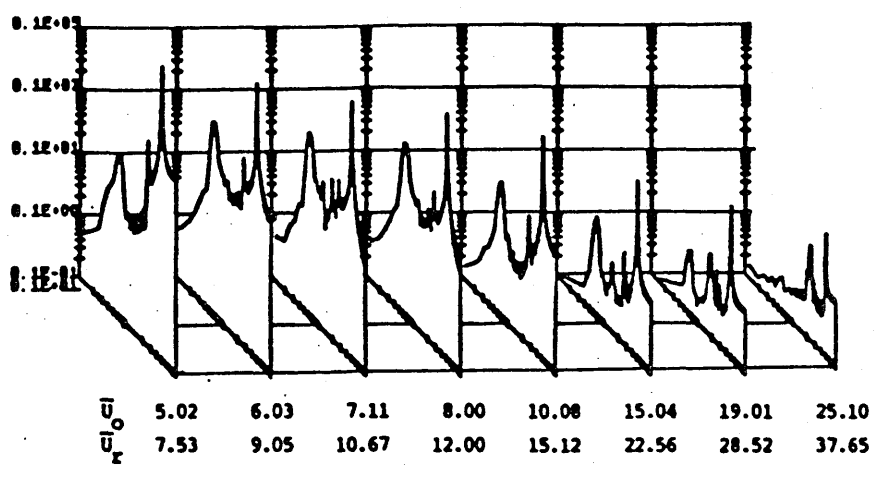


(d) $X_B = 8$
 $\hat{U}_r = 11.67$

Fig. 6.14(a) A collection of normalised torsional moment spectra for the upstream tower at four tandem configurations in uniform smooth flow for various reduced velocities.



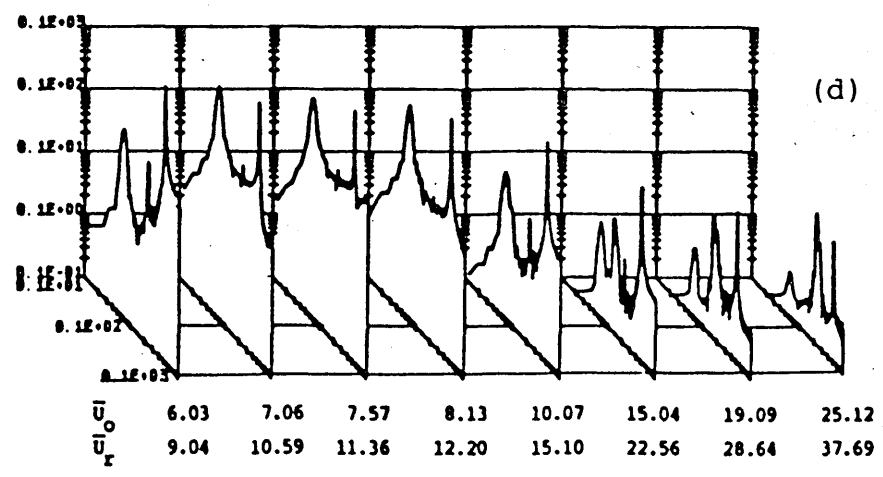
(b) $X_B = 4$
 $\hat{U}_r = 9.11$



(c) $X_B = 6$
 $\hat{U}_r = 11.55$

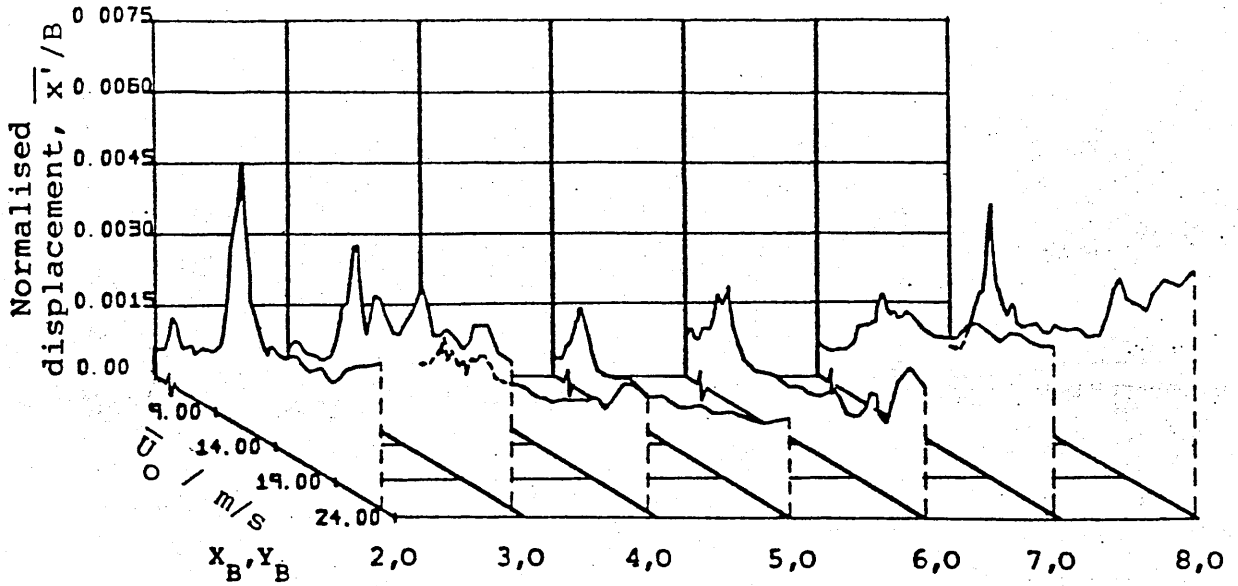
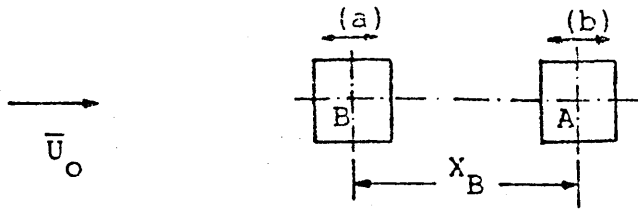
$$\frac{f S_M(f)}{(\frac{1}{2} \rho \bar{U}_O^2 B^2 H)^2}$$

Graph axes: \bar{U}_O, \bar{U}_r (horizontal), f (vertical)

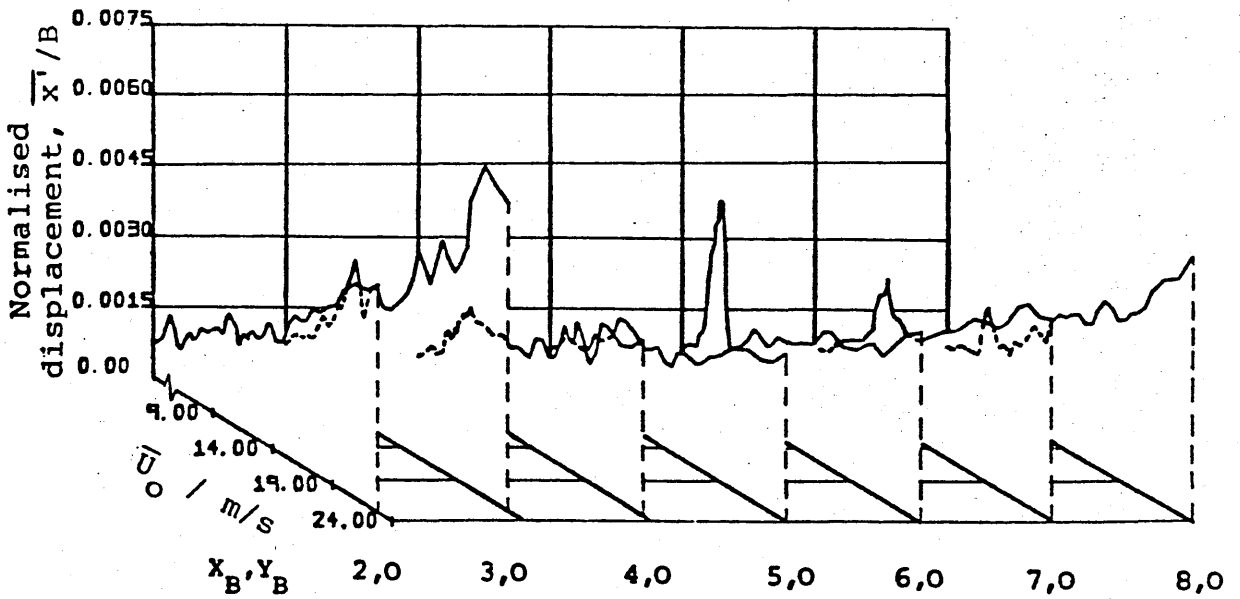


(d) $X_B = 8$
 $\hat{U}_r = 11.67$

Fig. 6.14(b) A collection of normalised torsional moment spectra for the downstream tower at four tandem configurations in uniform smooth flow for various reduced velocities.

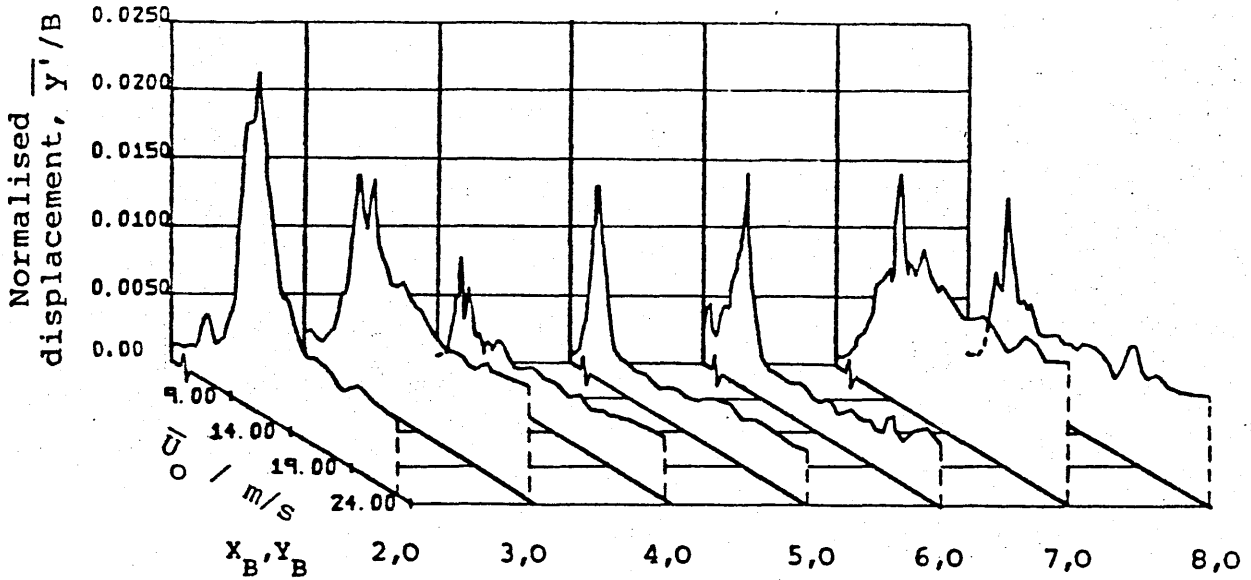
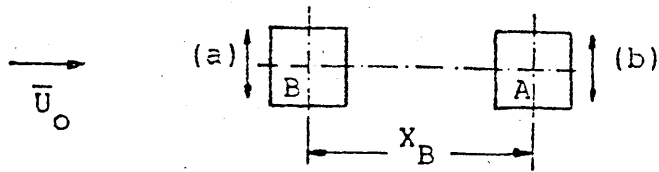


(a) along-wind response of model B

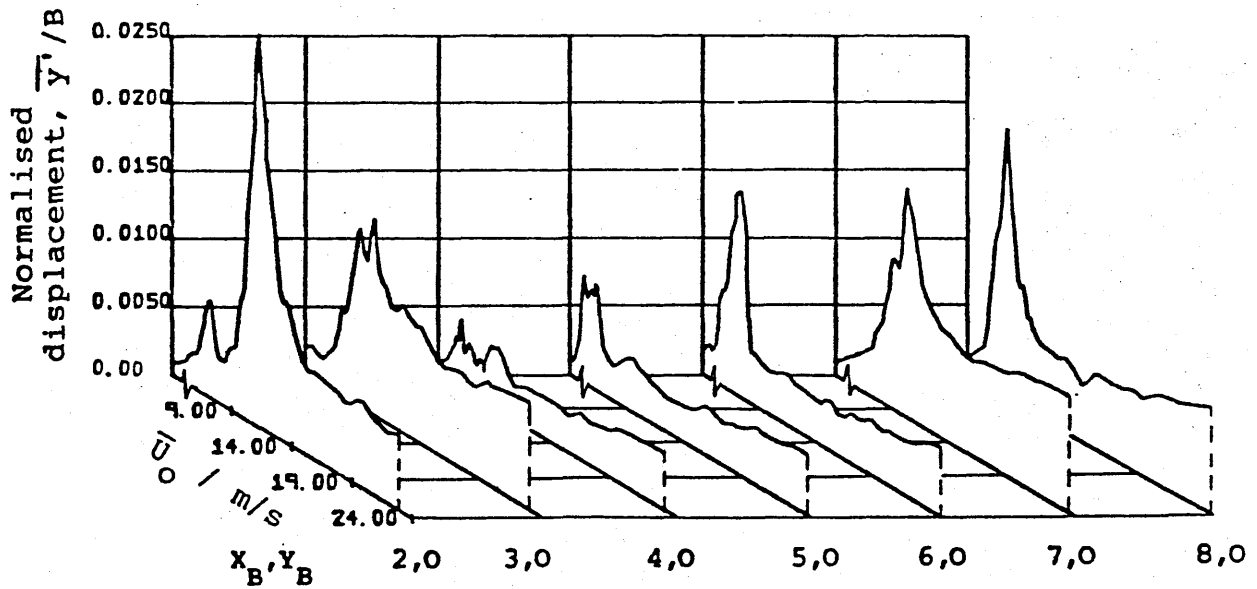


(b) along-wind response of model A

Figure 6.15 Variation of the normalised along-wind displacement at the top of the (a) upstream and (b) downstream tower with mean wind velocity in uniform smooth flow for various tandem arrangements.



(a) cross-wind response of model B



(b) cross-wind response of model A

Figure 6.16 Variation of the normalised cross-wind displacement at the top of the (a) upstream and (b) downstream tower with mean wind velocity in uniform smooth flow for various tandem arrangements.

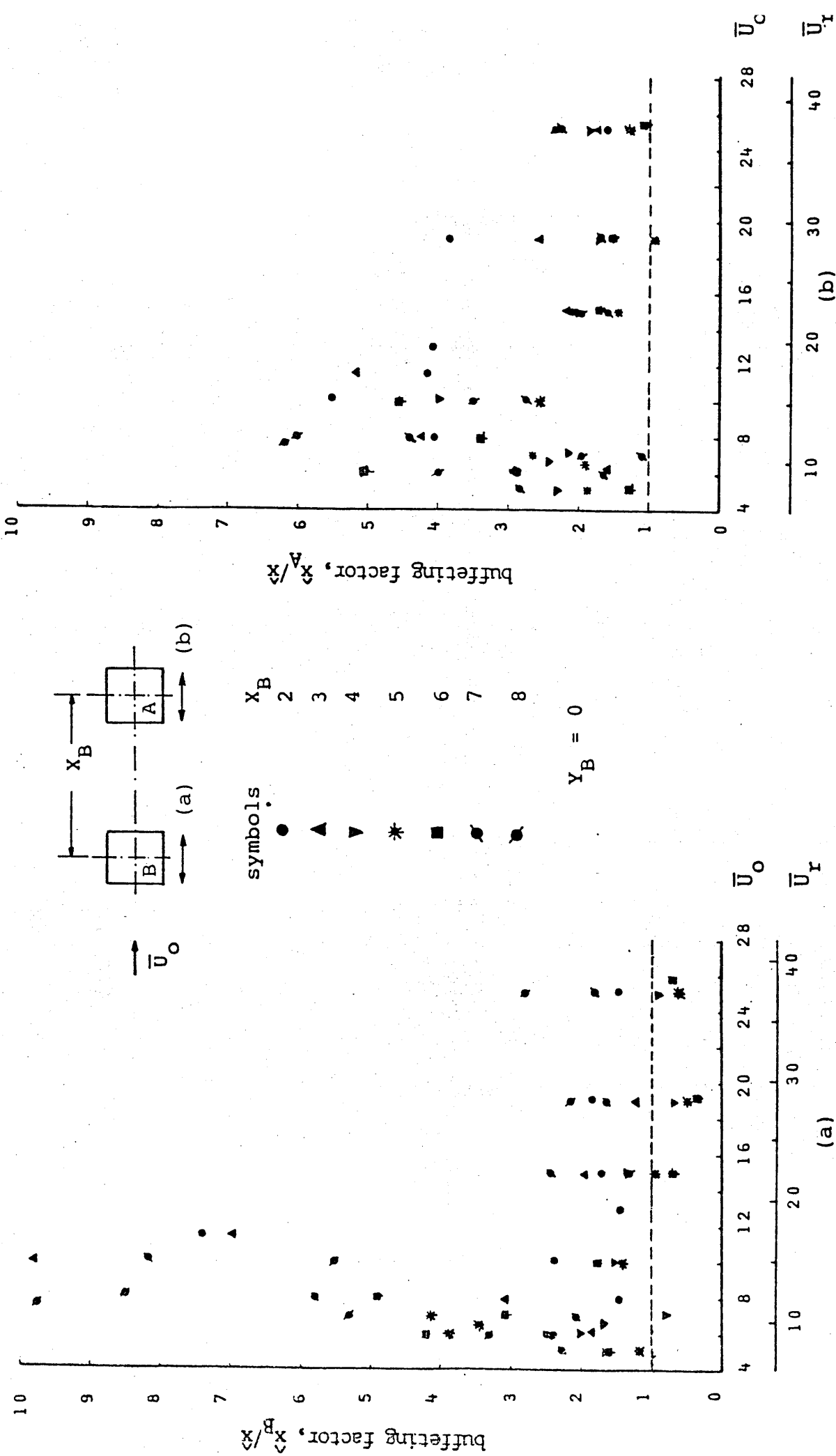


Figure 6.17 Normalised along-wind response of the (a) upstream model with interference from a downstream model and (b) downstream model with interference from an upstream model at various tandem arrangements in uniform smooth flow.

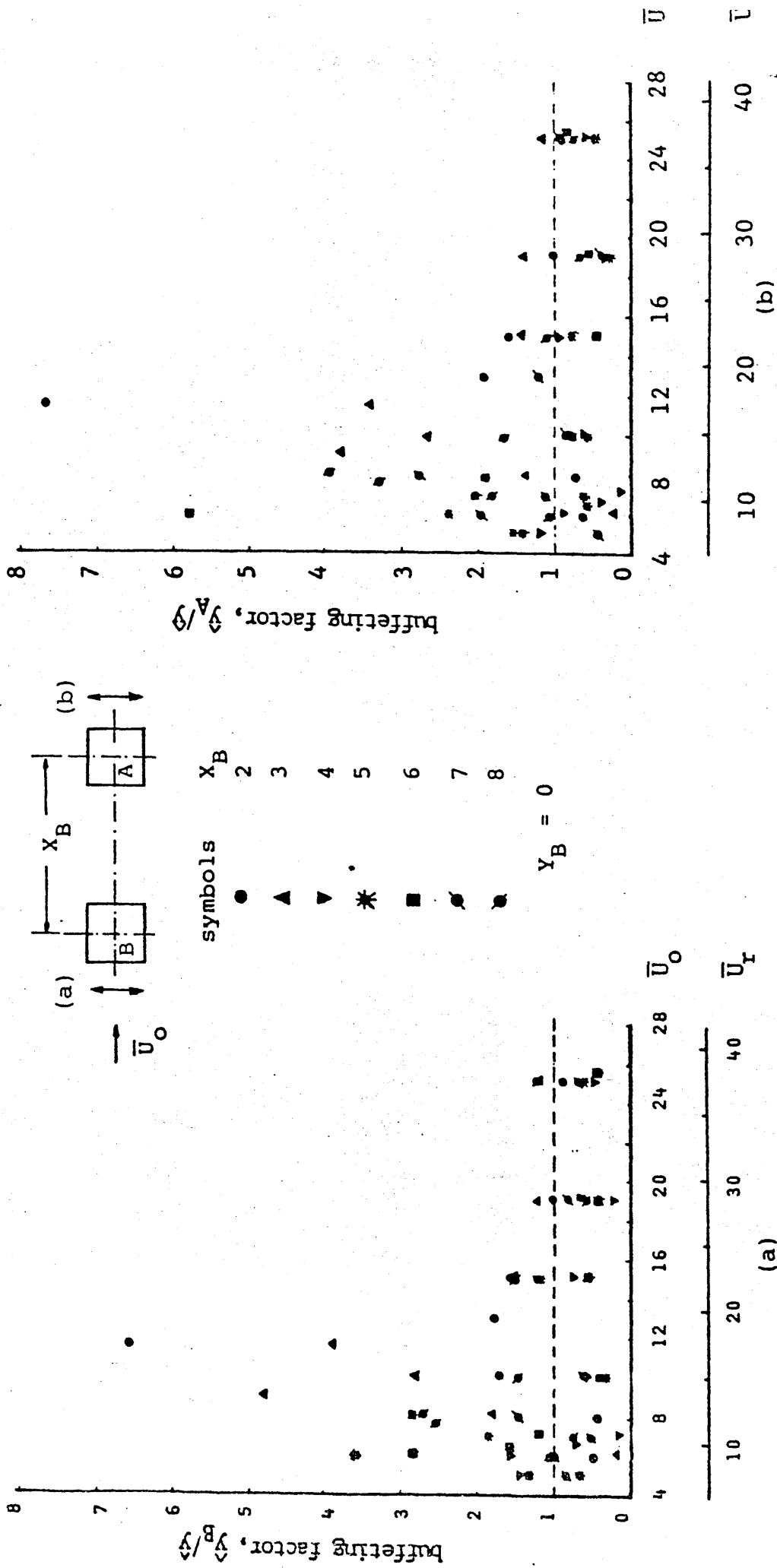


Figure 6.18 Normalised cross-wind response of the (a) upstream model with interference from a downstream model and (b) downstream model with interference from an upstream model at various tandem arrangements in uniform smooth flow.

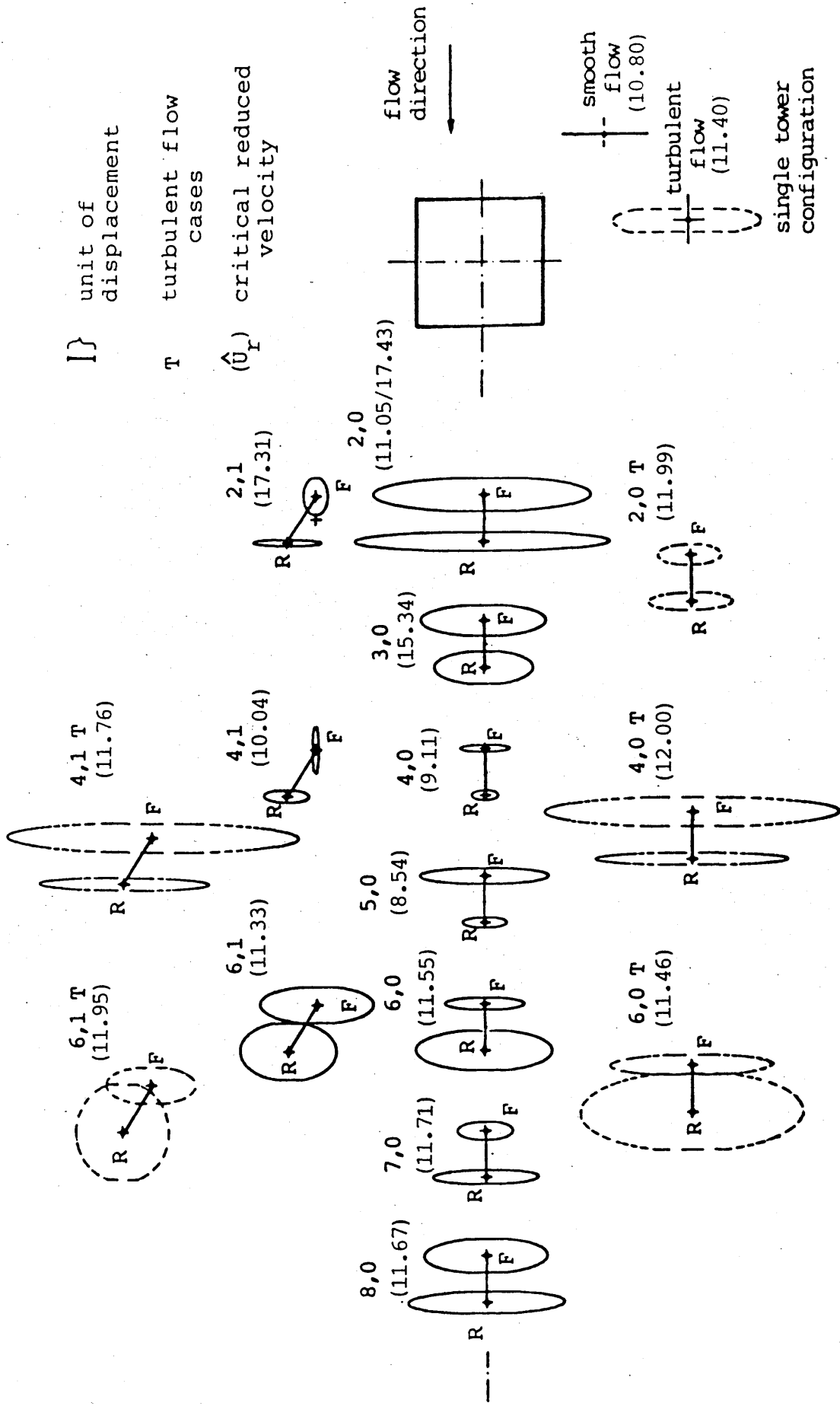
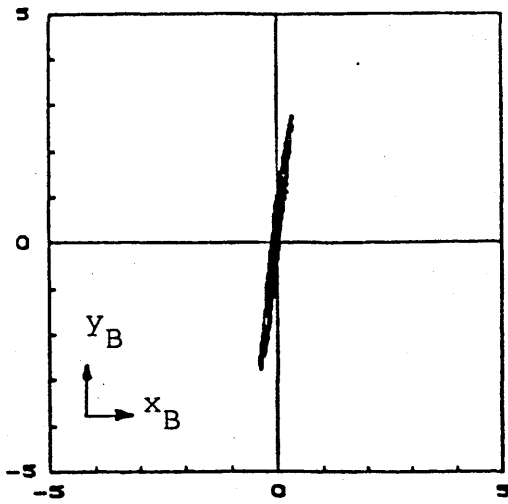


Figure 6.19 Oscillation loops composed from the maximum displacement (average peaks) measured at the top of the square towers of vortex excitation in both uniform smooth and turbulent flows, F-upstream and R-downstream tower.

Tower B



Tower A

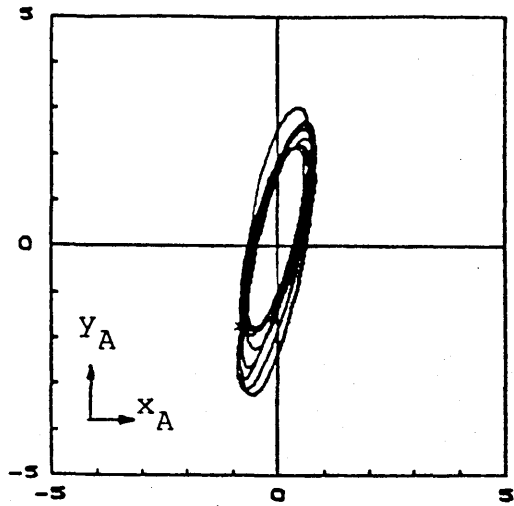
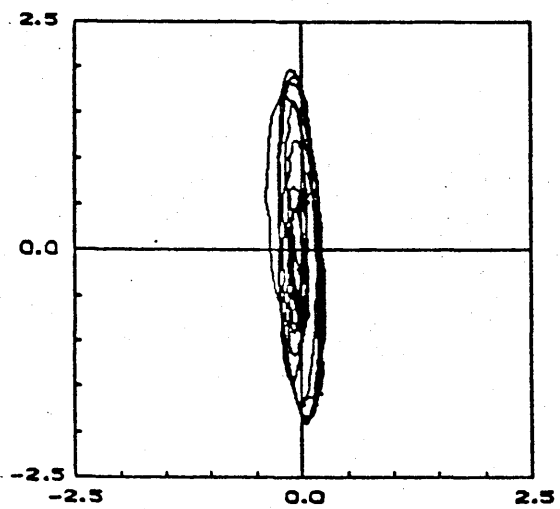
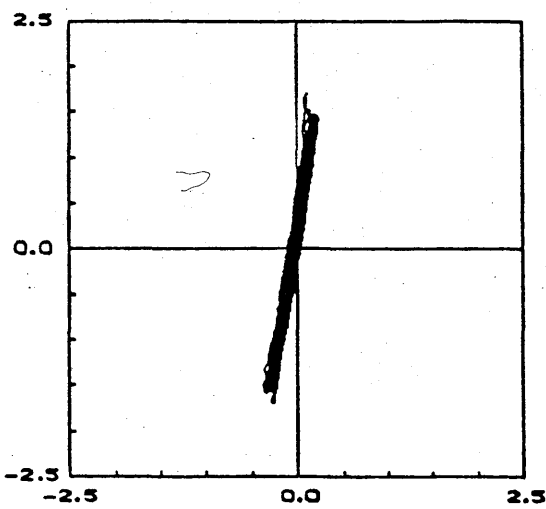
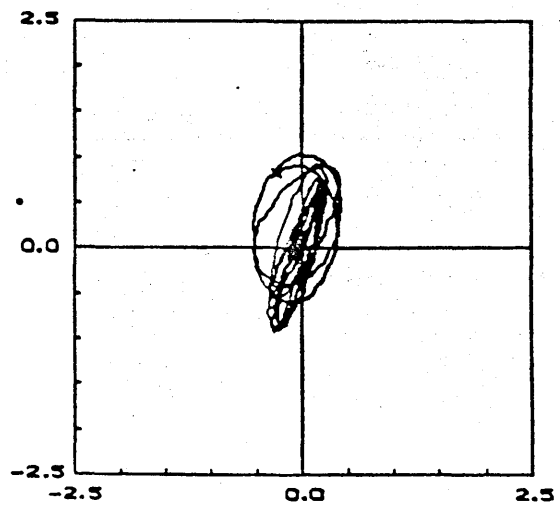
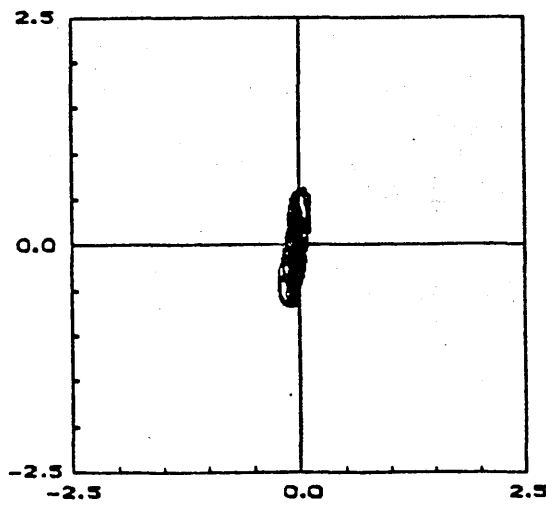
(a) $\bar{U}_O = 7.72$ m/s or $\bar{U}_r = 10.78$ (b) $\bar{U}_O = 8.00$ m/s or $\bar{U}_r = 12.11$ (c) $\bar{U}_O = 10.08$ m/s or $\bar{U}_r = 15.26$

Figure 6.20 X-Y plots of the displacement response at the tips of of the two towers separated by $6B$ in uniform smooth flow at $\bar{U}_r = 10.78, 12.11$ and 15.26 .

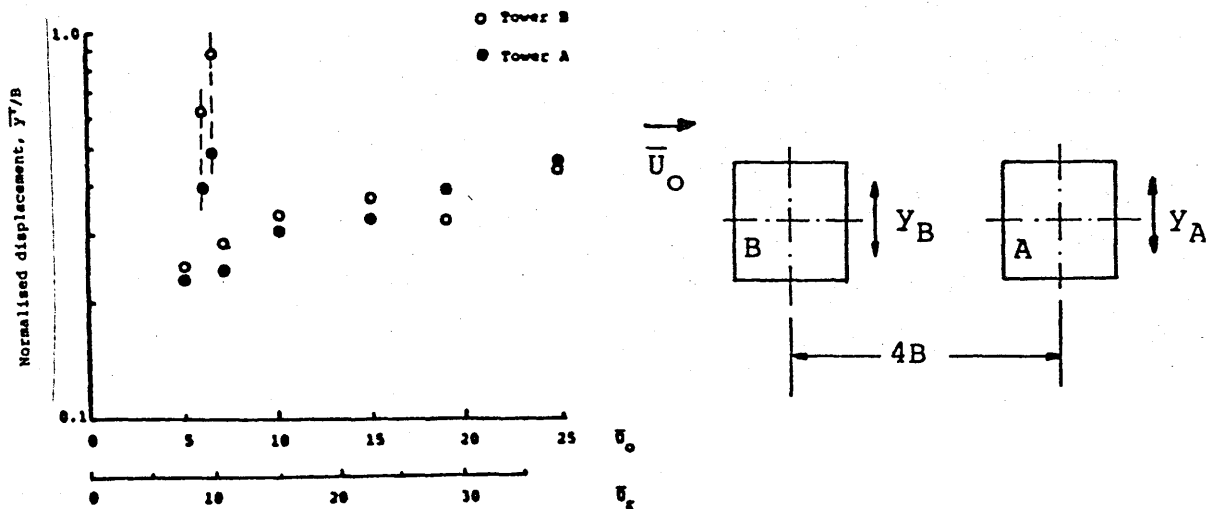
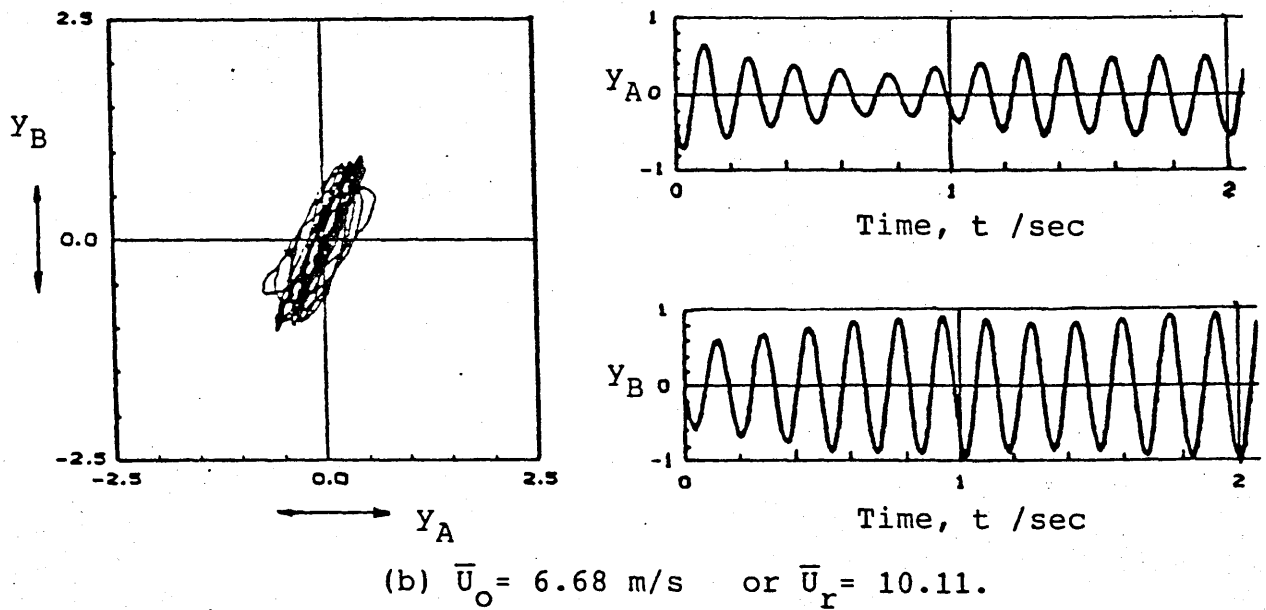
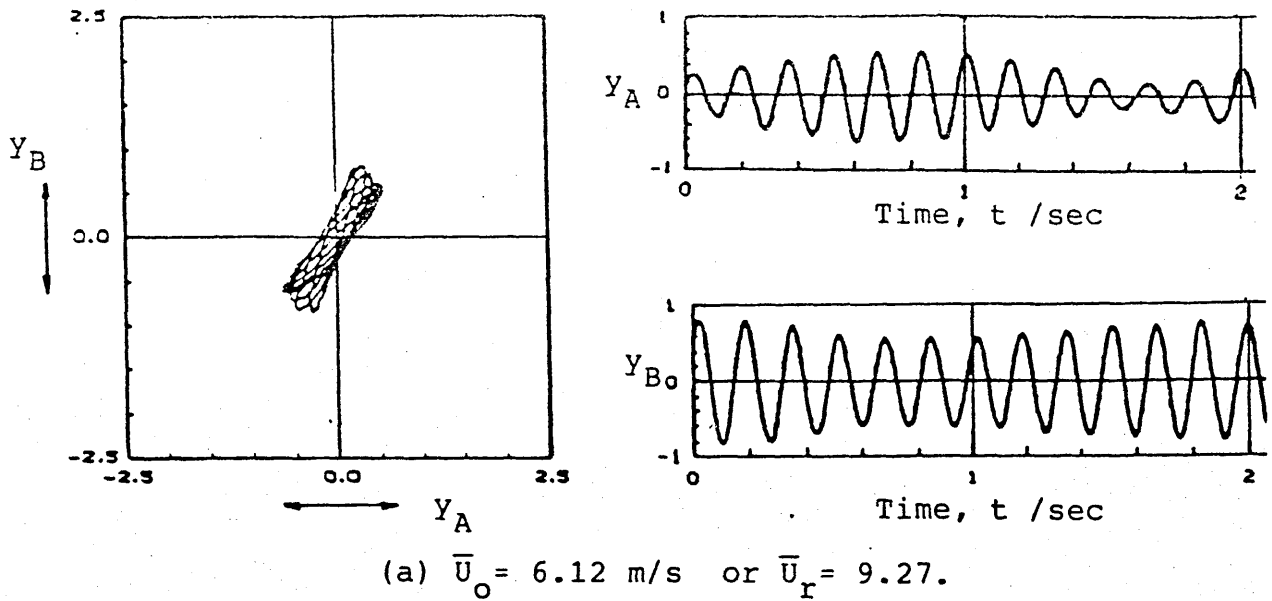
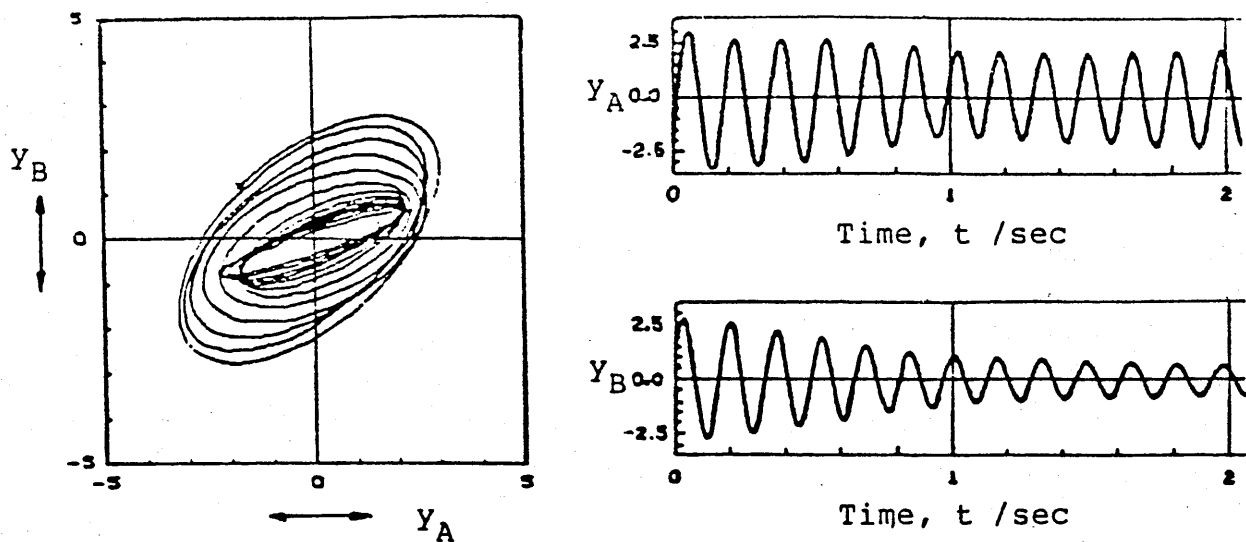
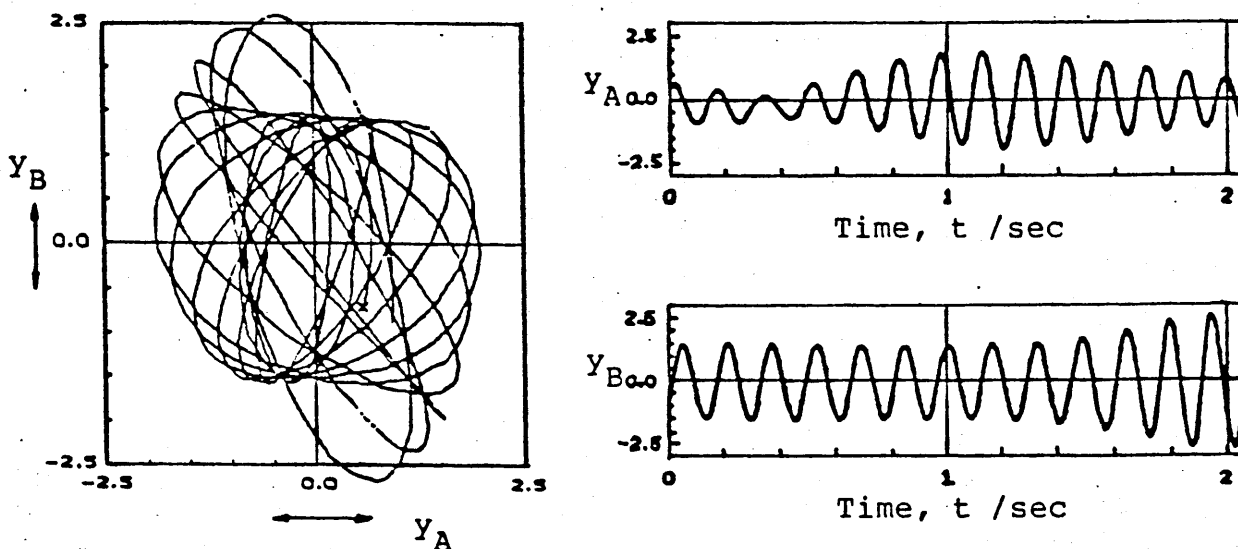


Fig. 6.21 Cross-wind displacement traces and oscillation loops composed from the cross-wind response of the two towers separated at a distance of $4B$ in uniform smooth flow at $\bar{U}_r = 9.27$ and 10.11 .



(a) $\bar{U}_O = 7.11$ m/s or $\bar{U}_r = 10.77$.



(b) $\bar{U}_O = 8.00$ m/s or $\bar{U}_r = 12.12$.

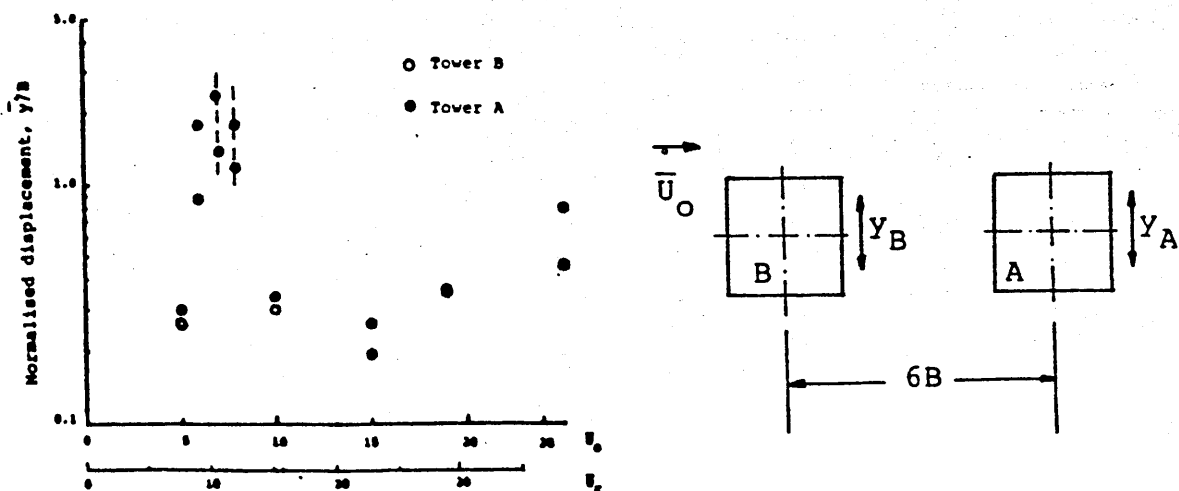


Fig. 6.22 Cross-wind displacement traces and oscillation loops composed from the cross-wind response of the two towers separated at a distance of $6B$ in uniform smooth flow at $\bar{U}_r = 10.77$ and 12.12 .

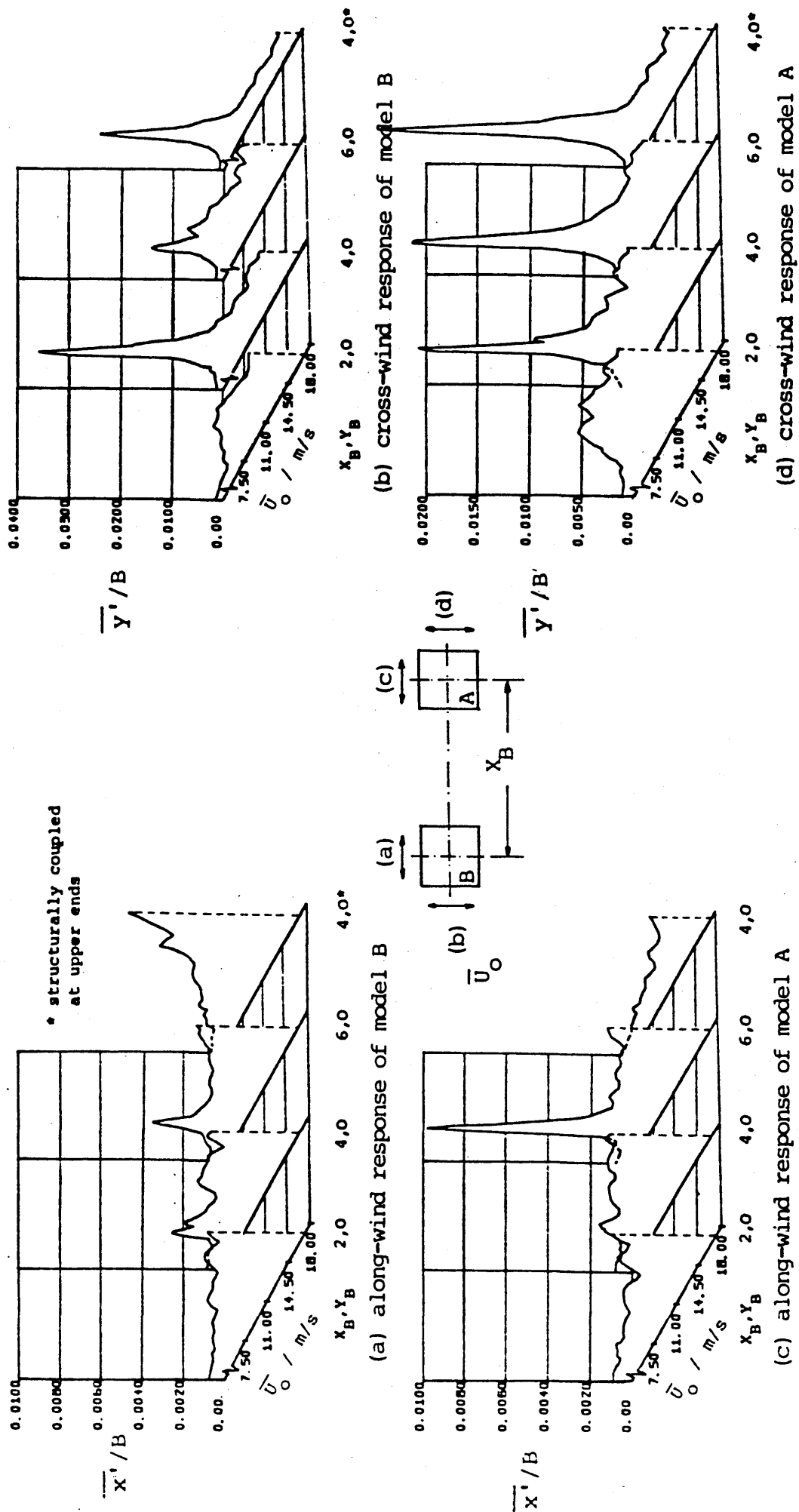
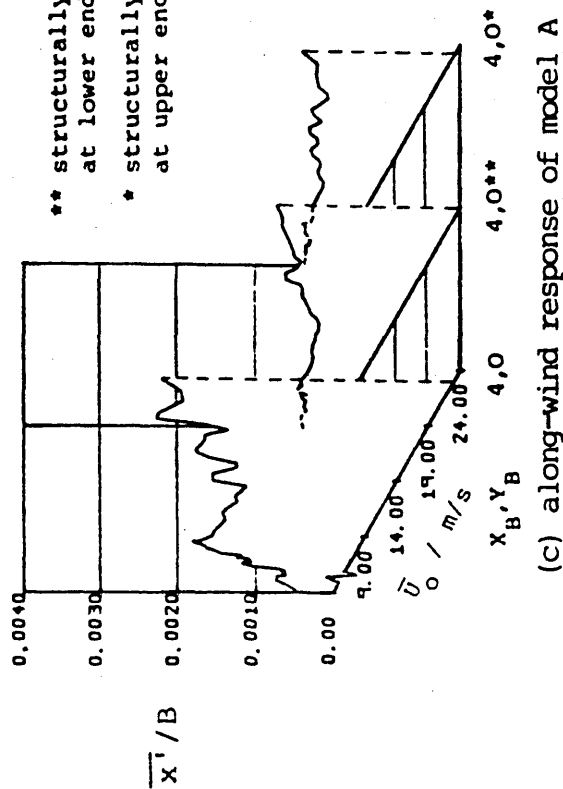
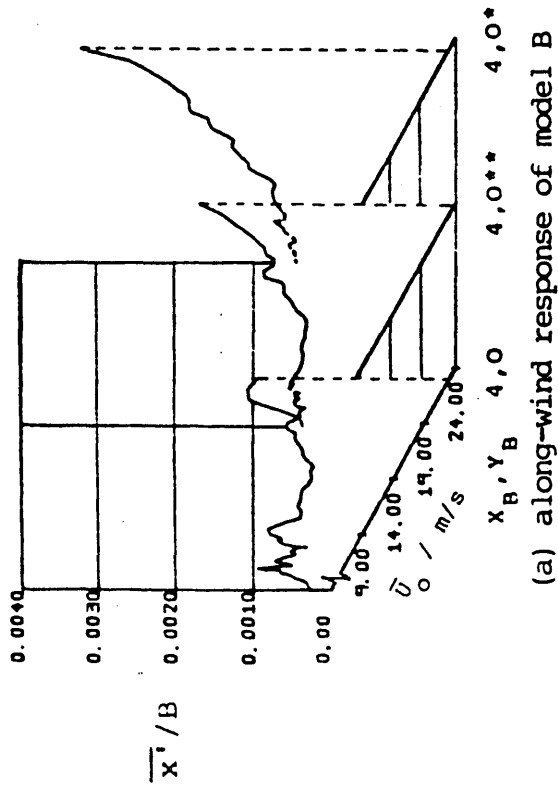


Figure 6.23 Variation of normalised displacement at the top of the upstream and downstream towers with mean wind velocity in uniform turbulent flow for various tandem arrangements.



** structurally coupled
at lower ends
* structurally coupled
at upper ends

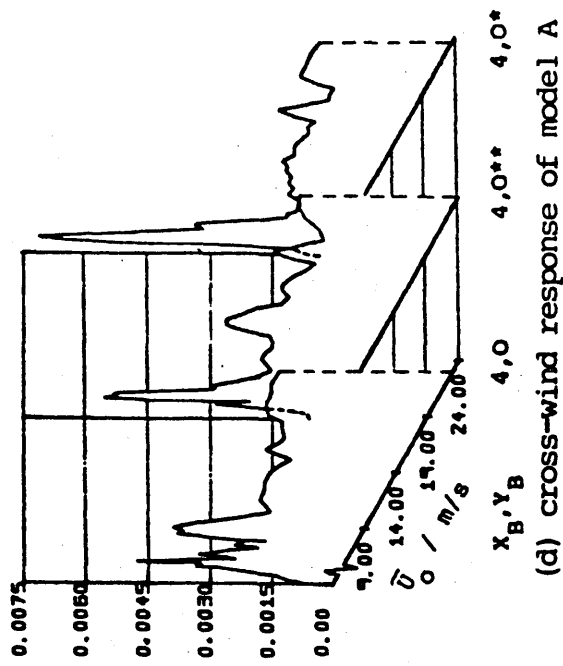
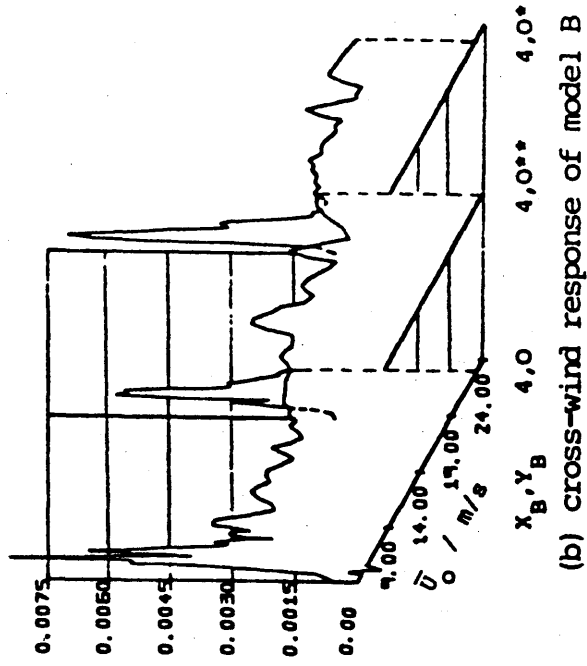
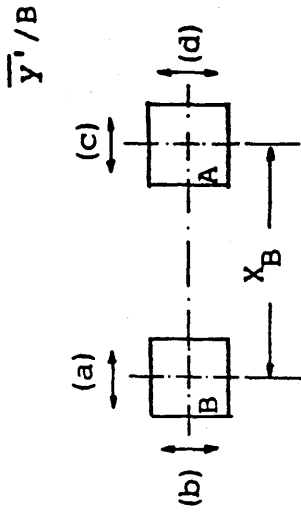
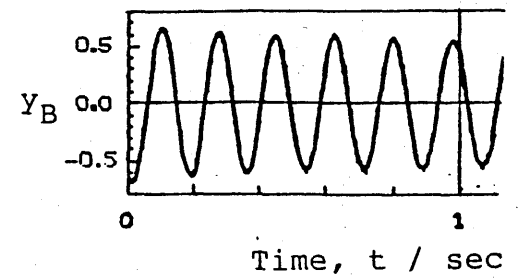
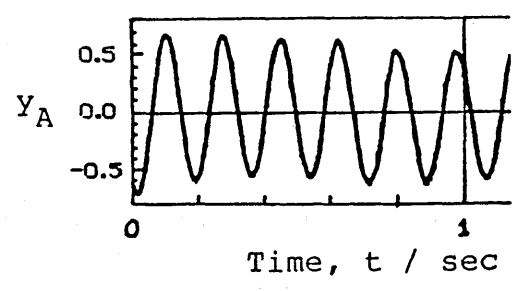
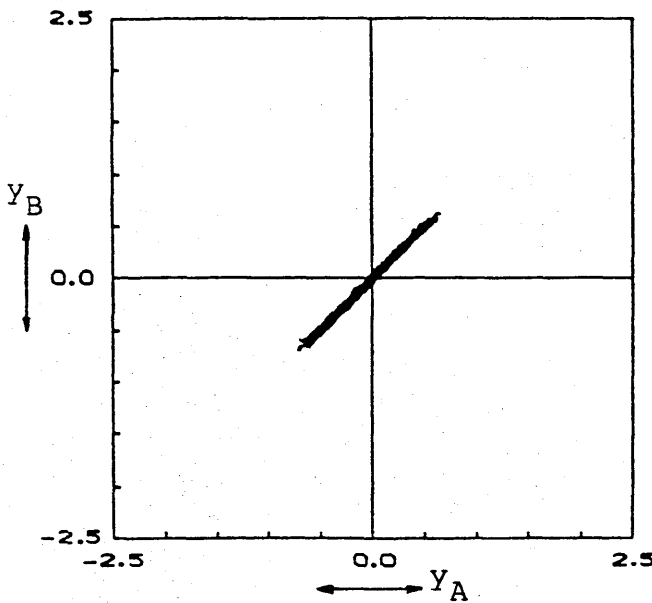


Figure 6.24 Variation of normalised displacement at the top of the upstream and downstream towers with mean wind velocity in uniform smooth flow for various tandem arrangements.



$\bar{U}_O = 5.95 \text{ m/s}$ or $\bar{U}_r = 9.01$

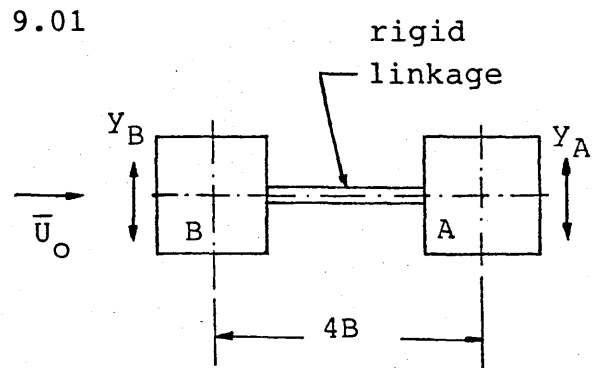
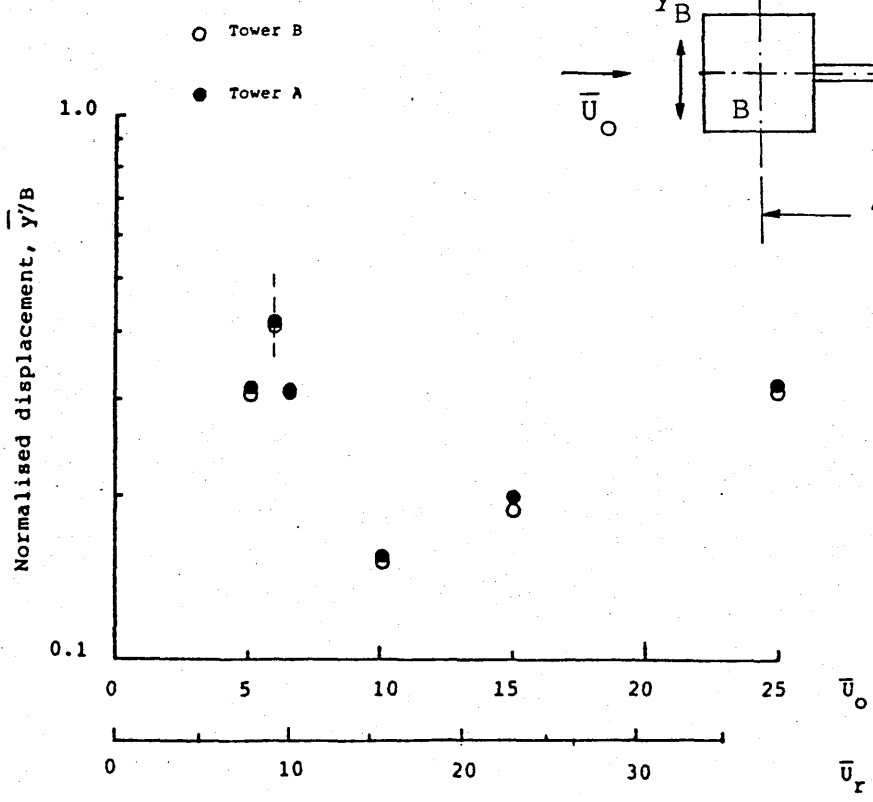
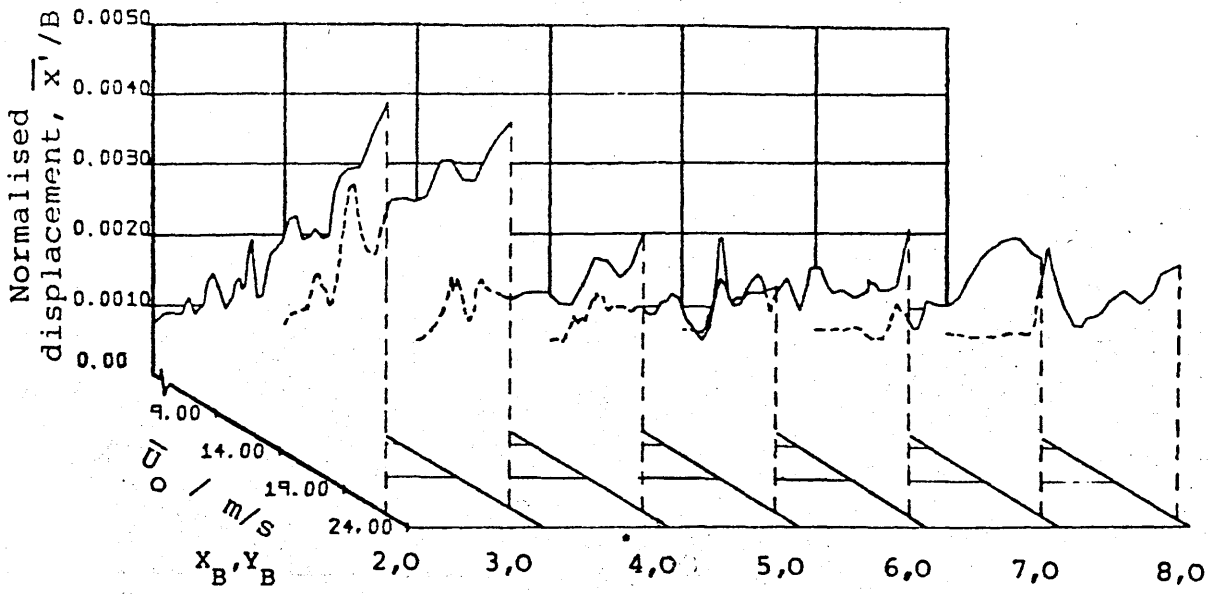
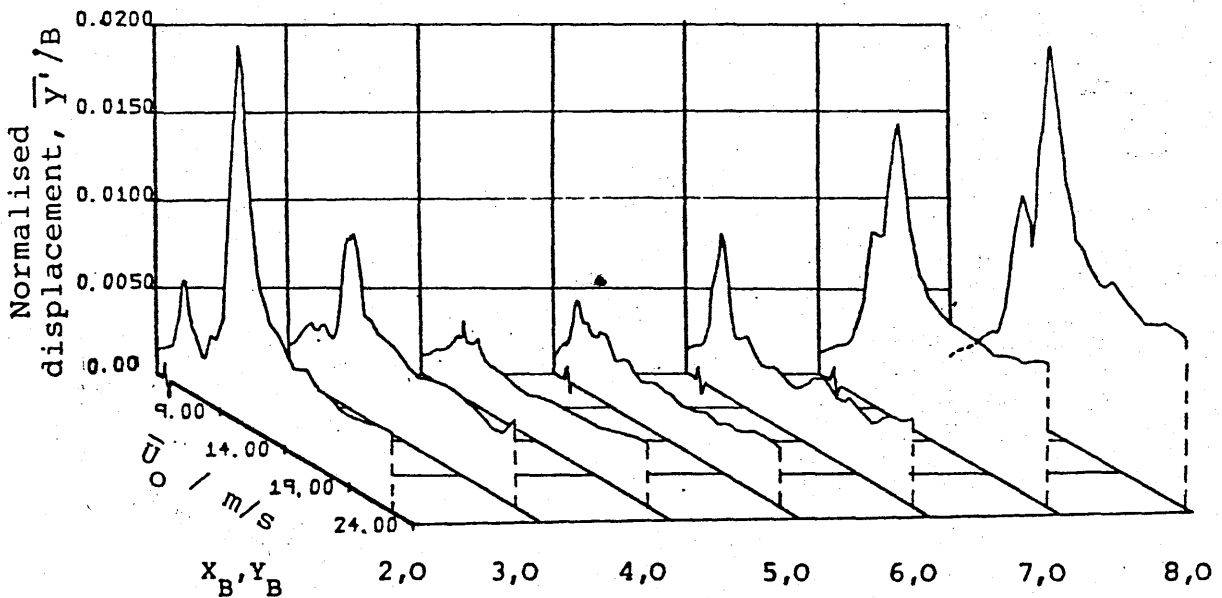
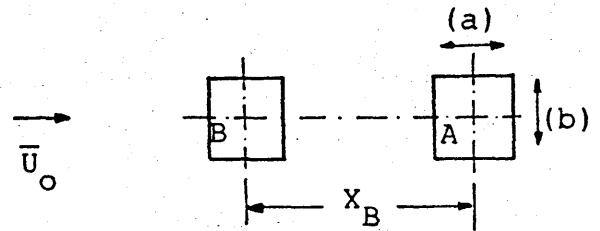


Figure 6.25 Cross-wind displacement traces and oscillation loops composed from the cross-wind response of the two towers separated $4B$ apart and with their free ends structurally coupled in uniform smooth flow at $\bar{U}_r = 9.01$.

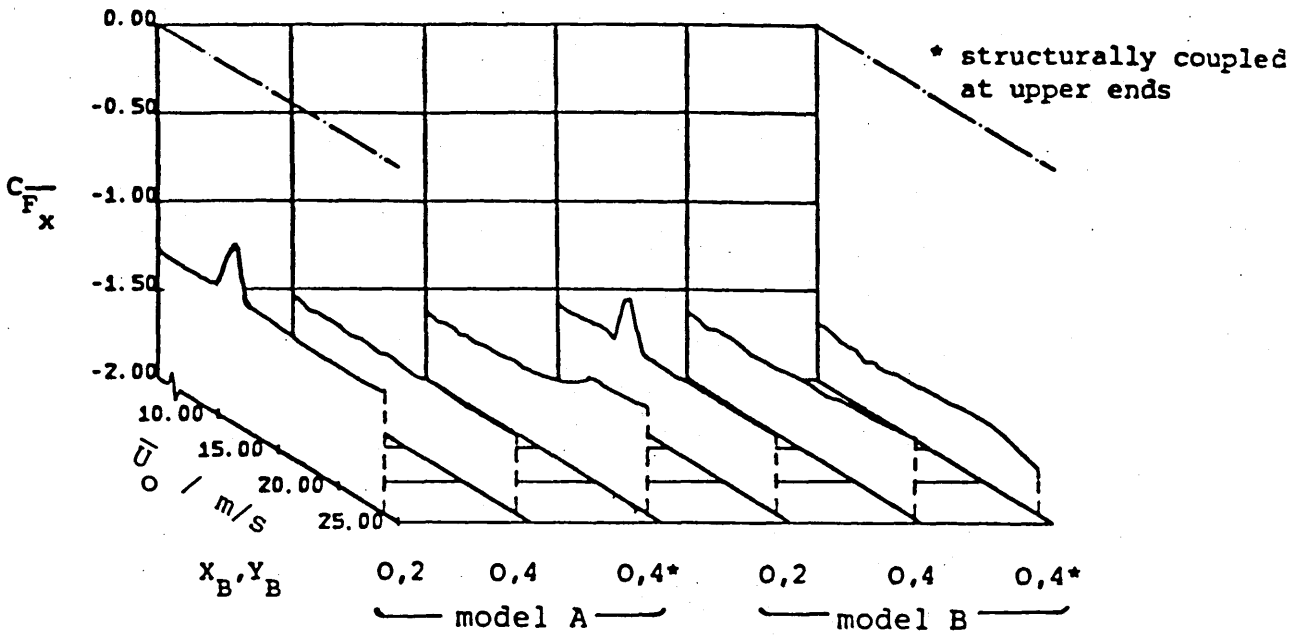
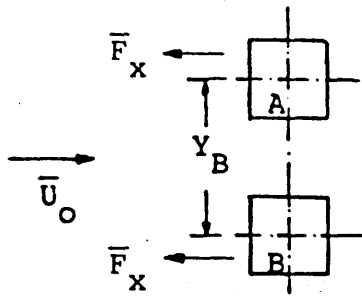


(a) along-wind response of model A

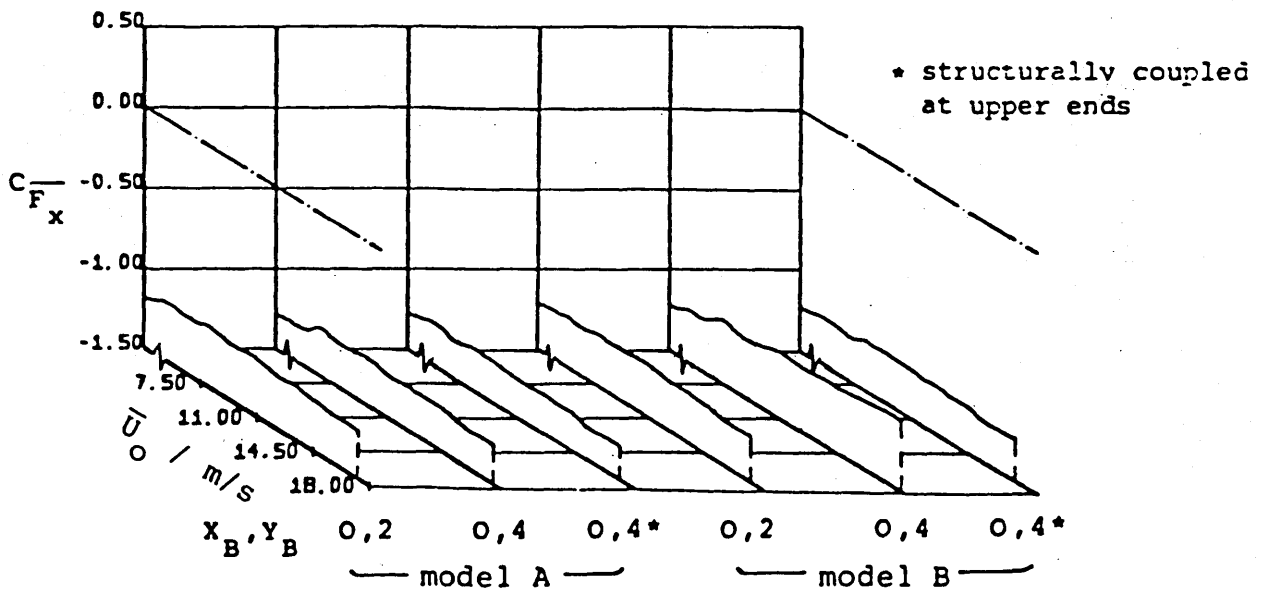


(b) cross-wind response of model A

Figure 6.26 Variation of normalised amplitude at the top of the downstream square tower with wind velocity in uniform smooth flow for various tandem arrangements. The upstream model (B) is wedged.

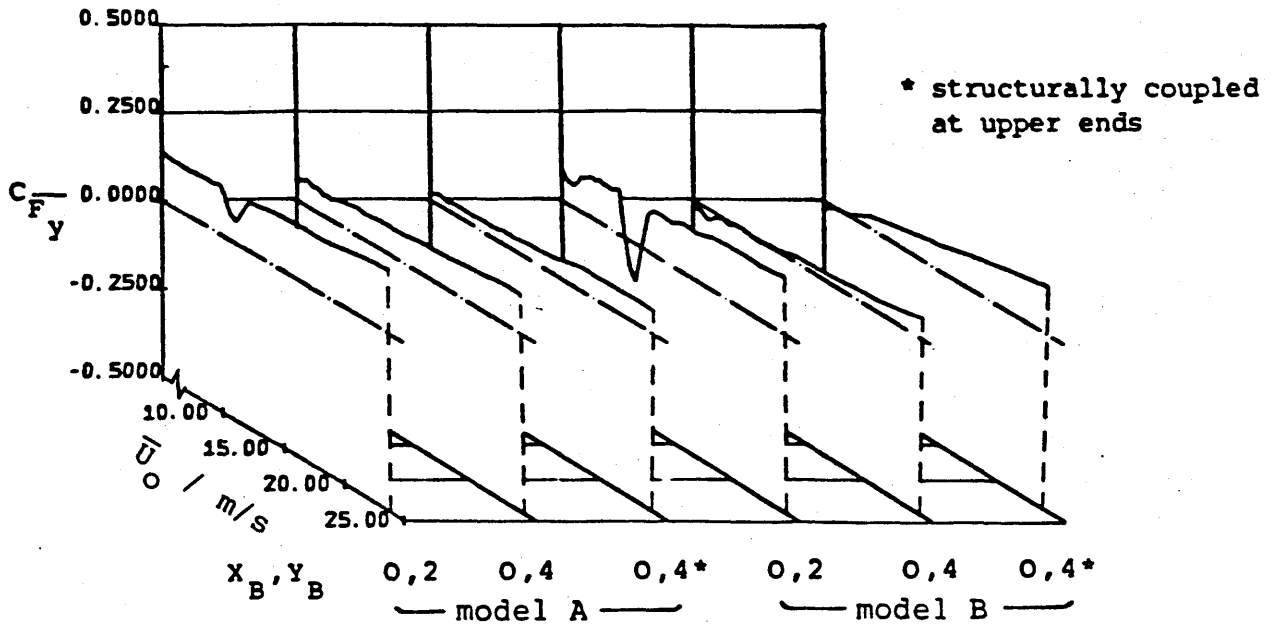
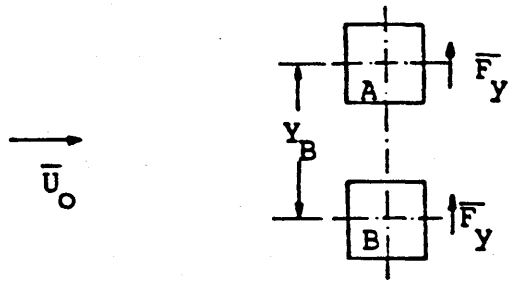


(a) Time-mean along-wind force response of model A and B in uniform smooth flow

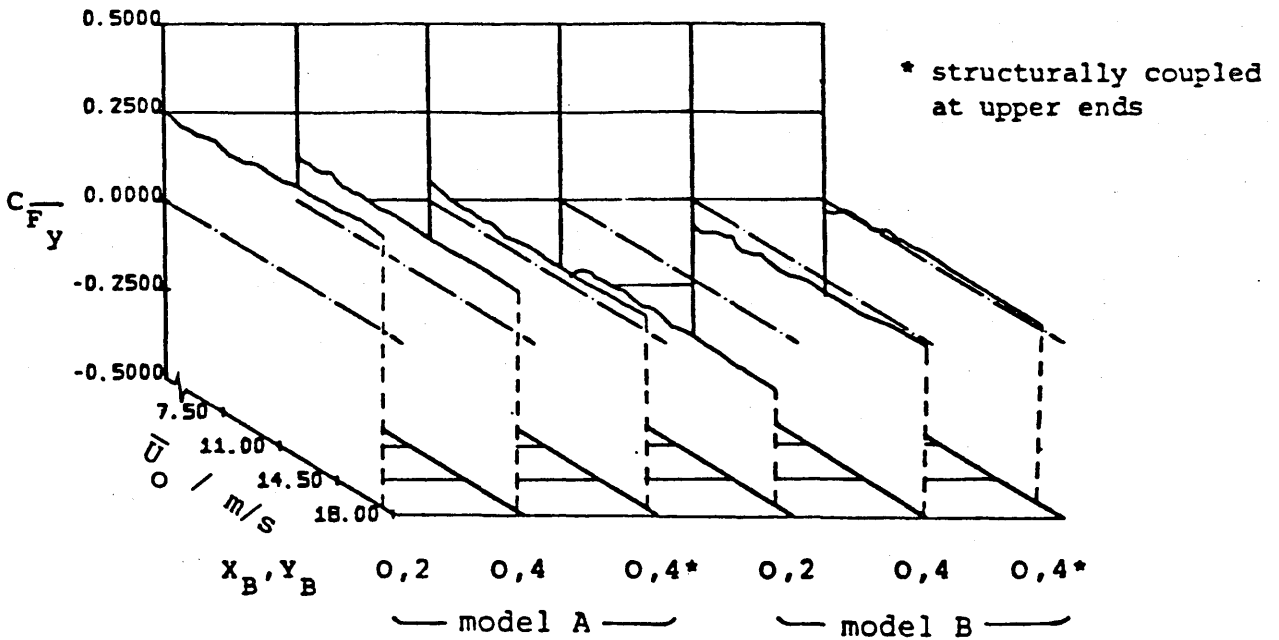


(b) Time-mean along-wind force response of model A and B in uniform turbulent flow

Figure 6.27 Variation in the coefficients of time-mean along-wind force on the towers with mean flow velocity in (a) uniform smooth and (b) uniform turbulent flow for various side by side arrangements.

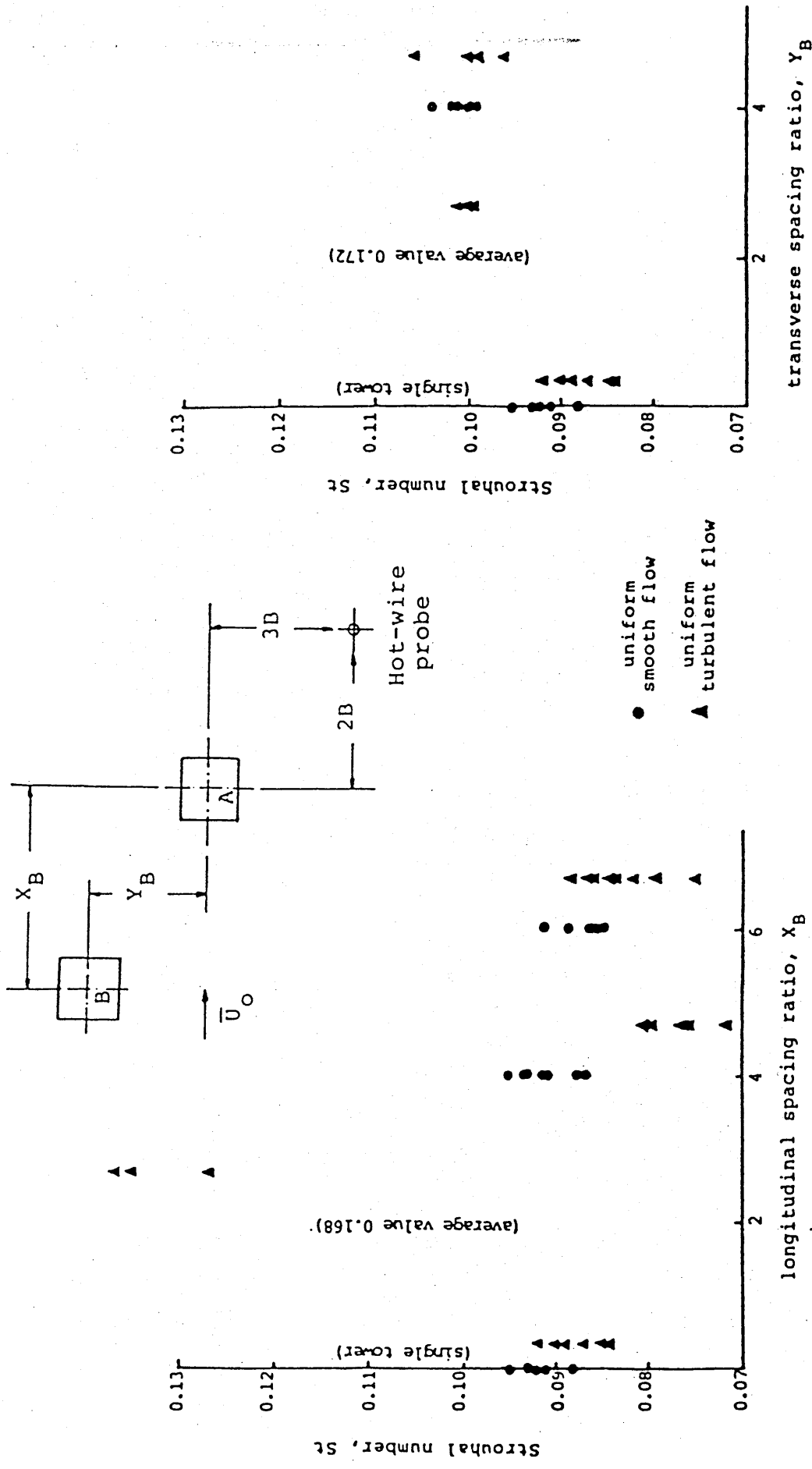


(a) Time-mean cross-wind force response of model A and B in uniform smooth flow



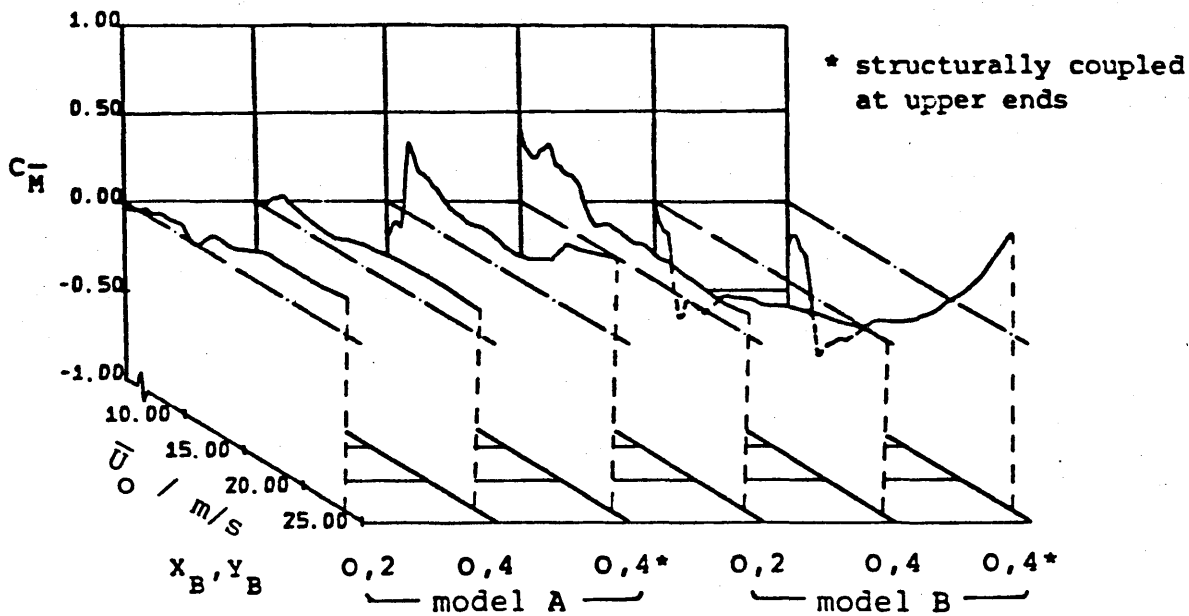
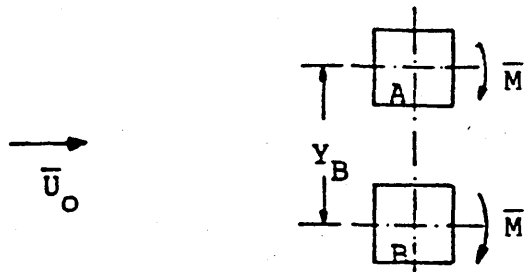
(b) Time-mean cross-wind force response of model A and B in uniform turbulent flow

Figure 6.28 Variation in the coefficients of time-mean cross-wind force on the towers with mean flow velocity in (a) uniform smooth and (b) uniform turbulent flow for various side by side arrangements.

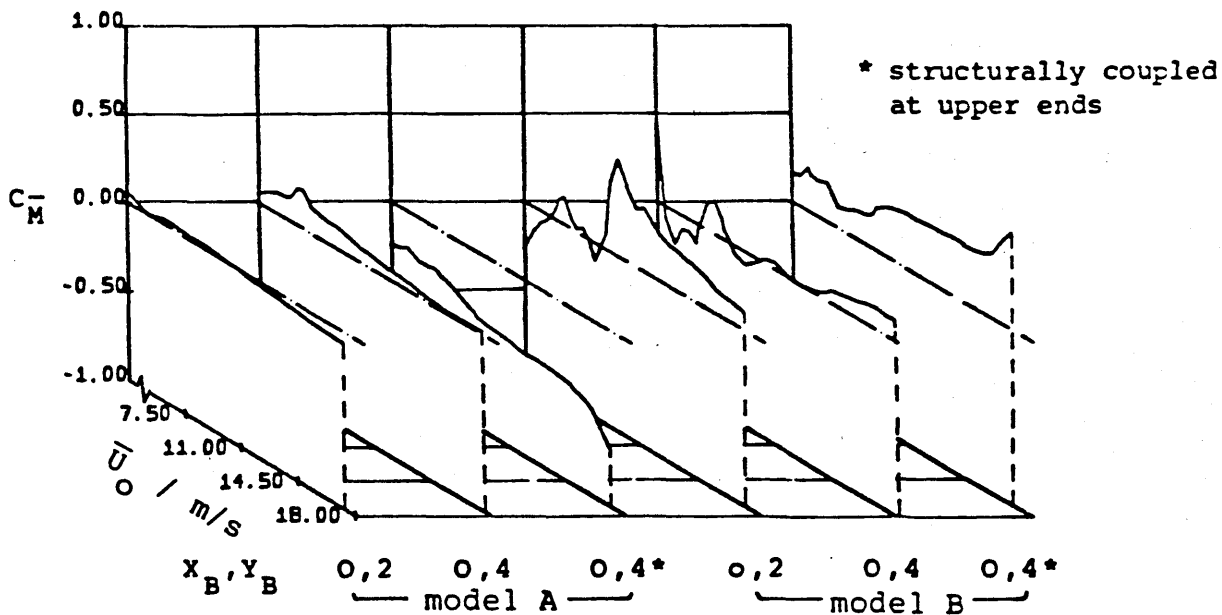


(a) Staggered arrangements ($Y_B = 1$)
 (b) Side by side arrangements

Figure 6.29 Strouhal number behind the downstream tower in either (a) staggered or (b) side by side arrangements in both uniform smooth and turbulent flows. Note that the values measured in turbulent flow are shown next to those measured in smooth flow for all arrangements.

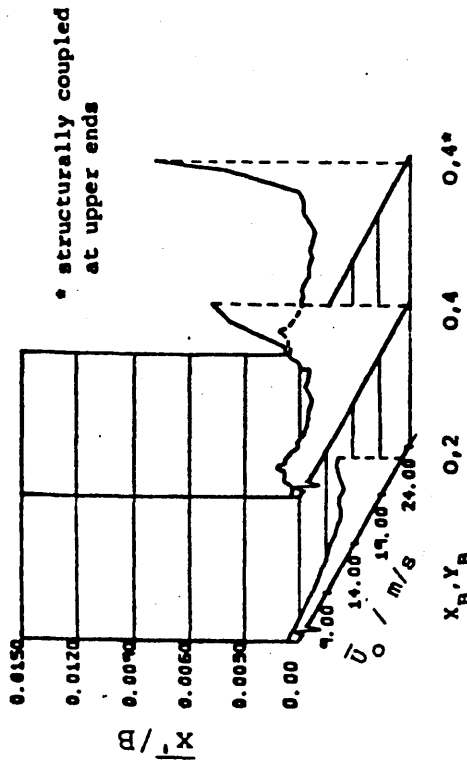


(a) Time-mean torsional response of model A and B in uniform smooth flow

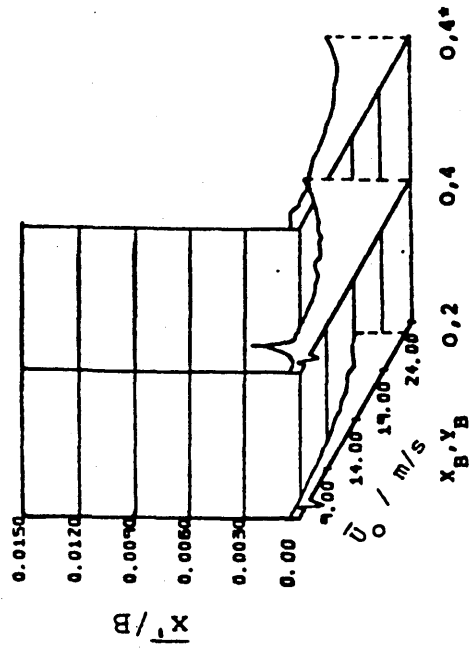


(b) Time mean torsional response of model A and B in uniform turbulent flow

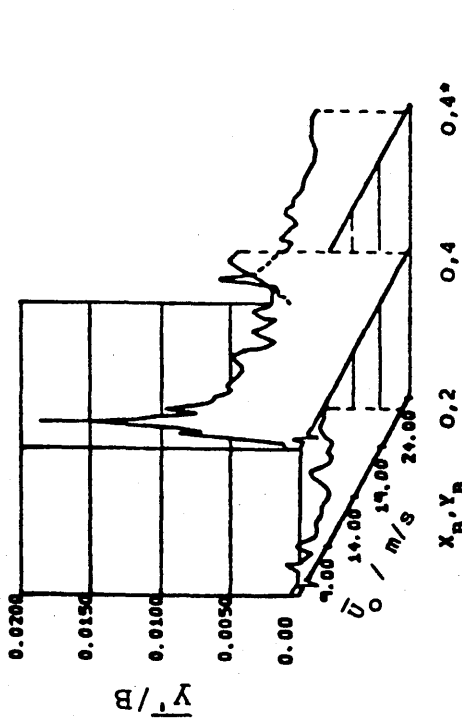
Figure 6.30 Variation in the coefficients of time-mean torsional moment on the towers with mean flow velocity in (a) uniform smooth and (b) uniform turbulent flow for various side by side arrangements.



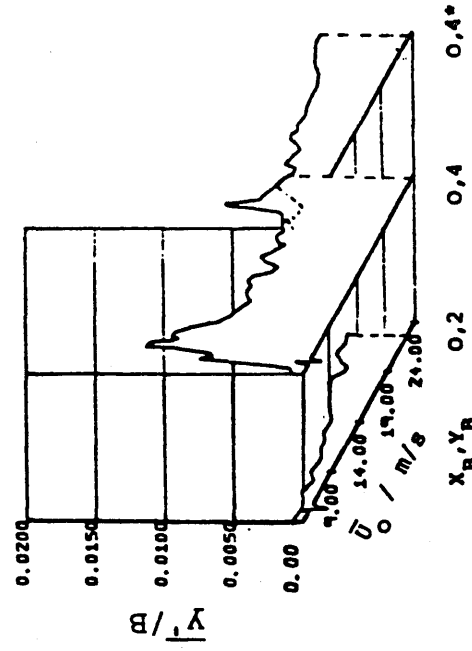
(a) along-wind response of model B



(c) along-wind response of model A



(b) cross-wind response of model B



(d) cross-wind response of model A

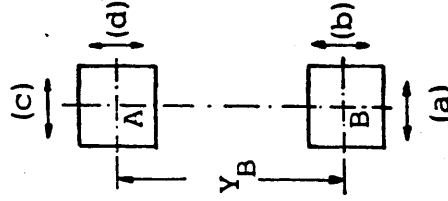


Figure 6.31 Variation of the normalised displacement at the top of the upstream and downstream towers with mean wind velocity in uniform smooth flow for various side by side arrangements.

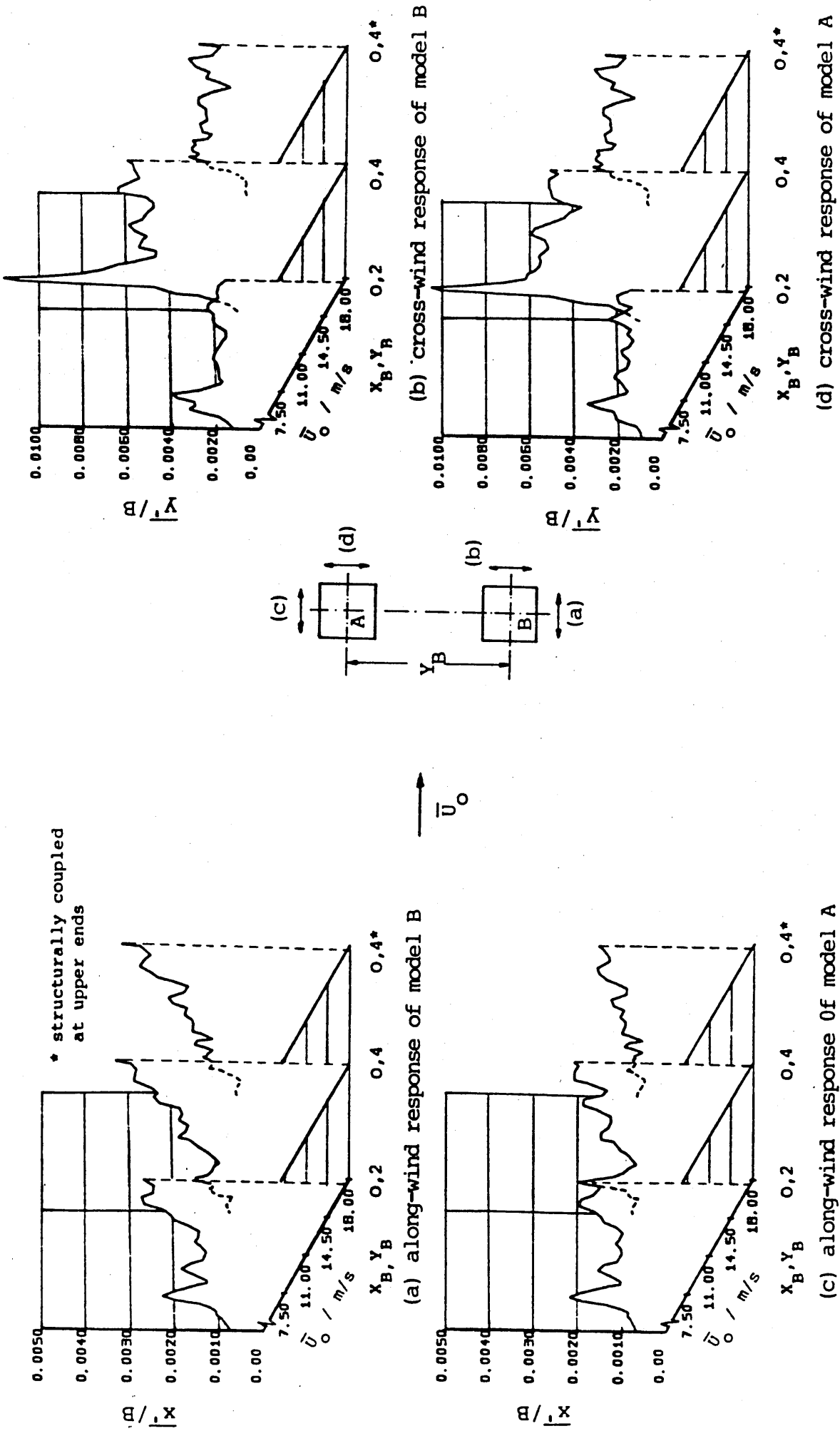
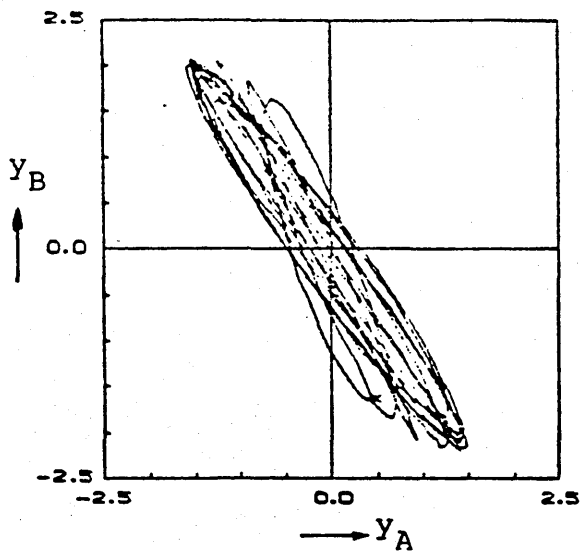
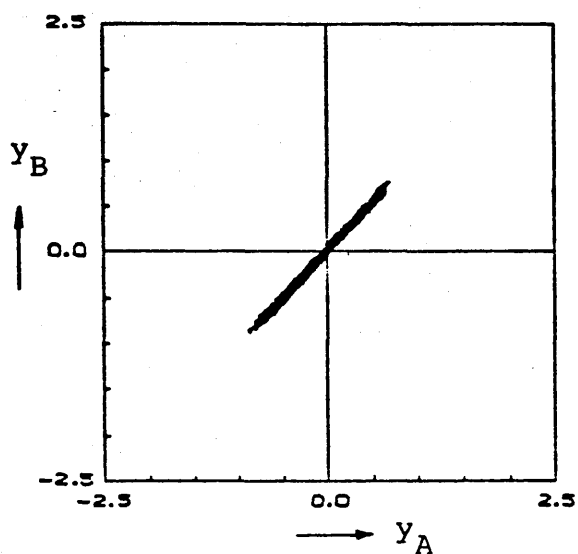
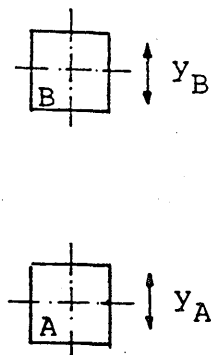


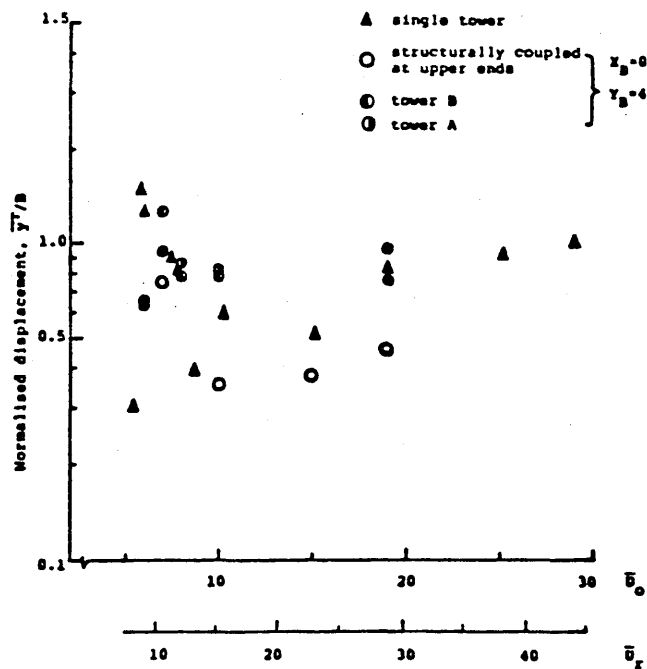
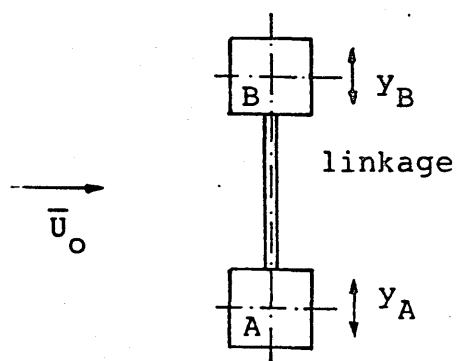
Figure 6.32 Variation of the normalised displacement at the top of the upstream and downstream towers with mean wind velocity in uniform turbulent flow for various side by side arrangements.



(a) $\bar{U}_O = 7.06$ m/s or
 $\bar{U}_R = 10.69$.

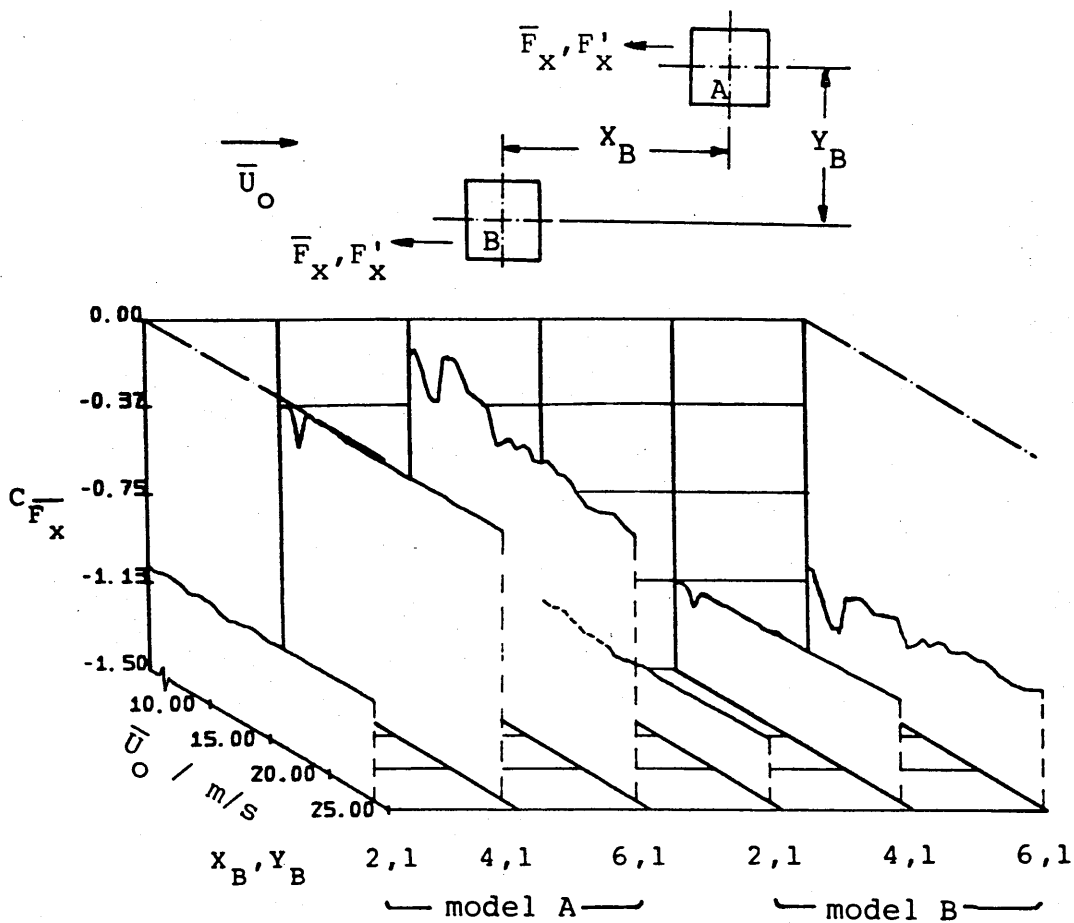


(b) $\bar{U}_O = 7.04$ m/s or
 $\bar{U}_R = 10.66$.

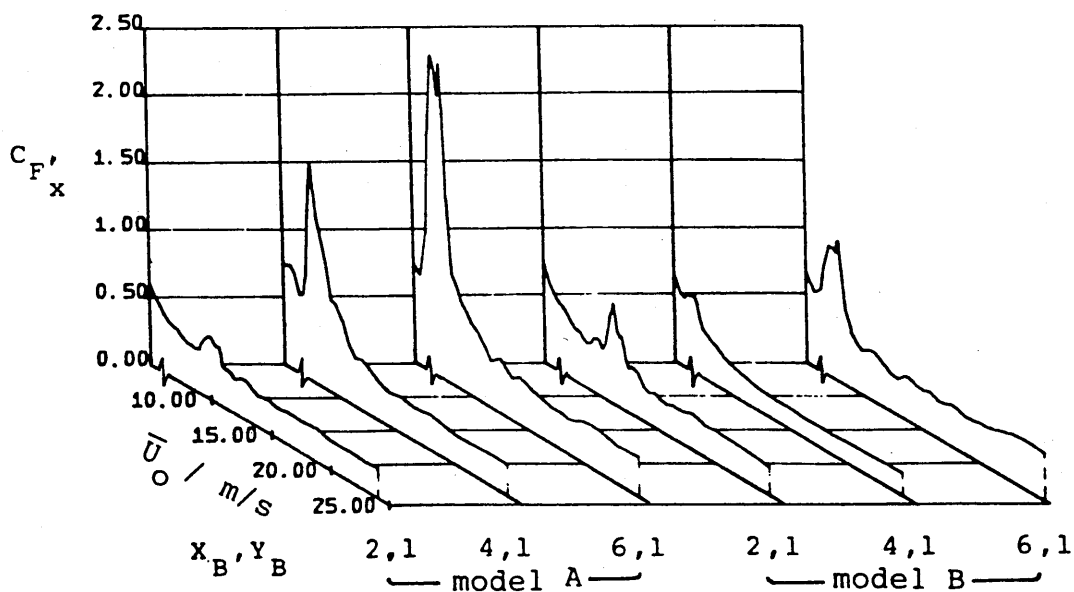


$X_B = 0$ and
 $Y_B = 4$

Figure 6.33 Oscillation loops composed from the cross-wind response of the two towers separated $4B$ apart (transversely) and (a) without and (b) with their free ends structurally coupled in uniform smooth flow.

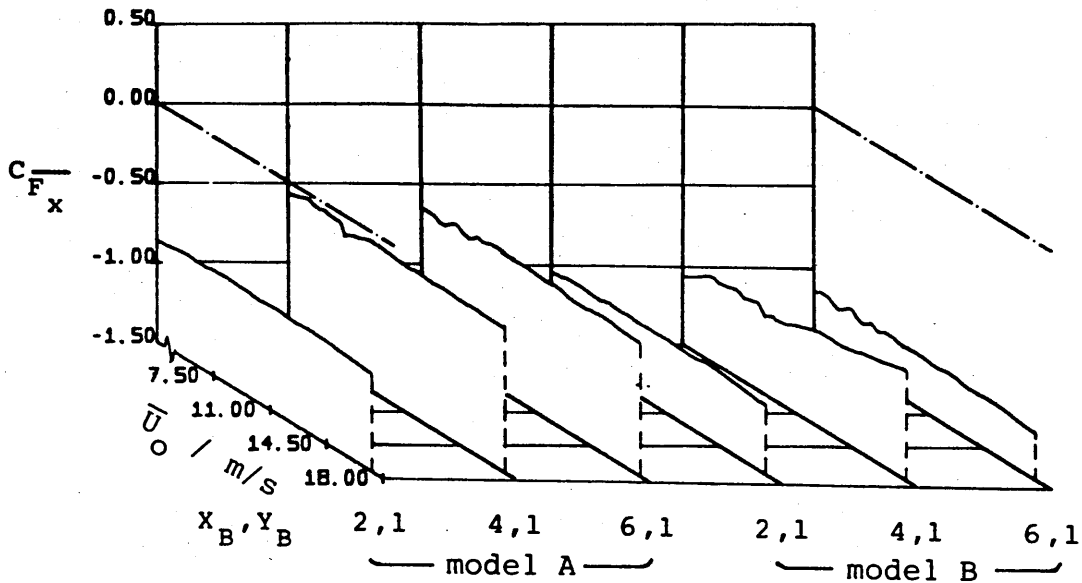
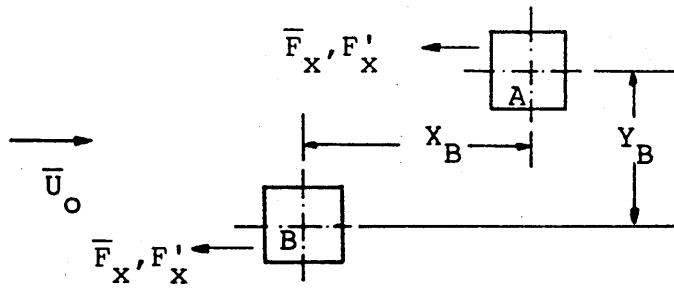


(a) Time-mean along-wind force coefficient of tower A and B

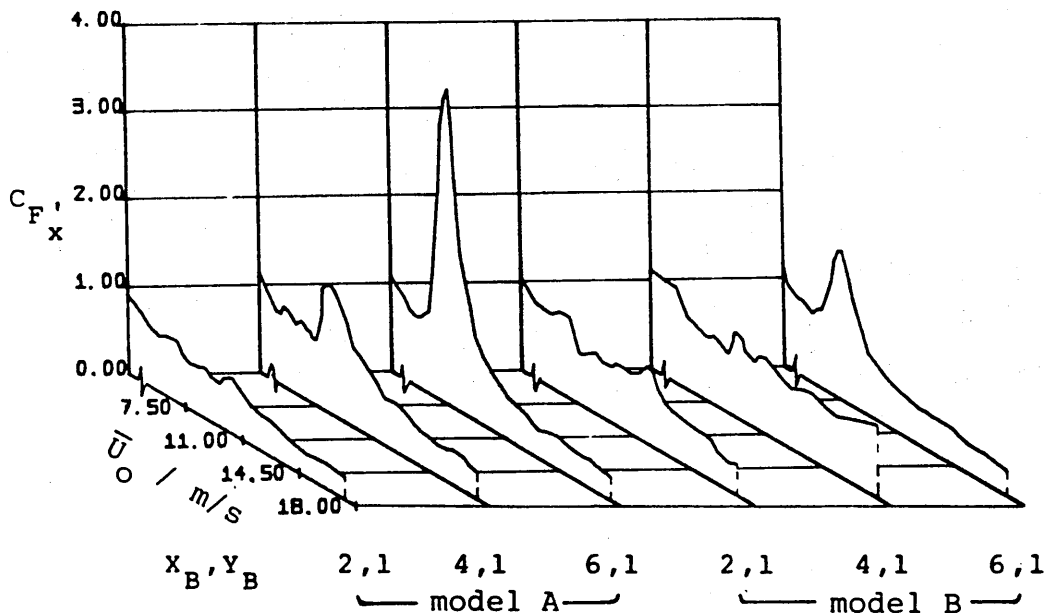


(b) Fluctuating along-wind force coefficient of tower A and B

Figure 6.34 Variation in the coefficients of (a) the time-mean and (b) the RMS values of the fluctuating along-wind force on the towers with mean wind velocity in uniform smooth flow for various staggered arrangements.

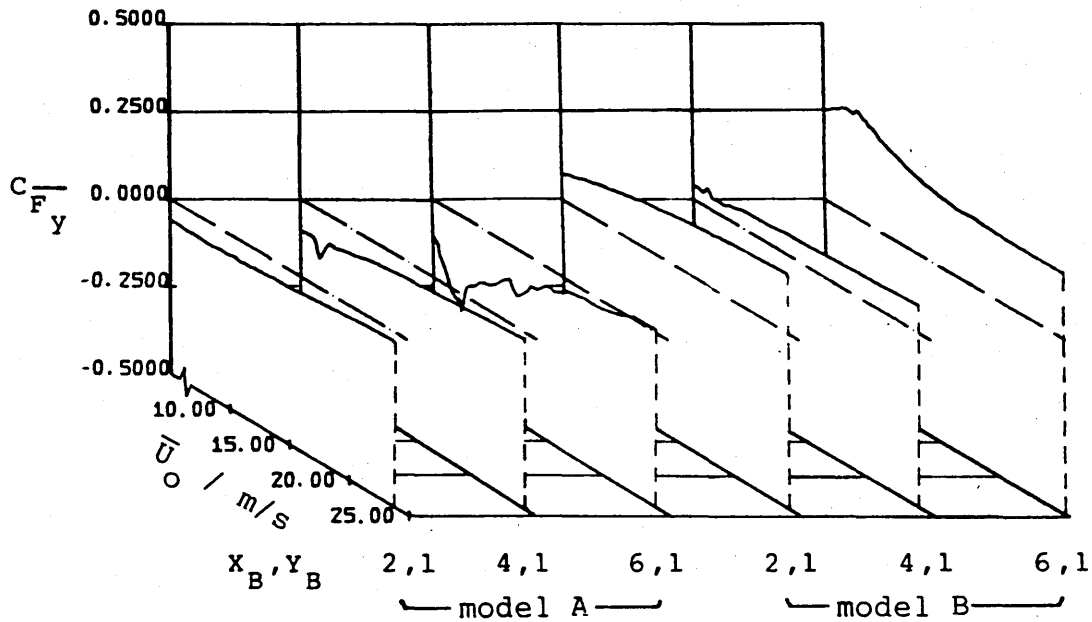
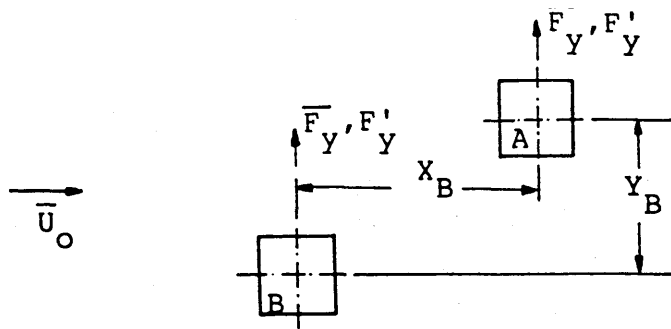


(a) Time-mean along-wind force coefficient of tower A and B

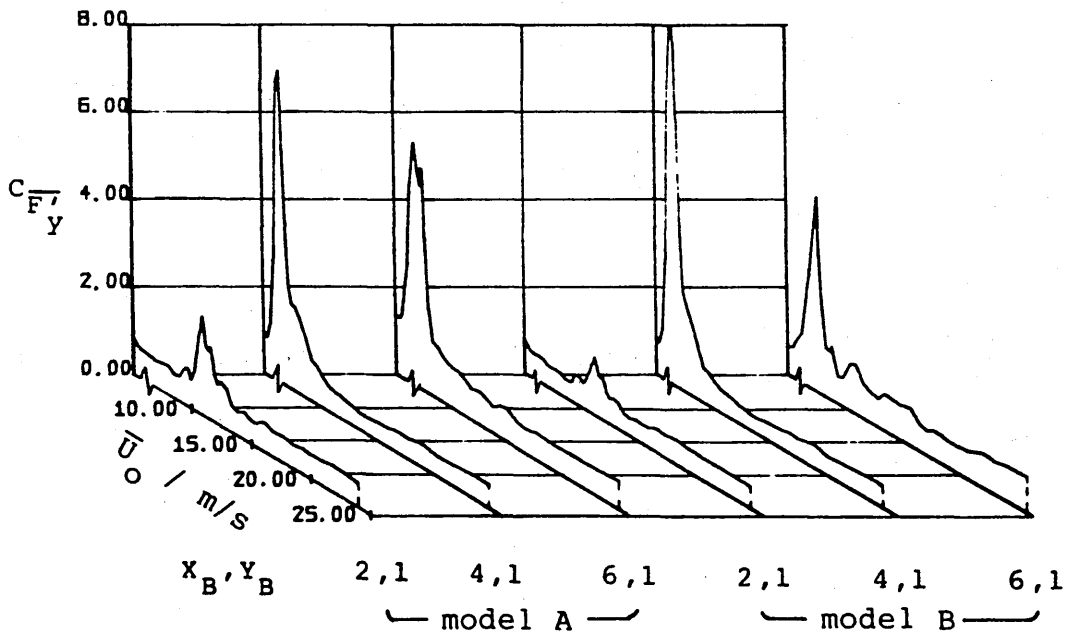


(b) Fluctuating along-wind force coefficient of tower A and B

Figure 6.35 Variation in the coefficients of (a) the time-mean and (b) the RMS values of the fluctuating along-wind force on the towers with mean wind velocity in uniform turbulent flow for various staggered arrangements.

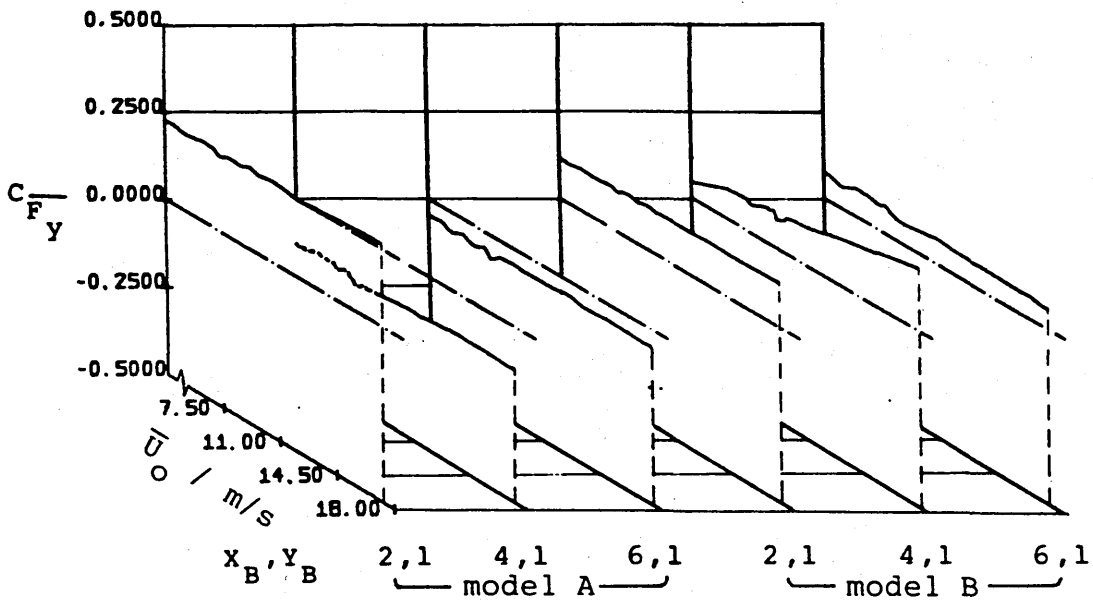
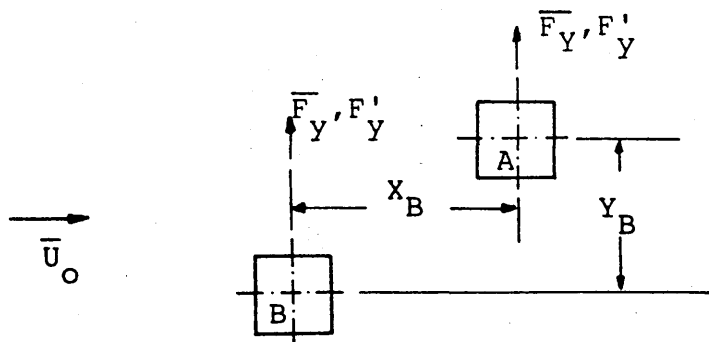


(a) Time-mean cross-wind force coefficient of tower A and B

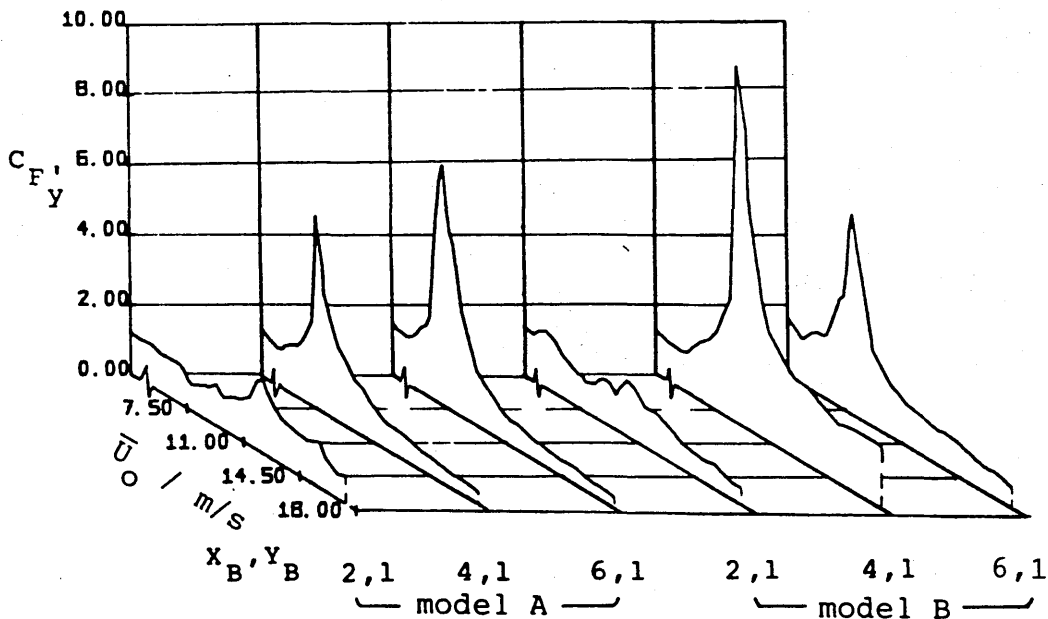


(b) Fluctuating cross-wind force coefficient of tower A and B

Figure 6.36 Variation in the coefficients of (a) the time-mean and (b) the RMS values of the fluctuating cross-wind force on the towers with mean wind velocity in uniform smooth flow for various staggered arrangements.

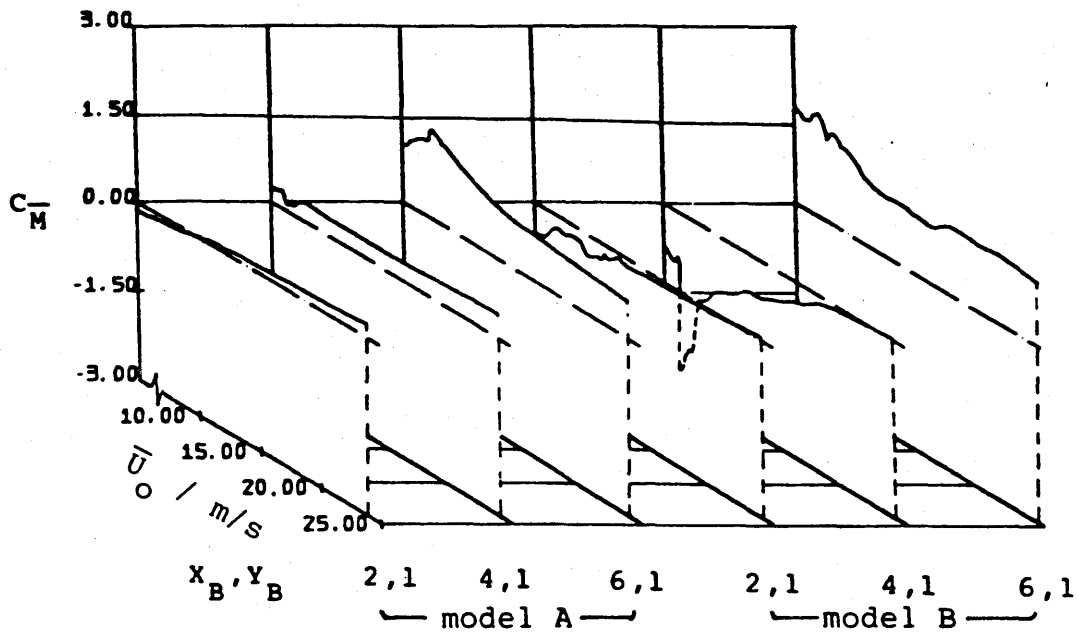
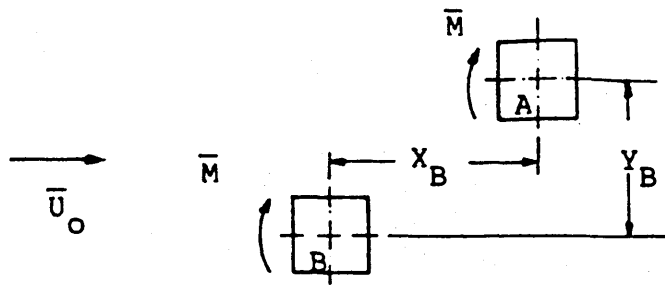


(a) Time-mean cross-wind force coefficient of tower A and B

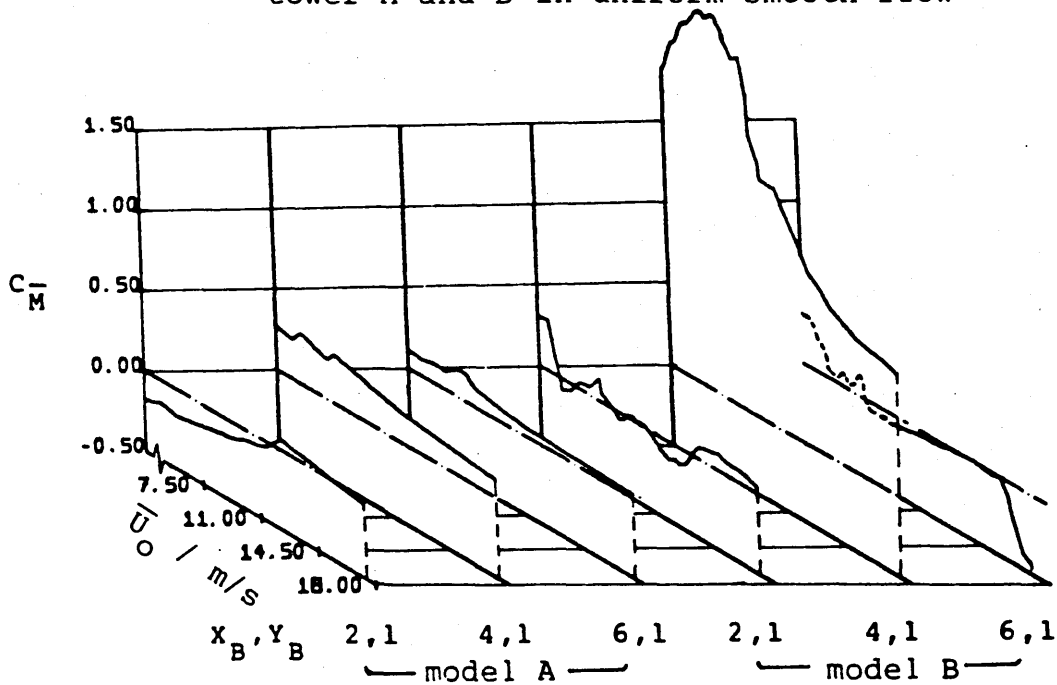


(b) Fluctuating cross-wind force coefficient tower A and B

Figure 6.37 Variation in the coefficients of (a) the time-mean and (b) the RMS values of the fluctuating cross-wind force on the towers with mean wind velocity in uniform turbulent flow for various staggered arrangements.

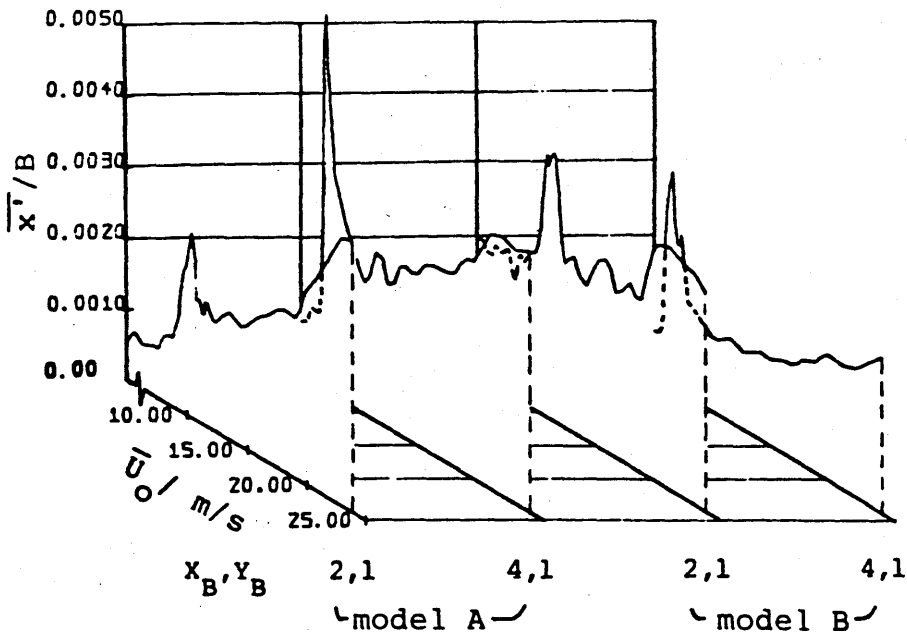


(a) Time-mean torsional moment coefficient of tower A and B in uniform smooth flow

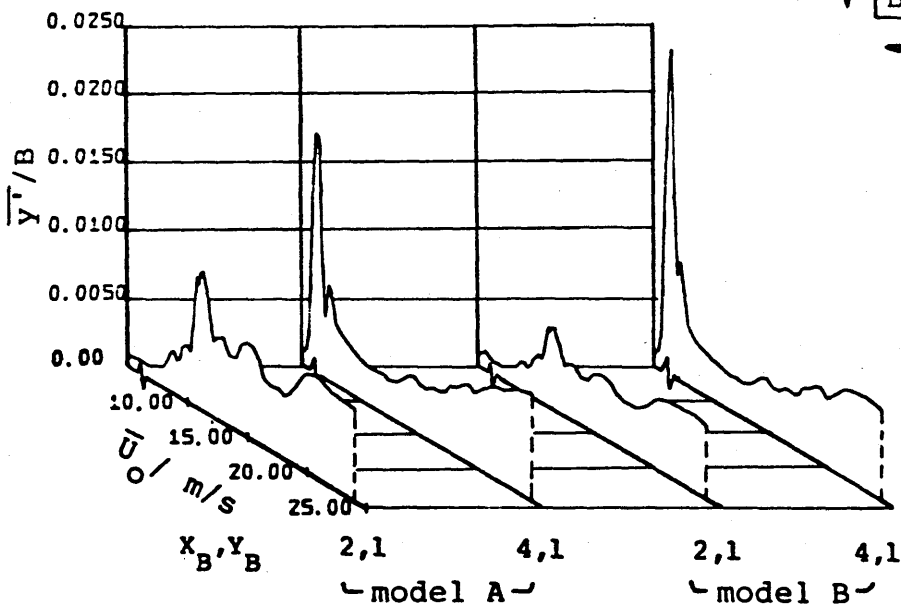
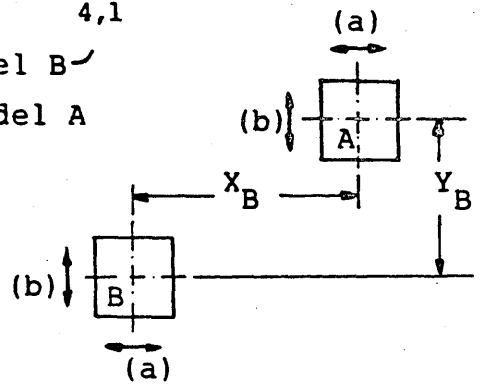


(b) Time-mean torsional moment coefficient of tower A and B in uniform turbulent flow

Figure 6.38 Variation in the coefficients of the time-mean torsional moment on the towers with mean wind velocity in (a) the uniform smooth and (b) the uniform turbulent flow for various staggered arrangements.



(a) along-wind response of model A and B



(b) cross-wind response of model A and B

Figure 6.39 Variation of the normalised displacement at the top of the upstream and downstream towers with mean wind velocity in uniform smooth flow for two staggered arrangements.

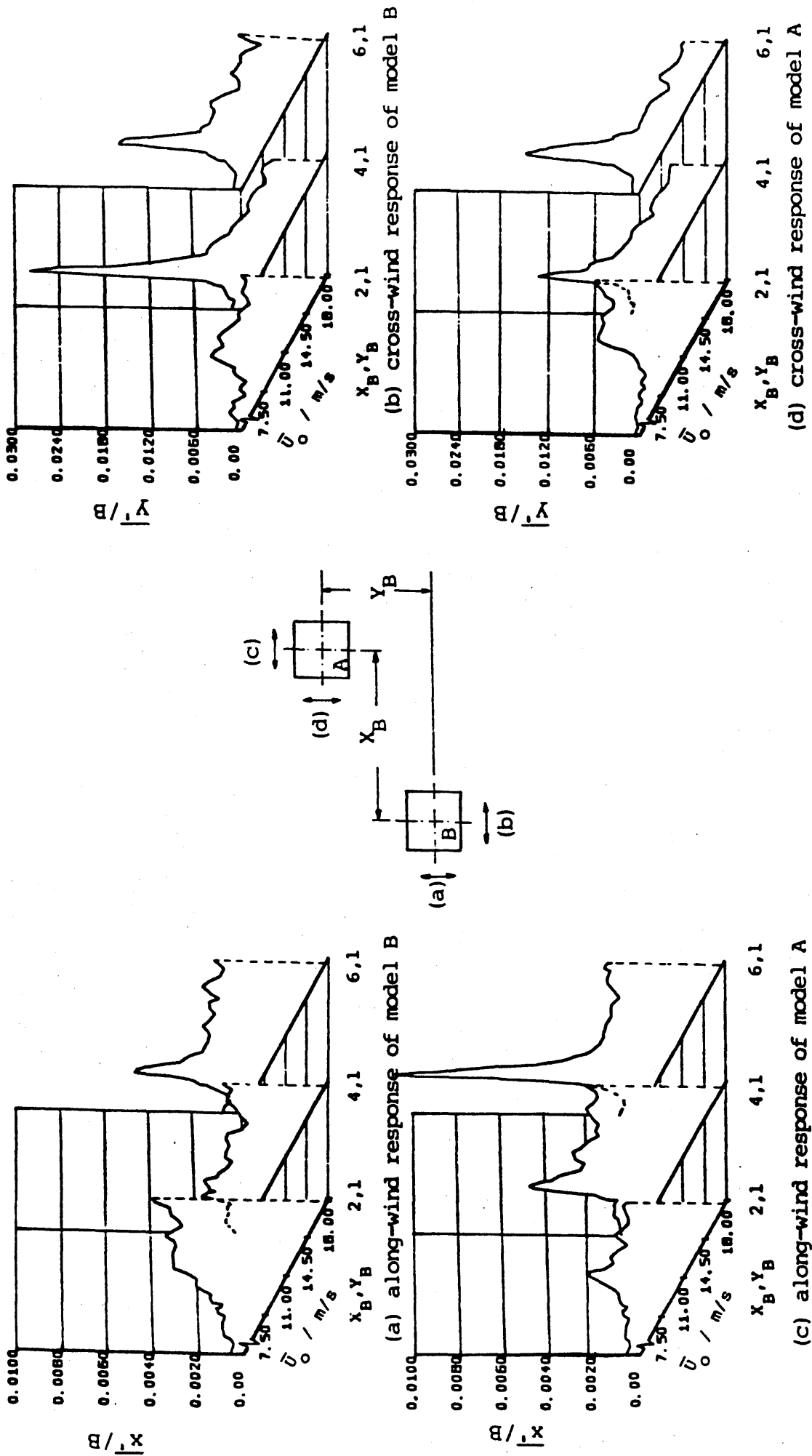
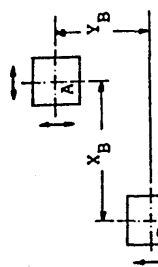
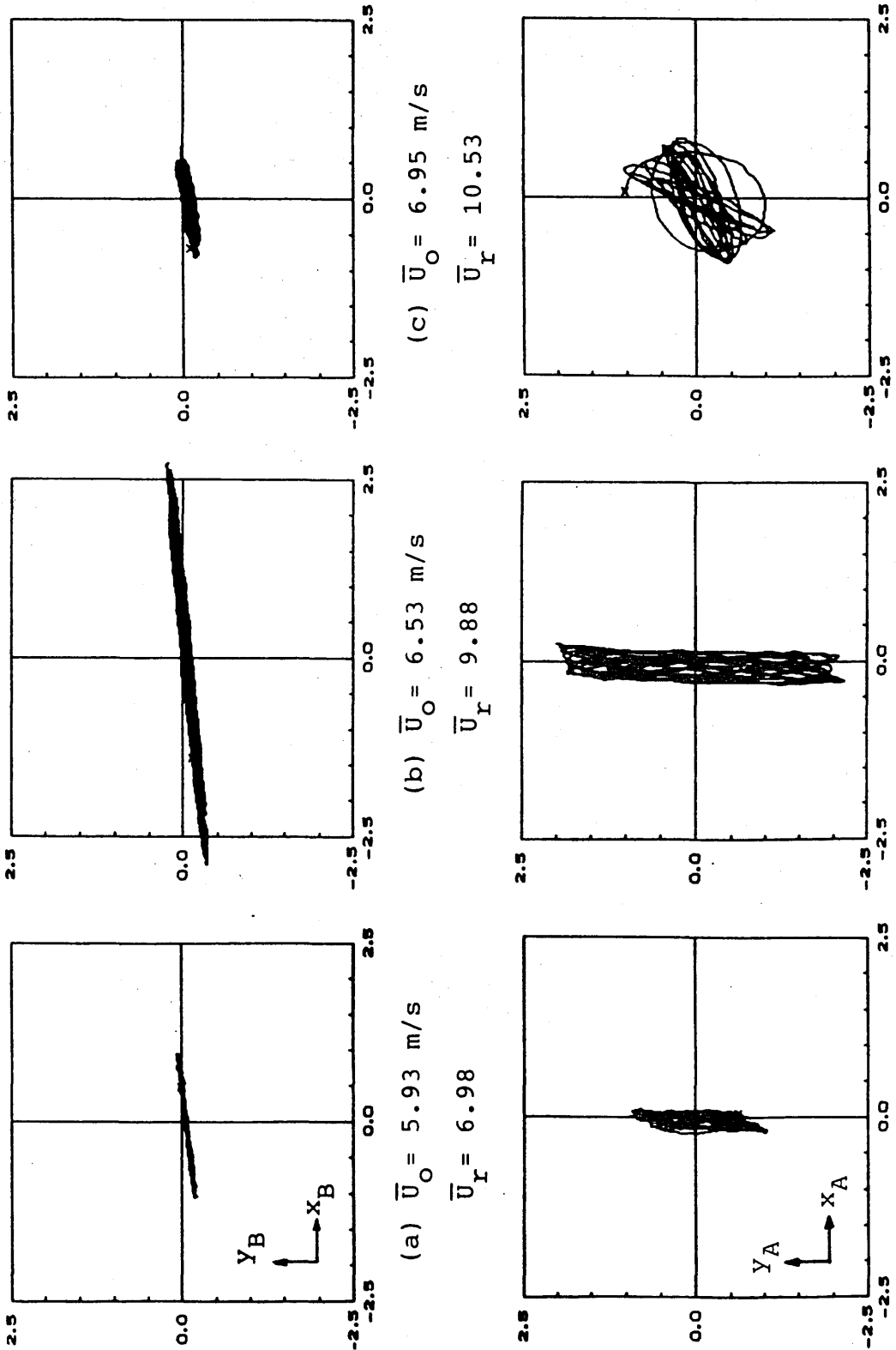


Figure 6.40 Variation of the normalised displacement at the top of the upstream and downstream towers with mean wind velocity in uniform turbulent flow for various staggered arrangements.



○ along-wind } model B
 ▲ cross-wind }
 ○ along-wind } model A
 ▲ cross-wind }

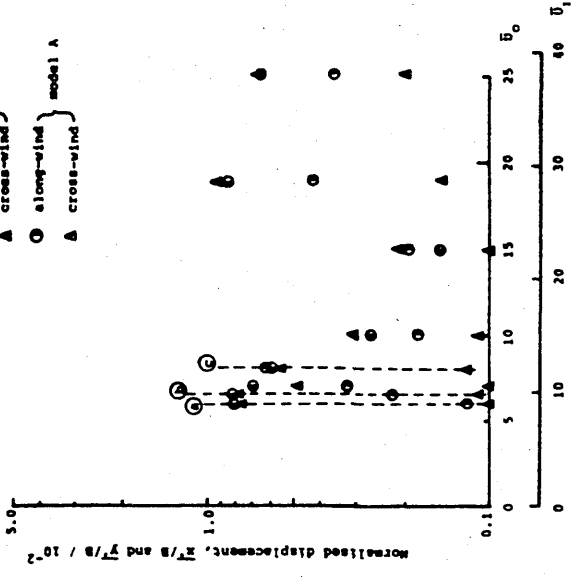


Figure 6.41 X-Y plots of the displacement response at the top of the two towers separated 4B (longitudinal) and 1B (transversely) apart in uniform smooth flow at $\bar{U}_r = 6.98, 9.88$ and 10.53

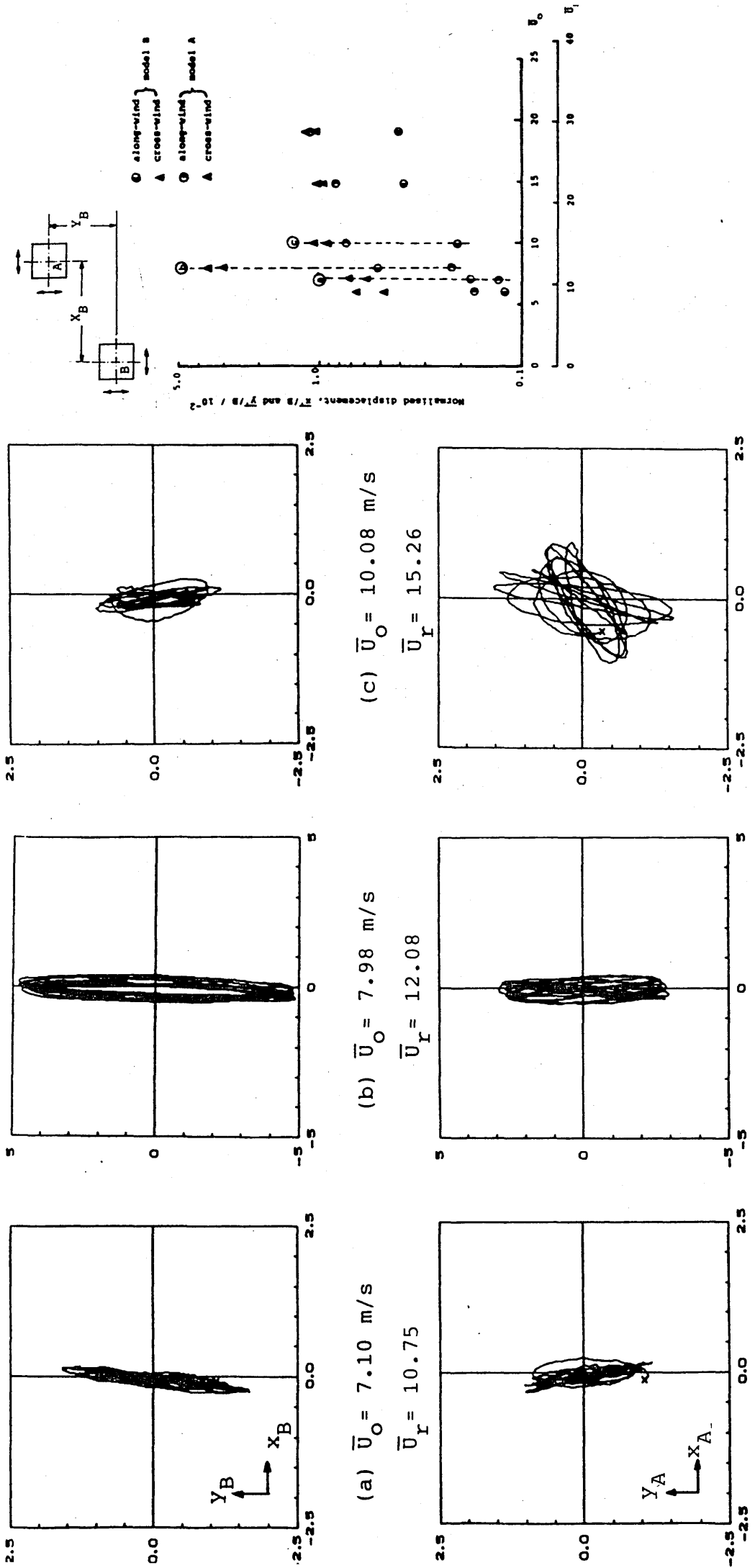


Figure 6.42 X-Y plots of the displacement response at the top of the two towers separated 4B (longitudinal) and 1B (transversely) apart in uniform turbulent flow at $\bar{U}_I = 10.75, 12.08$ and 15.26 .

CHAPTER SEVEN

CONCLUSIONS AND RECOMMENDATIONS FOR FURTHER RESEARCH

7.1 Introduction

The interactions of neighbouring tall buildings, in one way resulting from mutual interference of the fluid flow through the group and, in another, by mechanical coupling through their foundations, is known in many cases to have caused increased dynamic motions. To acquire an understanding of the excitation mechanisms and characteristics of the response process of a tall square tower block under interference excitation from neighbouring bodies, a series of wind-tunnel model tests was performed. The aim was:

- To investigate, in detail, the aerodynamic and mechanical characteristics of a single tower model under different flow conditions.
- To assess the interference effects, arising either from aerodynamic or mechanical coupling, on the response process for two identical tower models which were placed at various positions relative to each other and studied under different operating conditions.

These aims as stated have been achieved to a substantial degree.

The models used in this investigation were a pair of square cross-section towers with a height to breadth ratio of 10 to 1. Since the response of one tower in a twin tower configuration might be affected by the presence of the other, the mechanical characteristics of each were kept as close as possible and both were instrumented. In brief, the measuring system comprised an elastic model and a force balance column (dynamometer) which sat atop a steel framework. The combined model-force balance assembly resembled an elastic cantilever and could measure torsional moment about its elastic axis and the force components in the directions of the two principal axes of the model cross-section.

Tests were conducted in both uniform smooth and turbulent flows with the latter being generated by a uniform grid. A broad range of experimental measurements, including longitudinal and transverse force coefficients, torsional moment coefficients, dynamic response at the top of the towers in the translational directions and velocity fluctuations in the near wake, were recorded either in-line or off-line for detailed analysis.

The major conclusions of this study are listed in Sections 7.2 and 7.3. It is important to note that these conclusions were made within the scope of the present study, that is, they apply to the type of structure and wind models used in this work and within the test conditions investigated. With further investigation, some of these conclusions can be more explicit and have a wider application to other structures, wind environment and operating conditions. Section 7.4 is an assessment of the uncertainties created by the apparatus used in these tests. And finally, a number of recommendations for further research are suggested.

7.2 Conclusions from the Results Observed in Single Tower Configuration Cases

The oscillatory behaviour of a slender square tower in a flow field depends on many factors, such as the body's geometry and operating conditions. In this study, the effects of mean flow velocity (Reynolds number), wind exposure and angle of incidence on the response process of a single tower model and the resulting wake structures have been investigated. The following is a summary of all the major conclusions arising from experimental observations described in Chapter Five.

- (1) The natural frequencies and damping of the model-force balance combination depends almost entirely on the material and its construction. Both viscous and dry friction types of damping are found to be present on its decaying vibration traces. The values of the effective viscous damping coefficient obtained using different measuring techniques proved to be inconsistent.
- (2) This, together with the fact that the combined assembly is not a linear system, means that the wind-induced loading on the model can not be inferred from its response amplitudes (or vice versa). Hence, the forces and torsional moment acting on the model are measured by strain gauges on the force balance column and translational motions at the top of the model by accelerometers.
- (3) Under static loading conditions, the coupling of the orthogonal force components in the measuring system is minimal. But in dynamic conditions, due to the fact that the natural frequencies about each of its principal axes are nearly equal, coupling between the longitudinal and transverse modes of vibration can take place.
- (4) For flow normal to one face, (i.e. at $\alpha = 0$ degree), the response process of a square tower is mainly caused by the periodic shedding of large vortices into its wake and is predominantly in the cross-wind direction. Near a wind speed

for which the vortex-shedding frequency is close to the natural frequency of the model system, a sharp increase in response amplitude occurs. The critical reduced velocity of this measuring system is 10.8 in uniform smooth flow and 11.4 in uniform turbulent flow.

- (5) At close to the critical reduced velocity, the increase in cross-wind response associated with a decrease in total damping causes a significant interdependence between the cross-wind excitation and response which, as a result, exhibits a departure from the normal distribution and tends to follow the distribution of a sinusoid function plus a random noise.
- (6) At an operating reduced velocity away from the critical, the response is of very small amplitude and is random in character
- (7) At the resonant conditions, peaks of instability also occurred in the response process for the along-wind direction. But this is likely to be the result of the energy transfer between the motions in the two perpendicular directions and is produced at the expense of the cross-wind vibration. In general, the along-wind oscillation is primarily due to the turbulence in the incident flow and its magnitude increased almost linearly with increase in mean flow velocity.
- (8) Mean torsional moment can be found on a geometrically symmetrical prism due to non-uniformities in the flow field and for wind directions not aligned with the axes of the body geometry, whereas dynamic torque is caused by unbalance in the instantaneous pressure distribution. Hence torsional excitation of a square prism can be significantly increased by the turbulence in the approaching flow. However, due to the inherent high torsional rigidity, the magnitudes of output from the torsional strain gauge sets are small and are severely distorted by the background noise.
- (9) When the angle of incidence of the mean wind is increased, there is a tendency for the separated shear layer from the leading edge to re-attach itself onto the windward face of the square tower. As a result, the magnitudes of the excitation force and the transverse response are reduced. The changes in response amplitudes are considerable and are most rapid over the first 20 degrees.
- (10) The aerodynamic force acting on a square section body is proportional to the slope of the transverse force coefficient versus angle of incidence of the mean wind. It is apparent that at zero angle of incidence, the aerodynamic force on the present model system should be sufficient to cause galloping type oscillation in the uniform turbulent flow but not in the uniform smooth flow.

However, by applying a quasi-steady linear approximation of the aerodynamic force in association with the transverse force characteristics of the measuring system, it is also established that the total damping (mechanical damping plus aerodynamic damping) at the resonant reduced velocity is sufficiently high to prevent galloping from happening.

- (11) The major effects of an increase in free-stream turbulence is to increase the turbulent mixing in the shear layers and hence increase the rate of entrainment of the surrounding fluid. As a result, the magnitude of the drag force acting on the tower model is reduced, but the wind loads and response amplitudes in the cross-wind direction are significantly higher than would be obtained in smooth flow.
- (12) By measuring the turbulence intensity at various locations surrounding the tower model, the area enclosed by recirculation flow is defined. Inside this wake region and along its centre-plane, the turbulence intensity varies, reaching a maximum value at a distance downstream of about three times the tower's breadth. The boundary of this free stagnation zone seems to be dependent on the fluid entrainment from both side shear layers and that over the top of the tower. In turbulent flow, the recirculation zone is noticeably shortened and the distance to the position of maximum fluctuations is reduced to 1.5 times the tower's breadth.
- (13) When the square tower is excited by periodic vortex shedding forces, there is a complex, non-linear, interaction between the wake and the body. The vibration itself causes an increase in circulation which is probably the result of the periodic shifting of the position of re-attachment of the shear layer flow on the body surfaces. Consequently, the motion-induced vortices are stronger and the wake frequency, which is expressed as the Strouhal number, is different from that measured behind a stationary body of similar cross-sectional geometry.

7.3 Conclusions from the Results Observed in Twin Tower Configuration Cases

In total, seventeen configurations have been studied in this investigation which covered the tandem arrangements from 2 to 8 breadth spacing, the side by side arrangements from 2 to 4 breadth and a number of staggered arrangements within these limits. All tests were conducted in both uniform and turbulent flows. The positions covered by these measurements are still fewer than those presented by Zdravkovich [19] and Bailey et al. [11]; in both cases a large number of positions had

been studied and the curves of constant coefficients were drawn by interpolation between the measured values. However, based on the limited results presented in Chapter Six, a number of conclusions can be drawn as follows:

- (1) In all the cases being investigated, the response process of both towers (either in the upstream-downstream or side by side configurations) is affected by the presence of the other. Flow interference between them in various arrangements imposes continuous and discontinuous changes in the pattern of vortex shedding. The resulting oscillations induced by the vortex shedding are considerably modified by and, also, strongly depend on the arrangements of the two towers.
- (2) In most cases where the towers were in an upstream-downstream configurations, the strongest response was developed when the towers were offset normal to the flow direction. This was particularly evident when the downstream tower was located outside the highly turbulent, low-velocity, flow within the wake region.
- (3) Within the proximity interference region, the vortex shedding behind the front tower can be severely disrupted by the presence of the rear tower. The oscillatory behaviour of both towers is affected, resulting from the entrainment of fluid into the wake formed behind the upstream body and from the gap flow streaming between the two. In certain configurations, a strong gap flow can induce large transverse force components on both towers. A critically located downstream tower can alter the wake from the upstream tower in such a way that the modified wake can reach resonance with the upstream tower at a low reduced velocity, affecting both along-wind and cross-wind response.
- (4) In the tandem configurations where one tower is positioned directly behind the other, the presence of the upstream tower provides a significant degree of shielding for the downstream tower. In such cases, the downstream tower seems to be submerged in the low-velocity wake flow region enclosed by the shear layers emanating from the upstream tower. The size of this region can extend up to six times the breadth of the tower in the flow direction. However, even in such situations, significant fluctuating forces and moments are still found on both towers.
- (5) Beyond the critical spacing region, the flow patterns around the towers are drastically altered and vortex streets are formed behind both towers. The commencement of periodic wake flow behind the upstream tower strongly affects and synchronises with the vortex shedding behind the downstream one.

- (6) The flow interference between towers in side by side arrangements is mainly due to close proximity effects. In the cases being studied, narrow and wide wakes are observed to be formed behind the towers and are divided by a biased flow through the gap. When the transverse spacing between the towers is sufficiently large, a vortex street is formed behind each tower but these could be coupled in an out-of-phase mode.
- (7) With a few exceptions, the wind-induced oscillations are predominately in the cross-wind direction. But the amplitudes of the along-wind and cross-wind response of both towers are magnified by the presence of the other tower and clear peaks of instability due to vortex shedding are also evident in most cases. Due to the changes in the flow surrounding the towers, there is evidence that the torsional excitation on the towers has been increased. Unfortunately, results from measurements are marred by low sensitivity and high background noise. However, the fact that there is likely to be some error in the results does not negate this finding.
- (8) In turbulent flow, due to the reduction in the radius of curvature of the shear layers, the flow interference between the towers is reduced, particularly when they are close to each other. The process of vortex shedding, which is suppressed in the close proximity region in uniform smooth flow, reappears. In general, due to the higher fluctuating velocity in the incident flow, the wind loads and response amplitudes of the towers in the turbulent flow are significantly stronger than those measured in smooth flow.
- (9) From the results presented in this report, there is evidence to support the existence of mechanical interference between the towers (or the tower measuring system), such as beating. It has been shown that, in certain conditions, mechanical coupling between the towers through their foundation can take place and subsequently, the two towers behave as a single body. As might be expected, it appears that the magnitude of the mechanical coupling between the tower models decreases as the longitudinal distance between them is increased.

7.4 Some Uncertainties Associated with the Apparatus Used in the Measurements

(a) Force balance column---As mentioned before, the ideal force balance should have high sensitivity and high rigidity, but these two attributes are in fact contradictory to each other [100]. An alternative approach, as the one used in this study, is to measure the resonant response of an aeroelastic model by a low

frequency force balance system. The output from such a measuring system is high enough to give small force components accurately. However, one major drawback is that the response is greatly distorted for input frequencies near the fundamental frequency of the system.

If the natural frequencies of the combined model-balance assembly about each of its principal axes are nearly equal, coupling of the orthogonal force components take place. As a result, energy is transferred from one direction of motion to another.

Furthermore, as described in Chapter Three, the damping of the present measuring system arises almost entirely from its material and construction. It is therefore very difficult to adjust or even to measure accurately. Because of this, the forces on the model can not be inferred from the response measurements (or vice versa).

(b) Wind models---Two wind models were employed in this study, namely the uniform smooth and turbulent flows, the latter being grid-generated. The apparent advantage of using a turbulent flow model of this form, as compared to turbulent boundary shear layer flow, is its simplicity. Both the velocity and turbulence are near uniform and the effect of early re-attachment due to increase in free stream turbulence is more significant and better defined. However, because of the absence of velocity profile and turbulence intensity profile, the three-dimensional effects on the towers are less apparent. As results from other observations have shown, the interference or interaction study between two structures should be carried out in a turbulent flow that closely simulates the flow at the site of the full-scale structures.

(c) Interference effects--- One of the main objectives of this study is to clarify the mechanical interference between the two towers in different flow conditions. In the original design, it was hoped that the frame structures, on which the model-balance assemblies were mounted, would have sufficient rigidity to restrain their oscillations. But as the results presented in this thesis suggest, motions on one measuring system can induce oscillations on the other measuring system. As a result, coupling and consequently, transfer of energy could take place between them through the supporting structures. This explains the minimal effects on the response amplitudes when the two towers were linked by a rigid substructure at either their upper or lower ends.

7.5 Recommendations for Further Research

In this thesis, the excitation mechanism and response process of a single tower due to wake excitation have been clarified and defined. Changes in turbulence

characteristics, flow separation and vortex formation are found to be the basic interaction mechanisms between towers in close vicinity. Nevertheless, the excitation/interaction mechanism of a tower model under the influence of a neighbouring structure is very complex, being dependent on the operating conditions and a wide variety of variables, such as the distance between them. In this report, the effects of a number of such variables on the excitation/interaction mechanism have been studied. However, the relative contribution of each individual excitation mechanism in operation conditions where more than one mechanism is significant is still a subject of considerable interest and worthy for further investigation. In fact, one of the major difficulties is to formulate a method, either theoretical and experimental, which can be used to isolate effectively each individual mechanism. And as emphasised in this thesis, the choice of the apparatus used in the wind-tunnel measurements is very important.

On the other hand, because of the complexity, the probability of predicting the oscillatory behaviour of towers under the influence of neighbouring structures by analytical methods is very slight indeed. A wind-tunnel method still provides the most reliable techniques for identifying and quantifying the interference effects between neighbouring structures in the foreseeable future. Therefore, more efforts should be applied to collecting systematic data and preparing comprehensive guidelines for design purposes.

REFERENCE

- [1] Mahrenholtz, O. and Bardowicks, H., 'Wind-Induced Oscillations of Some Steel Structures', Symp. of Practical Experiences with Flow-Induced Vibrations, Karlsruhe, West Germany, Sept. 1979, Springer-Verlag, 1980, Paper F5, pp. 643-649.
- [2] 'Report of the Committee of Inquiry into Collapse of Cooling Towers at Ferrybridge', Central Electric Generating Board, Nov. 1965. (as cited by Sachs, P., *Wind Forces in Engineering*, Pergamon Press, 1972, pp. 277-281.)
- [3] Whitbread, R.E. and Wootton, L.R., 'An Aerodynamic Investigation for the Five 50-Storey Tower Blocks Proposed for the Ping Shek Estate, Hong Kong', NPL Aero Special Report 002, 1968.
- [4] Mair, W.A. and Maull, D.J., 'Aerodynamic Behaviour of Bodies in the Wakes of Other Bodies', Phil. Trans. Roy. Soc., London, Series A, Vol. 269, 1971, pp. 425-437.
- [5] Peterka, J.A. and Cermak, J.E., 'Adverse Wind Loading Induced by Adjacent Buildings', Journal of the Structural Division, ASCE, Vol. 102, No. ST3, Proc. Paper 11980, March 1976, pp. 533-548.
- [6] Ikenouchi, M., 'Experimental and Numerical Studies on the Aerodynamic Instability of Tower-Like Structures', Proc. Fifth Int. Conf. Wind Engineering, Fort Collins, Colorado, July 1979, Pergamon Press, 1980, pp. 747-756.
- [7] Cain, T.H. and Nelson, H.M., 'Wind Tunnel Tests on a 1/40 Scale Aeroelastic Model of the Kessock Road Bridge Pylons', Contract Report, Dept. of Aeronautics and Fluid Mechanics and Civil Engineering, University of Glasgow, Feb. 1981.
- [8] Kwok, K.C.S., 'Cross-Wind Response of Structures Due to Displacement Dependent Excitations', Ph.D. Thesis, Department of Mechanical Engineering, Monash University, Australia, Dec. 1977.

- [9] Reinhold, T.A., Tieleman, H.W. and Maher, F.J., 'Interaction of Square Prisms in Two Flow Fields', *Journal of Industrial Aerodynamics*, Vol. 2, 1977, pp. 223-241.
- [10] Ruscheweyh, H., 'Dynamic Response of High Rise Buildings under Wind Action with Interference Effects from Surrounding Buildings of Similar Size', *Proc. Fifth Int. Conf. Wind Engineering*, Fort Collins, Colorado, July 1979, Pergamon Press, 1980, pp. 725-734.
- [11] Bailey, P.A. and Kwok, K.C.S., 'Interference Excitation of Twin Tall Buildings', *Journal of Wind Engineering and Industrial Aerodynamics*, Vol. 21, 1985, pp. 323-338.
- [12] Cermak, J., 'Separation Induced Pressure Fluctuations on Buildings', *Proc. First U.S.A.-Japan Research Seminar on Wind Effects on Structures*, Oct. 1970, University Hawaii, Honolulu.
- [13] Rockwell, D.O., 'Organised Fluctuations Due to Flow Past a Square Cross Section Cylinder', *Journal of Fluids Engineering*, ASME, Vol. 97, Sept. 1977, pp. 511-516.
- [14] Hunt, J.C.R., 'The Effect of Single Buildings and Structures', *Phil. Trans. Roy. Soc., London, Series A*, Vol. 269, 1971, pp. 457-467.
- [15] Davies, M.E., Quincey, V.G. and Tindall, S.J., 'The Near-Wake of a Tall Building Block in Uniform and Turbulent Flows', *Proc. Fifth Int. Conf. Wind Engineering*, Fort Collins, Colorado, July 1979, Pergamon Press 1980, pp. 289-298.
- [16] Vickery, B.J., 'Fluctuating Lift and Drag on a Long Cylinder of Square Cross-Section in a Smooth and in a Turbulent Stream', *Journal of Fluid Mechanics*, Vol. 25, Pt. 3, 1966, pp. 481-494.
- [17] Lee, B.E., 'The Effect of Turbulence on the Surface Pressure Field of a Square Prism', *Journal of Fluid Mechanics*, Vol. 69, Pt. 2, 1975, pp. 263-282.
- [18] Bearman, P.W. and Obasaju, E.D., 'An Experimental Study of Pressure Fluctuations on Fixed and Oscillating Square-Section Cylinders', *Journal of Fluid Mechanics*, Vol. 119, 1982, pp. 297-321.

- [19] Zdravkovich, M.M., 'Flow Induced Oscillations of Two Interfering Circular Cylinders', Int. Conf. on Flow Induced Vibrations in Fluid Engineering, Reading, Sept. 1982, BHRA Fluid Engineering 1982, Paper D2, pp. 141-154.
- [20] Cooper, K.R. and Wardlaw, R.L., 'Aeroelastic Instabilities in Wakes', Proc. Third Int. Conf. Wind Effects on Buildings and Structures, Tokyo, 1971, Saikon Co. 1972, Paper IV.1, pp. 647-655.
- [21] Rosati, P.A., 'An Experimental Study of the Response of a Square Prism to Wind Load', M.Sc. Thesis, University of Western Ontario, Canada, 1968.
- [22] Isyumov, N. and Poole, M., 'Wind Induced Torque on Square and Rectangular Building Shapes', Journal of Wind Engineering and Industrial Aerodynamics, Vol. 13, 1983, pp. 183-196.
- [23] Simiu, E. and Scanlan, R.H., *Wind Effects on Structures: An Introduction to Wind Engineering*, John Wiley & Sons, New York, 1978.
- [24] Patrickson, C.P. and Friedmann, P., 'A Study of the Coupled Lateral and Torsional Response of Tall Buildings to Wind Loading', UCLA School of Engineering and Applied Sciences Rep. UCLA-ENG 76126, Dec. 1976.
- [25] Foutch, D.A. and Safak, E., 'Torsional Vibration of Wind-Excited Structures', Third ASCE/Eng. Mech. Div. Speciality Conf., Austin Texas, Sept. 1979.
- [26] Nakamura, Y. and Mizota, T., 'Torsional Flutter of Rectangular Prisms', Journal of the Engineering Mechanics Division, ASCE, Vol. 101, No. EM2, April 1975, pp. 125-142.
- [27] Nakamura, Y., 'On the Aerodynamic Mechanism of Torsional Flutter of Bluff Structures', Journal of Sound and Vibration, Vol. 67, Pt. 2, 1979, pp. 163-177.
- [28] Durgin, F.H. and Tong, P., 'The Effect of Twist Motion on the Dynamic Multimode Response of a Building', IUTAM-IAHR Symp. on Flow-Induced Structural Vibrations, Karlsruhe, West Germany, 1972, Springer-Verlag, 1974, pp. 383-400.

- [29] Kato, B. and Akiyama, H., 'Experimental Study on Buffeting Vibrations of Tall Buildings', Proc. Second U.S.A.-Japan Research Seminar on Wind Effects on Structures, Kyoto, 1974, University of Tokyo Press 1976, pp. 141-152.
- [30] Kareem, A., 'Wind Induced Torsional Loads on Structures', Eng. Struct., Vol. 3, April 1981, pp. 85-86.
- [31] Blessmann, J. and Riera, J.D., 'Interaction Effects in Neighbouring Tall Buildings', Proc. Fifth Int. Conf. Wind Engineering, Fort Collins, Colorado, July 1979, Pergamon Press, 1980, pp. 381-395.
- [32] King, R., Prosser, M.J. and Jones, D.J., 'On Vortex Excitation of Model Piles in Water', Journal of Sound and Vibration, Vol. 29, Pt. 2, 1973, pp. 189-218.
- [33] Liepmann, H.W., 'On the Application of Statistical Concepts to the Buffeting Problem', Journal of Aeronautical Sciences, Vol. 19, No. 12, Dec. 1952, pp. 793-800 and 822.
- [34] Davenport, A.G., 'The Application of Statistical Concepts to the Wind Loading of Structures', Proc. Institute of Civil Engineers, Vol. 19, 1961, pp. 449-472.
- [35] Davenport, A.G., 'Gust Loading Factors', Journal of the Structural Division, ASCE, Vol. 93, No. ST3, Proc. Paper 5255, June 1967, pp. 11-34.
- [36] Vellozzi, J. and Cohen, E., 'Gust Response Factors', Journal of the Structural Division, ASCE, Vol. 94, No. ST6, Proc. Paper 5980, June 1968, pp. 1295-1313.
- [37] Simiu, E., 'Gust Factors and Along-Wind Pressure Correlations', Journal of the Structural Division, ASCE, Vol. 99, No. ST4, Proc. Paper 9686, April 1973, pp. 773-783.
- [38] *Canadian Structural Design Manual, Supplement No. 4 to the National Building Code of Canada*, Associate Committee on the National Building Code and National Research Council of Canada, Ottawa, 1975.

- [39] *American National Standards Building Code Requirements for Minimum Design Loads in Buildings and Other Structures*, A58.1, American National Standards Institute, New York, 1972.
- [40] Simiu, E., Marshall, R.D. and Haber, S., 'Estimation of Along-wind Building Response', *Journal of the Structural Division, ASCE*, Vol. 103, No. ST7, July 1977, pp. 1325-1338.
- [41] Simiu, E. and Lozier, D.W., 'The Buffeting of Tall Structures by Strong Winds', *Building Science Series 74*, National Bureau of Standards, Washington D.C., 1975.
- [42] Simiu, E., 'Equivalent Static Wind Loads for Tall Building Design', *Journal of the Structural Division, ASCE*, Vol. 102, No. ST4, Proc. Paper 12057, April 1976, pp. 719-737.
- [43] Simiu, E., 'Revised Procedure for Estimating Along-Wind Response', *Journal of the Structural Division, ASCE*, Vol. 106, No. ST1, 1980, pp. 1-10
- [44] Solari, G., 'Along-Wind Response Estimation: Closed Form Solution', *Journal of the Structural Division, ASCE*, Vol. 108, No. ST1, 1982, pp. 225-235.
- [45] Saunders, J.W. and Melbourne, W.H., 'Tall Rectangular Building Response to Cross-Wind Excitation', *Proc. Fourth Int. Conf. on Wind Effects on Buildings and Structures*, London, 1975, Cambridge University Press, 1977, pp. 369-379.
- [46] McLaren, F.G., Sherratt, A.F.C. and Morton, A.S., 'The Interference Between Bluff Sharp-Edged Cylinders in Turbulent Flows Representing Models of Two Tower Buildings Close Together', *Building Science*, Vol. 6, Pergamon Press, 1971, pp. 273-274.
- [47] Lee, B.E. and Flower, G.R., 'The Mean Wind Forces Acting on a Pair of Square Prisms', *Building Science*, Vol. 10, Pergamon Press, 1975, pp. 107-110.
- [48] Biermann, D. and Herrnstein, W.H., Jr., 'The Interference Between Struts in Various Combinations', *NACA Tech. Rep. 468*, 1933.

- [49] Hori, E., 'Experiments on Flow Around a Pair of Parallel Circular Cylinders', Proc. Ninth Japan National Congress for Applied Mech., Tokyo, 1959, pp. 231-234.
- [50] Melbourne, W.H. and Sharp, D.B., 'Effects of Upwind Buildings on the Response of Tall Buildings', Proc. of the Regional Conf. on Tall Buildings, Hong Kong, Sept. 1976, pp. 174-191.
- [51] Melbourne, W.H., 'Cross-Wind Response of Structures to Wind Action', Proc. Fourth Int. Conf. on Wind Effects on Buildings and Structures, London 1975, Cambridge University Press, 1977, pp. 343-358.
- [52] Saunders, W.H. and Sharp, D.B., 'Buffeting Effects of Upstream Buildings', Proc. Fifth Int. Conf. Wind Engineering, Fort Collins, Colorado, July 1979, Pergamon Press, 1980, pp. 593-606.
- [53] Davenport, A.G., 'The Action of Wind on Suspension Bridges', Proc. Int. Symp. on Suspension Bridges, Laboratorio Nacional de Engenharia Civil, Lisbon, 1966, pp. 79-100.
- [54] Simiu, E., 'Modern Developments in Wind Engineering: Part 3', Engineering Structures, Vol. 4, April 1982, pp. 66-74.
- [55] Okajima, A., 'Strouhal Numbers of Rectangular Cylinders', Journal of Fluid Mechanics, Vol. 123, 1982, pp. 379-398.
- [56] Otsuki, Y., Washizu, K., Tomizawa, H. and Ohya, A., 'A Note on the Aeroelastic Instability of a Prismatic Bar with Square Section', Journal of Sound and Vibration, Vol. 34, Pt. 2, 1974, pp. 233-248.
- [57] Bishop, R.E.D. and Hassan, A.Y., 'The Lift and Drag Forces on a Circular Cylinder Oscillating in a Flowing Fluid', Proc. Roy. Soc., London, Series A, Vol. 277, 1964, pp. 32-74.
- [58] Hartlen, R.T. and Currie, I.G., 'Lift Oscillator Model of Vortex-Induced Vibration', Journal of Engineering Mechanics Division, ASCE, Vol. 96, No. EM5, 1970, pp. 577-591.

- [59] Griffin, O.M., Skop, R.A. and Koopmann, G.H., 'The Vortex-Excited Resonant Vibrations of Circular Cylinders'. *Journal of Sound and Vibration*, Vol. 31, Pt. 2, 1973, pp. 235-249.
- [60] Skop, R.A. and Griffin, O.M., 'A Model for the Vortex-Excited Response of Bluff Cylinders'. *Journal of Sound and Vibration*, Vol. 27, 1973, pp. 225-233.
- [61] Skop, R.A. and Griffin, O.M., 'On a Theory for the Vortex-Excited Oscillations of Flexible Cylindrical Structures'. *Journal of Sound and Vibration*, Vol. 41, Pt. 3, 1975, pp. 263-274.
- [62] Dowell, E.H., 'Nonlinear Elasticity', *Proc. Eng. Foundation Conf. Nonlinear Dynamics*, Monterey, Calif., Dec. 1979, SIAM.
- [63] Griffin, O.M. and Koopmann, G.H., 'The Vortex-Excited Lift and Reaction Forces on Resonantly Vibrating Cylinders'. *Journal of Sound and Vibration*, Vol. 54, 1977, pp. 435-448.
- [64] Sarpkaya, T., 'Transverse Oscillation of a Circular Cylinder in Uniform Flow'. *Journal of Waterway, Port, Coastal and Ocean Division, ASCE*, Vol. 104, No. WW4, 1978, pp. 275-290.
- [65] Toebes, G.H., 'Fluid Elastic Features of Flow Around Cylinders', *Proc. Int. Res. Seminar Wind Effects Buildings Struct.*, Ottawa, Canada, 1967, Vol. 2, University of Toronto Press, 1968, pp. 323-334.
- [66] Ramberg, S.E. and Griffin, O.M., 'Velocity Correlations and Vortex Spacing in the Wake of a Vibrating Cable'. *Journal of Fluids Engineering, ASME*, Vol. 98, 1976, pp. 10-18.
- [67] Ramberg, S.E. and Griffin, O.M., 'Vortex Formation in the Wake of a Vibrating, Flexible Cable'. *Journal of Fluids Engineering, ASME*, Vol. 96, 1974, pp. 317-322.
- [68] Sallet, D.W., 'The Drag and Oscillating Transverse Force on Vibrating Cylinders Due to Steady Fluid Flow'. *Ing.-Arch.*, Vol. 44, 1975, pp. 113-124.

- [69] Blevins, R.D. and Burton, T.E., 'Fluid Forces Induced by Vortex Shedding', *Journal of Fluids Engineering*, ASME, Vol. 95, March 1976, pp. 19-24.
- [70] Howell, J.F. and Novak, M., 'Vortex Shedding from Circular Cylinders in Turbulent Flow', *Proc. Fifth Int. Conf. Wind Engineering*, Fort Collins, Colorado, July 1979, Pergamon Press, 1980, pp. 619-629.
- [71] Sarpkaya, T., 'Vortex-Induced Oscillations, a Selective Review', *Journal of Applied Mechanics*, ASME, Vol. 46, 1979, pp. 241-257.
- [72] Fung, Y.C., 'Fluctuating Lift and Drag on a Cylinder in a Flow at Supercritical Reynolds Number', *Journal of Aerospace Science*, Vol. 27, Nov. 1960, pp. 801-814.
- [73] Scruton, C., 'On the Wind Induced Oscillation of Stacks, Towers and Masts', *Proc. Symp. Wind Effects on Buildings and Structures*, N.P.L. Teddington, England, 1965, pp. 798-832.
- [74] Wootton, L.R., 'The Oscillations of Large Circular Stacks in Wind', *Proc. Inst. Civil Eng.*, Vol. 43, 1969, pp. 573-598.
- [75] Vickery, B.J., 'Wind-Induced Vibrations of Towers, Stacks and Masts', *Proc. Third Int. Conf. Wind Effects on Buildings and Structures*, Tokyo 1971, Saikon Co. 1972, Paper IV.2, pp. 657-665.
- [76] Vickery, B.J. and Clark, A.W., 'Lift or Across-Wind Response of Tapered Stacks', *Journal of the Structural Division*, ASCE, Vol. 98, No. ST1, Jan. 1972, pp. 1-20.
- [77] Rosati, P.A., 'The Response of a Finite Rectangular Cylinder to Four Different Wind Flows', *Boundary Layer Wind Tunnel Laboratory Research Report*, BLWT-6-71, University of Western Ontario, Canada, 1971.
- [78] Gartshore, I.S., 'The Effects of Free Stream Turbulence on the Drag of Rectangular Two Dimensional Prisms', *Boundary Layer Wind Tunnel Laboratory Research Report*, BLWT-4-73, University of Western Ontario, Canada, 1973.

- [79] Sakamoto, H. and Arie, M., 'Vortex Shedding from a Rectangular Prism and a Circular Cylinder Placed Vertically in a Turbulent Boundary Layer', *Journal of Fluid Mechanics*, Vol. 126, 1983, pp. 147-165.
- [80] Saunders, J.W., 'Wind Excitation of Tall Buildings, with Particular Reference to the Cross-Wind Motion of Tall Buildings of Constant Rectangular Cross-Section', Ph.D. Thesis, Department of Mechanical Engineering, Monash University, Australia, 1974.
- [81] Kareem, A., Cermak, J.E. and Peterka, J.A., 'Cross-wind Response of High-Rise Buildings', Proc. Fifth Int. Conf. Wind Engineering, Fort Collins, Colorado, July 1979, Pergamon Press, 1980, pp. 659-672.
- [82] Zdravkovich, M.M., 'REVIEW-Review of Flow Interference Between Two Circular Cylinders in Various Arrangements', *Journal of Fluids Engineering*, ASME, Vol. 99, Dec. 1977, pp. 618-633.
- [83] Mair, W.A. and Maull, D.J., 'Bluff Bodies and Vortex Shedding-A Report on Euromech 17', *Journal of Fluid Mechanics*, Vol. 45, 1971, pp. 209-224.
- [84] Parkinson, G.V., 'Wind-Induced Instability of Structures', *Phil. Trans. Roy. Soc., London, Series A*, Vol. 269, 1971, pp. 395-429.
- [85] Ferguson, N. and Parkinson, G.V., 'Surface and Wake Flow Phenomena of the Vortex-Excited Oscillation of a Circular Cylinder', *Journal of Engineering for Industry*, ASME, Vol. 89, 1967, pp. 831-838.
- [86] Toebes, G.H. and Ramamurthy, A.S., 'Fluid Elastic Forces on Circular Cylinder', *Journal of Engineering Mechanics Division*, ASCE, Vol. 93, No. EM6, pp. 1-20.
- [87] Novak, M., 'Galloping and Vortex Induced Oscillation of Structures', Proc. Third Int. Conf. Wind Effects on Buildings and Structures, Tokyo 1971, Saikon Co. 1972, pp. 799-810.
- [88] Parkinson, G.V. and Smith, J.D., 'The Square Prism as an Aeroelastic Nonlinear Oscillator', *Quart. J. Mech. Appl. Math.*, Vol. 17, Pt. 2, 1964, pp. 225-239.

- [89] den Hartog, J.P., *Mechanical Vibrations*, Fourth ed., McGraw-Hill, New York, 1956.
- [90] Parkinson, G.V. and Brooks, N.P.H., 'On the Aeroelastic Instability of Bluff Cylinders', *Journal of Applied Mechanics*, ASME, Vol. 83, 1961, pp. 252-258.
- [91] Novak, M., 'Aeroelastic Galloping of Prismatic Bodies', *Journal of Engineering Mechanics Division*, ASCE, Vol. 95, No. EM1, Feb. 1969, pp. 115-142.
- [92] Novak, M., 'Galloping Oscillations of Prismatic Structures', *Journal of Engineering Mechanics Division*, ASCE, Vol. 98, No. EM1, Feb. 1972, pp. 27-46.
- [93] Novak, M. and Tanska, H., 'Effect of Turbulence on Galloping Instability', *Journal of Engineering Mechanics Division*, ASCE, Vol. 100, 1974, pp. 27-47.
- [94] Novak, M. and Davenport, A.G., 'Aeroelastic Instability of Prisms in Turbulent Flow', *Journal of Engineering Mechanics Division*, ASCE, Feb. 1970, pp. 17-39.
- [95] Laneville, A. and Parkinson, G.V., 'Effects of Turbulence on Galloping Bluff Cylinders', *Proc. Third Int. Conf. Wind Effects on Buildings and Structures*, Tokyo, 1971, Saikon Co. 1972, pp. 787-798.
- [96] Cooper, K.R., 'A Wind Tunnel Investigation of Twin Bundled Power Conductors', Report No. LTR-LA-96, NAE, NRC, Ottawa, Canada, 1972.
- [97] Ruscheweyh, H.P., 'Wind-Induced Vibrations of Towers and Stacks', *Symp. of Practical Experience with Flow-Induced Vibrations*, Karlsruhe, West Germany, Sept. 1979, Springer-Verlag, 1980, Paper G3, pp. 709-717.
- [98] Ruscheweyh, H.P., 'Aeroelastic Interference Effects Between Slender Structures', *Journal of Wind Engineering and Industrial Aerodynamics*, Vol. 14, 1983, pp. 129-140.
- [99] Scruton, C., *An Introduction to Wind Effects on Structures*, Engineering Design Guides 40, Oxford University Press, 1981.

- [100] Isyumov, N., 'The Aeroelastic Modelling of Tall Buildings', Proc. Int. Workshop on Wind Tunnel Modelling for Civil Engineering Applications, N.B.S., Gaithersbury, Maryland, April 1982, Cambridge University Press, pp. 373-407.
- [101] Gordon, R. et al., Private communication.
- [102] Whitbread, R.E., 'On the Introduction of Turbulence into Wind-Tunnel Investigations for the Determination of Wind-Induced Amplitudes of Oscillation', Symp. on Wind Effects on Buildings and Structures, Univ. of Technology, Loughborough, 1968, Paper 32, pp. 1-16.
- [103] Whitbread, R.E. and Scruton, C., 'An Investigation of the Aerodynamic Stability of a Model of the Proposed Tower Blocks for the World Trade Center, New York', Part II, NPL Aero. Special Report 001, Oct. 1967.
- [104] Vickery, B.J., 'On the Flow Behind a Coarse Grid and its Use as a Model of Atmospheric Turbulence in Studies Related to Wind Loads on Buildings', NPL Aero. Report 1143, 1965.
- [105] Davenport, A.G., 'The Spectrum of Horizontal Gustiness Near the Ground in High Winds', Quart. J. Roy. Met. Soc., Vol. 87, 1961, pp. 194-211.
- [106] Davenport, A.G., Isyumov, N. and Jandali, T., 'A Study of Wind Effects for the Sears Project', Faculty of Engineering Science Research Report, BLWT-5-1971, University of Western Ontario, Canada, 1971.
- [107] Kareem, A., 'Wind Excited Motion of Buildings', Ph.D. Thesis, Colorado State University, U.S.A., 1978.
- [108] Whitbread, R.E., 'The Measurement of Non-Steady Wind Forces on Small-Scale Building Models', Proc. Fourth Int. Conf. on Wind Effects on Buildings and Structures, London 1975, Cambridge University Press, 1977, pp. 567-574.
- [109] Tschanz, T., 'Measurement of Total Dynamic Loads Using Elastic Models with High Natural Frequencies', Proc. Int. Workshop on Wind Tunnel Modelling for Civil Engineering Applications, N.B.S., Gaithersbury, Maryland, April 1982, Cambridge University Press, pp. 296-312.

- [110] Evans, R.A. and Lee, B.E., 'A Modelling Technique for the Determination of Dynamic Wind Loads on Buildings', Int. Conf. on Flow Induced Vibrations in Fluid Engineering, Reading, Sept. 1982, BHRA Fluid Engineering, 1982, Paper D3, pp. 155-167.
- [111] Evans, R.A. and Lee, B.E., 'The Determination of the Model Forces Acting on Three Buildings Using Wind Tunnel Methods', Journal of Wind Engineering and Industrial Aerodynamics, Vol. 13, 1983, pp. 161-172.
- [112] Bruel & Kjaer, Type 2635 Charge Amplifier: Instruction Manual, Jan. 1980.
- [113] Bradshaw, P., *An Introduction to Turbulence and its Measurement*, Pergamon Press, First ed., 1971.
- [114] Sandborn, V.A., *Resistance-Temperature Transducers*, Metrology Press, First ed., 1972.
- [115] Kokkalis, A., 'An Investigation into the Wake Flow behind Circular Cylinders Fitted with Slat Devices', M.Sc. Thesis, Department of Aeronautics and Fluid Mechanics, University of Glasgow, April 1983.
- [116] DISA 56N21 Linearizer: Instruction Manual, DISA Information Department, 1980.
- [117] Bendat, J.S. and Piersol, A.G., *Measurement and Analysis of Random Data*, Wiley and Sons, New York, 1966.
- [118] Newland, D.E., *An Introduction to Random Vibrations and Spectral Analysis*, Longman, 1975.
- [119] McD. Galbraith, R.A. and Leishman, J.G., 'A Micro-Computer Based Test Facility for the Investigation of Dynamic Stall', Int. Conf. Use of Micros in Fluid Engineering, London 1983, Paper E3, BHRA Fluid Engineering, 1983, pp. 197-205.
- [120] McD. Galbraith, R.A., Barrowman, J. and Leishman, J.G., 'Description of the Sample and Hold Circuits for the Glasgow University Dynamic Stall Facility', GU Aero Report No. 8208, Dec. 1982.

- [121] Leishman, J.G. and McD. Galbraith, R.A., 'A software Enhancement Package for DEC MINC-11 Laboratory Programming', GU Aero Report No. 8307, Oct. 1983.
- [122] Hacker, M.J., 'A FORTRAN Callable MACRO-11 Routine for Fast Continuous A/D', MINC Techletter, Vol. 5, No. 2.
- [123] Digital Signal Processing Committee (Ed.), *Programs for Digital Signal Processing*, IEEE Press, 1979.
- [124] Rader, C.M., 'An Improved Algorithm for High Speed Autocorrelation with Application to Spectral Estimation', IEEE Trans. Audio Electroacoust., Vol. AU-18, No. 4, 1970, pp. 349-442.
- [125] Carter, G.C., Knapp, C.H. and Nuttall, A.H., 'Estimation of the Magnitude-Squared Coherence Function via Overlapped Fast Fourier Transform Processing', IEEE Trans. Audio Electroacoust., Vol. AU-21, No. 4, Aug. 1973, pp. 337-344.
- [126] Pollard, J.H., *A Handbook of Numerical and Statistical Techniques*, Cambridge University Press, 1977.
- [127] Olesen, H.P. and Randall, R.B., 'A guide to Mechanical Impedance and Structural Response Techniques', Bruel & Kjaer, Application Notes.
- [128] Broch, J.T., *Mechanical Vibration and Shock Measurements*, Bruel & Kjaer, June 1973.
- [129] Pendered, J.W. and Bishop, R.E.D., 'A Critical Introduction to Some Industrial Resonance Testing Techniques', Journal of Mechanical Engineering Science, Vol. 5, No. 4, 1963, pp. 345-367.
- [130] Beards, C.F., *Structural Vibration Analysis: Modelling, Analysis and Damping of Vibrating Structures*, Ellis Horwood Ltd., 1983.
- [131] Russel, J.B., 'Determination of the Damping of a System Using a Planimeter', Aeronautical Journal, Feb. 1976, pp. 82-84.

- [132] Perera, M.D.A.E.S., 'A Wind-Tunnel Study of the Interaction Between Along-Wind and Cross-Wind Vibrations of Tall, Slender Structures', *Journal of Industrial Aerodynamics*, Vol. 3, 1978, pp. 315-341.
- [133] Sykes, D.M., 'Dynamic Response of a Building Model with a Second Model in Proximity', *Proc. 4th Colloq. on Industrial Aerodynamics*, Aachen, West Germany, 1980, Part 2, pp. 205-221.
- [134] Lee, B.E., 'The Wind-Induced Vibration of a Pair of Model Stacks', *Proc. Inst. Civil Engineers*, Vol. 57, 1974, pp. 99-111.
- [135] *Fluid Force, Pressure and Moments on Rectangular Blocks*, Engineering Sciences Data Item No. 71016, 1971.
- [136] Davenport, A.G., 'The Influence of Turbulence on the Aeroelastic Response of Tall Structures to Wind', *IUTAM-IAHR Symp. on Flow-Induced Structural Vibrations*, Karlsruhe, West Germany, 1972, Springer-Verlag, 1974, pp. 681-695.
- [137] Wootton, L.R. and Scruton, C., 'Aerodynamic Stability', Paper 5 from *Modern Design of Wind Sensitive Structures*, Construction Research and Information Association, London, 1970.
- [138] Vickery, B.J., 'Load Fluctuations in Turbulent Flow', *Journal of Engineering Mechanics Division, ASCE*, Vol. 94, No. EM1, Feb. 1968, pp. 31-46.
- [139] Akins, R.E., Peterka, J.A. and Cermak, J.E., 'Mean Force and Moment Coefficients for Buildings in Turbulent Boundary Layers', *Journal of Industrial Aerodynamics*, Vol. 2, 1977, pp. 195-209.
- [140] Komatsu, S. and Kobayashi, H., 'Vortex-Induced Oscillation of Bluff Cylinders', *Journal of Wind Engineering and Industrial Aerodynamics*, Vol. 6, 1980, pp. 335-362.
- [141] Steinman, D.B., 'Problems of Aerodynamic and Hydrodynamic Stability', *Proc. Third Hydraulics Conf., Univ. Iowa Studies in Engin. Bull.*, Vol. 31, 1946.

- [142] Vellozzi, J. and Cohen, E., 'Dynamic Response of Tall Flexible Structures to Wind Loading', Proc. Tech. Meeting Concerning Wind Loads on Structures and Structures, Gaithersburg, Maryland, Jan. 1969, pp. 115-128.
- [143] Walker, J., 'Strange Things Happen When Two Pendulums Interact Through a Variety of Interconnections', Scientific American, Oct. 1985, pp. 160-164.
- [144] Ishigai, S., Nishikawa, E., Nishimura, K. and Cho, K., 'Experimental Study on Structure of Gas Flow in Tube Bands with Tube Axes Normal to Flow', Bulletin of the Japan Society, Mechanical Engineers, Vol. 15, No. 86, 1972, pp. 949-956.

APPENDIX A

PRINCIPLE OF THE STRAIN GAUGE BALANCE SYSTEM

The introduction of bonded foil type strain gauges for load measurement has led to new conceptions in wind tunnel balance design. As compared with the traditional balance linkages, the strain gauge dynamometry has less displacement and, at the same time, higher sensitivity. A few of these force measuring devices were examined by Rebuffet [A.1].

The principles of strain gauge dynamometry can be described by means of a bar equipped with strain gauges which are appropriately arranged in a Wheatstone bridge circuit. As shown in Fig. A.1(a), the prismatic bar AB has one end built-in and is subjected to a system of forces and moments applied at a point, O, on the axis. Let X, Y, M, N be the four components of the resultant forces and moments.

Consider four gauges glued on to the bar in the ZOY plane at two sections C and D which are located symmetrically with respect to O. These gauges detect the surface stresses of the bar caused by the four components. If gauges 1, 2, 3 and 4 are placed in a bridge circuit in such a way as to subtract the electrical effects corresponding to the strains in sections C and D, the resulting bridge unbalance potential is proportional to the difference between the bending moments at the two locations, i.e.

$$\text{unbalance potential} \propto \text{force } Y \times \overline{CD}$$

in which \overline{CD} is the distance between sections C and D. Fig. A.1(b) shows the bridge diagram which is usually called a differencing circuit.

Similarly, a summing circuit, Fig. A.1(c), yields a bridge unbalance potential proportional to the M component of the resulting moment.

Theoretically, if the interaction between each loading direction is zero, the gauges under consideration, located in the ZOY plane of the bar, would register zero strain due to action of the X and N components. The four active gauges bridge arrangement also eliminates the stresses due to axial strain.

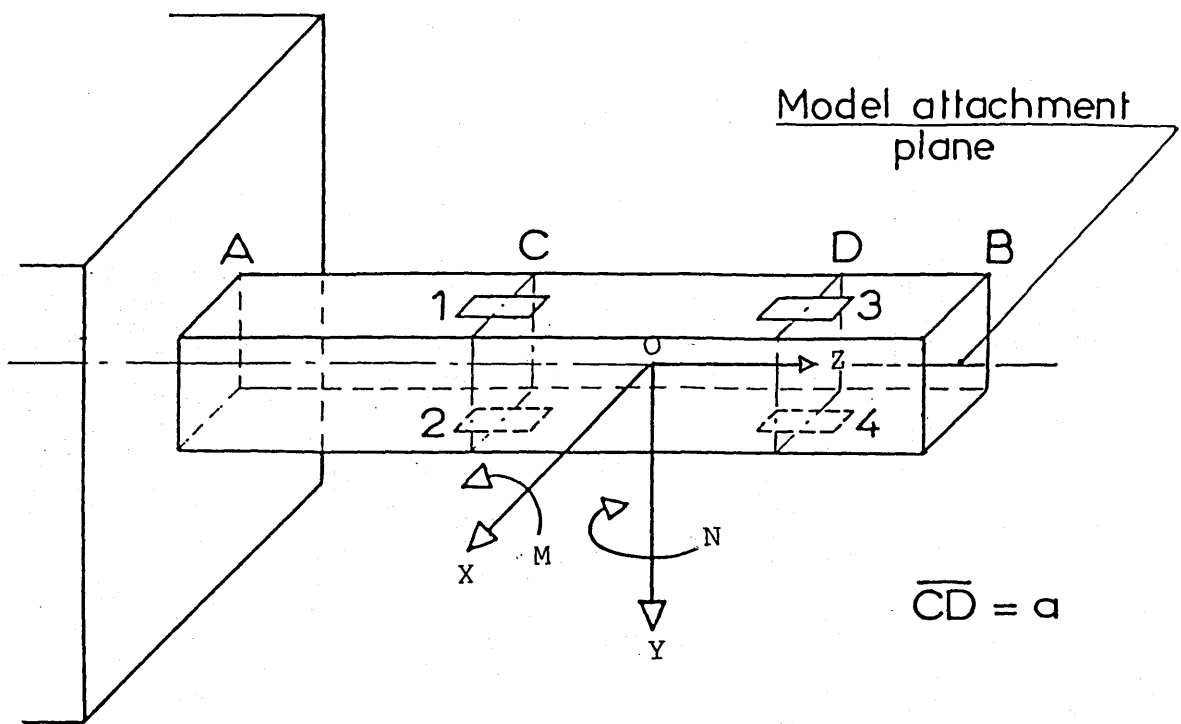
Similarly, four gauges bonded to the vertical faces at sections C and D could detect the surfaces stresses due to the X and N components. Therefore, with four pairs of gauges and appropriately connected to four halves of bridge circuits, this bar could measure the four components of the resultant forces and moments acting at its free end.

The bar is also generally associated with a torquemeter for measuring reaction torque, T , acting along its axis. Although torque can be measured by one or two gauges placed in the appropriate directions on the bar, the possibility of bending or axial strains affecting the reading can be eliminated by the use of four gauges as shown in Fig. A.2(a), and a bridge circuit diagram in Fig. A.2(b).

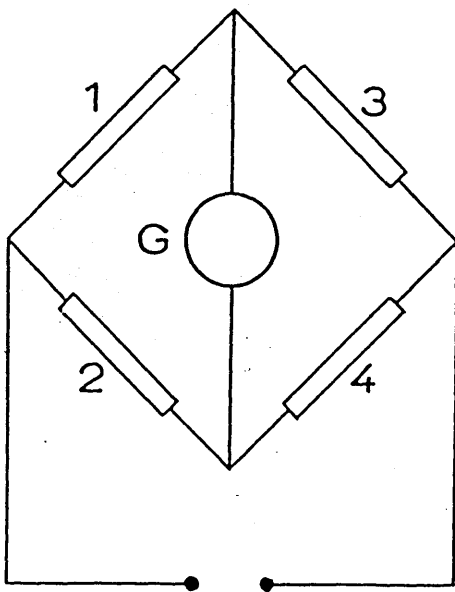
The use of gauges to form the four arms of the bridge, which acts as dummy for each other, ensures that the bridge output is unaffected by thermal drift and has extra benefit of a combined output which is four times as sensitive as for a single gauge.

REFERENCE

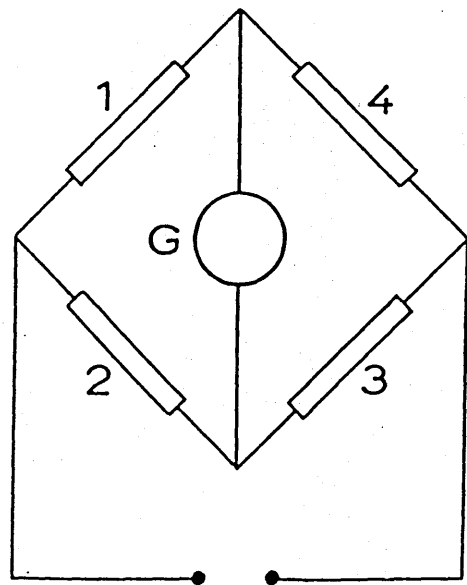
- A.1 Rebuffet, P.. 'Some Strain Gauge Balances Used in French Wind Tunnel'.
AGARD, Report 6-T, Feb. 1956.



(a) bar analyzer

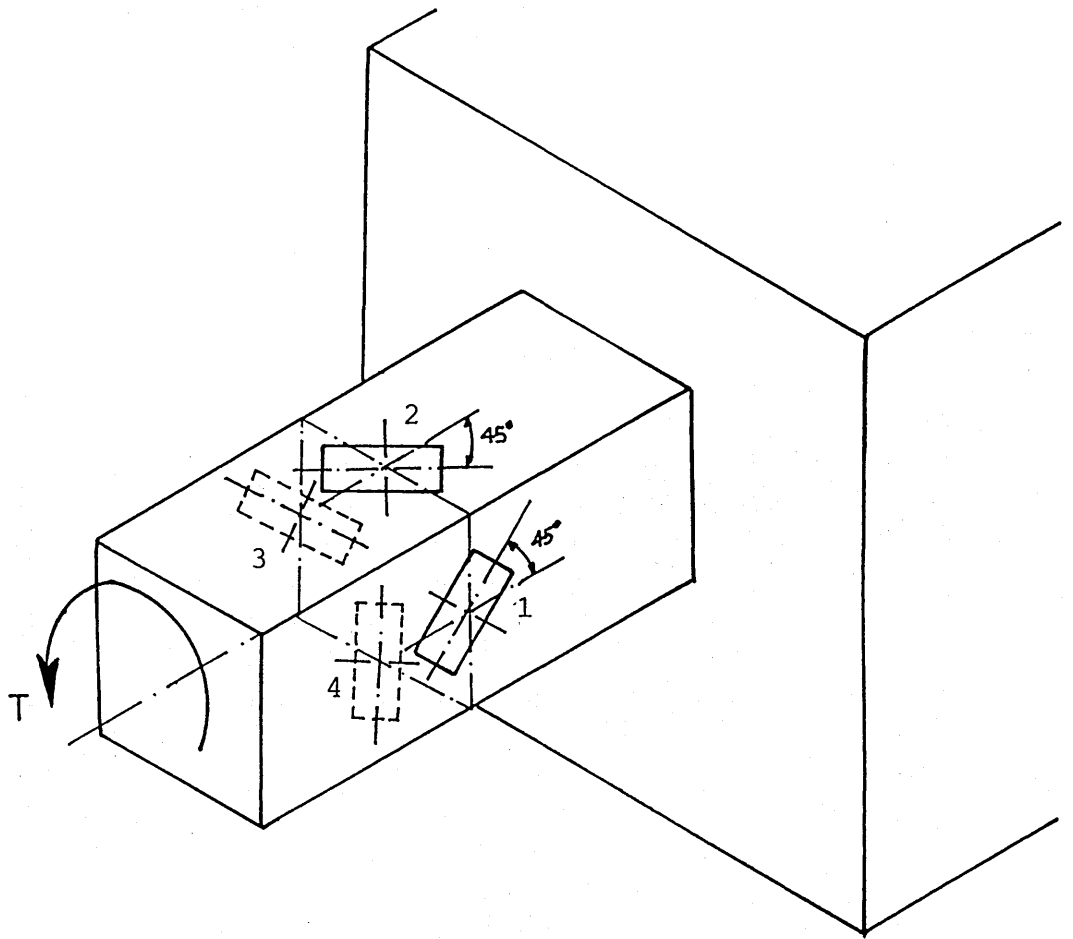


(b) Differencing circuit
Force Y

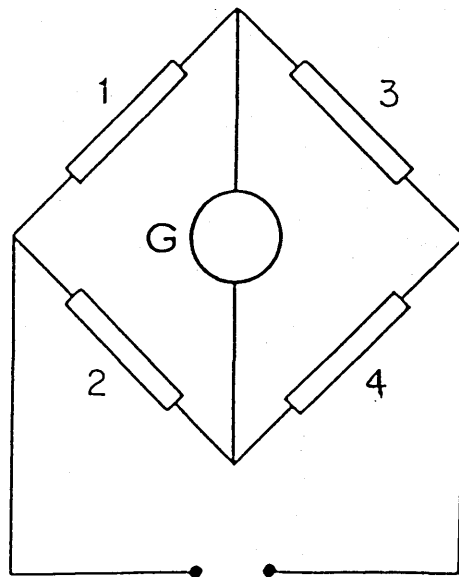


(c) Summing circuit
Moment M

Figure A.1 A schematic diagram of bar analyzer (for measuring forces) and bridge circuit diagrams.



(a) bar analyzer



(b) Summing circuit
Moment T

Figure A.2 A schematic diagram of bar analyzer (for measuring torque) and gauges circuit diagram.

APPENDIX B

STATISTICAL PROPERTIES OF RANDOM DATA

There are four main types of statistical functions used to describe the basic properties of random data, namely the mean square values, probability density functions, correlation functions and power spectral density functions. Their various descriptive properties of stationary random data are outlined in the following sections. More detailed description can be found in standard texts, such as Bendat & Piersol [B.1]. It is assumed here that the measured data in question are ergodic, so that the properties of the data can be determined from time average of individual sample records.

To help clarify the practical significance of these functions, four examples of some typical time history records, namely (a) sine wave, (b) sine wave plus random noise, (c) narrow-band random noise and (d) wide-band random noise, are shown in Fig. B.3 along side with their corresponding function plots.

B.1 Mean and Mean Square Values

The mean square value is the rudimentary term to describe the general intensity of any random data, which is simply the average of the square values of the time history record, $x(t)$. In equation form,

$$\overline{x^2} = \lim_{T \rightarrow \infty} \frac{1}{T} \int_0^T x^2(t) dt$$

On the other hand, the measured physical data are usually expressed in terms of a combination of a static and a fluctuating component. The static component may be described by a mean value which is simply the average of all values, i.e.,

$$\bar{x} = \frac{1}{N} \sum_{i=1}^{i=N} x_i.$$

and the fluctuating component may be described by a variance which is simply the mean square value about the mean, i.e.

$$\overline{x'^2} = \frac{1}{N} \sum_{i=1}^{i=N} (x_i - \bar{x})^2$$

The positive square root of the variance is called the standard deviation and is given by,

$$\sqrt{x'^2} = \left[\sum_{i=1}^{i=N} \frac{(x_i - \bar{x})^2}{(n-1)} \right]^{1/2}$$

The term (N-1) is used only to penalise a small sample size.

If the mean of the measured values is zero, the positive square root of the mean square values is usually called root mean square value (or RMS).

B.2 Probability Density Functions

The probability density function of random data describes the probability that the data will assume a value within some defined range at any instant of time. Considering the sample time history record, $x(t)$, as shown in Fig. B.1, the probability that $x(t)$ lies within the range between x and $(x + \Delta x)$ may be obtained by taking the ratio T_x / T , where T_x is the total amount of time that $x(t)$ falls inside the range $(x, x + \Delta x)$ during a sufficient long observation time T . In equation form,

$$Prob[x < x(t) \leq x + \Delta x] = \lim_{T \rightarrow \infty} \frac{T_x}{T}$$

For small Δx , the probability density function, $p(x)$, can be defined as,

$$p(x) = \lim_{\Delta x \rightarrow 0} \frac{Prob[x < x(t) \leq x + \Delta x]}{\Delta x}$$

Fig. B.3 shows the resultant probability density functions for four common signals.

The principal application of probability density function measurement for physical data is to establish a probabilistic description for the instantaneous values of the data, and in some cases, to distinguish between sinusoidal and random data.

B.3 Autocorrelation Functions

The autocorrelation function of random data describes the general dependence of the values at one time on the values at another time.

The autocorrelation between the values of $x(t)$ at times t and $t + \tau$, as shown in Fig. B.2, may be estimated by taking the product of the two values and averaging over the observation time, T , i.e.

$$R_x(\tau) = \lim_{T \rightarrow \infty} \frac{1}{T} \int_0^T x(t) x(t + \tau) dt$$

and is equal to \bar{x} if the time displacement becomes very long.

The autocorrelation function is usually normalised by dividing it, for sufficient large data size, by its variance. The resultant function has a value between ± 1 and is usually referred to as the autocorrelation coefficient, $\rho_x(t)$.

The principal application of an autocorrelation function measurement of physical data is to establish the influence of values at any one time over values at a future time. Any deterministic data will have an autocorrelation function which persists over all time displacements, whereas, for random data, the function diminishes to zero for large time displacements. Therefore, an autocorrelation function is always a useful tool for detecting deterministic data which might be masked in a random background.

A typical plot of autocorrelation function, $R_x(\tau)$, versus time displacement, τ , for four time records is illustrated in Fig. B.3.

B.4 Power Spectral Density Functions

The general frequency composition of random data can be identified by the power spectral density function in terms of the spectral density of its mean square value.

If a measured data has a frequency range between f and $f + \Delta f$, the mean square value of this data may be obtained by filtering the sample record with a band-pass filter having short cutoff characteristics, and computing the average of the squared output from the filter.

For small Δf , the power spectral density function, $S_x(f)$, can be defined such that

$$S_x(f) = \lim_{\Delta f \rightarrow 0} \lim_{T \rightarrow \infty} \left[\frac{1}{T} \int_0^T x'^2(t, f, \Delta f) dt \right]$$

Consequently, for stationary data, the power spectral density function can be related to the autocorrelation function by a Fourier Transform as follows.

$$S_x(f) = 2 \int_{-\infty}^{\infty} R_x(\tau) \exp(-j 2\pi f \tau) d\tau$$

In terms of the autocorrelation coefficient, the power spectral density function is given by.

$$S_x(f) = 4 x'^2 \int_0^{\infty} \rho_x(\tau) \cos(2\pi f \tau) d\tau$$

The principal application of power spectral density function measurement is to establish the frequency composition of some physical data which may contain

important information of the basic characteristics of the system involved. Examples of resultant power spectral density functions from four common signals are shown in Fig. B.3

B.5 Cross-Correlation Functions

The cross-correlation function of two sets of random data describes the general dependence of the values of one set of data on the other with respect to time. Analogous to the autocorrelation function, the cross-correlation function of the value $x(t)$ at time t and $y(t)$ at $t+\tau$ is evaluated by taking the average product of the two values over the observation time T . In equation form,

$$R_{xy}(\tau) = \lim_{T \rightarrow \infty} \frac{1}{T} \int_0^T x(t) y(t+\tau) dt$$

But unlike the autocorrelation function, $R_{xy}(\tau)$ does not necessarily have a maximum value at $\tau = 0$. However, if $x(t)$ and $y(t)$ are interchangeable, this function does display symmetry about the ordinate, i.e.

$$R_{xy}(-\tau) = R_{yx}(\tau)$$

The cross-correlation function can be normalised by divided it with the product of $\sqrt{x'^2}$ and $\sqrt{y'^2}$, and the resultant function is usually called cross-correlation coefficient, ρ_{xy} , which has values between ± 1 .

The main applications of the cross-correlation functions are in the measurement of time delay and the determination of transmission paths through a given system. Assuming the system is linear, the results from a cross-correlation measurement between the input and output signals will peak at that time displacement equal to the time required for the signal to pass through the system.

B.6 Cross-Spectral Density Functions (and Coherence Functions)

The cross-spectral density function of two sets of random data, say $x(t)$ and $y(t)$, is the Fourier Transform of the cross-correlation function. Because a cross-correlation function is not an even function, the cross-spectral density function, $S_{xy}(f)$, is generally a complex number, i.e.,

$$S_{xy}(f) = 2 \int_{-\infty}^{\infty} R_{xy}(\tau) \exp(-j 2\pi f \tau) d\tau$$

$$= C_{xy}(f) - jQ_{xy}(f)$$

in which the real part, $C_{xy}(f)$, is called the co-spectral density function and the imaginary part, $Q_{xy}(f)$, is called the quadrature spectral density function. In direct frequency terms, the co-spectral density function can be considered as the average product of $x(t)$ and $y(t)$ within a narrow interval between f and $f+\Delta f$, divided by the frequency interval, Δf , i.e.,

$$C_{xy}(f) = 2 \int_{-\infty}^{\infty} R_{xy}(\tau) \cos(2\pi f \tau) d\tau$$

The quadrature spectral density function is the same except that either $x(t)$ or $y(t)$, but not both, is shifted in time sufficiently to produce a 90-degree phase shift at frequency f , so that

$$Q_{xy}(f) = 2 \int_{-\infty}^{\infty} R_{xy}(\tau) \sin(2\pi f \tau) d\tau$$

It is convenient to express the cross-spectral density function in complex polar notation such that

$$S_{xy}(f) = |S_{xy}(f)| \exp(-j\theta_{xy}(f))$$

where the $|S_{xy}(f)|$ and $\theta_{xy}(f)$ are related by the magnitude, $S_{xy}(f)$, such as

$$|S_{xy}(f)| = \sqrt{C_{xy}^2(f) + Q_{xy}^2(f)}$$

and the phase angle,

$$\theta_{xy}(f) = \tan^{-1} \left| \frac{Q_{xy}(f)}{C_{xy}(f)} \right|$$

In dealing with physical problems, it is often more convenient to express cross-spectral information in a real-valued quantity given by,

$$\gamma_{xy}^2(f) = \frac{|S_{xy}(f)|^2}{S_x(f) S_y(f)}$$

Where $\gamma_{xy}^2(f)$ is called the squared coherence function which has magnitudes ranging from 0 to 1 for all values of f .

Cross-spectral density functions have many applications in the interpretation of data for a given system including the measurement of time delays and transmission paths as functions of frequency, and the detection and recovery of signals obscured by noise.

REFERENCE

- B.1 Bendat, J.S. and Piersol, A.G.. *Measurement and Analysis of Random Data*, J. Wiley and Sons, New York, 1966.

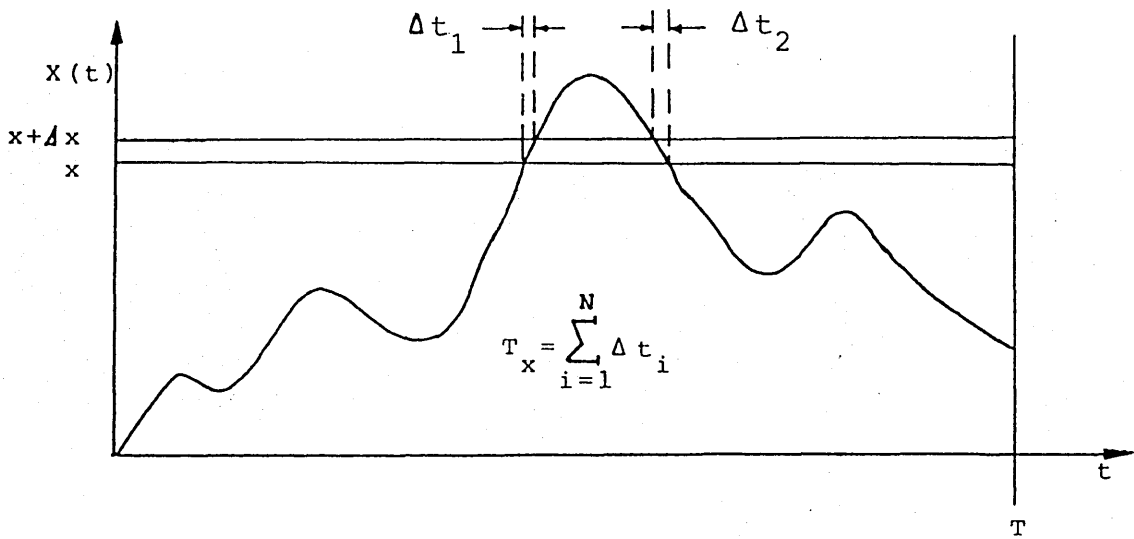


Figure B.1 Probability measurement.

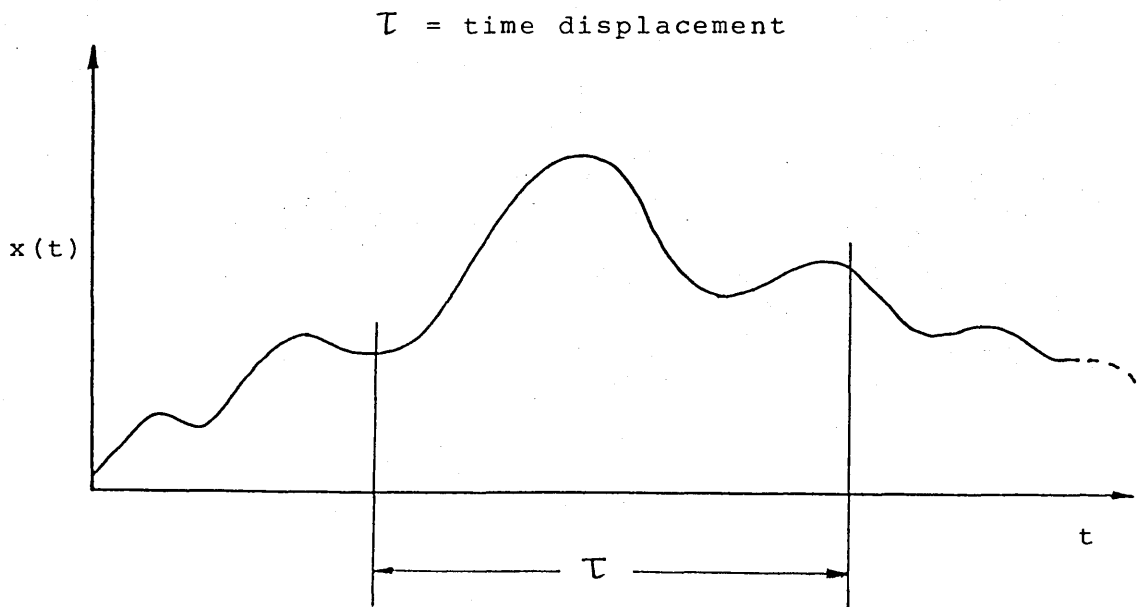


Figure B.2 Autocorrelation measurement.

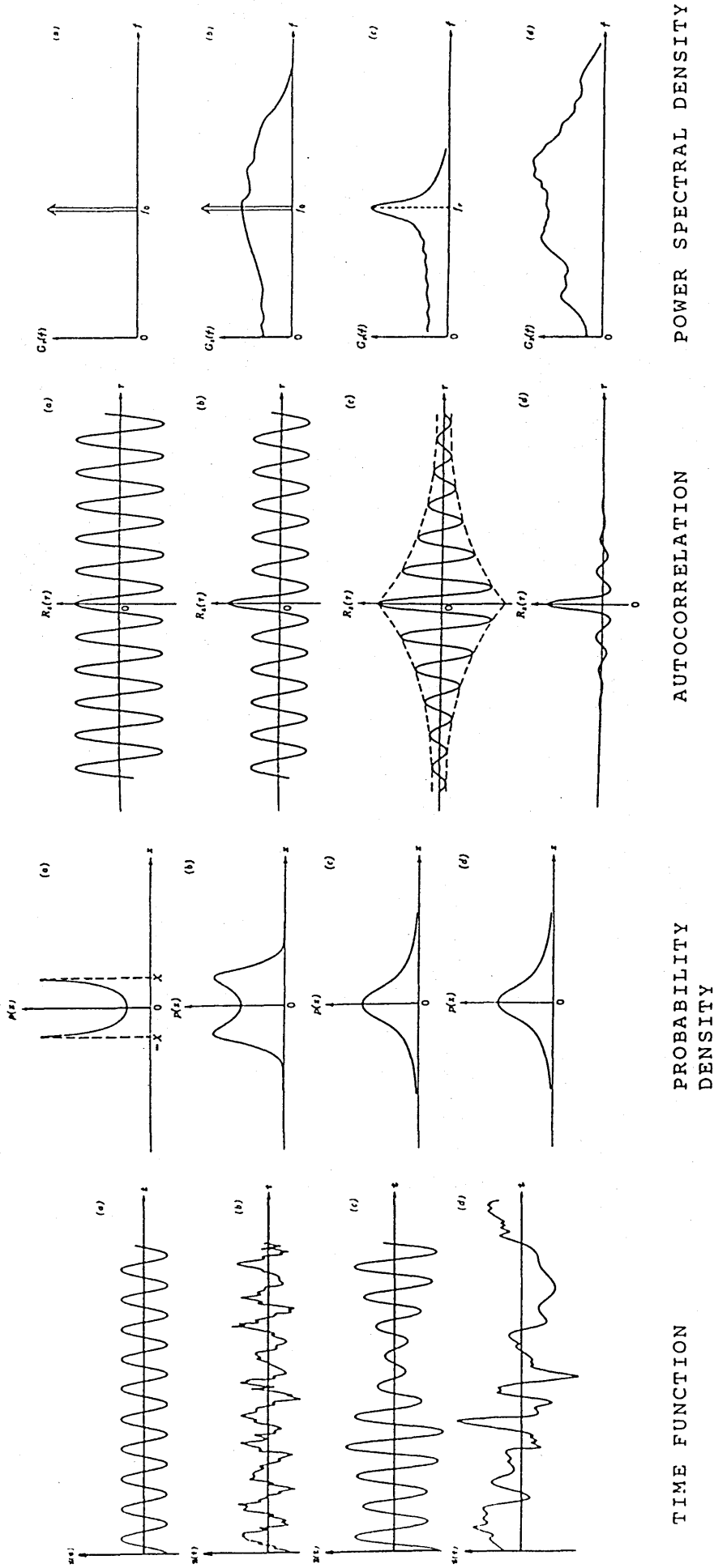


Figure B.3 Typical forms of analysis for four common signals: (a) sine wave, (b) sine wave plus random noise, (c) narrow band random noise and (d) broad band random noise.

APPENDIX C

EFFECTS OF VARIATION IN AERODYNAMIC FORCES ON A BODY DUE TO ITS MOTIONS

A factor that can be of considerable influence in the dynamic response of a flexible structure is the effect of the structure's movement on the aerodynamic force acting upon it. When a square section body moves through a constant airflow, the relative velocity of the wind to the body changes both in magnitude and direction. If the relative angle and velocity magnitude changes due to the motion are $\delta\alpha$ and δU respectively, then the change in force on the section is,

$$\delta F = \frac{dF}{d\alpha} \delta\alpha + \frac{dF}{dU} \delta U$$

in which the angle of incidence of the mean wind, α , is defined as the angle of the mean wind measured relative to the line normal to the windward face of the body.

If the force, F , per unit area is of the form,

$$F = \rho \bar{U}_o^2 C_F(\alpha)$$

in which $C_F(\alpha)$ is the quasi-steady aerodynamic force coefficient measured on a fixed body during a static test under the same angle of incidence of the mean wind.

The change in force can be expressed as,

$$\delta F = \rho \bar{U}_o^2 \left[2C_F \frac{\delta U}{\bar{U}_o} + \frac{dC_F}{d\alpha} \delta\alpha \right]$$

As shown in Fig. C.1, the body has wind-induced motions along its translational axes, \dot{x} and \dot{y} , such that

$$\delta U = -\dot{x} \cos \alpha - \dot{y} \sin \alpha$$

$$\delta\alpha = \frac{1}{\bar{U}_o} (\dot{x} \sin \alpha - \dot{y} \cos \alpha)$$

This leads to the following forces:

$$\delta F_x = \rho \bar{U}_o^2 \left[D_x \frac{\dot{x}}{\bar{U}_o} + E_x \frac{\dot{y}}{\bar{U}_o} \right]$$

$$\delta F_y = \rho \bar{U}_o^2 \left[D_y \frac{\dot{y}}{\bar{U}_o} + E_y \frac{\dot{x}}{\bar{U}_o} \right]$$

in which

$$D_x = -2C_F \cos \alpha + \frac{dC_F}{d\alpha} \sin \alpha.$$

$$D_y = -2C_{F_y} \sin \alpha - \frac{dC_{F_y}}{d\alpha} \cos \alpha.$$

$$E_x = -2C_{F_x} \sin \alpha - \frac{dC_{F_x}}{d\alpha} \cos \alpha, \text{ and}$$

$$E_y = -2C_{F_y} \cos \alpha + \frac{dC_{F_y}}{d\alpha} \sin \alpha.$$

The terms D_x and D_y are wind-induced damping forces per unit area which act on the body in parallel with the structural damping and are referred to as aerodynamic damping forces. Whereas E_x and E_y are coupling forces per unit area between the motions in the two axes [C.1]. If the natural frequencies of the body in the two lateral motion directions are close together, then there is a possibility that large quantities of energy will be exchanged between the two motions.

The damping forces, D_x and D_y , can be expressed as a critical damping ratio by considering the generalised damping force defined by,

$$C = \int_0^1 \delta F(z) \mu^2(z) dz$$

where $\mu(z)$ is the mode shape and z is the non-dimensional height of the body. The corresponding critical aerodynamic damping ratio then becomes,

$$(\zeta_x)_c = -\frac{1}{8\pi} \frac{\rho}{\rho_s} \frac{\bar{U}_o}{fB} D(x) \quad \text{---(C.1)}$$

$$(\zeta_y)_c = -\frac{1}{8\pi} \frac{\rho}{\rho_s} \frac{\bar{U}_o}{fB} D(y)$$

where ρ_s is the mass density of the body and,

$$D(x) = \int_0^1 \frac{\bar{U}_x}{\bar{U}_o} \left[2C_{F_x} \cos \alpha - \frac{dC_{F_x}}{d\alpha} \sin \alpha \right] \mu^2(z) dz \quad \text{---(C.2)}$$

$$D(y) = \int_0^1 \frac{\bar{U}_y}{\bar{U}_o} \left[2C_{F_y} \sin \alpha + \frac{dC_{F_y}}{d\alpha} \cos \alpha \right] \mu^2(z) dz$$

in which \bar{U}_x/\bar{U}_o is the velocity profile.

It is obvious that the aerodynamic damping forces are proportional to both the ratio of air density to average building density and the reduced velocity. The integrals, $D(x)$ and $D(y)$, are simply constants associated with the mode shape and steady aerodynamic coefficients.

The nature of the damping forces is best explained by reference to Fig. C2 which shows that for a square section body subjected to winds normal to its face the longitudinal oscillation induces forces opposing the motion, while transverse motion

induces forces that reinforce the motion. The latter is due to the properties of square shapes reported by Parkinson [C.2] in which a small change in relative wind direction from the normal produces an into-wind component of transverse force.

This property is also exhibited by the test results of the square tower model used in this study. The mean force coefficients, shown in Fig. C.3, indicate that the negative slope of the transverse force coefficient at zero degree and the positive slope at 90 degree position, both of which, according to eqn. (C.2), give rise to negative aerodynamic damping.

Instability occurs when the net damping in a system, including both the mechanical and aerodynamic, approaches zero. Under such conditions the amplitude of oscillation grows progressively until it reaches a steady magnitude governed by the non-linearity of the aerodynamic damping.

Therefore, the condition for instability is

$$\zeta_s + \zeta_a < 0$$

Even if the wind velocity and structural damping are such that the resulting damping is neither zero nor negative, the presence of a negative aerodynamic damping effectively reduces the total available damping of the structure. This results in an increase in response due to other excitations such as those associated with turbulence and the wake.

REFERENCE

- C.1 Davenport, A.G., 'The Treatment of Wind Loading on Tall Buildings', Proc. of Symp. on Tall Buildings, University of Southampton, April 1966, Pergamon Press, pp. 3-44.
- C.2 Parkinson, G.V., 'Aeroelastic Galloping in One Degree of Freedom', Proc. of Symp. on Wind Effects on Buildings and Structures, Vol. 1, N.P.L., Teddington, 1963, pp. 581-609.

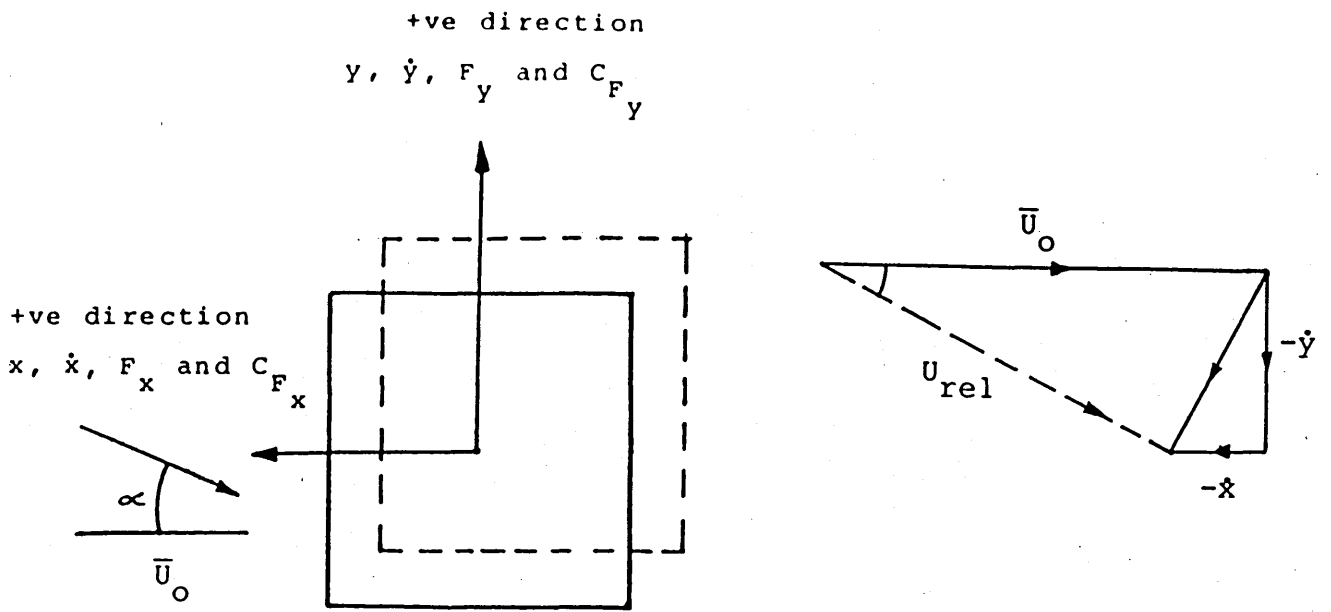
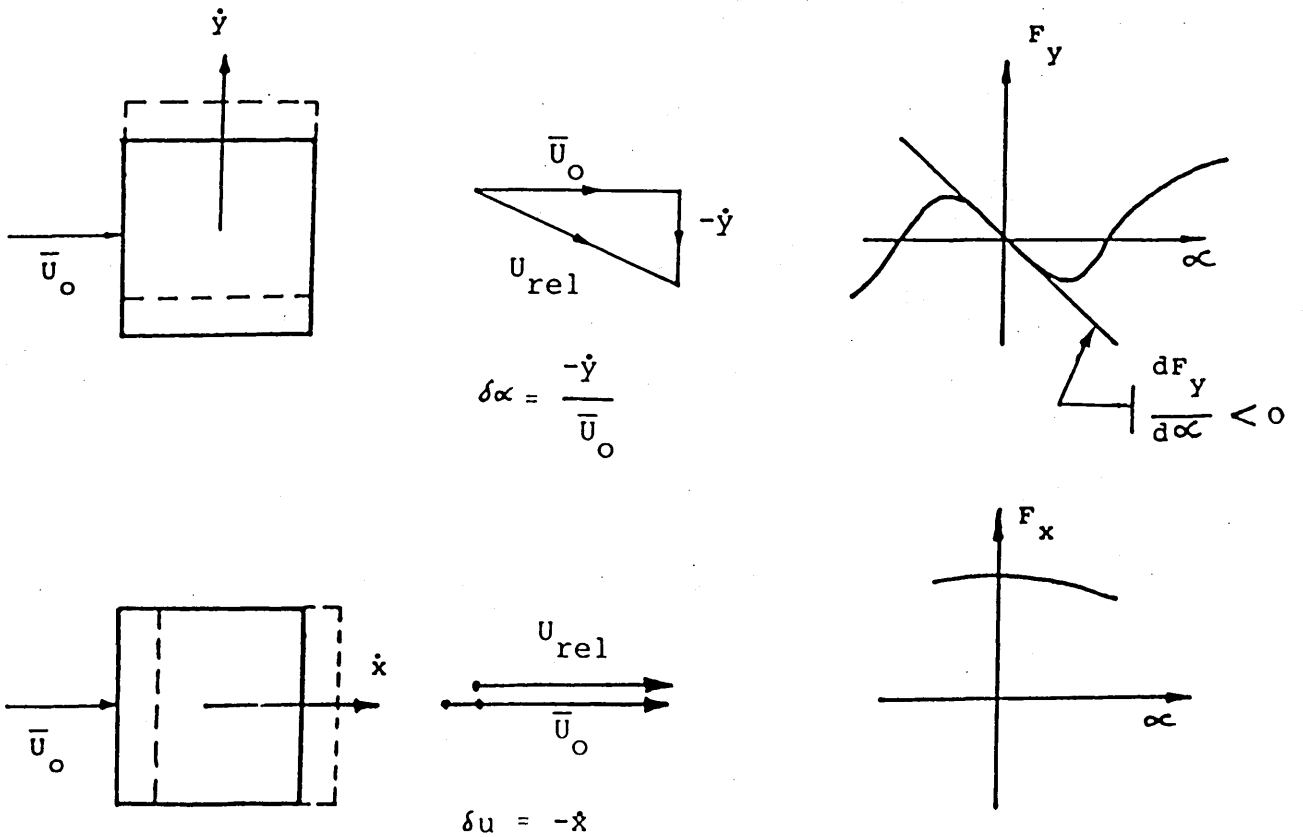


Figure C.1 Changes in magnitude and direction of wind relative to body due to its motion.



N.B. $\delta F_y > 0$ (-ve damping) and $\delta F_x < 0$ (+ve damping)

Figure C.2 Diagrams showing variation in aerodynamic forces on a square section due to its motion.

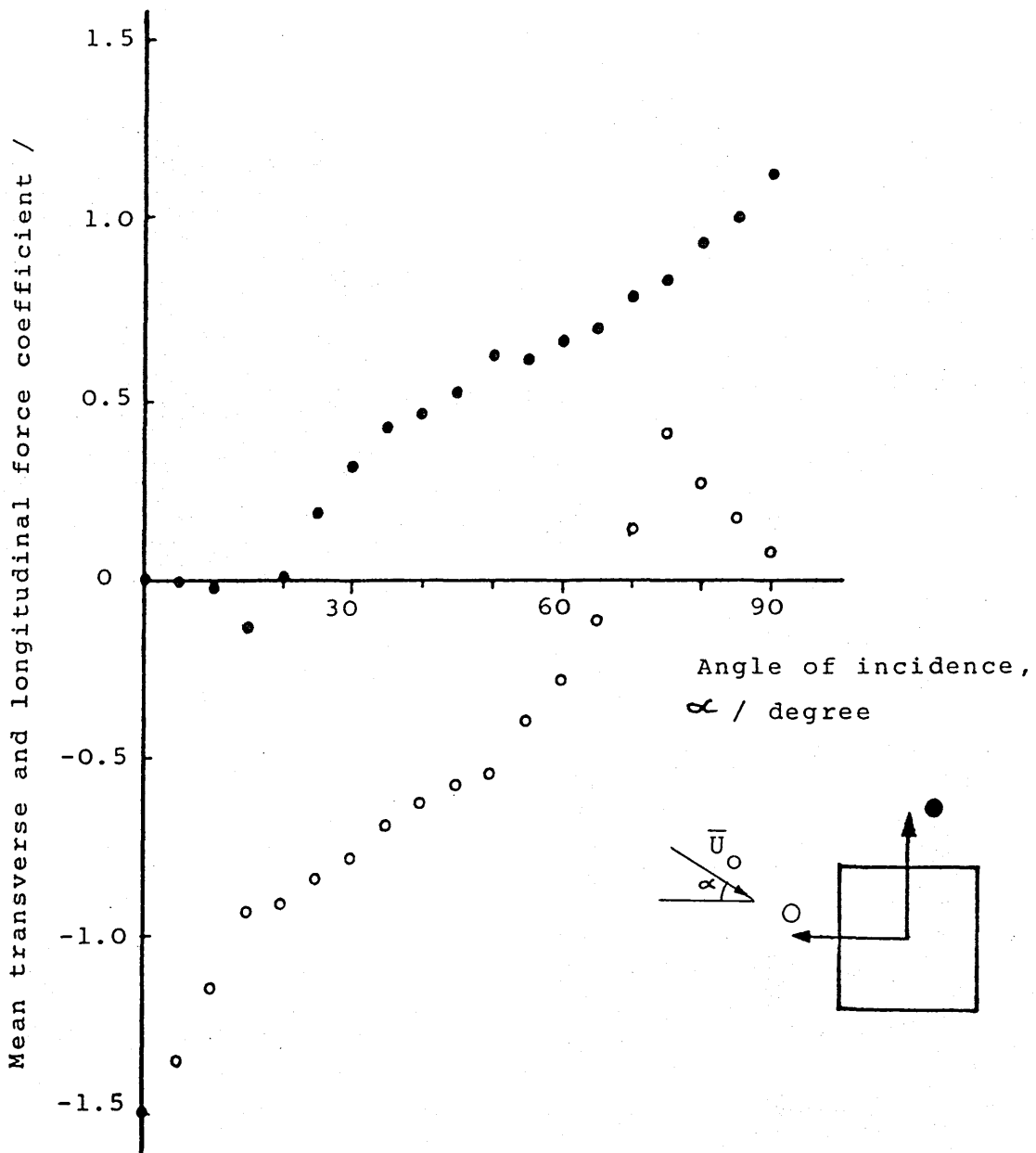


Figure C.3 Variation of the aerodynamic force coefficients of the 10x1x1 square tower model as a function of angle of incidence in smooth uniform flow.